AECL Research

International Conference on Nuclear Structure at High Angular Momentum

Ottawa, 1992 May 18-21

Workshop on Large Gamma-Ray Detector Arrays

Chalk River Laboratories, 1992 May 22-23

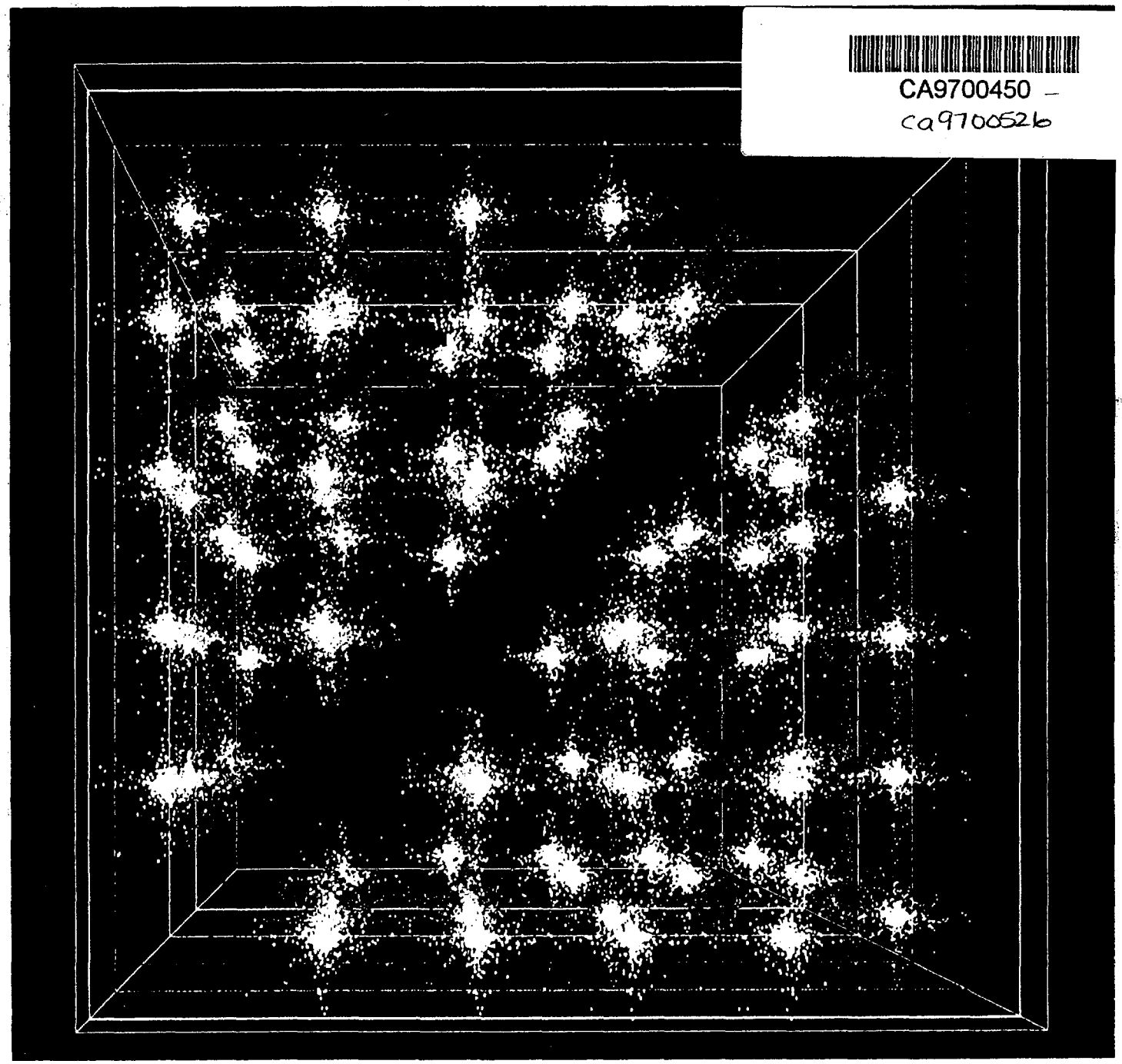

Volume 2
Proceedings

AECL 10613

International Conference on Nuclear Structure at High Angular Momentum

Ottawa

1992 May 18-21

Workshop on Large Gamma-ray Detector Arrays

Chalk River Laboratories

1992 May 22-23

Sponsored by McMaster University and University of Toronto (through NSERC) and by AECL Research, Chalk River Laboratories.

Chalk River, Ontario
1992 August

AECL-10613
(Volume 2)

Foreword

The proceedings of the conference/workshop have been published in two volumes. One-page abstracts of all contributed papers are in Volume 1. The present volume of proceedings (Volume 2) contains the text of most of the invited and contributed talks; by author request, it also contains expanded versions of the abstracts of some papers that were not presented orally.

The papers are arranged by session number in the order presented at the conference; the expanded abstracts appear at the end of the sessions to which they pertain.

Local organizing committee
1992 August

INTERNATIONAL CONFERENCE ON NUCLEAR STRUCTURE AT HIGH ANGULAR MOMENTUM

INTERNATIONAL CONFERENCE ON NUCLEAR STRUCTURE AT HIGH ANGULAR MOMENTUM

Ottawa

Session 1: Superdeformation in Nuclei (I)

Superdeformation in ^{191}Tl.

S. Pilotte†, J.M. Lewis, L.L. Riedinger and C.-H. Yu
Department of Physics, University of Tennessee, Knoxville, TN 37996- 1200, USA

M.P. Carpenter, R.V.F. Janssens, T.L. Khoo, T. Lauritsen, Y. Liang and F. Soramel
Physics Division, Argonne National Laboratory, Argonne, IL60439, USA

I.G. Bearden
Purdue University, West Lafayette, IN 47907, USA

Abstract

High spin states in ^{191}Tl have been populated via the ^{159}Tb(^{36}S,4n) reaction at 165 MeV. Two weak sequences of regularly spaced transitions have been identified. These bands exhibit many of the properties observed in many other superdeformed nuclei in the Hg region.

NUCLEAR REACTIONS ^{159}Tb(^{36}S,4n), E = 165 MeV, measured E_γ, I_γ, $\gamma\gamma$-coin., Enriched target, Compton-suppressed Ge detector array, BGO array. Cranked shell model.

I. Introduction

High-spin states in mercury nuclei have been the object of much interest following the discovery of superdeformation in ^{191}Hg [1]. Approximately 34 bands in 14 nuclei have now been reported in this region [1-14]. The majority of the bands exhibit a small monotonic increase of their dynamical moment of inertia of the order of 20% over the range of observed rotational frequencies ($\approx$ 0.2-0.4MeV). The ^{192}Hg nucleus plays a central role in this region since it has a doubly-closed gap at Z=80 and N=112 for superdeformed (SD) shapes that survives under rotation. It is instructive to relate the neighboring SD nuclei as particles or holes coupled to the ^{192}Hg core. The study of nuclei with proton or neutron numbers lower than ^{192}Hg is particularly interesting since the importance of specific orbitals can be addressed as one removes particles from orbits in the ^{192}Hg core.

This work focuses on the light SD nucleus ^{191}Tl which is two neutrons below the N=112 gap and has an additional proton outside the SD closed shell at Z=80. In addition to the usual spectroscopic methods used during the course of this investigation, a correlation search technique similar to the one outlined in Ref.[17] has been used and the results are briefly described. Finally, incremental alignments Δi [16] are examined.

II. Experimental Method

High-spin states in ^{191}Tl have been populated via the ^{159}Tb(^{36}S,4n) reaction at 165 MeV, using a beam from the ATLAS superconducting accelerator at the Argonne National Laboratory. This reaction was selected because it produces the residual nuclei at an excitation energy and angular momentum very similar to the successful reactions used throughout this region where discrete superdeformed bands were observed [(E*, ℓ_{max}) $\approx$ (24MeV,50$\hbar$)]. A stack of two thin ^{159}Tb foils ($\approx$ 500μg/cm^2) was used to allow the residual nuclei to recoil in vacuum. Coincidence events were collected with an array of 12 Compton-suppressed Ge detectors. Fifty BGO elements surrounding the target were used for multiplicity and total energy selection. In these measurements a multiplicity of K=6 was required. Thin Pb and Cd absorbers were placed in front of the Ge counters to reduce the count rate due to X rays. With 120x10^6 events written to tape, we subsequently sorted the Doppler-corrected data for different K cuts into symmetrical 2Kx2K E_γ-E_γ correlation matrices.

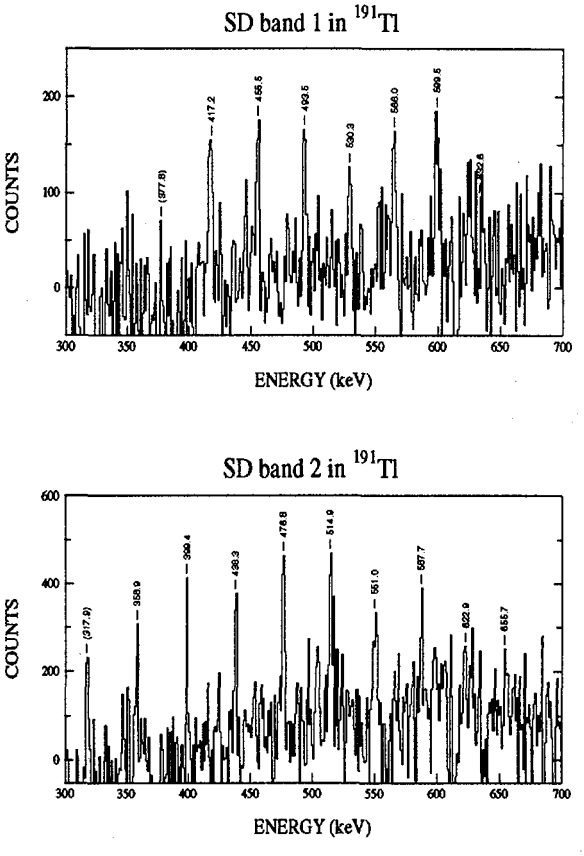

Fig. 1 Superdeformed bands observed in ^{191}Tl from the ^{159}Tb(^{36}S,4n) reaction at 165 MeV.

III. Results

High-spin events were selected by requiring a gamma multiplicity of at least K = 12. From conventional gating methods the resulting matrix revealed two very weak signals with an average spacing between consecutive transitions of 38 keV (Fig. 1). The intensity of these transitions was estimated to represent approximately 0.4% of all 4n reaction products. Due to the very weak intensities involved and the presence of contaminated peaks, it is difficult to observe all the coincidence relationships between

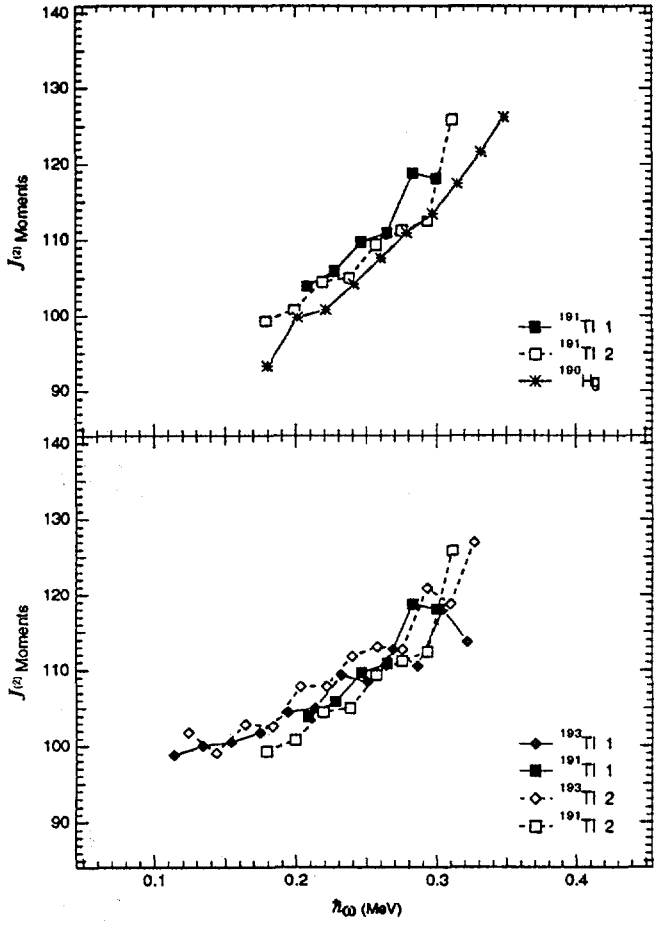

Fig. 2 Experimental dynamical moments of inertia ($\mathcal{J}^{(2)}$) for ^{191}Tl, ^{193}Tl, ^{190}Hg and ^{192}Hg.

transition members. Furthermore, the presence of ^{191}Tl yrast transitions in the SD-gated spectra depends strongly on the background subtracted. Since these yrast transitions are very intense and we are working at a low statistics level, we found this case to be particularly sensitive to the subtraction performed and has prevented us to make a firm assignment based solely on coincidence relationships. This difficulty is aggravated by contamination from transitions belonging to neighboring nuclei. This beam energy was selected in order to bring high angular momentum in the compound nuclei and the 4n and 5n channels were dominant (the 4n channel being strongest). No transition belonging to the 3n reaction channel could be identified. The fold and sum energy distributions associated with the observed SD bands peak slightly higher than the 4n channel. This is consistent with a feeding of SD states coming from the high-ℓ tail of the entry distribution [17, 18] and supports the ^{191}Tl assignment.

The characteristics of these bands agree very well with the systematics of other SD bands found in the Hg-Tl-Pb region. First, the dynamical moment of inertia of these proposed bands in ^{191}Tl increases with rotational frequency at a rate similar to that observed in the majority of neighboring SD bands (Fig. 2). It corresponds to a cascade of γ-rays with a decreasing energy spacing from 40 keV at the bottom of the band to 33 keV for transitions of 600 keV decaying higher spin levels. Secondly, their weak intensities of $\approx$0.5% also follow the trend present in the Hg nuclei where the ^{190}Hg SD band is populated at 0.8% [13] which is lower than in the heavier isotopes usually populated at the 1 to 2% level. The SD bands reported in ^{192}Tl [2], ^{193}Tl [3], ^{194}Tl [4] and ^{195}Tl [5] are more weakly populated than in their corresponding Hg isotones. The feeding and decaying out of the bands are typical of other SD bands with a gradual feeding spread over many transitions and a sudden drain of all the intensity. The point at which 50reached ($\hbar\omega \approx 0.6$MeV is compatible with other similar measurements in this region. Thirdly, the lowest transition of 377.8 keV indicates a decay out of the band at a higher frequency than for the heavier isotopes. This behavior is analogous to that in ^{190}Hg with a lowest transition of 360 keV. This last point agrees with a predicted reduction in the potential depth of the SD minimum with decreasing neutron number [20]. Experimentally, the γ-ray energy of the lowest observed transition of the Hg isotopes has a minimum at N=112. The Pb isotopes also show the same trend in their first transition energies. They are generally lower than their Hg and Tl counterparts, indicating a decay out of band at very low spins. The ^{191}Tl bands fit very well within this systematic.

IV. Grid search method

The grid search method [17] has been developed to enhance the presence of very weak and regularly spaced transitions occurring from the decay

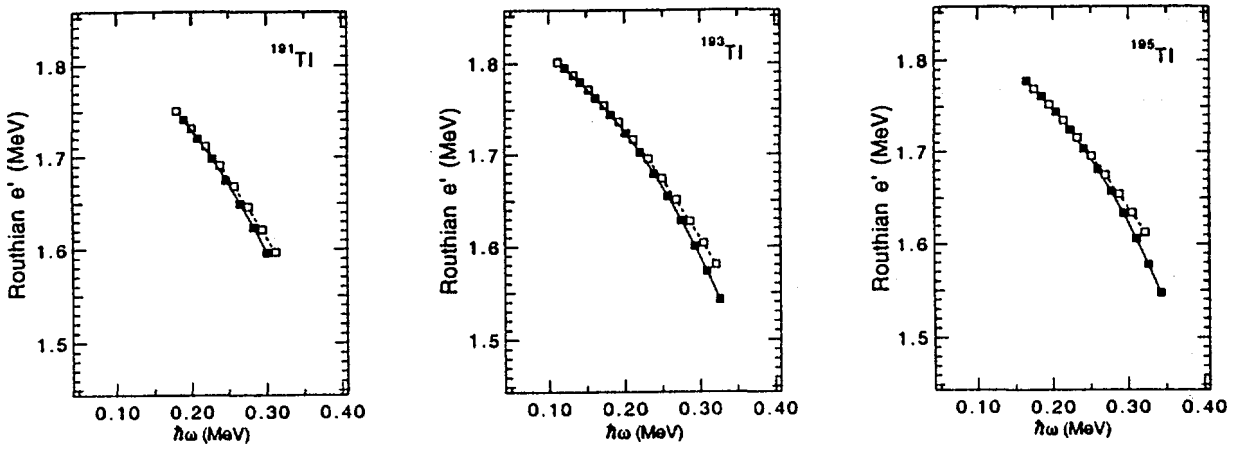

Fig. 3 Experimental signature splittings for ^{191,193,195}Tl.

of superdeformed nuclei in a matrix dominated by strong transitions decaying from normal nuclear states. The idea behind the method is simple and consists in moving a small grid of regularly spaced 2D gating elements centered along the diagonal of a subtracted matrix to create a *spectrum of merit* by adding the contributions from all the gating elements. Typically, the Waddington/Palameta [21] subtraction method can be applied successfully. If the postulated spacing corresponds to the spacing of an hidden signal then one expects peaks at regular intervals every time the grid overlaps with the signal.

However, a subtle problem arises when the background is not uniform. For this method to be effective we need to limit the contributions from intense peaks by applying an upper threshold on the number of counts allowed in a given gating element. This is easily done by fixing the maximum counts to a few standard deviations from the normal background fluctuations. This can be accomplished only if the background in the subtracted matrix is flat and ideally close to zero. We can see that fixing a threshold a given number of counts counts is meaningful only if it is valid on the entire range of the search.

From a very large number of spacing and stretching investigated, the only spectra of merit exhibiting such a structure were those with an initial spacing of 40 keV at 400 keV and a reduction of 1 keV for every member higher in the band. A comparison with single gates extracted from the γ-ray correlation matrix strongly suggests that this technique could effectively be used to find superdeformed signals more easily than the traditional gating method for these special cases.

However, this technique is strongly dependent on the smoothness of the hidden signal. If strong anomalies in the transition energies are present, the postulated spacing and spacing variation would be totally inadequate and would only produce uncorrelated noise in the diagonal spectrum of merit.

V. Discussion

A large majority of SD bands in the $A = 190$ region show a similar increase in their dynamical moment of inertia of approximately $\approx$20% over the observed frequencies. This smooth behavior has been interpreted in terms of consecutive $\nu j_{15/2}$ and $\pi i_{13/2}$ alignments in presence of pairing [1, 3, 12]. It is well known that cranked shell model (CSM) calculations can provide a useful guideline to explain many of the features observed. Despite its relative success, a global agreement with all the experimental results cannot be achieved (e.g. ^{189,190}Hg [13] and ^{193}Tl [3]) even by significantly changing parameters such

as deformation, pairing or interaction strength. Nevertheless, so far it as been instructive to assign "particle" configurations based on small differences in moments of inertia or signature splittings and comparing the observed features to predictions from the cranked shell model.

For ^{191}Tl, the expected yrast SD configuration would be built on the $6_{5/2}$ (note the convention N_Ω, where N is the principal quantum number of the state and Ω denotes the angular momentum projection on the symmetry axis) orbital occupied by the odd proton. Any excited proton configuration would likely involve the [514]9/2 or [411]1/2 Nilsson orbital located above and below the Fermi surface respectively. The neutron shell is filled with only 110 neutrons which is two neutrons below the $N = 112$ gap. Probable neutron excitations would be built on the [512]5/2, [624]9/2, [642]3/2, [640]1/2 Nilsson orbits or the $7_{3/2}$ intruder orbital near the Fermi surface.

Following blocking arguments, an yrast SD configuration based on the $\pi i_{13/2}\ 6_{5/2}$ orbital would lead to a smaller increase in $\mathcal{J}^{(2)}$ relative to the even-even core. The remaining crossing resulting from the unblocked $\nu j_{15/2}$ crossing. The two SD bands in ^{193}Tl seem to firmly support this interpretation when compared to ^{192}Hg. Similarly, if we examine the $\mathcal{J}^{(2)}$ moments of inertia of ^{191}Tl and ^{190}Hg (see Fig. 2) we notice that this trend seems also present but is not as clear due to scattering of the data

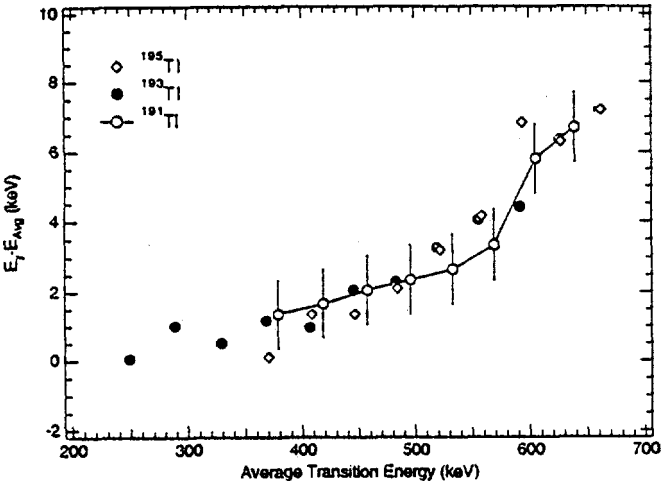

Fig. 4 Plots of the transition energy differences between signatures for ^{191,193,195}Tl.

points. At low frequencies, the odd $6_{5/2}$ proton is expected to provide the additional contribution to the moment of inertia present in both ^{191}Tl and ^{193}Tl data. Figure 2 shows the $\mathcal{J}^{(2)}$ moments for ^{191}Tl and ^{193}Tl, we also see that the slope of the ^{191}Tl trajectory is somewhat steeper than ^{193}Tl. This trend is consistent with CSM calculations which predict a lower deformation and an higher interaction strength resulting in a sharper rise in $\mathcal{J}^{(2)}$. Since we assign these new bands to the $6_{5/2}$ configuration we should find the same signature splitting as observed in ^{193}Tl [3] and ^{195}Tl [4]. The $6_{5/2}$ orbit exhibits very little splitting below a frequency of $\hbar\omega \approx 0.2$ MeV so we arbitrarily normalized the experimental Routhians accordingly. Figure 3 shows the extracted Routhians for the A=191, 193 and 195 Tl isotopes. We notice that the splitting develops in all three cases at a rotational frequency of 0.2 MeV. In extracting signature splittings, one has to provide the spins of the levels. We have applied a spin fitting procedure similar to the one proposed by *Becker et al.* [5] which is based on the Harris expansion [22, 23]. More importantly, the fit supports a staggering of one unit of angular momentum between both signatures. The exit spins at the bottom of the bands are relatively high as expected (see text above) at $33/2\ \hbar$ (band 1) and $31/2\ \hbar$ (band 2). The fitting procedure indicates that the J_0 and J_1 inertia parameters change significantly for ^{191}Tl. This behavior is also present for ^{190}Hg [13] where the $\mathcal{J}^{(2)}$ trajectory is significantly smaller than the ^{192}Hg reference SD band. In fact, even if no change in deformation at the 20% level is taking place [13], a difference of only a few percents in deformation could easily account for these differences. We have kept J_0 and J_1 constant for ^{193}Tl and ^{195}Tl and reduced them for ^{191}Tl in order to reproduce the overall trend. The extracted deformations from TRS calculations indicate that small changes in deformation of $\Delta\beta_2 \approx +0.008$ occur going from ^{190}Hg to ^{192}Hg or from ^{192}Hg to ^{193}Tl. For all practical purposes, the changes in deformation between ^{190}Hg and ^{191}Tl or from ^{191}Tl to ^{193}Tl are also predicted to be of the same order. So the expected deformation of ^{192}Hg and ^{191}Tl are predicted to be very similar. Interestingly, the transition energies of band 1 in ^{191}Tl are very close to the SD band observed in ^{192}Hg. We can examine the sig-

nature splitting independently of any parameters by plotting the difference in energy between the transition energies of a given signature and the average energy of the two neighboring transitions belonging to the other signature. In figure 4 we show such a plot for the three Tl isotopes A=191, 193 and 195. It is remarkable that the curves are tracking each other very closely and strongly indicate that these nuclei experience the same crossing at the same rotational frequency, again supporting the ^{191}Tl assignment.

In addition to the large Z=80 gap for the proton system, an equally important gap at N=112 in the neutron shell structure persists for all rotational frequencies observed experimentally. Due to the stabilizing effect of these two gaps, the ^{192}Hg nucleus plays a central role as a reference nucleus. The yrast superdeformed configuration of the ^{192}Hg core is commonly designated by its high-N orbital configuration and labeled as $\pi 6^4 \nu 7^4$. (In general, a configuration will be referred by $\pi(N_\pi)^n \nu(N_\nu)^m$ where N_i denotes the principal quantum number and n, m the number of nucleons in that particular subshell). Excited configurations in ^{192}Hg are energetically costly because of these large gaps and indeed no other SD states have been reported for this nucleus.

A different approach to compare superdeformed bands in various nuclei involve what has been called the incremental alignment Δi [16], where differences in γ-ray energies of the nucleus of interest with those of a reference nucleus are compared with the increase in energy between successive transitions of the reference. For ideal strongly-coupled bands, the resulting even-spin sequences will exhibit the same transition energies as the yrast band of the core whereas the odd-spin sequences are staggered at mid-energies. A detailed discussion on these aspects is presented in Ref[23]. The incremental alignment Δi, is simply related to spins through γ-ray energy differences and takes the values $\Delta i = 0, 1$ and $\pm 1/2$ for even-A and odd-A nuclei, respectively.

For ^{191}Hg the 111^{th} neutron is in the $\alpha = 1/2, 7_{3/2}$ orbit (favored signature) and represents the yrast SD configuration. Unlike ^{192}Hg, the high-N content is now $\pi 6^4 \nu 7^3$ and the Δi diagram (Fig. 5) translates in a strongly downsloping pattern indicating a different core than ^{192}Hg. Experimentally, two excited bands have been found [11]. The absence of

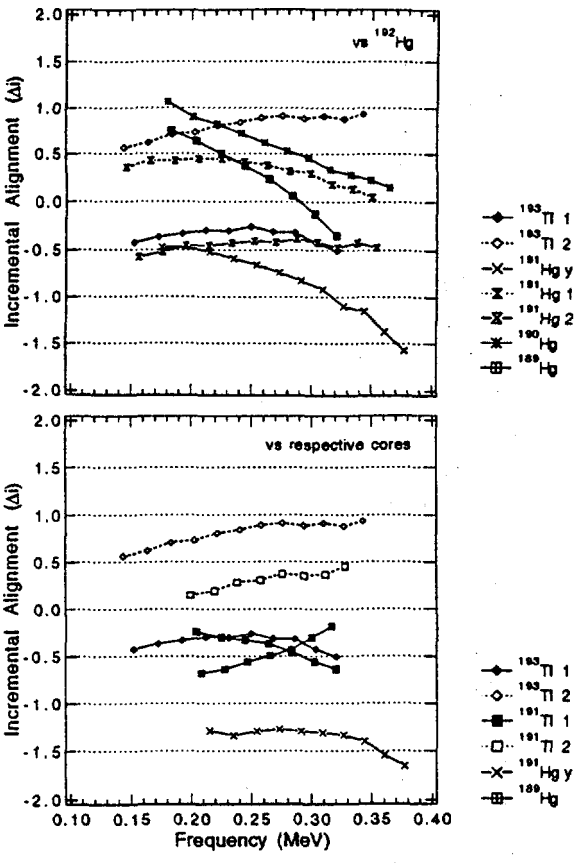

Fig. 5 Incremental alignments Δi of selected nuclei in the Hg-Tl-Pb region plotted relative to various cores, namely ^{190}Hg and ^{192}Hg.

signature splitting suggests that these bands are built on the [642]3/2 neutron orbital. They follow very well the prescription of a valence neutron strongly coupled to the ^{192}Hg core exhibiting a rather flat incremental alignments at $\Delta i = \pm 1/2$. This shows that these excited bands are similar to the SD band in ^{192}Hg and follow from the fact that they have the same $\pi 6^4 \nu 7^4$ high-N configuration as ^{192}Hg. The small differences in the $\mathcal{J}^{(2)}$ moments of inertia also support these assignments [1, 11].

The two SD bands observed in ^{193}Tl agree well with the expected single-particle configurations [3, 4]. For Tl isotopes, the valence proton is placed in the $6_{5/2}$, [642]5/2 orbital just above the Z=80 gap. The routhian signature splitting for the predicted $6_{5/2}$ orbital is zero at low frequency and develops only to modest values at higher frequencies (Fig. 3).

No other configurations (particle or hole) can provide an alternate explanation. The Δi plots (Fig. 5) show a gradual increase relative to ^{192}Hg from $\pm 1/2$ starting values.

Data on ^{190}Hg [13] and ^{189}Hg [14] revealed only one superdeformed band in these nuclei. The high-N configurations in the A=150 region are a good indicator of the most influential orbits in the SD cores. However, the ^{191}Tl core and neighboring nuclei are subject to pairing and the high-N orbitals are being pushed away from the Fermi surface as one depletes the core from nucleons. For example, the SD band in ^{190}Hg is built on the $(0,+)$ zero-quasiparticle [13] like ^{192}Hg. Thus it could be labeled by the same high-N configuration as ^{192}Hg but would likely misrepresent their occupation probabilities. In ^{190}Hg and ^{189}Hg, the Δi values again follow a downsloping trend relative to ^{192}Hg suggesting a different core.

Clearly, we see that comparing nuclei having different high-N configurations is not justified and indeed not very helpful. Here we can investigate the response of these different cores under the influence of the same $6_{5/2}$ proton orbital. To do so let us examine the incremental alignment Δi of ^{191}Tl relative to the ^{190}Hg core and Δi for ^{193}Tl versus the ^{192}Hg core (Fig.5). We have also plotted the incremental alignments of ^{189}Hg and ^{191}Hg yrast bands to illustrate the effect of changing to the more appropriate ^{190}Hg core reference. One common feature to both Tl isotopes is an increase in Δi relative to their respective cores. Due to the intruder character of the $6_{5/2}$ proton orbital, deviation from the strongly-coupled scheme is to be expected since polarizing effects are likely to be more important. The high-N content of ^{189,190}Hg and ^{191}Hg yrast bands is reduced and the ability to resist the deformation driving effect could be reduced. The proton $6_{5/2}$ orbital drives the core to larger deformation resulting in a greater increase in Δi for ^{191}Tl compared to ^{193}Tl. Other factors like pairing effects or structure details in the vicinity of the Fermi level could also be important and full calculations are required for those nuclei with their Fermi level below the SD gaps.

VI. Summary

Two bands of 8 transitions have been observed in the study of ^{191}Tl produced by the ^{159}Tb(^{36}S,4n) reaction at 165 MeV. These bands are interpreted as signature partners issued from the $6_{5/2}$ proton orbital directly above the $Z = 80$ gap at superdeformed shapes. Analysis using a grid-search method provided clear support for the presence of these two superdeformed decay sequences. These bands exhibit features which agree well with the systematics of other SD bands in the $A = 190$ region. A comparison of the effect of the valence proton with ^{193}Tl is not straightforward because the appropriate ^{190}Hg core is different than ^{192}Hg. Further investigation is clearly needed in order to understand the exact nature of these SD bands and the interplay between configurations and deformation driving effect in this region of superdeformation.

Acknowledgments

The research at the University of Tennessee is supported by the Department of Energy under contract no. DE-FG05-87ER40361. The Oak Ridge support is obtained through the Department of Energy under contract DE-FG05-3837366. This work was partially supported by the National Sciences and Engineering Research Council of Canada.

† Present address: Department of Physics, University of Ottawa, Ottawa, K1N-6N5, CANADA.

References

[1] E.F. Moore, R.V.F. Janssens, R.R. Chasman, I. Ahmad, T.L. Khoo, F.L.H. Wolfs, K.B. Beard, U. Garg, M.W. Drigert, Ph. Benet, Z.W. Grabowski and J.A. Cizewski, Phys. Rev. Lett. **63**, 360 (1989).

[2] Y. Liang, et al., *International Conference on Nuclear Structure at High Angular Momentum*, Contribution Vol 1, May, (1992).

[3] P.B. Fernandez, M.P. Carpenter, R.V.F. Janssens, I. Ahmad, E.F. Moore, T.L. Khoo, F. Scarlassara, I.G. Bearden, Ph. Benet, M.W. Drigert, U. Garg, W. Reviol, D. Ye and S. Pilotte, Nucl. Phys. A **517**, 386 (1990).

[4] F. Aziez, W.H. Kelly, W. Korten, M.A. Deleplanque, F.S. Stephens, R.M. Diamond, C.W. Beausang, J.A. Becker, E.A. Henry, J.E. Draper, M.J. Brinkman, S.W. Yates, A. Kuhnert and E. Rubel, Z. Phys. A **336**, 243 (1990).

[5] J.A. Becker, N. Roy, E.A. Henry, M.A. Deleplanque, C.W. Beausang, R.M. Diamond, J.E. Draper, F.S. Stephens, J.A. Cizewski and M.J. Brinkman, Phys. Rev. C **41**, R9 (1990).

[6] E.A. Henry, M.J. Brinkman, C.W. Beausang, J.A. Becker, N. Roy, S.W. Yates, J.A. Cizewski, R.M. Diamond, M.A. Deleplanque, F.S. Stephens, J.E. Draper, W.H. Kelly, R.J. McDonald, J. Burde, A. Kuhnert, W. Korten, E.Rubel and Y.A. Akovali, Z. Phys. A **355**, 361 (1990).

[7] C.W. Beausang, E.A. Henry, J.A. Becker, S.W. Yates, N. Roy, M.A. Deleplanque, R.M. Diamond, J.E. Draper, F.S. Stephens, W.H. Kelly, R.J. McDonald, J. Burde, E. Rubel, M.J. Brinkman, J.A. Cizewski and Y.A. Akovali, Z. Phys. A **335**, 325 (1990).

[8] D.M. Cullen, M.A. Riley, A. Alderson, I. Ali, T. Bengtsson, M.A. Bentley, A.M. Bruce, P. Fallon, P.D. Forsyth, F. Hanna, S.M. Mullins, W. Nazarewicz, R.J. Pounter, J.W. Roberts, W. Satula, J.F. Sharpey-Schafer, J. Simpson, G. Sletten, P.J. Twin, R. Wadsworth and R. Wyss, Phys. Rev. Lett. **65**, 1547 (1990).

[9] T.F. Wang, et al., LLNL preprint (1991).

[10] D. Ye, R.V.F. Janssens, M.P. Carpenter, E.F. Moore, R.R. Chasman, I. Ahmad, K.B. Beard, Ph. Benet, M.W. Drigert, P.B. Fernandez, U. Garg, T.L. Khoo, S.D. Ridley and F.L.H. Wolfs, Phys. Rev. C **41**, R13 (1990).

[11] M.P. Carpenter, R.V.F. Janssens, E.F. Moore, I. Ahmad, P.B. Fernandez, T.L. Khoo, F.L.H. Wolfs, D. Ye, K.B. Beard, U. Garg, M.W. Drigert, Ph. Benet, R. Wyss, W. Satula, W. Nazarewicz and M.A. Riley, Phys. Lett. B **240**, 44 (1990).

[12] M.A. Riley, D.M. Cullen, A. Alderson, I. Ali, T. Bengtsson, M.A. Bentley, A.M. Bruce, P. Fallon, P.D. Forsyth, F. Hanna, S.M. Mullins, W. Nazarewicz, R. Pounter, J.W. Roberts, J.F. Sharpey-Schafer, J. Simpson, G. Sletten, P.J. Twin, R. Wadsworth, and R. Wyss, Nucl. Phys. A **512**, 178 (1990).

[13] M.W. Drigert, M.P. Carpenter, R.V.F. Janssens, E.F. Moore, I. Ahmad, P.B. Fernandez, T.L. Khoo, F.L.H. Wolfs, I.G. Bearden, Ph. Benet, P.J. Daly, U. Garg, W. Reviol, D. Ye, R. Wyss, Nucl. Phys. A **530**, 452 (1991).

[14] I.G. Bearden, et al., private communication.

[15] J. Kuehner, BANDAID code, private communication.

[16] F.S. Stephens, M.A. Deleplanque, J.E. Draper, R.M. Diamond, A.O. Machiavelli, C.W. Beausang, W. Korten, W.H. Kelly, F. Aziez, J.A. Becker, E.A. Henry, S.W. Yates, M.J. Brinkman, A. Kuhnert and J.A. Cizewski, Phys. Rev. Lett. **65**, 301 (1990).

[17] T.L. Khoo, R.V.F. Janssens, E.F. Moore, K.B. Beard, Ph. Benet, I. Ahmad, M.P. Carpenter, R.R. Chasman, P.J. Daly, M.W. Drigert, U. Garg, Z.W. Grabowski, F.L.H. Wolfs, D. Ye and P.B. Fernandez, Nucl. Phys. A **520**, 169c (1990).

[18] R.V.F. Janssens and T.L. Khoo, Ann. Rev. Nucl. Part. Sci. **41**, 321 (1991).

[19] G. Palameta and J.C. Waddington, Nucl. Inst. and Meth. A **234** 476 (1985).

[20] R.R. Chasman, Phys. Lett. B **219**, 227 (1989).

[21] G. Palameta and J.C. Waddington, Nucl. Inst and Meth. A **234**, 476 (1989).

[22] S.M. Harris, Phys. Rev. B **509**, 138 (1965).

[23] R. Wyss and S. Pilotte, Phys. Rev. C **44** R602 (1991).

HIGHER SUPERDEFORMED BAND MEMBERS IN ^{190}Hg: EVIDENCE FOR A BAND INTERACTION?

I. G. Bearden[1], R. V. F. Janssens[2], M. P. Carpenter[2], I. Ahmad[2], P. J. Daly[1], M. W. Drigert[3], U. Garg[4], T. L. Khoo[2], T. Lauritsen[2], Y. Liang[2], W. Reviol[4], R. Wyss[5]

1: Purdue University, West Lafayette, IN 47907, U.S.A.
2: Argonne National Laboratory, Argonne, IL 60439, U.S.A.
3: Idaho National Engineering Laboratory, EG&G Idaho Inc., Idaho Falls, ID 83415, U.S.A
4: University of Notre Dame, Notre Dame, IN 46556, U.S.A.
5: Joint Institute for Heavy-Ion Research, Oak Ridge, TN 37831, U.S.A

Abstract: The superdeformed band of ^{190}Hg has been traced up to a frequency $\hbar\omega \geq 0.4$ MeV by combining data from several experiments. A distinct change in the slope of the dynamic moment of inertia $J^{(2)}$ vs $\hbar\omega$ is observed at $\hbar\omega = 0.32$ MeV. This result is interpreted as evidence for a band interaction at the highest frequencies. Possible interpretations are reviewed.

The evolution of the dynamic moment of inertia $J^{(2)}$ as a function of rotational frequency for superdeformed (SD) bands in the mass A = 150 region is characterized by pronounced isotopic and isotonic variations[1] attributed to differences in the occupation of specific high-N intruder orbitals[2]. In contrast, the vast majority of the SD bands in the mass A = 190 region displays the same smooth and rather pronounced increase of $J^{(2)}$ with $\hbar\omega$[1]. The occupation of specific high-N intruders cannot account for this rise[1,3-5] in $J^{(2)}$. The results of lifetime measurements[6] rule out the possibility that a change in deformation with $\hbar\omega$ causes this increase. It has been suggested that quasiparticle alignments and the resulting changes in pairing play an essential role[4-8]. Calculations using the cranked Woods-Saxon Strutinsky model (CSM) with pairing are able to account for the 40 % rise in $J^{(2)}$ observed for $0.12 \leq \hbar\omega \leq 0.40$ MeV in ^{192}Hg by the combined alignment of a pair of N = 6 ($i_{13/2}$) protons and a pair of N = 7 ($j_{15/2}$) neutrons[6]. These calculations predict that, after the quasiparticle alignments have taken place, $J^{(2)}$ will exhibit a downturn with increasing $\hbar\omega$ and will approach the static moment of inertia $J^{(1)}$.

We have recently reported on a new investigation[9] of ^{192}Hg, in which the SD band was extended to higher frequencies. As can be seen from figure 1, $J^{(2)}$ rises with $\hbar\omega$ over the entire frequency range and there is no sign of the predicted downturn. Thus, the data at high rotational frequencies lead one to question the validity of the calculations as well as of the proposed interpretation.

In order to assess whether this result is unique, i.e. whether (for example) the SD band in ^{192}Hg has a peculiar behavior because of the "doubly magic" SD character of this nucleus[1], we have now performed a similar study for ^{190}Hg. It has been noted[10] that CSM calculations for this nucleus indicate that the interaction strength between the ground state and the aligned configurations is much weaker in ^{190}Hg than in ^{192,194}Hg and, hence, alignment effects should result in more distinct variations of $J^{(2)}$.

Coincidence data obtained with the ^{160}Gd(^{34}S, 4n) reaction at three beam energies (159, 162, 165 MeV) were used. The experimental details can be found in ref. 10. In the analysis, a coincidence matrix was constructed from signals recorded in 12 Compton suppressed Ge detectors. Events corresponding to high-multiplicity cascades in ^{190}Hg were enhanced by careful gating on the γ-ray multiplicity and sum-energy recorded in the 50 element inner array of the Argonne Notre Dame BGO γ-ray facility. The gates were adjusted at each beam energy, in order to reflect corresponding changes in input angular momentum and excitation energy. The final matrix obtained in this way contained 3.5×10^7 events.

The spectrum obtained by adding the cleanest coincidence spectra (gates placed on the 360, 443, 483 and 558 γ rays) is shown in fig. 2. The SD band and the yrast transitions reported earlier[10] are clearly visible. From the data we were able to establish more precisely the energy of the 727 keV transition and add three new γ rays with energies of 756, 784 and 812 keV. These three transitions correspond to intensities of 15, 12 and 5% of the most intense transition in the SD band.

The behavior of the dynamic moment of inertia $J^{(2)}$ at high rotational frequency in the ^{190}Hg SD band is also presented in fig. 1. It can be seen that two markedly different slopes in $J^{(2)}$ are present. At frequencies $\leq$ 0.32 MeV, there is a smooth rise with a slope similar to that of ^{192}Hg. However, for the higher frequencies, a clear upbend in the data points is observed and, as a result, the $J^{(2)}$ values for ^{190}Hg become even larger than those for ^{192}Hg. Such a change in slope is very similar to those seen in many rotational bands at normal deformation and strongly suggests the presence of a crossing between the SD "ground state" band and another band.

A comparison between the data and the results of CSM calculations is presented in figure 3a. The solid line in the figure represents the result of a calculation with the reduced neutron pairing gap and the increased proton pairing

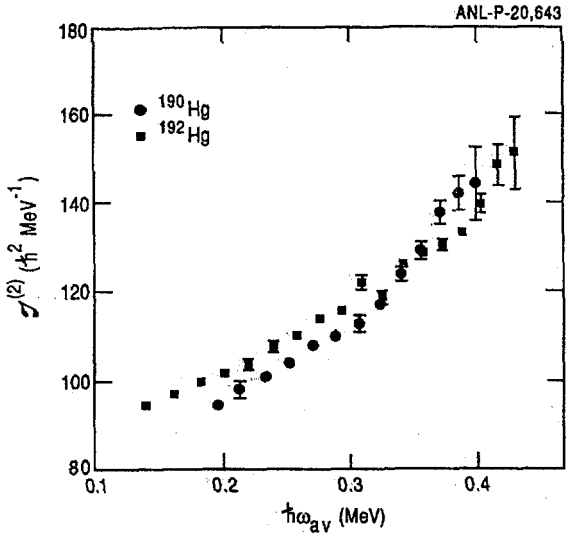

Fig. 1

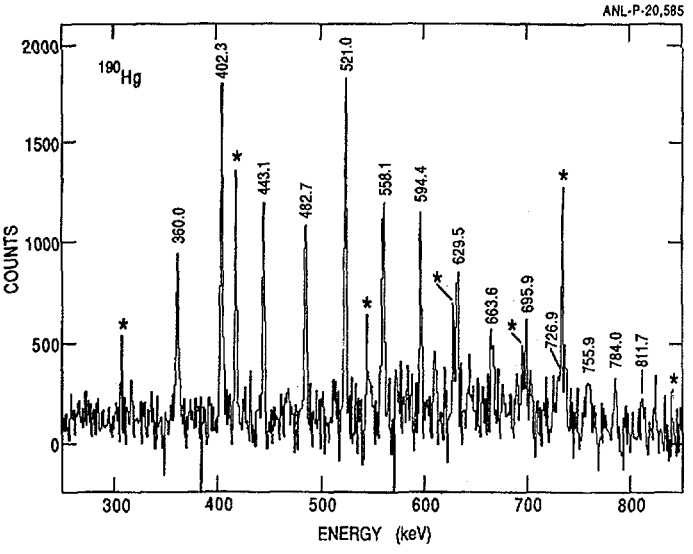

Fig. 2

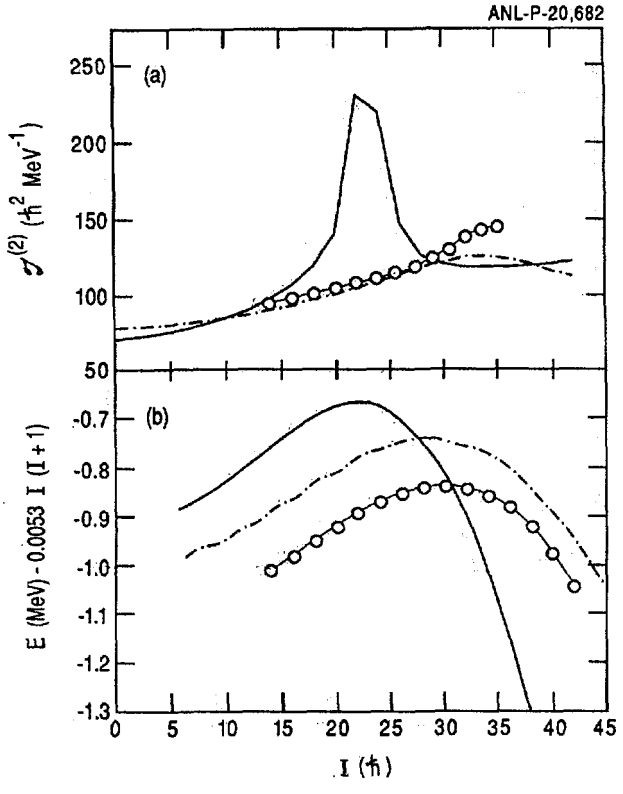

Fig. 3

Fig. 1: Dynamic moments of inertia $J^{(2)}$ vs $\hbar\omega$ for the latest data sets on the SD bands in ^{190}Hg and ^{192}Hg.

Fig. 2: Spectrum of the SD band in ^{190}Hg. Known yrast transitions associated with the decay out of the SD band are marked with a *.

Fig. 3: Comparison for the moments of inertia (a) and the energies with respect to a reference (b) between the data on ^{190}Hg (open circles) and CSM calculations with (i) reduced neutron pairing and enhanced proton pairing (solid line) and (ii) with a shifted aligned $\nu(j_{15/2})^2$ configuration and an increased interaction strength (dashed line).

gap used to reproduce the moments of inertia in ^{192,194}Hg (see ref. 7 for details). This calculation shows a sharp rise in the moment of inertia brought about mainly by the relatively weak interaction strength (~ 100 keV compared to ~ 500 keV in ^{192,194}Hg) between the ground state and the aligned $\nu(j_{15/2})^2$ SD band. This sharp rise is not present in the data. In figure 3b the calculations and the data are presented with a reference subtracted. At the highest spins (or frequencies) the data exhibit a downward slope which can be interpreted as a crossing with a configuration having larger aligned angular momentum. The comparison between data and calculations then suggests that the alignment process is (1) delayed in frequency and (2) occurs with a larger interaction strength than predicted. There is at present no satisfactory explanation for these observations. However, some possible interpretations are worth discussing.

Within the CSM, variations of several parameters which influence the evolution of $J^{(2)}$ with $\hbar\omega$ have been explored. Neither the small changes in the deformation parameters β_2 and β_4 allowed by the lifetime measurements[10] nor the introduction of a static octupole deformation as suggested in ref. 11 result in significant changes in $J^{(2)}$ with $\hbar\omega$. In ref. 10 it was proposed that a strong residual neutron-proton (np) interaction may be present which would result in a lowering in energy of the yrast SD configuration with respect to all other orbitals and would shift the interaction frequency and modify the interaction strength. A motivation for this approach comes from the fact that delays in frequency, changes in interaction strength and/or non-observation of expected alignments have been reported in some nuclei with normal deformation when intruder configurations are involved[12]. Furthermore, for the SD configuration discussed here, the protons and the neutrons occupy the same number of intruder orbitals which could result in an enhanced np interaction. The dashed lines in figs. 3a and 3b are the result of a calculation where this possibility has been "simulated" by artificially shifting up the aligned $(\nu j_{15/2})^2$ band by 350 keV relative to the yrast band while keeping the interaction strength between the two crossing bands to a value of the order of 200-400 keV. Clearly, this calculation comes closer to the data. It is hoped that detailed calculations will further explore this suggestion.

In most CSM calculations which attempt to reproduce the evolution of $J^{(2)}$ with $\hbar\omega$ in the A = 190 region, the most critical parameter appears to be the monopole pairing strength. However, this strength has thus far mainly been used as a parameter for which a detailed microscopic treatment is not yet available.

Pairing is sensitive to the overlap between orbitals of interest. At very large deformation, states originating from different shells approach the Fermi surface, and these states should have a reduced pairing interaction. If the monopole pairing strength is reduced, higher order corrections such as quadrupole pairing may become important. Efforts to explore this possibility are currently under way for the SD nuclei[13,14], and preliminary calculations of quadrupole pairing in the $\nu j_{15/2}$ system result in a higher crossing frequency. Here too a more definite conclusion is still lacking.

To summarize, recent analysis of data on the SD bands of ^{192}Hg and ^{190}Hg has shown that the dynamic moments of inertia $J^{(2)}$ are not reproduced well by the available calculations. Two suggestions for possible explanations of the deviations were briefly discussed: a strong neutron-proton interaction and/or higher order corrections to the pairing field. It is, of course, also possible that neither of these effects will provide a satisfactory account of the data and the fascinating possibility that these data will require the introduction of "new physics" may still have to be contemplated.

This work was supported in part by the Department of Energy, Nuclear Physics Division, under contracts nos W-31-109-ENG-38, DE-AC07-76ID01570 and DE-FG02-87ER40346, by the National Science Foundation under grant PHY91-00688.

References:

1. R.V.F. Janssens and T.L. Khoo, Ann. Rev. Nucl. Part. Sci. 41, (1991) 321
2. T. Bengtsson, I. Ragnarsson and S. Aberg, Phys. Lett. B208, (1988) 39; W. Nazarewicz, R. Wyss and A. Johnson, Phys. Lett. B225, (1989) 208
3. E.F. Moore et al., Phys. Rev. Lett. 63, (1989) 360
4. D. Ye et al., Phys. Rev. C41, (1990) R13
5. M.P. Carpenter et al., Phys. Lett. B240, (1990) 44
6. E.F. Moore et al., Phys. Rev. Lett. 64, (1990) 3127
7. M.A. Riley et al., Nucl. Phys. A512, (1990) 178
8. R.R. Chasman, Phys. Lett. B242, (1990) 317
9. T. Lauritsen et al., Phys. Lett. B279 (1992) 239
10. M.W. Drigert et al., Nucl. Phys. A530, (1991) 452
11. D. Cullen et al., Phys. Rev. Lett. 65, (1990) 1547
12. R. Wyss and A. Johnson, Proc. Conf, High Spin Physics and Gamma-soft Nuclei, Pittsburgh 1990,J.X. Saladin, R.A. Sorensen and C.M. Vincent ed., World Scientific 1991, p. 123
13. W. Nazarewicz, Recent Advances in Nuclear Structure, D. Bucurescu, G. Cata-Danil and N.V. Zamfir ed., World Scientific 1991, p. 175
14. R. Wyss, to be published

Superdeformation in the A = 190 Region: the Lead Nuclei

E.A. Henry, J.A. Becker, M.J. Brinkman, A. Kuhnert,
M.A. Stoyer, T.F. Wang, and S.W. Yates
Lawrence Livermore National Laboratory, Livermore, CA 94550

F.A. Azaiez, C.W. Beausang, J. Burde, M.A. Deleplanque, R.M. Diamond,
J.E. Draper, W.H. Kelly, W. Korton, A.O. Macchiavelli, J. Oliveira,
E. Rubel, and F.S. Stephens
Lawrence Berkeley Laboratory, Berkeley, CA 94720

J.A. Cizewski
Rutgers University, New Brunswick, NJ 08903

Introduction

Superdeformed (SD) bands have been identified in the four even-even lead nuclei ^{192}Pb, ^{194}Pb, ^{196}Pb, and ^{198}Pb [1-4]. The discovery of SD bands in these nuclei extended the region of superdeformation in the A = 190 region to Z = 82, and to neutron numbers up to N = 116. All of the SD bands in these nuclei are observed with transition energies ranging from about 250 keV to about 600 keV, with the lowest energy SD band transition for the entire region of 169 keV in ^{194}Pb. The spins deduced for the lowest levels in the SD bands are (10,11), 6, 8, and 12 for ^{192,194,196,198}Pb, respectively. The dynamic moments of inertia of ^{192}Pb and ^{194}Pb are similar to each other, and to those of many other SD bands in this mass region. The dynamic moments of inertia of ^{196}Pb and ^{198}Pb are somewhat lower than those of ^{192,194}Pb at a given frequency. The experimental lifetimes in ^{194}Pb and the deduced transition quadrupole moments ($Q_t \approx$ 20 eb) [5] are equal to those of other nuclei in the region within errors [6,7]. While SD bands have been observed in the odd-neutron Hg and Tl nuclei, SD bands have not been reported for the odd-neutron Pb nuclei.

In this contribution we discuss briefly three topics on superdeformation in the lead nuclei. First, we have recent experimental data on ^{196}Pb that extends our knowledge of the SD band in that nucleus. Next we review briefly the population of low-lying yrast levels from the decay of the SD bands in ^{192,194,196}Pb. Finally, we summarize our efforts to identify superdeformation in the odd-A Pb nuclei. All of the experiments described here were performed using the HERA spectrometer at the 88-Inch Cyclotron facility located at Lawrence Berkeley Laboratory.

New results for ^{196}Pb SD band

We have recently performed a backed thick target experiment which gave additional results for the ^{196}Pb SD band. For this experiment the ^{176}Yb(^{26}Mg,6n) reaction was used at a beam energy of 138 MeV. The ^{176}Yb target was 3 mg/cm^2 thick with a gold

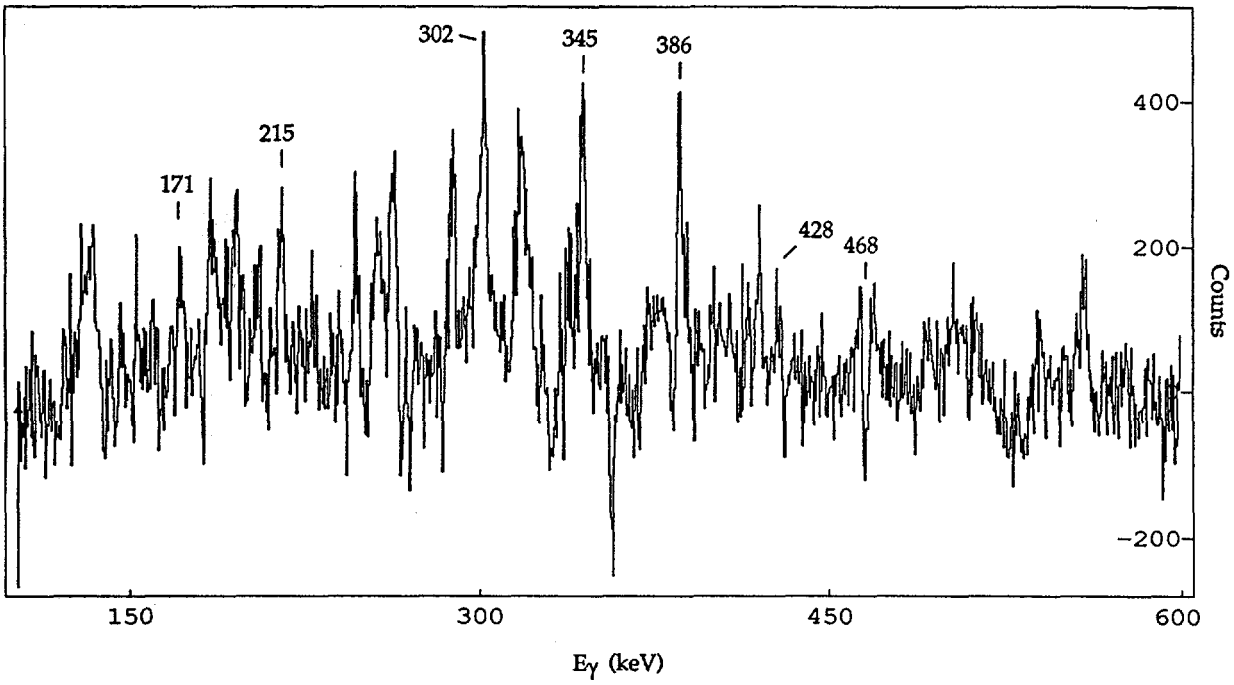

Figure 1. The spectrum in coincidence with the 259-keV member of the ^{196}Pb SD band, taken with a thick target. The newly observed transition at 171 keV is identified. Loss of intensity in the prompt peaks starting at 428 keV is indicative of the short lifetimes of the higher SD levels. Peaks at 468 keV and higher are completely shifted in this thick target experiment.

---

backing 12 mg/cm^2 thick. The statistics for ^{196}Pb SD band transitions was increased by a factor of more than five in this experiment compared to those of the previous experiments [1,3].

Figure 1 shows the spectrum in coincidence with the 259-keV member of the ^{196}Pb SD band. The previously known members of the ^{196}Pb SD band are clearly identified as is a transition at 171 keV. The higher statistics of this experiment and the reduction in contaminating peaks in the 171 keV region (possibly due to the differences in target thickness and backing) make this peak evident. A gate on this 171 keV transition brings back the SD band members. The intensity of the 171-keV transition (including internal conversion) is approximately one-half of the maximum SD band intensity. We propose this transition as the $8 \rightarrow 6$ transition in the ^{196}Pb SD band.

Also evident in Figure 1 is the loss of intensity in the prompt peaks of the higher energy transitions in the ^{196}Pb SD band, starting with the 428-keV transition. The pattern of intensities in the prompt peaks is similar to that obtained in an experiment using a ^{22}Ne beam with the same target to produce the ^{192}Hg SD band. The similarity of the SD transition spectra in these two experiments is a qualitative indication that the level lifetimes in the ^{196}Pb SD band are comparable to those of ^{192}Hg.

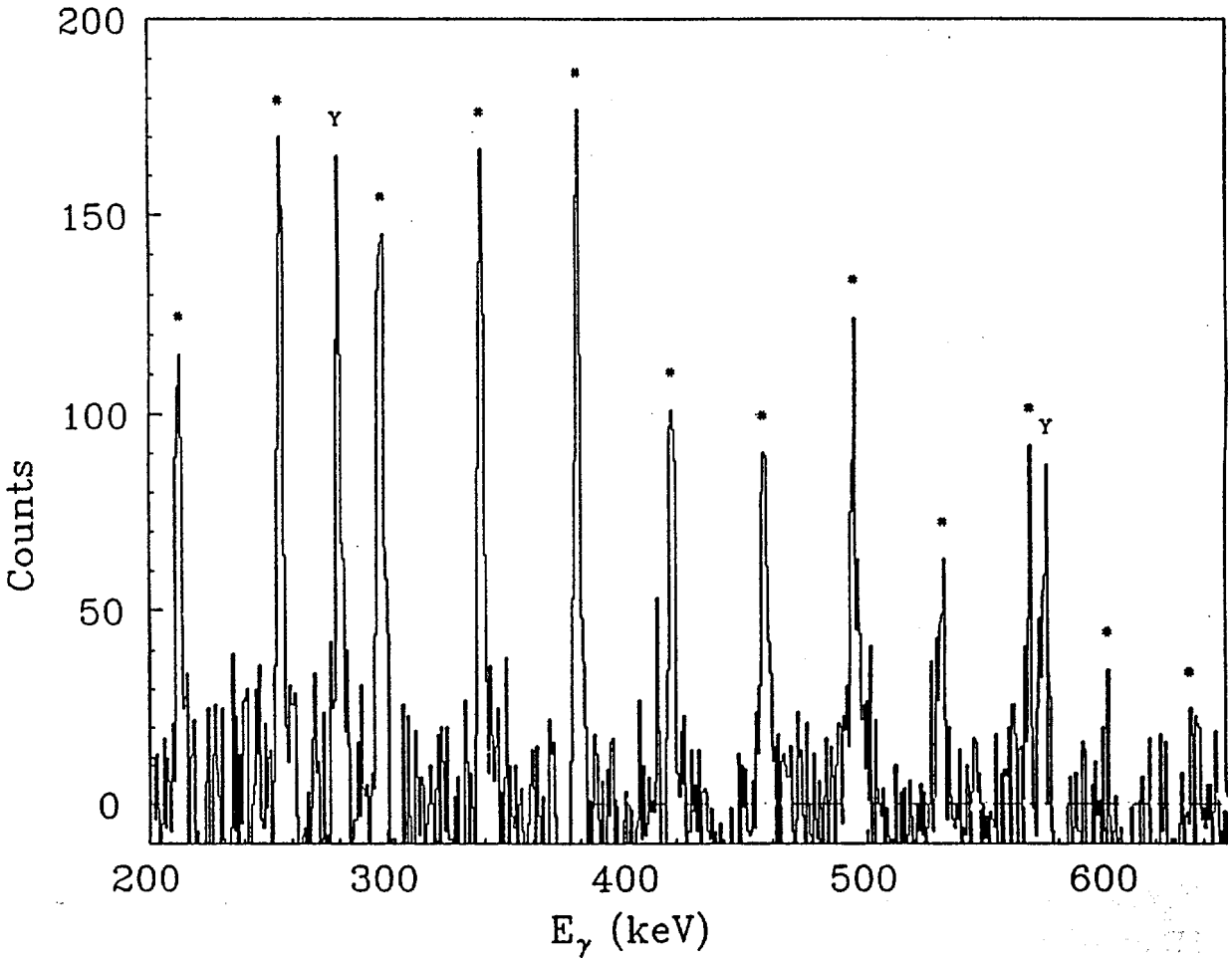

Figure 2. A spectrum of the ^{194}Pb SD band from double-gated triples data (transitions used in gates are indicated by asterisks). The low-lying $5^- \rightarrow 4^+$ transition at 280 keV and $4^+ \rightarrow 2^+$ transition at 575 keV are clearly observed, and indicated by Y on this spectrum.

Population of low-lying states by decay of lead SD bands

Spectra gated on SD band members in ^{192,194,196}Pb show transitions among the low-lying levels in the corresponding nuclei. We have projected spectra from the triple coincidence data by setting double gates on the cleanest SD band transitions. This technique minimizes contamination from the strong transitions between low-lying states, and reduces background subtraction problems. Shown in Figure 2 is the spectrum of ^{194}Pb obtained with double gates on SD band transitions. Clearly visible in this spectrum are the $5^- \rightarrow 4^+$ transition at 280 keV, and the $4^+ \rightarrow 2^+$ transition at 575 keV (the $2^+ \rightarrow 0^+$ transition is at 965 keV and not shown in this spectrum). Not observed is the $6^+ \rightarrow 4^+$ transition at 595 keV; an upper limit of 20% of the maximum SD band intensity can be established for that transition. Thus a large fraction of the SD band intensity decays through the 5^- level.

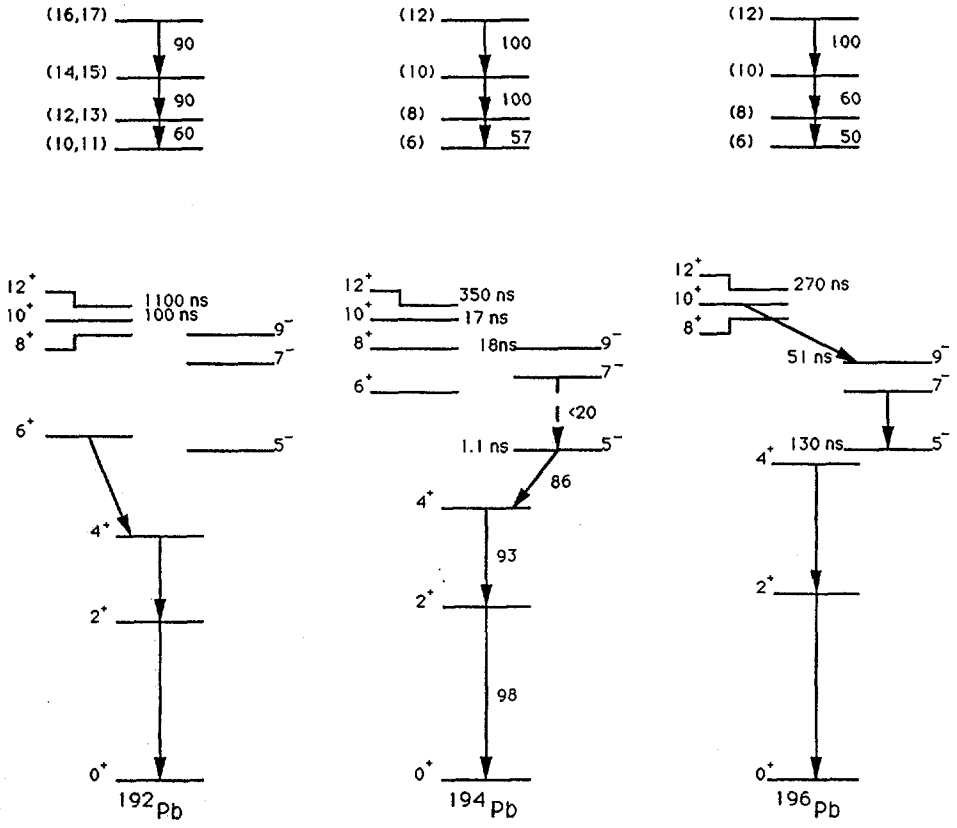

Figure 3. Schematic diagrams of the low-lying yrast levels and the lower portion of the SD bands for ^{192,194,196}Pb. The solid arrows indicate low-lying transitions observed in coincidence with the SD bands. The typical uncertainty of the intensities given is ±20%.

In a similar way spectra were projected for ^{192}Pb and ^{196}Pb. For ^{192}Pb the low-lying $2^+ \rightarrow 0^+$, $4^+ \rightarrow 2^+$, and $6^+ \rightarrow 4^+$ transitions at 853, 502, and 565 keV, respectively, are evident. The $5^- \rightarrow 4^+$ transition at 504 keV would be part of a triplet including an SD band member and the $4^+ \rightarrow 2^+$ transition, but it is quite weak if it is present at all. Though analysis is still underway for the ^{196}Pb SD band, a spectrum double-gated on SD band transitions shows the $10^+ \rightarrow 9^-$ and $7^- \rightarrow 5^-$ transitions at 337 and 372 keV. A number of long-lived isomers (>50 ns) complicates the determination of the intensity for the transitions between low-lying levels compared to SD band transitions in ^{196}Pb.

Figure 3 summarizes the population of low-lying yrast levels following the decay of the SD bands in ^{192,194,196}Pb nuclei. Low-lying transitions observed in coincidence with the SD band transitions are indicated by solid arrows. The intensities for the low-lying transitions in ^{194}Pb are indicated; uncertainties in these values are ±20%. As the next generation of detector arrays come on line, the anticipated increase in statistics will help us decide if the suggested differences among these three similar nuclei indicate structure effects in the decay of their SD bands.

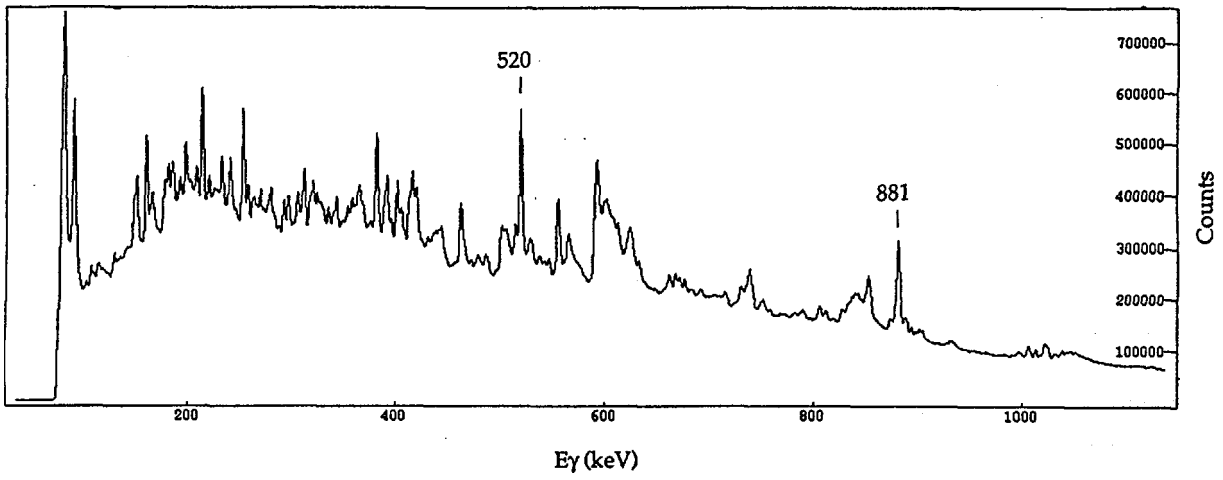

Figure 4. Total projection of the ^{193}Pb spectrum obtained with the reaction ^{24}Mg + ^{174}Yb at 134 MeV. This spectrum is typical of the lead spectra obtained in such reactions, including those for even-even lead nuclei where SD bands are observed.

Searches for SD bands in odd-A lead nuclei

Superdeformed bands have been identified in the odd-A mercury nuclei ^{189,191,193}Hg, and in the odd-odd thallium nuclei ^{192,194}Tl. However, SD bands have not been reported in the odd-A lead nuclei ^{193,195,197}Pb, even though SD bands are known in the neighboring even-even lead isotopes.

We have performed a number of experiments designed specifically to search for SD bands in the odd-A lead nuclei, or which populated odd-A lead nuclei as part of another study. These experiments include:

^{197}Pb:	^{48}Ca + ^{154}Sm at 205 and 210 MeV, ^{26}Mg + ^{176}Yb at 130 and 135 MeV,
^{195}Pb:	^{24}Mg + ^{176}Yb at 122, 127 and 132 MeV, and
^{193}Pb:	^{24}Mg + ^{176}Yb at 129 and 134 MeV.

No SD bands have been identified in any of these data for the odd-neutron lead nuclei. Interestingly, in the ^{24}Mg + ^{176}Yb reaction at 122, 127, and 132 MeV, SD bands were identified that belong to ^{194}Pb and ^{196}Pb, but no SD band that could be attributed to ^{195}Pb, even though the data on ^{195}Pb had twice the statistics of that of the adjacent even-even lead isotopes..

Shown in Figure 4 is a total projection of coincidence data obtained with the ^{24}Mg + ^{174}Yb reaction at 134 MeV to populate ^{193}Pb. This beam energy is somewhat above that for the peak of the 5n channel, and the 6n channel is about 40% of the 5n channel; this beam energy is ideally suited to populate SD bands in ^{193}Pb. Approximately 160

million and 307 million γ-γ coincidence events were collected at 129 and 134 MeV beam energies, respectively. These coincidence data were searched channel-by-channel for evidence of SD bands, but none have been identified. The triple coincidence data were scanned with a seven transition template, requiring two of the three coincident γ rays to be in the template and creating a spectrum of the third. The energy spacings of the ^{192}Pb SD band (which are nearly equal to those of ^{194}Pb) were used as the template spacings. The template used 2.5 keV wide gates. The initial position of the template ranged from 220 to 300 keV at 2 keV intervals. No evidence for a SD band in ^{193}Pb has been observed in any of these spectra projected from the triple coincidence data.

Several recent theoretical papers have presented results of quasiparticle calculations for superdeformed nuclei in the A = 190 region [see for example refs. 8, 9]. One result of these calculations is that there are a number of low-lying neutron quasiparticle states in the superdeformed second minimum near N = 112. For example, Meyer, et al., (ref. 8) calculate four to seven neutron quasiparticle states within 500 keV of each other for the superdeformed lead nuclei of interest here. This result suggests one explanation for the failure to identify SD bands in odd-A lead nuclei so far, that the reaction cross section leading to superdeformation is fragmented over so many bands that none of them has enough intensity to be identified with present spectrometer arrays. The arrays now under construction will be much more sensitive and may make it possible to identify SD bands in odd-A lead nuclei.

1. M. J. Brinkman, et al., Z. Phys. A 336, 115 (1990).
2. K. Theine, et al., Z. Phys. A 336, 113 (1990).
3. T. F. Wang, et al., Phys. Rev. C 43, R2465 (1991).
4. E. A. Henry, et al., Z. Phys. A 338, 469 (1991).
5. P. Willsau, et al., Proceedings of the International School of Nuclear Physics, Erice, Sicily, (Progress in Particle and Nuclear Physics, Vol. 28, Pergamon Press, Oxford).
6. E. F. Moore, et al., Phys. Rev. Lett. 63, 360 (1989).
7. E. F. Moore, et al., Phys. Rev. Lett. 64, 3127 (1990).
8. M. Meyer, et al., Phys Rev. C 45, 233 (1992).
9. W. Satula, et al., Nucl. Phys. A529, 289 (1991).

Lifetimes of the Low Spin States in the Superdeformed Band of ^{192}Hg

I.Y. Lee, C. Baktash, D. Cullen, J.D. Garrett, N.R. Johnson,
F.K. McGowan, and D.F. Winchell

Oak Ridge National Laboratory, Oak Ridge, TN 37831

C.H. Yu

University of Tennessee, Knoxville, TN 37996

I. INTRODUCTION

Superdeformed (SD) states with a 2:1 axis ratio have been observed in nuclei in the A = 150, 190, and the actinide regions. These states depopulate into normally deformed (ND) states by gamma decay, but so far the linking transitions have not been observed and the depopulation mechanism is not fully understood. As shown in Table I, nuclei in different mass regions decay out at states with different spin (I), excitation energy above the ND yrast line (U) and lifetime (τ). This variation is due to differences in the nuclear properties such as the barrier penetration probability, the level densities and the gamma transition strength of SD and ND states. One important factor is the competition between the collective E2 decay along the SD band and the statistical decay to the ND states. These transition rates, or the partial lifetimes, can be determined if the lifetime and the intensity of the gamma rays depopulating the SD states are known.

Table I. Decay out properties of superdeformed states

	I	U(MeV)	τ
^{152}Dy	26	6	0.06 psec
^{192}Hg	10	4	
^{236}U	0	2.7	166 nsec

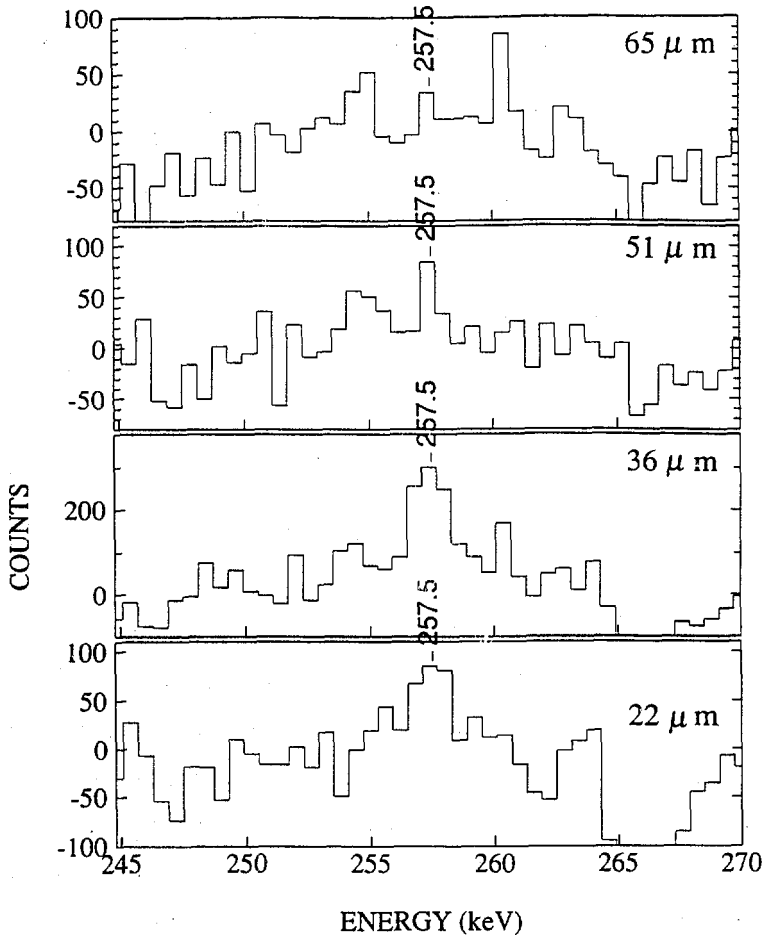

Fig. 1. Spectra of the 257-keV gamma ray for four target-stopper distances. A stopped peak and two moving peaks corresponding to the ± 45° detectors are observed.

II. EXPERIMENT AND RESULTS

In the mass 190 region, the lifetimes of the states at the end of the SD cascade have not been measured. Since the expected lifetime is in the range of few picoseconds, the recoil distance method is best suited for such a measurement. The lifetimes of the 257- and 300-keV transitions in the SD band of ^{192}Hg produced via the ^{160}Gd(^{36}S,4n) reaction have been measured with a 159-MeV beam from the HHIRF at ORNL. With an array of 20 Compton shielded Ge detectors and a recoil distance device, gamma-gamma coincidence data were taken at target-stopper distances of 22, 36, 51 and 65 micrometers.

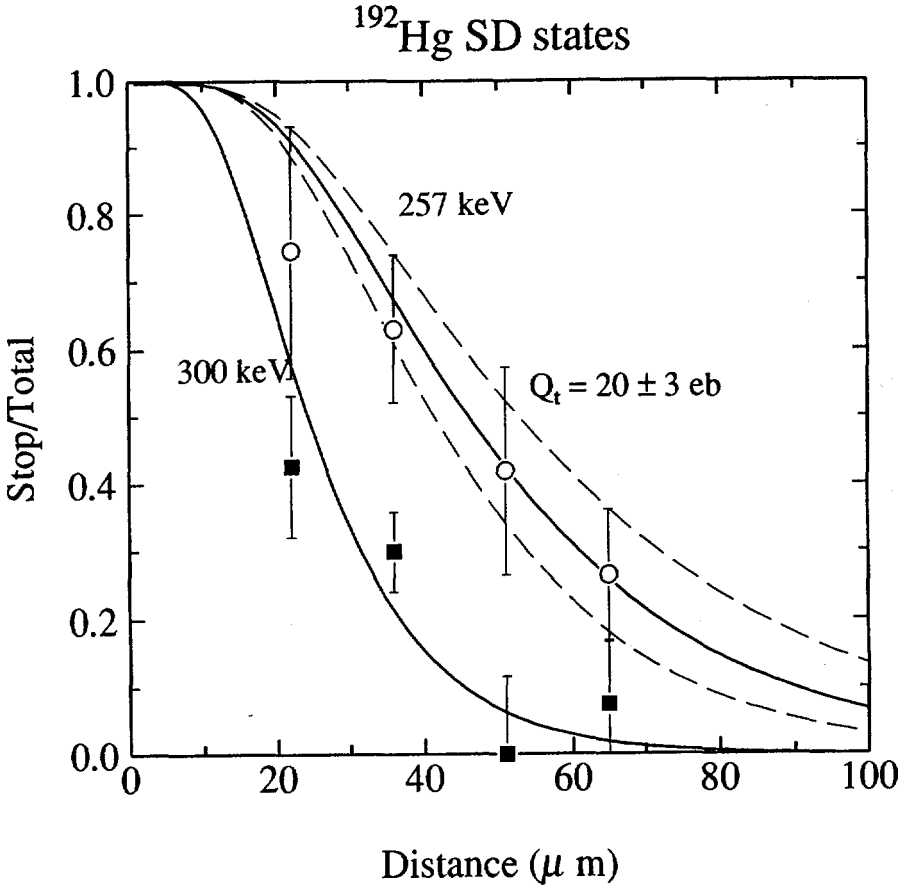

Fig. 2. Measured and calculated ratios of stopped and peak to total intensity.

One-dimensional spectra from the eight detectors at ± 45 degrees were obtained by gating on SD transitions above the transitions of interest. Figure 1 shows spectra for the 257-keV gamma ray [the $(12^+) \rightarrow (10^+)$ transition] at the four distances. For each transition, one stopped peak and two moving peaks corresponding to the ± 45 degree detectors are observed.

Figure 2 shows the ratio of the intensity of the stopped peak to the total intensity at each distance for the 257- and 300-keV transitions. Also shown are the calculated decay curves based on a Q_t value of 20 eb, determined from previous lifetime measurements[1] of the higher-spin SD states. The comparison indicates that the measured lifetimes are consistent with collective E2 decay if there is no branching to the ND states. However, the intensity of the 257-kev transition obtained from an average of the results of this and two previous experiments[1,2] is about 84 ± 7 % of the intensity of the 300-keV transition indicating a 16% branch to the ND state. This would produce an 8% reduction

of the Q_t value for the 257-keV gamma ray. Such a reduction is smaller than the uncertainty of the lifetime measurement. Therefore, in the subsequent analysis a Q_t value of 20 eb is used for the SD E2 transition. This value gives a partial lifetime of 5.2 psec for the 257-keV transition.

The total transition rate of a state is the sum of transition rates in the SD and ND wells. For ^{192}Hg, the transition in the SD well is dominated by collective E2 decay and in the ND well by statistical E1 decay. The ratio of the gamma-ray intensities is proportional to the ratio of the partial transition rates, T, and inversely proportional to the lifetimes, τ. Thus

$$\frac{I_N}{I_S} = \frac{T_N(E1)}{T_S(E2)} = \frac{\tau_S(E2)}{\tau_N(E1)} .$$

Therefore, the partial lifetime of decay in the ND well can be determined from the intensity ratio and the known SD E2 partial lifetimes.

$$\tau_N(E1) = \frac{I_S}{I_N}\tau_S(E2)$$

A value τ_N (E1)= 27.5 ps is obtained for the (12^+) state. A calculated partial lifetime of ND decay of 2.9 ps also is obtained for the (10^+) state observed in a previous experiment[2] to decay by a 214.6-keV transition with 18% of the intensity of the 257-keV transition.

These values of the E1 lifetime are longer than the expected lifetime of statistical E1 decay. This is because only a fraction of the wavefunction of the state is in the ND well. Indeed the ratio of the statistical E1 lifetime to the measured E1 partial lifetime provides a measure of the amplitude, α, of the wavefunction in the ND well. In the statistical model τ_N^{stat} (E1) can be calculated as

$$\tau_N^{stat}(E1) = 1 / \int_o^{U_i} \frac{\rho(U_f)}{\rho(U_i)} f_{GDR}(E_\gamma) E_\gamma^3 dE_\gamma$$

where $U_f = U_i - E\gamma$,

$\rho(U)$ is the level density at an excitation energy of U, and f_{GDR} is the E1 strength function based on the shape of the giant dipole resonance.

Therefore, $\alpha^2 = \frac{\tau_N^{stat}(E1)}{\tau_N(E1)}$

We have calculated values of τ_N^{stat} (E1) and α^2, using $U_i = 4$ MeV and 4.4 MeV for the 12^+ and 10^+ states respectively. These values are shown in Table II. The amplitude of the wavefunction in the ND well increases from 8.9×10^{-4} to 6.5×10^{-3} as the spin decreases from I = 12 to 10. Also shown are similar results for ^{152}Dy and ^{236}U. The values are 7.9×10^{-2} and 2.9×10^{-7}, respectively.

Table II. E1 lifetimes of superdeformed decay

	I	U(MeV)	τ_s(E2)	τ_N(E1)	τ_N^{stat}(E1)	α^2	log(Γ/D_n)
^{152}Dy	26	6	0.6 ps	0.09 ps	0.007 ps	$7.9\ 10^{-2}$	-1.5
^{192}Hg	12	4	5.2 ps	27.5 ps	0.024 ps	$8.9\ 10^{-4}$	-3.5
	10	4.4	13 ps	2.85 ps	0.019 ps	$6.5\ 10^{-3}$	-2.6
^{236}U	0	2.7	166 nsec	263 ns	0.075 ps	$2.9\ 10^{-7}$	-6.9

III. DISCUSSION

In a barrier penetration model, the amplitude of the wavefunction in the ND well is related to the barrier penetration width Γ and the level density of the normal deformed states. Using a model similar to that of ref. 3, we obtained

$$\Gamma/D_n = \pi/8\ \alpha^2$$

where D_n is the average spacing of ND states.

This result indicates that a large value of α could be the result of either a large barrier penetrability or a large level density, or both. The values of log(Γ/D_n) consistent with these results also are shown in Table II. Theoretical calculations[4] for ^{192}Hg indicate that from spin 12 to 10 the barrier penetrability increases by a factor of 3.3. When combined with the factor of 2.1 increase in the normally-deformed level density for I = 10 relative to I = 12 described in the preceding section, a total enhancement of a factor of 6.9 is predicted for α^2 of I = 10 relative to that for I = 12. The corresponding experimental ratio of α^2(I=10)/α^2(I=12) is 7.3; hence the agreement is excellent.

This analysis indicates that the "sudden" decay out of the SD well is due to three factors all of which favor decay to the normal deformed states at low spin. They are: 1) the reduction of inband SD E2 decay rate due to the lower E2 transition energy; 2) the increase of the ND statistical E1 transition rate due to the increase of excitation energy of the SD state relative to the ND yrast line; and more importantly, 3) the increase of the amplitude of the state in the ND well. The last factor is due to an increased barrier penetrability and a higher level density at lower spin.

Oak Ridge National Laboratory is managed by Martin Marietta Energy Systems, Inc., for the U.S. Department of Energy under Contract No. DE-AC05-84OR21400. Nuclear physics research at the University of Tennessee is supported by the U.S. Department of Energy under contract DE-FG05-87ER40361.

REFERENCES

1. E.F. Moore et. al. Phys. Rev. Lett. **64** (1990) 3127.
2. J.A. Becker et. al. Phys. Rev. **C41** (1990) R9.
3. E. Vigezzi et. al. Nucl. Phys. **A520** (1990) 179c, and private communication.
4. Y.R. Shimizu et. al. Phys. Letts. **B274** (1992) 253, and private communication.

LIFETIMES OF SUPERDEFORMED STATES IN ^{194}Pb

P. WILLSAU[1)], H. HÜBEL[1)], F. AZAIEZ[2)], M.A. DELEPLANQUE[2)], R.M. DIAMOND[2)], W. KORTEN[2)], A.O. MACCHIAVELLI[2)], F.S. STEPHENS[2)], H. KLUGE[3)], F. HANNACHI[4)], J.C. BACELAR[5)], J.A. BECKER[6)], M.J. BRINKMAN[6)], E.A. HENRY[6)], A. KUHNERT[6)], T.F. WANG[6)], J.A. DRAPER[7)], E. RUBEL[7)]

[1)] *Institut für Strahlen- und Kernphysik, Universität Bonn, D-5300 Bonn, Germany*
[2)] *Nuclear Science Division, Lawrence Berkeley Laboratory, Berkeley, California 94720, USA*
[3)] *Hahn-Meitner-Institut für Kernforschung, D-1000 Berlin, Germany*
[4)] *Centre de Spectrométrie Nucléaire et de Spectrométrie de Masse, F-91405 Orsay, France*
[5)] *Kernfysisch Versneller Instituut, Zernikelaan 25, 9747 AA Groningen, The Netherlands*
[6)] *Lawrence Livermore National Laboratory, Livermore, California 94550, USA*
[7)] *University of California, Davis, California 95611, USA*

The superdeformed (SD) rotational bands that have been found in the A=190 region all show very similar dynamical moments of inertia $J^{(2)}$ that rise by about 40% over the observed frequency range. This rise may be caused by an increase of the quadrupole deformation (e.g. by centrifugal stretching), by a gradual alignment of nucleons or by a decrease in pairing. The latter effects, which are probably correlated, require the presence of pair correlations in the SD states. It is important to decide this question experimentally by lifetime measurements. Since the SD bands in this mass region extend down to rather low spins and the transition energies at low and medium spin are small, the lifetimes of the states are of the order of a few *ps* down to a fraction of a *ps*. Doppler-shift methods can therefore be applied to determine their values. Recently, lifetimes of SD states in ^{192}Hg were measured by the Doppler-shift attenuation method (DSAM) (Moore *et al.*, 1990). The transition quadrupole moments derived from these lifetimes are rather constant, around 19 eb. They confirm the large deformation, which remains constant over the whole frequency range.

Here we report on a DSAM measurement of lifetimes of SD states in ^{194}Pb (Theine *et al.*, 1990; Hübel *et al.*, 1990; Brinkman *et al.*, 1990). High-spin states in this nucleus were populated in the reaction ^{150}Sm(^{48}Ca,4n) at the LBL 88-inch cyclotron with a beam energy of 205 MeV. A 1.1 mg/cm^2 thick metal Sm foil, enriched in ^{150}Sm, on a 10 mg/cm^2 gold backing was used as a target. The γ-rays were detected with the HERA spectrometer array consisting of 20 Compton-suppressed Ge detectors and an inner BGO ball with 32 elements. The analysis was based on 200×10^6 events with a requirement of at least 2 Ge detectors and 7 ball elements firing and a minimum sum

energy of 2.2 MeV.

The data were sorted into $\gamma\gamma$-coincidence matrices subdivided into the different angle groups of the Ge detectors: forward (37°) or backward (153°) detectors on the projection axes and any detector on the gate axes. Spectra were created by setting gates on the lowest members of the SD band (213 to 380 keV); these γ-rays were emitted by completely stopped nuclei. The spectra were added up in various combinations to get the cleanest spectra for the considered transitions.

The SD transitions above 380 keV show line shapes for which a DSAM analysis could be performed. To derive the lifetimes of the SD states a program package was used with Monte Carlo simulation for the path of the recoiling nuclei in the target and stopper, least squares fits to reproduce the experimental line shapes, and routines to solve Bateman's system of coupled differential equations (J. Gascon *et al.*, 1990). The intensities of the SD transitions and the contaminants as well as the quadrupole moments were simultaneously treated as free parameters in the fits. Only spectra from backward detectors were clean enough for line shape analysis. Side feeding intensities were neglected in the considered frequency range because of the intensity pattern of the band produced in a comparable reaction (Theine *et al.*, 1990; Hübel *et al.*, 1990). Fig. 1 shows two examples of fits to the 458 and 496 keV transitions. The results are summarized in the table. The transition quadrupole moments derived from the lifetimes using the rotational model expression (Bohr and Mottelson, 1975) are displayed as a function of the rotational frequency in fig. 2.

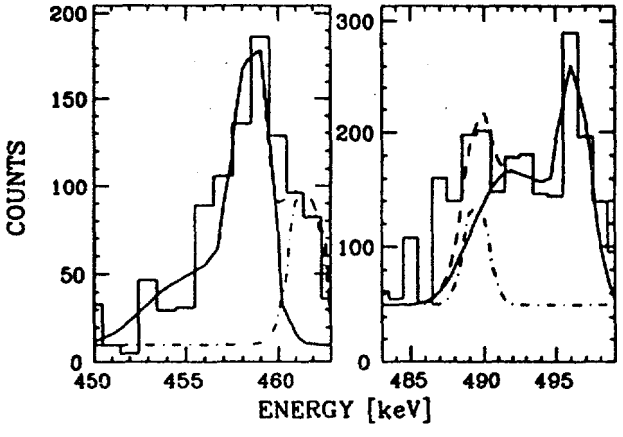

Fig. 1. DSAM fits to the 458 and 496 keV SD transitions in ^{194}Pb measured by the backward detectors. Solid line: fitted line shape; dot-dashed line: fitted contaminant; dashed line: line shape plus contaminant (total fit).

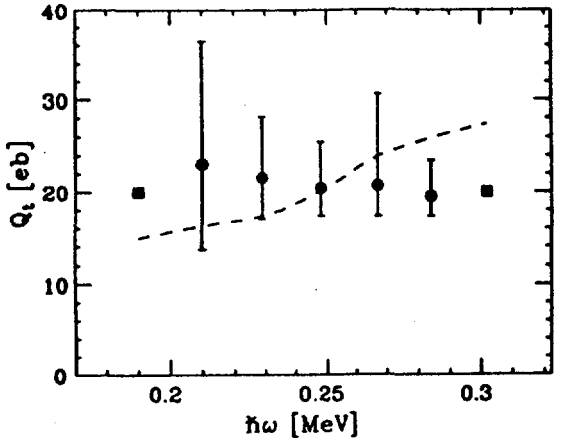

Fig. 2. Experimental transition quadrupole moments of SD states in ^{194}Pb as a function of rotational frequency. Dashed curve: calculated quadrupole moments assuming that the increase in $J^{(2)}$ is due only to centrifugal stretching.

Table. Experimental lifetimes and transition quadrupole moments of SD states in ^{194}Pb.

$E_\gamma[keV]$	$\tau[ps]$	$Q_t[eb]$
≤ 380	> 0.7	
419	$0.31^{+0.27}_{-0.37}$	$23.8^{+13.5}_{-10.0}$
458	$0.26^{+0.10}_{-0.17}$	$21.1^{+6.5}_{-4.5}$
496	$0.19^{+0.06}_{-0.07}$	$20.3^{+3.7}_{-3.3}$
533	$0.12^{+0.05}_{-0.14}$	$20.8^{+10.0}_{-4.0}$
568	$0.10^{+0.03}_{-0.05}$	$19.5^{+4.5}_{-2.5}$

Within the experimental uncertainties the quadrupole moments are constant over the whole frequency range. The point at the highest frequency (square) was not obtained from a fit, but represents the quadrupole moment that was used as an input parameter in the fits to the line shapes of the transitions of the lower states. The 380 keV transition shows no line shape. This would be the case, if the quadrupole moment was around 20 eb or smaller and is indicated by the square at the low frequency end.

The dynamical moments of inertia $J^{(2)}$ of the SD bands in the A=190 region show a steady increase with increasing rotational frequency. The dashed curve in fig. 2 indicates the slope of the quadrupole moments that would be obtained if the observed (Theine *et al.*, 1990; Hübel *et al.*, 1990; Brinkman *et al.*, 1990) increase in $J^{(2)}$ in ^{194}Pb was due only to centrifugal stretching (Moore, 1991). Since it is not in agreement with the data we may conclude that the deformation of the SD band in ^{194}Pb, as in the previously investigated band in ^{192}Hg (Moore *et al.*, 1990) remains stable and the increase of the $J^{(2)}$ moment of inertia is probably due to an alignment effect rather than to centrifugal stretching.

The target was fabricated by J. Heagney. This work was supported by the U.S. Departement of Energy.

REFERENCES

Bohr, A. and B. Mottelson (1975) *Nuclear Structure, Vol. II.* Benjamin, Reading, MA.

Brinkman, M.J. *et al.* (1990). Superdeformation in lead nuclei. *Z. Phys.* **A336**, 115.

Gascon, J. *et al.* (1990). Configuration-dependent transition rates in ^{157}Ho. *Nucl. Phys.* **A513**, 344.

Hübel, H. *et al.* (1990). Superdeformation in ^{194}Pb. *Nucl. Phys.* **A520**, 125c.

Moore, E.F. *et al.* (1990). Lifetime measurements in the superdeformed band of ^{192}Hg. *Phys. Rev. Let.* **64**, 3127.

Moore, E.F. (1991). Private communication.

Theine, K. *et al.* (1990). Superdeformation in ^{194}Pb. *Z. Phys.* **A336**, 113.

INTERNATIONAL CONFERENCE ON NUCLEAR STRUCTURE AT HIGH ANGULAR MOMENTUM

Ottawa

Session 2: Superdeformation in Nuclei (II)

NEW VISTAS IN SUPERDEFORMATION

W. Nazarewicz*
Joint Institute for Heavy-Ion Research, Holifield Heavy Ion Research Facility,
P.O. Box 2008, Oak Ridge, Tennessee 37831, U.S.A.

1. INTRODUCTION

The issue of nuclear shape coexistence, or nuclear superdeformation dates back to the mid-fifties; see the recent review[1]. Already in 1956 Morinaga[2] interpreted the deformed band in ^{16}O built upon the $I^\pi=0^+$ state at 6.049 MeV in terms of deformed $4p$–$4h$ configuration†. Another early example of multiple shape coexistence is the spectrum of ^{40}Ca with two well-deformed bands associated with $4p$–$4h$ and $8p$–$8h$ states at 3.352 MeV and 5.213 MeV, respectively[4].

In heavy nuclei, three regions of superdeformed (SD) shapes have been established: fission isomers in actinides, high spin SD states around ^{152}Dy, and SD bands around ^{192}Hg. An impressive experimental and theoretical effort has been devoted to exploring the underlying physics. There is no doubt that these investigations have opened up a new exciting field of nuclear superdeformed spectroscopy.

In this short contribution I would like to concentate on several aspects of nuclear superdeformation. The area of interest is so huge, and the space available is so limited, that a dramatic selection of the material had to be made. Some issues, such as the structure of collective excitations built on SD states, new symmetries of SD states, new predictions, etc., have been covered in other contributions to this Conference (Dudek, Matsuyanagi, Skalski, Delaroche, Sugawara-Tanabe, and others).

2. HYPERDEFORMATIONS

Hyperdeformed nuclei, i.e., with quadrupole deformations significantly larger than β_2=0.6 are known or predicted in several mass regions.

Good examples of very elongated configurations can be found in light nuclei. For example, the hyperdeformed state in ^{12}C (three aligned alpha particles) built on the 0^+ resonant state at 10.3 MeV becomes yrast already $I^\pi=4^+$. The calculated low-lying reflection-asymmetric hyperdeformed minimum (ε_2=1, ε_3=0.3) in ^{24}Mg[5] can be associated with the asymmetric ^{16}O+α+α (or ^{16}O+^{8}Be) structures or the symmetric hyperdeformed α+^{16}O+α states[6]. Other examples are the hyperdeformed states in ^{36}Ar (^{16}O+^{16}O+α),^{48}Cr (^{16}O+^{16}O+^{16}O) (see discussion in ref.[7]), or a six-α chain structure in ^{24}Mg reported by Wuosmaa *et al.*[8], and see the contribution by R.R. Betts.

In heavy nuclei the best hyperdeformed states are the so-called third minima in nuclei around ^{232}Th. In these nuclei the second saddle point is split leading to the weak reflection-asymmetric minimum with $\beta_2\sim$0.85, $\beta_3\sim$0.35[9-11]. Experimentally, the third minimum shows

*On leave of absence from the Institute of Theoretical Physics, Warsaw University.

†For the $4\hbar\omega$ shell model calculations for ^{16}O, see ref.[3] and the contribution by W.C. Haxton.

up as an alternating-parity microstructure of resonances near the (n,f) fission thereshold[12]. Recent calculations based on the Gogny–HF model[13] or the Woods–Saxon model[14] predict the the third minima to be deeper than in the previous calculations based on the Nilsson model[11]. Figure 1 displays the Woods–Saxon potential energy surface for ^{232}Th. The heights of the

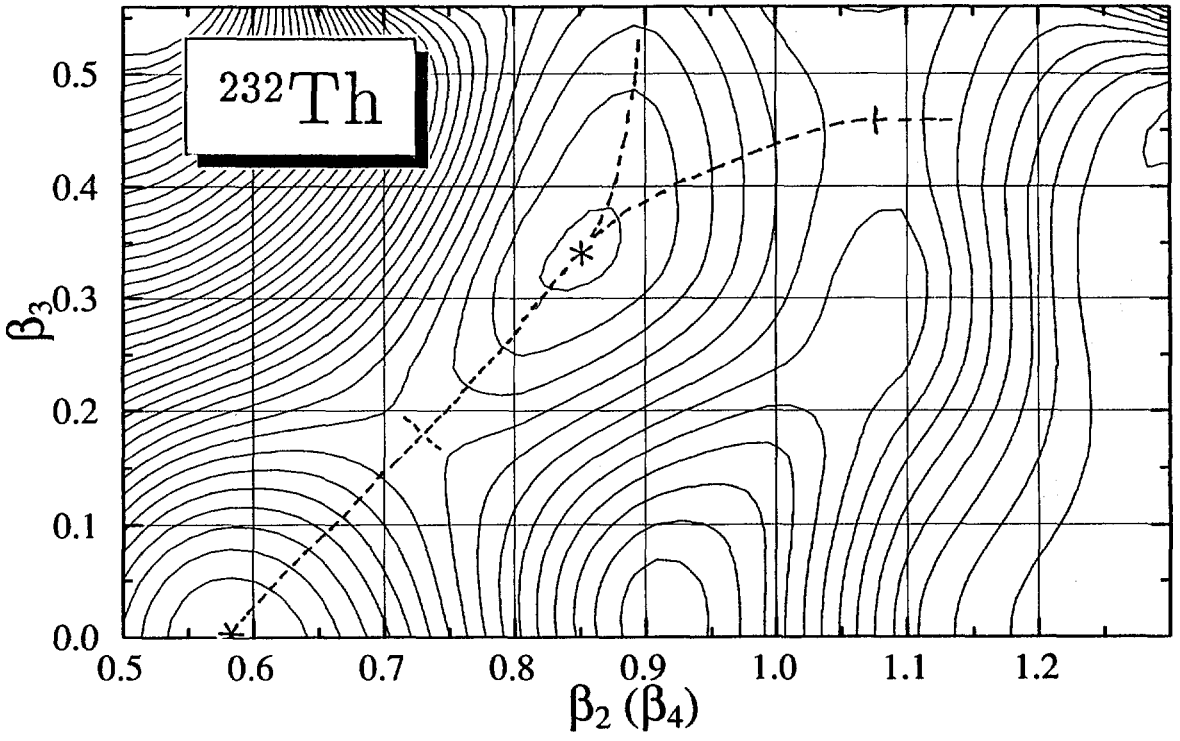

Fig. 1. The Woods–Saxon–Strutinsky total potential energy for ^{232}Th as a function of β_2 and β_3. At each (β_2, β_3) point the energy was minimized with respect to β_4–β_6. The distance between the contour lines is 0.5 MeV. (From ref.[14].)

second and third barrier (saddle point) are 1.4 MeV and 2.9 MeV, respectively. This should be compared with the value of ~400 keV from ref.[11].

For recent evidence for hyperdeformation in ^{152}Dy around I=80 $\hbar$; see the contribution by A. Galindo–Uribarri *et al.*.

3. SUPERDEFORMATIONS FAR FROM STABILITY

According to the model predictions (see, e.g., refs.[15, 16]) low–lying super and hyperdeformed configurations are expected in various mass regions, many of them being practically inaccessible with the present detector systems (too low cross sections), or inaccessible at all using combinations of stable beams and targets. Some of those "white spots" will, hopefully, be investigated in the future – thanks to the new–generation multidetector arrays (EUROGAM, GAMMASPHERE, EUROBALL), or exotic (radioactive) ion beam facilities currently being constructed in Europe, U.S.A., and Japan.

According to predictions of the mean field theory nuclei in the N=Z≃40 mass region favor 2:1 shapes. This tendency remains at high spins, and superdeformed configurations in nuclei around $^{82}_{38}Sr_{44}$ or $^{88}_{44}Ru_{44}$ are predicted to be yrast at spins ∼30–40 $\hbar$[17–20]. Interestingly, cranked Skyrme Hartree–Fock calculations, cranked Woods–Saxon calculations, and cranked calculation based on the relativistic mean field theory give rather similar results. Since neutron and proton numbers are rather close, the neutron and proton SD configurations are similar, corresponding to the alignment of one or two $1h_{11/2}$ protons and neutrons. At very high spins also the lowest $1i_{13/2}$ orbitals become occupied. On the neutron rich side, the best prospects for superdeformation are expected to be in nuclei around $^{108}_{44}Ru_{64}$. Indeed, by combining the SD gaps at Z=44 and N=64 one obtains very favored SD structure which becomes yrast around I=35 $\hbar$[20, 21].

Very little is known about the very neutron–deficient Hg nuclei with N∼96. The lightest system known from in–beam studies is ^{180}Hg[22]. The nucleus ^{178}Hg has lifetime τ∼49 s whilst for ^{176}Hg τ drops to 34 ms (see ref.[23]), and ^{174}Hg is expected to be proton–unstable.

The potential energy surfaces for ^{170}Hg (proton unstable), ^{180}Hg (τ=5.9 s), ^{190}Hg (τ=20 m),

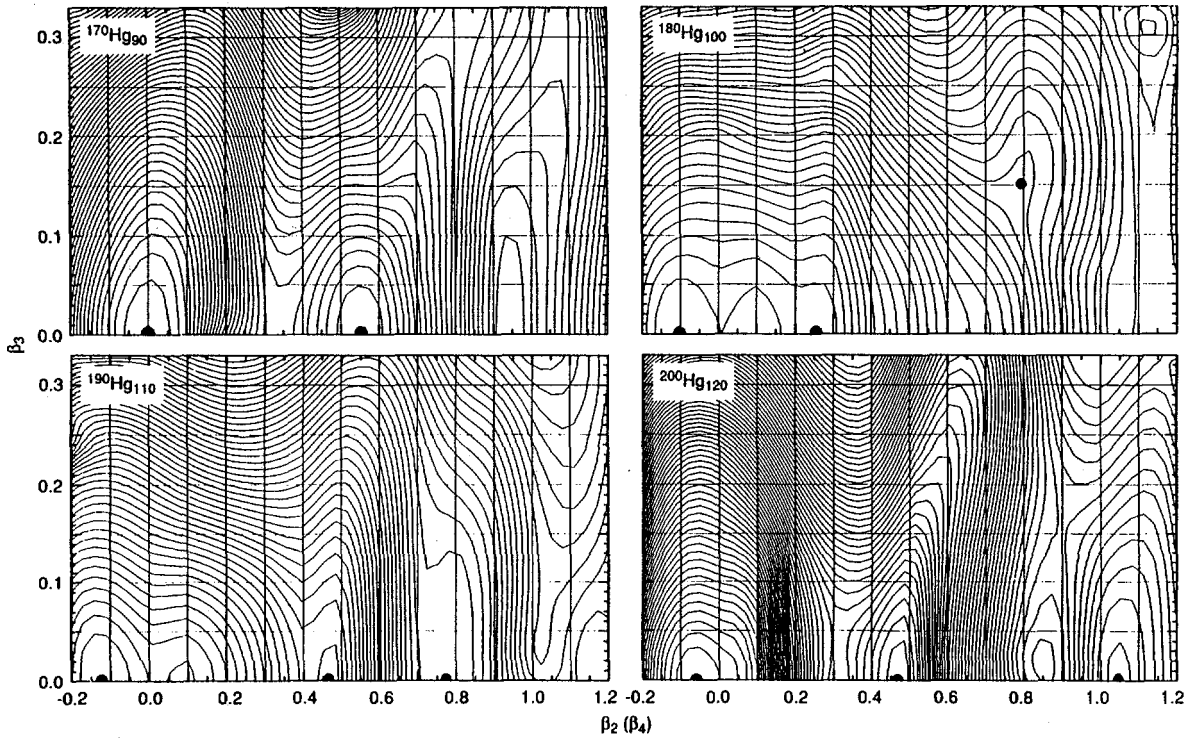

Fig. 2. The Woods–Saxon–Strutinsky total potential energy for ^{170,180,190,200}Hg as a function of β_2 and β_3. At each (β_2, β_3) point the energy was minimized with respect to β_4–β_8. The distance between the contour lines is 0.3 MeV.

^{200}Hg (stable), are shown in fig. 2. The SD minimum seen in ^{190,200}Hg disappears in ^{180}Hg[‡].

[‡]Note the presence of reflection–symmetric hyperdeformed minima in ^{190}Hg (β_2∼0.8), ^{200}Hg (β_2∼1.05), and

However, when decreasing neutron number the SD states reappear again; see the map for ^{170}Hg. Detailed calculations presented in fig. 3 indicate that the excitation pattern of low–deformation

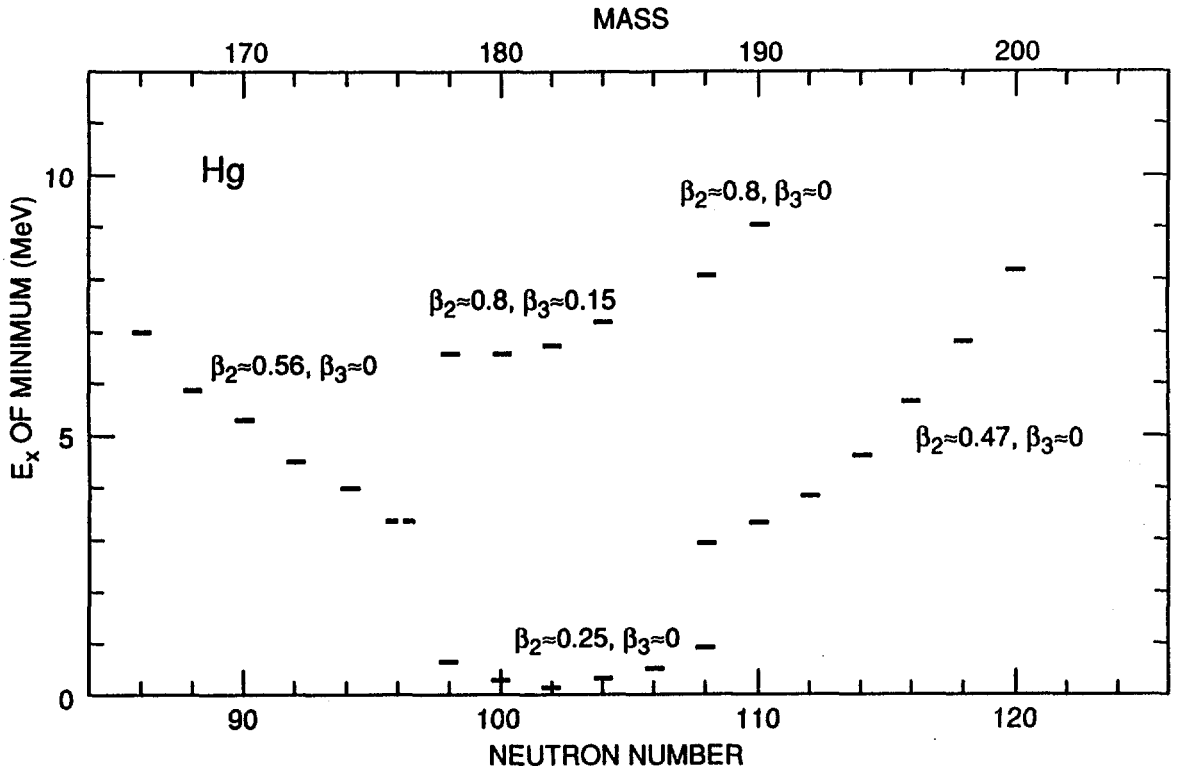

Fig. 3. Calculated energies of excited shape–coexisting states in even–even Hg isotopes with $86\leq N\leq 120$.

shape–coexisting configurations and SD states is symmetric with respect to the middle of the shell, i.e., N$\sim$102. A similar situation has also been calculated for Pt and Pb isotopes.

A new region of hyperdeformed shapes has been predicted around ^{120}Ce[24]. These structures involve N=6 protonns and N=7 neutrons and are expected to become yrast around I=50 $\hbar$.

As discussed in the proposal for the Oak Ridge Radioactive Ion Beam Facility RIB[25], the new beams at RIB will provide the necessary tools to access high-spin states in the N=Z$\simeq$ 40 mass region, the region around ^{120}Ce, and around ^{176}Hg; see the contribution by J.D. Garrett.

4. EFFECTIVE INTERACTIONS, EFFECTIVE OPERATORS

The structure of single–particle states around the Fermi level in SD nuclei is significantly different from the pattern familiar from normal deformations. Indeed, the SD supershells consist of states with very different spatial character. Consequently, the commonly used effective and residual interactions are probably different in the superdeformed world.

reflection–asymmetric hyperdeformed minima in ^{180}Hg ($\beta_2\sim0.8$, $\beta_3\sim0.15$).

It is well known that the low and high–frequency nuclear vibrations can be associated with the residual multipole–multipole interactions. Do the standard multipole–multipole forces describe correctly collective excitations at SD shapes? Sakamoto and Kishimoto[26, 27] have introduced the doubly–stretched multipole moments,

$$Q''_{\lambda K} = f_{\lambda K}(r'')Y_{\lambda K}(\Omega''), \quad x''_i \equiv \frac{\omega_i}{\omega_o}x_i, \ (i = 1, 2, 3), \tag{1}$$

where ω_i is the i–th oscillator frequency. The corresponding multipole–multipole doubly–stretched interaction can be viewed as an improved conventional multipole–multipole force. Firstly, it satisfies the nuclear–selfconsistency rigorously even if the system is deformed. Secondly, it yields the zero–energy RPA spurious modes, i.e., it automatically separates the translational (λ=1, T=0) and reorientation (λ=2, K=1, T=0) modes. Last but not least, for the doubly–stretched interaction the coupling between octupole and dipole modes disappears.

At normal deformations, the spatial difference between doubly–stretched and normal multipole–multipole forces is rather small. At large deformations, however, these interactions give markedly different predictions[26, 27]. For instance, the presence of large dipole moments (or enhanced B(E1) rates at SD shapes) is a direct consequence of the doubly–stretched octupole force. The K=0 and K=1 $(r^3Y_{3K})''$ operators are linear combinations of the ordinary octupole fields, r^3Y_{3K} and the compressional dipole fields, r^3Y_{1K}[28]. Again, if the doubly–stretched residual interaction is realised in nature, strong dipole transitions de-exciting superdeformed octupole states should be present. For more discussion, see the contributions by K. Matsuyanagi and J. Skalski.

The influence of large shape-elongations on the pairing field is still not well understood. For example, in the "doubly-magic" SD nucleus ^{152}Dy pairing is expected to play a minor role[29–32]. Indeed, due to the very low level density of single-particle states the superfluid-type correlations in this band are expected to be seriously quenched and mainly of a dynamical character. In ^{150}Gd the large increase of thy dynamical moment of inertia, $\Im^{(2)}$, in the lower part of SD band[33] has been interpreted as a *paired* band crossing associated with an alignment of the N=7 neutron pair[34, 31]. A similar crossing has been found in the first excited SD band in ^{149}Gd[35]. Another piece of experimental evidence suggesting the presence of pairing at SD shapes is a steady increase of $\Im^{(2)}$ in the SD bands in the A$\sim$190 region, which can be attributed[36, 37] to the alignment of N=7 neutrons and N=6 protons. Calculations without pairing yield fairly constant moments of inertia.

However, there are also many pieces of evidence that pairing correlations are extremely weak at large elongations. For instance, the moments of inertia in SD bands are very close to their rigid-body values and even a strongly reduced pairing field yields too strong quasiparticle alignment[37, 38]. Moreover, only very weak evidence for blocking effects in SD configurations has been found in the A$\sim$190 region[39].

Let us consider the general pairing interaction

$$H_{pair} = -\sum_{i,j,k,l} G_{ij;kl}c_i^+c_j^+c_{\bar{l}}c_k, \tag{2}$$

where $G_{ij;kl} = < i\bar{j}|v|k\bar{l} >_{AS}$ is the antisymmetrized matrix element of the two-body pairing interaction. The matrix elements $G_{ij;kl}$ have been calculated by many authors using various

residual interactions like the delta force, the surface delta interaction, the Skyrme force, the finite-range D1S interaction, or a density dependent delta interaction[40–43] (see also refs.[44, 45]). It has been found that the pairing matrix elements are relatively enhanced for orbitals with similar values of $\langle n_z \rangle / \langle N \rangle$, i.e., orbitals with good angular overlap. In particular, it has been observed that the pairing matrix elements between the high-j intruder orbitals (such as [660]1/2 and [651]3/2) are rather large, as are those between high-j intruder states and the natural-parity orbitals with j=N–1 and similar Ω-values (such as [660]1/2 and [541]1/2). At normal deformations the single-particle unique-parity orbitals are relatively close to each other and to normal-parity states with similar spatial overlap. However, at large deformations states originating from completely different shells approach the Fermi level. These states are very weakly coupled through pairing interaction. Moreover, the "favored" coupling between unique-parity levels is diminished because of their large deformation splitting. In view of the above it is likely that the pairing correlation energy should decrease with deformation – an effect that is analogous to the fragmentation of pairing matrix elements caused by the Coriolis force.

A simple parametrization of the particle–particle interaction is usually based on the multipole expansion. Usually, only the monopole term (seniority pairing) is considered since for the delta force the L=0 component is about five times stronger than the L=2 (quadrupole) term[46]. At superdeformed shapes, however, most single–particle orbits close to the Fermi level are, on the average, of definite prolate character. That suggests that the quadrupole pairing interaction should play an important role. In particular, it is expected, that the inclusion of quadrupole pairing should shift the crossing frequency towards higher values[47] – a welcome effect in light of the recent data on SD band ^{192}Hg[38] (as shown in the contribution by R.V.F. Janssens). The previously obtained good fit for the dynamical moment of inertia[48] can easily be retained by adjusting the relative strengths of the L=0 and L=2 (M=0,1,2) components[47]. Preliminary results of calculations involving the quadrupole pairing interaction by R. Wyss[49] are very encouraging.

A new area of interest concerns spin polarization and the structure of the magnetic moment operator at large deformations. The measurement of the g factor of the fission isomer in ^{237}Pu[50] has put strict limits on the parameters of existing mean-field-based models: the value $g = -0.45(3)$ indicates that the parameters of the deformed single-particle potential exhibit a significant deformation dependence[51]. The intrinsic spin g-factors are usually reduced with respect to their free values to account for spin polarization of the core, i.e. g_s=$f g_s^{free}$, with f typically varying between 0.6 and 0.7 at normal deformations. However, for large elongations, the spin polarization may make contributions to the magnetic moments that cannot be simply accounted for in terms of the renormalization of the free values. Indeed, the spin-polarization effect in spin-unsaturated orbitals due to an odd particle is associated with the spin-dependent components of the effective nucleon-nucleon force, e.g., the spin-spin interaction[52]. The renormalization of g_s is, in the first order, due to the spin interaction between spin-orbit partners with j=l±1, and should exhibit a deformation dependence. Moreover, even within first-order perturbation theory, one can argue that spin- and isospin-dependent nuclear forces may lead to a renormalization of the orbital g_l factors and the presence of the tensor component[52, 53], which is expected to have a significant deformation dependence.

4. SPIN ASSIGNMENTS AND IDENTICAL BANDS

Parametrization of rotational spectra dates back to more than thirty years ago when Bohr and Mottelson used a phenomenological formula to characterize properties of rotational bands[54]. Later on, extended and revised versions of this early formalism were used to classify collective properties of the *ground state bands* in a wide range of nuclei[55, 56]. The problem of spectral fitting has recently been revisited in the context of the superdeformed bands in the Hg region[57]. Although a large number of high-spin superdeformed bands have been found around the doubly-magic SD ^{152}Dy and ^{192}Hg nuclei, their *absolute* spin assignments are so far lacking. This is because of the fact that the gamma rays that connect the SD bands to the known levels at lower spins have not been identified experimentally[§]. The correct angular momentum assignment has become a central issue after the discovery of *twinned bands* (i.e., bands having identical transition energies) in neighboring odd and even nuclei[58, 59].

In refs.[60, 61] a detailed analysis of the spin-fitting procedure has been made and several criteria have been introduced that are crucial for a meaningful spin assignment. The relative alignments of the twinned SD bands in the Hg region have been then obtained from a power-series expansion of angular momenta in terms of the measured transition energies.

Subsequent studies of such fitting procedures have pointed out[62, 63] that, because of the lack of knowledge about the low-lying transitions in the SD bands, the fitted spins are subject to uncertainties. In a recent ref.[64] it has been pointed out that possible presence of a non-zero initial alignment, i_o, can lead to a serious uncertainty in the absolute-spin determination of the *excited bands*. Since this quantity *cannot* be determined from a least-squares fitting procedure, the above fitting formalisms could yield incorrect spins, despite the superb quality of these fits as judged by their χ^2 values. The problem of non-zero initial alignment was recognized in refs.[65, 60]. However, the authors assumed a zero value as being the most plausible choice at superdeformed shapes where the deformation alignment (strong coupling) dominates. As briefly discussed in[62, 63], this problem seriously limits the applicability of the suggested fitting formalisms to the excited bands, which can potentially have non-zero initial alignments. Results of our extensive investigation of this problem in the normally-deformed excited bands where spins are known show that: (i) the fitting procedure oftentimes leads to wrong spin assignments even if γ-ray energies of all low-lying members of the band are known; (ii) there is no simple relationship between the angular momentum obtained from the optimization procedure and the experimentally determined spins; and (iii) the fitted spins are usually dependent on which data points are included in the fitting procedure.

Recently, several models have been proposed to explain identical SD bands, as well as the alignment patterns that have been obtained from phenomenological spin-fitting procedures, despite the problems alluded above. Among them are microscopic models based on the mean field approach (Hartree-Fock, Nilsson-Strutinsky) or the shell model (pseudo-SU_3 model, Fermion Dynamical Symmetry Model), formulas obtained from the symmetry limits of specific group theoretical models (Interacting Boson Model, supersymmetric schemes, models based on quantum groups), or other scenarios (triplet pairing). A critical review of several of the models

[§]As we have learnt during this Conference, such a connection has just been found in the nucleus ^{143}Eu, see the contribution by A. Ataç *et al.*

and scenarios that purport to explain the origin of the identical bands, or the patterns of the fitted alignments has also been presented in ref.[64]. It has been concluded that many of these formulations can be reduced to simple expressions for energies which strongly resemble the standard VMI model. However, a large majority of these models either explicitly *assume* identical moments of inertia, or *impose* an ad hoc symmetry on the model Hamiltonian to obtain the desired outcome of identical bands. Similarly, gross approximations made by some other models cast serious doubts on their ability to address such subtle effects as the constancy of moments of inertia. In spite of many efforts and new and interesting ideas and suggestions, none of the scenarios proposed so far addresses the fundamental question at hand, namely the microscopic origin of identical moments of inertia that have been observed in a wide range of normally–deformed and superdeformed nuclei. A more complete discussion is given in the contribution by C. Baktash.

Acknowledgements The author would like to thank P. Semmes for useful comments. The Joint Institute for Heavy Ion Research has as member institutions the University of Tennessee, Vanderbilt University, and the Oak Ridge National Laboratory; it is supported by the members and by the Department of Energy through Contract Number DE–FG05–87ER40361 with the University of Tennessee. This work was also partly supported by the Polish Committee for Scientific Research (KBN).

REFERENCES

1. J.L. Wood *et al.*, Phys. Rep. (1992) in print.
2. H. Morinaga, Phys. Rev. **101**, 254 (1956).
3. W.C. Haxton and C. Johnson, Phys. Rev. Lett. **65**, 1325 (1990).
4. R.W. Bauer *et al.*, Phys. Lett. **14**, 129 (1965).
5. G.A. Leander and S.E. Larsson, Nucl. Phys. **A239**, 93 (1975).
6. H. Flocard *et al.*, Prog. Theor. Phys. **72**, 1000 (1984).
7. W.D.M. Rae and A.C. Merchant, Phys. Lett. **B279**, 207 (1992).
8. A.H. Wuosmaa *et al.*, Phys. Rev. Lett. **68**, 1295 (1992).
9. V.V. Pashkevich, Nucl. Phys. **A169**, 275 (1971).
10. P. Möller, Nucl. Phys. **A192**, 529 (1972).
11. R. Bengtsson *et al.*, Nucl. Phys. **A473**, 77 (1987).
12. J. Blons, Nucl. Phys. **A502**, 121c (1989).
13. J.F. Berger, M. Girod and D. Gogny, Nucl. Phys. **A502**, 85c (1989).
14. S. Ćwiok *et al.*, *to be published.*
15. T. Bengtsson *et al.*, Phys. Scr. **24**, 200 (1981).
16. S. Åberg, H. Flocard and W. Nazarewicz, Ann. Rev. Nucl. Part. Sci. **40**, 439 (1990).
17. W. Nazarewicz *et al.*, Nucl. Phys. **A435**, 397 (1985).

18. P. Bonche, H. Flocard, and P.-H. Heenen, Nucl. Phys. **A523**, 300 (1991).
19. W. Koepf and P. Ring, Nucl. Phys. **A511**, 279 (1990).
20. S. Åberg, Nucl. Phys. **A520**, 35c (1990).
21. J. Skalski and W. Nazarewicz, to be published.
22. G.D. Dracoulis *et al.*, Phys. Lett. **208B**, 365 (1988).
23. J.R.H. Schneider *et al.*, Z. Phys. **A312**, 21 (1983).
24. R. Wyss and W. Nazarewicz, to be published.
25. *A Proposal for Physics with Exotic Beams at the Holifield Heavy Ion Research Facility*, ed. by J.D. Garrett and D.K. Olsen, Physics Division, ORNL, February 1991.
26. H. Sakamoto and T. Kishimoto, Nucl. Phys. **A501**, 205 (1989).
27. H. Sakamoto and T. Kishimoto, Nucl. Phys. **A501**, 242 (1989).
28. S. Mizutori, Y.R. Shimizu, and K. Matsuyanagi, Prog. Theor. Phys. **85**, 559 (1991); Prog. Theor. Phys. **86** (1991).
29. Y.R. Shimizu, E. Vigezzi and R.A. Broglia, Phys. Lett. **198B**, 33 (1987).
30. J. Dudek *et al.*, Phys. Rev. **C38**, 940 (1988).
31. W. Nazarewicz, R. Wyss and A. Johnson, Nucl. Phys. **A503**, 285 (1989).
32. Y.R. Shimizu, E. Vigezzi and R.A. Broglia, Nucl. Phys. **A509**, 80 (1990).
33. P. Fallon *et al.*, Phys. Lett. **218B**, 137 (1989).
34. W. Nazarewicz, R. Wyss and A. Johnson, Phys. Lett. **225B**, 208 (1989).
35. B. Haas *et al.*, Phys. Rev. **C42**, R1817 (1990).
36. D. Ye *et al.*, Phys. Rev. **C41**, R13 (1990).
37. M.A. Riley *et al.*, Nucl. Phys. **A512**, 178 (1990).
38. T. Lauritsen *et al.*, Phys. Lett. **B279**, 239 (1992).
39. P. Fallon *et al.*, Phys. Lett. **B276**, 427 (1992).
40. R.R. Chasman, Phys. Rev. **C14** (1976) 1935.
41. R.R. Chasman *et al.*, Rev. Mod. Phys. **49**, 833 (1977).
42. J. Dobaczewski, H. Flocard and J. Treiner, Nucl. Phys. **A422**, 103 (1984).
43. S.J. Krieger *et al.*, Nucl. Phys. **A517**, 275 (1990).
44. D. Glas and U. Mosel, Nucl. Phys. **A216**, 563 (1973).
45. R.E. Griffin, A.D. Jackson and A.B. Volkov, Phys. Lett. **36B**, 281 (1971).
46. A.M. Lane, *Nuclear Theory* (Benjamin, New York, 1964).
47. M. Diebel, Nucl. Phys. **A419**, 221 (1984).
48. E.F. Moore *et al.*, Phys. Rev. Lett. **64**, 3127 (1990).
49. R. Wyss, Annual Report, Physics Division, ORNL 1991.

50. M.H. Rafailovich *et al.*, Phys. Rev. Lett. **48**, 982 (1982).

51. J. Dudek, W. Nazarewicz and A. Faessler, Nucl. Phys. **A412**, 61 (1984).

52. A. Bohr and B.R. Mottelson, *Nuclear Structure*, vol. 2 (W.A. Benjamin, New York, 1975).

53. I. Hamamoto, Phys. Lett. **61B**, 343 (1976).

54. A. Bohr and B.R. Mottelson, Kg. Danske Videnskab. Selskab, Mat.–Fys. Medd. **27**, No. 16 (1953).

55. S.M. Harris, Phys. Rev. **138**, B509 (1965).

56. M.A.J. Mariscotti, G. Scharff–Goldhaber, and B. Bruck, Phys. Rev. **178**, 1864 (1969).

57. J.A. Becker *et al.*, Nucl. Phys. **520**, 187c (1990).

58. T. Byrski *et al.*, Phys. Rev. Lett. **64**, 1650 (1990).

59. F.S. Stephens *et al.*, Phys. Rev. Lett. **64**, 2623 (1990); Phys. Rev. Lett. **65**, 301 (1990).

60. J.E. Draper *et al.*, Phys. Rev. **C42**, R1791 (1990).

61. J.A. Becker *et al.*, preprint (1991).

62. C.–L. Wu, D.H. Feng and M.W. Guidry, Phys. Rev. Lett. **66**, C1377 (1991).

63. R. Wyss and S. Pilotte, Phys. Rev. **C44**, R602 (1991).

64. C. Baktash, W. Nazarewicz and R. Wyss, Nucl. Phys. **A** (submitted).

65. J.A. Becker *et al.*, Phys. Rev. **C41**, R9 (1990).

DECAY OUT OF THE SUPERDEFORMED BAND IN ^{143}Eu

A. Ataç[a], M. Piiparinen[a,1], B. Herskind[a], J. Nyberg[a,2], G. Sletten[a], G. de Angelis[b], S. Forbes[c], N. Gjørup[a], G. Hagemann[a], F. Ingebretsen[d], H. Jensen[a], D. Jerrestam[e], H. Kusakari[a], R. Lieder[a], G. M. Marti[f], S. Mullins[c], D. Santonocito[a], H. Schnare[f], K. Strähle[f], M. Sugawara[a], P. O. Tjøm[d], A. Virtanen[a] and R. Wadsworth[g]

[a] *The Niels Bohr Institute, University of Copenhagen, Copenhagen, Denmark.*
[b] *Laboratori Nazionali di Legnaro, Legnaro, Italy.*
[c] *Oliver Lodge Laboratory, University of Liverpool, Liverpool, U.K.*
[d] *Department of Physics, University of Oslo, Oslo, Norway.*
[e] *The Studsvik Science Laboratory, Nykøbing, Sweden.*
[f] *Institut für Kernphysik, Jülich, Germany.*
[g] *Department of Physics, University of York, York, U.K.*

During the last years, more than 33 SD bands have been observed at very high spins in various mass regions (see e.g. review articles ref. 1,2 and ref.3). In all cases studied so far the connection between the SD and the normal-deformed (ND) states has been unknown, most probably due to a highly fragmented decay path out of the SD bands. This has left the spin, the parity and the excitation energy of the SD bands undetermined. In this paper we are presenting results of a new experimental approach where we take advantage of triple and higher fold coincidences to study the decay out of a SD band. The method provides us with an excitation energy and spin assignment for a SD band for the first time.

It is known from previous works[1,2)] that the feeding out of a SD band starts from a few of the lowest lying observed states of the band and ends in a few near yrast ND states. We assume that a large fraction of the decay proceeds through cascades of only two transitions. Due to the high level density there are a large number of intermediate levels in the cascade, but the sum of the two consecutive γ-ray energies has a well defined value. In the triple coincidence events we set a gate on one γ-ray transition of the SD band and sum up the two other γ-ray energies to produce a sum spectrum. In this spectrum we would like to identify discrete peaks related to the deexcitation of the SD band.

[1]Permanent address: Dept. of Physics, Univ. of Jyväskylä, Jyväskylä, Finland
[2]Permanent address: The Svedberg Lab., Univ. of Uppsala, Uppsala, Sweden

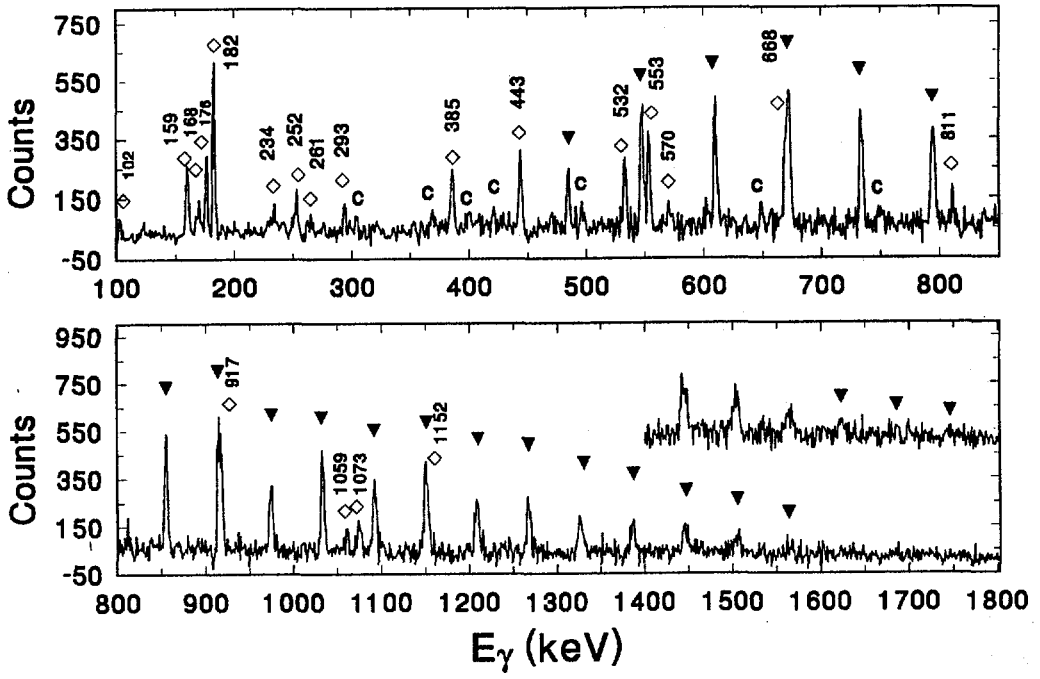

Fig.1: Gamma-ray spectrum coincident with two SD band members. The band members with energies 483.7, 546.5, 609.3, 671.7, 732.9, 793.9, 854.1, 913.3, 972.9, 1031.8, 1090.7, 1148.6, 1207.6, 1266.0, 1325.0, 1384.3, 1443.8, 1503.1, 1563.5, 1623, 1684, 1743 keV (errors ranging from 0.2 keV for the strongest transitions up to 2 keV for the weakest peaks) are marked by (▼) and known ND states in ^{143}Eu are denoted by (◇). Contaminations from ^{140}Pm, ^{142}Eu and ^{144}Eu are indicated by (C). The spectrum is shown with a background subtraction and it is corrected for the detector efficiencies. The insert is a sum of all double gated spectra with both gates on the SD band members. The highest energy transitions are enhanced in this spectrum.

The experiment was carried out at the Niels Bohr Institute Tandem Accelerator Laboratory using the NORDBALL detector array which consisted of 19 Compton-suppressed Ge detectors, 1 Ge LEP detector and a BaF_2 inner ball for multiplicity and sum energy selection. The states in ^{143}Eu were populated by the reaction ^{110}Pd(^{37}Cl,4n)^{143}Eu at a beam energy of 160 MeV. About 10^9 triple and higher fold events were collected during the experiment, 10% of them being 4-fold Ge-coincidences.

Fig.1 shows a double gated γ-ray spectrum with both gates on transitions of the SD band. The spectrum is a sum of 42 gate combinations and shows the SD band with twenty two members. Twenty of them were previously reported[4)] and assigned to ^{142}Eu. However, our results which were obtained with the same reaction

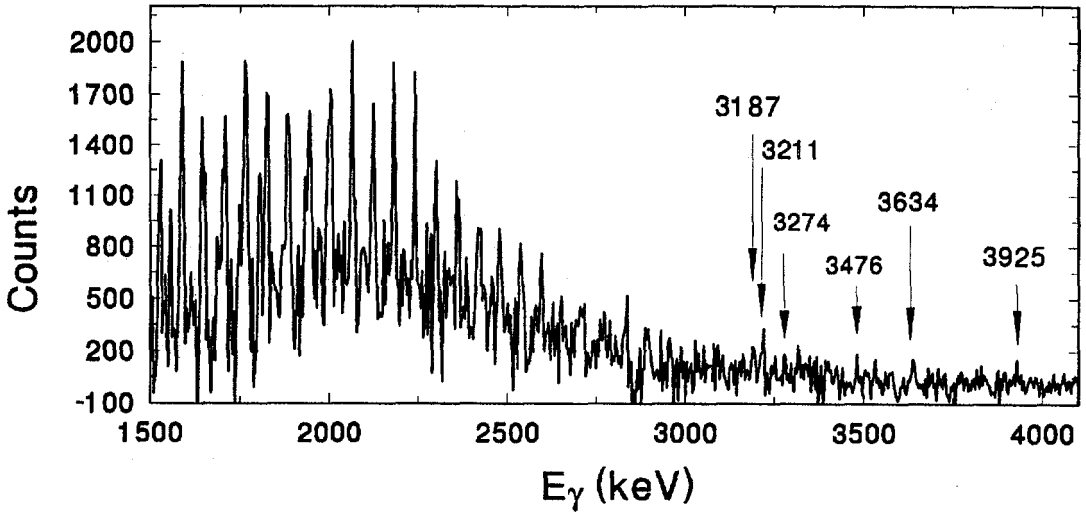

Fig.2: Sum spectrum, a sum of two γ-ray energies which are in coincidence with one of the SD band members, is shown with a resolution of 4 keV/ch. It is obtained by adding 15 clean gates and subtracting an appropriate background. The peaks which are identified as sum of two linking transitions are marked by arrows. Their energies are given with an uncertainty of 4 to 5 keV.

and beam energy, unambiguously show that the SD band belongs to ^{143}Eu. By double gating and selecting clean gates we have obtained a spectrum which shows strongly the known transitions in ^{143}Eu but only weakly ^{142}Eu or other contaminants.

To establish the connection between the SD band and the ND structure we have to know the ^{143}Eu yrast level scheme in the region where the SD band feeds in. The level scheme, previously known[5] up to spin 35/2 has been extended[6] up to I=75/2 at 15.6 MeV excitation energy, using the same NORDBALL data. A partial level scheme is shown in fig. 3. In the γ-ray spectrum of fig.1 all strong ^{143}Eu transitions up to the I = 35/2 level at 4949 keV are seen in coincidence with the band. The 168 keV and 261 keV transitions higher up in the level spectrum are also observed weakly, indicating that at least part of the decay from the SD band feeds into the higher lying levels.

The sum spectrum of two γ-ray energies which are in coincidence with one of the SD transitions is shown in fig. 2. In the energy region between 1.5 MeV to about 3.0 MeV, all the prominent peaks are identified as being the sum of two transitions in the SD band. The intensities of these peaks are strongly enhanced since many sums fall in the same energy due to a very constant moment of inertia $\mathcal{J}^{(2)}$ in the band. Above 3.0 MeV, we have identified 6 peaks as being the sum of two linking transitions between the SD band and the ND states. We have identified them by comparing the energy differences between pairs of such peaks to the level energy differences

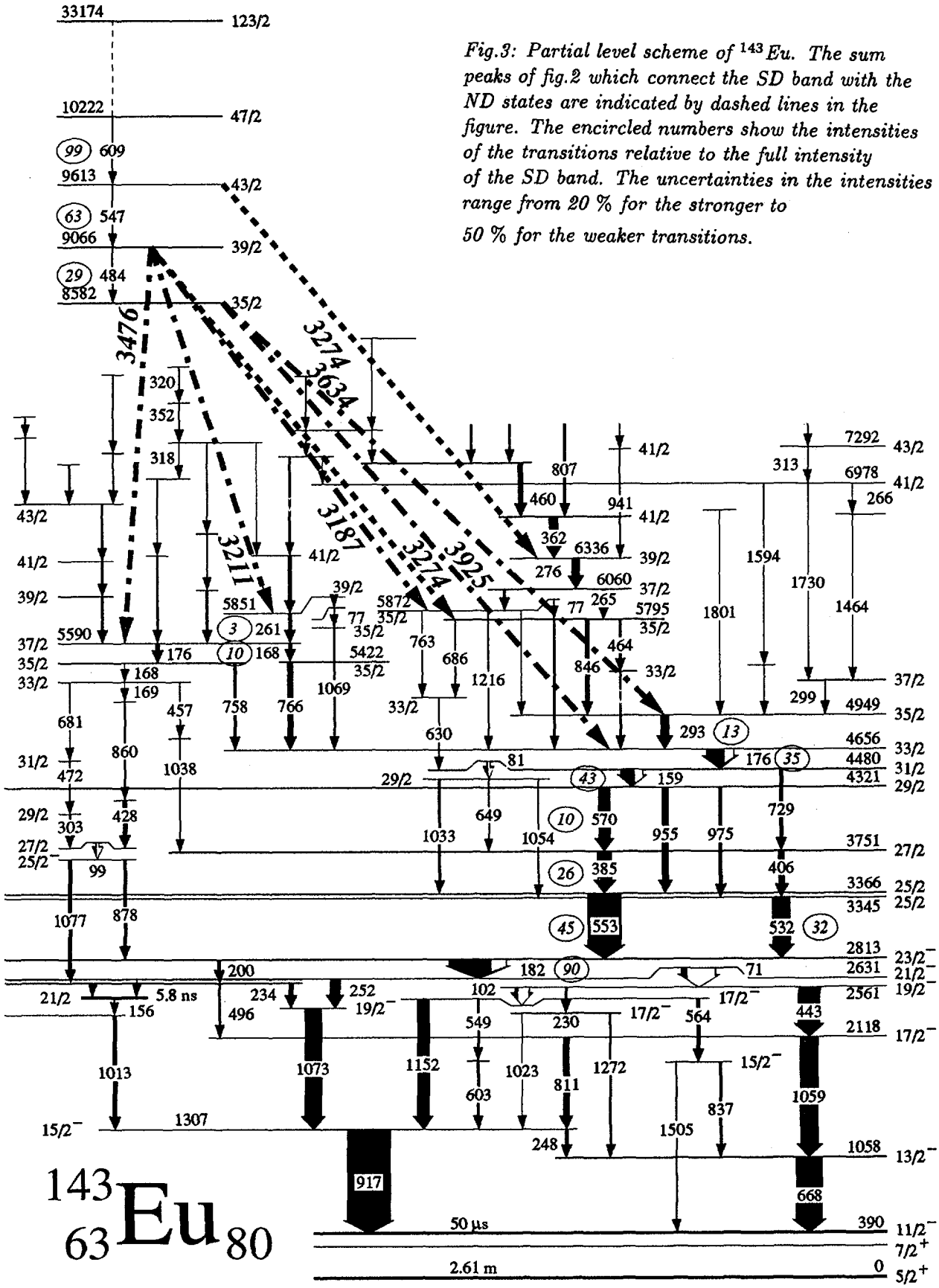

Fig.3: Partial level scheme of ^{143}Eu. The sum peaks of fig.2 which connect the SD band with the ND states are indicated by dashed lines in the figure. The encircled numbers show the intensities of the transitions relative to the full intensity of the SD band. The uncertainties in the intensities range from 20 % for the stronger to 50 % for the weaker transitions.

in the region where the SD band feeds the yrast structure. We found only one solution where the energy differences match each other.

In the partial level scheme which is displayed in fig. 3 the SD band is shown together with the ND states taken from ref. 6. Cascades of two transitions whose energies add up to the sum peaks of fig. 3 are marked in the figure. As an example : The energy difference between the 3925 keV and 3634 keV sum peaks is 291 $\pm$ 6 keV and is within the experimental uncertainty the same as 293.3 $\pm$ 0.2 keV which is the energy difference between the I=33/2 level at 4656 keV and the I=35/2 level at 4949 keV in the ND regime. This provides us with the energy of the initial SD state which is determined to be 8582 $\pm$ 4 keV. The encircled numbers in fig. 3 show the intensity flow into the ND states relative to the full intensity in the SD band. They are obtained from the double gated spectrum (fig.1).

Two consecutive γ rays which link the SD band to the ND states are most likely[7] stretched or nonstretched E1 transitions taking away 0 or 1 unit of angular momentum each. With this in mind, the spins of the two lowest states in the SD band are assigned as 35/2 and 39/2 so that the decay routes with two γ-rays take away 0, 1 or 2 units of spin. These routes will not change the parity between the SD and the ND states. A possibility of assigning the spins of the two lowest states as 37/2 and 41/2 can not be excluded if the decay out of the SD band proceeds by an E1 transition followed by an E2 transition.

The SD band is 3634 keV higher than the yrast line at I=35/2 $\hbar$ and it extends to I = 123/2 $\hbar$ at an excitation energy of 33174 keV. The SD band crosses the yrast line at a spin of 40 $\hbar$. These properties are compared to the TRS calculations[8] with pairing. The experimental results are in good agreement with the theoretical predictions[9].

References :

1. J.F. Sharpey-Schafer, New Aspects of Nuclear Dynamics, Edited by J.H. Koch and P.K.A.de Witt Ruberts (Plenum Publ. 1989), p. 147.
2. R.V.F. Janssens and T.L. Khoo, Annu. Rev. Nucl. Part. Sci. 41(1991)321.
3. SD Data Tables, Compilation by X.L. Han and C.L. Wu (1992).
4. S.M. Mullins et al., Phys. Rev. Lett. 66(1991)1677.
5. M. Müller-Veggian et al., Z.Phys. A330(1988)343.
6. M.J. Piiparinen et al., Z.Phys. in press.
7. B. Herskind et al., Phys. Rev. Lett. 59(1987)2416.
8. W. Nazarewicz, R. A. Wyss and A. Johnson, Nucl. Phys. A503(1989)285.
9. A. Ataç et al., submitted to Phys. Rev. Lett..

NEW FEATURES IN THE SPECTRUM OF ^{152}Dy: EVIDENCE FOR HYPERDEFORMATION

A. Galindo-Uribarri[1], H.R. Andrews[1], G.C. Ball[1], T.E. Drake[3], V.P. Janzen[1,2], J.A. Kuehner[2], S. Mullins[2], L. Persson[2], D. Prevost[2], D.C. Radford[1], J.C. Waddington[2], D. Ward[1] and R. Wyss[4]

[1] AECL Research, Chalk River Laboratories, Ontario, Canada, K0J 1J0
[2] Department of Physics and Astronomy, McMaster University, Hamilton, Ontario, Canada L8S 4K1
[3] Department of Physics, University of Toronto, Toronto, Ontario, Canada M5S 1A7
[4] Joint Institute for Heavy Ion Research, Oak Ridge, TN 37831, USA

One of the most important recent developments in nuclear structure physics has been the prediction and observation of superdeformed (SD) shapes at high angular momentum in several nuclei in the rare earth region. The first experimental observation was a ridge-valley structure in a γ-γ coincidence matrix for the ^{152}Dy nucleus[1]. The ridge was found to be generated by sequences of stretched E2 transitions and corresponded to a moment of inertia $J^{(2)}$ of 85 $\hbar^2$MeV^{-1}. Subsequently a discrete SD band was discovered in ^{152}Dy[2] and the lifetimes were measured[3]. More recently the discovery of SD bands in several nuclei in the neighbourhood of ^{152}Dy[4], the discovery of multiple SD bands in some nuclei[5], and the discovery of new SD regions at mass A~190[6] and A~140[7] have stimulated intense research activity in this area of nuclear physics.

The theories that have been successful in explaining superdeformation also predict other exotic shapes[8]. Rotational bands built upon hyperdeformed (HD) shapes with axis ratios around 3:1 are expected. In the most favourable cases, these states might become yrast at spins as low as 70 $\hbar$, and could therefore be populated in heavy-ion fusion reactions, but very strong competition would be expected from the fission process.

In searching for a manifestation of HD we have used a reaction channel in which a charged particle was evaporated, namely ^{37}Cl + ^{120}Sn $\rightarrow$ ^{152}Dy + 4n + p. The rationale was two fold: firstly at the high input angular momenta needed to populate HD bands there is considerable fractionation of the fusion cross section into (xn, yp, zα) channels, even where the compound nucleus is not very neutron deficient. Thus tagging on a particular charged particle enhances the contribution of a particular nuclide to the γ-γ coincidence data, and results in a cleaner data set. Secondly, there is some possibility that charged particle evaporation could be a trigger for the formation of highly-deformed nuclear shapes. This follows from the argument that the lowering of the Coulomb barrier at the tips of a very deformed nucleus might lead to an enhanced evaporation of charged particles compared to that from a more spherical shape.

An experiment to search for hyperdeformation in ^{152}Dy was performed at the Tandem Accelerator Superconducting Cyclotron (TASCC) facility at Chalk

River with the 8π spectrometer and a 24-element CsI(Tl)-photodiode charged-particle detector array[9]. Gamma-rays were detected with the 8π spectrometer, which consists of a ball of 70 bismuth germanate (BGO) crystals and an array of twenty high-resolution Compton-suppressed Ge detectors. A beam of 187 MeV ^{37}Cl ions bombarded two self-supporting ^{120}Sn foils with a thickness of 0.6 mg/cm^2 each. Approximately $4x10^8$ events characterized by two-fold and higher Ge coincidences above a multiplicity-10 trigger on the BGO ball were recorded during the run, of which $2.7x10^8$ corresponded to γ-γ with no particles in coincidence (leading mainly to ^{153}Ho and ^{152}Ho) and $1.3x10^8$ to γ-γ-particle coincidences (^{152}Dy, ^{150}Tb). The data, corrected online for Doppler shifts, were sorted with a requirement of a single identified proton and a γ-ray sum energy of H>19 MeV registered in the BGO ball, which nearly eliminated events in ^{151}Dy. After this cut on the data, $3x10^7$ events remained in the γ-γ coincidence matrix. A cube was also generated from proton gated γ-γ-γ Ge coincidences.

We studied the ridge-valley structures in the γ-γ coincidence matrix generated from proton γ-γ coincidences. We subtracted uncorrelated events from the matrix using the procedure of Palameta and Waddington[10]. A striking feature observed was a ridge with a 30±3 keV separation running from about 1.2 to 1.5 MeV. Such ridges result from coincidences between transitions in rotational bands with similar moments of inertia. The dynamic moment of inertia of the rotational bands is related to the separation of the ridges by $J^{(2)}=4\hbar^2/\Delta E$; therefore this ridge corresponds to $J^{(2)}$ of about $130\hbar^2 Mev^{-1}$. Fig. 1 shows the spectrum of $\Delta E=E\gamma_1-E\gamma_2$ obtained with a cut in the energy range of $1375\leq(E\gamma_1+E\gamma_2)/2\leq1500$ keV. The ridges appear as peaks at energies of $\Delta E=\pm30\pm3$ keV.

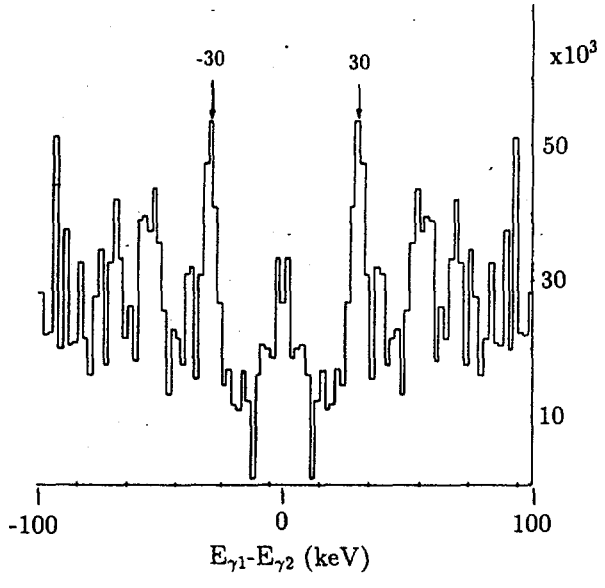

Figure 1. Spectrum of $\Delta E=E\gamma_1-E\gamma_2$ obtained with a cut in the energy range of $1375\leq(E\gamma_1+E\gamma_2)/2\leq1500$ keV. The ridges appears as peaks at energies of $\Delta E=\pm30\pm3$ keV.

Figures 2a and 2b show the spectra of $\Delta E=E\gamma_1-E\gamma_2$ obtained with cuts 100 keV wide in a lower (1200-1300 keV) and a higher (1400-1500 keV) energy range. The peaks at $\Delta E=\pm48$ keV in the lower energy range correspond to the well known superdeformed ridge[1]. In the higher energy spectrum, the SD ridge is much weaker, and the 30 keV ridge structure predominates.

In a second replay of the data, two γ-γ coincidence matrices were generated: one in which both γ rays were detected in the most forward and backward detectors (±37°) and one in which both γ rays were detected in the rings closest to 90°, namely ±79°. The γ-γ directional correlation ratios (DCO) showed that this structure was consistent with stretched quadrupole character.

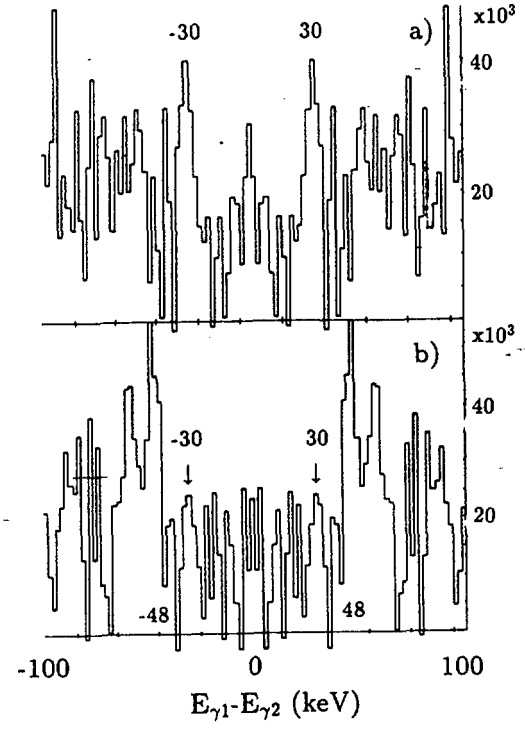

Figure 2. Spectra of $\Delta E=E\gamma_1-E\gamma_2$ obtained with cuts 100 keV wide in a higher (a) 1400-1500 keV and lower (b) 1200-1300 keV energy range. The peaks at $\Delta E=\pm 48$ keV in the lower energy range correspond to the superdeformed ridge.

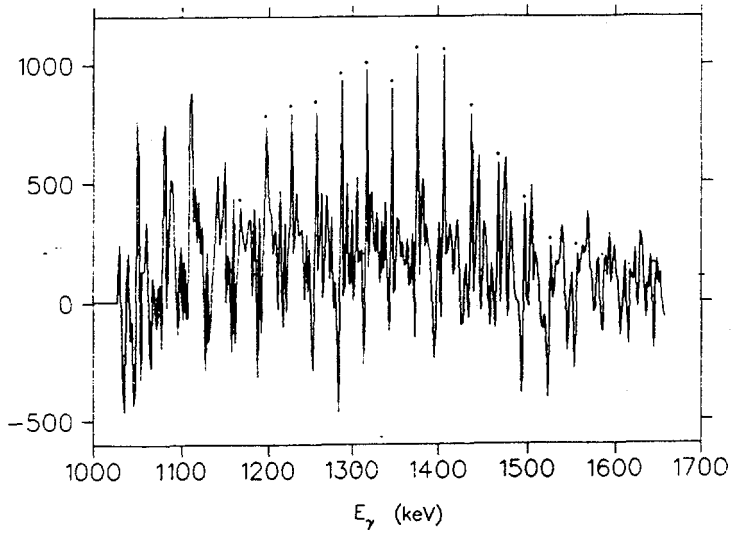

Figure 3. Two-dimensional correlation spectrum obtained with the program BANDAID[11]. A grid of twelve gates with a constant separation of 30 keV was used.

Two- and three-dimensional correlation techniques, BANDAID and CUBEAID[11], were used to search the γ-γ matrix and γ-γ-γ cube for coincidence patterns indicative of a rotational cascade with constant $J^{(2)}$. The code generates a figure of merit spectrum measured along the $E\gamma_1=E\gamma_2$ diagonal (or $E\gamma_1=E\gamma_2=E\gamma_3$ in the case of a cube) an example of which is shown in Figure 3. By figure of merit we mean the net sum of counts at the grid points defined by the m cascade transitions assumed in the trial band evaluated for a particular placement of the grid over the data. Where a rotational band is present with a spacing close to that assumed in the trial, the figure of merit is large wherever the grid happens to overlap the data points. The figure of merit spectrum generated by moving the trial grid along the diagonal therefore exhibits a sequence of sharp peaks separated by the energy spacings of the band. An example for a grid of 12 gates separated by 30 keV is shown in Figure 3.

The envelope of these peaks also gives information on where the signal is strong relative to the noise. A similar analysis made on the cube with the program CUBEAID[11] supports these findings. Figure 4 shows a summed coincidence γ-spectrum obtained by setting gates at the positions of the band members located by the correlation method.

The known SD band and the low deformation prolate band in ^{152}Dy[3] were also seen in the data. Charged-particle spectra associated with these bands will be reported elsewhere.

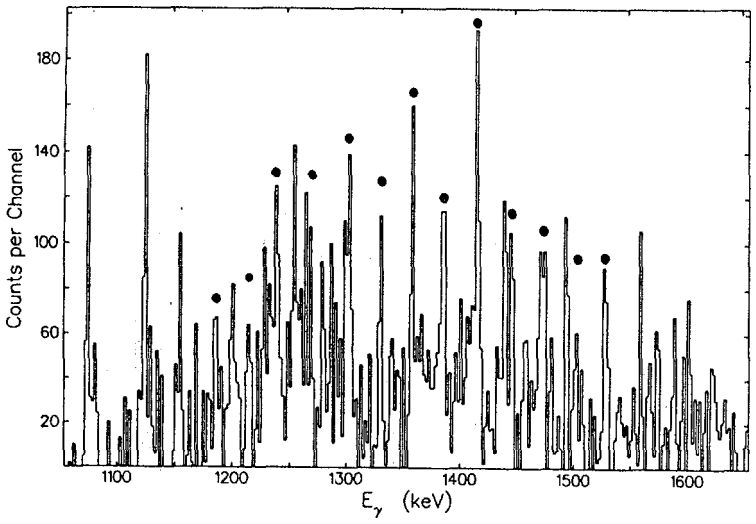

Figure 4. Summed γ-ray spectrum obtained for the band located by the correlation method.

The energy spectrum of the simple anisotropic harmonic oscillator has pronounced degeneracies at deformations with major axis ratios 1:1, 2:1, 3:1 etc. The shell structure at a 2:1 shape has been related to the occurrence of superdeformation in nuclei in the A=150 and A=190 regions. The nucleus ^{152}Dy is considered to be a doubly-magic superdeformed core because of the very large gaps present in the single-particle spectrum. This is true for a realistic potential[12] as well as for the harmonic oscillator potential. An HD structure in the same nucleus raises the question as to what extent a similar shell structure might be responsible?

Total Routhian Surface (TRS) calculations have been performed for nuclei in the vicinity of ^{152}Dy. The shape parameters β_2, β_4 and γ of the nucleus in the rotating frame were minimized (for details see ref. [12]). In the calculations, there is a deep minimum corresponding to the SD shape, β_2~0.6. However, at a frequency of $\hbar\omega$=0.66 MeV, a new minimum occurs in the surface, corresponding to a value of β_2 ~ 0.9. At very high rotational frequencies, corresponding to spins of about 80 $\hbar$, the HD structure becomes yrast in these calculations.

The calculations show that the underlying physics of the HD band is very different from that of the SD band. There are no pronounced shell effects at the calculated equilibrium deformation in contrast to the SD band. However, static pairing correlations are strong whereas static pairing is reduced even at spin 0 for the SD shape.

It was predicted in ref [12] that the SD band is expected to be crossed at $\hbar\omega$ =0.8 MeV by aligned $j_{15/2}$ protons. This high-j intruder configuration originating from two shells above those active at β_2~0 will tend to polarize the nuclear shape to greater prolate deformation. The TRS calculations confirm that the quadrupole deformation increases after the $j_{15/2}$ crossing. The next calculated crossing involves $k_{17/2}$ neutrons. The occupation of the ν N=8, "super"-intruder orbitals polarizes the shape to an even larger deformation. In addition, both these ν and π orbitals contribute a large aligned angular momentum to the total spin of the nucleus. A "super backbend" is thus the possible origin of the minimum in the TRS calculation at HD shapes. This is in sharp contrast to the SD minima which are caused by shell structure.

It is difficult to estimate the spins of the observed structure. If we assume that $J^{(2)}$ equals the static moment of inertia $J^{(1)}$ then the observed structure extends from about spin 78 $\hbar$ to spin 98 $\hbar$. Alternatively, taking the spins from the TRS calculation, the observed γ-ray energies in the frequency region of 0.45-0.75 MeV correspond to a spin region of 50-80$\hbar$. This lower estimate arises because of the large amount of aligned angular momentum in the calculation, which implies that $J^{(2)} \neq J^{(1)}$.

These high spins are surprising since one would expect very strong competition with fission above spin 70 $\hbar$. However the disappearance of the fission barrier does not set an upper limit on the angular momentum that a compound nucleus can sustain since the entrance channel is in a very different part of the potential energy surface from the fission channel. The time scales involved in dissipating the initial excitation energy through light particle emission might also play a role of stabilizing the residues against fission. Theoretically, the maximum angular momentum a nucleus in this mass region is able to sustain against the centrifugal force is around 90 $\hbar$[13]. These calculations are based on the liquid drop model and the shell structure is not taken into account. In addition, when states carry aligned angular momentum, the collective rotation, which is of relevance to the fission limit is correspondingly reduced. The calculations give an aligned angular momentum of ~12-14 $\hbar$, implying that the collective rotation should be lowered by that amount. The possibility of angular momentum alignment as well as the presence of shell structure will affect the spin dependence of the fission limit considerably. It is interesting to note that recent calculations[14], derived from the liquid drop model and including nuclear proximity effects, show that very high angular momenta can be sustained by nuclei in elongated shapes without fissioning. The same authors predict for nuclei like ^{152}Dy the existence of an isomeric state with a ratio s = 0.3 between the neck diameter and the elongation of the system[15], corresponding to β_2 = 0.9 for spins between 70 and 115 $\hbar$ with a moment of inertia of about 110 $\hbar^2 Mev^{-1}$.

In conclusion, ridges have been found in energy-correlation spectra for ^{152}Dy with a constant energy separation corresponding to an extremely large moment of inertia $J^{(2)}$ of about 130$\hbar^2 Mev^{-1}$. The ridges consist of stretched E2 transitions. Such a large moment of inertia suggests the existence of a strongly deformed shape with a $\beta_2 \geq 0.9$. Furthermore, two- and three-dimensional correlation techniques used to search the data found strong regular coincidence patterns. A cascade of about 10 discrete transitions with an average energy spacing of 30 keV has also been found. Still more powerful instrumentation such as the third generation of spectrometers will be needed in order to measure lifetimes for this structure.

This work has been partially funded by the Natural Sciences and Engineering Research Council of Canada and by AECL Research. This work has benefited from discussions with G. Smith and J. Sharpey-Schafer from University of Liverpool, J.P. Vivien from Strasbourg, W. Nazarewicz from Warsaw and G. Royer from Nantes.

References

1. B.M. Nyako et al., Phys. Rev. Lett. 52 (1984)507.

2. P.J. Twin et al., Phys. Rev. Lett. 57 (1986)811.

3. M.A. Bentley et al., Phys. Rev. Lett. 59 (1987)2141 and J. Phys. G17 (1991) 481.

4. B. Haas, Nucl. Phys. A538 (1992) 595c.

5. J.K. Johansson et al., Phys. Rev. Lett. 63 (1989) 2200.

6. E.F. Moore et al., Phys. Rev. Lett. 63 (1989) 360.

7. S.M. Mullins et al., Phys. Rev. Lett. 66 (1991) 1677.

8. J. Dudek, T. Werner and L.L. Riedinger, Phys. Lett., B211 (1988) 252.

9. A. Galindo-Uribarri, Prog. Part. Nucl. Phys. 28 (1992) 463.

10. G. Palameta and J.C. Waddington, Nucl. Instr. & Methods A234 (1985) 476.

11. J.A. Kuehner, Bandaid and Cubeaid programs, Proc. of the Int. Conf. on Nuclear Structure at High Angular Momentum, Ottawa, Ontario, 1992 May 18-21, AECL-10613, Vol. 1, p. 19 and these proceedings.

12. W. Nazarewics et al., Nucl. Phys. A503 (1989) 285.

13. S. Cohen et al., Ann. Phys. 82 (1974) 557; R.A. Broglia et al., Nucl. Phys. A349 (1980) 496.

14. G. Royer and J. Mignen, to be published in J. Phys. G (1992); G. Royer and B. Remaud J. Phys. G10 (1984) 1057.

15. G. Royer and F. Haddad, private communication.

INTERNATIONAL CONFERENCE ON NUCLEAR STRUCTURE AT HIGH ANGULAR MOMENTUM

Ottawa

Session 3: Fusion and High Angular Momentum Residues

Entrance Channel Effects and the Superdeformed Band in ^{152}Dy

C.W. Beausang[1], A. Alderson[1], I. Ali[1], M.A. Bentley[3], P.J. Dagnall[1], G. deFrance[2], G. Duchene[2]P. Fallon[1], S. Flibotte[2], P.D. Forsyth[1], B. Haas[2], P. Romain[2], G. Smith[1], Ch. Theisen[2], P.J. Twin[1], and J.P. Vivien[2]

1: University of Liverpool

2: Centre de Recherches Nucleaires Strasbourg

3: SERC Daresbury.

Since the first observation of a high-spin superdeformed band in ^{152}Dy in 1986 [1], the phenomenon of superdeformation has been observed in many nuclei in three different mass regions. While much progress has been made in the study of such exotic nuclear structures, basic questions regarding the population mechanism of the superdeformed minimum still remain to be answered. One open question is whether the population intensity in the superdeformed minimum depends on the mass-asymmetry of the projectile and target in the entrance channel of the compound nuclear system. Indeed, recent results for ^{152}Dy and ^{147,148}Gd [2, 3] indicate an enhancement of the superdeformed band population, by a factor of 1.5 – 2.0, relative to the normal deformed nuclear states, when populated via a mass-symmetric entrance channel versus a mass-asymmetric channel.

The present data for ^{152}Dy, summarised in Fig. 1, represent the combined results of many experiments carried out over several years using the TESSA3 array [4] in Daresbury. The reactions used, ^{36}S + ^{120}Sn, 170 – 176 MeV, ^{48}Ca + ^{108}Pd, 185 – 212 MeV, and ^{82}Se + ^{74}Ge, 324 – 346 MeV, were chosen to populate ^{152}Dy in each case via the 4n evaporation channel and, in addition, the beam energies were chosen to populate the compound system ^{156}Dy over similar ranges of excitation energy and maximum angular momentum. Recently two new points have been added to the data set as a result of early commissioning experiments using the Eurogam array.

The data, see Fig. 1, reveal that a minimum excitation energy (or angular momentum l_{max}) is required in order to populate the superdeformed band. Above the threshold, the SD population increases rapidly to reach a saturation value of 1.1%, 1.5%, and 2.2% of the ND intensity for the ^{36}S, ^{48}Ca and ^{82}Se induced reactions, respectively. At the highest measured excitation energies the data suggests that the ratio SD/ND remains constant or perhaps decreases slightly.

The dependence of the SD/ND intensity ratio on the mass-asymmetry in the entrance channel was very unexpected and possibly reflects differences in the compound nuclear formation time for different entrance channels. A longer formation time, or equilibration time, for the compound system at very high angular momentum allows neutron evapora-

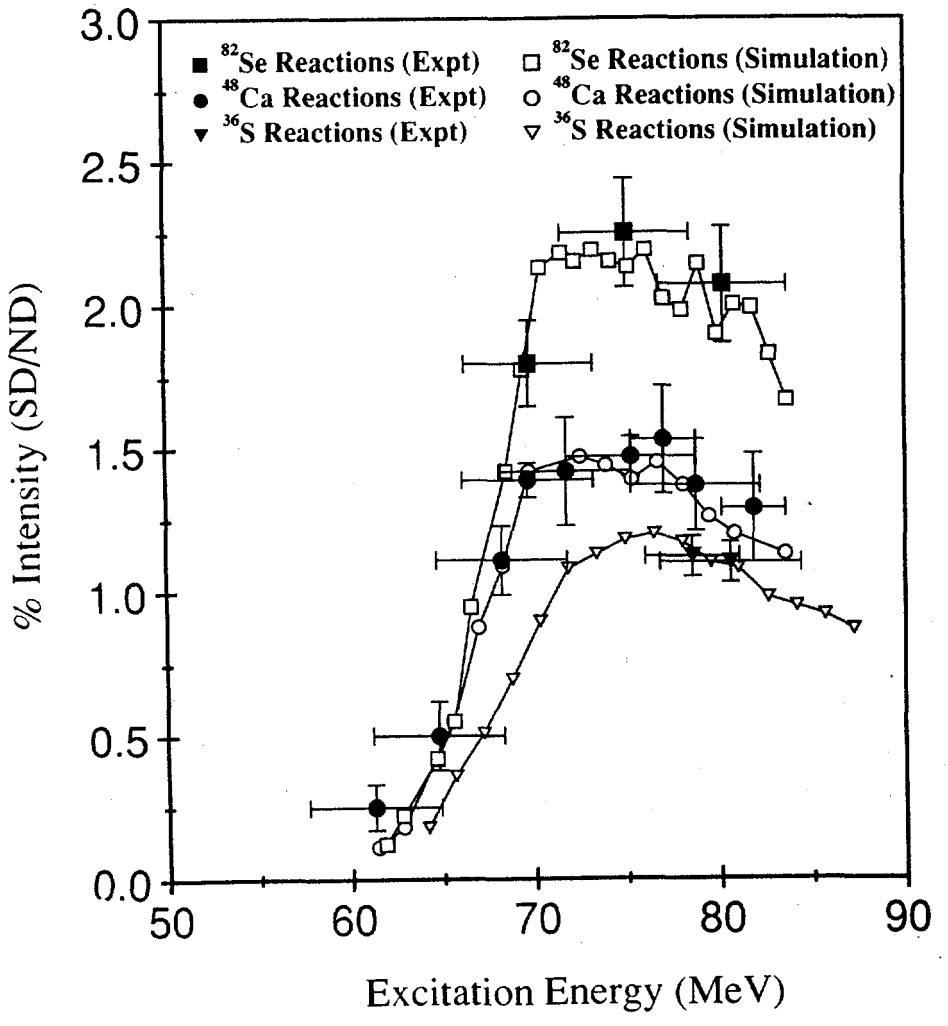

Figure 1: Experimental and calculated SD/ND intensity ratios for ^{152}Dy plotted as a function of the excitation energy in the compound nucleus (^{156}Dy).

tion, leading ultimately to ^{152}Dy, to more readily compete with fission. The SD population in the mass 150 region may be especially sensitive to such a phenomenon as the SD bands in this region are only populated at very high angular momenta. Thus, the SD population is acting as a microscope which focuses attention only on the very highest l-waves which eventually form compound nuclear states. Any enhancement of the fusion probability at high l-waves should also be associated with an enhanced feeding into the high spin members of the SD band.

To simulate these results we have carried out a series of calculations using the statistical code CASCADE [5], to predict the entrance population cloud for ^{152}Dy, coupled with a Monte-Carlo code to calculate the SD and ND spectra following γ decay [6]. The results are summarised in Fig. 2 and are also compared to the experimental data in Fig. 1. The

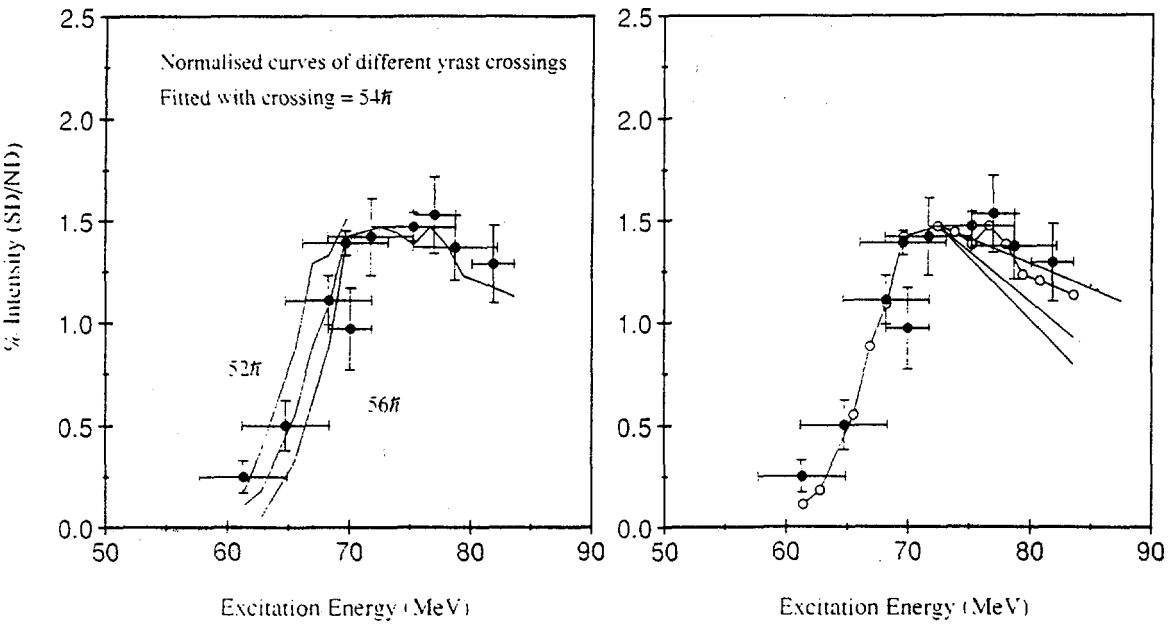

Figure 2: Experimental SD/ND intensity ratios for ^{1552}Dy for the ^{48}Ca induced reaction. The lines show the results of the calculation indicating (left) the result of varying the position of the SD and ND yrast crossing and (right) changing the ratio of level density parameters in the SD. and ND potential wells from $a_{SD} = 0.9a_{ND}$ (top) to $a_{SD} = 1.4a_{ND}$ (bottom). The open circles show the calculated intensity ratio for $a_{SD} = 1.1a_{ND}$. The level density parameter a_{ND} used was 8 MeV^{-1}.

results of the calculations can briefly be summarised as follows, while full details will be found in ref [7].

- The low excitation energy (or angular momentum) threshold in the SD population is especially sensitive to the yrast SD/ND crossing point. The best fit to the experimental data is found by setting this crossing to 54$\hbar$, see Fig. 2.

- At very high excitation energies (or angular momenta) the behaviour of the SD/ND population is sensitive to the ratio of level densities in the first and second wells. The available data seem best fit by a value of a_{SD}/a_{ND} slightly less than 1.0, see Fig. 2. Changing the ratio ρ_{SD}/ρ_{ND} does not appreciably effect the equilibrium value of the population intensity, but only effects the slope at high excitation energy.

- In order to reproduce the measured SD/ND intensity ratio, see Fig. 1, we have increased the fission barrier used in the calculation by $\sim 3.3\hbar$ for the ^{82}Se induced reaction relative to the ^{36}S induced reaction. This enhanced fusion probability at high l-waves should also result in an enhancement of the population of the higher

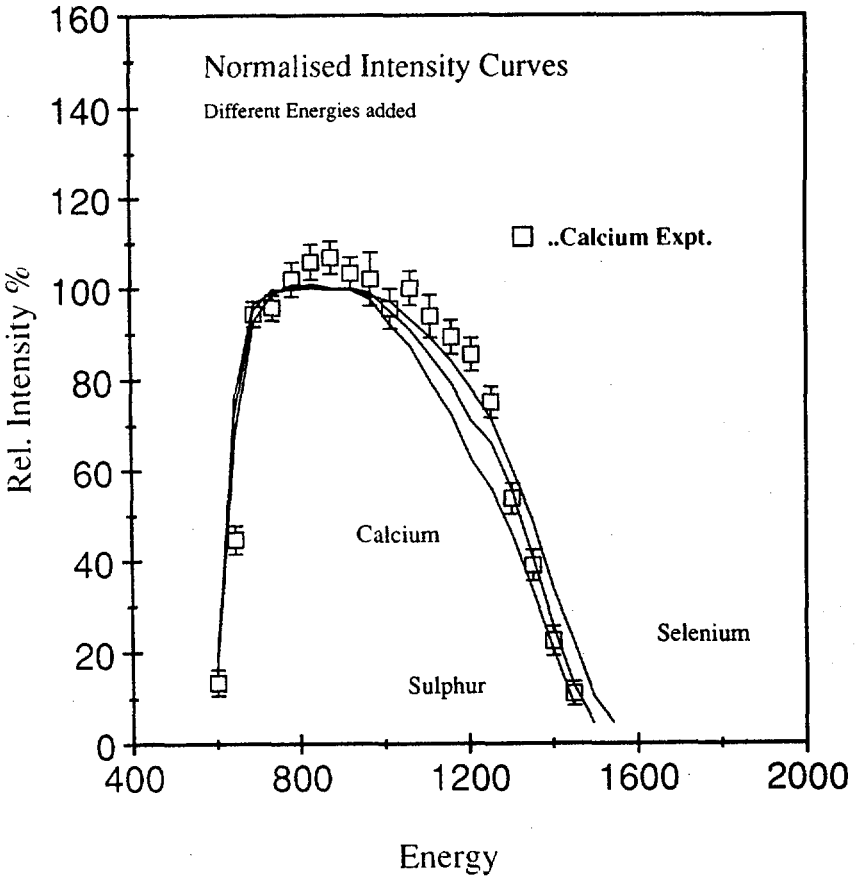

Figure 3: Calculated SD band intensities for the three reactions. The experimental intensities for the ^{48}Ca induced reaction at 197 MeV (the largest and best quality data set available to date) are superimposed to indicate the quality of the data required for an accurate measurement of the SD intensity at the highest spins in the SD band.

spin SD band members when populated via a mass-symmetric reaction, as shown in Fig. 3. To confirm this prediction we plan a series of experiments using the new Eurogam array.

To prepare for these experiments, and as part of the commissioning program of the Eurogam array, two experiments were performed to populate ^{152}Dy. The first, using the ^{36}S + ^{120}Sn reaction at 170 MeV used 26 escape suppressed Ge detectors. A coincidence between at least 3 suppressed Ge detectors was demanded before recording data to tape. In twelve hours beam time a total of $\sim 180 \times 10^6$ unfolded $\gamma - \gamma$ events were recorded, comparable to the statistics obtained in one week running on the TESSA3 array! The second experiment used the ^{82}Se + ^{74}Ge reaction at a beam energy of 335 MeV. Thirty Ge detectors were used and a total of $\sim$ 200 million events ($\sim 40\% \geq 3$ Ge an $\sim 60\% \geq 2$ Ge

plus isomer event) were collected in 12 shifts of beam time. The analysis of the data from these test experiments is still underway, however the following points can already be made

- An extrapolation of the data rate achieved in the ^{36}S induced reaction indicates that $\sim$ 12000 unfolded triples per second will readily be achieved with the full Eurogam phase 1 array of 45 Ge detectors. This data rate implies $\geq$ 1000 counts per day in a 100% superdeformed peak when double gates are placed on eight other SD band members.

- The SD/ND intensity ratio measured in these reactions is consistent with previously measured values using the TESSA3 array.

- Using a triples analysis, two new band members, with transition energies of 557 keV and 1495 keV have been assigned to the SD band in ^{152}Dy.

- Preliminary measurements on the data obtained following the ^{82}Se induced reaction indicate that insufficient statistics were obtained to allow an accurate measurement of the intensity of the high spin band members to compare with data obtained with ^{48}Ca induced reaction. This comparison must await the analysis of the results of forthcoming experiments using the completed Eurogam array.

References

[1] P.J. Twin *et al* Phys. Rev. Lett. **57**, 811 (1986).

[2] G. Smith *et al* Phys. Rev. Lett. **68**, 158, (1992).

[3] S. Flibotte *et al* Phys. Rev. **C45**, R889, (1992).

[4] P.J. Nolan and P.J. Twin, Ann. Rev. Nucl. Part. Sci. **38**, 532, (1988).

[5] F. Puhlhofer, Nucl. Phys. **A280**, 267, (1977).

[6] K. Schiffer and b. Herskind, Nucl. Phys. **A520**, 521c, (1990).

[7] G. Smith *et al*, thesis, Liverpool University and to be published.

ENTRANCE CHANNEL DEPENDENCE IN THE POPULATION OF THE SUPERDEFORMED BANDS IN ^{191}Hg AND A MODEL FOR THE FEEDING MECHANISM

T. Lauritsen[1], F. Soramel[1,2], T.L. Khoo[1], R.V.F. Janssens[1], I. Ahmad[1], M.P. Carpenter[1], Y. Liang[1], B. Fornal[3], I. Bearden[3], Ph. Benet[3], P. Daly[3], Z.W. Grabowski[3], R. Maier[3], D. Ye[4], U. Garg[4], W. Reviol[4], M.W. Drigert[5]

[1]Argonne National Laboratory, Argonne, IL 60439, USA. [2]On leave from Padova University, I-35131 Padova, Italy. [3]Purdue University, West Lafayette, IN 47907, USA. [4]University of Notre Dame, Notre Dame, IN 46556, USA. [5]INEL, EG&G Idaho Inc., Idaho Falls, ID 83415, USA.

Abstract: The population of the superdeformed bands in ^{191}Hg has been measured for two reactions with different mass asymmetry. No entrance channel effect was observed, in contrast to similar measurements in the A=150 region. To further elucidate this problem, the entry distribution for the superdeformed band in ^{192}Hg was measured and a Monte Carlo model for the feeding was developed. The simulations suggest that the decision on trapping in the superdeformed well is made at the barrier between the normal and superdeformed wells rather than at the entry point.

Recent measurements of the total intensity flowing through the superdeformed (SD) bands in the A=150 region[1,2] suggest the existence of an entrance channel effect: mass-symmetric reactions have been reported to enhance the population of SD bands. This has been explained by invoking a dynamic effect in the entrance channel, i.e., the formation time of the compound nucleus is longer for symmetric reactions than for asymmetric ones, favoring neutron evaporation over fission.

We have investigated this problem in the A=190 region by comparing SD bands yields in ^{191}Hg produced either in the ^{130}Te(^{64}Ni,3n) or ^{160}Gd(^{36}S,5n) reaction. The experiments were carried out using ATLAS beams and the Argonne–Notre Dame γ-ray facility consisting of 12 ACS Ge detectors and a 50 element inner BGO array.

For the symmetric and asymmetric reactions, the SD bands in ^{191}Hg were found to have 3.0(8)% and 3.7(5)%, respectively, of the ground state intensity. The results for each SD band (there are 3 known SD bands[3,4]) and for the total SD yield in ^{191}Hg are compared in fig.1a. Within errors the measured yields are the same for the two reactions, in contrast to the observation near A=150. This is illustrated in fig.2 where the SD intensities as a function of the "degree of symmetry" parameter, $S=A_{beam}/A_{target}$, are shown. We conclude that no enhancement is observed in the A=190 region.

These results do not rule out the possibility of an entrance channel effect, though they underline the importance of other effects which should also be examined carefully. In particular, since the SD band population is very sensitive to the higher partial waves of the l-distribution, it becomes very important to measure the entry points for the different reactions. We measured both K (fold) and H (sum energy, unfolded to the total energy E) for the two reactions leading to ^{191}Hg. As can be seen in fig.1b, the experimental entry points for normal deformed (ND) and SD states are very close in the two cases; this ensures that the same partial waves are involved in the two reactions

and rules out the possibility of an entrance channel effect at least in this mass region. It would be useful to have similar data for the nuclei in the A=150 region in order to understand if the increase in SD bands population observed in this case reflects an entrance channel memory or, more likely, can be attributed to differences in the tails of the l-distributions involved in the reactions. We expect such differences to be present, based on the more diffuse tail in the compound nucleus l-distribution in the symmetric channel and on the l-dependent survival probability against fission. Our results for ^{191}Hg can be understood within the framework of a model describing the formation and decay of the SD bands. This is discussed below.

Entry distributions both for the γ cascades feeding the SD and ND bands in ^{192}Hg have been measured. The nucleus was populated with the reaction ^{160}Gd(^{36}S,4n)^{192}Hg at 162 MeV. Double coincidence gates were placed on the Ge spectra and the coincident fold (K) and energy (H) measured in the inner array were recorded. The response function for the inner array was measured and used to unfold the (K,H) distribution. Finally the entry distribution was constructed using the mean angular momentum removed per photon, obtained from an analysis of the quasicontinuum γ rays. Thus, we have measured the population distribution in spin and energy from where the γ cascades start after the last neutron has been evaporated (and after successful competition with fission).

The entry distributions were measured, *both* in coincidence with the SD lines and ND lines. They are shown in fig.3a,b. It is seen that the SD distribution is located at higher spin and somewhat lower energy (for a given spin) than the ND distribution. As the double gates on the ND transitions were placed on γ transitions which are also fed in the decay of the SD band, the ND entry distribution is the total entry distribution for *all* γ cascades in ^{192}Hg.

A model was developed to follow, by a Monte Carlo approach[5,6,7], the γ cascades starting from this measured total entry distribution. The model has two wells, ND and SD, separated by a barrier. The states in the nucleus are considered to be either in one or the other well. The initial selection of the well in which a γ cascade starts is based on the relative level densities in the two wells at the given spin and energy. In order to calculate the γ transitions, the Γ-decay widths in the two wells are computed and the levels in the two wells are allowed to mix as described by Vigezzi et al[8,9]. The mixing allows the nucleus to change shape while it γ decays. Thus, γ cascades can be followed from the entry point till they enter a region close to the ND or SD yrast lines. By tracing back the sub-set of the γ cascades that feed the SD well, the entry distribution for the SD band can be found. This is shown in fig.3c. The principal feature, viz. that the SD states originates from the higher spin portion of the normal states, is clearly seen; but some differences in details are apparent (fig.3d,e).

The model contains the excitation energy of the SD band, the barrier between the ND and SD wells and the quadrupole moments and levels densities in the two wells as

parameters. We have determined the best values of the parameters in order to reproduce the following observables: the SD entry distribution, the intensity of the SD band and its variation with spin and the energy of the quasicontinuum γ rays. All observables are reproduced only for a narrow range of SD excitation energies and barrier heights. Thus, the model allows us to set constraints on these parameters. The excitation energy over the normal yrast line for the SD band when it decays around spin 10 is 3.3–4.3 MeV and the barrier height at spin 40 is 3.5–4.5 MeV (assuming a barrier frequency of $\hbar\omega$=0.6 MeV[8]). In the model, trapping in the SD well is made near the barrier between the two wells rather than at the entry point. It was found that $\approx$ 95% of the cascades that feed the SD well started out from ND states. The model is able to reproduce all observables associated with SD γ cascades in the nucleus, and indicates trapping in the SD well occurs 10^{-14} s after formation of the compound nucleus.

In summary, we have measured the population of the SD bands in ^{191}Hg with two reactions having different mass-asymmetry. No entrance channel effect was seen, in contrast to results in the A=150 region. For ^{191}Hg, the average entry points and spin distributions (not shown here) have been determined to be similar. The results indicate it is unlikely that there is a memory of the entrance channel when trapping in the SD well occurs. This is not unexpected since the time when trapping occurs is around 10^{-14} s, which is much later than the characteristic time for shape relaxation of the compound nucleus (commonly thought to be around 10^{-20} s, although it could be as long as 10^{-18} s) or the time for emission of the last neutron ($\approx 10^{-18}$ s). The possibility that the observed effect in the A=150 region is due to an angular momentum effect should be checked by measurements of the entry distributions so that a distinction can be made between a memory or an angular momentum effect. The entry distributions for both the ND and SD cascades in ^{192}Hg have been measured and a Monte Carlo model has been developed to follow the γ cascades. In addition, the model puts constraints on the excitation energy of the SD band and on the barrier between the ND and SD wells.

This work was supported by the Department of Energy, Nuclear Physics Division, under contracts Nos W-31-109-ENG-38, DE-AC07-76ID01570 and DE-FG02-87ER40346 and by the National Science Foundation under grant PHY91-00688.

References:

[1]G. Smith et al., Phys. Rev. Lett. **68**(1992)158
[2]S. Flibotte et al., Phys. Rev. **C45**(1992)R889
[3]E.F. Moore et al., Phys. Rev. Lett. **63**(1989)360
[4]M.P. Carpenter et al., Phys. Lett. **B240**(1990)44
[5]R. Holzmann et al., Phys. lett. **195**(1987)321
[6]K. Schiffer et al., Z. Phys. **A332**(1989)17
[7]K. Schiffer et al, Nucl. Phys. **A520**(1990)521c
[8]E. Vigezzi et al., Phys. Lett. **249**(1990)163
[9]S. Bjørnholm et al., Rev. Mod. Phys. **52**(1980)725

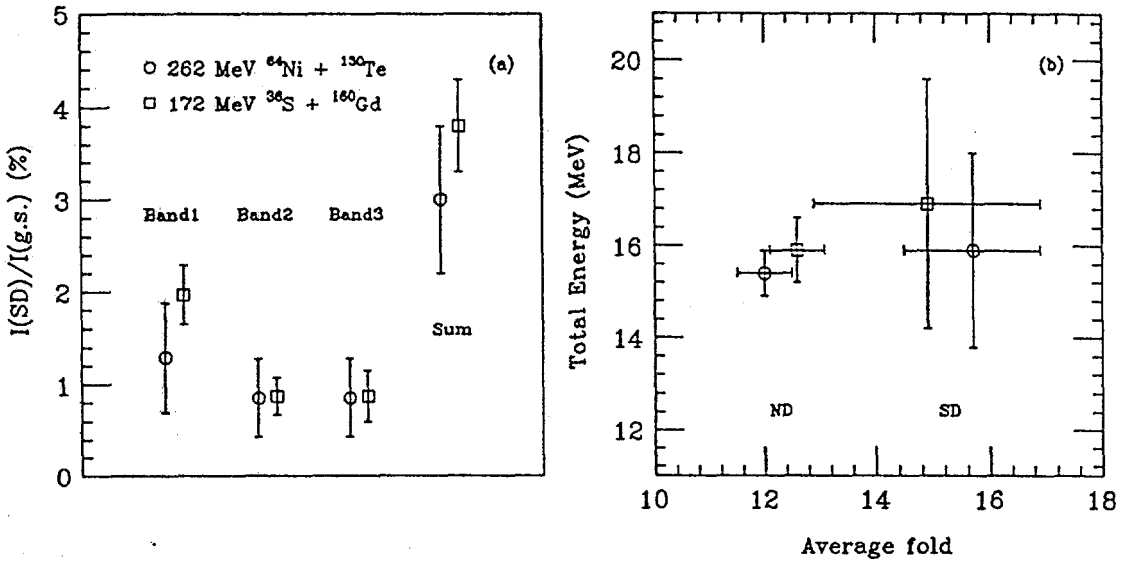

Figure 1: a: Relative intensities of each SD band and total SD flux in ^{191}Hg for different reactions. b: Experimental entry points for ND and SD states.

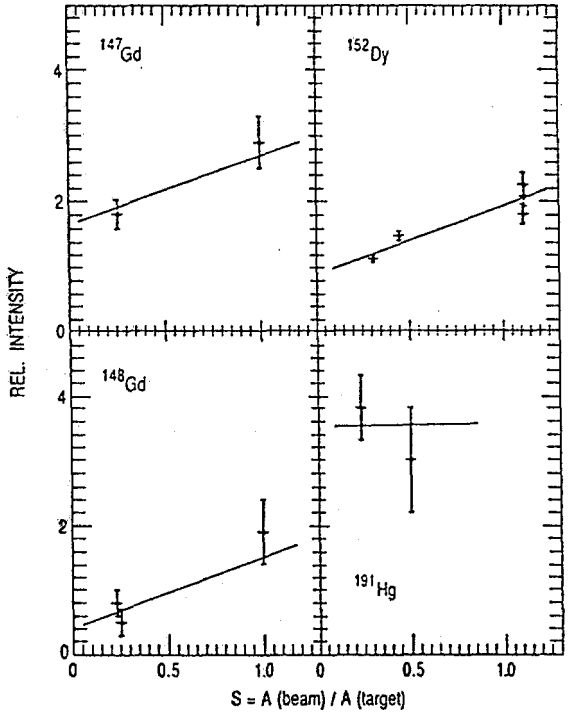

Figure 2: Total SD intensity in various nuclei as function of the "degree of symmetry" of the reaction. The lines are drawn to guide the eye.

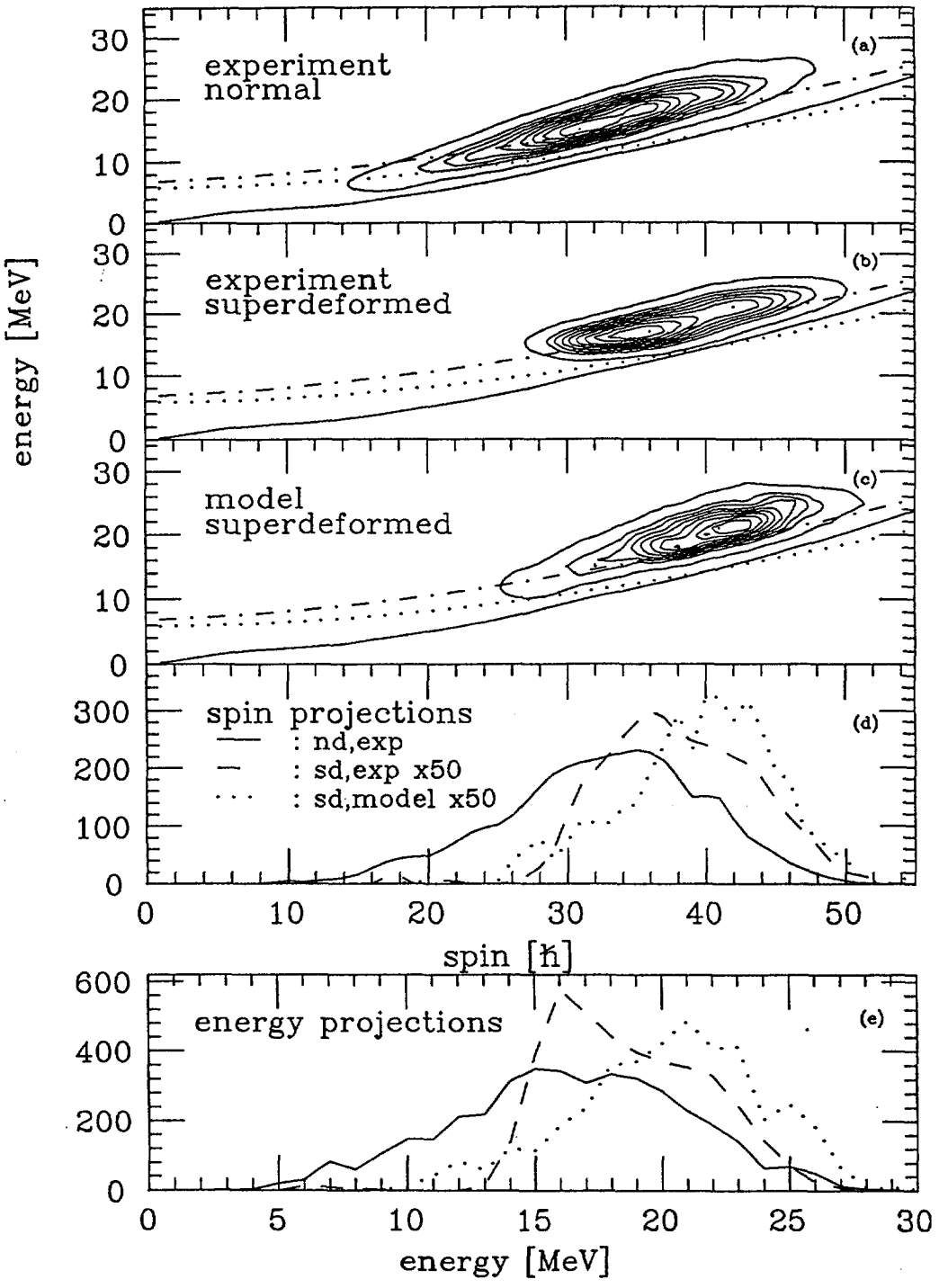

Figure 3: a,b: measured entry distribution in ^{192}Hg for ND and SD cascades, respectively. Each contour represents a change of 10% of maximum value. c: calculated entry distribution. d,e: projections of the entry distributions on the spin and energy axes, respectively.

INTERNATIONAL CONFERENCE ON NUCLEAR STRUCTURE AT HIGH ANGULAR MOMENTUM

Ottawa

Session 4: Nuclei at High Temperature

Spin Dependence of Rotational Damping by the Rotational Plane Mapping Method

S.Leoni[a], B. Herskind[b], T. Døssing[b], P. Rasmussen[b], A. Ataç[b] , M. Bergström[c], A. Bracco[a], A. Brockstedt[c], H. Carlsson[c], P. Ekström[c], H. J. Jensen[b], G. B. Hagemann[b], F. Ingebretsen[d], R. M. Lieder[b], T. Lönnroth[e], A. Maj[b], B. Million[a], A. Nordlund[c], J. Nyberg[b], M. Piiparinen[b], H. Ryde[c], M. Sugawara[b], P. O. Tjøm[d], A. Virtanen[b]

[a] *Dipartimento di Fisica, Università di Milano*
[b] *The Niels Bohr Institute, Copenahgen*
[c] *Department of Physics, University of Lund, Sweden*
[d] *Department of Physics, University of Oslo, Norway*
[e] *Department of Physics, Åbo Akademi, Finland*

The nuclear structure and rotational motion of deformed nuclei is well studied by discrete γ ray spectroscopy. In the best studied nuclei up to 15 regular rotational bands are identified in the range from the yrast line to a few hundred keV up in excitation energy.

The γ ray cascades from high spin states formed in compound reactions decay mainly through the warm region of high level density $\approx$ 3-5 MeV above yrast. However, very little specific information has been obtained about the rotational motion in this region.

From the studies of $E_{\gamma_1} * E_{\gamma_2}$ correlation spectra it has been found [1,2] that the large collective quadrupole transitions strength known from rotational bands at high excitation energy may be distributed over all final states of a given parity within an interval defined as the rotational damping width Γ_{rot}. As a consequence a theoretical model [3] was developed to describe the average properties of the nuclear E2 decay through the regions of high level density. The model also predicts a temperature and spin dependence of Γ_{rot} and a decrease of Γ_{rot} at higher temperature due to the so called motional narrowing effects in analogy to the line narrowing observed in NMR from heated solids. Values for $\Gamma_{rot} \approx$100 keV were estimated on the basis of an indirectly comparison of spectrum shapes of the data and simulation calculations.

A new method for analyzing triple $E_{\gamma_1} * E_{\gamma_2} * E_{\gamma_3}$ correlations data, the Rotational Plane Mapping Method, has been developed recently to directly measure the rotational damping width Γ_{rot} [4]. Fig.1 illustrates in a schematic way how undamped and damped rotational cascades generate a central valley flanked by ridges in the $E_{\gamma_1} * E_{\gamma_2}$ spectra. In the rotational damping region (Fig.1d,1e,1f) the independent selection of damped transition energies at (I+2)$\rightarrow$I and at I$\rightarrow$(I-2) causes the spike at the grid points(Fig.1a,1b,1c) to be smeared into a round hill having a width Γ_{rot} in all directions(Fig.1e). As shown in Fig.1f, when $\Gamma_{rot} > 4/\Im^{(2)}$ the smeared hills merge, resulting in a flat spectrum, except for a shallow diagonal valley, since there are no spikes to be smeared out at the diagonal $E_{\gamma_1} = E_{\gamma_2}$. The width of the valley is equal to the rotational damping width Γ_{rot}. Therefore, the spectrum can be expressed by a constant

spectrum minus a component of Gaussian or Breit-Wigner shape along the diagonal $E_{\gamma_1} = E_{\gamma_2}$.

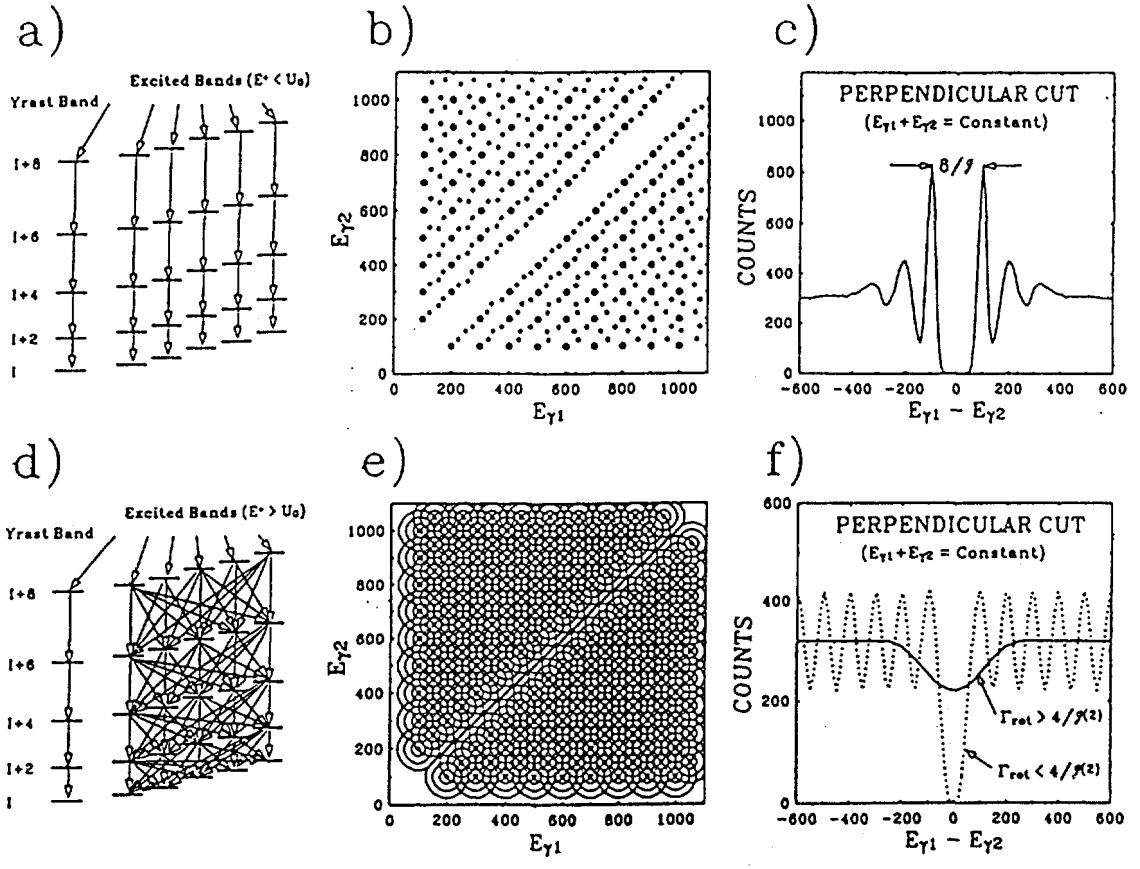

Fig. 1. *The schematic figure shows the expected patterns for $E_{\gamma_1} * E_{\gamma_2}$ spectra in b) and e) when the decay paths are regular rotational cascades (a) or when the pathway goes through a region where the rotational damping is dominating (d). The spectra c) and f) correspond to diagonal cuts for constant $E_{\gamma_1} + E_{\gamma_2}$ at b) and e) respectively.*

In the three dimensional spectrum, the average transition energies will also form grids in the three planes obeying the equations $E_{\gamma_1} = E_{\gamma_2}$, $E_{\gamma_1} = E_{\gamma_3}$, $E_{\gamma_2} = E_{\gamma_3}$. The damping is also smearing the three dimensional grid points with the missing points in the three planes each forming a valley. The three dimensional spectrum can therefore be represented by a constant spectrum minus three valleys superimposed. The three valleys join at the "great valley" at $E_{\gamma_1} = E_{\gamma_2} = E\gamma_3$. The width of the great valley is proportional to Γ_{rot}, and it can be displayed in tilted rotational planes, obeying the equations $E_{\gamma_1} - E_{\gamma_2} = N(E_{\gamma_3} - E_{\gamma_2})$, with N taking the values 1,2,3,4, is directly proportional to Γ_{rot}. We find it to be an advantage if the data in the tilted planes are divided by the total projection of the cube in order to reduce many of the unwanted effects from discrete lines, feedings and impurities. The corresponding 3D/2D analytical function is used in the fit of the spectrum shape to extract the values of Γ_{rot}.

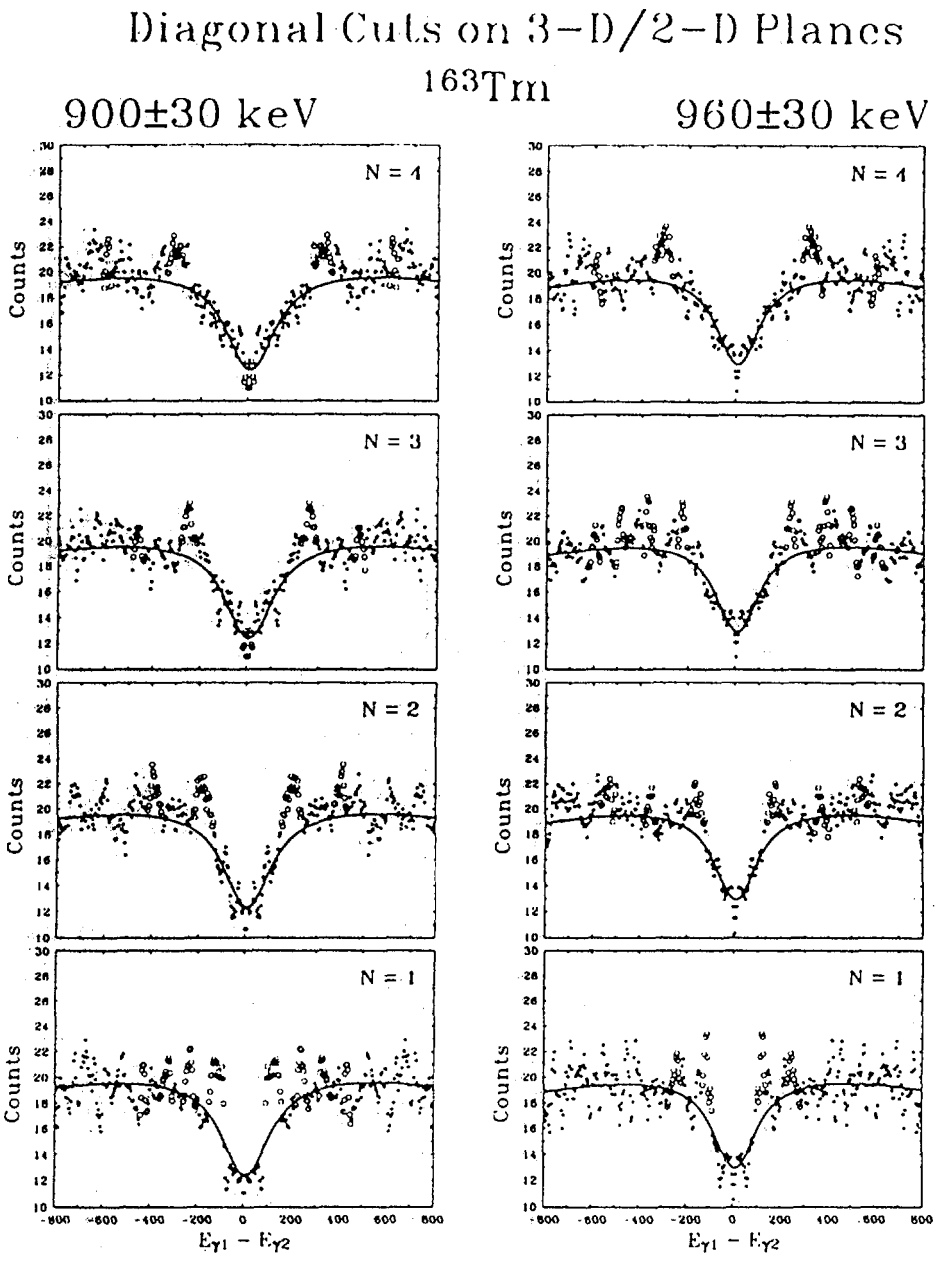

Fig. 2 *Spectra of diagonal cuts on the ratio planes 3D/2D for N=1,2,3,4 for transition energies* $(E_{\gamma_1} + E_{\gamma_2})/2$*=900 and 960 keV for intervals of 60 keV on the data of* ^{163}Tm*, high temperature gate. The open circles indicate the regions of peaks which have not been included in the last square fitting procedure.*

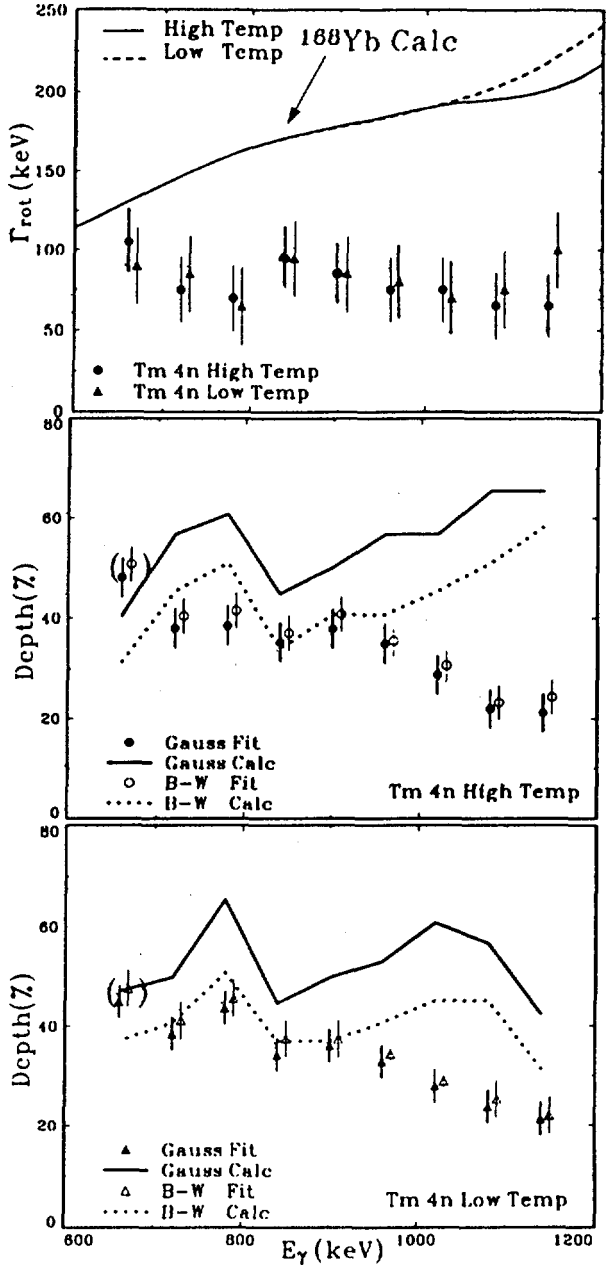

Fig. 3. *The values of Γ_{rot} shown are extracted for the high and low temperature gates on ^{163}Tm (upper part) together with the theoretical calculations including the motional narrowing effect. The analytical function used to reproduce the spectrum shapes includes a Gaussian shaped valley. The valley depths extracted from the ^{163}Tm high (middle part) and low (lower part) temperature gates are compared to the expected values (lines) both for a Gaussian and Breit-Wigner shaped valley, assuming that 20% of the transitions for each energy interval in a single spectrum consists of statistical E1 transitions.*

The method was applied to a high spin triple experiment on $^{162,163}Tm$, made by the use of *NORDBALL* and the heavy ion accelerator of the Niels Bohr Institute, by the $^{37}Cl + ^{130}Te$ [5] reaction. The data were analyzed with 4 gating conditions, making use of information from multiplicity and sum energy of the 4π BaF_2 ball, filtering in the best possible way the reaction channels (5n)-low-spin and (4n)-high-spin, each with a low and high sum-energy gate. Perpendicular cuts on the N=1,2,3 and 4 3-D/2-D planes for energy intervals of 60 keV and transition energy of $(E_{\gamma_1} + E_{\gamma_2})/2$=900 and 960 keV are shown in Fig.2. The ridge structures (open circles) changing from plane to plane are carefully stripped off by hand, keeping the expected pattern from the cold region in mind. The full drawn curves are obtained by first fitting a second order polynomial to the spectrum on the wings, leaving out the valley region, to take the influence from feeding into account to first order. Secondly the remaining intensity in the valley region is fitted by multiplying this polynomial function by the 3D/2D analytical function.

The experimental Γ_{rot} values obtained for the 2 different 4n regions are shown in Fig.3 and compared to the only existing microscopic calculations [4] made for ^{168}Yb. The results are constant within the statistical error yielding in average Γ_{rot} = 81 keV and 74 keV for the (4n)-high-spin and (5n)-low-spin regions respectively, almost independent of transition energy, perhaps with a tendency to raise in the region of the first backband. Only a very small effect of motional narrowing may be observed in the data points at 1080 and 1140 keV for the (4n)-high-spin data set. In contrary to the constant Γ_{rot}, a large variation in the valley depth is seen (Fig.3). A reasonable agreement is found between the depth of the valley and the corresponding Γ_{rot} up to 960 keV transition energies, especially when a Breit-Wigner function is used, but above this transition energy an increasing deviation is found.

The extracted Γ_{rot} values are significantly smaller than the theoretical predictions although calculation only is made for the ^{168}Yb nucleus. Thus the present results cast serious doubts upon the cranking model picture [3,6] of rotational damping, at least for rotational frequencies up to about 0.5 MeV. At higher rotational frequencies the more shallow valleys than predicted by a single Breit-Wigner component may suggest that the rotational width is probably composed of several different components and that the RPM method focuses more sensitively on the small Γ_{rot} values.

References:

[1] J.C. Bacelar, G.B. Hagemann, B. Herskind, B. Lauritzen, A. Holm, J.C. Lisle and P. Tjøm Phys. Rev. Lett. 55, (1985) 1858

[2] J.E. Draper, E.L. Dines, M.A. Deleplanque, R.M. Dimond and F.S. Stephens Phys. Rev. Lett. 56 (1986) 309

[3] B. Lauritzen, T. Døssing, R.A. Broglia Nucl. Phys. A457 (1986) 61

[4] B. Herskind, T. Døssing, D. Jerrestam, K. Shiffer, S. Leoni, J. Lisle, R. Chapman, F. Kazaie and J.N. Mo, Physics Letter B 276 (1992) 4-10

[5] B. Herskind, T. Døssing, S. Leoni, M. Matsuo and E. Vigezzi "Progress in Particle and Nuclear Physics", Vol.28, Erice 1991

[6] Vlasenko S., R.A. Broglia, T. Døssing and E. Ormand (1988). In: Proceedings of the Conference on High-Spin Nuclear Structure and Novel Nuclear Shapes, Argonne National Laboratory, Argonne, Illinois ANL-PHY-88-2

Statistical Gamma Transitions in ^{174}Hf

L.P.Farris, J.A.Cizewski, M.J.Brinkman, R.G.Henry, C.S. Lee
Rutgers University, New Brunswick, New Jersey 08903 USA
T.L.Khoo, R.V.F.Janssens, E.F.Moore, M.P.Carpenter, I.Ahmad, T.Lauritsen
Argonne National Laboratory, Argonne, Illinois 60439 USA
J.J.Kolata, K.B.Beard, D.Ye, U.Garg
University of Notre Dame, Notre Dame, Indiana 46556 USA
M.S.Kaplan, J.X.Saladin, D.Winchell
University of Pittsburgh, Pittsburgh, Pennsylvania 15213 USA

Abstract: Statistical spectrum extracted from the ^{172}Yb(α,2n)^{174}Hf reaction was fit with Monte Carlo simulations using a modified GDR E1 strength function and several formulations of the level density.

I. Introduction

After formation in a fusion-evaporation reaction, the compound nucleus decays by a combination of three types of gamma-transitions:[1] (i) statistical transitions, which remove excitation energy over the yrast line, but not much spin; (ii) quasi-continuum, collective, stretched, dipole and quadrupole transitions, which remove angular momentum, but not much energy; and (iii) discrete transitions, deexciting known, near-yrast levels. The quasi-continuum, quadrupole transitions go down collective bands that are approximately parallel to the yrast line, and form a bump on the continuum spectrum at $E_\gamma \approx 1$ MeV in rare-earth nuclei formed at high spin, as in (heavy-ion,xn) reactions. The statistical spectrum depends on the average gamma-transition strength and the level density, and we hope to extract data on these quantities. An accurate determination of the statistical spectrum is also important to studies of the E2 quasi-continuum spectrum, for the accurate removal of the statistical background.

II. Experiment

In order to isolate the statistical spectrum, it is necessary to populate the target nucleus with low angular momentum, minimizing the yield of quasi-continuum quadrupoles. The ^{172}Yb(α,2n)^{174}Hf reaction was used with a beam of 28 MeV α particles from the Notre Dame Tandem Van de Graaff accelerator. Reaction γ rays were recorded using the University of Pittsburgh Gamma Array, which consists of 6 Compton suppressed Ge detectors and 14 BGO scintillators. The Ge detectors were in-plane: two at 30°, two at 150°, one at 90° and one at 105° relative to the beam direction. Thirty million γ-γ coincidence events were recorded up to $E_\gamma = 5$ MeV. In addition, response functions of the Ge detectors were measured using 14 radioactive gamma sources with energies ranging from 0.122 to 2.754 MeV. The total projected gamma-coincidence spectrum (Fig. 1), shows a smoothly decreasing exponential, with no broad structure at 1 MeV, which is expected in a fusion reaction with heavy ions.

III. Extraction of Statistical Spectrum

In order to extract the continuum spectrum from the data, the following procedure was used. For each detector, spectra were gated on the $4^+ \rightarrow 2^+$, $6^+ \rightarrow 4^+$, and the $8^+ \rightarrow 6^+$ lines in order to select only ^{174}Hf transitions. The lines from the (n,n'γ) reactions were then fitted and subtracted out. The background from Compton-scattered γ rays was removed by the unfolding procedure[2] of Radford, et al. After their Compton spectra were removed, the discrete lines were fitted and subtracted from the unfolded spectrum. The remaining spectra for the six detectors were corrected for the relative efficiencies of the individual detectors as a function of E_γ. The intensity as a function of angle was assumed to follow a Lengendre polynomial, with the coefficient of $P_4(\cos\theta)$, $A_4 = 0$. The A_0 and A_2 coefficients can then

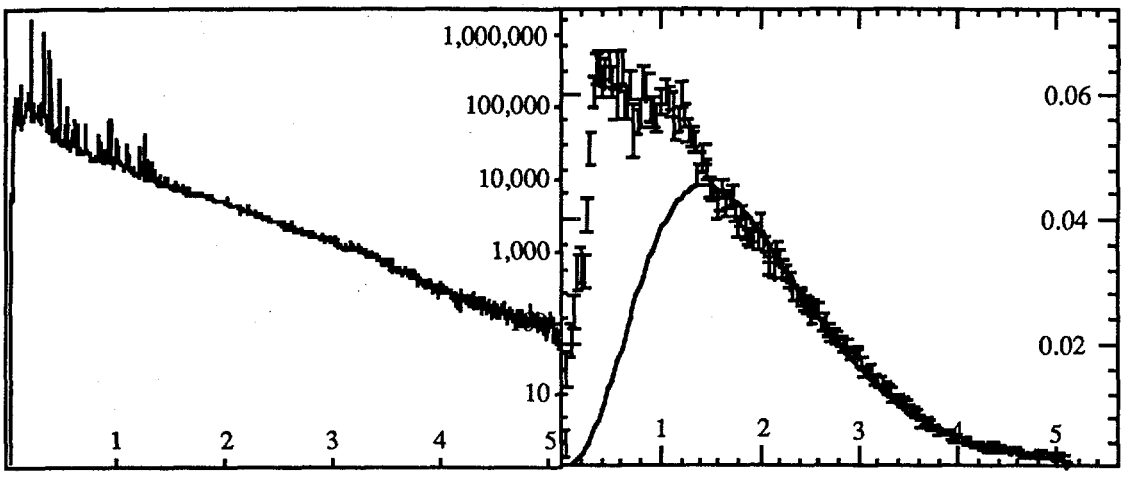

Fig.1. Total projected spectrum.

Fig.2. Spectrum of statistical transitions compared to single transition prediction (solid line)

be determined from the spectra at two angles. Figure 2 displays the isotropic portion of the continuum spectrum, normalized to the $2^+ \rightarrow 0^+$ total intensity.

To determine the average energy and angular momentum at which the statistical gamma cascade is entered and exited, it is first assumed that all cascades go through the $2^+ \rightarrow 0^+$ transition, so that the total number of cascades, N_c, is given by the $2^+ \rightarrow 0^+$ intensity, corrected for conversion. The average multiplicity, $\langle m_\gamma \rangle$, for each transition is determined by dividing its intensity by N_c. For discrete lines, the fitted intensity is used, and for the statisticals, the number of counts in the energy bin is used. The energy per cascade removed by a transition is given by $E_\gamma \langle m_\gamma \rangle$, where E_γ is the fitted peak energy for discrete transitions, and the average energy of a bin for the statisticals. The angular momentum removed is $\Delta I_\gamma \langle m_\gamma \rangle$. ΔI_γ is known for most of the discrete transitions, and is assumed to be 0.5 $\hbar$ for the statistical transitions. Table 1 gives the calculated total values.

IV. Calculation of the Statistical Spectrum

The spectral distribution, $\nu(E_\gamma)$, of primary γ rays is proportional to the average gamma-transition probability and the level density. If the statistical gammas were only electric dipole in nature[3], then

$$\nu(E_\gamma) \propto E_\gamma^3 f_{E1}(E_\gamma) \sum_{I_f} \rho(E_i - E_\gamma, I_f) / \rho(E_i, I_i) \qquad (1)$$

where f_{E1} is proportional to the average B(E1) value, ρ is the level density, i is the initial state, f is the final state, and I is the spin. In general, the spectral distribution would be composed of a sum of contributions of different multipolarities of both electric and magnetic transitions. For simplicity, in the present study it was assumed that the statistical cascade is composed of electric dipole transitions only, since these are the strongest in single particle

Table 1. Multiplicities of transitions, and energy and angular momentum removed.

	discrete	statistical	total
$\langle m_\gamma \rangle$	4.202 ± 0.475	4.262 ± 0.018	8.464± 0.493
E_γ [MeV]	1.680 ± 0.131	6.565 ± 0.121	8.245± 0.252
I_γ [$\hbar$]	6.705 ± 0.853	2.146± 0.009	8.851± 0.862

estimates. We take f_{E1} to be dominated by the giant E1 resonance, and that it exhausts the E1 sum rule[4,5], so that

$$f_{E1} = 50NZA^{-5/3}(1 + 0.8x)\, E_\gamma \Gamma_G \left\{(E_\gamma^2 - E_G^2)^2 + (\Gamma_G E_\gamma)^2\right\}^{-1} \qquad (2)$$

where x = 0.5 is the fraction[6] of exchange forces in the nuclear force. The energy and width of the GDR are estimated by $E_G \simeq 80\ A^{-1/3}$ MeV, which correspond to $E_G \simeq 14.6$ MeV for ^{174}Hf, and $\Gamma_G \simeq 5$ MeV, respectively. This expression matches the measured strength function from the photoabsorption spectrum, but overestimates the strength at low energies[7] ($E_\gamma < 5$ MeV) by about 30%.

Kadmenskii, Markushev, and Furman[8] (KMF) address this by including quasiparticle fragmentation in a microscopic calculation of the strength function. The result is to multiply f_{E1} at low E_γ by a factor

$$g = 0.7(E_\gamma^2 + 2U_f/3g(\varepsilon_F))/E_\gamma E_G \qquad (3)$$

where U_f is the energy of the final state of the transition and the density of single particle states at the Fermi energy is $g(\varepsilon_F)$. Since eq.3 fits the measured strength function[8], the KMF formulation of the E1 strength function is adopted for this work.

The other major component in eq.1 is the level density. The effect of pairing on the level density is to reduce the number of states below the pairing gap to zero, but this effect decreases as a function of spin. This was simulated with a level density yrast line (LDYL), which was determined by fitting $E_{LDYL} = E_0 + (\hbar^2/2\mathcal{J})I(I+1)$ to the first levels lying above the ground state and beta-vibrational band for each spin, where $\mathcal{J}$ is an effective moment of inertia for the LDYL. The intrinsic excitation energy U is measured relative to the LDYL: $U = E_{ex} - E_{LDYL}$. The spin dependence of the level density is taken to be [9]

$$\rho(E_{ex},I) = (2I+1)\left(\hbar^2/2\mathcal{J}\right)^{3/2}\rho(U,0) \qquad (4)$$

Three level density formulas have been used: the Constant Temperature formula (CT), the Fermi-gas model formula [9] (FG), and the Grossjean and Feldmeier Fermi-gas formula[10] (GFFG):

$$\textbf{CT}: \qquad \rho(U) = 1/T \exp(U/T) \qquad (5)$$

$$\textbf{FG}: \qquad \rho(U) = (\sqrt{a}/24)\frac{\exp(\sqrt{aU})}{(E+(3/2)T)^2} \qquad (6)$$

$$T = \sqrt{U/a + 9/16a} + (3/4)\,a$$

$$\textbf{GFFG}: \qquad \rho(U) = \delta(U) + \frac{\exp((U/T) + aT)}{\sqrt{48U}}\,\frac{1 - \exp(-aT)}{\sqrt{1 - (U/2T)\exp(-aT)}} \qquad (7)$$

$$U = aT^2/(1 - \exp(-aT))$$

The level density parameter $\mathbf{a} = \pi^2 g(\varepsilon_F)/6$, and the nuclear temperature $T \approx \sqrt{U/\mathbf{a}}$.

The CT formula arises from assuming a nuclear temperature, and using the Fermi-distribution for a simple calculation of the level density based on the density of single-particle states near the Fermi energy.

The FG formula arises from a detailed statistical mechanical calculation, in which it is assumed that the density of single particle states is a smooth function.

The GFFG formula is calculated following the same procedure as the FG formula, except that the ground state is taken into account with a delta function, thus fixing the divergence at low energy arising from the denominator in the standard Fermi-gas formula.

The statistical cascade, from an entry distribution in phase space, to within 1 MeV of the yrast line was modeled in a Monte Carlo simulation[11], using eq. 1 with the KMF strength function and the three level density expressions. The probability of decay by a given transition is given by $\nu(E_\gamma)$, and the cascades typically proceed through several transitions. The average entry point of the cascade was fixed at the value calculated from the experimental data. When using the CT level density, T was varied, and when using the two FG formulas, a was varied. The resulting spectra were normalized to the number of cascades.

In Fig.2, the experimental spectrum has been fit with the expression $A\ E_\gamma^3\ \exp(-E_\gamma/T)$, where A is an amplitude, and T is analogous to temperature in eq. 5. This corresponds to a cascade consisting of a single γ ray, with a constant temperature level density, no change in spin, and a constant f_{E1} as a function of energy. This and related expressions[1,12,13] have typically been used to fit the continuum spectrum above 2.5 MeV, to then subtract the fit as the background to the quasi-continuum spectrum. In Fig.2, for an α-induced reaction, this fit is only good above 1.5 MeV, whereas for rare-earth nuclei formed at high spin, the quasi-continuum bump typically is centered around 1 MeV. Therefore, this expression is not adequate to determine the background of the quasi-continuum.

Figure 3 shows the results of the Monte Carlo simulations. These simulations consist of cascades of several statistical transitions, with realistic expressions for the level density

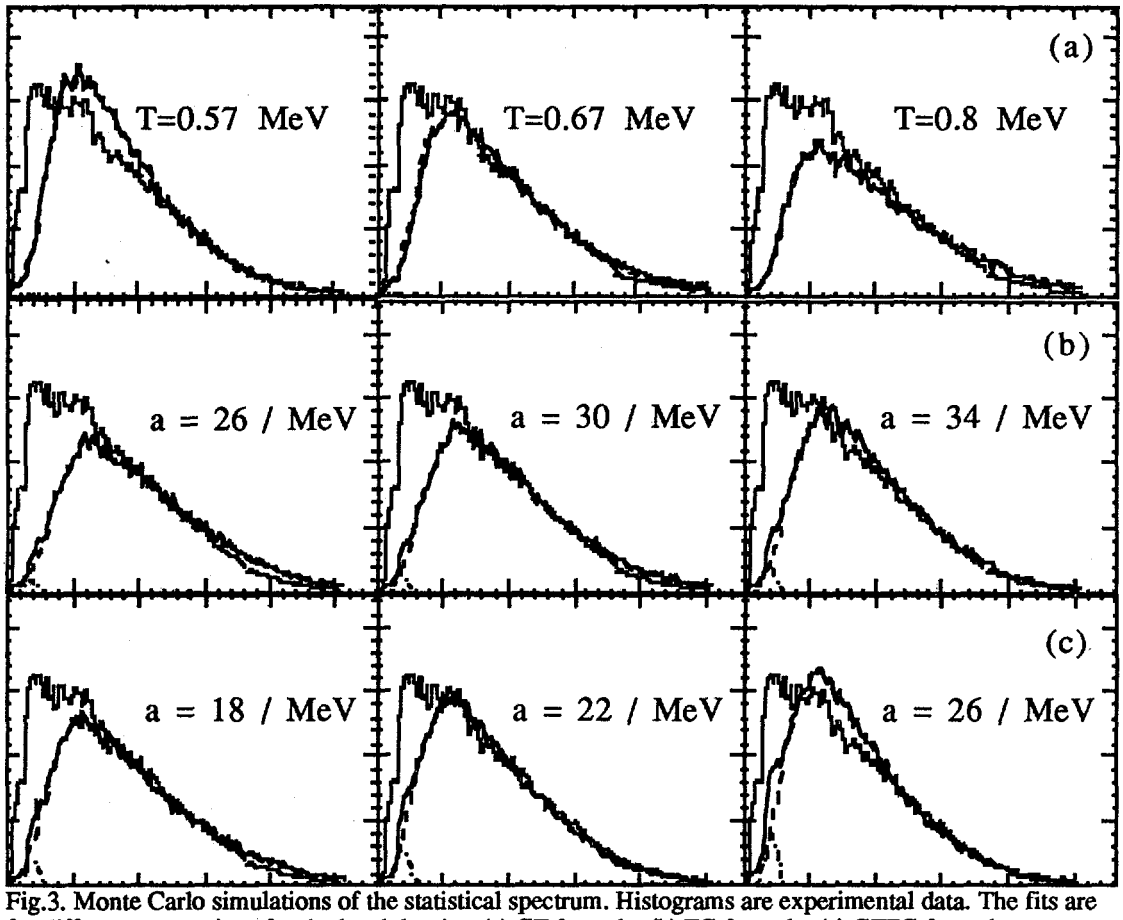

Fig.3. Monte Carlo simulations of the statistical spectrum. Histograms are experimental data. The fits are for different expressions for the level density: (a) CT formula, (b) FG formula, (c) GFFG formula

and the E1 strength function. All three expressions for the level density are able to produce a good fit of the data down to 1 MeV, with the GFFG formula giving the best fit, although comparable to the CT formula. In particular, we note that for the GFFG formula, the level density parameter, **a** = 22/MeV, is consistent with both a diffuse Fermi-gas formula estimate,[14] **a** = (A/14.61) (1 + 4 $A^{-1/3}$) = 20.44 / MeV, and **a** = A/8 = 21.75 / MeV, determined from a fit of neutron resonance densities across a wide range of nuclear mass.[15] Similarly, if we take **a** = 21 / MeV and U = **a**T^2 for the constant temperature formula, for an intrinsic excitation of 9 MeV, T = 0.65 MeV.

V. Summary and Conclusions

The spectrum of statistical gamma transitions was measured in the $^{172}Yb(\alpha,2n)^{174}Hf$ reaction. This spectrum was fit to a simple formula corresponding to a single transition in the statistical cascade, and to Monte Carlo simulations with multiple transitions in the cascade, using realistic expressions for the average gamma-transition probability, but considering only E1 transitions.

The data could not be fit with the single-transition model below E_γ = 1.5 MeV. With the Monte Carlo simulations it is possible to fit the data down to E_γ = 1 MeV. The GFFG formula gives the best fit, with level density parameter close to that expected, but the CT formula gives a comparable fit.

The yield of statisticals is underestimated by the realistic models at low energy. However, M1 and E2 transitions are expected to become more important as the cascade approaches the vicinity of the yrast line, and the statistical nature of the transitions eventually gives way to domination by nuclear structure effects.

In the study of quasi-continuum transitions, the use of the expression A E_γ^3 exp(-E_γ/T) is not recommended, because it can only reproduce the observed statistical spectrum down to $E_\gamma \approx$ 1.5 MeV. An improved determination of the statistical background can be obtained by using a Monte Carlo simulation of a multiple transition cascade, using eq.1 to determine the transition probabilities, with a Constant Temperature level density and the KMF gamma-strength function. To determine the temperature, the data can be fit above E_γ > 2.5 MeV.

This work supported in part by the National Science Foundation and the U.S. Department of Energy, Nuclear Physics Division, under Contract No. W-31-109-ENG-38.

1. D.C.Radford, et al., Phys.Rev.Lett **55**,1727(1985).
2. D.C.Radford, et al., Nucl. Inst. Meth. **A258**,111(1987).
3. G.A.Bartholomew, et al., Adv. Nucl. Phys. **7**, 229(1973).
4. P.Axel, Phys. Rev. **126**, 671(1962).
5. G.A.Leander, Phys.Rev.C38,728(1988).
6. J.M.Eisenberg and W.Greiner, *Nuclear Theory, Vol.II* (1987).
7. C.M.McCullagh, M.L.Stelts, and R.E.Chrien, Phys. Rev. **C23**, 1394(1981).
8. S.G.Kadmenskii, et al., Sov. J. Nucl. Phys. **37** 165(1983).
9. D.W.Lang, Nucl.Phys.**77**, 545(1966).
10. M.K.Grossjean and H.Feldmeier, Nucl. Phys. **A444**, 113(1985).
11. R. Holzmann, et al., Phys. Lett. **B195**, 321 (1987).
12. S.H.Sie, et al., Nucl. Phys. **A352**, 279(1981).
13. R.M.Diamond and F.S.Stephens, Ann. Rev. Nucl. Part. Sci. **30**, 85(1980).
14. J.Toke and W.J.Swiatecki, Nucl. Phys. **A372**, 141 (1981).
15. A.Bohr and B.R.Mottelson, *Nuclear Structure, Vol I*, 187 (1969).

The giant dipole resonance and the shape of hot nuclei

A. Bracco, F. Camera, B. Million, M. Pignanelli

Dipartimento di Fisica, Universitá di Milano and INFN sez. Milano, via Celoria,16 20133 Milano (Italy).

J.J. Gaardhøje, A. Maj, A. Atac

The Niels Bohr Institute, Copenhagen

Information on the nuclear shapes and on their changes with spin (I) and excitation energy (E^*) for hot rotating compound nuclei can be obtained through the study of the gamma decay of the Giant Dipole Resonance (GDR). However, because the shape and orientation of nuclei at finite temperature display large fluctuations the measured GDR response functions reflect effective nuclear deformations which can be different from the equilibrium deformation. These effective deformations depend not only on the size of the fluctuations but also on the dynamics of the coupling of the GDR vibrations to quadrupole surface vibrations. A systematic study of the angular distribution of the gamma rays emitted by the GDR has been undertaken. They are expected to provide a stringent test of the exsisting theoretical models (cf. refs. 1 and 2). Contrary to the angular integrated response, angular distributions do not require a statistical model analysis and are expected to have a larger sensitivity to orientation fluctuations. Some of the most recent results are here discussed, the central theme being the dependence of the angular anisotropy on spin for two mass regions, namely A$\sim$160-170 ($^{165-167}$Er, ^{162}Yb) and A$\sim$110 ($^{109-110}$Sn).

The Sn isotopes are spherical in their ground states and are expected to become oblate under the stress of rotations, with a deformation that increases with the size of the nuclear spin. The situation is different for $^{161-162}$Yb and $^{165-167}$Er which have prolate ground states and which are expected to become first spherical and then oblate as a function of rotational frequency ω and temperature T. The critical values of ω and T at which these transitions take place are rather small for soft nuclei like $^{161-162}$Yb and considerably larger for mid-shell nuclei like $^{165-167}$Er (N=97-99).

The compound nucleus reactions that were employed are listed in table 1. The γ rays emitted by the reactions were measured by the detection system HECTOR. It consists of 8 large volume BaF_2 detectors (14.5 cm in diameter x 17.5 cm in length) positioned at 4 different angle pairs ($\pm 165^0$, $\pm 135^0$, $\pm 90^0$, and $\pm 45^0$) that measure the energy and the time of the high energy gamma rays and 14 small BaF_2 (5.54cm x 5.54 cm covering all together 30 % solid angle) placed around the target used as a multiplicity filter for low-energy γ transitions. Gain drifts of the

large volume BaF_2 were corrected to better that 0.2% using the light pulses of an LED system.

The quadrupole coefficients a_2 were extracted as a function of the γ energy E_γ by fitting the measured spectra of the high energy γ rays with the function $N(E_\gamma,\theta) = N_0(E_\gamma)[1+a_2(E_\gamma)P_2(cos\theta)]$, where $P_2(cos\theta)$ is the Legendre polinomy.

The $a_2(E_\gamma)$ distributions for the nuclei $^{165-167}$Er are presented in figure 1. In spite of the fact that the average angular momenta imparted to the $^{166-167}$Er nuclei ($24\hbar$ and $26\hbar$) are approximately twice of the value for ^{165}Er ($14\hbar$) the measured anistropies are almost identical and very small (2-3%). This result indicates that the GDR sees an effective deformation that is very small. In principle, this is not incompatible with the fact that because of the modest temperature of the system under study shell effects are expected to be important. This,together with the fact that the rotational frequencies in question are small, suggests that the expected deformation cannot be much different to that of the equilibrium which is characterized at T=1.3 MeV by $\beta \sim 0.2$. In spite of this fact the anisotropies calculated at the equilibrium deformations (dashed-dotted lines of figure 1) are much larger than those observed experimentally. Consequently, one can expect thermal fluctuatuions to play a central role. To check this point a detailed theoretical analysis is needed. We will only discuss the most straighforward calculations.

The a_2 predictions presented in this report were obtained making use of the

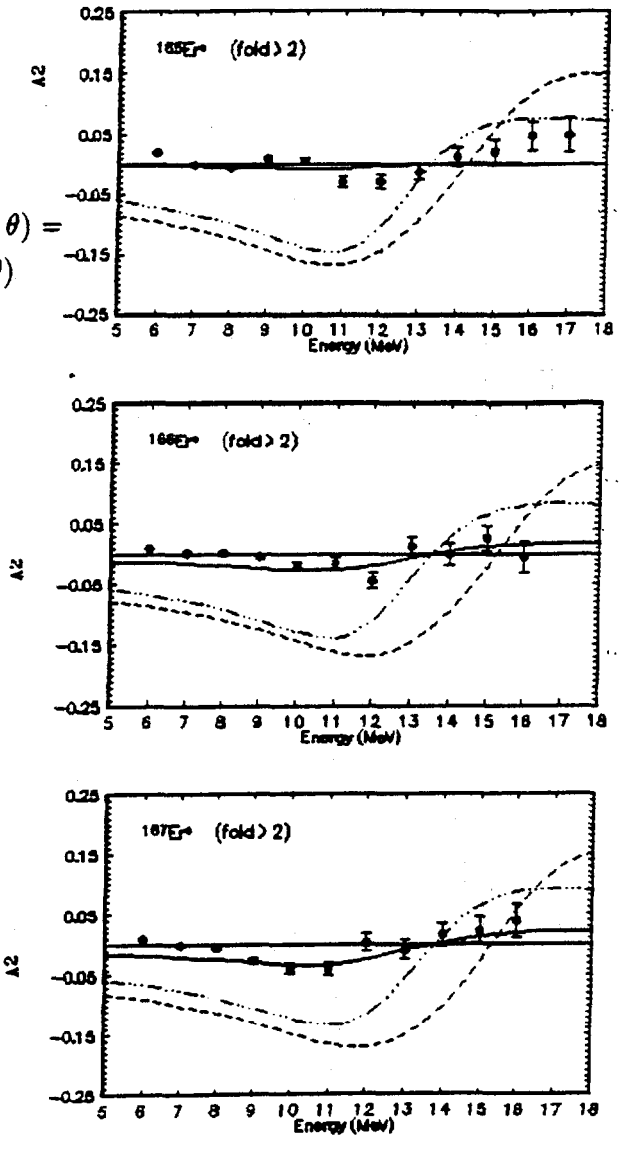

Fig. 1 a_2 coefficients as a function of the transition energy of the gamma rays emitted by $^{165-167}$Er with excitation energy and spin given in the table. The curves correspond to: equilibrium deformation (dotted-dashed lines), adiabatical model with shape fluctuations (dashed lines) and with shape and orientation fluctuations (full lines).

Reaction	E_k (MeV)	E^* (MeV)	$\langle J \rangle (\hbar)$
$^{17}O + ^{150}Nd \rightarrow ^{167}Er$	85	64	~ 26
$^{18}O + ^{148}Nd \rightarrow ^{166}Er$	78	56	~ 24
$^{17}O + ^{148}Nd \rightarrow ^{165}Er$	70	48	~ 14
$^{48}Ti + ^{114}Cd \rightarrow ^{162}Yb$	223	75	~ 46
$^{48}Ti + ^{62}Ni \rightarrow ^{110}Sn$	223	92	~ 40
$^{48}Ti + ^{61}Ni \rightarrow ^{109}Sn$	209	80	~ 40

Table 1 In this table the incident laboratory energy E_k, the excitation energy E^* and the average angular momentum $\langle J \rangle$ of the compound nuclei are given for all the reactions used in the present study.

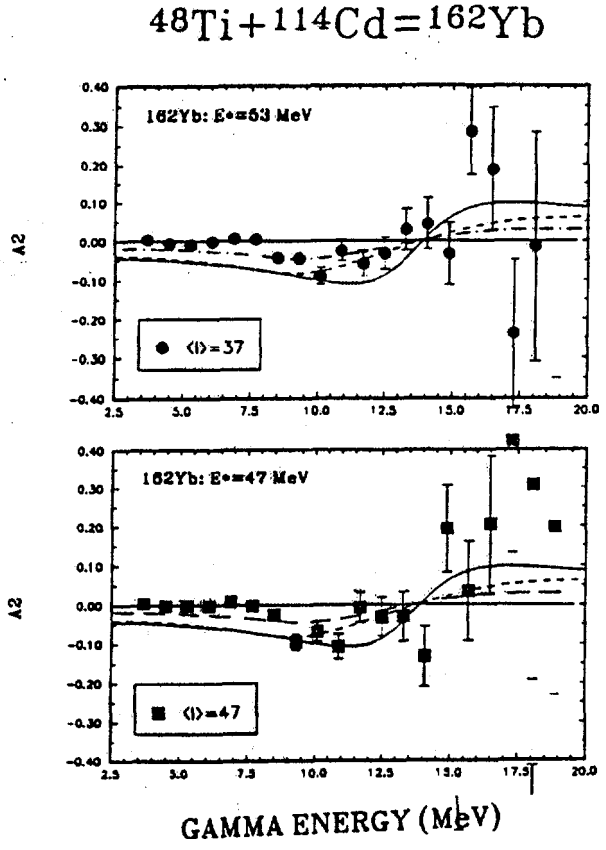

Fig. 2 a_2 coefficients as a function of the transition energy of the gamma rays emitted by ^{162}Yb. In these legenda E^* is the excitation energy above yrast. In the top panel the data correspond to an average spin of $37\hbar$, in the bottom to $47\hbar$. The curves correspond to: equilibrium deformation (full lines), adiabatical model with shape fluctuations (short dashed lines) and with orientation and shape fluctuations (dotted-dashed and long-dashed lines).

models of references 1 and 2. In the most general model of thermal shape and orientation fluctuations the time dependence of these fluctuations may play a central role. Two limits of this model are the adiabatic and that in which the frequency with which the shape and orientation change is much larger that the spreading in frequency induced by the coupling of the GDR to the surface. In the first case the GDR sees the nucleus as an ensemble of static shapes. In the second, the GDR approximately only sees the average deformation of the system**. The dashed and full drawn lines of figure 1 are adiabatical calculations, the first accounting only for shape fluctuations and the second including also orientation fluctuations. While the magnitude of the low spin data are underestimated by the calculations with shape and orientation fluctuations, the two other sets of data are fairly well reproduced. This fact indicates that orientation fluctuations are overestimated at low spins. A possible explanation is connected to the form of the shape and orientation probability at low rotational frequency. It has been found [ref 3] that this probability is different when it is calculated at constant E* and I instead of constant T and ω (used for these calculations). To investigate if this has an effect on the GDR response one needs data corresponding to a well defined and narrow region of spin, especially at low spin where the rate of change of the a_2 with the rotational frequency is predicted to be large. In the case of figure 1 the calculations were made at the rotational frequency associated to the average spin of the triangular spin distribution of the compound.

Some of the data obtained for ^{162}Yb are shown in figure 2. The two sets correspond to the same CN reactions and to different gates on the coincidence folds in the multiplicity filter. The associated average spins are 37 and 47 for the top and bottom part, respectively. These data evidence spin effects since the experimental anisotropies increase almost a factor of two when the average angular momentum is increased by only 10 $\hbar$ and the temperature goes from 1.35 to 1.25. The comparison with the model predictions shows that it is difficult to choose among the three different calculations for both spin gates.

The situation is different in the case of $^{109-110}$Sn as it is shown in figure 3 in which the experimental and calculated values of the a_2 averaged in the interval E_γ=11-14 MeV are plotted. In this interval of γ transition energies, the angular anisotropies as in the cases of $^{165-167}$Er and ^{162}Yb have small errors and their absolute values are the largest. Two remarks can be made observing the data alone: first the a_2 are basically unchanged at the two excitation energies 80 MeV (open squares) and 92 MeV (filled circles), second the increase of the magnitude of the a_2 with spin is more pronounced than in ^{162}Yb. The comparison with calculations displays that the results for the equilibrium deformation substantially overpredict the magnitude of the observed a_2 in all range of angular momenta, except the

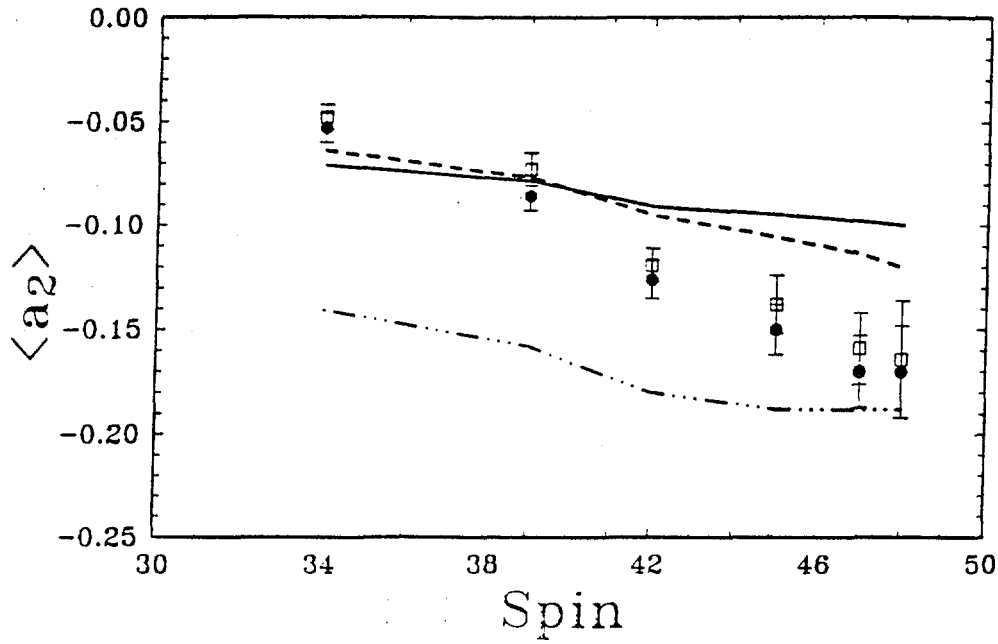

Fig. 3 Averaged values of the a_2 coefficients in the interval $11 \leq E_\gamma \leq 14$ MeV for ^{109}Sn (open squares) and ^{110}Sn (filled circles). The excitation energies are 80 and 92 MeV, respectively. The calculated curves correspond to: equilibrium deformation (dotted-dashed line), adiabatical model with shape and orientation fluctuations (solid line) and adiabatical model with shape and orientation fluctuations and with more realistic line shapes(dashed line).

better the magnitude of the observed a_2 at the lower angular momentum, but underpredicting the data at higher angular momenta.

To which extent these results reflect the rate of change with angular momentum of the hopping in the nuclear shape and orientation (motional narrowing) is an open question. We are currently investigating this point with data obtained with a better multiplicity filter consisting of 38 elements and covering 85% solid angle. With this increased experimental sensitivity and with a better theoretical description we expect to learn more on shapes, fluctuations and on their coupling to the GDR.

1) W.E. Ormand et al., Phys. Rev. Lett. 64,2254 (1990) and to be published

2) Y. Alhassid et al., Phys. Rev. Lett 65,2527 (1990).

3) A. Goodman, Nucl. Phys. A258,348(1991) and to be pubblished

** To be noted that calculations at the equilibrium deformation provide an approximate estimate of the effect of time dependence of the fluctuations in the limit where the hopping frequency in the orientation and shape fluctuations is infinite.

STATISTICAL ORIENTATION FLUCTUATIONS: CONSTANT ANGULAR MOMENTUM VERSUS CONSTANT ROTATIONAL FREQUENCY CONSTRAINTS

Alan L. Goodman
Physics Department, Tulane University
New Orleans, Louisiana 70118

ABSTRACT

Statistical orientation fluctuations are calculated with two alternative assumptions: (1) the rotational frequency remains constant as the shape orientation fluctuates, and (2) the average angular momentum remains constant as the shape orientation fluctuates.

1. INTRODUCTION

If a hot rotating even-even nucleus is in an equilibrium state, then the rotation axis is usually parallel to a principal axis of the intrinsic shape. However thermal fluctuations can populate non-equilibrium states in which the rotation axis does not coincide with a principal axis [1]. In such states, the orientation of the intrinsic principal axes with respect to the rotation axis is defined by the angles (θ,ϕ). The statistical orientation fluctuations generate an orientation probability distribution $P(\theta,\phi)$. Two alternative methods for calculating this distribution will be compared.

2. ORIENTATION DISTRIBUTIONS

The conventional assumption is that the nuclear rotational frequency remains constant as the orientation angles fluctuate [1,2]. If the nucleus has specified frequency ω and temperature T, then the equilibrium state minimizes the free energy in the rotating frame

$$F'(\theta,\phi;\omega,T) = E - TS - \underset{\sim}{\omega}\bullet\underset{\sim}{I}, \tag{1}$$

where $E=<H>$ is the energy, S is the entropy, and $\underset{\sim}{I}=<\underset{\sim}{J}>$ is the angular momentum. The probability that the nucleus has an orientation (θ,ϕ) is [1,2]

$$P(\theta,\phi;\omega,T) \propto e^{-F'/T}. \tag{2}$$

The constant frequency distribution (2) may be defective. As an example, let the nuclear shape be axially symmetric. The limiting values of the orientation angle θ are 90° (rotation axis perpendicular to symmetry axis) and 0° (rotation axis parallel to

symmetry axis). For $\theta=90^\circ$, the spin is $\mathcal{I}_x\omega$, and at $\theta=0^\circ$, the spin is $\mathcal{I}_z\omega$. If ω is the same for all orientations, then the ratio of these spins is

$$\frac{I(\theta=90^\circ)}{I(\theta=0^\circ)} = \frac{\mathcal{I}_x}{\mathcal{I}_z} \quad . \tag{3}$$

For a deformation $\beta=0.3$, this spin ratio is ~1.35. For example, if $I(\theta=0^\circ)=30\hbar$, then $I(\theta=90^\circ) = 40\hbar$. Since the nucleus is an isolated system, its angular momentum should be conserved during the orientation fluctuations. However in this simple example, spin conservation is violated by $10\hbar$. This unphysical result is caused by the assumption that ω remains constant during the orientation fluctuations. Furthermore the variable which is quantized and observed is the spin, not the rotational frequency.

Consequently the nuclear spin should remain constant as the orientation angles fluctuate. If the nucleus has specified I and T, then the equilibrium state minimizes the free energy

$$F(\theta,\phi;I,T) = E - TS, \tag{4}$$

and the orientation probability distribution is

$$P(\theta,\phi;I,T) \propto e^{-F/T}. \tag{5}$$

Mean field theories generate wave functions for deformed nuclei which do not conserve angular momentum. Instead one considers the *average* spin, defined by

$$I(I+1) = \langle J_x \rangle^2 + \langle J_y \rangle^2 + \langle J_z \rangle^2 , \tag{6}$$

where (x,y,z) are the intrinsic principal axes. Consequently if mean field theories are used to calculate orientation fluctuations, then the spin cannot be conserved. Instead we apply the less stringent requirement that each orientation (θ,ϕ) has the same *average* spin, i.e., the same value of I defined in eq. (6).

3. j = 13/2 MODEL

Is the constant ω orientation distribution (2) a good approximation to the correct constant I orientation distribution (5)? Consider an axially symmetric quadrupole potential, where z is the symmetry axis. Restrict the model space to the j=13/2 shell. For axial symmetry, all values of ϕ are equivalent, so let $\phi=0^\circ$. Then the potential in the rotating frame is

$$h'(\omega,\theta) = \frac{-\hbar\omega_0}{b^2}\beta Q_{20} - \omega J_x \sin\theta - \omega J_z \cos\theta - \mu N, \tag{7}$$

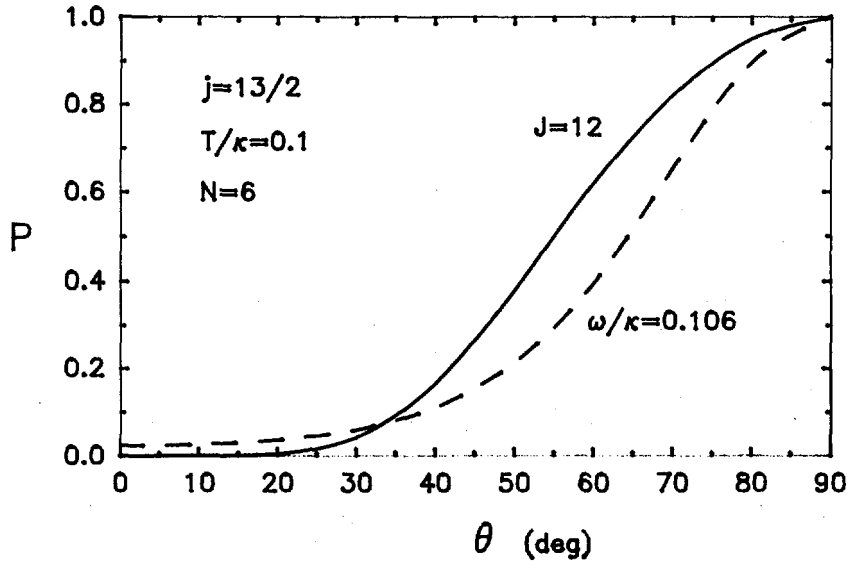

Fig. 1. The orientation probability P versus the orientation angle θ for the j=13/2 model. The constant average spin constraint is compared to the constant rotational frequency constraint.

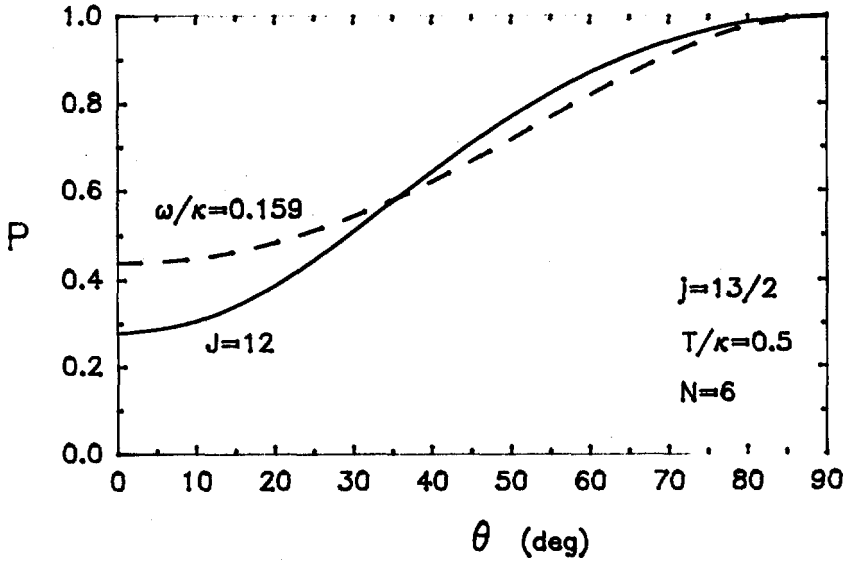

Fig. 2. See Fig. 1.

where θ is the angle between the rotation axis and the symmetry axis, β is the quadrupole deformation, ω_0 is the oscillator frequency, b is the oscillator length, and μ is the chemical potential.

The constant spin distribution (5) will now be compared to the constant frequency distribution (2). Consider the equilibrium state with the properties $T/\kappa = 0.1$, $J = [I(I+1)]^{1/2} = 12$, $\omega/\kappa = 0.106$, and $\theta = 90^\circ$. (The constant κ is proportional to β, where $\kappa = 2.6$ MeV for a rare-earth nucleus with $\beta=0.3$.) The orientation fluctuations about this equilibrium state are calculated (a) with constant $J=12$, and (b) with constant $\omega/\kappa = 0.106$. The two orientation distributions are compared in Fig. 1. Fig. 2 gives a similar comparison for fluctuations around the equilibrium state with $T/\kappa = 0.5$, $J = 12$, $\omega/\kappa = 0.159$, and $\theta = 90^\circ$. The differences between the constant spin probability and the constant frequency probability are as large as 0.22, and differences on the order of 0.1 seem to be typical. For orientations near $\theta=90^\circ$, the constant spin constraint gives larger relative probabilities than the constant frequency constraint. For orientations near $\theta=0^\circ$, the reverse occurs.

If we use the constant ω constraint, then each orientation θ will have a different *average* spin J. Fig. 3 shows $J(\theta)$ for the two equilibrium states in Figs. 1 and 2. For $T/\kappa=0.5$ and $\omega/\kappa = 0.159$, the spin varies from 12.0ħ at $\theta=90^\circ$ to 7.5ħ at $\theta=0^\circ$. Therefore angular momentum conservation is violated by 4.5ħ during the orientation fluctuations. Fig. 2 shows that this violation occurs with a large relative probability of 0.44 ($\theta=0^\circ$). Similarly for $T/\kappa=0.1$ and $\omega/\kappa = 0.106$, the spin varies from 12.0ħ at $\theta=90^\circ$ to 5.2ħ at $\theta=0^\circ$. Angular momentum conservation is violated by 6.8ħ. These violations of spin conservation are unphysical consequences of the constant ω constraint.

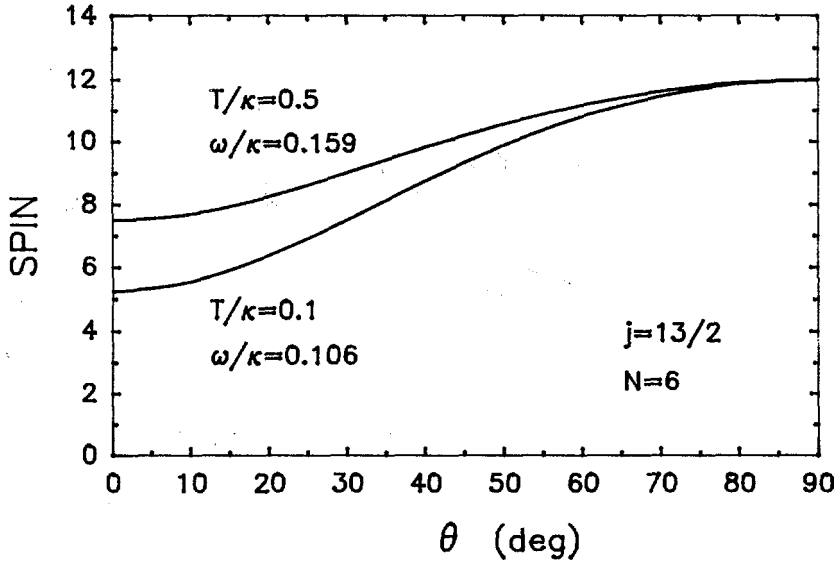

Fig. 3. The average spin J versus the orientation angle θ for the j=13/2 model. The constant rotational frequency constraint is used. The equilibrium orientation ($\theta=90^\circ$) has J=12.

4. LANDAU MODEL

The Landau model of shape transitions developed by Alhassid et.al. [1,2] can also be used to compare the two constraints. Consider an axially symmetric shape. The constant ω orientation distribution is [1,2]

$$P(\theta;\omega,T) \alpha \exp [(\mathcal{I}_x \sin^2\theta + \mathcal{I}_z \cos^2\theta)\ \omega^2/2T], \tag{8}$$

and the constant I orientation distribution is

$$P(\theta;I,T) \alpha \exp \left[- \left[\frac{\mathcal{I}_x \sin^2\theta + \mathcal{I}_z \cos^2\theta}{\mathcal{I}_x^2 \sin^2\theta + \mathcal{I}_z^2 \cos^2\theta} \right] \frac{I(I+1)}{2T} \right]. \tag{9}$$

For a prolate shape, the ω in eq. (8) and the I in eq. (9) are related by the equilibrium constraint

$$[I(I+1)]^{1/2} = \mathcal{I}_x \omega. \tag{10}$$

The differences between the constant ω distribution (8) and the constant I distribution (9) are comparable to the differences found with the $j=13/2$ model. Since $\mathcal{I}_x/\mathcal{I}_z$ increases with β, the difference between the two constraints is larger for a superdeformed shape than for a normal deformed shape.

5. CONCLUSIONS

Statistical orientation fluctuations should be calculated with a constant spin constraint, or at least with a constant average spin. The constant ω orientation distribution may be a poor approximation to the constant I orientation distribution. The constant ω constraint causes large violations of angular momentum conservation.

ACKNOWLEDGEMENT

This work was supported in part by the National Science Foundation.

REFERENCES

1. Y. Alhassid and B. Bush, Phys. Rev. 65, 2527 (1990).
2. Y. Alhassid and B. Bush, Nucl. Phys. A531, 39 (1991).

INTERNATIONAL CONFERENCE ON NUCLEAR STRUCTURE AT HIGH ANGULAR MOMENTUM

Ottawa

Session 5: Nuclear Spectroscopy (I)

Delayed Band Crossing in the Unfavoured Signature Partner of the $h_{9/2}[541]1/2^-$ Band in ^{163}Tm

H.J. Jensen[1], G.B. Hagemann[1], P.O. Tjøm[2], A. Ataç[1], M. Bergström[3], A. Bracco[5], A. Brockstedt[3], H. Carlsson[3], P. Ekström[3], J.M. Espino[4], B. Herskind[1], F. Ingebretsen[2], J. Jongman[6], S. Leoni[5], R.M. Lieder[1], T. Lönnroth[7], A. Maj[1], B. Million[5], A. Nordlund[3], J. Nyberg[1], M. Piiparinen[8], H. Ryde[3], M. Sugawara[1] and A. Virtanen[1].

There is a close relation between the occupation of the configurations in which the single particle energy has the largest slope with respect to a deformation of the nuclear mean field and the nuclear shape and shape stability. The high-j intruder states play a dominant role in this respect.

The strongly shape driving $\pi h_{9/2}[541]1/2^-$ configuration with $\alpha = +1/2$ exhibits some anomalous, and so far unexplained, features concerning the crossing frequency, $\hbar\omega_c$, the aligned angular momentum, i_x, and interaction strength, at the alignment of the first pair of $i_{13/2}$ quasineutrons in several odd Z-rare earth-nuclei. The expected change in equilibrium deformation for this $h_{9/2}[541]1/2^-$ configuration, obtained from self consistent calculations[1], can explain a fraction of the observed shift in $\hbar\omega_c$ varying from 20 - 60 % only, in the cases where these shifts are large[2]. In ^{163}Tm an observed[3] shift of $\sim$ 80 keV relative to the other proton configurations, in particular the $\pi h_{11/2}$ bands, as well as the neighbouring even-even nuclei, has been discussed[3] in terms of a possible shape change and a shape induced neutron pairing change, with no satisfactory explanation.

Similar information on the unfavoured $\alpha = -1/2$ signature partner of the $h_{9/2}[541]1/2^-$ configuration has usually not been established in high spin spectroscopy, since this band is very weakly populated due to the expected large energy signature splitting. Furthermore, a large signature splitting may cause the inband rotational decay sequence, which is the experimental signature of a rotational band, to be diluted by competing M1 transitions of rather large energies and with no outstanding energy pattern. In many rare earth nuclei large E1 matrix elements have been established between specific configurations. For example, in the isotope ^{167}Tm there are many connections[4] between both the favoured and unfavoured partners of the $[411]1/2^+$ and the $[541]1/2^-$ bands by E1 transitions, which may be explained[5] as a consequence of coupling to octupole degrees of freedom. Such E1 transitions may complicate the decay pattern even further, but, on the other hand also serve as a guideline for recognizing this particular band.

---

1. The Niels Bohr Institute, University of Copenhagen, Denmark.
2. Department of Physics, University of Oslo, Norway.
3. Department of Physics, University of Lund, Sweden.
4. Departamento di Fisica Atomica, Molecular y Nuclear, Universida de Sevilla, Spain.
5. Dipartimento di Fisica, Universita di Milano, Italy.
6. Kernfysisch Versneller Instituut, Groningen, The Netherlands.
7. Department of Physics, Åbo Akademi, Finland.
8. Department of Physics, University of Jyväskylä.

In this communication we report on a band in ^{163}Tm which due to its structure and decay properties may be interpreted as the unfavoured $\alpha = -1/2$ signature partner of the $h_{9/2}[541]1/2^-$ configuration.

The nucleus ^{163}Tm was populated in the (^{37}Cl, xn) reaction. The γ-rays were detected using the NORDBALL array equipped with 20 Compton suppressed Ge-spectrometers, and an inner BaF_2 ball used to select the 4n reaction channel. A total of more than $2 \cdot 10^9$ two and higher fold coincidence events were collected. The results from this data concerning the $h_{9/2}[541]1/2^-$, $\alpha = +1/2$ and $h_{11/2}[523]7/2^-$, $\alpha = \pm 1/2$ configurations are given in ref.[3].

A more detailed analysis of the data has revealed a new, weakly populated band, which decays to both the known $h_{9/2}[541]1/2^-$, $\alpha = +1/2$ band as well as the $[411]1/2^+$, $\alpha = +1/2$ band. In this analysis a clean "cube" of $\sim 1.3 \cdot 10^8$ triple fold events selected from the 4n channel has been utilized. The data were sorted with an energy dependent dispersion to reduce the necessary disc space for the cube. For establishing such weak band structures it is crucial that the main gates in which the weak transitions are observed can be checked for contaminations. Even though the triple statistics was not sufficient to establish the relative intensities of the weak transitions in the new band in double gating, valuable information about contamination and coincidence relationship in the related band structures could be obtained.

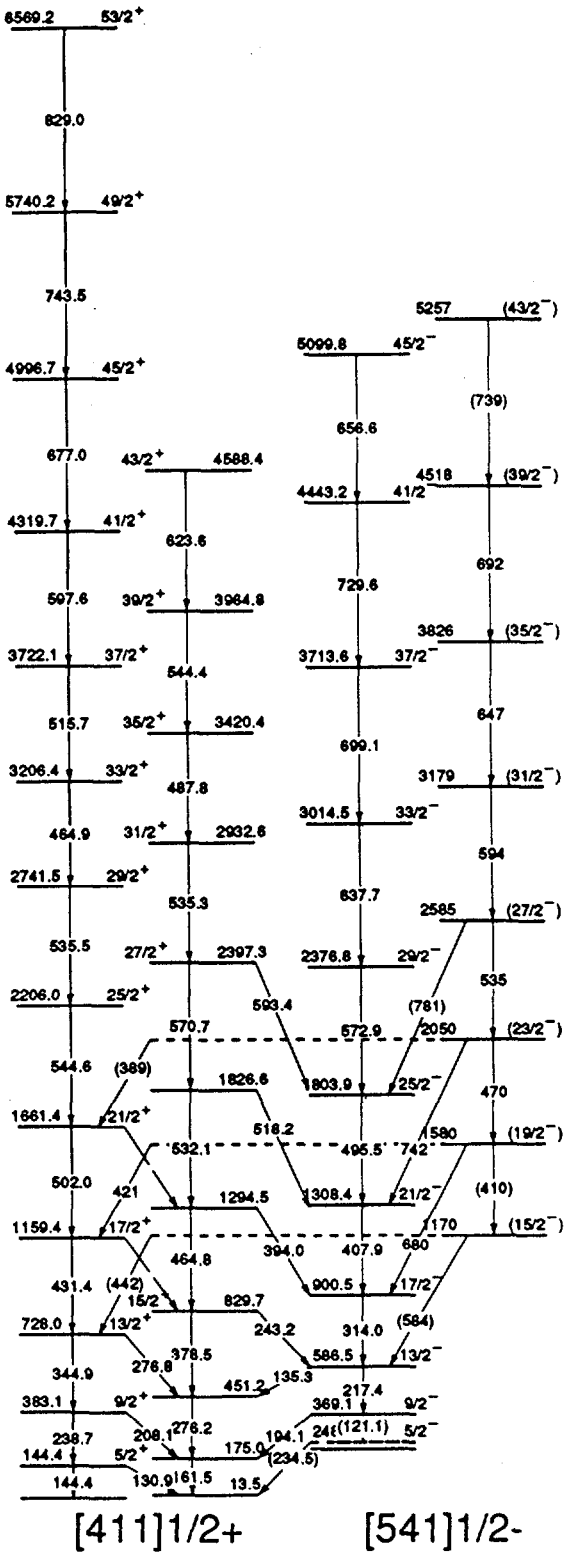

Figure 1: Partial level scheme of ^{163}Tm. The new band shown to the right-hand side decays to both the $h_{9/2}[541]1/2^-$, $\alpha = +1/2$ band as well as the $[411]1/2^+$, $\alpha = +1/2$ band. Weak transitions are given in parenthesis.

The most strongly populated bands in ^{163}Tm are built on the [523]7/2$^-$ configuration. Relative to these the favoured [541]1/2$^-$ has a population[3] of $\sim$ 20% at I $\sim$ 15$\hbar$, whereas the new band has a strength of $\sim$ 2% only, in accordance with a large signature splitting of $\sim$ 0.5 MeV.

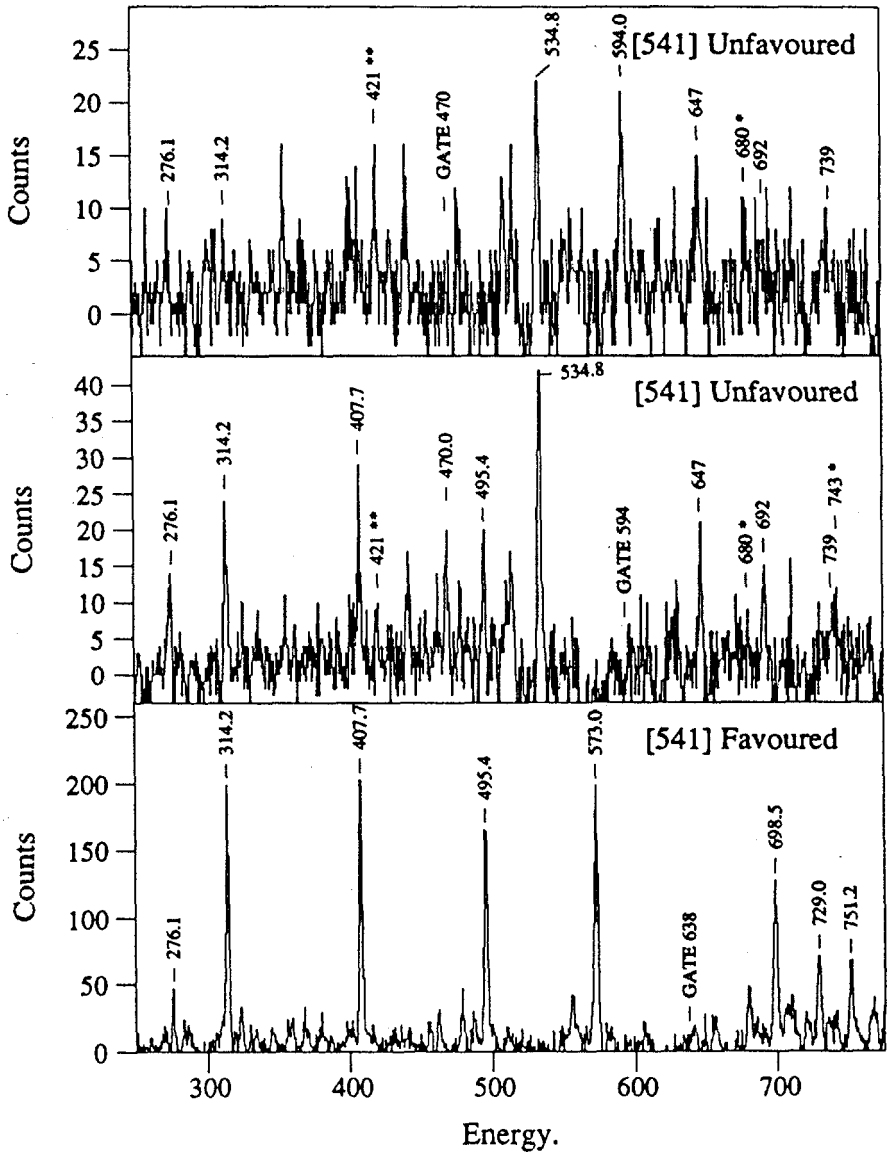

Figure 2: Spectra of transitions in ^{163}Tm corresponding to a gate on the 33/2$^-$ $\rightarrow$ 29/2$^-$ transition in the favoured [541]1/2$^-$ band (lower part) together with gates on the (31/2$^-$) $\rightarrow$ (27/2$^-$) (middle part) and (23/2$^-$) $\rightarrow$ (19/2$^-$) (upper part) transitions in the new (unfavoured [541]1/2$^-$) band. The competing (M1,I$\rightarrow$I$-$1) transitions are marked with an asterisk and the (E1,I$\rightarrow$I$-$1) transitions to the [411]1/2$^+$ band with two asterisks.

The decay properties of the new band are illustrated in fig. 2. It is indeed these decay properties that determines the signature of the new band to be $\alpha = -1/2$ and the most likely parity to be negative, since there is no positive parity band expected at this excitation energy with matching properties. The [402]5/2$^+$ configuration is known at the

lowest spins and is too low in excitation energy for the new band to be its extension. The $[411]3/2^+$ configuration also known at the lowest spins is higher in energy. If the new band is the high spin extension of this configuration, then the multipolarity of the transitions marked with one and two asteriks would be reversed. The $[411]3/2^+$ configuration is well established[4] in ^{167}Tm. It has some decay strength to the $[411]1/2^+$ band but no decay to the $[541]1/2^-$ band. Furthermore, the $[411]3/2^+$ band in ^{167}Tm has both signatures established and M1 transitions observed between them. On this basis we tentatively assign the new band as the unfavoured signature partner of the $h_{9/2}[541]1/2^-$ configuration. The intensity by which the new band decays out of band relative to the inband rotational cascades corresponds, if interpreted as the unfavoured $h_{9/2}[541]1/2^-$ band, to B(M1) and B(E1) values in qualitative agreement with the observations[4] in ^{167}Tm.

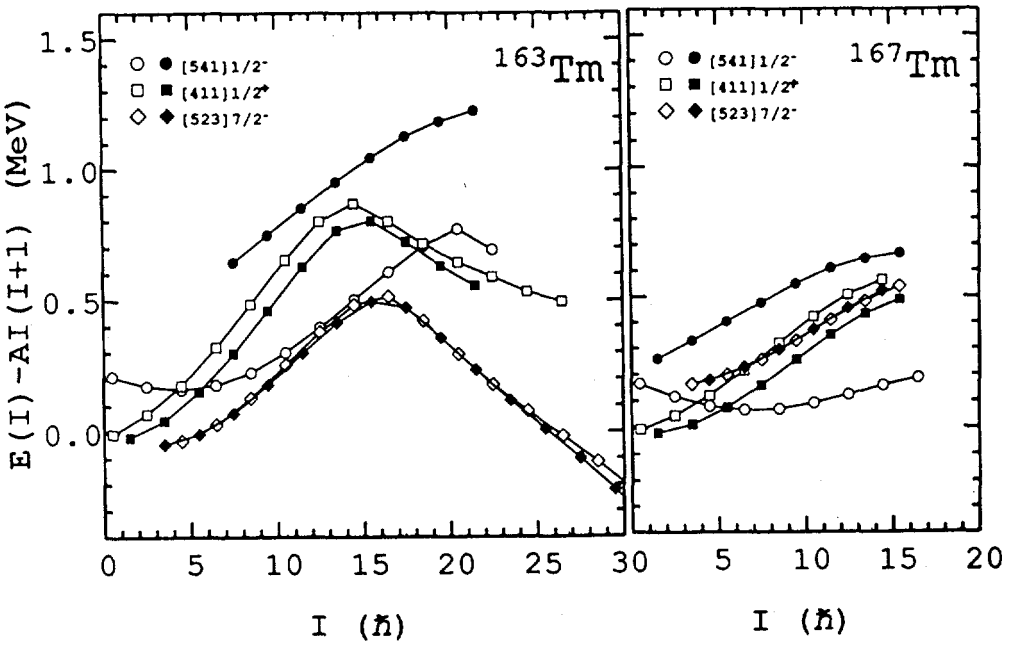

Figure 3: Excitation energy versus spin for both signature partners of the $\pi h_{9/2}[541]1/2^-$, the $[411]1/2^+$ and the $\pi h_{11/2}[523]7/2^-$ bands relative to a rigid rotor with moment of inertia $\Im = 60\hbar^2 MeV^{-1}$ for ^{163}Tm and ^{167}Tm.

In the following we compare the observed features of the new band with those in the isotope ^{167}Tm, for which the unfavoured $[541]1/2^-$ band is firmly established[4] up to a spin value of I=31/2. In fig. 3 the relative excitation energies for the $h_{9/2}[541]1/2^-$, the $[411]1/2^+$ and also the $h_{11/2}[523]7/2^-$ bands are displayed for the two Tm isotopes as a function of I. The signature splitting in $[541]1/2^-$ is $\sim$ 12 % smaller in ^{163}Tm than in ^{167}Tm. From cranking calculations based on the modified oscillator potential the signature splitting for ^{163}Tm is not expected to depend on deformation. The experimental trend in both Tm and Lu isotopes with neutron number N $\sim$ 100, though, show a decrease of the signature splitting with decreasing neutron number (i.e decreasing deformation[1]) in agreement with the present case. The relative positions of the $[411]1/2^+$ and $[541]1/2^-$configurations are very similar in the two isotopes, which is a good reason

to expect the E1 matrix elements to be comparable, as observed.

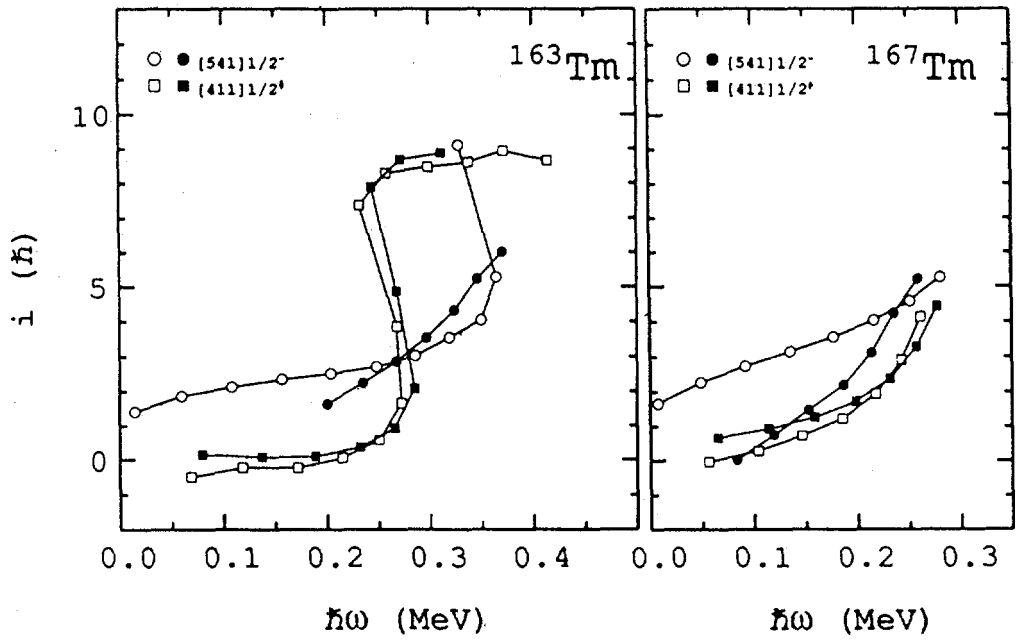

Figure 4: Experimental alignment of the two signatures of the $[541]1/2^-$ band (open and filled circles) and the $[411]1/2^+$ band (open and filled squares) in ^{163}Tm and ^{167}Tm as a function of rotational frequency, $\hbar\omega$ relative to the same reference with Harris parameters $\Im_0 = 40\hbar^2\text{MeV}^{-1}$ and $\Im_1 = 40\hbar^4\text{MeV}^{-3}$.

The aligned angular momentum for the $[411]1/2^+$ and $[541]1/2^-$ bands in both ^{163}Tm and ^{167}Tm are shown in fig. 4. It should be noted that all the other bands in ^{163}Tm observed to sufficiently high rotational frequency show the AB neutron crossing roughly at the same frequency as the $[411]1/2^+$ bands, but are left off the figure here to simplify the picture. The unfavoured $[541]1/2^-$ band in both nuclei show a gradual increase in alignment which causes the unfavoured signature partner to have a larger alignment than the favoured signature partner above $\hbar\omega \sim 0.25$ MeV in contrast to an expected difference in alignment of $\sim 1\hbar$ between the two signatures. A possible explanation for this could be a large interaction with the closest negative parity band of the same signature, which would be the next $h_{11/2}$ orbit i.e. $[514]9/2^-$ or $[532]5/2^-$. It is in this respect interesting to note that the interaction between the favoured $h_{9/2}[541]1/2^-$ and $h_{11/2}[523]7/2^-$ configurations is measured to be 7.5 keV in ^{163}Tm and in ^{171}Lu the interaction between the unfavoured $h_{9/2}[541]1/2^-$ and $[514]9/2^-$ configurations can be estimated to be smaller than 4 keV from the level distances[6]. An alternative explanation could be mixing of especially the unfavoured $[541]1/2^-$ to a gamma vibration built on $[541]1/2^-$ with $K = |1/2 - 2| = 3/2$. This gamma band has possibly been observed[4] in ^{167}Tm at an excitation energy relative to the favoured and unfavoured $[541]1/2^-$ configurations of $\sim$ 800 and 350 keV respectively, at I$\sim 10\hbar$. Mixing between such bands can be large since they have $\Delta K = 1$. Furthermore, the unfavoured signature will mix much stronger due to the smaller energy difference.

The shifts in frequency of the AB crossing is at least as large for the unfavoured signature of the $\pi h_{9/2}[541]1/2^-$ band as for the favoured signature partner. This new observation therefore rules out the possibility of a smaller crossing frequency shift when averaged over both signatures. It can be noted that in ^{163}Tm with the Fermi level below the $[541]1/2^-$ configuration the unfavoured signature partner is expected to have the same equilibrium shape as the favoured one[7]. The delayed crossing in strongly shape driving intruder bands could be caused by a neutron-proton interaction as suggested in ref.[8]. A calculation within the particle-rotor model and a $Q_N \cdot Q_P$ interaction expressed in double stretched coordinates, though, cannot explain[9] the delay observed in ^{163}Tm.

Future analysis of the M1 decay pattern may hopefully provide additional information about the structure of the wave function of these strongly shape driving intruder bands.

This project was supported by the Danish Natural Science Foundation, the NORDBALL collaboration, the Nordic Committee for Accelerator Based Research, the Swedish Natural Science Research Council, the Finish Academy, Commemoration Association for the Japan World Exposition [Quantum Physics Exchange Program between Japan and Denmark (NBI)], the Danish Research Academy, the Humboldt Foundation and Istituto Nazionale di Fisica Nucleare (INFN).

References

[1] W. Nazarewicz, M.A. Riley and J.D. Garrett. Nucl Phys. **A512** (1990) 61.

[2] C.-H. Yu, G.B. Hagemann, J.M. Espino, K. Furuno, J.D. Garrett, R. Chapman, D. Clarke, F. Khazaie, J.C. Lisle, J.N. Mo, M. Bergström, L. Carlén, P. Ekström, J. Lyttkens and H. Ryde. Nucl. Phys. **A511** (1990) 157.

[3] H.J. Jensen et al. Z. Phys. A340 (1991) 351.

[4] S. Olbrich, V. Ionescu, J. Kern, C. Nordmann and W. Reichardt. Nucl. Phys. **A342** (1980) 133.

[5] I. Hamamoto, J. Höller and X.Z. Zhang, Phys. Lett. **B226** (1989) 17

[6] P. Kemnitz, L. Funke, K.-Kaun, H. Sodan, G. Winther and M.I. Baznat. Nucl. Phys. **A209** (1973) 271.

[7] From TRS calculations. R, Wyss, R. Bengtsson, W. Nazarewicz and J. Nyberg. Private Communication and to be published.

[8] R. Wyss and A. Johnson. Proc. Int. Conf. on High Spin Physics and Gamma-Soft Nuclei, Pittsburgh Sept. 1990, Edt. J.X. Saladin, R.A. Sorensen and C.M. Vincent, World Scientific Publ. Co. 1991, p. 123.

[9] G.B. Hagemann and I. Hamamoto, Phys. Rev. C. in press.

Spectroscopy of Very Neutron-Deficient Hafnium and Tungsten Isotopes

G.D. Dracoulis, B. Fabricius and P.M. Davidson
Department of Nuclear Physics, RSPhysSE, Australian National University,
GPO Box 4, Canberra ACT 2601, Australia;
A.O. Macchiavelli, J. Oliviera, J. Burde, F. Stephens and M.A. Deleplanque
Lawrence Berkeley Laboratory, Berkeley, California

Abstract: Level schemes of the very neutron-deficient isotopes ^{158}Hf and ^{162}W have been identified, and that for ^{164}W extended. Alignment of the $h_{9/2}$ neutrons is suggested.

As the neutron number approaches the closed shell at N=82, the isotopes of tungsten (Z=74) and hafnium (Z=72) should correspondingly be less deformed. Figure 1 shows the deformations predicted from the potential-energy-surface calculations of Nazarewicz, Riley and Garrett [1] and Möller and Nix [2] (combined only approximately because they are derived from different potentials). Examination of the Nilsson scheme for deformation $\beta_2 \lesssim 0.1$ places the neutron Fermi level at N ~ 86, close to the low-Ω orbitals of the $h_{9/2}$ neutron, and well below the Ω = 1/2 orbital of the $i_{13/2}$ neutron. Since the proton Fermi level is still high in its $h_{11/2}$ shell (relative to lower-Z nuclei such as erbium), band-crossings due to competing particle alignments, for the first time in this region should favour the $h_{9/2}$ neutron. This can be seen from Figure 2 which shows the crossing frequencies calculated with the CSM for a hypothetical ^{158}Hf nucleus as a function of a fixed quadrupole deformation. A deformation $\varepsilon_2 \lesssim 0.1$ also corresponds to the region where the pseudo-spin partner orbitals derived from the $f_{7/2}$ and $h_{9/2}$ neutrons at sphericity, exchange character. This may be manifested as a change in signature favouring in the 1-, 2- and 3-quasiparticle bands containing these orbitals, since an $f_{7/2}$ character favours $\alpha = -1/2$, whereas $h_{9/2}$ favours $\alpha = +1/2$. These nuclei may also be susceptible to octupole effects since the neutron number N ~ 86 is optimal and quadrupole deformation is weak.

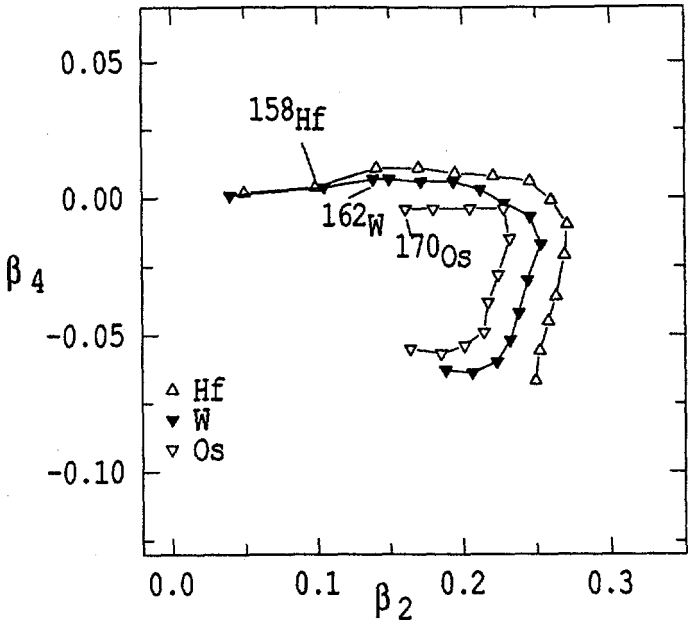

Figure 1

The lightest hafnium isotope whose level scheme is known, except for the closed shell case ^{154}Hf which was observed through the decay of a seniority isomer [3], is ^{160}Hf, studied by Murzel et al [4]. The lightest tungsten isotope previously studied is ^{164}W, whose yrast band was recently reported by Simpson et al [5].

Population of such neutron-deficient nuclei in (heavy ion, xn) reactions becomes problematic because of fission competition which reduces the residue cross-section, and because of fragmentation of the cross-section in a particular channel when charged-particle emission becomes

competitive. Nevertheless, astute choice of reactions which use heavy beams near the Coulomb barrier and *involve* proton emission and also *minimises* the number of evaporated particles make some cases accessible. This tactic was recognised by the Munich [6] and Purdue/Argonne groups [7] and successfully employed in our identification of the lightest platinum and mercury isotopes known to date [8,9]. It should be remembered however, that if fission is the main limitation, level schemes extending to high spins cannot be obtained since the fission channel depletes the high ℓ-values. This limitation will be evident when new nuclei become accessible, in principle, using neutron-deficient, radioactive beams.

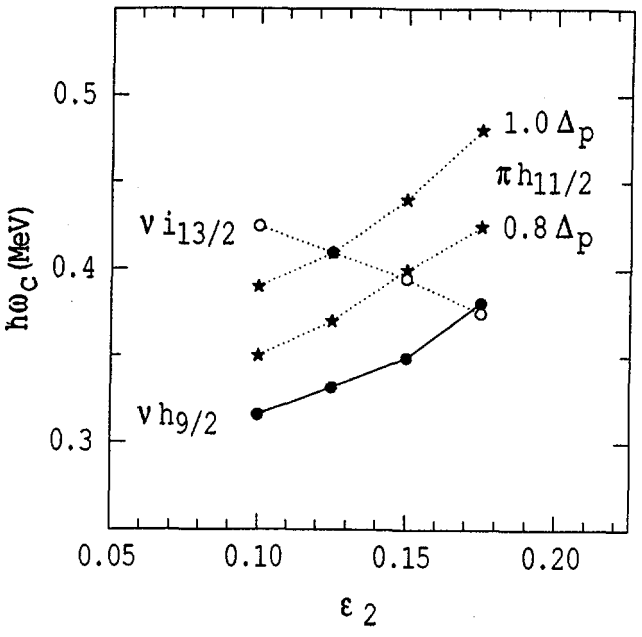

Figure 2

We have confirmed and extended the level scheme of ^{164}W using the ^{109}Ag(^{58}Ni,p2n) reaction and identified for the first time levels in ^{158}Hf (N=86) and ^{162}W (N=88) using, respectively, ^{107}Ag(^{58}Ni, p2n)^{162}W and ^{107}Ag(^{54}Fe,p2n)^{158}Hf reactions. As a by-product, level schemes were also obtained for ^{163}W and ^{159}Hf, the latter being observed in two of the bombardments. The bulk of the measurements were carried out using 253 MeV, ^{58}Ni and 233 MeV, ^{54}Fe beams from the 88-inch cyclotron (in combination with the ECR source) at the Lawrence Berkeley Laboratory. Gamma-rays were observed in the 21-detector array, HERA. Additional measurements were carried out, and are still in progress at the ANU, 14 UD Pelletron facility.

Assignment to a specific proton number was made on the basis of coincidences between the main transitions and characteristic X-rays, examples of which are shown in Figure 3. (Note that this requires minimal absorbers and due attention to time-walk for low-energy transitions.) The main products in the bombardments are the odd-odd nuclei ^{162}Ta and ^{158}Lu for which level schemes are also being constructed. X-ray coincidences in these cases are generally more intense because of the presence in the level schemes of relatively low energy MI transitions which, through their large conversion coefficients, lead to high X-ray production.

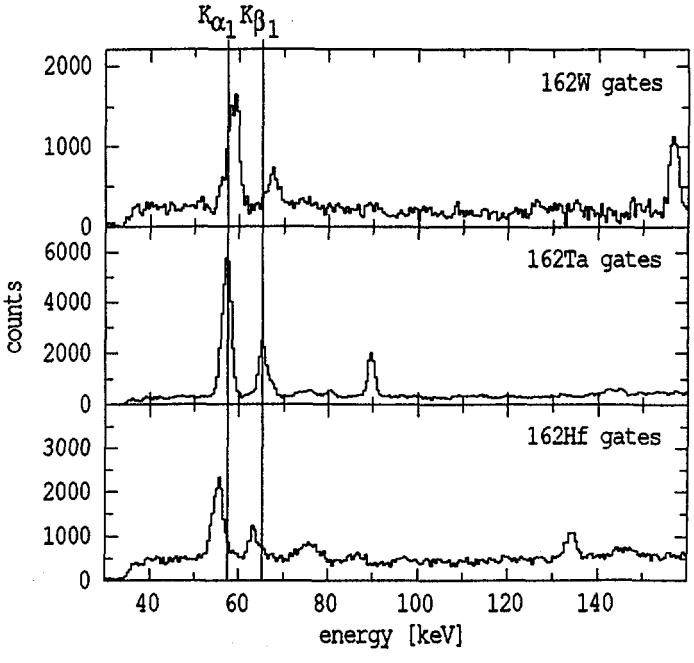

Figure 3

For ^{164}W, two sidebands which collect a substantial part of the yrast intensity, were identified. They are similar in structure to the negative parity bands known [10,11] in the isotone ^{162}Hf and presumably arise from the $\nu(h_{9/2}i_{13/2})$ (or AE and AF) configurations. These become increasingly more competitive with decreasing neutron number.

Coincidence gates on the proposed $2^+ \rightarrow 0^+$ transitions in ^{158}Hf and ^{162}W are shown in Figure 4. Neither shows a regular structure, and both overlap with transitions in identified

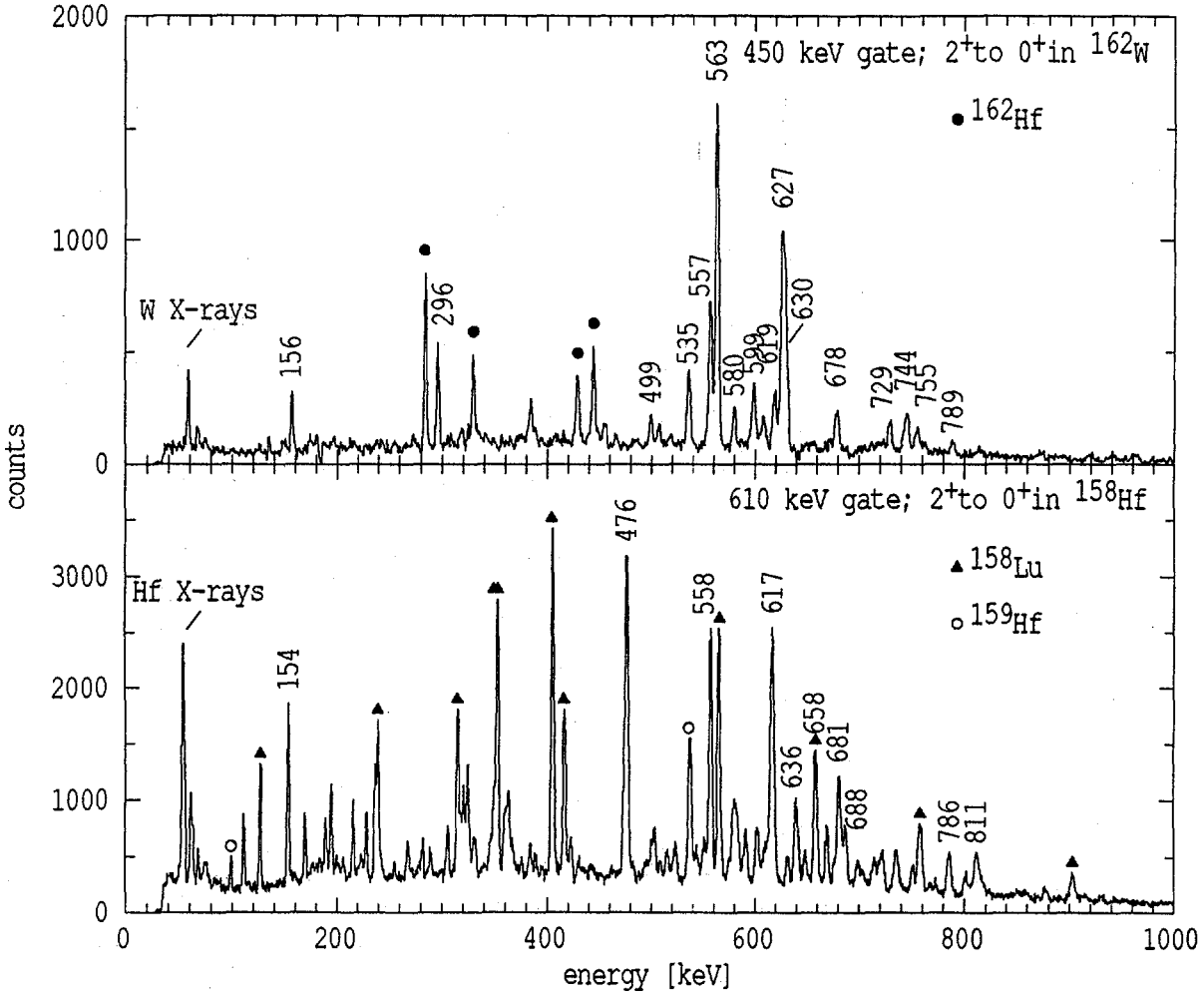

Figure 4

contaminants, the products of competing channels. Preliminary schemes have been constructed for both isotopes, but there are at present ambiguities in the schemes, particularly in the ordering of transitions in the sidebands, and in the feeding connections to the low-spin yrast bands. It is expected that these will be resolved with additional measurements. A single band is observed in ^{163}W and it is assumed to be associated with the $i_{13/2}$ neutron, decoupled sequence. In ^{159}Hf, the main band populated probably arises from the $h_{9/2}$ neutron configuration.

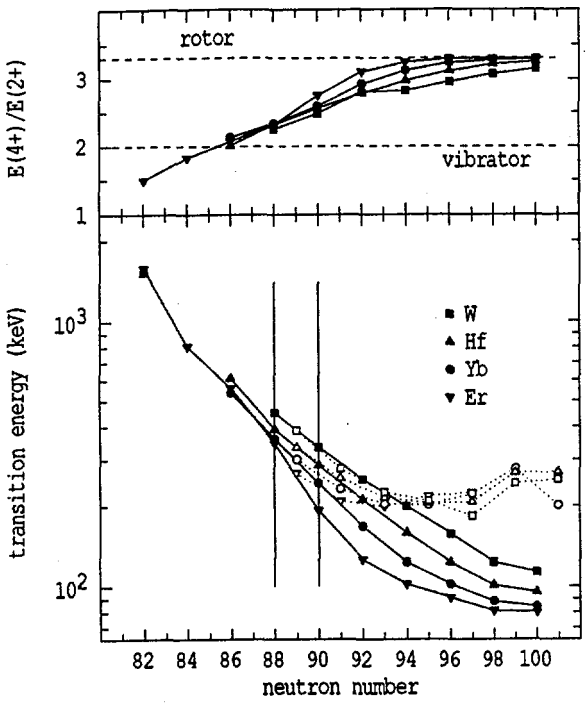

The proposed $2^+ \rightarrow 0^+$ transition energies and the E_4+/E_2+ ratios fit smoothly into the systematics shown in Figure 5, as does the proposed $17/2^+ \rightarrow 13/2^+$ transition in ^{163}W (of energy 385 keV). The E_4+/E_2+ ratio in ^{158}Hf is close to the vibrational limit.

Net alignments for the range of even-even and odd-N isotopes, collecting previously published data [4,5,10,11,12] and the new results on ^{164}W, ^{163}W, ^{162}W, ^{158}Hf and ^{159} Hf, are shown in Figures 6 and 7. (The same reference parameters have been used for each even-even nucleus and its A+1, odd neighbour.) The alignment gain near $\hbar\omega$=0.3 MeVin the positive parity yrast band in ^{162}W is low and similar to that in ^{160}Hf. Both are distinctly different from the ^{162}Hf and ^{164}W isotones, which show a large alignment, assigned to the $(i_{13/2})^2$ neutrons [5,10,11]. The curve for ^{158}Hf is irregular, even at low spins.

Figure 5. Open symbols represent the $17/2^+ \rightarrow 13/2^+$ transitions.

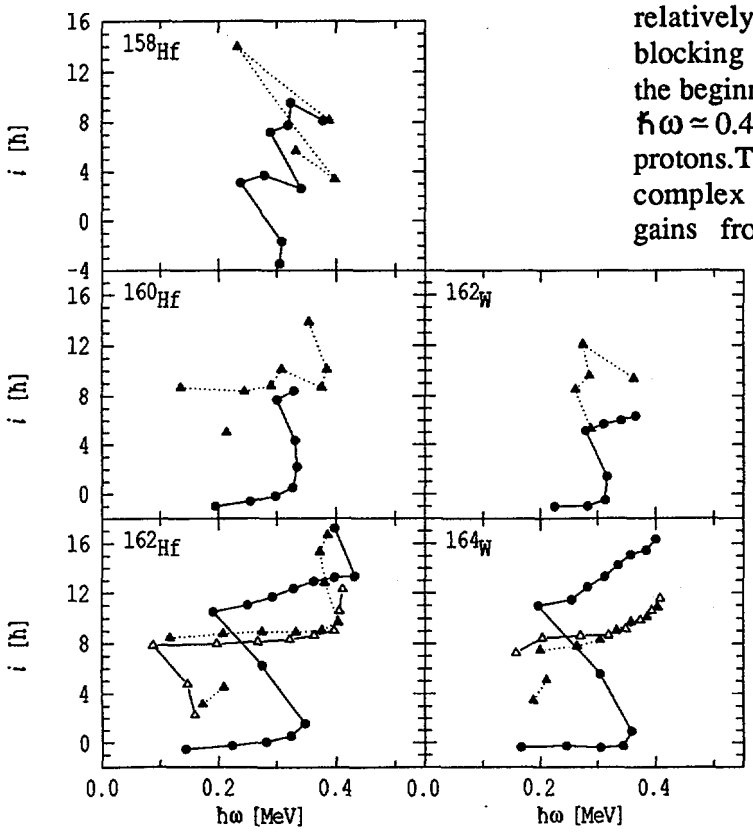

The negative-parity bands in ^{164}W show a relatively constant alignment, consistent with blocking of both $h_{9/2}$ and $i_{13/2}$ neutrons, until the beginning of a weak alignment gain near $\hbar\omega \simeq 0.40$ MeV, presumably from the $(h_{11/2})^2$ protons.The $i_{13/2}$ neutron band in ^{163}W has a complex shape, compatible with alignment gains from the $h_{9/2}$ neutrons and the $h_{11/2}$ protons, in close proximity. This directly supports the proposition of Simpson et al [5], that the irregular alignment gain in ^{164}W after the major crossing due to the $(i_{13/2})^2$ neutrons is due to the same two alignments – both trajectories are similar. (This is also consistent with the prediction [2] that the deformation of ^{163}W will resemble ^{164}W rather than ^{162}W.)

Figure 6. Net alignment in even-even isotopes (circles are positive parity states; triangles are negative parity states)

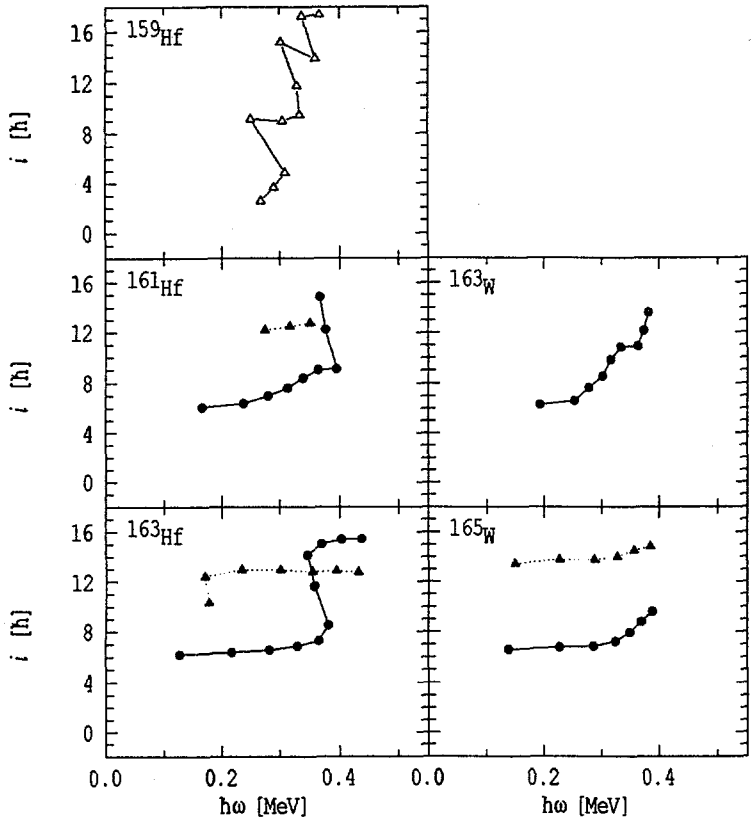

Figure 7. Net alginment in odd-neutron isotopes.

The alignment gain in the yrast band of ^{162}W is proposed to be due to the $h^2_{9/2}$ neutrons (with $\Delta i \simeq 7\hbar$) consistent in frequency and alignment with the CSM calculations. The small magnitude of the alignment gain in ^{160}Hf, attributed to $(i_{13/2})^2$ neutron in ref [4] remains problematic (as noted by those authors). No regularity is discernible in the side-band sequences, assumed to be of negative parity, in either ^{162}W or ^{158}Hf, but further analysis is necessary to confirm the spin assignments.

Characterisation of the alignment gains is also being pursued through the structure of the bands in the neighbouring odd-odd isotopes ^{158}La and ^{162}Ta, currently under evaluation.

References

[1] W. Nazarewicz, M.A. Riley and J.D. Garrett, Nucl. Phys. A512 (1990) 61.
[2] P. Møller and J.R. Nix, Atomic Data and Nuclear Data Tables 26 (1981) 165.
[3] J.H. McNeill et al. Phys. Rev. Lett 63 (1989) 860.
[4] M. Murzel et al., Nucl. Phys. A516 (1990) 189.
[5] J. Simpson et al., J. Phys. G 17 (1991) 511.
[6] E. Nolte et al., Z. Phys. A 306 (1982) 211.
[7] Y.H. Chung et al., Phys. Rev. C29 (1984) 2153.
[8] G.D. Dracoulis et al., Phys. Rev. C 44 (1991) R1246.
[9] G.D. Dracoulis et al., Phys. Lett. 208B (1988) 365.
[10] H. Hübel et al., Z. Phys. A 329 (1988) 289.
[11] C.R. Bingham et al., J. Phys. G 14 (1988) L77.
[12] J. Simpson et al., to be published.

Collective Oblate Bands in Pb Nuclei

H. Hübel, G. Baldsiefen, D. Mehta, B.V. Thirumala Rao, U. Birkental, G. Fröhlingsdorf, M. Neffgen, N. Nenoff, S.C. Pancholi, N. Singh, W. Schmitz, K. Theine and P. Willsau
Institut für Strahlen- und Kernphysik, Universität Bonn, Nussallee 14-16, D-5300 Bonn, Germany

H. Grawe, J. Heese, H. Kluge, K.H. Maier, M. Schramm and R. Schubart
Hahn-Meitner-Instiut für Kernforschung, Glienicker Str. 100, D-1000 Berlin, Germany

F. Azaiez, C. Bourgeois, D. Hojman, A. Korichi, N. Perrin and H. Sergolle
Institut de Physique Nucleaire, F-91106 Orsay, France

H.J. Maier
Ludwig-Maximilians-Universität München, Am Coulombwall 1 D-8046 Garching, Germany

The coexistence of different nuclear shapes is a well established phenomenon in the Hg-Pb region where spherical, oblate, prolate and superdeformed prolate shapes have been observed. In this work we report on several new rotational bands in the normally spherical nuclei $^{199-201}$Pb [1-3]. Similar structures were also found recently in the lighter isotopes ^{197,198}Pb [4-6].

High-spin states in $^{199-201}$Pb were populated by bombarding ^{192}Os targets with ^{12,13,14}C beams of 70-82 MeV and ^{186}W targets with ^{18}O of 94 MeV. Some details of the experiments are summarized in Table 1. The analysis of the γ-ray coincidence data revealed 10 cascades with rather regular energy spacings in the three investigated nuclei. An example of the coincidence spectra is displayed in Fig. 1. The decay out of the bands occurs mainly at the two lowest-energy states. At high energies the intensities decrease smoothly from 300 to 600 keV. These intensity patterns are very similar to the ones observed for superdeformed bands. Also, as for the superdeformed bands, it was not yet possible to establish the links to the known yrast states, except for one band in ^{199}Pb.

Table 1: Summary of experiments to investigate high-spin states in $^{199,200,201}Pb$

Reaction	E_{beam} (MeV)	target thickness (mg/cm^2)	spectro-meter	place
$^{192}Os(^{12}C,5n)^{199}Pb$	82	2 x 0.4	OSIRIS6	Bonn
$^{192}Os(^{13}C,6n)^{199}Pb$	81	2 x 0.4	OSIRIS12	Berlin
$^{186}W(^{18}O,5n)^{199}Pb$	94	12	OSIRIS12	Berlin
$^{192}Os(^{13}C,5n)^{200}Pb$	76	2 x 0.4	OSIRIS12	Berlin
$^{192}Os(^{14}C,5n)^{201}Pb$	70	2 x 0.4	Chateau	Orsay

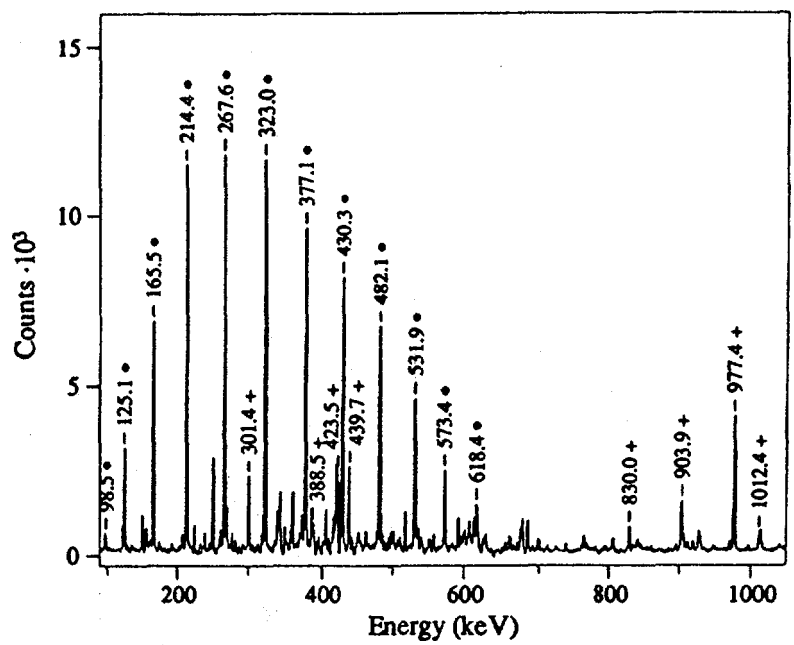

Fig. 1: Coincidence spectrum measured in the reaction $^{186}W(^{18}O,5n)^{199}Pb$. Spectra with gates on several of the dipole transitions have been added. The new band transitions are marked by dots, the previously known ^{199}Pb transitions are marked by plus signs.

The evaluation of directional correlation (DCO) ratios shows that the strong regular transitions within the bands are stretched dipoles (with possible small quadrupole admixtures). We also observe crossover transitions for some of the bands, but their intensities are too weak to determine DCO ratios. Only linear polarisation or conversion coefficient measurements can finally decide whether the transitions are electric or magnetic dipoles, but all the presently existing evidence favours M1 multipolarity.

The assignments of the bands to the three different isotopes $^{199-201}$Pb is based on the coincidences with known transitions between the spherical states; as an example see the transitions marked by plus signs in the spectrum of Fig. 1.

The properties of the observed bands can be summarized as follows:

(i) The transitions within the bands are stretched dipoles, probably M1, with small E2 admixtures.

(ii) The crossover E2 transitions are weak. The $B(M1, \Delta I = 1)/B(E2, \Delta I = 2)$ ratios lie between 10 and 40 μ^2/eb^2.

(iii) The bands show no signature splitting.

(iv) The dynamical moments of inertia $J^{(2)}$ are small (~ 20 $\hbar^2$/MeV) over most of the frequency range. Fig. 2 gives a few examples.

(v) Some of the bands have almost identical transition energies and very similar moments of inertia (see Fig. 2).

As mentioned above, the linking transitions to the normal states are still missing for most of the bands, but from the decay pattern estimates of the band head spins can be made [1-6]. These estimated spins can be plotted as a function of the rotational frequency (taken as E_γ for dipole transitions). For most of the bands this gives a linear relationship except for one of the bands in ^{199}Pb where a pronounced backbending is observed, see Fig. 3. For the

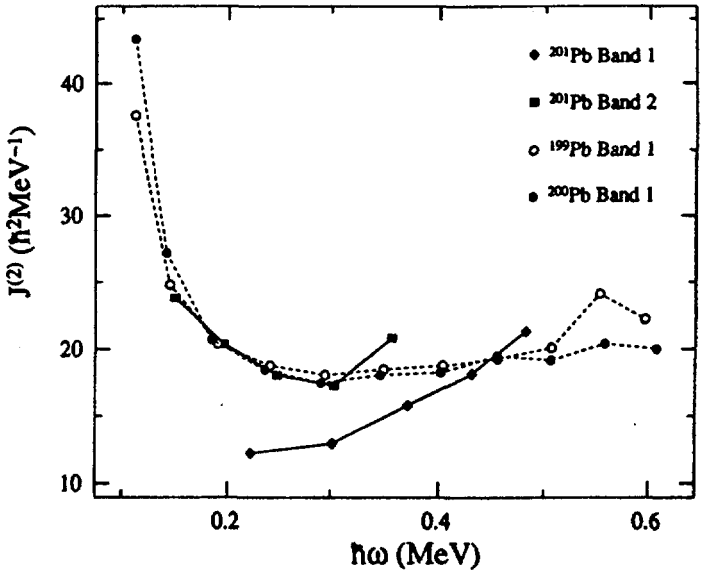

Fig. 2: Dynamic moments of inertia as a function of rotational frequency for the two bands in ^{201}Pb compared to one of the bands in ^{199}Pb and ^{200}Pb.

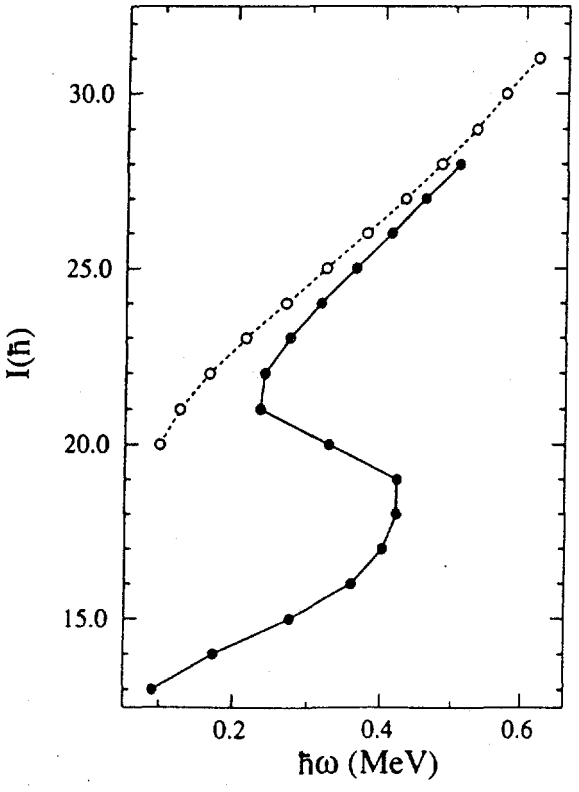

Fig. 3: Spin as a function of rotational frequency for two of the new bands in ^{199}Pb. The spins are uncertain within ± 1 ħ.

backbending band the band head spin is probably 25/2 or 27/2 (for this band the connection to the spherical states is established), but for the other band in ^{199}Pb, which is shown for comparison in Fig. 3, the spin is only estimated as 39/2 from the decay pattern to the normal states. Fig. 3 suggests that the bandcrossing observed in the backbending band is blocked in the other band. It is most likely due to the alignment of a pair of $i_{13/2}$ neutrons (comparison with the Hg isotopes [7] suggests that it is the BC alignment). The band head of the backbending band probably has a configuration with one aligned $i_{13/2}$ neutron (A) and that of the other band with three $i_{13/2}$ neutrons (ABC).

The observed properties of the bands suggest an interpretation in terms of high-K multi-quasiparticle band heads on which the rotation is built. Such states can be expected from the Nilsson model for oblate deformation in this mass region. For instance, Bengtsson and Nazarewicz [8] predict $I^{\pi}=11^{-}$ ($h_{9/2}$ x $i_{13/2}$) two-proton states with oblate deformation in the light Pb isotopes. In ^{194}Pb and ^{196}Pb such states and collective structures built on the isomeric 11^{-} and on other states have been found [9-11]. Similar proton excitations, coupled to one or more aligned neutrons could be responsible for the new structures observed here. The large extrapolated alignment at $\hbar\omega=0$ (see Fig. 3) is evidence for a rapid initial alignment of several quasiparticles. For oblate deformation the Fermi level lies within the upper part of the neutron $i_{13/2}$ multiplet

with low-K orbitals which are easy to align. We therefore suggest that the observed rotational bands are based on configurations with proton particle-hole excitations involving the $h_{9/2}$ and $i_{13/2}$ orbitals which are deformation-aligned with high K values along the symmetry axis of the oblate nucleus coupled to rotation aligned neutron $i_{13/2}$ orbitals. The band head spins can then be understood for Fermi-aligned coupling. For instance, for the backbending band the experimentally determined band head spin is 25/2 or 27/2, and for a $\{(\pi h_{9/2}\, i_{13/2}) \times \upsilon i_{13/2}\}$ Fermi-aligned coupling one estimates a spin of 25/2 ($\pm$ 2). Similarly, for the other observed bands (where only estimates for the band head spins can be deduced from the experimental data) configurations with two, three or four aligned $i_{13/2}$ neutrons can explain the estimated spins.

This work was supported by BMFT, Germany

References

1. G. Baldsiefen et al., Phys. Lett. 275B, 252 (1992)
2. H. Hübel et al., Prog. Part. Nucl. Phys. 28, 427 (1992)
3. G. Baldsiefen et al., Z. Phys. in press
4. R.M. Clark et al., Phys. Lett. 275B, 247 (1992)
5. A. Kuhnert et al., Phys. Rev. C in press
6. R.M. Clark et al., Z. Phys. in press
7. D. Mehta et al., Z. Phys. A339, 317 (1991)
8. R. Bengtsson and W. Nazarewicz, Z. Phys. A334, 269 (1989)
9. B. Fant et al., J. Phys. G17, 319 (1991)
10. J. Penninga et al., Nucl. Phys. A471, 535 (1987)
11. J.J. Van Ruyven et al., Nucl. Phys. A449, 579 (1986)

Transition Probabilities up to I = 36+ in ^{160}Yb

N. R. Johnson,[a] F. K. McGowan,[a] D. F. Winchell,[a] J. C. Wells,[a,b] C. Baktash,[a]
L. Chaturvedi,[c] W. B. Gao,[c] J. D. Garrett,[a] I. Y. Lee,[a] W. C. Ma,[c]
S. Pilotte,[d] and C.-H. Yu[d]

[a]*Oak Ridge National Laboratory, Oak Ridge, TN 37831*

[b]*Tennessee Technological University, Cookeville, TN 38505*

[c]*Vanderbilt University, Nashville, TN 37235*

[d]*University of Tennessee, Knoxville, TN 37996*

I. INTRODUCTION

During the past dozen years or so, numerous groups have worked on the properties of the ytterbium nuclei and we at Oak Ridge have been actively involved in the study of many of these nuclei. We have concentrated on lifetime measurements of their high-spin states because it is from the lifetime of a state that one can determine Q_t, the transition quadrupole moment. The importance of obtaining a Q_t value is in that it reflects the intrinsic part of the wave function and, hence, provides an indicator of the collectivity.

It is well known that the family of Yb nuclei possesses some rather interesting and unusual features. One striking pattern of behavior is found in an examination of a plot of Q_t vs. A for the $2^+ \rightarrow 0^+$ and $17/2^+ \rightarrow 13/2^+$ transitions in Yb nuclei from mass 158 through mass 170. Here one sees a steady and almost linear increase in collectivity in this family up to ^{165}Yb, at which point the Q_t values begin to level off. This is an interesting pattern of behavior when it is compared with that for other nuclei in this region, e.g., for the Gd or the Er nuclei. For the latter two families there is a sharp increase in the collectivity in going from neutron number 88 to N = 90, followed by a rather gradual but non-linear increase in collectivity up to mass 160.

Not only do we find that the quadrupole deformation in these Yb nuclei shows no dramatic increase at neutron number 90 (^{160}Yb), but an examination of the potential energy surface and the total routhian surface of ^{160}Yb reveals that they are extremely

shallow in both the β and γ degrees of freedom, even more so than are its other N = 90 isotonic neighbors. Thus, we expect this very soft nucleus to be quite susceptible to polarization effects that may well change both its collectivity and its shape at high rotational frequencies.

Although this paper presents the results from recent Doppler broadened line shape (DBLS) measurements in ^{160}Yb at very large rotational frequencies of $\hbar\omega \approx 0.36$-0.50 MeV ($I = 22^+ - 36^+$), it is helpful to review briefly some of the recoil-distance (RD) lifetime results from our early measurements[1,2] on the Yb nuclei around N = 90. Figure 1 shows a summary of the Q_t values obtained for ^{159}Yb, ^{160}Yb, and ^{161}Yb in the RD measurements[1,2] several years ago. What we found there was a distinct drop-off in the collectivity above a rotational frequency of about 0.25 MeV. For these nuclei, where the Fermi surface lies near the bottom of the $i_{13/2}$ shell, we were able to understand our lifetime results – at least qualitatively – in terms of cranked shell model (CSM) and cranked Hartree-Fock-Bogoliubov (CHFB) calculations (e.g., see Refs. 2,3). After the backbend, these nuclei undergo a shape change (driven by the aligned $i_{13/2}$

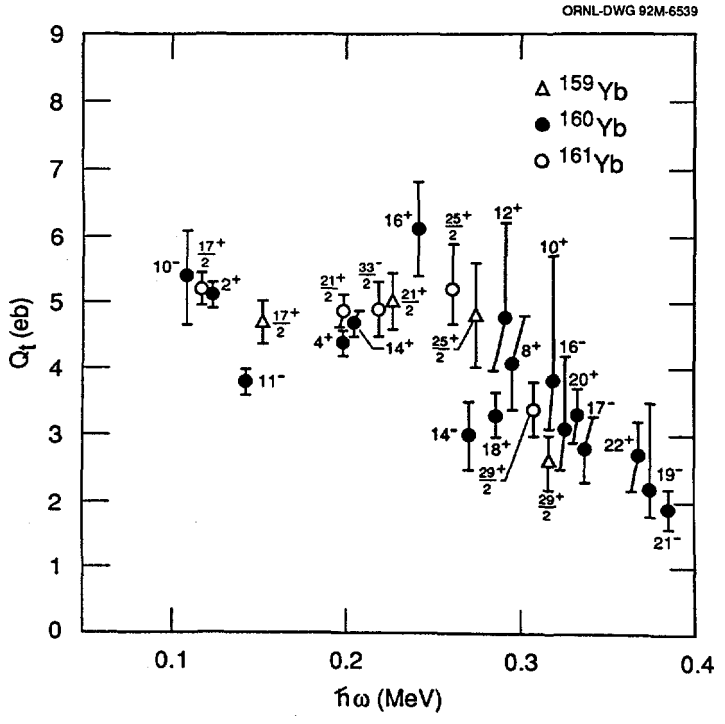

Fig. 1. Transition quadrupole moments for states in ^{159}Yb, ^{160}Yb, and ^{161}Yb.

quasineutrons) to a triaxial shape that is oriented so as to reduce the collectivity of the rotation, i.e., to positive γ values, while at the same time undergoing some reduction in β_2.

Having gained some insight into the ways these nuclei near N = 90 adapt to the forces exerted at moderately high rotational frequencies, we now address the question of what happens to their collectivity under the stress of extremely rapid rotation. In particular, there has remained much curiosity and speculation on what will happen to the collectivity of the yrast sequence in the spin 22^+-40^+ range for ^{160}Yb: will the Q_t values remain at about 3eb, the level we had found for the 20^+-22^+ states in our earlier RD measurements; will the decreasing trend continue, arriving at a near total collapse of the collective properties by spin 30^+; or will there be a return to collective behavior similar to that seen in the ground band? However, due to the very short lifetimes of such states ($\leq$ 1 ps), the RD method could not be employed. Instead, we used the Doppler broadened line shape (DBLS) method where one backs the target with a stopping medium and determines the line-shape distribution of the decays as the recoiling nuclei come to rest.

II. EXPERIMENT AND RESULTS

For these DBLS experiments the ^{160}Yb was produced in the reaction ^{120}Sn(^{44}Ca,4n)^{160}Yb at a beam energy of 200 MeV. The beam was provided by the 25-MV Tandem Accelerator at Oak Ridge. Measurements were made on two different targets. In one case, 1.05 mg/cm^2 ^{120}Sn evaporated onto a 10 mg/cm^2 Au backing was employed and in the other, the same thickness of ^{120}Sn was used, but the backing was 28 mg/cm^2 Pb. We collected these γ-ray data in the coincidence mode with the Oak Ridge Compton Suppression Spectrometer System which consists of 20 Compton-suppressed Ge detectors. Four of the detectors are located at 45° with respect to the beam direction and four at 135°. The data stored are from coincidences in each of these detectors with any other detector. With the Au-backed target we collected a total of 394 x 10^6 γ-γ coincidence events, while for the Pb-backed target, 90 x 10^6 such events were accumulated.

To analyze DBLS data we utilized the program LINESHAPE[4] based on a program originally obtained from Jules Gascon[5] at the Niels Bohr Institute. We[4] have incorporated several new features into LINESHAPE to facilitate the analysis of DBLS data. For example, we have added the least-squares minimization routine MINUET[6] which was used in our program LIFETIME[7] for the analysis of RD data; also added is the

stopping power routine STOPO[8] which provides the option of three prescriptions to generate a set of stopping powers for the recoiling nuclei.

The time-dependent decay yield for a level is determined by both its lifetime and the lifetimes of levels that feed into it. The decay information from the known precursors cascading into the level of interest is handled in a straightforward manner by the analytical solutions of the Bateman equations. However, it is necessary to set up a model for the side feeding from the γ-ray continuum. We have tried both two-step cascade side feeding and five-state rotational-band side feeding where a moment of inertia of 65 MeV^{-1} was used. The results from both types of modeling were used in the final lifetime averaging process and the resulting ^{160}Yb Q_t values (averages of Pb-backed and Au-backed Sn targets) are shown in Fig. 2, along with our[1,2] earlier RD results for the lower-spin states.

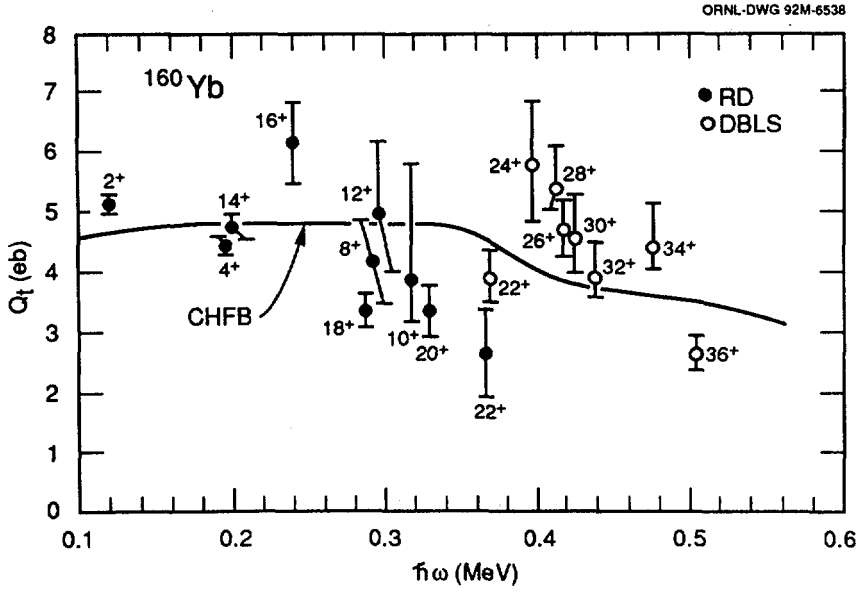

Fig. 2. Transition quadrupole moments (Q_t) for members of the yrast sequence in ^{160}Yb. The solid lines are from the earlier recoil-distance measurements[1,2] and the open circles are from the current Doppler broadened line shape experiments.

III. DISCUSSION

The data in Fig. 2 show that there is a definite recovery in the collectivity between spins of 24^+ and 34^+ in the ^{160}Yb yrast sequence, with a possible falloff again at $I = 36^+$. This pattern of a falloff followed by a recovery of collectivity in the yrast band is very difficult to account for within the framework of current theories, and obviously deserves additional study.

In an attempt to better understand this behavior we felt that it may be helpful to look at all of the available Q_t values for the yrast sequences of even Yb nuclei. These data are shown in Fig. 3. Note that also in ^{162}Yb McGowan *et al.*[9] have found what appears to be a loss in collectivity for the states beyond the first band crossing by $vi_{13/2}$ quasiparticles, with the loss extending up to the highest state measured, $I = 18^+$; but no experimental data are available for the higher-spin states of ^{162}Yb to tell us if it too experiences a recovery in collectivity in the $I = 20^+$-36^+ range. Our recent DBLS results (Xie *et al.*[10-12]) for the high-spin region of ^{164}Yb coupled with the lifetime results of Bochev *et al.*[13] for the lower spins reveal a fairly constant range of Q_t values up to $I = 28^+$, with an apparent dropoff at $I = 30^+ - 32^+$. As reported by Bacelar *et al.*[14] a similar dropoff in the Q_t values of ^{166}Yb is also present in the $I = 28^+$ to 34^+ states ($\hbar\omega \approx 0.4$-0.5 MeV). In the case of ^{168}Yb, lifetimes of the 26^+ to 34^+ members have been measured by Lisle *et al.*[15] and, as seen, the Q_t values of these states show a steady decrease as a function of rotational frequency.

The fundamental question is can we better understand what is happening at the microscopic level to lead to these patterns of collectivity at high rotational frequencies. For this, we use the deformation parameters from the Total Routhian Surface (TRS) calculations of these Yb nuclei by Wyss *et al.* [16] With these deformation parameters the theoretical Q_t values for the Yb nuclei are determined by use of the expression

$$Q_t = \frac{6}{\sqrt{15\pi}} Z e r_0^2 A^{2/3} \beta_2 (1 + 0.36\beta_2) \cos(30° + \gamma)$$

where Ze is the charge on the nucleus and $r_0 = 1.2$ fm. The computed values are shown as solid lines in Fig. 3. It is seen that the theoretical Q_t values do predict the trends of the data at high spins, but do not provide quantitative agreement with experiment. Probably the two main features of agreement are: (1) at low $\hbar\omega$ values, theory provides the trend

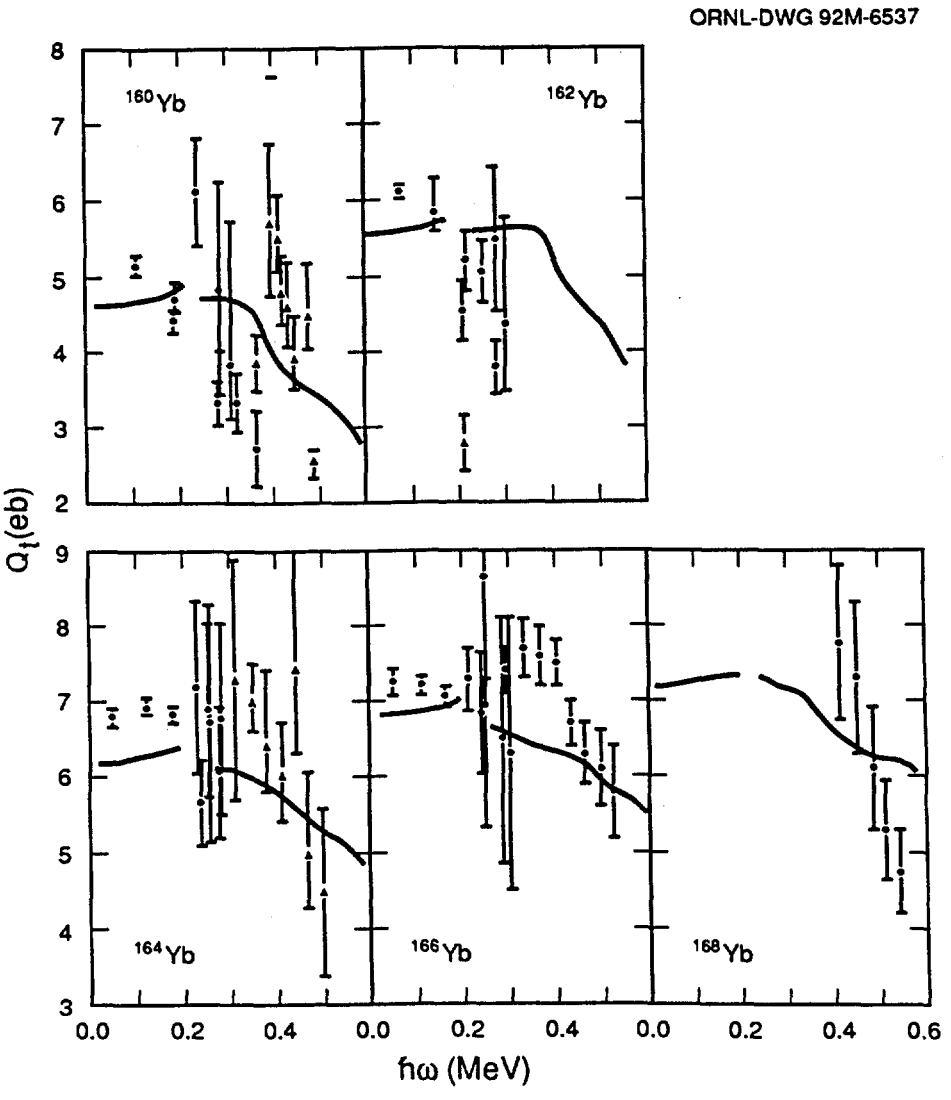

Fig. 3. Systematics of transition quadrupole moments for even-mass ytterbium nuclei plotted as a function of the rotational frequency ($\hbar\omega$). The solid points for ^{160}Yb are from the earlier RD measurements[1,2] and the triangles are from the current measurements. The ^{162}Yb data are from Ref. 9. The low-spin data for ^{164}Yb are from Ref. 13, while the high-spin data (triangles) for this case are from Refs. 10-12. Data for ^{166}Yb are from Ref. 14 and those for ^{168}Yb are from Ref. 15. The theoretical curves are based on deformation parameters from the TRS calculations in Ref. 16.

of increasing Q_t values with neutron number as we move up from the N = 90 case; and (2) theory predicts a trend of decreasing Q_t values in each nucleus in the range of $\hbar\omega \approx$ 0.25–0.50 MeV. We must add that part of the problem may be in the approximate nature of our calculation of Q_t from the deformation parameters. For a precise treatment of lifetime data, one really needs the wave functions of the initial and final states for each transition but, unfortunately, these are not available.

In conclusion, it is evident that we are making progress at a microscopic level in our understanding of rapidly-rotating nuclei. At the same time, however, it is clear that a fuller understanding of the evolution of collectivity and the accompanying changes in the shapes of nuclei such as these demands both experimental data of higher quality and more refined theoretical treatments. Vast improvements in both the quantity and the quality of the experimental data are now on the horizon with the much larger Compton-suppressed arrays currently being constructed.

Research sponsored by the U.S. Department of Energy, under contract DE-AC05-84OR21400 with Martin Marietta Energy Systems, Inc. Work at Vanderbilt University and the University of Tennessee is supported by the U.S. Department of Energy under contracts DE-FG05-88ER40407 and DE-FG05-87ER403611, respectively.

REFERENCES

1. N. R. Johnson, in *Proc. INS International Symposium on Dynamics of Nuclear Collective Motion,* ed. K. Ogawa and K. Tanabe, (Inst. for Nuclear Study, Univ. of Tokyo, Tokyo, 1982) p. 144.
2. M. P. Fewell, N. R. Johnson, F. K. McGowan, J. S. Hattula, I. Y. Lee, C. Baktash, Y. Schutz, J. C. Wells, L. L. Riedinger, M. W. Guidry, and S. C. Pancholi, *Phys. Rev.* C **31,** 1057 (1985); and *Phys. Rev.* C **37,** 101 (1988).
3. R. Bengtsson, Y-S. Chen, J-Y. Zhang, and S. Åberg, *Nucl. Phys.* **A405**, 221 (1983).
4. J. C. Wells and N. R. Johnson, LINESHAPE; A Computer Program for Doppler-Broadened Lineshape Analysis. *ORNL Physics Division Progress Report for Period Ending September 30, 1991*, ORNL-6689.
5. J. Gascon, private communication. (1989).
6. F. James and M. Roos, Comput. Phys. Commun. **10**, 343 (1975).
7. J. C. Wells, M. P. Fewell, and N. R. Johnson, *Oak Ridge National Laboratory Report* ORNL/TM-9105 (1985).
8. W. T. Milner, private communication.
9. F. K. McGowan, N. R. Johnson, C. Baktash, I. Y. Lee, Y. Schutz, J. C. Wells, and A. Larabee, *Nucl. Phys.* **A539,** 276 (1992).
10. Hong Xie, Ph.D. thesis presented to Vanderbilt University, Nashville, Tennessee (1990). Unpublished.

11. H. Xie, F. K. McGowan, C.-H. Yu, N. R. Johnson, J. D. Garrett, C. Baktash, I. Y. Lee, J. C. Wells, J. H. Hamilton, and L. L. Riedinger, in *Proc of Conf. on Nuclear Structure in the Nineties*, Oak Ridge, Vol. 1, (1990) p. 162; and *ORNL Physics Division Progress Report for Period Ending September 30, 1989*, ORNL-6578, 47.
12. H. Xie, J. D. Garrett, F. K. McGowan, R. Wyss, C-H. Yu, N. R. Johnson, I. Y. Lee, C. Baktash, and J. H. Hamilton, in *Proc of Conf. on Nuclear Structure in the Nineties,* Oak Ridge, Vol. 1, (1990) p. 164.
13. B. Bochev, S. A. Karamian, T. Kutsarova, K. Nadjakov, and Yw. Ts. Oganessian, *Nucl. Phys.* **A267,** 344 (1976).
14. J. C. Bacelar, R. M. Diamond, E. M. Beck, M. A. Deleplanque, J. Draper, and F. S. Stephens, *Phys. Rev.* C **35,** 1170 (1987).
15. J. C. Lisle, D. Clarke, R. Chapman, F. Khazaie, J. N. Mo, H. Hübel, W. Schmitz, K. Theine, J. D. Garrett, G. B. Hagemann, B. Herskind, and K. Schiffer, in *Nuclear Structure in the Nineties*, ed. N. R. Johnson (Elsevier Science Publishers B. V., Amsterdam, 1990) p. 451; and *Nucl. Phys.* **A520,** 451 (1990).
16. R. Wyss, R. Bengtsson, and W. Nazarewicz, private communication.

High-Spin Rotational States in ^{179}Os

J. Burde
Racah Institute of Physics, Hebrew University of Jerusalem, Israel
and
Nuclear Science Division, Lawrence Berkeley Laboratory, Berkeley, California 94720
M. A. Deleplanque, R. M. Diamond, A. O. Macchiavelli,* F. S. Stephens and C. W. Beausang **
Nuclear Science Division, Lawrence Berkeley Laboratory, Berkeley, California 94720

* Permanent address: Comision National de Energia Atomica, Buenos-Aires, Argentina.
** Present address: Oliver Lodge Laboratory,University of Liverpool, Liverpool, L69 3BX,UK

I. Introduction

The rotational bands of the osmium isotopes display very interesting properties that vary with the neutron number [1,2]. On the one hand the yrast bands of $^{182,184,186}Os$ display a sudden and rather strong gain in aligned angular momentum, whereas the lighter osmium nuclei such as $^{176,178,180}Os$ show a more gradual increase of alignment characteristic of strongly interacting bands. In addition, an unusual rotational band has been found [3] in ^{178}Os. It consists of seven regularly spaced transitions about 36 keV apart which correspond closely to the spacing of the superdeformed band in ^{152}Dy after an $A^{5/3}$ normalization. This band populates the yrast band directly, and the moment of inertia $J^{(1)}$ is found to be much smaller than $J^{(2)}$. The most likely interpretation of this is a band with large deformation which is undergoing systematic changes in deformation, pairing and/or alignment.

This latter finding in particular motivated us to carry out research on the higher spin states in ^{179}Os. Dracoulis et al. [4] have published their results on 5 rotational bands in ^{179}Os. In the present work we found six new bands and extended appreciably the spin limits in the other five.

II. Results and analysis

The nucleus ^{179}Os was produced at the 88-Inch Cyclotron of the Lawrence Berkeley Laboratory in the ^{154}Sm (^{30}Si,5n) ^{179}Os reaction using a 20 enA beam of 155 MeV ^{30}Si. The enriched ^{154}Sm target was composed of three self-supporting foils, each 0.5 mg/cm^2 thick. The γ rays emitted by the reaction products were observed in the 20 Compton-suppressed Ge detectors of the HERA array. Only three-fold and higher-fold events were recorded on magnetic tape. The prompt γ rays were Doppler shifted, hence the gains of the detectors were adjusted so that all the spectra had the same energy calibration and could be added.

The three-fold and higher-fold events were broken into pairs, altogether 220 millions, for double-coincidence analysis. Extensive projections were made by gating various prominent lines and observing in each case the coincident spectrum.

Based on many coincidence projections we have constructed the level scheme given in Fig. 1. The 11 bands are numbered at the top of the figure and below are given the proposed band assignments.

A. Band assignments

In Ref. [4] the yrast band was assigned as the $1/2^-$ [521] band and the other two pairs of signature partners as the $7/2^-$ [514] and the $9/2^+$ [624] bands. The $1/2^-$ [521] α=+1/2 sequence was extended up to spin $45/2^-$ and is displayed in Fig. 1 as band 2. The α=-1/2 signature partner has been found in the present work and is shown as band 1. There is a rather characteristic indication for the appearance of

such Ω=1/2 bands. Both signature components of the Ω=1/2 band are decoupled due to the Coriolis interaction. The moment-of-inertia parameter [E(I)-E(I-1)]/(2I) can be obtained as: [E(I) -E(I-1)]/(2I) = $\hbar^2$/(2J) [1+a(-1)$^{I+1/2}$] , where a is the decoupling parameter.This is plotted as a function of I^2 in Fig. 2. The experimental values of sequences 1 and 2 that comprise the two signature components of the 1/2$^-$ [521] band are marked by diamonds and show a strong oscillation.

The assigned [4] 7/2$^-$ [514] α=-1/2 and α=+1/2 partners which were extended in the present work up to spins 57/2$^-$ and 63/2$^-$ are displayed in Fig. 1 as bands 7 and 8, respectively. Their moment-of-inertia parameter is also plotted in Fig. 2 as stars, and, in contrast to the previous plot, this curve is rather smooth as one would expect of a K=7/2 band.

The 9/2$^+$[624] α=-1/2 and α=+1/2 sequences are also displayed. The moment-of-inertia parameter of this band shows a very pronounced signature-splitting oscillation. Such strong oscillations were observed for K=7/2 and K=9/2 $i_{13/2}$ bands in the neighboring odd neutron osmium and platinum.

The bands 4 and 5 are newly found bands. Sequence 5 is fed by band 7 through the 339.7- and 318.0-keV transitions and de-excites to sequence 8 by the 238.5-keV line. It seems also that the 15/2$^-$ level in sequence 4 is partially de-excited to the 11/2- level in band 8, defining most probably the band head of the two sequences as the 5/2$^-$ 115.1 keV state. The logical assignment following the systematics in the neighboring osmium and platinum nuclei, is: α=-1/2 and α=+1/2 5/2$^-$ [512] for bands 4 and 5, respectively. The moment-of-inertia parameter is plotted in Fig. 2 for bands 4 and 5 and seems to be a rather smooth curve as expected for this configuration.

B. Experimental Routhians and band crossings.

Additional important properties of the bands can be obtained by examining the experimental Routhians. The reference parameters were taken as J_0=25 MeV$^{-1}\hbar^2$ and J_1=60 MeV$^{-3}\hbar^4$. Only two bands (band 4 and band 10) have rather pronounced backbendings. In all the other sequences the alignment and the Routhian energies as a function of frequency have mainly a smooth behavior. However, the band- crossing positions were determined from the Routhian energy plots .

1. The 5/2$^-$[512] band

In this way the crossing frequency was determined as 0.24 MeV for band 4 , assigned as the 5/2$^-$ [512] band and the change in alignment as Δi=8.5. These are in good agreement with the CSM calculation of 0.24 MeV and Δi=10.6 for the AB crossing, which is expected for this negative-parity band. The signature partner of this band, sequence 5 follows rather closely curve 4 and backbends at about the same position, but, has not been observed to high enough frequency to be able to deduce the crossing frequency and Δi accurately.

2. The 1/2$^-$[521] band

Bands 1 and 2, that comprise the 1/2$^-$[521] band, display a rather gradual alignment as can be seen from Fig. 3. The dynamic moment of inertia plots, show definite irregularities in these sequences. The band crossings deduced from the Routhian energy curves are, 0.23 and 0.26 MeV, respectively, and the alignment increments are Δi>4.5 and >8.5 , in good agreement with the AB crossing expectations.

3. The 7/2$^-$[514] band

The alignments of bands 7 and 8 which comprise the 7/2$^-$[514] band, are more pronounced. Their irregularities are strongly displayed by the peaks of their dynamic moment of inertia plots. Their crossing frequencies, are 0.28 and 0.27 MeV, and their alignment increases are Δi=11 and 10.5 for the α=+1/2 sequence 7 and α=-1/2 sequence 8, respectively. The Δi values agree very well with the CSM prediction for the AB crossing, but the crossing frequencies are a little higher. It is interesting to note,

however, that similar values were deduced [1] for the corresponding bands in ^{181}Os from previous experimental data and also in the isotone [5] ^{181}Pt.

4 The 9/2$^+$[624] $i_{13/2}$ band

The two signature partners of the 9/2$^+$[624] band, sequences 9 (α=-1/2) and 10 (α=+1/2), display quite different features in the alignment plot. Whereas the α=+1/2, curve 0 backbends around 0.3 MeV, the α=-1/2, curve 9, exhibits a more gradual alignment increase. This behavior was attributed to possible differences in interaction strength. The crossing frequencies deduced from the Routhians are 0.31 and 0.30 MeV and the alignment increases are Δi=6.5 and 5.5 for the α=+1/2 and α=-1/2 components, respectively. Taking into account that the AB crossing is blocked for those two sequences, there is good agreement with the CSM prediction for the BC crossing frequency of 0.30 MeV and Δi=8.2 for the α=+1/2 component. The α=-1/2 component crossing, however, appears to be lower in frequency experimentally, although the CSM value is slightly higher (0.31 MeV).

5 . Second band crossings in the $i_{13/2}$ sequences

At the top of bands 9 and 10 are observed additional irregularities in the alignment plot i, and in the dynamic moment of inertia curves. The crossing frequencies as deduced from the Routhian and alignment curves are 0.44 and approximately 0.5 MeV and the alignment Δi increments are about 2.5 and >3 for the α=-1/2 and α=+1/2 signature partners, respectively. While the crossing frequency of band 9 occurs at the predicted proton ab crossing value we do not understand why the crossing of band 10 appears at a visibly higher frequency. In Ref. [5] a possible upbending was observed at $\hbar\omega$=0.4 MeV in the 9/2$^+$ band of the ^{181}Pt isotone. This was attributed to the alignment of two $h_{9/2}$ quasiprotons. The rather sharp upbend at the top of band 11 signifies a possible band crossing due to an alignment of two $h_{9/2}$ quasiprotons at $\hbar\omega_c$=0.43 MeV.

III. Summary

The structures in ^{179}Os have been studied via a HI-induced fusion reaction. Six new bands have been identified, and the spin limit in each of the previously known five bands have been significantly extended. Eight of the sequences comprise four signature-partner pairs identified as the 1/2$^-$[521], 5/2$^-$[512], 7/2$^-$[514] and 9/2$^+$[624] Nilsson neutron orbitals. Another single sequence extending up to spin (37/2$^-$) is tentatively assigned as a component of the 5/2$^-$[523] band. Two other sequences which decay to the 9/2$^+$[624] and the 7/2$^-$[514] bands are found up to spins 61/2$^+$ and 65/2$^-$ respectively. The experimental Routhians are compared with the CSM theoretical predictions for all the sequences. The first crossings are indentified in all the first ten sequences as due to the alignment of a pair of $i_{13/2}$ neutrons. Second band crossings are found in the two positive-parity bands 9 and 10 and in the negative-parity sequence that decays in the 7/2$^-$[514] band. These second band crossings are probably due to an alignment of two $h_{9/2}$ 1/2$^-$[541] protons, and this proton alignment probably appears also in sequence 11. The B(M1)/B(E2) ratios are discussed and compared with theory.

References

[1] J. D. Garrett and S. Frauendorf, Phys. Lett. **108B,** 77 (1982).
[2] A. Neskakis, R. M. Lieder, G. Sletten and J. D. Garrett, Phys. Lett. **118B**, 49 (1982).
[3] J. Burde, A. O. Macchiavelli, M. A. Deleplanque, R. M. Diamond, F.S. Stephens, C.W. Beausang, R. J. McDonald, and J .E. Draper, Phys. Rev. **C 38,** R2470 (1988).
[4] G. D. Dracoulis, C. Fahlander and A. P. Byrne, Nucl. Phys. **A401,** 490 (1983).
[5] M. J. A. De Voigt, R. Kaczarowski, H. J. Riezebos, R. F. Noorman, J. C. Bacelar, M. A. Deleplanque, R. M. Diamond and F. S. Stephens, Nucl. Phys. **A507,** 447 (1990).

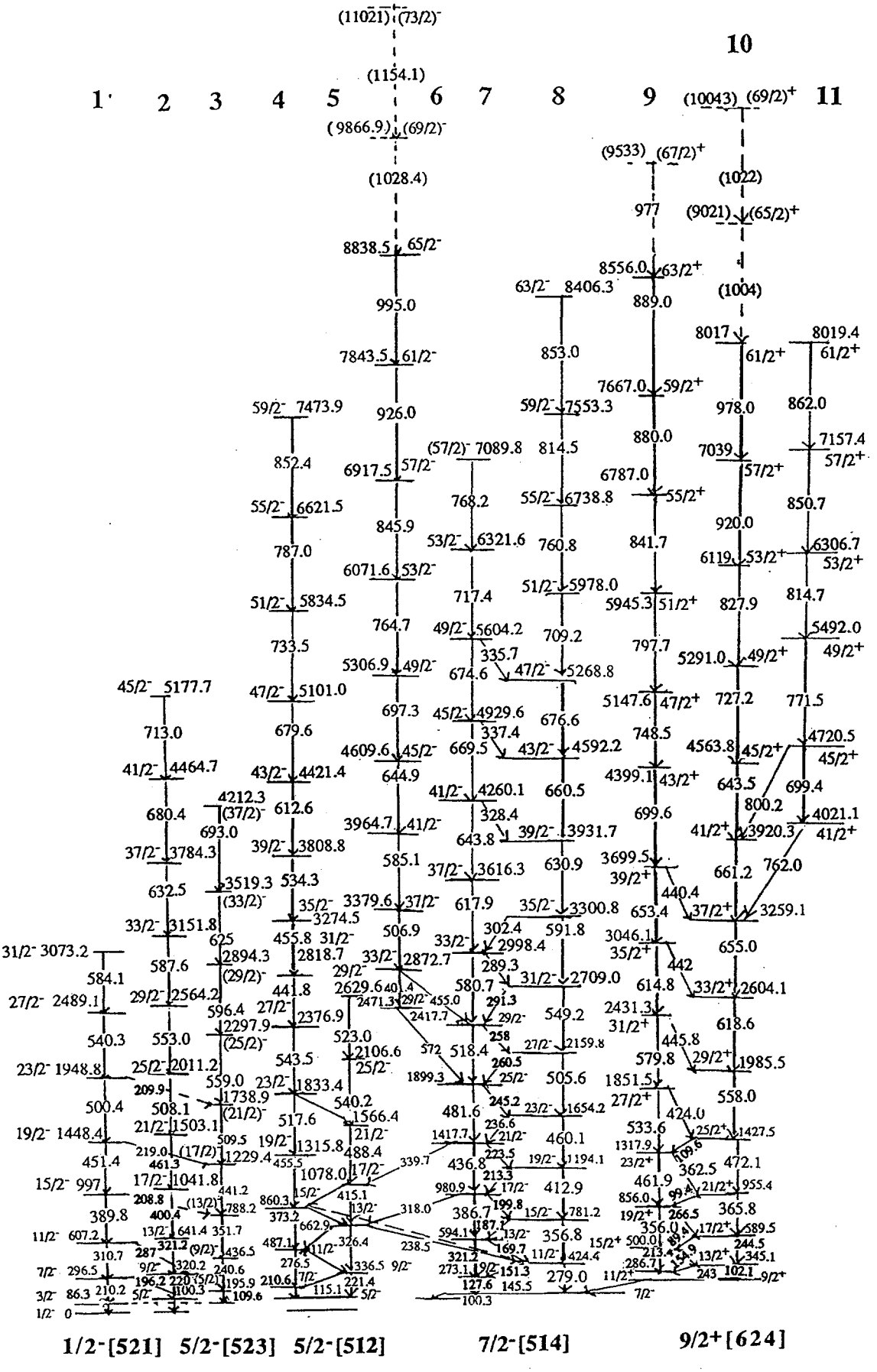
1
2
3
4
5
6
7
8
9
10
11
1/2-[521]
5/2-[523]
5/2-[512]
7/2-[514]
9/2+[624]

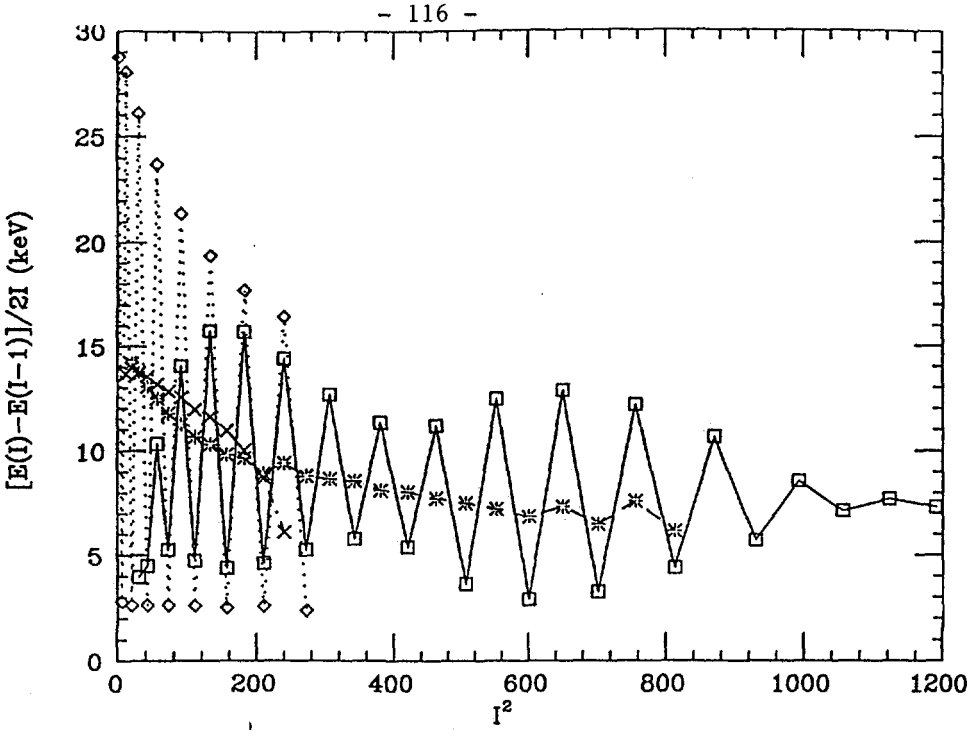

Fig. 2 The moment-of-inertia parameter as a function of I^2. The experimental points for bands 1 and 2, identified as the 1/2⁻[521] band, are marked by diamonds. Those of 4 and 5, comprising the 5/2⁻[512] band are indicated by x-es. Those of 7 and 8, identified as the 7/2⁻[514] band are marked by stars. The 9/2⁺[624] band is indicated by squares.

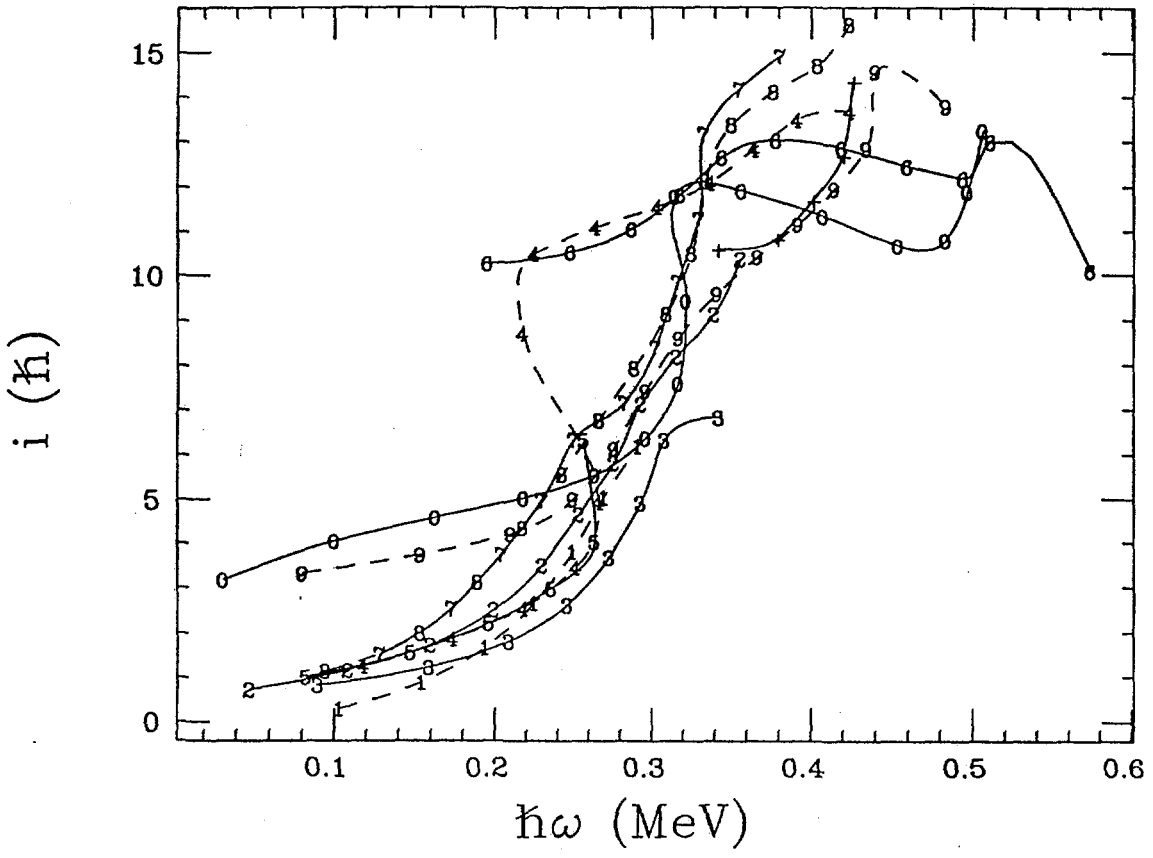

Fig. 3 Alignment i in units of ħ as a function of frequency ħω in MeV of the 11 bands in ^{179}Os. The curves are indicated by the corresponding numbers of the bands (see fig. 3), except for band 10 and 11 which are marked by 0 and +, respectively. Curves 1 and 2 are assigned as the α=-1/2 and α=+1/2 of 1/2⁻[521], 3 as the 5/2⁻[523], 4 and 5 as the α=-1/2 and α=+1/2 of 5/2⁻[512], 7 and 8 as the α=+1/2 and α=-1/2 of 7/2⁻[514], and 9 and 0 as the α=-1/2 and α=+1/2 of 9/2⁺[624] bands, respectively. The reference parameters are taken as: J_0=25 MeV^{-1}ħ^2 and J_1=60 MeV^{-3}ħ^4.

Discrete Spectroscopy in ^{180}Os at High Spins

G.Martí[1*], Ts. Venkova[1§], T.Morek[1¤], H.Schnare[1], W.Gast[1],
A. Georgiev[1§], K.M.Spohr[1], R.M.Lieder[1], K.H.Maier[2] and K.O.Zell[3]

1 Institut für Kernphysik, KFA-Jülich, Germany
2 Hahn-Meitner-Institut, Berlin, Germany
3 Institut für Kernphysik, Universität Köln, Germany

The Os nuclei lie at the begining of the transitional region between well deformed and spherical shapes. Nuclei in this region are believed to be soft with respect to deformation changes. The detailed theoretical analysis of [1], shows that the alignment behaviour in the mass A=180 region is strongly correlated with shape changes. Properties such as triaxiality and/or shape coexistence, may arise due to softness of the nuclear potential and its sensitivity to particle configuration and alignment. This results in a large variation of the backbending behaviour of the neutron deficient Os nuclei [2,3,4], and the existence of highly deformed intruder bands [5,6] and high-K isomerism in this mass region [7,8,9]. Furthermore, superdeformed structures were predicted [10] and evidence for a superdeformed band was obtained in previous studies [6]. Therefore, we re-investigated ^{180}Os to search for a discrete superdeformed band. The results presented here were obtained as a byproduct. A more detailed paper is under preparation.

The nucleus ^{180}Os has been produced through the ^{150}Nd (^{36}S, 6n) reaction at 177 MeV using the pulsed ^{36}S beam delivered by the **VICKSI** accelerator of the HMI, Berlin. In the first experiment (thin target) a self supporting ^{150}Nd foil of ≈ 0.5 mg/cm^2 thickness, was used to search for fast transitions with a minimum Doppler broadening, whereas in the second one (thick target) a ≈ 1 mg/cm^2 ^{150}Nd foil backed by ≈ 7 mg/cm^2 of ^{197}Au was used. The emitted γ-radiation was detected with the **OSIRIS** spectrometer. For each coincidence event the γ-ray energies, the times $t_{\gamma\text{-beam}}$ and the number of BGO elements fired together with the corresponding sum-energy were recorded. A total number of ≈ 340 and ≈ 450 millon two-fold events were recorded in the thin and thick target experiments, respectively. These data were subsequently sorted to obtain several matrices by setting suitable windows on the time spectra. Due to the comparatively low statistics of the data set for the thin target experiment fold and sum-energy windows were set just to suppress contaminations resulting from Coulomb excitation of the target, radioactive decay and (n,n'γ) reactions. In the thick target experiment a relatively high fold condition (f≥9) was set which resulted in very clean matrices containing only events belonging to the nuclei ^{180,181}Os.

The nucleus ^{180}Os was already previously the subject of very detailed studies [11,12], but some new interesting features observed in the present study deserve to be discussed in more detail. A revised partial level scheme of ^{180}Os resulting from the present work is shown in fig. 1. The bands are labelled by the parity π, signature α and a running index n as $(\pi,\alpha)_n$ following the same order as in ref. [12]. The placement of the transitions are based on the prompt-prompt, delayed-prompt and prompt-delayed coincidence relationships. A partial level scheme containing all the identified delayed transitions deexciting the 7^- isomer at 1928 keV, will be published elsewhere [13] and are not included; here we want

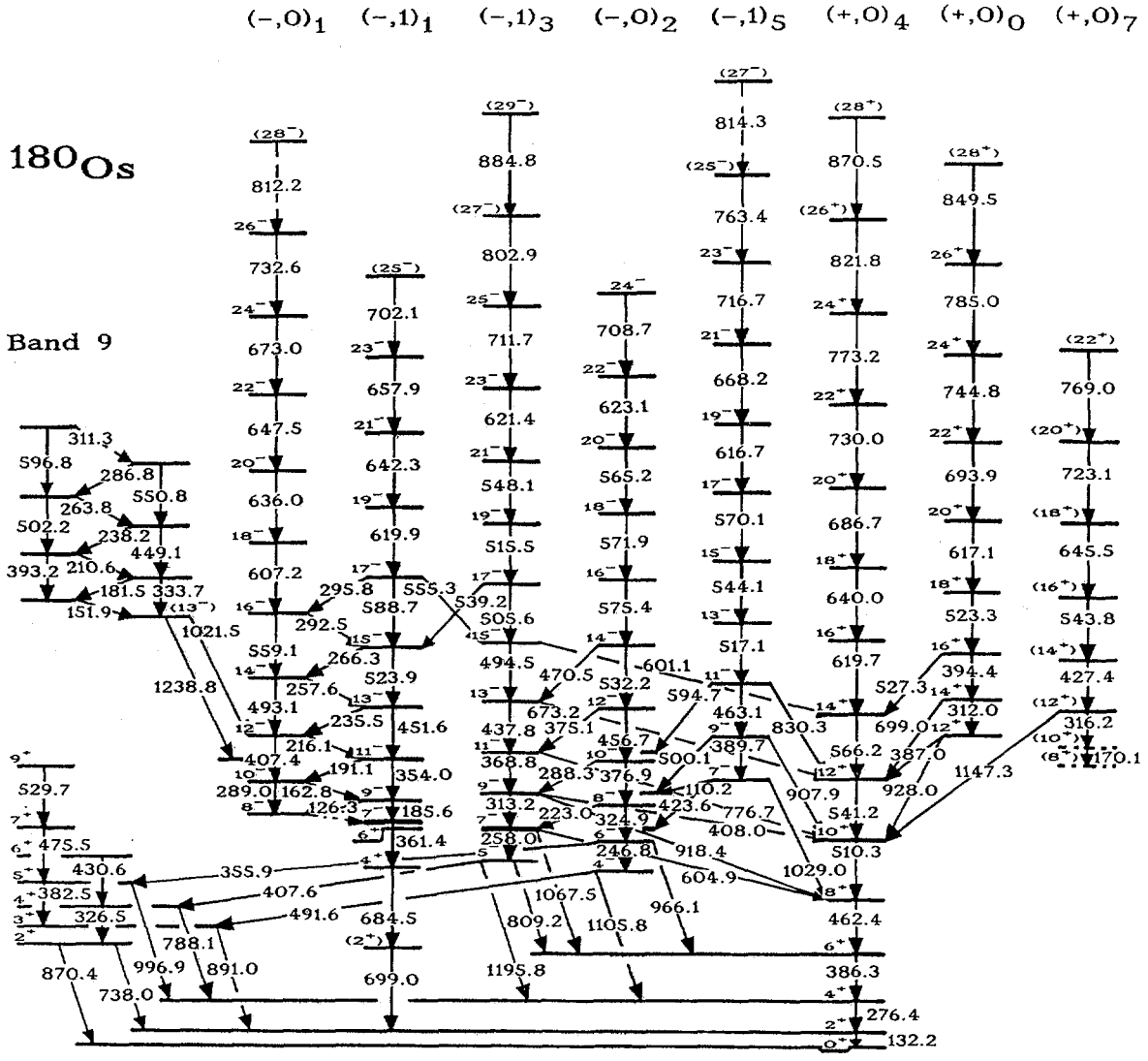

Figure 1: Partial level scheme of ^{180}Os. All assignments are based on coincidence relations. Uncertain placements are indicated by dashed lines.

to concentrate mainly on the high-spins states ($I \geq 10$). We shall summarize and discuss the most important results in comparison to those obtained in previous studies [11,12]. Differences with previous level schemes will be emphasized.

A new weakly populated strongly-coupled rotational band labelled as band 9 in fig. 1 ($\approx$ 1.8% of the $2^+ \rightarrow 0^+$ ground state transition) with cascade and crossover transitions was identified. It deexcites, respectively, into the 12^- and 11^- states of the $(-,0)_1$ and $(-,1)_1$ sequences of band 1, through the two high energy 1021.5 and 1238.8 keV transitions. We assigned $I^\pi = (13^-)$ to the band head relying on the DCO ratios of the two relatively strong 1021.5 and 1238.8 keV transitions. Due to the low intensity g_K-factors based on branching and M1/E2 mixing ratios, could not be determined for this band and therefore no configuration assignment was carried out. Assuming $\Delta I = 1$ for the cascade transitions and

$\Delta I = 2$ for the crossover transitions the moment of inertia parameter $\Delta E(I \rightarrow I-1)/2I$ was plotted versus I^2 in fig. 2. No signature staggering is observed for the identified members of the band. We searched for a half-life for the band head of band 9. Within the limits of our experiment ($T_{1/2} \geq 5$ ns) no half-life was measured for the 1021.5 and 1238.8 keV transitions.

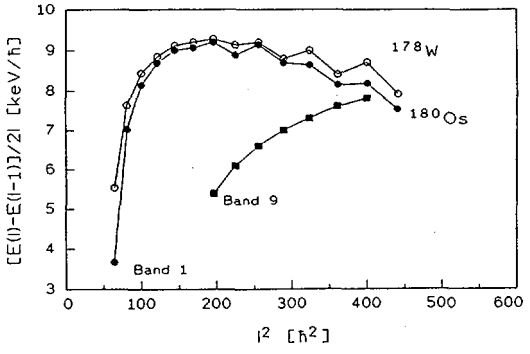

Figure 2: Moment of inertia parameter ΔE $(I \rightarrow I-1)/2I$ plotted as a function of the spin for bands 1 and 9 in ^{180}Os and for the isomeric 7^- band in ^{178}W.

A new transition of 185.6 keV belonging to the $(-,1)_1$ sequence of band 1 was identified which directly feeds the 7^- isomer at 1928 keV as a result of the analysis of the prompt-delayed, delayed-prompt and prompt-prompt γ-γ coincidence matrices from the thick target experiment. Its placement in the level scheme was confirmed through several coincidence spectra. The 185.6 keV line is placed as $9^- \rightarrow 7^-$ transition. A stretched quadrupole assignment is consistent with the observed DCO ratios, although a $\Delta I = 0$, M1/E2 assignment cannot be excluded. The $8^- \rightarrow 7^-$ transition of $\approx$ 60 keV has not been observed. The observation of this new transition allows furthermore to place two relatively strong interband transitions of 539.2 and 555.3 keV connecting the $(-,1)_3$ and $(-,1)_1$ sequences. This gives additional support for the placement of the 185.6 keV line as the $9^- \rightarrow 7^-$ transition in the $(-,1)_1$ sequence of band 1. As a consequence of its placement results a new spin and signature assignments for band 1. The spins increase by one unit and the signatures of both sequences are exchanged as compared to previous results [11,12]. In fig. 2 plots of the moment of inertia parameter versus I^2 for the bands built on the 7^- isomers in the isotones ^{180}Os and ^{178}W [14] are included. The agreement between both curves is noteworthy. One should remark that the difference in the phase of the oscillations discussed in [11] was removed. These facts support the assumption that the same two-quasineutron configuration ν {7/2$^+$[633] $\otimes$ 7/2$^-$[514]} can be assigned to the 7^- bands in both nuclei.

A possible explanation for the observation of the transitions connecting the $(-,1)_3$ and $(-,1)_1$ sequences of same parity and signature could be related to a configuration mixing between the levels of the same spin which the 539.2 and 555.3 keV transitions deexcite, respectively. This feature was also found in ^{175}Os [15], ^{181}Os [16], ^{186}Pt [17] and ^{181}Ir [18]. A rough estimate of the interaction strength can be obtained from the energy differences [19] between levels of equal spin. The upper limit of the interaction strength is $|V| \leq 24$ keV for the 17^- levels assuming that it is half of the energy difference between the levels. A better estimate can be obtained using the four level approximation of [20]

assuming that the interaction is proportional to I and mixes only states of the same spin. Using the experimental branching ratios for the 17^- level of the $(-,1)_3$ band at 3982.0 keV a value of V = 18.1 $^{+0.3}_{-0.4}$ keV was obtained for the interaction strength of the 17^- levels. Using this value the calculated branching ratio for the transitions deexciting the 17^- level at 4031.8 keV gives $\lambda(555.3/588.7)_{th}$= 0.29 in good agreement with the experimental branching ratios of 0.27 ± 0.10 obtained as a weighted average from gated spectra on the 621.4 and 642.3 keV transitions respectively.

An important discrepancy between the level schemes of ^{180}Os reported in [11] and [12] is a different assignment of the yrast and yrare bands of positive parity and signature α = 0. One of the main arguments in ref. [12] for the spin assignment of the yrast and yrare states [21,22], is based on the observation of the interband transitions of 1050.5, 1093.4 and 1240.2 keV. We could not confirm the existence of these transitions. Furthermore, we have accurately determined the DCO ratio for the 527.3 keV transition giving 0.98 $\pm$ 0.08 (gating on the 523.3 keV transition) and 1.02 $\pm$ 0.1 (gating on the 566.2 keV transition) in agreement with stretched quadrupole character [23]. The spin assignment for the level deexcited by the 527.3 keV transition could not be unambiguosly determined from the angular distribution measurements and/or DCO ratio determinations, but conversion electron coefficients are needed in addition. Combining the results of conversion electron measurements of ref. [21] with the limits for the mixing E2/M1 ratio resulting from angular distribution measurment lead to the conclusion that the only possible multipolarity for the 527.3 keV transition is stretched quadrupole. These results strongly support the previous assignment of ref. [11] and our revised assignment in the present work.

New information about the states lying above spin I ≥ 24 was obtained for most of the bands. The high spin transitions producing the second band crossing [12] could not be confirmed, but several new transitions were identified. All of them were confirmed in several coincidence relations in both experiments. The dotted transitions in fig. 1 have a confident level of ≈ 80%. Out of the ten side bands in ^{180}Os reported in [12] only 7 bands could be confirmed. In fig. 3a and 3b the alignment plots for the negative and positive parity bands, respectively, are plotted as a function of the rotational frecuency in the frame of the CSM [19].

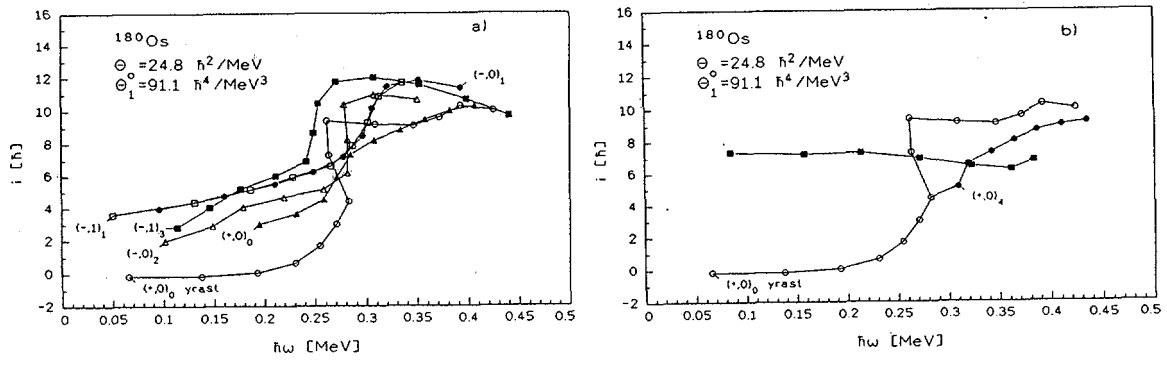

Figure 3: **a)** alignment plots for the negative parity bands in ^{180}Os . The yrast band is shown as a reference. **b)** idem a) but for the positive parity bands.

It can be seen that for all the bands the second band crossing, previously interpreted [12] as a consequence of $h_{11/2}$ proton alignments, vanishes. In the region $0.24 \leq \hbar\omega \leq 0.30$ all the bands display only one crossing. Furthemore, due to the new identified transitions the yrast band shows a forward bending after the first crossing at $\approx$ 0.28 MeV.

In summary, a new strongly-coupled rotational band starting at a relatively high excitation energy was found; the observation and placement of the 185.6 keV transition in the level scheme, gives strong support to the considered 2-quasineutron configuration ν {7/2$^+$[633] $\otimes$ 7/2$^-$[514]} assigned to the 7$^-$ isomeric bands in ^{180}Os and the isotone ^{178}W; band mixing between the $(-,1)_1$ and $(-,1)_3$ bands of same parity and signature was observed and the interaction strength was estimated from experimental branching ratios; our results confirm the previous assignment of ref. [11] for the yrast and yrare sequences in this nucleus and with the identification of the new transitions above the states with I $\approx$ 24 previous bands assigned had to be revised with the result that the second band crossing vanishes.

References

1 R.Wyss et al., Nucl. Phys. A511 (1990) 324.
2 R.M.Lieder et al., Adv. Nucl. Phys 10 (1978) 1.
3 J.D.Garrett et al., Phys. Lett. 108B (1982) 77.
4 M.J.A. de Voigt et al., Rev. Mod. Phys. 55 (1983) 949.
5 J.Burde et al., Phys. Rev. C38 (1988) 2470.
6 T.Rzaca-Urban et al., Z.Phys. A328 (1987) 379.
7 J.Pedersen et al., Z.Phys. A321 (1985) 567.
8 A. Krämer-Flecken, Ph. D.Thesis, Jül-Spez 458 (1988).
9 P.Chowdhury et al., Nucl. Phys. A485 (1988) 136.
10 R.Chassman, Phys. Lett. B219 (1989) 227.
11 G.Dracoulis et al.,Nucl. Phys. A383 (1982) 119.
12 R.M.Lieder et al., Nucl. Phys. A476 (1988) 545.
13 Ts. Venkova et al., to be published.
14 C.L.Dorrs et al., Nucl. Phys. A314 (1979) 61.
15 B.Fabricious et al., Nucl. Phys. A511 (1990) 345.
16 T.Kutsarova et al., to be published.
17 G.Hebbinghaus et al., Nucl. Phys. A514 (1990) 225.
18 G.Dracoulis et al. private comunication.
19 R.Bengtsson et al., Nucl. Phys. A314 (1979) 27 and Nucl. Phys A327 (1979) 139.
20 E.M.Beck et al., Nucl. Phys. A464 (1987) 472.
21 G.Dracoulis et al., Nucl. Phys. A509 (1990) 605.
22 A.Neskakis et al. Phys. Rev. Letters 50, 20 (1988) 1628.
23 R.M.Lieder et al., Nucl. Inst. and Meth. A275 (1989) 333.

* Permanent address: Departamento de Físca, CNEA, Av. del Libertador 8250 (1429) Bs. As. Argentina.
§ Permanent address: Institute of Nuclear Research and Nuclear Energy, Boul. Trakia 72, 1184 Sofia, Bulgaria.
¤ Permanent address: Institute of Experimental Physics, University of Warsaw, ul. Hoza 69, PL-00681, Warsaw, Poland.

Collective Dipole Rotational Bands in the A~200 Region.

R.M.Clark[1], R.Wadsworth[1], E.S.Paul[2], C.W.Beausang[2], I.Ali[2], A.Astier[3], D.M.Cullen[2], P.J.Dagnall[2], P.Fallon[2], M.J.Joyce[2], M.Meyer[3], N.Redon[3], P.H.Regan[1], J.F.Sharpey-Schafer[2], and W.Nazarewicz[4], R.Wyss[4]

[1] Department of Physics, University of York, York, Y01 5DD, UK
[2] Oliver Lodge Laboratory, University of Liverpool, Liverpool, L69 3BX, UK
[3] Institut de Physique Nucléaire de Lyon, IN2P3-CRNS, France
[4] Joint Institute for Heavy Ion Research, Oak Ridge, TN 37831, USA

Rotational oblate bands consisting of regular sequences of magnetic dipole transitions have recently been identified in $^{196-201}$Pb [1-8]. Their observation indicates a drastic change in the high spin configuration between the Hg, Tl and ^{194}Pb nuclei, in which SD bands are clearly observed, and the heavier Pb isotopes, where these weakly deformed oblate structures seem to dominate.

The high spin structures of ^{197,198}Pb have been studied in two experiments carried out on the 20MV tandem Van de Graaf at the Daresbury Laboratory, using the TESSA3 spectrometer, which consists of 16 escape suppressed Ge detectors and a 50 element inner ball of bismuth germanate (BGO). In the first experiment high spin states in $^{197-199}$Pb were populated via the ^{186}W(^{17}O,xn) reactions at beam energies of 92 and 98 MeV. The data comprised the energy deposited in each Ge detector and the sum-energy and fold recorded by the BGO ball for each event. A total of 18×10^6 events were recorded at 92 MeV with 100×10^6 events at 98 MeV. $E_{\gamma1}$–$E_{\gamma2}$ matrices of coincidence events were formed for both beam energies which preferentially selected the $^{197-199}$Pb nuclei by requiring a BGO fold condition of $\geq$10. In the second experiment the same reaction was used but now at a beam energy of 110MeV. This resulted in the population of states in ^{196,197}Pb. A total of 140×10^6 coincidence events were recorded.

The analysis of these data has resulted in the observation of ten rotational structures, one in ^{199}Pb, five in ^{198}Pb, three in ^{197}Pb, and one in ^{196}Pb. The bands can be assigned to their respective nuclei since γ-rays in the cascades are in coincidence with known transitions of the yrast sequences. The assignments are further supported by excitation function data.

The bands in $^{196-201}$Pb have many intriguing features in common. For instance, several of the structures are observed to have identical transition energies to within 3 or 4 keV (a property also displayed by superdeformed nuclei in this mass region, eg [9]). Other properties of the bands can be demonstrated by considering the structures seen only in ^{198}Pb, and then extending the discussion to include all the sequences observed in the other Pb nuclei.

The previous energy level scheme of ^{198}Pb is given in [10]. A revised scheme, deduced from the present work is presented in Fig 1. A typical spectrum for band 1 is presented in Fig 2. Five ΔI=1 cascades are found to dominate the level scheme above a spin of around 18$\hbar$. Detailed accounts for each of the bands can be found in [4,5], which also give the measured values of the transition energies, relative intensities, and angular correlation ratios.

Several general features common to all the bands can be emphasized here. The assignments of the bands to ^{198}Pb are based on the fact that all the transitions in each of the sequences are in coincidence with known γ-rays of this nucleus (for instance the 929 keV $14^+ \rightarrow 12^+$ transition; yrast transitions below this are generally not seen since the 12^+ state is isomeric). The assignments are also supported by excitation function data.

Angular correlation measurements have been extracted from the coincidence data. In this case γ-γ coincidence data were sorted into matrices which contained events from detectors at 35° and 90°, thus enabling the angular correlation ratio W(35°,35°,ψ)/W(90°,35°,ψ) to be deduced for each transition. Theoretical angular correlation ratios have also been calculated using the TRIFAC code [11], averaged over various ψ angles for detectors located in different planes and assuming full alignment for the population of the substates. The results of these calculations yield ratios of 1.58 for a stretched quadrupole–stretched quadrupole correlation and 0.74 for a pure stretched dipole–stretched dipole correlation. Experimental correlation ratios for various known E2–E2 sequences are all slightly lower than 1.50, suggesting an incomplete alignment of the substate populations.

Unfortunately, it was not possible (due to contamination) to obtain correlations for known stretched dipole–stretched dipole transitions. However, it was clear from the measured values (typically $\leq$0.7) for each of the sequences that the transitions are dipoles. Moreover, these ratios tend to be smaller, on average, than predicted for a fully aligned pure stretched dipole–stretched dipole correlation. Incomplete alignment of the magnetic substates would tend to increase the correlation values for pure dipoles. Thus, the low experimental values tentatively suggest that there is a small negative E2/M1 mixing ratio, $\delta_{E2/M1}$ (using the definition and sign convention of [12]) for each of the ΔI=1 cascades. Furthermore, since

$$\mathrm{sgn}(\delta_{E2/M1})=\mathrm{sgn}[Q_o/(g_K\text{-}g_R)]$$

(see [13]), we can explicitly define the shape of the nucleus for a given strucure provided that g_K-g_R is known (see below).

The magnetic nature of the dipoles can be inferred experimentally. Observed feed-out from the structures only appears to occur from near to the bandhead, and the intensity down the cascades should be constant if gates are set on transitions higher up. The decrease in the observed intensity for the transitions below the gate can only be accounted for by M1 conversion, which is about 15 times stronger than E1 conversion. We therefore conclude that sequences 1-5 are ΔI=1 bands consisting of magnetic dipole transitions.

No associated ΔI=2 E2 crossover transitions could be confirmed for any of the bands. The experimental lower limits for the ratio of the reduced transition probabilities B(M1:I$\rightarrow$I-1)/B(E2:I$\rightarrow$I-2) vary between 12 and $\geq$30 $(\mu_N/\mathrm{eb})^2$ over wide ranges of spin.

In order to characterize the bands several points must be considered. The fact that dipoles are seen without observed quadrupoles suggests that the sequnces are built on high-K configurations that are weakly deformed. Configuration constrained shell correction calculations [14] predict that the $K^\pi=11^-$ isomeric state observed in ^{194,196}Pb [15,16] is based on a two proton configuration, namely $\pi(h_{9/2}\otimes i_{13/2})$. Measured g-factors [16] turn out to be consistent with this interpretation. The calculated deformation of this state varies between β_2=-0.18 (^{192}Pb) to β_2=-0.15 (^{200}Pb) (ie, weakly oblate). The dipole bands reported in [1-8] have been interpreted in terms of being built on this and other similar high-K two proton configurations (eg, $\pi(i_{13/2})^2_{K=12}$, $\pi(h_{9/2})^2_{K=8}$, $\pi(h_{9/2}\otimes s^{-1}_{1/2})_{K=5}$), which will also be weakly oblate. The bands in ^{198}Pb can be interpreted in similar terms.

The generally low stretched dipole–stretched dipole angular correlations suggest small negative E2/M1 mixing ratios, $\delta_{E2/M1}$, for the bands. From the equation above it is clear that if the structures are based on proton configurations (large positive g-factors) then the quadrupole moment, Q_o, must be negative, and therefore the structures are oblate.

The variation of the dynamic moments of inertia, $\Im^{(2)}=dI/d\omega(=1/\Delta E_\gamma)$ for bands 1-4 are shown in Fig 3. The $\Im^{(2)}$ moments of inertia are generally small varying between 10–25 $\hbar^2\mathrm{MeV}^{-1}$ over quite a range of frequency. These values are comparable to the dynamic moments of inertia of the many-quasiparticle oblate collective bands in the neighbouring Hg isotopes [17]. Band 1 shows a rise at a frequency of $\hbar\omega$ ~0.2 MeV. Bands 2, 3, and 4 all have very similar $\Im^{(2)}$ plots which show a rise at $\hbar\omega$ ~0.4 MeV. A rise in $\Im^{(2)}$ indicates that an alignment of a pair of quasiparticles occurs at these frequencies. At weak oblate deformation for ^{198}Pb (N=116) $i_{13/2}$, $p_{3/2}$, and $f_{5/2}$ neutrons all lie close to the Fermi surface. The observed rises in $\Im^{(2)}$ can be explained in terms of alignments involving these neutrons.

A striking feature of the bands is the varying degree of regularity that they display. Band 1 is highly regular with a roughly constant energy spacing of ΔE_γ ~43 keV. Bands 2,3, and 4 show larger differences in ΔE_γ varying in the range 30-60 keV. Band 5 is highly irregular with ΔE_γ varying considerably over the cascade. These differences may be indicative of a varying degree of the collective behaviour of the configurations upon which these structures are based. TRS calculations indicate that the $\pi(h_{9/2}\otimes i_{13/2})$ configuration is the most oblate deformed with β_2 ~-0.15. Band 1 may be based on this configuration. The $\pi(h_{9/2})^2$ configuration is less oblate deformed with β_2 ~-0.10. It is sugested here that bands 2, 3, and 4 may have this as their underlying structure. The $\pi(h_{9/2}\otimes s^{-1}_{1/2})$ configuration is predicted to be only weakly deformed with β_2 ~-0.05. This configuration may be responsible for the highly irregular band 5.

The interpretation discussed above can be extended to include all the ΔI=1 bands observed to date in $^{196-201}$Pb. For example, the bands reported in $^{199-201}$Pb [7,8] are very similar to band

1. They have highly regular energy spacings (~50 keV), and large experimental B(M1)/B(E2) ratios ($\geq 30(\mu_N/\mathrm{eb})^2$). They also display low frequency alignments ($\hbar\omega$ ~0.2 MeV). They have been interpreted as bands built on the same high-K two proton configuration as band 1, namely $\pi(h_{9/2}\otimes i_{13/2})$, coupled to either one (^{199,201}Pb) or two (^{200}Pb) $i_{13/2}$ neutrons.

Three bands have been observed in ^{197}Pb [2,3]. Two of these are fairly regular (ΔE_γ ~ 50–60 keV) and may be based on either the $\pi(h_{9/2})^2$ or $\pi(h_{9/2}\otimes i_{13/2})$ proton configurations. The observation of associated E2 crossover transitions in one of the bands (see Fig 4) suggests that the former configuration is the most likely (since it will have lower B(M1)/B(E2) ratios). Both the bands display a higher frequency alignment at $\hbar\omega$ ~0.4 MeV, and these may be explained if the proton configurations are coupled to aligned neutrons such as $\nu(i_{13/2})^3$. The lower frequency alignment of $\nu(i_{13/2})$ neutrons, predicted by CSM calculations to occur at $\hbar\omega$ ~0.2 MeV, would then be blocked and the higher frequency alignments would then correspond to negative parity neutron orbitals ($f_{5/2}$, $p_{3/2}$). The third band in ^{197}Pb is highly irregular and is possibly based on the $\pi(h_{9/2}\otimes s^{-1}_{1/2})$ configuration.

The ΔI=1 band seen in ^{196}Pb [1] is very weak, but has characteristics similar to bands 2, 3 and 4 in ^{198}Pb, implying that it may be based on either the $\pi(h_{9/2})^2$ or $\pi(h_{9/2}\otimes i_{13/2})$ proton configurations.

Further studies of these structures in the Pb nuclei, and the neighbouring Tl and Bi isotopes are clearly required. For instance, lifetime measurements may shed light on the underlying configurations of these structures. Detailed spectroscopy, using large detector arrays such as EUROGAM or GAMMASPHERE, would enable the systematic behaviour of these cascades to be established. More information of the decay out from these bands may also yield information on the mechanisms of decay of other low intensity collective structures, such as superdeformed bands.

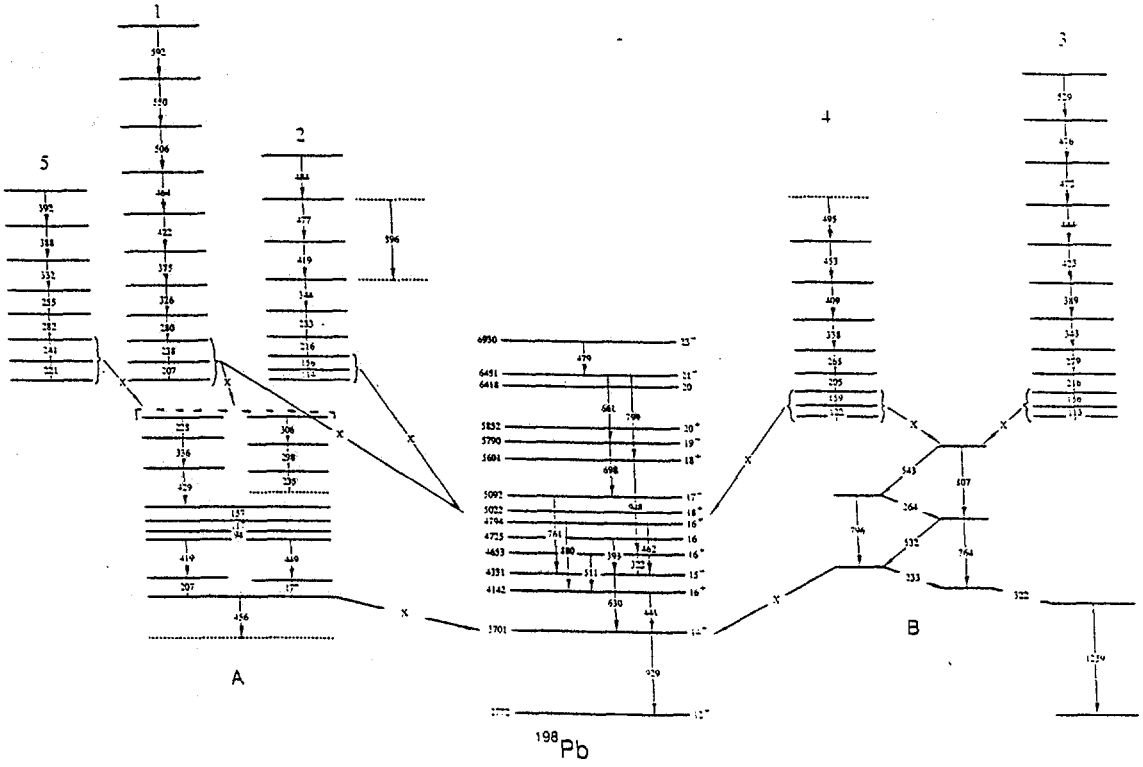

Fig 1: Level scheme for ^{198}Pb. Transition enrgies given in keV.

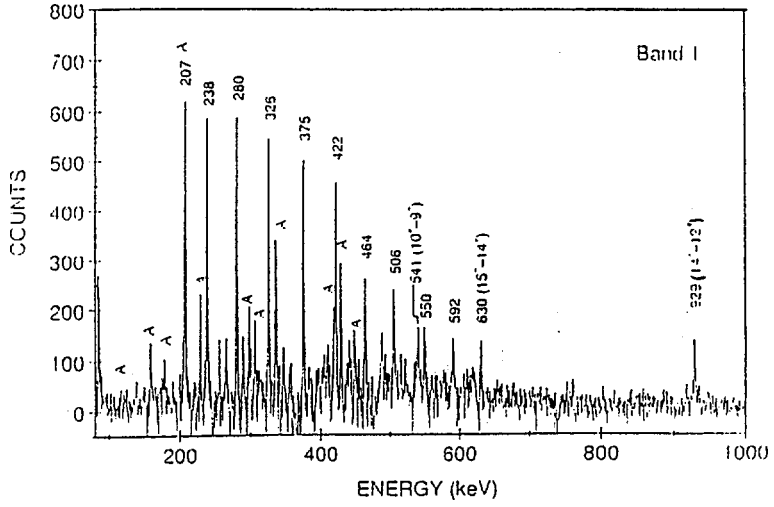

Fig 2: Summed coincidence spectrum for band 1. Transition energies are labelled in keV. Previously known γ-rays are labelled with their transition energy and spin assignments. Other γ-rays marked A are associated with the strucure A, which lies beneath the band (see Fig 1). The spectrum represents the summation of the 464, 506, and 550 keV gates.

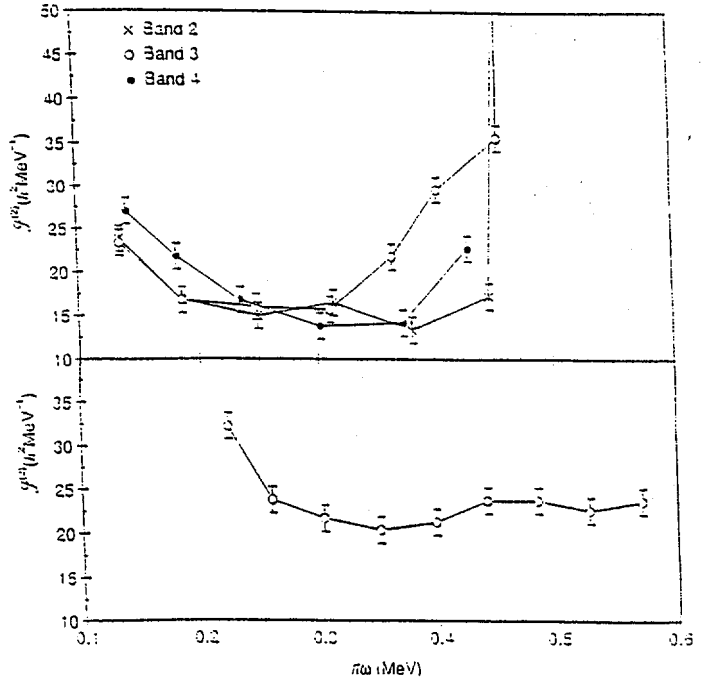

Fig 3: Dynamic moments of inertia, $\Im^{(2)}$, plotted as functions of rotational frequency for band 1 (bottom), and bands 2,3, and 4 (top).

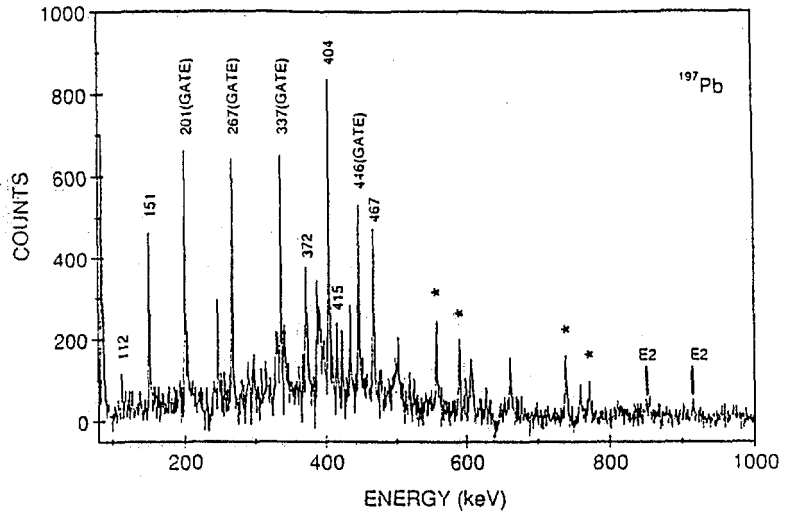

Fig 4: Summed coincidence spectrum for the strongest band in ^{197}Pb. Transition energies are labelled in keV. Known γ-rays in the Yrast sequence are labelled with an asterisk. Also marked are the two strongest E2 crossover transitions at 850 and 914 keV. The gates used to generate the spectrum are indicated in the figure.

References

(1) P.Dagnall et al., to be published
(2) A.Kuhnert et al., submitted to Phys. Rev. C
(3) R.M.Clark et al., Z. Phys. A 342 (1992) 372
(4) R.M.Clark et al., Phys. Lett. B 275 (1992) 247
(5) R.M.Clark et al., to be published
(6) T.F.Wang et al., to be published
(7) G.Baldsiefen et al., Phys. Lett. B 275 (1992) 252
(8) G.Baldsiefen et al., Z. Phys. A, in press
(9) D.M.Cullen et al., Phys. Rev. Lett 65 (1990) 1547
(10) K.Honkanen et al., Nucl. Phys. A 451 (1986) 141
(11) G.I.Harris et al., Phys. Rev. C 139 (1965) 1113
(12) T.Yamazaki, At. and Nucl. Data Tables A 3 (1967) 579
(13) K.Nakai, Phys. Lett. B 34 (1971) 269
(14) R.Bengtsson and W. Nazarewicz, Z. Phys. A 334 (1989) 269
(15) J.J.Van Ruyven et al., Nucl. Phys. A 449 (1986) 579
(16) J.Penninga et al., Nucl. Phys. A (1987) 535
(17) H.Hubel et al., Nucl. Phys. A 453 (1986) 316

THE ONSET OF COLLECTIVITY IN ^{196}Po

L.A. Bernstein[a], J.A. Cizewski[a], H.Q. Jin[a], R.G. Henry[a], L.P. Farris[a], T.L. Khoo[b], M.P. Carpenter[b], R.V.F. Janssens[b], T. Lauritsen[b], I. G. Bearden,[b,c] and D. Ye[d]

[a] Rutgers University, New Brunswick, NJ 08903 USA
[b] Argonne National Laboratory, Argonne, IL 60439 USA
[c] Purdue University,West Lafayette, IN 47907 USA
[d] Notre Dame University, Notre Dame, IN 46556 USA

Abstract

We have studied the in-beam γ-ray spectroscopy of ^{196}Po, which is the first Po isotope to exhibit collective vibrational structure. The onset of collective motion occurs in this isotope because of the large overlap between valence protons in $h_{9/2}$ and valence neutrons in $i_{13/2}$ orbitals.

1. Introduction

The polonium isotopes with two valence protons provide an excellent laboratory in which to study the transition between single particle and collective behavior in a nuclear system. Polonium isotopes with N ≈ 126 have structure characteristic of shell-model behavior with yrast energy spacings of a two-particle j^2 configuration. As the number of neutrons is decreased, the large number of valence particles makes a shell-model description of the low-lying structure difficult and the onset of collective structure is expected.

2. Experiment

We used the ^{172}Yb(^{28}Si,4n) reaction to study ^{196}Po at the ATLAS facility with beam energies of 141 and 145 MeV. The Argonne-Notre Dame BGO γ-ray facility which consists of 12 Compton suppressed Ge detectors and a 50-element inner BGO ball was used. Approximately 35 million γ–γ events with an inner ball multiplicity K≥3, as well as all higher fold Ge data, were recorded to tape. The data were sorted off-line into a series of matrices, of which the one with K≥5 was used for the majority of the analysis. Angular momentum assignments were determined through the use of DCO ratios. Earlier work[1] by Alber, et al., studied the delayed γ rays depopulating the 850 ns 11$^-$ isomer in ^{196}Po. As summarized in Fig.1, we have extended this earlier level scheme with our prompt spectroscopy measurements and have determined spins and probable parities of the levels.

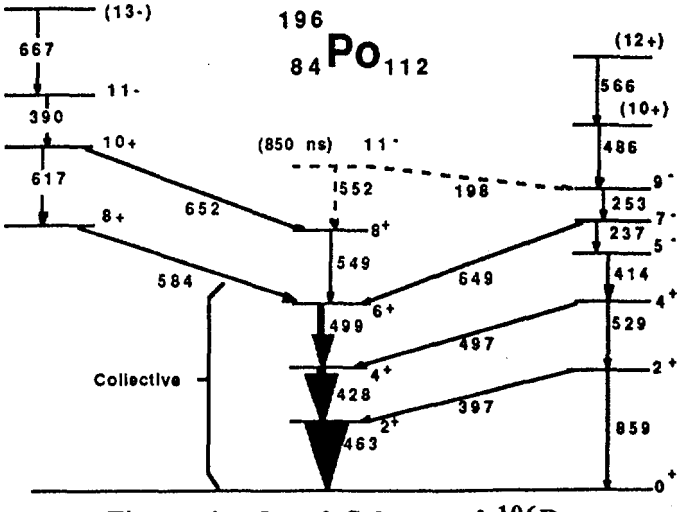

Figure 1: Level Scheme of ^{196}Po

The study of neutron deficient Po nuclei via (HI,xn) reactions is greatly hampered by competition with fission and multi-particle transfer reactions. As the number of neutrons is decreased Coulomb-enhanced fission becomes the prefered channel, especially at high angular momenta. However, through the use of the higher multiplicity cut on the BGO calorimeter, we were able to filter out most of the fission as well as some of the Coulomb excitation and transfer channels. The low-lying transitions in ^{196}Po are the strongest γ-ray lines in the spectrum, after appropriate filtering, near $E_\gamma \approx$ 400- 500 keV.

3. Energy Systematics

The structure of Po nuclei can be expected to be similar to that of Te nuclei, which also have two valence protons. Earlier work[2,3] by Lee, et al., and Henry on Te isotopes showed that as the neutron number decreased from singly magic ^{134}Te to ^{118}Te the structure became collective vibrational. The absolute B(E2; $2^+ \rightarrow 0^+$) values are exceptionally well-reproduced by the expectations of the vibrational limit of the interacting boson approximation (IBA) model. Also, relative B(E2) values are in better agreement with vibrational than rotational predictions.

In Fig. 2a we display a simple qualitative indicator[4] of the transition between shell-model and collective structure in Te isotopes. The ratio, R(6/4), of the energies of the yrast 6^+ to 4^+ states are plotted as a function of the R(4/2) ratio of the energies of the yrast 4^+ to 2^+ states. Such a plot can be divided into four regions. The portion of the plot with R(4/2) $\geq$ 2.0 and R(6/4) $\geq$ 1.5 can be labeled as collective, with the lower limits the expectations for a simple harmonic vibrator. The quadrant with R(4/2) < 2.0 and R(6/4) < 1.5 is indicative of shell-model structures. The remaining two quadrants are "forbidden" in the sense that although one of the two energy ratios is characteristic of collectivity, the other is associated with single-particle behavior.

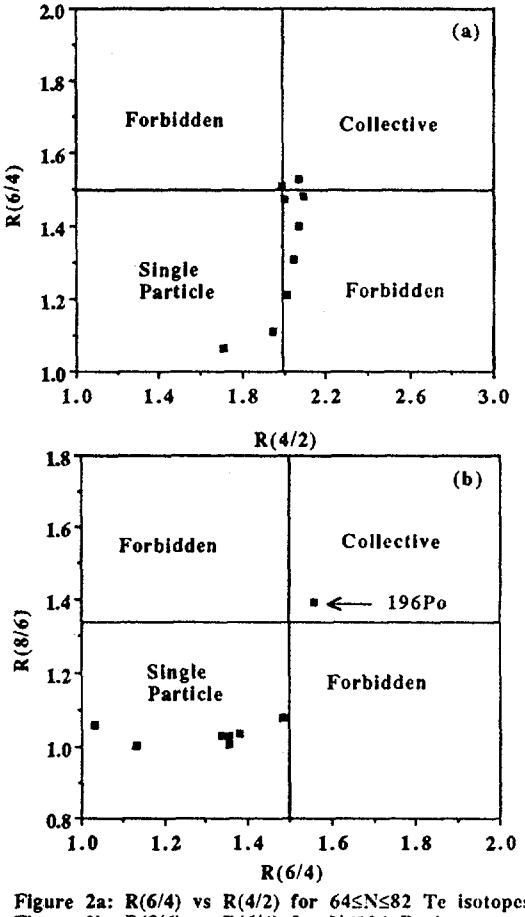

Figure 2a: R(6/4) vs R(4/2) for 64≤N≤82 Te isotopes
Figure 2b: R(8/6) vs R(6/4) for N≤126 Po isotopes
Data taken from ref. 1,3,5 and present work.

The ratios of various yrast energies can be used to determine the collective versus single-particle behavior. However, one needs to be judicious in the choice of the ratios plotted. Te nuclei have their valence protons in the $g_{7/2}$ orbital; therefore, the maximum angular momentum of two $g_{7/2}$ protons is 6. In Po the valence protons are in the $h_{9/2}$ orbital, with a maximum angular momentum of 8. To show the comparison between Te and Po more clearly we have plotted in Figure 2b the R(8/6) vs R(6/4) ratios, where again the solid lines demarcate the boundaries between collective (R(8/6) $\geq$ 1.33) and non-collective structures. Although the Te nuclei show a gradual tracking from the single-particle to the collective regimes, the behavior of the Po nuclei is radically different. The Po R(8/6) ratio stays tenaciously in the shell-model region from 0 to 12 valence neutrons (corresponding to ^{210}Po to ^{198}Po) and does not enter the collective area until it has 14 valence neutrons. However, ^{196}Po is clearly inside of the collective region of the plot.

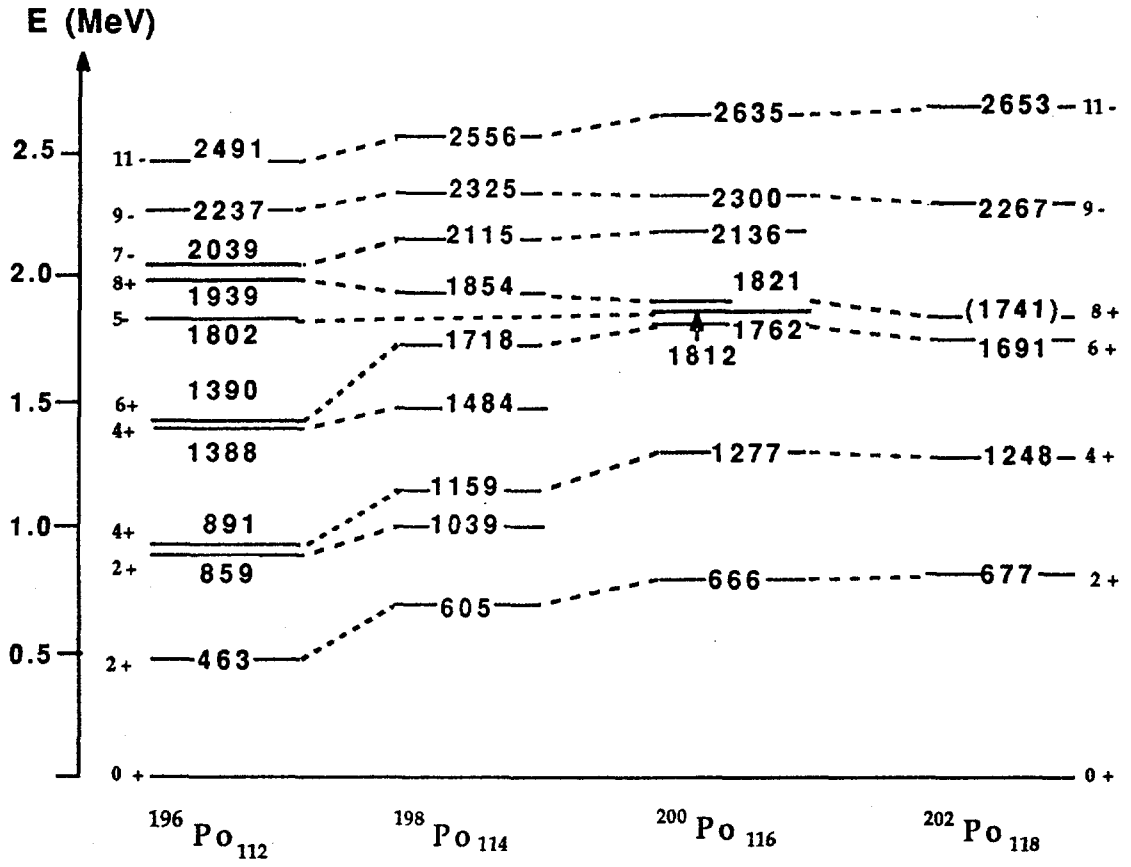

Figure 3: Even-A Polonium Systematics
Data taken from ref. 1,5 and present work

Figure 3 shows the systematics of the light Po nuclei. It is evident that as we go from ^{198}Po to ^{196}Po the energies of the yrast 2^+, 4^+ and 6^+ states decrease, whereas the energy of the yrast 8^+ state rises. It is this combination of energy spacings that signals the onset of vibrational structure in ^{196}Po. In addition, the 2_2^+ and 4_2^+ levels are now nearly degenerate with the yrast 4^+ and 6^+ states, respectively, as would be expected if these non-yrast states are members of multi-phonon multiplets.

If the low-lying structure in ^{196}Po is vibrational, then the selection rule, $\Delta N_{ph} = \pm 1$, for transitions between phonon multiplets should hold. Although no absolute B(E2) values were obtained, the ratio of B(E2) values can be calculated from the ratio of the intensities of the two transitions as seen in a gate taken on the gamma ray feeding the initial level. The comparison between experiment and the expectations of the vibrational model are given in Table 1, with the assumption that the observed transitions are of pure E2 character. The relative B(E2) ratios of the non-yrast transitions, together with the energy spacings, are a strong indication of vibrational collective structure. We propose that the last two neutron holes play a major role in the onset of collectivity in ^{196}Po.

Table 1: Ratios of B(E2) values

B(E2) ratios	Vibrator	Experiment
$B(E2;4_2 \rightarrow 2_2)/B(E2;4_2 \rightarrow 4_1)$	0.91	0.95
$B(E2;2_2 \rightarrow 2_1)/B(E2;2_2 \rightarrow 0_1)$	0	0.02

4. The p-n Interaction and Collectivity

The orderings of the single particle states for N < 126 and Z > 82 are shown in Figure 4.

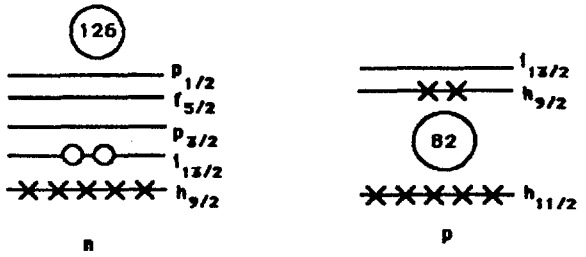

Figure 4: Shell Model levels for protons and neutrons in ^{196}Po

In a naive picture N=112 is the first Po isotope in which there are holes in the neutron $i_{13/2}$ intruder orbital, which is well known to drive the onset of deformation. In addition, Casten[6] has shown that the proton-neutron (p-n) interaction plays a major role in the onset of deformation. In particular, with the use of the parameter $P = N_pN_n / (N_p + N_n)$, which is a normalized ratio of the p-n interaction to the pairing interaction, systems with P > 4-5 are usually deformed.[7]

However, P is an incomplete representation of the p-n interaction, since it does not take into account the actual overlap of the proton and neutron orbitals. If the protons and neutrons are in states with very different quantum numbers, then it is unlikely that they will have a large interaction. If, however, there is a high degree of spatial overlap, then the p-n interaction could cause a large amount of mixing between the states and a corresponding lowering of the energy that is a signature of collectivity.

Casten has also developed a simple way to quantify the amount of overlap of single-particle wave functions with the use of a semi-classical angle. When two angular momentum vectors are added to form a resultant, the three vectors obey the law of cosines, which can be written as[6]

$$\theta_{j1,j2} = \cos^{-1}\{(J^2 - j_1^2 - j_2^2) / (2 \cdot |j_1| \cdot |j_2|)\}$$

If we replace the vectors with operators and extract the expectation value of the operators then[6]

$$\theta_{j1,j2} = \cos^{-1}\{[(J(J+1) - j_1(j_1+1)] - j_2(j_2+1)] / [2 \cdot j_1(j_1+1) \cdot j_2(j_2+1)]^{1/2}\}$$

This semi-classical angle can be viewed as the angle two single-particle states make with respect to one another in order to form a total angular momentum, J, of a given state.It gives a quantitative measure of the distribution in angles of the nucleons in a state with a particular J.

Table 2 presents the semi-classical angles of several $|(j^2,J)>$ configurations located near the Fermi surface in ^{196}Po. The angles for the neutron $(i_{13/2})^2$ and proton $(h_{9/2})^2$ configurations at moderate angular momenta are similar. This indicates that there is a larger overlap between this neutron intruder orbital and the valence proton orbital than was the case in heavier Po isotopes, in which the $i_{13/2}$ orbital is fully occupied. This large overlap means more p-n interaction, which then in turn drives the collective motion.

Table 2: Semi-classical angles (in degrees) for $|j^2,J>$ configurations

j (single particle)	J=2	J=4	J=6	J=8
$i_{13/2}$	160	144	127	108
$h_{9/2}$	152	127	99	63
$f_{7/2}$	144	111	71	-
$f_{5/2}$	131	82	-	-
$p_{3/2}$	90	-	-	-
$p_{1/2}$	-	-	-	-

5. Conclusion

The onset of collective vibrational motion has been observed in the low-lying structure of ^{196}Po. The energy spacings of the yrast 2^+, 4^+ and 6^+ states, as well as the 2_2^+ and the 4_2^+ states, are consistent with the spacings of one, two, and three phonon multiplets. The ratios of the B(E2) values for decays from the 4_2^+ and 2_2^+ states are also consistent with those for vibrational structure.

The transition at moderate angular momenta from single-particle behavior in ^{198}Po to collective behavior in ^{196}Po can be attributed mainly to the valence $i_{13/2}$ neutrons, since the $i_{13/2}$ neutrons have a large overlap with the valence $h_{9/2}$ protons. The p-n interaction causes mixing for configurations with spins less than 8, which yields collective wave functions and a lowering of excitation energies.

This work has been funded in part by the National Science Foundation and the U.S. Department of Energy, Nuclear Physics Division, under contract no. W-31-109-ENG-38.

References

1. D. Alber, et al., Z. Phys. **A339**, 225 (1991).
2. C.S. Lee, et al., Nucl. Phys. **A528**, 381 (1991); C. S. Lee, et al., Nucl. Phys. **A530**, 58 (1991); and to be published.
3. R.G.Henry, Ph.D. dissertation, Rutgers University (1992).
4. J.A. Cizewski, Phys. Lett. **B219**, 189 (1989).
5. Evaluated Nuclear Structure Data Files, Brookhaven National Laboratory Upton, NY.
6. Nuclear Structure from a Simple Perspective, R.F. Casten, Oxford University Press, New York NY, 1990.
7. R.F. Casten, D.S. Brenner, and P.E. Haustein, Phys. Rev. Lett. **58**, 658 (1987).

INTERNATIONAL CONFERENCE ON NUCLEAR STRUCTURE AT HIGH ANGULAR MOMENTUM

Ottawa

Session 6: Physics of High Spin Nuclear States

PHYSICS OF HIGH SPIN NUCLEAR STATES

R. Wyss
Joint Institute for Heavy–Ion Research, Holifield Heavy Ion Research Facility,
P.O. Box 2008, Oak Ridge, Tennessee 37831, U.S.A.
and
MSI, Frescativ. 24, 104 05 Stockholm

ABSTRACT

High spin physics is a vast topic addressing the variety of nuclear excitation modes. In the present paper, some general aspects related to recent highlights of nuclear spectroscopy are discussed. The relation between signature splitting and shape changes in the unique parity orbitals is elucidated. The relevance of the Pseudo SU(3) symmetry in the understanding of rotational band structure is addressed. Specific features of rotational bands of intruder configurations are viewed as a probe of the neutron-proton interaction.

1. INTRODUCTION

High spin spectroscopy aims to investigate the interplay of collective motion and single particle excitations as a function of angular momentum and nucleon number, N and Z. During the recent years an increasing amount of detailed high spin data has become available. In many nuclei states with same quantum numbers (angular momentum and parity) have been reported to be very close in energy (sometimes only $\approx$ 1 keV). In case of odd-N or Z nuclei, it indicates that certain single particle configurations remain orthogonal to rather high spins, implying, that it makes sense to label different rotational bands by means of additional quantum numbers. In other cases, it is related to a difference of the collective degree of freedom, e.g. two 12^+-states of prolate and oblate shape. The single particle and collective degree of freedom can of course not be separated and in general we deal with a mixture of them. Spectroscopic data from the last years reveal an extremely high degree of order, far from chaotic motion. The expected transition from order to chaos at higher excitation energy and higher spin is at present not observed. In the following, we focuse on the aspects of high spin physics which are related to the order of nuclear excitations.

Nuclei are generally classified as being either spherical, transitional or deformed. The region of deformed nuclei is then divided in nuclei with prolate and oblate shapes. These ground-states properties, although interesting and very important, give a very limited discription of the richness of nuclear excitations. The Pb isotopes have served as text book examples of spherical shell model nuclei. Recent high spin data reveals the presence of highly collective superdeformed prolate shapes,[1] see also E.A. Henry's contribution in this issue.

In addition, very recent reports give evidence for the most regular collective oblate bands observed hitherto.[2] Similarly, Sb-nuclei which show characteristic excitation energies of spherical nuclei, have collective rotational bands reaching frequencies of more than 2MeV, associated with stable prolate shapes (see V Janzen's contribution in this issue). Fast rotation is still one of the most efficient tools to access the inner structure of nuclei.

2. SHAPE CHANGES AND SIGNATURE INVERSION

Even-even nuclei in mass A=120-130 region exhibit moderatly deformed prolate shapes.[3,4] However, at higher spins the picture changes. Coexisting collective 12^+ states in Ba-nuclei have been interpreted as having prolate and oblate shapes, respectively.[5] Most recent high data spin in mass A=120 region give evidence for transition from collective rotational bands to single particle excitations.[6,7] A new region of non-collective high spin states is being explored (see also E Pauls contribution in this issue).

Direct measurement of the quadrupole moment of even-even nuclei at high spin is a rather difficult task. On the other hand, the odd nucleon is a much more sensitive probe to the shape degree of freedom. Rotational bands in odd-A nuclei exhibit a characteristic spectrum depending on whether the shape is prolate or oblate: If the Fermi level is among the low-Ω orbitals, one expects decoupled rotational bands, the favored sequence considerably lower in energy than the unfavored. If the Fermi level is among the high-Ω orbitals, rotational bands are strongly coupled, with no or little signature splitting between the favored and unfavored sequence. In the latter case, one frequently observes $\Delta I = 1$ sequences, which are merely a realization of the strong coupling scheme and not necessarely an indication for tilted cranking.

For the unique parity states the low-(high-)Ω orbitals are low (high) in the shell for prolate (oblate) nuclei, whereas they are high (low) in the shell at oblate (prolate) shape. Since the Fermi energy is rather well determined, the pattern of the rotational band is directly realated to the shape. Prolate-oblate shape transition and coexistence of collective rotational states in odd-proton nuclei has been established in the mass A=120-130 region since some time ago.[8,9]

Rotational bands in odd-A nuclei in the mass A=130 built on the $h_{11/2}$ neutron orbital region show an increasing signature splitting with N, $N \geq 71$. Since at prolate shape, the Ω-value is increasing with N, one expects the signature splitting to decrease. The present data can be understood in terms of a shape change from predominantly prolate to triaxial and oblate.[10]

Total Routhian Surface (TRS) calculations have been performed for the $h_{11/2}$ configurations. The TRS calculations minimize the equilibrium shape (β_2,$\beta_4$and γ) as a function of rotational frequency.[11,12] The signature splitting between favored and unfavored sequence can be obtained from the energy difference at equilibrium shape of each signature, respectively. Figure 1 compares

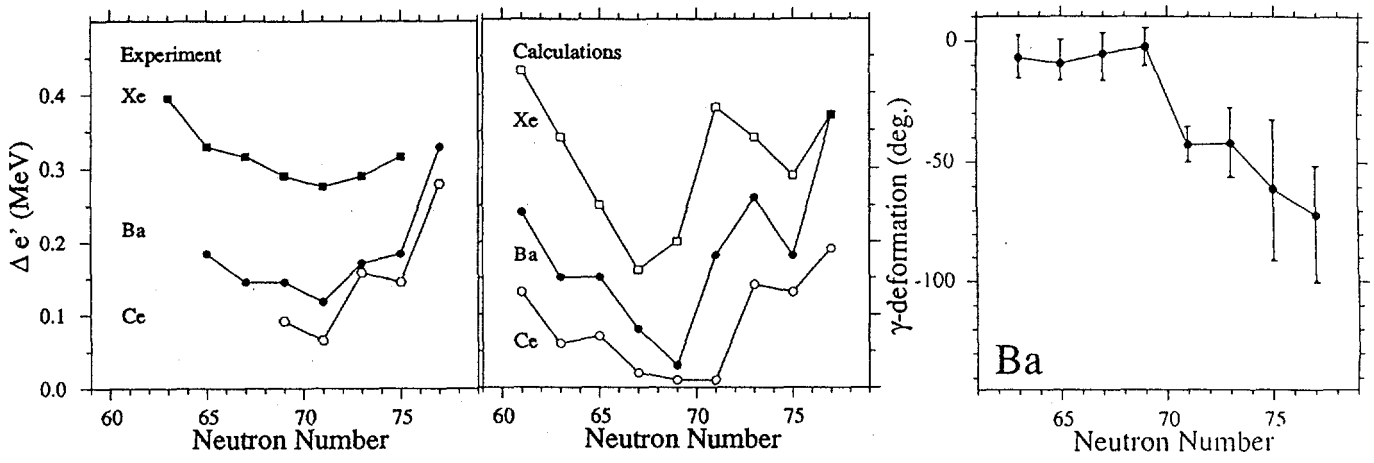

Fig. 1. *Experimental and calculated signature splitting in $h_{11/2}$ neutron bands. The calculated γ-values as a function of neutron number are indicated to the left. The error bars indicate the softness of the Routhian surface, within 100keV. (From ref. 10.)*

the calculated and experimentally observed signature splitting in. The calculated change of γ-deformation of the favored signature is also indicated for the Ba-isotopes. In all these cases, the favoured signature is lowest in energy, which is the most common case.

In odd-odd nuclei, however, signature inversion has been reported for rotational bands, especially involving the unique parity high-j orbitals. This has been taken as a 'fingerprint' of triaxiality with positive γ-values.[13] (According to the Lund convention [14], γ- value of $0°(-60°)$ corresponds to collective prolate (oblate) rotation and γ- value of $60°(-120°)$ to non-collective oblate (prolate) states.) Alternative explanations have been given by particle core coupling scheme[15,16], introducing a residual neutron-proton interaction[17,18] or by the coupling to gamma vibrational states.[19]

Experiments in the mass A=120 region show strong signature inversion in odd-odd Cs nuclei, the effect being considerably larger than previous data in the Rare Earth region.[20] The lack of firm spin assignment hade made the results from the Cs-isotopes difficult to interprete. Recently the group from Tsukuba university has performed an extensive study of ^{124}Cs, leading to more reliable spin assignments.[21] The signature splitting of ^{120}Cs is even larger than that of ^{124}Cs and is present up to spin $15\hbar$, ie even for $I > j_\pi + j_\nu$. Particle Rotor calculations including a residual proton neutron interaction have been performed for ^{120}Cs.[22] The experimental signature inversion can roughly be accounted for by either positive γ-values or by the residual neutron-proton (np) interaction. The excitation energies alone ar not enough to distinguish between the two scenar-

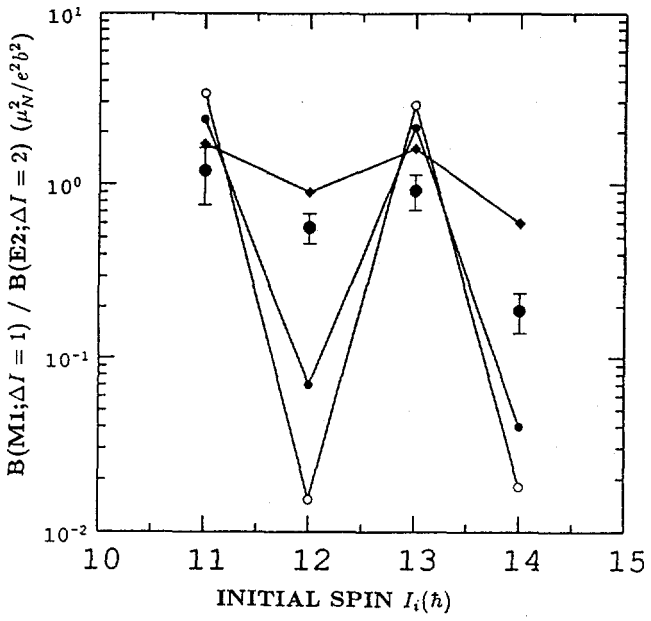

Fig. 2. *Experimental and calculated values (from Two-Particle plus Triaxial Rotor model calculations) of* $B(M1;I \rightarrow I-1)/B(E2;I \rightarrow I-2)$ *vs* I *for the* $\pi h_{11/2} \otimes \nu h_{11/2}$ *band (band 1).*
Experimental values: filled circles (with error bars)
The calculated points are connected with solid lines:
Axially symmetric shape and **no** *residual p-n interaction: filled circles.*
Triaxial shape, $\gamma = 20°$ *and* **no** *residual p-n interaction: open circles.*
Axially symmetric shape with a residual p-n interaction: diamonds.
(From ref. 22.)

ios. However, the BM1/BE2 ratios are impossible to account for by assuming triaxial shapes with positive gamma. On the other hand the ratios are easily reproduced by the inclusion of the residual np interaction (fig.2).[22]

In order to further investigate the possibility of triaxial shapes, Total Routhian Surface (TRS) calculations have been performed for the relevant high-j configurations. The calculations for the $\nu h_{11/2} \otimes \pi h_{11/2}$ configurations in CS-isotopes only yield slight positive gamma values, far from being enough to acount for the signature inversion. The same results are obtained for the $\nu i_{13/2} \otimes \pi h_{11/2}$ configurations in odd-odd nuclei in the Rare Earth region (Eu- and Ho-isotopes).

We can thus conclude, that the signature inversion observed in high-j orbitals in odd-odd nuclei is less likely to be related to triaxiality than to the dynamical coupling of protons and neutrons. One should also note that it is the central term of the neutron-proton interaction, which gives rise to the signature inversion and the resulting BM1/BE2 ratios.[18] Previous calculations based on a $Q \cdot Q$ force in a single-j shell result in a ten times weaker effect.[17]

3. ELECTROMAGNETIC PROPERTIES IN THE PSEUDO SU(3) SCHEME

The role and importance of the high-j unique parity orbitals in high spin physics has been studied extensively. However, the pattern of the normal parity states is much more complex, since a far greater number of single particle states are distributed in a more intricate way close to the Fermi surface. A simplified classification of the normal parity states has been given in terms of the Pseudo SU(3) scheme.[23-26] The spin-orbit interaction ($l \cdot s$) of the Nilsson potential of medium and heavy deformed nuclei is roughly four times as large as the orbit-orbit ($l \cdot l$) part, (corresponding to a Nilsson parameter of μ=0.5). Therefore, one can map the normal parity Nilsson states into a Pseudo SU(3) oscillator Hamiltonian with degenerate levels (doublets) of same pseudo $\tilde{\Lambda}$.($[Nn_z\Lambda] - \frac{1}{2}, [Nn_z\Lambda - 2] + \frac{1}{2}, \rightarrow [Nn_z\tilde{\Lambda}] \pm \frac{1}{2}$, $\tilde{\Lambda} = \Lambda - 1$, see also the discussion in 27) How well is this symmetry realized in medium and heavy nuclei?

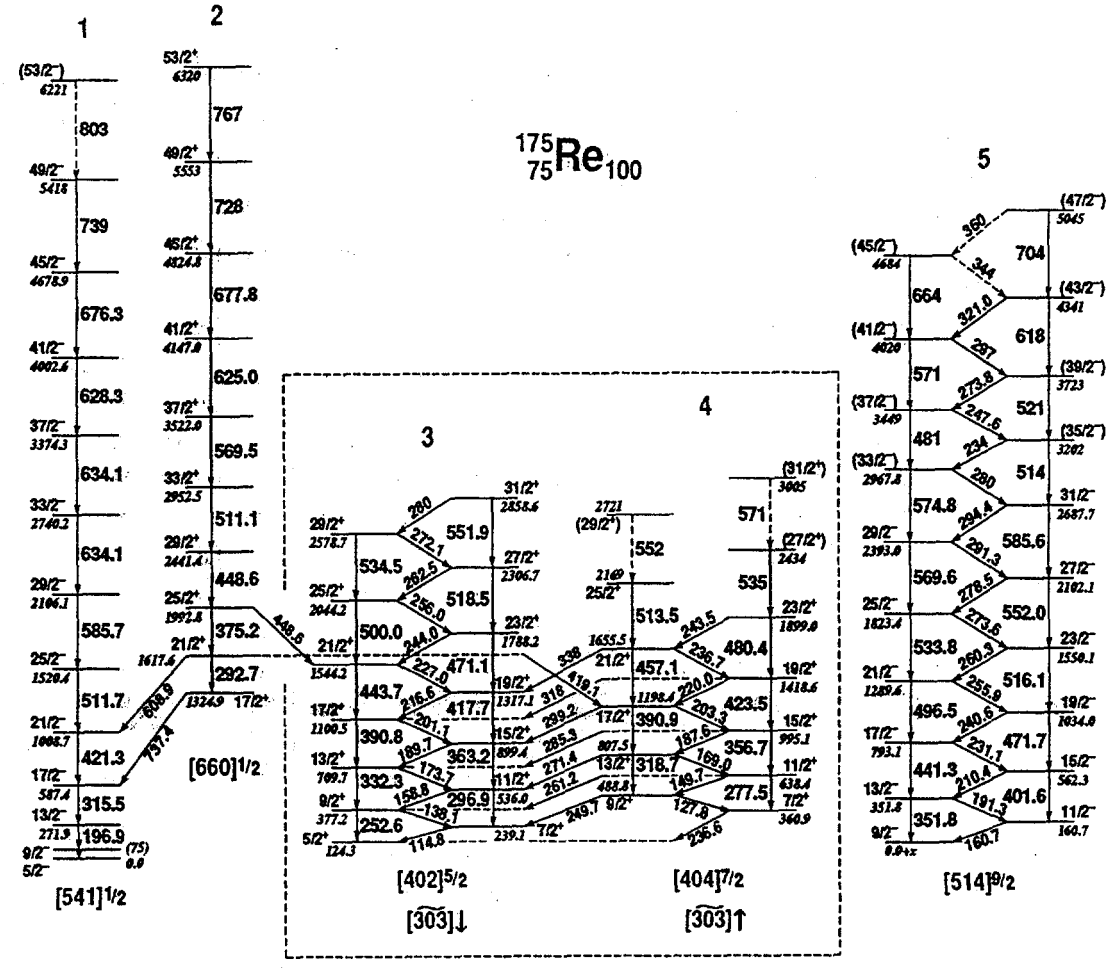

Fig. 3. *Levelschem of* ^{175}*Re, (from ref. 28)*

A most beautiful example of pseudo spin doublets has been found recently in the odd-proton nucleus ^{175}Re,[28] see fig.3. Two rotational bands built upon the [402]5/2 and [404]7/2 orbital are very close in energy and linked by strong interband M1 transitions (band 3 and 4). In the pseudo-SU(3) scheme, they correspond to the $[\widetilde{303}]\uparrow,\downarrow$ orbitals, respectively, originating from the spherical $\tilde{l}=3$ state.

The in-band BM(1) transition probability is proportional to the gyromagnetic factor $(g_\Omega - g_R)^2$ resulting in very different transition rates for the [402]5/2 and [404]7/2 orbital, since the orbital angular momentun is once coupled parallel and once antiparallel ($g_\Omega = g_l + (g_s - g_l)\langle s_z\rangle$). In this particular case, there is no contribution from $\tilde{l}=1$ and g_Ω can be calculted rather easily within the Pseudo SU(3) formalism.

$$g_\Omega = g_l - \frac{(\frac{1}{3}+2\alpha)}{\Omega}(g_s - g_l)\langle \tilde{s}_z\rangle, \qquad (1)$$

where $\alpha = 2/9$ for the $\tilde{\Lambda}=3$ orbital (for details see ref 25,28). Note also the opposite expectation value for $\langle \tilde{s}_z\rangle$ and $\langle s_z\rangle$ as well as the opposite sign in front.

Using g_s=0.7 g_{free} (=3.9) and g_l=1 for protons, one obtains $g_{7/2}$=0.67 for the $[\widetilde{303}]\uparrow$ and $g_{5/2}$=1.47 for the $[\widetilde{303}]\downarrow$ configuration. These values can be compared with the asymptotic Nilsson values of 0.59 and 1.58 and experiment, 0.75 and 1.67.[29] The results obtained within the pseudo-SU(3) model agree rather well with the data and are better than the predictions from the Nilsson model. (see further 25,28.)

Within the Nilsson model, the inter-band transitions are forbidden since $\Delta\Lambda = 2$. However, they are allowed within the pseudo SU(3) scheme since the pseudo angular momentum $\tilde{\Lambda}$ is preserved. As shwon in fig.4, the calculated transitions from band 4 $\uparrow$ to band 3 $\downarrow$ are almost an order of magnitude smaller than the experimental values. The drop (rise) of the intra-band BM1/BE2 transition rates in band $\downarrow(\uparrow)$ suggests that mixing between the pseudo spin doublets is present. In order to investigate the transition rates in the pseudo spin doublet, three different version of the calculations were carried out:

i) no Coriolis mixing between band 3 and 4 ($\eta = 0$)

ii) calculations within the symmetry limt, i.e. full Coriolis mixing ($\eta = 1$)

iii) calculations with Coriolis attenuation, to fit the experimentally observed energy spectrum as well as transition rates ($\eta = 0.4$)

In Fig. 4 the results of the three sets are demonstrated. In the presence of Coriolis mixing, one is able to account for the BM1/BE2 transition rates, as well as for the rather strong intra band transitions. The calculations within the symmetry limit, which are essentially parameter free, very nicely account for the observed trend. On the other hand, within the symmetry limit, band 4 would be lower in energy than band 3 and one is not able to reproduce the energy splitting of the levels. If one aims at to reproduce both energy levels and transition

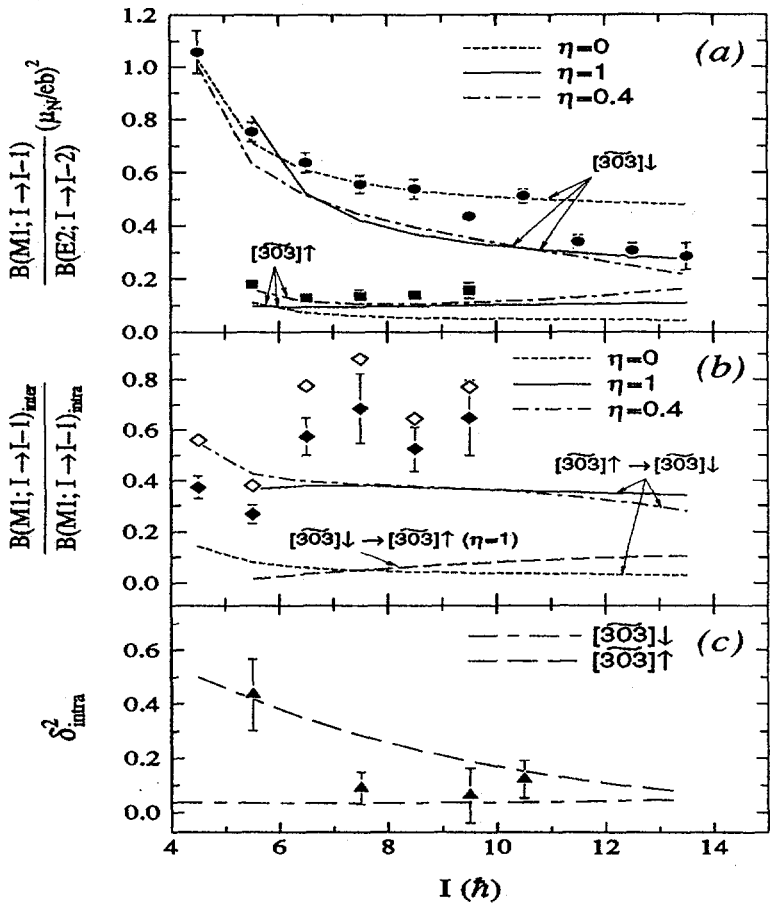

Fig. 4. *Comparisons of experimental (points) and calculated (curves) branching ratios for the pseudo-spin doublet in* ^{175}Re. **(a)** *Results for intraband* $B(M1)$ *and* $B(E2)$ *ratios. The measured values for the* $[\widetilde{303}]\downarrow$ *band are denoted by filled circles and for the* $[\widetilde{303}]\uparrow$ *band by filled squares.*
(b) *Results for* $B(M1)_{inter}/B(M1)_{intra}$ *ratios from band* $[\widetilde{303}]\uparrow$ *to band* $[\widetilde{303}]\downarrow$. *The filled points (experimental data) are not corrected for* $E2/M1$ *mixing ratios, whereas the open points are corrected for the* $B(E2; I \rightarrow I-1)_{intra}$ *using the calculated* δ_{intra} *values shown in portion (c). Three variants of calculations with three different Coriolis attenuation factors (*η*) are performed: no-mixing in the symmetry limit (*η*=0), full Coriolis mixing in the symmetry limit (*η*=1), and finally an attenuation factor which reproduces the energy spectrum (*η*=0.4). The calculated* $B(M1)_{inter}/B(M1)_{intra}$ *values for the case of* $[\widetilde{303}]\downarrow \rightarrow [\widetilde{303}]\uparrow$ *also are shown in portion (b).*
(c) *Calculated mixing ratios* δ^2_{intra} *for the* $[\widetilde{303}]$ *pseudo-spin doublet. The experimental mixing ratios for a similar configuration (*$[\widetilde{303}]\downarrow$*) in* ^{173}Ta *(from ref.* [30]*) are shown as filled triangles. (from ref. 28)*

rates, the resulting Coriolis mixing turns out to be strongly attenuated, i.e far from the symmetry limit. (The symmetry limit also implies that the difference in alignment between band 3 and 4 is $1\hbar$.) Different effects might be responsible for the attenuation: The deformation of band 3 and 4 is calculated to be

slightly different, which will weaken the Coriolis mixing. Deformation changes are expected to occure in this massregion, which have influence on the energy spectrum and mask the true mixing. The Pseudo SU(3) limit is not a very good symmetry in real nuclei - e.g. the calculated energy separation between pseudo partners is always much smaller than the experimental value[31]. To shed light on this issue, more experimental information about the pseudo partner orbitals is needed.

4. RESIDUAL NEUTRON PROTON INTERACTION IN INTRUDER BANDS

Rotational bands built upon intruder configurations belong to the most beautiful examples of regular rotational sequences. They reveal the distinct features of intruder like orbitals and the strong interplay of the single particle with the collective degree of freedom. Intruder orbitals origin from one shell above the valence shell and carry a large single particle quadrupole moment. The combination of particle like character and the large quadrupole moment results in a corresponding polarizing effect of the average deformed field.

It has been noticed, that the $i_{13/2}$ neutron crossing frequency is shifted in proton $h_{9/2}$ intruder bands (for a summary see [32] and references therein). A shift of the crossing frequency is commonly attributed to a reduction in the pairing field due to blocking effects. In odd-A neutron bands e.g., the neutron crossing is shifted to lower frequencies. In the case of intruder like orbitals, however, the odd-proton seem to affect the neutron crossing and it is shifted in the opposite direction. (Similarly, in neutron intruder configurations the proton crossing frequency is affected.) These phenomena seem to be a general feature of all intruder like configurations and have been attributed to the presence of a residual np interaction, not present in standard mean field calculations.[34,35] When the Fermilevel approaches the intruder like configuration, as is the case for the $h_{9/2}$ proton intruder orbital when Z$\approx 73-75$, the intruder becomes more of a quasi-particle, less particle like and the effect is reduced.[34] In the following we will focuse on the case where the odd particle is a proton (neutron) and the bandcrossing is occuring in the even neutron (proton) system.

In odd-A nuclei the band-crossing between the one-qp and three-qp configuration is essentially determined by the energy gap, ΔE, between the zero and two-qp aligned configuration and their interaction $\mathcal{V}$. The energies of the yraste and yrare configuration can be calculated by solving a 2×2 matrix, with $\mathcal{V}$ as the off-diagonal term, the diagonal being determined by ΔE. The odd particle remains essentially a spectator. The purpose of the np interaction is to involve it directly in the alignment process.

The crossing frequency depends on the diagonal term, ΔE, which in standard Cranked Shell Model (CSM) calculations, is determined by the deformation and the pairing gap. Since the intruder polarizes the nuclear shape to a larger

deformation, there is a trivial dependence of the crossing frequency and interaction $\mathcal{V}$ on deformation. In most cases, the crossing frequency and interaction strength increase with deformation. However, the deformation effect alone is not enough to account for the observed shifts of crossing and interaction.

A full analysis of this effect has to take into account the self consistent change of the mean field in the presence of the nucleonic interactions. This is very difficult to carry out. A qualitative understanding can be gained by investigating a residual np interaction of $Q \cdot Q$ type on top of the calculted mean field, in the sense of perturbation theory.

Since the $Q \cdot Q$ interaction is one of the main ingredients in the deformed mean field one has to subtract the expectation value of the average single particle quadrupole moment (core) from the interaction (we do not want to calculate the interaction twice):

$$\overset{\circ}{Q}{}^{2\mu}_{ik} = Q^{2\mu}_{ik} - \langle\tilde{Q}\rangle, \qquad Q_{ik} = \sum_{\mu} <i|r^2 Y_{2\mu}|k>, \quad \langle\tilde{Q}\rangle = \frac{\sum_{i=1,A} <i|r^2 Y_{2\mu}|i>}{A} \tag{2}$$

The average single particle quadrupole moment for neutrons and protons is given by $\langle\tilde{Q}\rangle$. The residual $Q \cdot Q$ interaction, is a force which is left when the contribution from the core ($\langle\tilde{Q}\rangle$) has been removed. One realizes e.g., that at spin 0 $\hbar$ the diagonal term of the residual $Q \cdot Q$ interaction vanishes, since $\sum(\overset{\circ}{Q}{}^{2\mu}_{ii} - <\tilde{Q}>) = 0$. This means that within this simple analysis, there is no additional diagonal term at spin $I = 0\hbar$.

However, the density of the rotating nucleus changes with spin. The largest change occurs at the bandcrossing. The reason for the change relates to the fact that the configuration is changing from zero-qp to two-qp, leading to changes in the Fermi energy, the pairing gap and related scattering from positive parity orbitals into negative parity and vice versa. The residual change of the quadrupole moment can be investigated by calculating the quadrupole tensor at fix deformation as a function of frequency. Note that this change is present at all deformations.

Since we are mainly interested in axial symmetric shapes associated with intruder like orbitals, only the residual Q_{20} term is calculted. In fig. 5, the calculated residual Q_{20} moment for Z=60 is shown, where the Fermi level λ and the pairing gap Δ are determined selfconsistently at each frequency according to the rotating BCS scheme. Proton number 60 was chosen since this corresponds to a case, where the BCS equation does not brake down after the bandcrossing as it does usually. The deformation corresponds to values of the highly deformed $i_{13/2}$ neutron intruder bands, observed in several Z=60 Nd-isotopes, where one expects the $h_{11/2}$ protons to align. The pronounced drop in the quadrupole moment is associated with the $h_{11/2}$ proton crossing (see fig.5). It implies that the quadrupole moment of the nucleus becomes smaller after the bandcrossing, although the deformation values are fixed. In other words, the deviations between single particle potential and the nuclear density increase with spin, especially

after the first band-crossing. In fully self consistent HFB calculations, this effect is taken into account.

When the aligning particles are within the unique parity sub-shell, one always obtains a drop in the microscopically calculated quadrupole moment after the bandcrossing. Since the quadrupole moment of the intruder orbital is always larger than that of the core nucleus, $Q_{20}^{int} > \tilde{Q}_{20}$ the residual np-interaction $Q_{20}^{int} \cdot Q_{20}$ becomes negative after the band-crossing, shifting the two-qp configuration to higher energies. In this particular case, using the selfconsistent coupling strength[29] one obtains a loss of the np interaction by $\approx$ 200keV, which will shift the S-band by that amount. If the aligning particles are below the unique parity shell, i.e. they will become occupied because of the bandcrossing, then the quadrupole moment will increase resulting in a positive residual $Q_{20}^{int} \cdot Q_{20}$ interaction. Then the band-crossing frequency is expected to become lower. This prediction can be tested in the Sb- and Sn region, where intruder orbitals associated with $h_{11/2}$proton have been observed (see V Janzens contribution in this issue).

If the residual np interaction shifts the crossing frequency to higher value in intruder configurations, what will be the effect for configurations close to the Fermi surface? Such orbitals are mainly of quasi-particle character and deviate little from the average core quadrupole moment, i.e. $Q_{20}^{odd} - \tilde{Q}_{20}$ is rather small. This holds expecially for the normal parity states close to the Fermi surface. (Deep hole states will give rise to a large residual quadrupole moment.) The high-j unique parity orbitals are also of dominant quasi-particle character at low frequency. However, the Coriolis interaction mixes in low-Ω states, giving rise to a with frequency increasing residual quadrupole moment (although smaller than that of the intruder). In the $h_{11/2}$ odd-proton bands in rare earth nuclei as Ho and Tm e.g. , the low-Ω component is of hole character, yielding a *negative* residual quadrupole moment. In that case the residual $Q \cdot Q$ interaction becomes *positive*, since the residual quadrupole moment of the aligned 2qp configuration also is negative. The $i_{13/2}$ neutron crossing frequency thus becomes *lower* in these high-j unique parity orbitals, ie the effect is opposite to intruder like orbitals.

In addition to the shift in crossing freuency, one also observes an additional band-interaction between the one-qp intruder configuration and the three qp configuration built on the intruder plus the aligned particles [34,35]. In the CSM there is no additional coupling between neutrons and protons, besides trivial dependence on deformation. The np interaction gives rise to additional off diagonal terms, mixing one and three-qp configurations. The additional interaction $\mathcal{V}$ can smooth out the bandcrossing. Instead of an expected backbend only an upbend is observed, instead of an upbend one observes a smooth rise in the moment of inertia, etc.

The off-diagonal matrix element $\mathcal{V}$ of a $\mathring{Q} \cdot \mathring{Q}$ interaction calculated from the solution of the CSM, is too small as compared to experiment. This might relate to the simplicity of the force. The short range components of the np

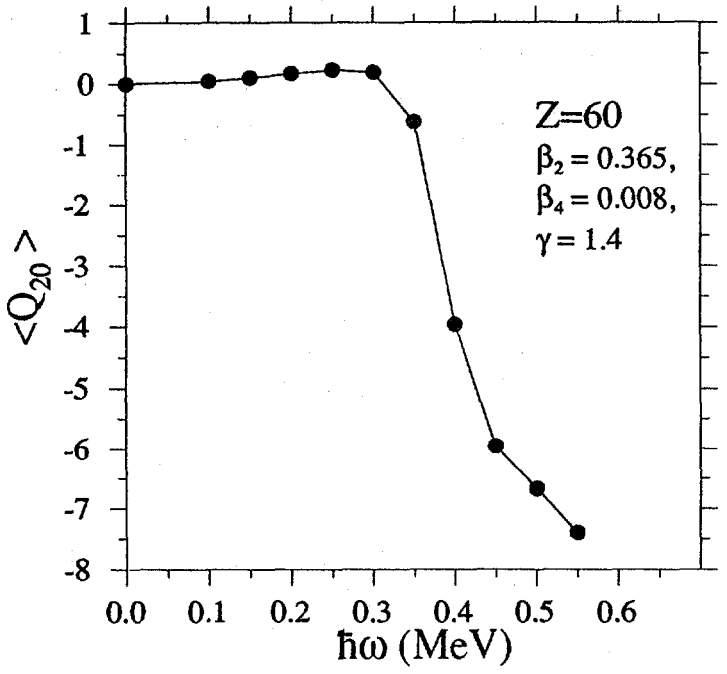

Fig. 5. *Change of the microscopically calculated residual Quadrupole moment* $\sum(Q_{20} - \langle\tilde{Q}_{20}\rangle)$ *for protons at fix deformation,* β_2*=0.365,* β_4*= 0.01 and* γ*=1.0°. The sudden drop is associated with the alignment of* $h_{11/2}$ *protons. Both the Fermi energy* λ *and the pairing gap* Δ *are adjusted to its selfconsistent value at each frequency* $\hbar\omega$*. The residual* Q_{20} *moment is given in dimensionless units. i.e.* $\langle 2z^2 - x^2 - y^2\rangle$ *is divided by the harmonic oscillator length. Contributions from 14 harmonic oscillator shells are taken into account in this calculation*

force might be important as well as influence on np-pairing. On the other hand, the additional interaction $\mathcal{V}$ is larger and has opposite sign in intruder configurations than e.g. high-j unique parity configurations. We can thus conclude that one gains valuable insight from the $\mathring{Q} \cdot \mathring{Q}$ interaction, however more refined approaches are necessary in order to fully understand the high-spin behavior of intruder configurations.

Rotational bands built upon intruder configurations have in general been associated with enhanced collectivity at prolate shape. The recently discovered oblate bands in Pb-region, can in a similar manner be classified as *oblate* intruder configurations, where very distinct oblate deformation driving orbitals have become occupied as e.g. the $i_{13/2}$ $\Omega = 13/2$ proton orbital. Again very regular rotational sequences are observed. Similar effects on crossing frequencies and band-interactions are expected. One can note, that the $i_{13/2}$ neutron crossing in the oblate $h_{9/2}$ proton band in ^{189}Tl, is considerably delayed as compared to the cranked shell model calculations [36].

4. CONCLUSIONS

The increased sensitivity and efficiency of todays detector systems has enhanced the richness of nuclear spectroscopy considerably. Weak transition between different rotational bands conrresponding to different single particle configurations challenge theoretical models and set new constraints. Shape coexistence is observed more frequently, pushing for unified models of nuclear structure theory.

There is a definite beauty present in many level-schemes, related to the pattern of rotational motion we can recognize. A nuclear level-scheme might remind us of a tree, which has been growing higher for each year. We see more and more of the details and the different branches but are still far from a complete picture. The progres in high spin nuclear physics is generally not related to one single discovery, but to the systematic exploration of many nuclei. Our hope is that more detailed high spin spectroscopy will lead to a better understanding of the nuclear many body problem as a whole. We are a bit on that way.

Acknowledgements The Joint Institute for Heavy Ion Research has as member institutions the University of Tennessee, Vanderbilt University, and the Oak Ridge National Laboratory; it is supported by the members and by the Department of Energy through Contract Number DE–FG05–87ER40361 with the University of Tennessee. This work is also party supported by the swedish research council for natural science (NFR).

REFERENCES

1. K. Theine et al., Z. Phys. **A336** (1990) 113, and
   M.J. Brinkman et al., Z. Phys. **A336**(1990)115

2. R.M. Clark et al., Phys. Lett. **275B** (1992) 247 and
   G. Baldsiefen et al., Phys. Lett. **275B** (1992) 252

3. R. Bengtsson, P. Möller, J.R. Nix and J.Y. Zhang Phys. Scr. Vol. 29 (1984)402

4. R. Wyss, A. Granderath, W. Lieberz, R. Bengtsson. P. von Brentano, A. Dewald, A. Gelberg, A. Gizon, J. Gizon, S. Harrisopulos. A. Johnson, W. Nazarewicz, J. Nyberg and K. Schiffer, Nucl Phys **A505**(1989)337

5. R. Wyss, J. Nyberg, A. Johnson, R. Bengtsson and W. Nazarewicz, Z. Phys. **A329** (1988) 255

6. Y. Liang, D. B. Fossan, J.R. Hughes, D.R. La Fosse, R. Ma, E. S. Paul, P. Vaska, M.P. Waring, N. Xu, R. Wyss', Phys Rev C44 (1991)R44

7. J.Simpson, H.Timmers, M.A.Bentley, S.M.Mullins, F.Hanna, J.F.Sharpey-Schafer, R.Wyss and T.Bengtsson, Phys Lett **B**262 (1991)388

8. E.S. Paul, C.W. Beausang, D.B. Fossan, R. Ma, W.F. Piel, Jr., N. Xu, L. Hildingsson, and G.A. Leander, Phys. Rev. Lett. **58** (1987) 984

9. Y. Liang, R. Ma, E.S. Paul, D.B. Fossan, N. Xu, J.-y. Zhang and F. Dönau, Phys. Rev. Lett.,**64**(1990)29

10. A. Granderath, P. Mantica, R. Bengtsson, R. Wyss, P. v Brentano A. Gelberg and F. Seiffert subm to Nucl Phys **A**

11. W. Nazarewicz, R. Wyss and A. Johnsson, Nucl. Phys. **A503** (1989) 285

12. R. Wyss, J. Nyberg, A. Johnson, R. Bengtsson and W. Nazarewicz, Phys.Lett. **215B**, 211 (1988)

13. R. Bengtsson, H. Frisk, F.R. May and J.A. Pinston, Nucl. Phys. **A415** (1984) 189

14. Andersson, G., Larsson, S.E., Leander, G., Möller, P., Nilsson, S.G., Ragnarsson, I.,Åberg, S., Bengtsson, R., Dudek, J., Nerlo-Pomorska, B., Pomorski, K., Szymański, Z.: Nucl. Phys. **A268**, 205 (1976)

15. A.J. Kreiner and M.A.J. Mariscotti, Phys. Rev. Lett. **43** (1979) 1150

16. I. Hamamoto, Phys. Lett. **235B** (1990) 221

17. I. Hamamoto, Phys. Lett. **179B** (1986) 327

18. P.B. Semmes and I. Ragnarsson, *Conference on Future Directions in Nuclear Physics with* 4π *Detection Systems of the New Generation, Strasbourg, March 1991*

19. M. Matsuzaki, Y.R. Shimizu and K. Matsuyanagi, Prog. Rep. Theo. Phys. 79 (1988)836

20. T. Komatsubara et al., Z. Physik **A335** (1990) 1113

21. T. Hosoda et al., *Proceedings of the INS Workshop on Nuclear Structure at High Spin and High Excitation,* Genshikaku Kenkyu, Vol. 35, No. 4, February 1991, p 59.

22. B. Cederwall, L. Hildingsson, F. Lidén, A. Johnson, R. Wyss, J. Nyberg, S. Miterai, J. Mukai, P. Ahonen, I. Ragnarsson and P Semmes Nucl. Phys. **A542**(1992)454

23. K.T. Hecht and A. Adler, Nucl. Phys. **A137** (1969) 129.

24. A. Arima, M. Harvey and K. Shimizu, Phys. Lett. **30B**, 517 (1969).

25. R.D. Ratna-Raju, J.P. Draayer and K.T. Hecht, Nucl. Phys. **A202**, 433 (1973).

26. A. Bohr, I. Hamamoto and B.R. Mottelson, Phys. Scr. **26**, 267 (1982).

27. C. Bahri, J.P. Drayer and S.A. Moszkowski Phys. Rev. Lett. **68**(1992)2133

28. H.-Q Jin, L.L. Riedinger, C.-H. Yu, W. Nazarewicz, R. Wyss, J.-Y. Zhang, C. Baktash, J.D. Garrett, N.R. Johnson, I.Y. Lee and F.K. Gowan, Phys. Lett. **277B**(1992)387

29. A. Bohr and B.R. Mottelson, Nuclear Structure, vol. 2 (W.A. Benjamin, New York, 1975).

30. J.C. Bacelar et al., Nucl. Phys. **A442**, 547 (1985).

31. W. Nazarewicz, M.A. Riley and J.D. Garrett, Nucl. Phys. **A512**, 61 (1990).

32. H.J. Jensen et al., Zeit. Phys. A **340**, (1992)351

33. R. Wyss, J. Nyberg, A. Johnson, R. Bengtsson and W. Nazarewicz, Phys.Lett. **215B**, 211 (1988)

34. R. Wyss and A. Johnson, Proc. of the Int. Conf. on High Spin Physics, ed. J.X. Saladin, R.A. Sorensen and C.M. Vincent, (World Scientific, Singapore), 1991, p.123

35. R. Wyss, Int. Symp. on Reflections and Directions in Low Energy Heavy-Ion Physics, Oct. 1991 to be published in World Scientific, Singapore

36. W. Reviol et.al., Nucl. Phys. **A**, in press

HIGH-K STRUCTURES IN ^{180}W and ^{181}W

K.C.Yeung,[1] P.M.Walker,[1] B.D.D.Singleton,[1] W.Urban,[2] J.C.Lisle,[2] J.Copnell,[2] J.N.Mo,[2] M.J.Joyce,[3] N.L.Gjørup[4] and G.Sletten[4]

[1]Department of Physics, University of Surrey, Guildford, UK
[2]Schuster Laboratory, University of Manchester, Manchester, UK
[3]Oliver Lodge Laboratory, University of Liverpool, Liverpool, UK
[4]Niels Bohr Institute, Risø, DK-4000 Roskilde, Denmark

Abstract: *In each of the prolate-deformed isotopes ^{180}W and ^{181}W, a very high-K non-collective state has been found which decays directly into the corresponding collective ground-state rotational band. There is complete breakdown of the K-selection rule, in contrast to the partial breakdown observed recently in ^{174}Hf and ^{182}Os. Nevertheless, the non-collective states themselves retain characteristics associated with a prolate axially symmetric shape, implying that K is still a useful quantum number.*

High-angular-momentum intrinsic states in nuclei are frequently long lived as a consequence of angular-momentum selection rules. In prolate-deformed nuclei with axial symmetry, the projection, K, of the angular momentum on the symmetry axis is a constant of the motion, though rotational perturbations, e.g. the Coriolis interaction, lead to the mixing of K-states. The selection rule for the multipolarity, λ, of electromagnetic transitions, $\lambda \geq \Delta K$, is violated, but such "forbidden" transitions are strongly retarded, in proportion[1,2] to the degree of K-forbiddenness, $\nu = \Delta K - \lambda$. The observation that the favoured decay path minimises the degree of forbiddenness is called the "K-selection rule".

The best examples of high-K isomers are found in the A=180 region of nuclei. A celebrated case is the K=16 isomer in ^{178}Hf, with a half life of 31 years. Macroscopic quantities of this exotic isomer have recently been prepared[3] as a target for nuclear structure experiments. Although, in principle, higher-spin isomers are expected to exist in ^{178}Hf, there is no stable beam-target combination with which significantly more angular momentum can be generated in ^{178}Hf, even though it has a stable ground state. Coulomb excitation does not in general lead to population of intrinsic states. Other isomers in the A=180 region have been studied at high angular momentum in recent years,[4-10] but the available data show that the most energetically favoured very-high-spin intrinsic states are simply not accessible with stable beams and targets. Perhaps the most favourable possibility with present technology, and the closest to ^{178}Hf, is the reaction of ^{48}Ca with ^{136}Xe, with which high-spin states, potentially up to about 60$\hbar$, in ^{180}W and ^{181}W can be populated. Use of the inverse reaction, combined with the recoil-shadow technique, previously enabled[10] the identification of new isomers, but without the associated level structures.

We have employed a cryogenically frozen ^{136}Xe target[11] in the centre of the TESSA3 array[12] of γ-ray detectors, together with a ^{48}Ca beam, to study these tungsten isotopes. The bunched and chopped beam of ^{48}Ca was

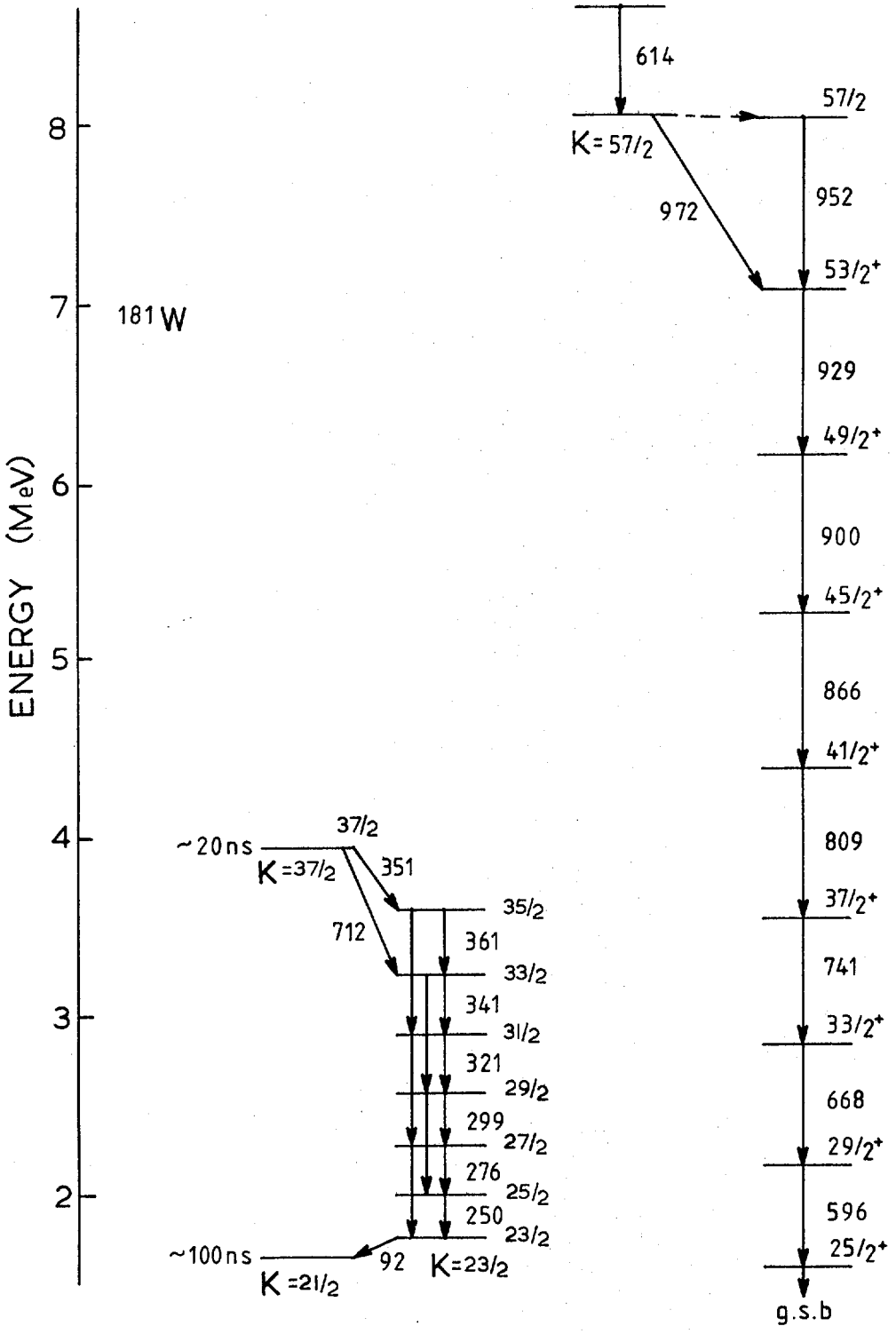

Fig.1 Partial level scheme for ^{181}W, illustrating newly found structures.

provided by the 20MV tandem accelerator at the Daresbury Laboratory. About 65 million γ-γ-BGO coincidences were obtained. The experimental signature of the very-high-spin isomeric decay in ^{161}W is remarkable: gating on γ-ray transitions in the rotational band based on the 9/2[624] Nilsson configuration (previously known[13] tentatively up to the 668keV, 33/2$\rightarrow$29/2 transition) a series of sharp γ-ray peaks is observed, up to almost 1MeV in energy. Severe Doppler broadening would normally be expected, as the recoiling ^{161}W nuclei decay during the time that they slow down and stop in the lead target backing. The sharp peaks show that the nuclei have already stopped before they decay, and hence that a long lifetime is involved ($>$2ps) which is considerably greater than the ~50fs collective rotational-decay lifetimes. In contrast, the Doppler-broadening effect is clearly evident in the ^{160}W spectra gated on ground-state-band transitions.

In ^{161}W, isomeric population of the rotational band is the only reasonable explanation for the sharp γ-ray peaks. Part of the associated level structure is shown in fig.1. Gating on the 614keV transition itself, it is apparent that over 50% of the isomer decay proceeds through the 9/2[624] ground-state rotational band. No other decay path from the K=(57/2) isomer has been identified. An upper limit of 3ns for the half life of the K=(57/2) intrinsic state is obtained from the lack of any significant shift in the time centroid between the beam bursts and the associated γ-γ-coincidence events.

The ^{160}W ground-state-band gated spectrum, which shows significant Doppler line-broadening for transition energies above 600keV, at first sight appears to be as expected for a rotor, with collective sub-picosecond transition rates. However, comparison with centroid-shift and line-shape calculations shows that there must be a significant long-lived ($>$2ps) component at I=24. About 70% of the total population of states in ^{160}W comes through a known[14] K=14 2μs isomer at 3.3MeV. A complex decay pattern from a $<$1ns isomer at 6.3MeV, with I=K=(25), has now been identified, a simplified version of which is illustrated in fig.2. A rotational sequence of states is found above the isomer, the lowest-energy and strongest transition being 430keV. Remarkably, the 430keV transition is seen in coincidence with members of the ground-state band up to I=24. Although the implied 93keV linking transition is not itself observed, this is consistent with a high electron conversion coefficient and low γ-ray detection efficiency. About 90% of the K=(25) isomer decay proceeds through the other high-K structures.

The K=(25) isomer decay in ^{160}W can be compared directly with that in the N=106 isotone ^{162}Os, where there is an I=25$^{(+)}$ isomer[4] which has a surprisingly strong (2%) branch directly to the I=24 member of the ground-state band. If both isomers have I$^{\pi}$=25^{+}, then the implied M1 Weisskopf hindrance factor for ^{160}W is even smaller (by a factor $>10^{5}$) than for ^{162}Os. The situation for ^{161}W is similar to ^{160}W. The hindrance per degree of K-forbiddenness, $f_{\nu}=(F_{W})^{1/\nu}$, is (assuming ν=22 and 24 for the 972keV (E2) and 93keV (M1) transitions in ^{161}W and ^{160}W, respectively) $1.0<f_{\nu}<1.4$: the transitions are essentially unhindered, and there is complete breakdown of the K-selection rule.

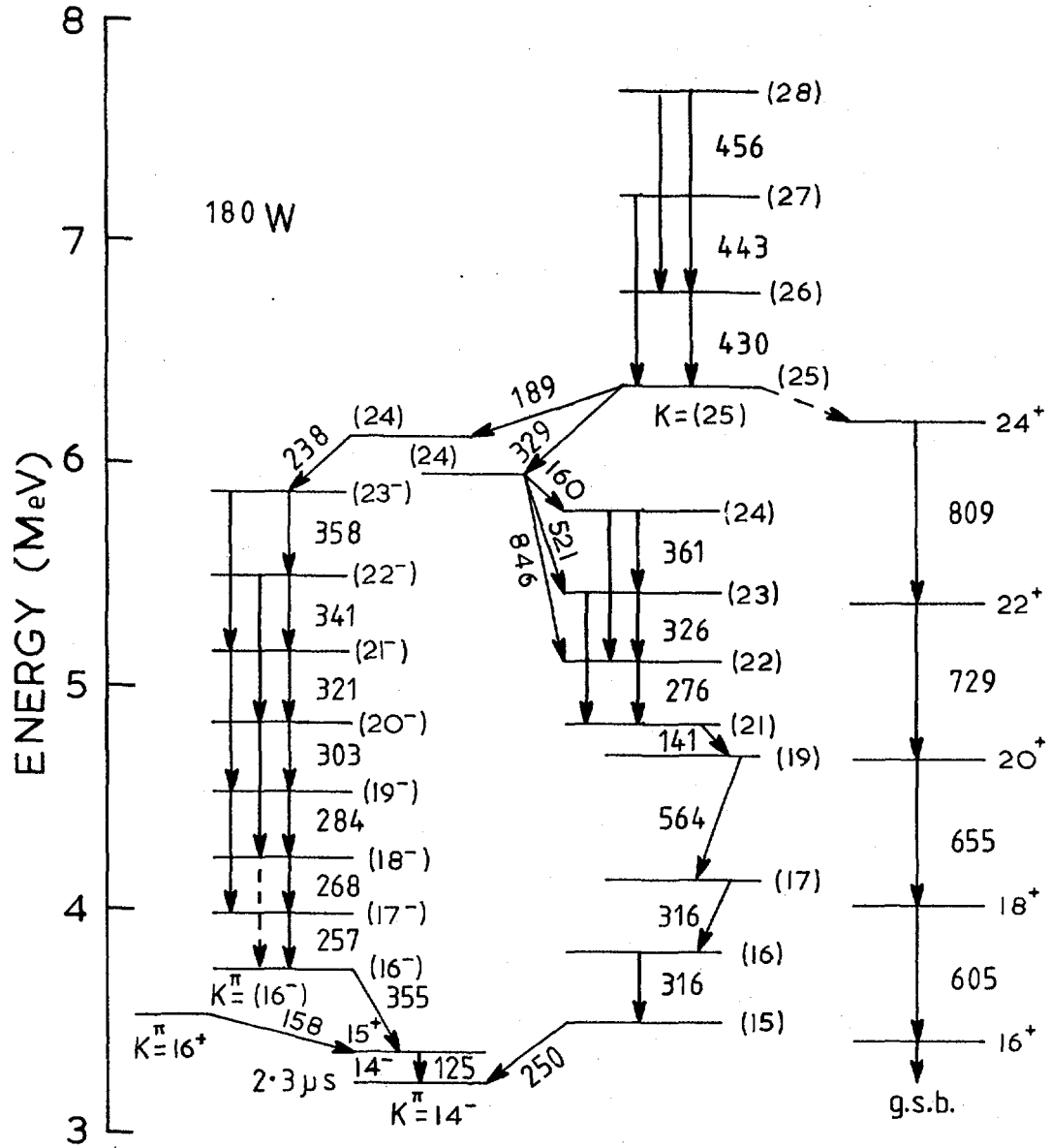

Fig.2 Partial level scheme for ^{180}W, illustrating newly found structures. The ground-state band has recently been extended[17] to I=26, (28).

The question remains as to whether the drastic K mixing arises in the intrinsic non-rotating isomeric states, in the low-K rotational states, or in both. An important indicator of high-K intrinsic structure is the sequence of rotational levels above a band head. Above the K=(25) isomer in ^{180}W, there are three clearly identified levels with rotational energy spacings, decaying by both $\Delta I=1$ (M1/E2) and $\Delta I=2$ (E2) transitions. There is no signature splitting. Furthermore, the sharpness of the observed $\Delta I=2$ γ-ray transitions above the K=(25) isomer is consistent with the expected quadrupole moment, $Q_0 \sim 6.5$b, providing K>20. We therefore suggest that the intrinsic states themselves have high and well-defined K-values; it is the high-spin states to which they decay that involve drastic K-mixing. This conclusion is consistent with the detailed observations[7] of many branches from a K=14 isomer in ^{174}Hf.

The mechanism, by which high-K components enter into the apparently low-K rotational bands, has been clarified by recent experiments[8] on ^{179}W. In this nucleus, it was found that at the first band crossing, the aligned band (usually called the s-band) has high K. The Fermi-aligned coupling scheme is involved for the two $i_{13/2}$ neutrons, and Frauendorf has incorporated[15] this feature into the cranking model by allowing the cranking axis to "tilt" away from the principal axes of the spheroidal shape. The aligned band is then called a tilted band, or "t-band". Thus, high-K components are present with large amplitude above the first band crossing, which is important for understanding the high-K isomer decays in ^{174}Hf, ^{182}Os, ^{179}W, ^{180}W and ^{181}W, all of which decay into low-K states at or above the t-band crossing. This provides at least a partial explanation for the extremely low hindrance factors for the isomeric transitions. The role of the hexadecapole (ε_4) deformation may also be important in understanding the lower hindrance factors in the heavier tungsten isotopes. The ε_4 deformation is known to be particularly large in these isotopes,[16] and increasing with neutron number, causing the low-Ω $i_{13/2}$ orbitals to be brought closer to the Fermi surface and increasing the effects of Coriolis K-mixing.

References:

1 K.E.G.Lobner, Phys Lett 26B, 369 (1968)
2 P.M.Walker, J Phys G16, L233 (1990)
3 Y.T.Oganessian et al, J Phys G18 393 (1992)
4 P.Chowdhury et al, Nucl Phys A485, 136 (1988)
5 N.L.Gjørup et al, Z Phys A337, 353 (1990)
6 G.Sletten et al, Nucl Phys A520, 325c (1990)
7 P.M.Walker et al, Phys Rev Lett 65, 416 (1990)
8 P.M.Walker et al, Phys Rev Lett 67, 433 (1991)
9 N.L.Gjørup et al, contributions to this conference
10 J.Pedersen et al, Z Phys A321, 567 (1985)
11 W.Urban et al, KVI Annual Report, 144 (1989)
12 J.F.Sharpey-Schafer and J.Simpson, Prog Part Nucl Phys 21, 293 (1988)
13 T.Lindblad et al, Nucl Phys A210, 253 (1973)
14 S.R.Faber, PhD Thesis, MSU (1979) unpublished
15 S.Frauendorf, contribution to this conference, and to be published
16 F.M.Bernthal et al, Phys Rev Lett 33, 915 (1974)
17 B.Crowell et al, BAPS 37, 1029 (1992), and private communication

Low-Spin Identical Bands in Odd-A Nuclei

C. Baktash, J.D. Garrett, D. F. Winchell *, and A. Smith **

Physics Division, Oak Ridge National Laboratory, Oak Ridge, TN 37831-6371

ABSTRACT

A comprehensive study of odd-A rotational bands in normally-deformed rare-earth nuclei indicates that a large number of seniority-one configurations (30% for odd-Z nuclei) at low spin have moments of inertia nearly identical to that of the seniority-zero configuration of the neighboring even-even nucleus with one less nucleon. It is difficult to reconcile these results with conventional models, based on the traditional picture of nuclear pair correlation in vogue for more than three decades, which predict variations of about 15% in the moments of inertia of configurations differing by one unit in seniority.

More than thirty years ago Bohr, Mottelson and Pines[1] suggested that short-range pairing interactions may be responsible for the observed reduction of the moment of inertia of deformed nuclei compared to that of a rigid rotor. Shortly afterwards, this expectation was confirmed by the first detailed application of the BCS pairing theory[2] to nuclei[3]. A consequence of this interpretation is that the moments of inertia associated with one-quasiparticle states in odd-A nuclei should be larger than that of the ground-state configurations of the neighboring even-even nuclei[4].

Therefore, the recent discovery[5] of superdeformed rotational bands in several[6-8] odd- and even-mass nuclei differing by a single nucleon that have identical γ-ray transition energies to within a few keV, has received a great deal of attention. Explanations of these "identical bands" (IB) range from a simple, "accidental" cancellation of the various terms associated with the contributions of the valence nucleons to the moment of inertia,[9,10] to strong-coupling of pseudo SU(3) orbitals to the even-even core,[11] and finally, to a suggestion of rotational alignment of pseudospin[6,7]. All these explanations assume that the largest contributing factor to the odd-even difference in the moments of inertia, namely the pair force, is substantially weakened for high-spin superdeformed states. However, these scenarios would fail to explain identical bands at *low spin,* where the blocking of the pairing contributions of the odd nucleon is predicted to reduce the nuclear superfluidity, thereby increasing the moment of inertia of an odd-A nucleus by about 15% for rare-earth nuclei[3,12]. (Recent reports of IB's in nearby even-even nuclei[13,14] compare bands which have the same number of quasiparticles and, thus, do not probe the effects of blocking on moments of inertia.)

This work reports a systematic comparison of nearly two hundred odd-A bands in normally-deformed rare-earth nuclei with their neighboring even-even isotone or isotope having *one less neutron or proton.* The difference in the moments of inertia of the neighboring odd-Z and even-even isotones is $\lesssim$2% for the low-spin part of nearly 30%

of the bands. This is much smaller than the expected 15% increase. Such data present a serious challenge to the traditional picture of monopole pairing correlations which has been in vogue for more than three decades. In order to characterize this unexpected result, the Z, N, configuration, and excitation-energy dependence of the normally-deformed identical bands were investigated.

As an example, the decay sequences of three "identical bands" in ^{171}Lu are compared in Fig. 1 with a rotational core defined by the yrast sequence of ^{170}Yb, the neighboring isotone with one less proton[15]. The variations between the transition energies of the [404]7/2 band in ^{171}Lu and the corresponding values in the ^{170}Yb core (shown in parenthesis in Fig. 1a) are small, indicating nearly equal dynamical moments of inertia for these bands. In the context of the present paper, bands in neighboring odd- and even-mass nuclei with nearly identical moments of inertia are termed "identical". Since bands which have identical moments of inertia have constant alignments, i, constancy of alignment has been used as a signature for identifying identical bands. (Alignment is defined as the difference in spin at constant γ-ray energy.)

The alignments of the [404]7/2, [402]5/2, and [514]9/2 single quasiproton bands in ^{171}Lu are shown in Fig. 1c. The alignments for all three configurations remain nearly constant, indicating that all these seniority-one (i.e., one-quasiproton) configurations have nearly identical moments of inertia to that of the seniority-zero yrast configuration of ^{170}Yb. In Fig. 1b, the plots for the [404]7/2 and [402]5/2 configurations of ^{171}Lu and the yrast configuration of ^{170}Yb fall on nearly identical curves, resulting in nearly zero alignments. In contrast, the [514]9/2 plot parallels the ^{170}Yb curve, but is displaced upward by an average alignment of $i_{av} = 0.93\ \hbar$.

Values of the average alignment , i_{av}, and the variation of i relative to i_{av}, V(i), expressed as a percentage, have been extracted for 174 single-proton bands with Z = 67-77 and N = 90-110 for which spin, parity, and configuration assignments exist in data bases[15,16] Explicitly, V(i) is defined as:

$$V(i) = (100 / N) \sum_{n=1}^{N} \left(|i_n - i_{av}| \right) \left[\frac{(\Delta E_\gamma)_n}{2(E_\gamma)_n} \right], \qquad (1)$$

where $(\Delta E\gamma)_n$ represents the difference in the energies of the two stretched E2 transitions that populate, $(E\gamma)_{n+1}$, and deexcite, $(E\gamma)_n$, the nth member of the rotational band. N, the total number of transitions in each band, varies from 3 to 14. While the first term in the above summation measures the constancy of the alignment curve, the second term ensures that the contributions of the low- and high-spin members of the band receive equal weight. The signature partners of K=1/2 bands, which have a large signature splitting, were analyzed separately. The average alignments, i_{av}, and the corresponding percentage variations, V(i), for the 52 bands with an alignment variation of $\leq$ 1% are displayed in Table I as a function of Z, N, and Nilsson configuration. The last three rows of the table show, for each of the listed configurations, the number of bands analyzed, the average variation, and the percentage of the bands with alignment variations of less than 1%. Surprisingly, 30% of the bands analyzed have alignment variations of less than 1%, and nearly 12% have alignment variations of less than 0.5%, comparable to the variations of the best examples of the superdeformed identical bands. The occurrence of IB becomes even more prevalent if configurations that contribute large terms to the moments

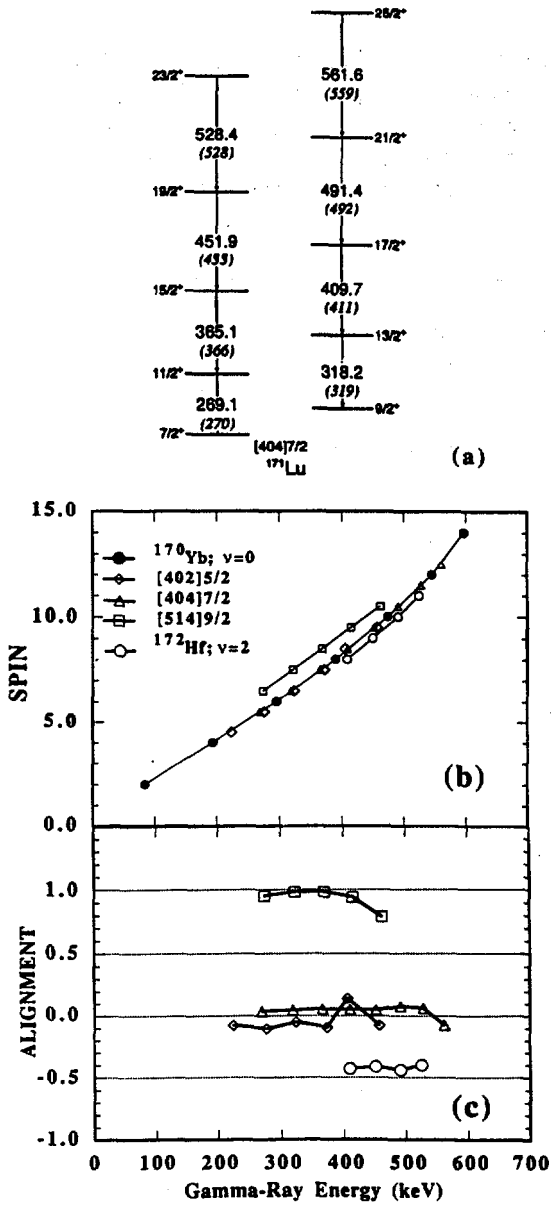

Fig. 1. (a) Level scheme for the [404]7/2 configuration in ^{171}Lu. The corresponding transition energies for the ^{170}Yb "core" are given for comparison in parenthesis below the ^{171}Lu transition energies. (b) Comparison of the distribution of spin as a function of gamma-ray transition energy for a variety of seniority-one configurations in ^{171}Lu and the $\pi[404]7/2 \otimes \pi[402]5/2$ configuration in ^{172}Hf with that of the ground-state band in ^{170}Yb. (c) Alignment plots of the seniority-one and -two configurations shown in Fig. 1b relative to the ground-state band of the ^{170}Yb as a function of the gamma-ray energy.

of inertia (e.g., [660]1/2 or [541]1/2) and nuclei with N < 93, which are easily polarized by the valence nucleons, are omitted from the analysis. Indeed, there is a clear increase in the tendency to encounter IB for nuclei with N > 100. These nuclei are among the best rotors and have stable β_2 deformations. A preliminary analysis of odd-neutron rare-earth

Table 1. Average alignment, i_{av}, and percent variation in alignment, V(i), of rotational bands with alignment variations V(i) ≤ 1% as a function of element, neutron number (N) and Nilsson asymptotic quantum numbers. Dashes indicate known bands with V(i) > 1%. The last three rows give the total number of bands analyzed, the average alignment variation, and the percentage of the known bands with V(i) ≤ 1% for each configuration.*

Element N	[402]5/2	[404]7/2	[411]1/2	[411]3/2	[541]1/2	[523]7/2	[514]9/2	[505]11/2
$_{67}$Ho 90		0.07,0.4			–	–		
94		0.40,0.9	–	–		1.1,0.8		
96		0.32,0.8	0.25,0.5	-0.20,0.8	–	–		
$_{69}$Tm 90		0.36,0.5				–		
92		0.03,0.5			–	–		
94		–	0.63,0.7		–	1.9,0.7		
98		0.13,1.0	–	–	–	1.2,0.8		
100		0.06,0.3	–		–	–		
$_{71}$Lu 92		0.36,0.5					–	
94	-0.17,0.6	0.18,0.7	–		–		–	
96	-0.04,0.6	–	–		–		–	
98	-0.06,0.7	–	–		–		–	
100	-0.05,0.8	0.04,0.2	–		–		0.93,0.6	
102	-0.20,0.4	-0.08,0.1	–		–		0.38,0.1	
104	-0.05,0.2	-0.02,0.4	–		–		0.15,0.1	
106	0.12,0.8	-0.03,0.1	-0.59,0.3				0.41,0.5	
$_{73}$Ta 98	-0.03,0.6	–			2.7,0.8		–	
100	-0.07,0.2	–			–		–	
102	-0.22,0.5	–			3.2,0.8		–	
104	0.00,0.2	-0.18,0.3			–		0.17,0.6	
106	–	0.13,0.6			–		0.64,0.9	
108		0.02,0.2					0.58,0.8	
$_{75}$Re 102	–				3.4,0.2		–	
106	–				–		0.40,0.4	
108	0.06,0.5				–		0.31,0.4	
110	0.02,0.4						–	
$_{77}$Ir 98					–			1.6,0.7
100	–				2.9,0.8		–	
108	–				3.2,0.8 4.1,0.6			–
Total # of Bands	27	24	23	6	41	11	26	3
Average V(i)	2.8	0.9	2.9	2.6	5.5	3.8	3.2	1.5
Freq. as IB	48%	67%	13%	17%	15%	27%	35%	33%

*No IB are observed in 7 occurrences of the [660]1/2 configuration having an average V(i) of 5.9.

nuclei indicates that though many neutron-based identical bands with similar characteristics exist, their occurrence is less frequent than those based on protons.

The clearest trend emerging from this study is the fact that 56% of the observed identical bands arise from the deformation-aligned [404]7/2 and [402]5/2 orbitals. Nearly 60% of the bands based on these orbitals fall into the IB category. In contrast, the percentages of the rotational-aligned identical bands are 15% and 0% for the [541]1/2 and [660]1/2 orbitals, respectively. Indeed, deformation- and rotational-aligned bands, which exert opposite polarizing forces experience, respectively, the smallest and largest susceptibility to alignment. These two factors strongly influence the moments of inertia. However, such systematics may also be associated with configuration-dependent short-range interactions.

An examination of the frequency of the IB as a function of the excitation energy of the bandhead reveals that about 57% of the bands with alignment variations of less than 0.5% have excitation energies of less than 100 keV. However, this lopsided distribution is a result of the large density of the deformation-aligned orbitals near the Fermi surface in this region. Indeed, the average value of $V(i)$ for the deformation-aligned [402]5/2, [404]7/2, and [514]9/2 orbitals is nearly independent of the band-head energy. This result is counterintuitive in that the largest contributions to pair correlations are from orbitals near the Fermi surface, whose occupation should produce the largest effect on nuclear superfluidity and, hence, the largest variation in the moment of inertia. It also is noted that adopting as a core either the even-even isotone having one more proton, or an average of the two neighboring even-even isotones produces substantially fewer identical bands. Indeed, such systematics also are counter to the expectations of a paired system, which would require comparison with the average of the neighboring isotones.

Perhaps the strongest challenge to the conventional BCS theory of pairing comes from identical bands differing by two quasiparticles. The K^π values of these excited bands in the seniority-two systems suggest the involvement of the two orbitals that also give rise to identical bands in the neighboring seniority-one systems. For example, the $K^\pi = 6^+$ identical band in ^{172}Hf is consistent with the coupling of $\pi[404]7/2 \otimes \pi[402]5/2$ configuration to the ^{170}Yb core. Indeed, the systematic occurrence of seniority-two $K^\pi = 6^+$ identical bands in $^{172\text{-}178}$Hf ($i_{av} = -0.42, -0.57, -0.02$, and -0.12, respectively) coincides with the occurrence of [404]7/2 and [402]5/2 identical bands in the neighboring odd-A $^{171\text{-}177}$Lu nuclei (see Table I). Analogous to ^{192}Hg, ^{170}Yb acts as a core for many of the seniority-one and -two identical bands in its neighboring nuclei. Other examples of nearly identical bands which may be built around the ^{170}Yb core include the $\{\nu[521]1/2 \otimes \nu[512]5/2\}$ configuration in ^{172}Yb ($K^\pi = 3^+$, $i_{av} = 1.3$), and the $\{\nu[521]1/2 \otimes \pi[404]7/2\}$ bands in ^{172}Lu ($K^\pi = 3^-$, $i_{av} = 0.6$; $K^\pi = 4^-$, $i_{av} = 1.1$). (The similarity of the $K^\pi = 4^-$ band in ^{174}Lu and the [404]7/2 bands in the neighboring ^{173,175}Lu nuclei has been noted previously[17].) The systematic existence of seniority-zero, -one and -two configurations with identical moments of inertia defy the conventional interpretation of moments of inertia in terms of the mean-field approach. Such configurations must have significantly different pairing correlations and, therefore, for an occupation of two quasiparticles are expected to exhibit as much as a 30% increase in their moments of inertia.

To further investigate the deformation dependence of IB, bands with $A \simeq 130$ [Ref. 18] having deformations of $\beta_2 \simeq 0.35$ (i.e., intermediate between that of normally-deformed and superdeformed bands) were also examined. Two identical bands based on neutron excitation, ^{132}Ce – ^{136}Nd ($V(i) = 0.14\%$) and ^{135}Nd – ^{136}Nd ($V(i) = 0.2\%$), were

identified. Because the spins of these bands are not known, only their incremental alignment Mod(i,2) = 1.8$\hbar$ and 0.67$\hbar$ respectively, could be determined. The existence of identical bands at a variety of deformations is a clear indication that these bands are not critically linked to the β_2 (or β_4) shape parameters via any yet-to-be discovered symmetries. Rather, large, stable quadrupole deformations may simply facilitate their occurrence.

An important question raised in connection with the superdeformed IB's is whether or not their alignments are integer[7]. In contrast to the superdeformed cases, the spins, excitation energies, and configurations of the identical bands studied here are known, allowing unambiguous determination of their alignments. In view of the common occurrence of the IB's based on a variety of configurations and at various deformations, it is doubtful that any microscopic mechanism based on accidental cancellations [9,10] can provide a viable explanation. Therefore, we compare the alignments shown in Table I with predictions of two phenomenological models which *ob ovo* assume identical moments of inertia for the core and the neighboring odd-A systems. In the strong-coupling limit of the particle-rotor model, alignments of the K=1/2 bands are given as $2i = (-1)^{I-1/2}\, a$, where I is the spin and a is the decoupling parameter. Relative alignment is zero for the K≠1/2 states. In the pseudo SU(3) model and its phenomenological variants that invoke $\tilde{L}$-$\tilde{S}$ coupling to explain alignments of the identical bands, $i = \pm$ 0.5 $\hbar$ for the *normal-parity* seniority-one bands relative to their even-even cores. The seniority-two bands in the pseudospin-one ($\tilde{S}$=1) state have an alignment of 1$\hbar$. relative to their seniority-zero configurations. (The "triplet pairing" scenario suggested in Refs. 6,7 postulates that integer alignments may result from the $\tilde{S}$=1 state of the vacuum.) The intruder orbitals fall outside the scope of this model.

Alignments of the normal-parity orbitals, and in particular the [402]-[404] pseudospin doublets, provide a unique opportunity to clearly distinguish between the strong-coupling, the pseudo SU(3), and the "triplet pairing" scenarios which give, respectively, i = 0, 0.5, and 1 $\hbar$ for the K≠1/2 orbitals. Barring a few exceptions, the observed alignments shown in Table I are in good accord with the predictions of the strong-coupling scheme, and provide no evidence for quantized alignments of 0.5 or 1 $\hbar$. The fact that constant alignments: (i) exist for both normal-parity and intruder states, (ii) are generally nonquantized, (iii) are present at very low frequencies, and (iv) are occasionally negative (e.g., $i \simeq -$ 0.5 $\hbar$ for the lowest $K^{\pi} = 6^+$ bands in ^{172,174}Hf) argues against rotational alignment of pseudospin as a general explanation for IB's. Nearly all the N=5 identical bands exhibit (non-quantized) anomalous alignments. Within the particle-rotor model, these alignments arise naturally from the mixing of the highly alignable [550]1/2 intruder orbital into the [523]7/2, [514]9/2, and [505]11/2 Nilsson-model states by the Coriolis force. The particle-rotor model, however, is not able to describe the experimental alignments quantitatively.

In summary, a systematic analysis of more than 200 one- and two-quasiparticle bands in the rare-earth region reveals an anomalously large number of identical bands (30% for odd-Z nuclei) at low spin and normal deformation. The existence of the identical bands at deformations intermediate between normal and superdeformed was also established. The frequent existence of identical bands for an extended range of deformations (varying from β_2 = 0.25 to 0.6) indicates that such occurrences are not restricted to the domain of superdeformed nuclei. The systematics of the identical bands suggest that they share a common basis and that the large stable deformation and the

weaker pairing correlations of the superdeformed bands simply facilitate the manifestation of this phenomenon. The alignments of these bands in normally-deformed nuclei, unambiguously determined, are not quantized, and do not seem to be the result of the rotational alignment of pseudospin. It is doubtful that any of the conventional mean field theories can explain the origin of these bands or the systematics of their alignments. In particular, the reduction of the BCS pairing correlations due to the blocking of one and two orbitals implies large changes (up to 30%) in the moments of inertia and cannot be reconciled with these systematics. Likewise, both the lack of a dependence of IB's on the bandhead excitation energy and the fact that IB's are nearly always observed for an odd-A nucleus and the even-even system with one less particle instead of the average of the two neighboring even-even systems are counterintuitive to pair correlations. It remains to be seen whether extensions of the present mean field theories will succeed in accounting for the data, or whether a new, fresh approach to account for short-range interactions is necessary.

ACKNOWLEDGMENTS

The authors acknowledge many fruitful discussions with W. Nazarewicz, R. Wyss, and P. Semmes. Oak Ridge National Laboratory is managed by Martin Marietta Energy Systems, Inc. for the Department of Energy under contract No. DE-AC05-84OR21400.

REFERENCES

* Partial support from the Joint Institute for Heavy-Ion Research.
** Participant in the Oak Ridge Science and Engineering Research Semester from Saint Joseph's College, Rensselaer, Indiana.

1. Aa. Bohr, B. R. Mottelson, and D. Pines, Phys. Rev. **110** (1958) 936.
2. J. Bardeen, L.N. Cooper, and J.R. Schriefer, Phys. Rev. **106** (1957) 162.
3. S. T. Belyaev, Mat. Fys. Medd. Dan. Vid. Selsk. 31, No. 11 (1959).
4. A. B. Migdal, Nucl. Phys. **13** (1959) 655 .
5. T. Byrski et al., Phys. Rev. Lett. **64** (1990) 1650.
6. F. S. Stephens et al., Phys. Rev. Lett. **64** (1990) 2623.
7. F. S. Stephens et al., Phys. Rev. Lett. **65** (1990) 301.
8. B. Haas et al., Phys. Rev. C**42** (1990) R1817.
9. I. Ragnarsson, Phys. Lett. **B264** (1991) 5.
10. J. Dudek, Z. Szymanski and T. Werner, Phys. Rev. C (submitted).
11. W. Nazarewicz, et al., Phys. Rev. Lett. **64** (1990) 1654.
12. Aa. Bohr and B. R. Mottelson, Nuclear Structure (Benjamin, 1975 Reading), Vol. II, p. 310-318.
13. I. Ahmad et al., Phys. Rev. C **44** (1991 1204.
14. R. F. Casten et al., Phys. Rev. C **45** (1992) R1413.
15. Evaluated Nuclear Structure Data File edited and maintained by the national Nuclear Data Center, Brookhaven National Laboratory. Summary of file contents and published documentation may be found on page ii of any issue of the Nuclear Data Sheets.
16. The Oak Ridge - Univ. of Tenn. High Spin Data Base, as described by J.D. Garrett et al., in ORNL, Physics Division Progress Report (1988) ORNL-6508, p. 70.
17. A.J. Kreiner, Phys. Rev. C**38** (1988) R2486.
18. X. L. Han and C. L. Wu, At. Data Nucl. Data Tables (in press).P. J. Nolan and P. J. Twin, Ann. Rev. Nucl. Part. Sci. **38** (1988) 533.

High-K Rotational Bands in ^{174}Hf and ^{175}Hf.

N.L.Gjørup, G.Sletten. The Niels Bohr Institute, DK-4000 Roskilde, Denmark.

P.M.Walker. Department of Physics, Univ. of Surrey, Guildford GU2 5XH, UK.

M.A.Bentley. NSF, Daresbury Laboratory, Daresbury, WA4 4AD, UK.

D.M.Cullen, J.F.Sharpey-Schafer, P.Fallon and G.Smith. Oliver Lodge Laboratory, Univ. of Liverpool, Liverpool L69 3BX, UK.

Abstract: *High sensitivity experiments with ^{48}Ca, ^{18}O and ^{9}Be induced reactions using the ESSA-30, TESSA-3 and NORDBALL arrays have provided extensive new information on the high spin level structures of ^{174}Hf and ^{175}Hf. During the series of experiments, several new bands have been found and most known bands have been extended considerably. Spin and excitation energy ranges for ^{174}Hf are now $\sim 35\hbar$ and ~ 13 MeV, respectively, and for ^{175}Hf ranges are $\sim 30\hbar$ and ~ 7 MeV, respectively. Several new high-K structures have been found in ^{174}Hf and the structure of these and the already known high-K bands in both nuclei together with the new Tilted Axis Cranking approach might explain the small K-hindrances observed for K-isomers in this region.*

The apparent breakdown of the K-selection rule observed in ^{182}Os[1] where a $K^{\pi}=25^{+}$ isomer decays directly into the yrast band has stimulated an experimental as well as theoretical activity in order to understand the mechanism behind this feature. The experimental activity has revealed several other high seniority states with unexpectedly low hindrance in their decays. In particular, the finding of low hindrance factors in the Hf-nuclei[2] as well, where a high degree of axial symmetry has been demonstrated, has removed some of the ambiguity in the conclusions of reference 1). The softness towards non-axial symmetry in ^{182}Os would in itself shed doubt on the validity of the K-selection rule.

We have therefore concentrated our research on W- and Hf-nuclei where axial symmetry is prevailing and where we expect to isolate other causes of the small K-hindrance. Here we will discuss two experiments on the rotational band structure built on high and low seniority states in ^{174}Hf and ^{175}Hf. The new theoretical approaches involves cranked shell model (CSM) calculations with cranking about an axis tilted with respect to the principal axes. We will present a comparison of our new experimental results to such calculations and discuss the implications for the decay of high-K isomers.

The experiments were performed with the TESSA-3 array at Daresbury Laboratory, U.K., and with the NORDBALL array at the Niels Bohr Institute. In the former, the reaction ^{130}Te(^{48}Ca,4n)^{174}Hf at an energy of 195 MeV and bunched beam was used. In the latter, the reaction ^{170}Er(^{9}Be,4n)^{175}Hf at 43 MeV was used. The two experiments yielded about $5\cdot10^{7}$ and $4\cdot10^{6}$ two-fold γ-coincidence events, respectively.

Figure 1 shows the ^{174}Hf ground state band and the β-vibrational band extended to I=34$\hbar$. This has allowed a clarification of the previously reported[3] double-crossing at I=24$\hbar$. The β-band crosses the ground state band at $\hbar\omega$=0.37 MeV and remains energetically favoured up to the highest spin identified at I=34$\hbar$. The gsb is crossed by an unidentified structure beyond $\hbar\omega$= 0.4 MeV. The favoured signature part of the $K^\pi=(1)^-$ octupole band has been extended to I=39$\hbar$, where the nature of this band probably is a 4-q.p. structure. This band crosses the gsb and the extension of the β-band at frequencies of $\hbar\omega$=0.45 and 0.5, respectively (see Fig. 2). Three new band structures have been identified in addition to the 20 known beforehand[4]. Two of these are probably of 2 q.p. nature. The lowest spin level identified in one of these cascades at 2685 keV has previously been proposed as the 12^+ member of the S-band[2]. This band has now been extended to I=32$\hbar$. The second new band structure starting at 1910 keV has a most probable spin of 5^-, 7^- or 6^+ deduced from its transitions to the gsb. A structure starting from a band head at 1563 keV is proposed as a $K^\pi=4^+$ two quasi-neutron configuration and is identified up to I=25$\hbar$.

The nature of the many quasi-particle structures available as final states is important for the understanding of the highly fragmented decay[2,5] from the $K^\pi=14^+$ isomeric state. Equally important is the structure of the isomeric state itself which is a 4-q.p. 2 quasi-neutron, 2 quasi-proton band head. The band built on the 3312 keV $K^\pi=14^+$ isomer is identified to I=27$\hbar$ and has the nature of a strongly coupled band without signature splitting (see Fig. 2). Two new high-seniority structures involving two signatures have been identified. A band-head at 4403 keV is assigned $K^\pi=18^+$ from its decay pattern into the $K^\pi=14^+$ band, and a band-head at 5203 keV is assigned $K^\pi=(21^-)$ from its decay pattern into the $K^\pi=18^+$ band and systematic arguments. The tentative assignment of $K^\pi=21^-$ should be pointed out since many degenerate transition energies are observed. With the $K^\pi=21^-$ assignment this band extends to I=30$\hbar$ and becomes yrast at I=26$\hbar$. In this way, the nature of the yrast line changes from rotational aligned structures to deformation aligned structures at a frequency of about $\hbar\omega$=0.36 MeV (see Fig. 2).

In ^{175}Hf, the known[6,7] level scheme has been verified and the 1- and 3-q.p. bands have all been extended to higher spin values, the $5/2^-$ [512] ground state band to I=45/2$\hbar$ and the $7/2^+$[633] band to I=57/2$\hbar$. This extension of the $7/2^+$[633] band shows that the $K^\pi=35/2^-$ 1.2μs 5 q.p. isomer at 3015 keV becomes the yrast configuration until it loses this character to a $K^\pi=(45/2^+)$ 7 q.p. isomer with microsecond half-life at 4636 keV[7]. It can also be seen that the two known 9 q.p. intrinsic states will not be yrast as they are 110 keV and 160 keV higher in energy compared to the $7/2^+$[633] band, respectively. A competition between rotational alignment and deformation alignment for the yrast priority is clearly demonstrated.

An interesting fact about the high-seniority bands in these two nuclei is that they do not show any signs of signature splitting up to the highest spins. This indicates persistance of deformation alignment and small mixing with low-Ω structures. Bands of this type have been discussed by Frauendorf[8] as uniform rotation about an axis pointing in

a direction different from the principal axes. It has been shown that these socalled TAC solutions (Tilted Axis Cranking) in TDHF can have lower energy than the usual PAC (Principal Axis Cranking) solutions. Because of the tilted axis, signature is no longer a good quantum number and the corresponding rotational bands will be $\Delta I=1$ bands, a unique feature of high-K bands. The absence of signature splitting in the high-K 3-, 4-, 5-, and 6-q.p. bands observed in the two nuclei (see Figs. 2,3) is taken as experimental evidence for observation of TAC solutions. It is also demonstrated that intrinsic high-K states become yrast, as shown for the $K^{\pi}=35/2^{-}$ isomer in ^{175}Hf and the band built on the $K^{\pi}=(21^{-})$ intrinsic state in ^{174}Hf. The TAC calculations demonstrate the presence of energy minima for high-K structures at tilting angles ϑ between 0° and 90°. Such minima could work as virtual stepping stones in a complicated decay sequence from isomeric high-K states to rotational aligned low-K states with $\vartheta=90°$ and thereby reduce the apparent K-forbiddenness.

In conclusion: New experimental information on band structures in ^{174}Hf and ^{175}Hf has demonstrated a competition for yrast between rotational and deformation aligned structures. The density of high-K structures near yrast seems to be a cause of the apparent breakdown of the K-selection rule. The tilted axis cranking calculations shows that band members in high-K structures have energy minima which competes with principal axis cranking solutions.

References:

1) P.Chowdhury *et al.*, Nucl. Phys. **A485**, 136 (1988).
2) P.M.Walker *et al.*, Phys. Rev. Lett. **65**, 416 (1990).
3) P.M.Walker *et al.*, Phys. Lett. **168B**, No. 4, 326 (1986).
4) N.L.Gjørup, Thesis, University of Copenhagen, (1990).
5) G.Sletten *et al.*, Nucl. Phys. **A520**, 325c (1990).
6) G.D.Dracoulis and P.M.Walker, Nucl. Phys. **A342**, 136 (1980).
7) N.L.Gjørup *et al.*, Z. Phys. **A337**, 353 (1990).
8) S.Frauendorf, Preprint, January 1991, and contributions to this conference.

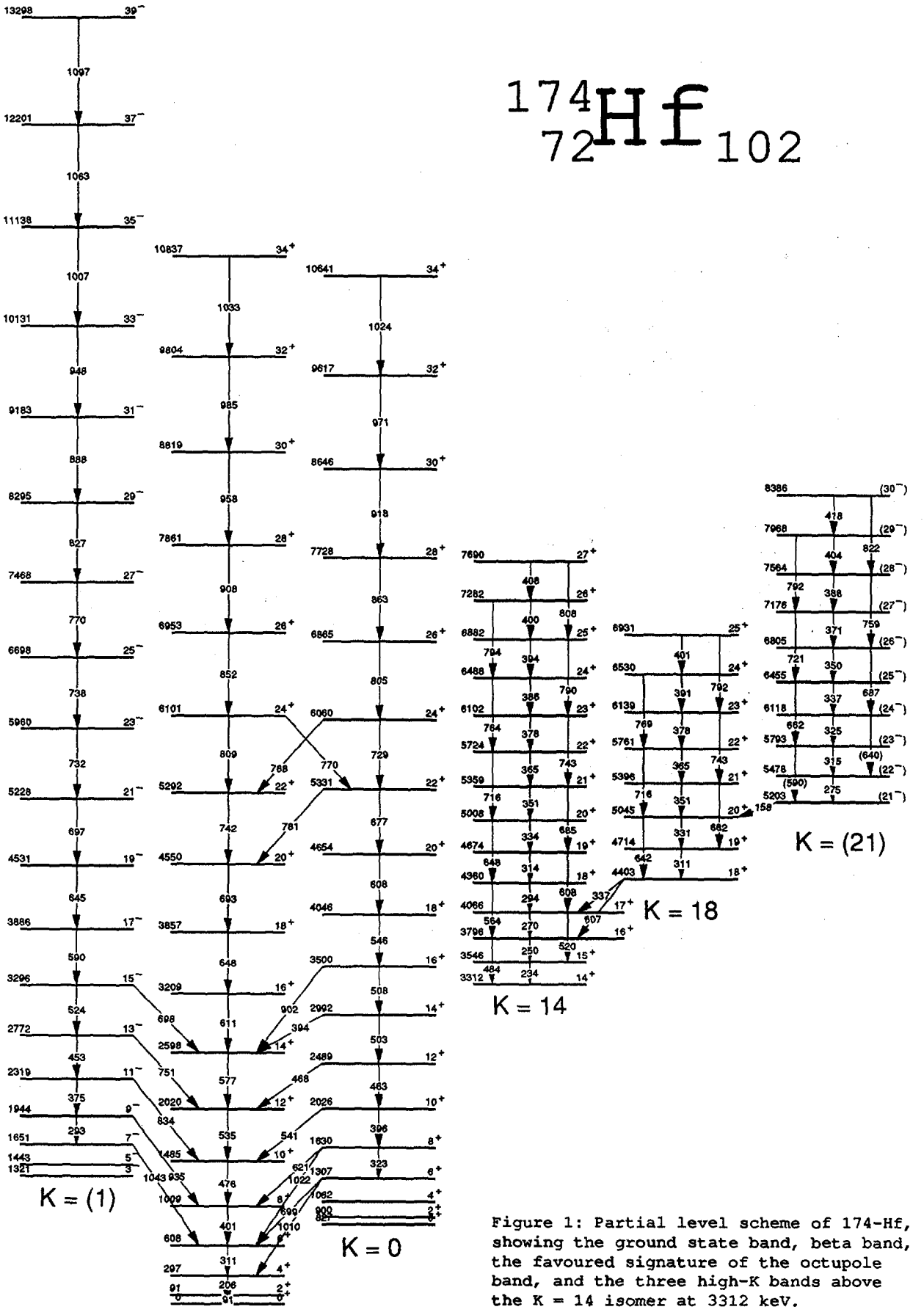

Figure 1: Partial level scheme of 174-Hf, showing the ground state band, beta band, the favoured signature of the octupole band, and the three high-K bands above the K = 14 isomer at 3312 keV.

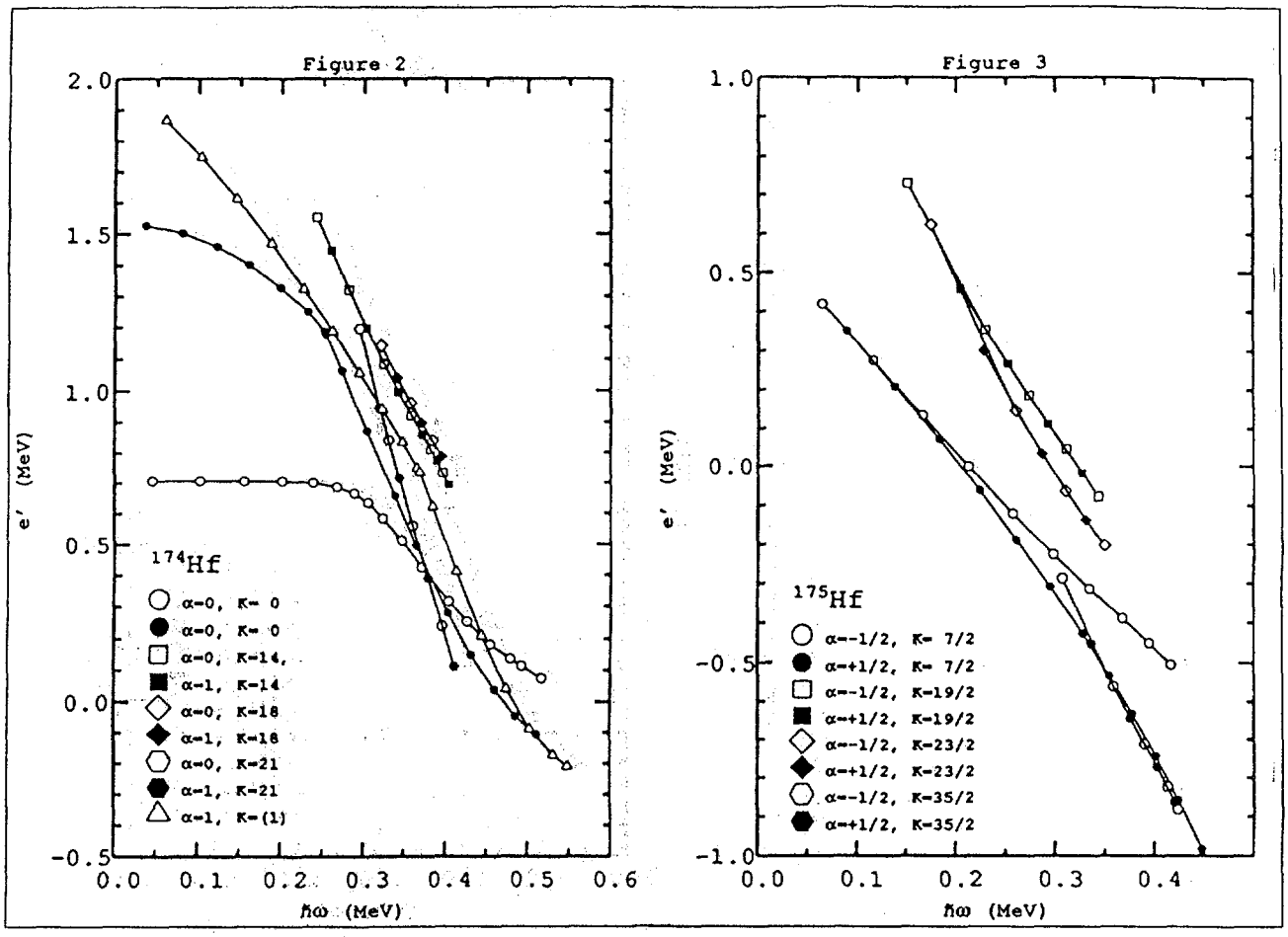

Figure 2 and 3: Experimental Routhians for ^{174}Hf and ^{175}Hf, showing the yrast-configurations and the 3-6 q.p. high-K bands. A Harris reference with the parameters J_0=32.7 MeV$^{-1}\hbar^2$ and J_1=112.4 MeV$^{-3}\hbar^4$ was used in both cases.

INTERNATIONAL CONFERENCE ON NUCLEAR STRUCTURE AT HIGH ANGULAR MOMENTUM

Ottawa

Session 7: Nuclear Theory (I)

OCTUPOLE CORRELATIONS IN SUPERDEFORMED STATES

T. Nakatsukasa, K. Arita and K. Matsuyanagi
Department of Physics, Kyoto University, Kyoto 606-01, Japan

S. Mizutori
Institute for Nuclear Study, University of Tokyo, Tanashi 188, Japan

Y. R. Shimizu
Department of Physics, Kyushu University, Fukuoka 812, Japan

ABSTRACT

We suggest that properties of single-particle motions in superdeformed nuclei may be significantly affected by coupling effects with low-frequency octupole vibrational modes with $K = 0, 1, 2$ and 3. We also indicate a possible relationship between octupole instability of superdeformed shape and supershell effects. In this connection, stability of classical periodic orbits and of KAM tori for single-particle motions in a reflection-asymmetric superdeformed potential are investigated.

INTRODUCTION

As is well known, properties of nuclear surface vibrations are strongly dependent on shell structures of average potentials. Since we have a new shell structure in superdeformed nuclei, which is drastically different from that of ordinary deformed nuclei, we expect that new kinds of nuclear surface vibrational mode to emerge above the superdeformed yrast states. In fact, the RPA calculation in the uniformly rotating frame, with the use of the single-particle states obtained by the cranked Nilsson-Strutinsky-BCS procedure, has indicated that we can expect highly collective, low-frequency octupole vibrational modes (with K =0, 1, 2 and 3) about the superdeformed equilibrium shape.[1,2] The main reason why the octupole* is more favorable than the quadrupole is that each major shell consists of about equal numbers of positive- and negative-parity single-particle levels which are approximately degenerate in energy at the superdeformed shape.

---

* Rigorously speaking, these reflection-asymmetric modes are not pure octupole, but are superpositions of odd-multipoles.

Existence of low-frequency octupole modes would imply that particle-hole or quasiparticle modes of motion in superdeformed nuclei might be significantly affected by the coupling effects with these vibrational modes. In this talk, we report some results of theoretical calculation which indicate the importance of such particle-vibration coupling effects to understand the properties of Landau-Zener band-crossing phenomena recently observed in ^{193}Hg.[3]

In the latter half of this talk, we would like to suggest a possible relationship between octupole instability of the superdeformed shape and supershell effects. We also discuss stabilities of periodic orbits and of KAM tori for the single-particle motions in reflection-asymmetric superdeformed potentials.

OCTUPOLE VIBRATIONS BUILT ON SUPERDEFORMED YRAST STATES

We solve the RPA equations for the Hamiltonian

$$H = h' - \frac{1}{2}\sum_K \chi_{3K} Q''^{\dagger}_{3K} Q''_{3K} \ , \tag{1}$$

where h' is a cranked single-particle Hamiltonian of the Nilsson-plus-BCS type,

$$h' = h_{\rm Nilsson} - \Delta\sum_i (c_i^\dagger c_{\bar{i}}^\dagger + c_{\bar{i}} c_i) - \lambda\hat{N} - \omega_{\rm rot}\hat{J}_x \ , \tag{2}$$

and Q''_{3K} are the doubly-stretched octupole operators.[4] We determine the equilibrium quadrupole deformation by means of the Strutinsky method and use a large configuration space composed of 9 major shells (for both protons and neutrons) when solving the coupled RPA dispersion equations.

As an example, we show in Fig. 1 octupole strengths evaluated at $\omega_{\rm rot} = 0$ for the superdeformed ^{192}Hg. We see that the collectivity is highest in this case for the $K = 2$ octupole mode. Figure 2 represents how the octupole strength distribution changes at a finite value of the rotational frequency $\omega_{\rm rot}$. In this figure, we can clearly see the K-mixing effects due to the Coriolis force; for instance, considerable mixing among the $K = 0$, 1 and 2 components is seen for the RPA eigenmode with excitation energy $\hbar\omega \approx 0.8$MeV.

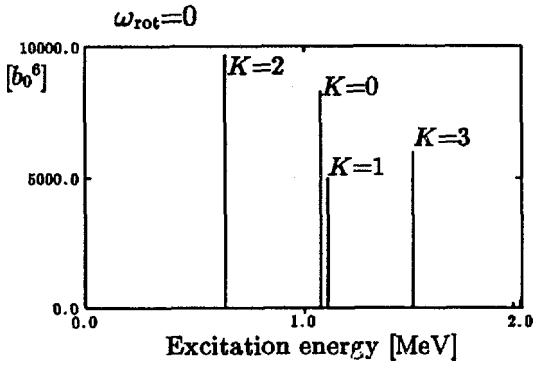

Fig. 1

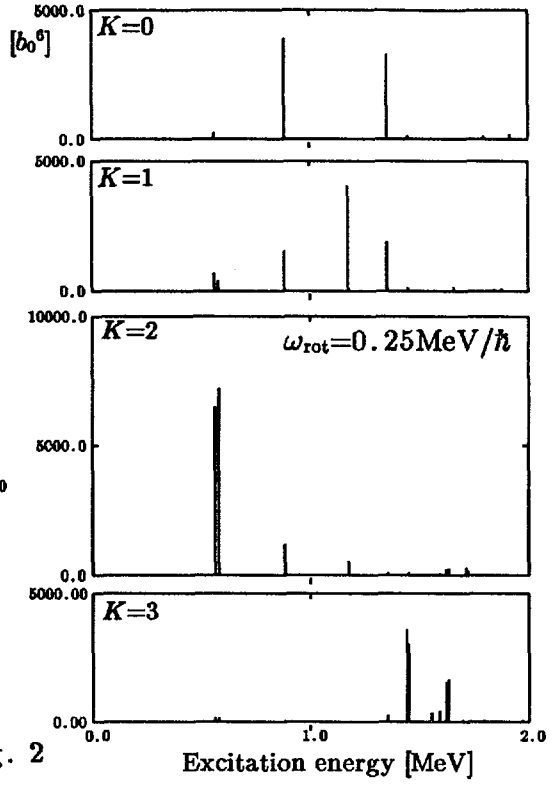

Fig. 2

Fig. 1 Octupole strengths $|\langle n|(r^3Y_{3K})''|0\rangle|^2$ calculated for the superdeformed states of ^{192}Hg at $\omega_{rot} = 0$. The neutron gap $\Delta = 0.9$MeV and the doubly-stretched octupole interaction strengths $\chi_{3K} = 1.1\chi_{3K}^{HO}$, with χ_{3K}^{HO} being the self-consistent values for the harmonic-oscillator potential,[4] are used.

Fig. 2 The same as Fig. 1 but for $\omega_{rot} = 0.25$MeV/$\hbar$.

OCTUPOLE VIBRATIONAL EFFECTS ON QUASIPARTICLE MODES IN SUPERDEFORMED ^{193}Hg

Starting from the microscopic Hamiltonian (1), we can derive the following effective Hamiltonian describing excited states composed of quasiparticle $a_\mu^\dagger$ and octupole vibrations $X_n^\dagger$

$$\mathcal{H} = \sum_\mu E_\mu a_\mu^\dagger a_\mu + \sum_n \hbar\omega_n X_n^\dagger X_n + \sum_n \sum_{\mu\nu} f_n(\mu\nu)(X_n^\dagger + \tilde{X}_n)a_\mu^\dagger a_\nu \ . \quad (3)$$

After diagonalization of $\mathcal{H}$, state vectors are written as

$$|\phi\rangle = \sum_\mu C_0(\mu)a_\mu^\dagger|0\rangle + \sum_n \sum_\nu C_1(\nu n)a_\nu^\dagger X_n^\dagger|0\rangle + \cdots \ . \quad (4)$$

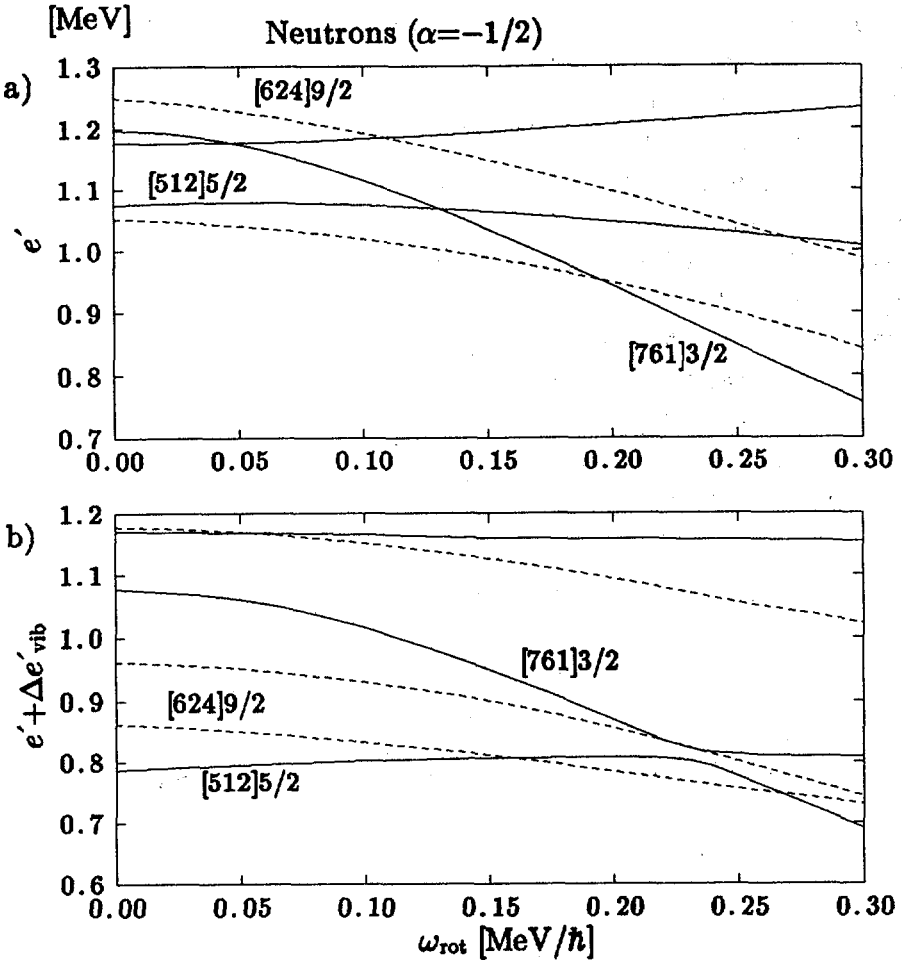

Fig. 3 a) Quasiparticle energy diagram for neutrons with signature $\alpha = -1/2$ in ^{193}Hg, plotted as a function of $\omega_{\rm rot}$.
b) The same as a) but the energy shifts $\Delta e'_{\rm vib}$ due to the coupling effects with the octupole vibrations are included. Parameters used in the calculation are the same as in Figs. 1 and 2. Notations like [512]5/2 indicate the main components of the wave functions.

Recently, experimental data suggesting octupole correlations in superdeformed states have been reported by Cullen et al.[3] for ^{193}Hg. Figure 3 shows a result of calculation for excitation spectra in the rotating frame of this nucleus. By comparing the conventional quasiparticle energy diagram (Fig. 3-a)) with the result of diagonalization of $\mathcal{H}$ (Fig. 3-b)), we can clearly identify effects of the octupole vibrations: Energy shifts $\Delta e'_{\rm vib}$ of 50∼400keV due to

the coupling effects are seen. In particular, we note that the Landau-Zener crossing frequency between Band 1 (whose main component is the [512]5/2 quasiparticle state) and Band 4 (associated with the [761]3/2 quasiparticle) is considerably delayed in agreement with experiment.[3] We also note that the interaction between these bands is increased. This is because interactions between different quasiparticle states through intermediate configurations composed of one quasiparticle and octupole vibrations are now possible. Although quantitative details depend on the parameters entering into the calculation (the force-strength χ_{3K}, the pairing gap Δ, etc.), which are not necessarily well known at present, we show here an example of wave functions for Band 1 and Band 4 at $\omega_{\rm rot} = 0$ in order to indicate qualitative characteristics:

$$
\begin{aligned}
|\phi_{\rm Band1}\rangle = \; & 0.88\,|[512]5/2(\alpha=-1/2)\rangle \\
& +0.10\,|[752]5/2(\alpha=-1/2)\rangle \\
& -0.32\,\left|[624]9/2(\alpha=-1/2)\otimes\omega^{(+)}_{K=2}\right\rangle \\
& +0.32\,\left|[624]9/2(\alpha=+1/2)\otimes\omega^{(-)}_{K=2}\right\rangle \\
& +\cdots\,, \\
|\phi_{\rm Band4}\rangle = \; & -0.96\,|[761]3/2(\alpha=-1/2)\rangle \\
& +0.17\,\left|[642]3/2(\alpha=+1/2)\otimes\omega^{(-)}_{K=0}\right\rangle \\
& -0.16\,\left|[640]1/2(\alpha=-1/2)\otimes\omega^{(+)}_{K=1}\right\rangle \\
& +0.16\,\left|[640]1/2(\alpha=+1/2)\otimes\omega^{(-)}_{K=1}\right\rangle \\
& +\cdots\,.
\end{aligned}
$$

Here $\omega^{(+)}_{K=1,2,3}$ and $\omega^{(-)}_{K=0,1,2,3}$ represent the octupole vibrations with positive- and negative-signatures, respectively. We note that the mixing effects of the $K = 2$ octupole vibrations are especially strong in the [512]5/2 quasiparticle state.

SUPERSHELL STRUCTURE AND OCTUPOLE INSTABILITY OF SUPERDEFORMED SHAPE

In recent years, octupole softness of superdeformed nuclei has been suggested[5–8] in shell-structure energy calculations by means of the Strutinsky method. As is well known, octupole instability takes place when the frequency of the octupole vibration evaluated by RPA becomes imaginary.

To understand the origin of the octupole instability, Nazarewicz and Dobaczewski[9] have discussed dynamical symmetry of the harmonic-oscillator potential with frequencies in rational ratio, and suggested that the octupole instability might occur in the superdeformed closed-shell configurations whose uppermost shell quantum numbers $N_{\rm sh} = 2n_\perp + n_z$ are even.

Figure 4 shows the shell-structure energies as functions of particle number N for the single-particle potential

$$V = \frac{1}{2}M\omega_0^2(r^2)'' - \lambda_{30}M\omega_0^2(r^2Y_{30})'' , \qquad (5)$$

where the double primes indicate that the quantities in parenthesis are defined in terms of the doubly-stretched coordinates $x_i'' = (\omega_i/\omega_0)x_i$. The frequency ω_0 is determined at each value of the octupole-deformation parameter λ_{30} so that the volume conservation condition is fulfilled. We can clearly see deep minima at $N = 62$ and 112 for the case of $\lambda_{30} = 0.38$. These new magic numbers are connected to the superdeformed magic numbers $N = 60$ and 110 where the single-particle levels are filled up to the major shells with $N_{\rm sh} = even$. In contrast, the minima at $N = 80$ and 140 associated with the major shells with $N_{\rm sh} = odd$ decline when one goes from the case of $\lambda_{30} = 0$ to the case of $\lambda_{30} = 0.38$. This result nicely agrees with the suggestion by Nazarewicz et al.[9] It also agrees qualitatively with the result of realistic calculation by Höller and Åberg[6].

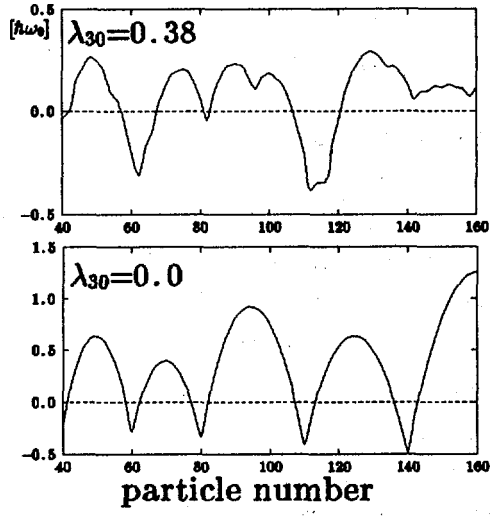

Fig. 4 Comparison between the shell-structure energies for the reflection-asymmetric case ($\lambda_{30} = 0.38$) and for the reflection-symmetric case ($\lambda_{30} = 0.0$). The unit is $\hbar\omega_0$.

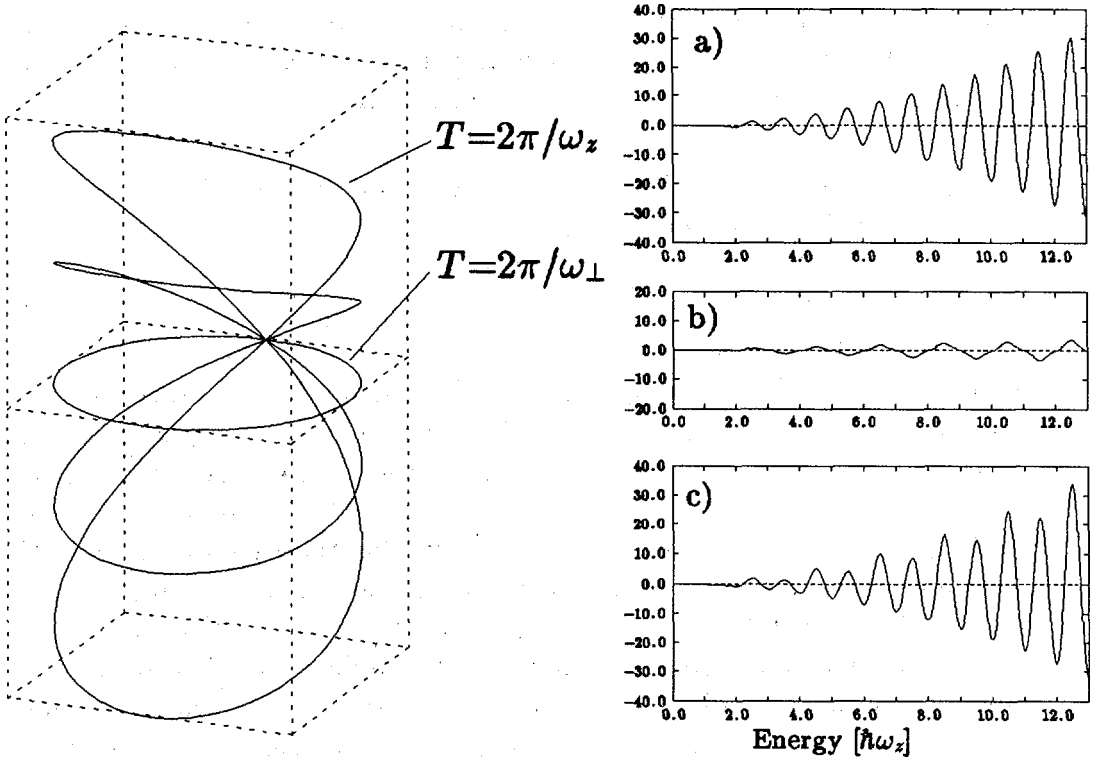

Fig. 5 Classical periodic orbits in the axially-symmetric harmonic-oscillator potential with $\omega_\perp = 2\omega_z$ and their contributions to the oscillating level density. a) represent those from three-dimensional orbits with the period $T = 2\pi/\omega_z$, b) those from planar orbits with $T = 2\pi/\omega_\perp$, and c) the sum of a) and b). The smoothing width $\gamma = 0.5\hbar\omega_z$ is used.

The odd-even effect in $N_{\rm sh}$ discussed above corresponds to the supershell effect[10] in the semiclassical theory of shell structure.[11] Figure 5 shows how the supershell effect arises in the case of the axially-symmetric oscillator potential with the frequency ratio $\omega_\perp : \omega_z = 2 : 1$. It arises from interference between three-dimensional classical closed orbits with the period $T = 2\pi/\omega_z$ and planar orbits in the (x, y) plane with the period $T = 2\pi/\omega_\perp$.

Figure 6 shows the oscillating components of the single-particle level density for the potential (5). We can clearly see that the beating pattern arising from the interference effect becomes more significant at $\lambda_{30} = 0.38$ compared to the reflection-symmetric case ($\lambda_{30} = 0$). This result strongly suggests that the octupole instability of the superdeformed shape is intimately connected with growth and decline of the supershell structure.

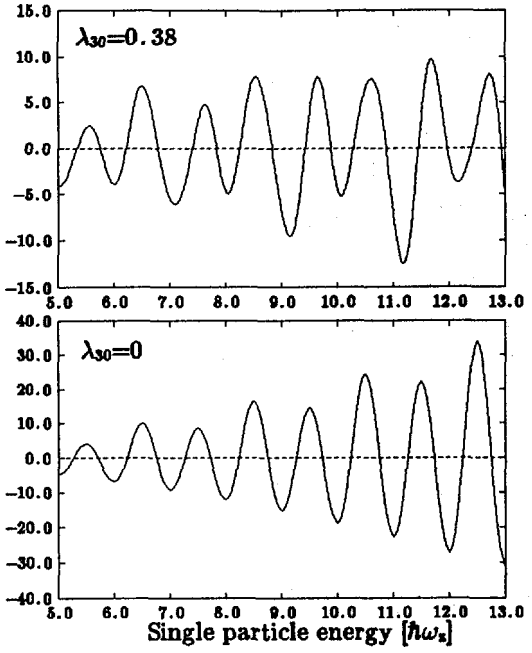

Fig. 6 Comparison between the oscillating components of the single-particle level density for the reflection-asymmetric case ($\lambda_{30} = 0.38$) and for the reflection-symmetric case ($\lambda_{30} = 0.0$). The smoothing width $\gamma = 0.5\hbar\omega_z$ is used.

STABILITY OF PERIODIC ORBITS IN REFLECTION-ASYMMETRIC SUPERDEFORMED OSCILLATOR POTENTIAL

In order to understand physical reason why certain superdeformed nuclei tend to break reflection symmetry and favor reflection-asymmetric shapes, let us investigate, on the basis of the semiclassical theory of shell structure,[11] stabilities of classical periodic orbits in the potential (5). Using the cylindrical coordinates (ρ, z) and after a suitable scale transformation, we can write the Hamiltonian as

$$h = \frac{1}{2}(p_\rho^2 + p_z^2) + \frac{m^2}{2\rho^2} + \frac{1}{2}(4\rho^2 + z^2) - \lambda\sqrt{\frac{7}{4\pi}}\frac{z^3 - 6z\rho^2}{\sqrt{4\rho^2 + z^2}} . \qquad (6)$$

Note that this Hamiltonian is non-integrable when $\lambda \neq 0$, and has some similarities with the Hénon-Heiles Hamiltonian well known in the study of quantum chaos.

Figure 7 shows, for the case of $m = 0$, a Poincaré surface of section (p_z, z) in the four-dimensional phase space (p_ρ, p_z, ρ, z) and several closed orbits with relatively short periods.

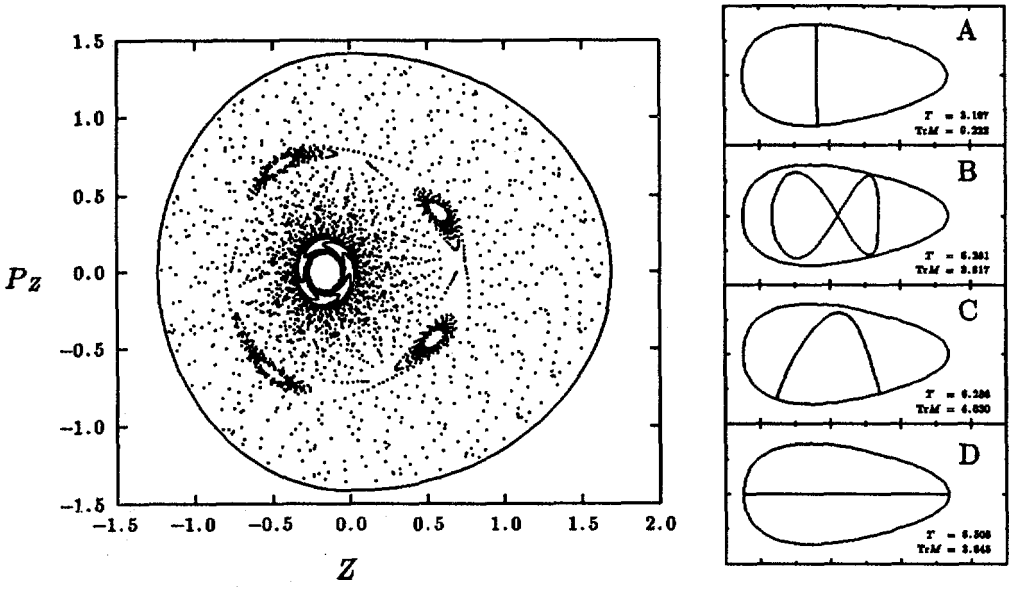

Fig. 7 Poincaré surface of section (p_z, z) and classical periodic orbits with $m = 0$ for the Hamiltonian (6) with $\lambda = 0.2$.

Let us evaluate stabilities of these periodic orbits by calculating the traces of the monodromy matrices,[12] Tr M, associated with them. As an example, we show Fig. 8 which indicates that the value of Tr M for the figure-eight orbit (B in Fig. 7) becomes negative at $\lambda \gtrsim 0.4$ implying an occurrence of instability. Thus, a period-doubling bifurcation of the figure-eight orbit occurs at $\lambda \simeq 0.4$, and the KAM torus associated with this closed orbit disappears thereafter. This is shown in Fig.9 together with the appearance of new tori associated with other period-doubling and -tripling bifurcations.

It is a very interesting open problem to clarify how the stabilities of these periodic orbits and of the KAM tori are related with growth and decline of the supershell structure in the single-particle spectra which arises from interferences between different periodic orbits.

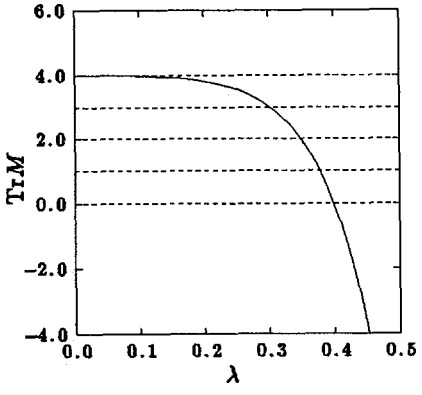

Fig. 8 Trace of the monodromy matrix M for the figure-eight orbit B evaluated as a function of λ.

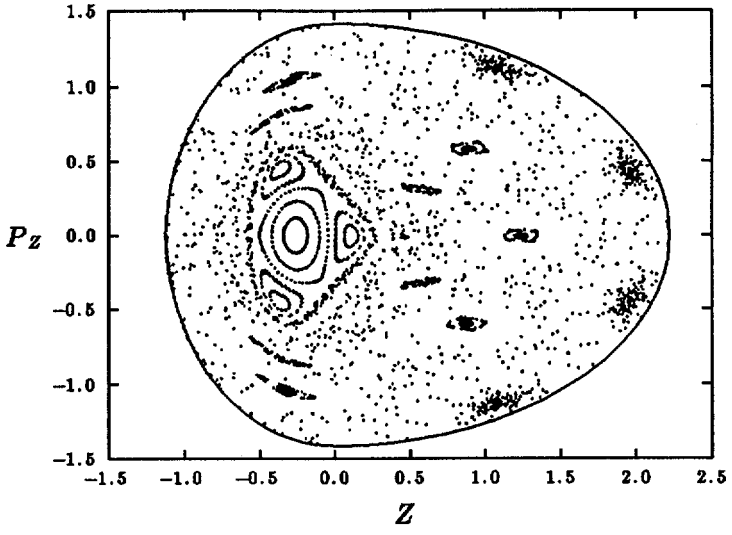

p_ϕ=0, λ=0.4

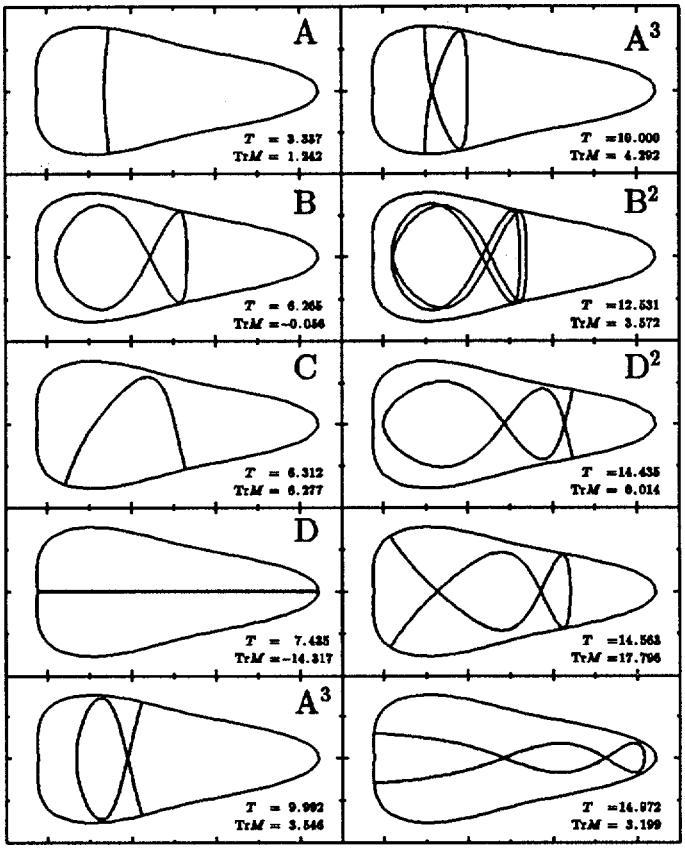

Fig. 9 The same as Fig.7 but for $\lambda = 0.4$.

REFERENCES

1. S. Mizutori, Y.R. Shimizu and K. Matsuyanagi, *Prog. Theor. Phys.* 83, 666(1990); 85, 559(1991); 86, 131(1991); in *Proceedings of the Workshop-Symposium on "Future Directions in Nuclear Physics with 4π Gamma Detection Systems of the New Generation"*, Strasbourg, March 1991 (American Institute of Physics, New York, in press).
2. T. Nakatsukasa, S. Mizutori and K. Matsuyanagi, *Prog. Theor. Phys.* 87, 607(1992).
3. D.M. Cullen et al., *Phys. Rev. Lett.* 65, 1547(1990).
4. H. Sakamoto and T. Kishimoto, *Nucl. Phys.* A501, 205(1989).
5. J. Dudek, T.R. Werner and Z. Symanski, *Phys. Lett.* B248, 235(1990).
6. J. Höller and Åberg, *Z. Phys.* A336, 363(1990).
7. R.R. Chasman, *Phys. Lett.* B266, 243(1991).
8. J. Skalski, *Phys. Lett.* B274, 1(1992).
9. W. Nazarewicz and J. Dobaczewski, *Phys. Rev. Lett.* 68, 154(1992); see also T.Bengtsson et al., *Phys. Scr.* 24, 200(1981).
10. A. Bohr and B.R. Mottelson, *Nuclear Structure* (Benjamin, New York, 1975), Vol.2, p.604.
11. V.M. Strutinsky and A.G. Magner, *Sov. J. Part. Nucl.* 7, 138(1976).
12. M.A.M. de Aguiar, C.P. Malta, M. Baranger and K.T.R. Davies, *Ann. Phys.* (N.Y.) 180, 167(1987).

Tilted Cranking Classification of Multibandspectra

S. Frauendorf

IHK FZ-Rossendorf, PF 19, O-8051 Dresden, Germany and
Nuclear Science Division, Lawrence Berkeley Laboratory, 1 Cyclotron Road, Berkeley, Ca 94720, USA

and

F. R. May

Niels Bohr Institute, Blegdamsvej 17, 2100 Copenhagen, Denmark and
Department of Mathematical Physics, Lund University of Technology, P. O. Box 118, S-221 00 Lund, Sweden

1. Introduction

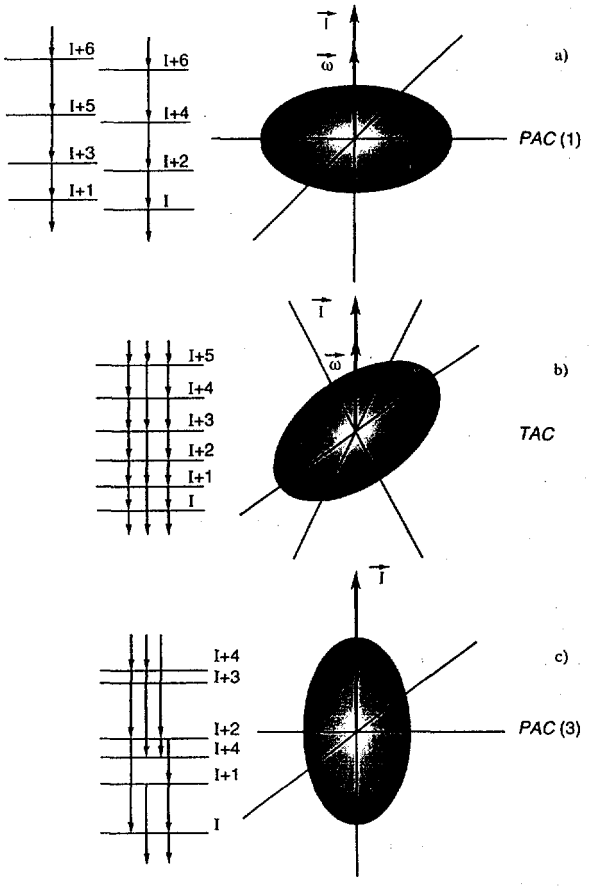

Fig. 1 Types of Rotation

Excited bands above the Yrast line can be sucessfully classified as quasiparticle configurations (conf.) in a deformed potential rotating uniformely about one of its principle axes. In the case of collective rotation this analysis is called CSM [1]. As sketched in fig. 1 a the bands are grouped into $\Delta I = 2$ sequences connected by fast stretched E2 transtions, each of which is interpreted as a quasiparticle conf. of fixed signature. In the case of rotation about the symmetry axis of the potential the method is

referred to the as "sloping Fermisurface" [1]. As shown in fig. 1c, it describes the yrast spectrum of individual high spin states not forming bands. The states are irregularely spaced, connected by noncollective transitions and are often isomeric (yrast traps). They are the heads of of $\Delta I = 1$ bands of the type shown in fig. 1 b. In addition to the stretched E2 crossover transitions there are strong stretched M1 and $\Delta I = 1$ E2 transitions. We shall demonstrate that these very common bands may be interpreted as quasiparticle conf.s in a deformed potential that rotates *uniformely* about an axis that is tilted with respect to its principal axes PA. If the rotational axis is a principle axis we shall speak of principle axis cranking (PAC) if not of tilted axis cranking (TAC). The calculation of electromagnetic transition probabilities by means of TAC has been discussed in ref. [2]. We restrict ourselve to the energies of the $\Delta I = 1$ bands above the yrast line.

2. Selfconsistency and Symmetry

The meanfield solutions in a frame rotating uniformely about the z-axis are obtained by applying the HF approximation to the routhian

$$H' = H - \omega_z j_z = h_{sp} - \frac{\kappa}{2} \sum_\lambda q_\lambda q^*_\lambda - \omega_z j_z \tag{1}$$

where we take the separable QQ-interaction. Then , the meanfield routhian is

$$h' = h_{sp} - \kappa \sum_\lambda Q^*_\lambda q_\lambda - \omega_z j_z \tag{2}$$

and selfconsistency is reduced to the five relations for the components of the quadrupole tensor

$$Q_\lambda = < q_\lambda >, \tag{3}$$

Here $|>$ denotes the single particle configuration. We define the PA 1,2,3 as the frame in which $Q'_1 = Q'_{-1} = 0$ and $Q'_2 = Q'_{-2}$, i. e. the quadrupole tensor is given by the two intrinsic moments Q'_0 and Q'_2 and the the angles ϑ and φ that fix the orientation of the PA relative to the z-axis,

$$Q_\lambda = D^{*2}_{0\lambda}(0,\vartheta,\varphi)Q'_0 + (D^{*2}_{2\lambda}(0,\vartheta,\varphi) + D^{*2}_{-2\lambda}(0,\vartheta,\varphi))Q'_2 \tag{4}$$

There always exist PAC solutions for which the PA coincide with the lab axes x,y,z (fig. 1 a). However, there may be additional TAC solutions of lower energy whose PA are different from the lab axes (fig. 1 b).

The selfconsistent solutions $|>$ are stationary, i. e. $\delta E' = 0$. Consider the special variations generated by infinitesimal rotations about the x- and y-axes

$$\delta E' = i\delta\phi < [H', j_x] >= \delta\phi < j_y >= 0 \tag{5}$$

$$\delta E' = i\delta\phi < [H', j_y] >= -\delta\phi < j_x >= 0 \tag{6}$$

which show that for the selfconsistent solutions

$$I_x =< j_x >= 0, \quad I_y =< j_y >= 0, \quad I = I_z =< j_z > \tag{7}$$

Hence, selfconsistency ensures that the axis of rotation $\vec{\omega}$ and the expectation value of angular momentum $\vec{I}$ are parallel, what is the well known condition for uniform rotation in classical mechanics. The stationarity of $|>$ implies also the familiar canonical relations

$$\frac{dE'}{d\omega} = -I, \quad \frac{dE}{dI} = \omega, \quad E' = E - \omega I \tag{8}$$

Considering $E' =< H' >$ as a function of the Q_λ, its extrema are the the solutions of the selfconsistency eqs. (3). According to eq. (4) we may find the minima in two steps: For given Q'_0, Q'_2 we minimize E' with respect to the orientation angles ϑ, φ. Then, $E'(Q'_0, Q'_2)$ is minimized with respect to the deformation parameters Q'_0 and Q'_2. In the following we consider stiff nuclei, i. e we assume that the deformation parameters Q'_0 and Q'_2 are not changed by rotation. Hence, we keep them fixed to the values found for the ground state and to minimizes E' only with respect to the orientation angles. Restricting ourselve to axial nuclei the deformed meanfield routhian reads in the PA system

$$h' = h_{sp} - \kappa Q'_0 q_0 - \omega(sin\vartheta j_1 + cos\vartheta j_3) \tag{9}$$

where ϑ measures the angle between the symmetry and the rotational axes. We choose h_{sp} such that h becomes the Nilsson hamiltonian with a monopole pairfield. The equilibrium angles are found by minimizing

$$E'(\omega, \vartheta) =< h' > \tag{10}$$

with respect to ϑ. The condition for uniform rotation, $\vec{I} \| \vec{\omega}$, is fullfilled at these points (c. f. ref. [2] for a more explicite discussion). A sequence of equilibrium confs. $|\omega >$ is associated with a rotational band.

Due to the symmetry of the deformed potential the parity π is a good quantum number independent of the orientation of the rotational axis. The PAC solutions can additionally be classified by the signature α, which is the eigenvalue of the rotation $\mathcal{R}_1(\pi) = e^{i\alpha\pi}$. The fact that $\mathcal{R}_1(\pi)$ defines a subgroup of the full rotational rotational group has the consequence that $I = \alpha \ mod \ 2$. Each quasiparticle configuration represents a ΔI =2 band with given π (c. f. fig. 1 a) Since TAC solution are not eigenfunctions of $\mathcal{R}_1(\pi)$ they cannot be classified by signature and there is no spin selection rule. Each qp conf. considered as function of the frequency ω represents a ΔI =1 rotational band of given π (c. f. fig. 1 b) The absence of signature splitting is the experimental evidence for the observation of a TAC solution.

3. The TAC Spectrum

Fig. 2 shows the single neutron spectrum obtained by diagonalizing the routhian (9) with a zero pairfield. The occupation corresponds to ^{174}Hf which has 102 neutrons. In the left part the nucleus is spinned up from $\omega = 0$ to $\hbar\omega = 0.3MeV$ along the symmetry axis 3. When levels cross the Fermilevel, the yrast conf. changes. The different conf.s encountered may be characterized by the angular momentum component $I_3 = K$, which is a good quantum number. The yrast squence is : $I_3^\pi = 0^+$, 6^-, 10^- and 15^-.

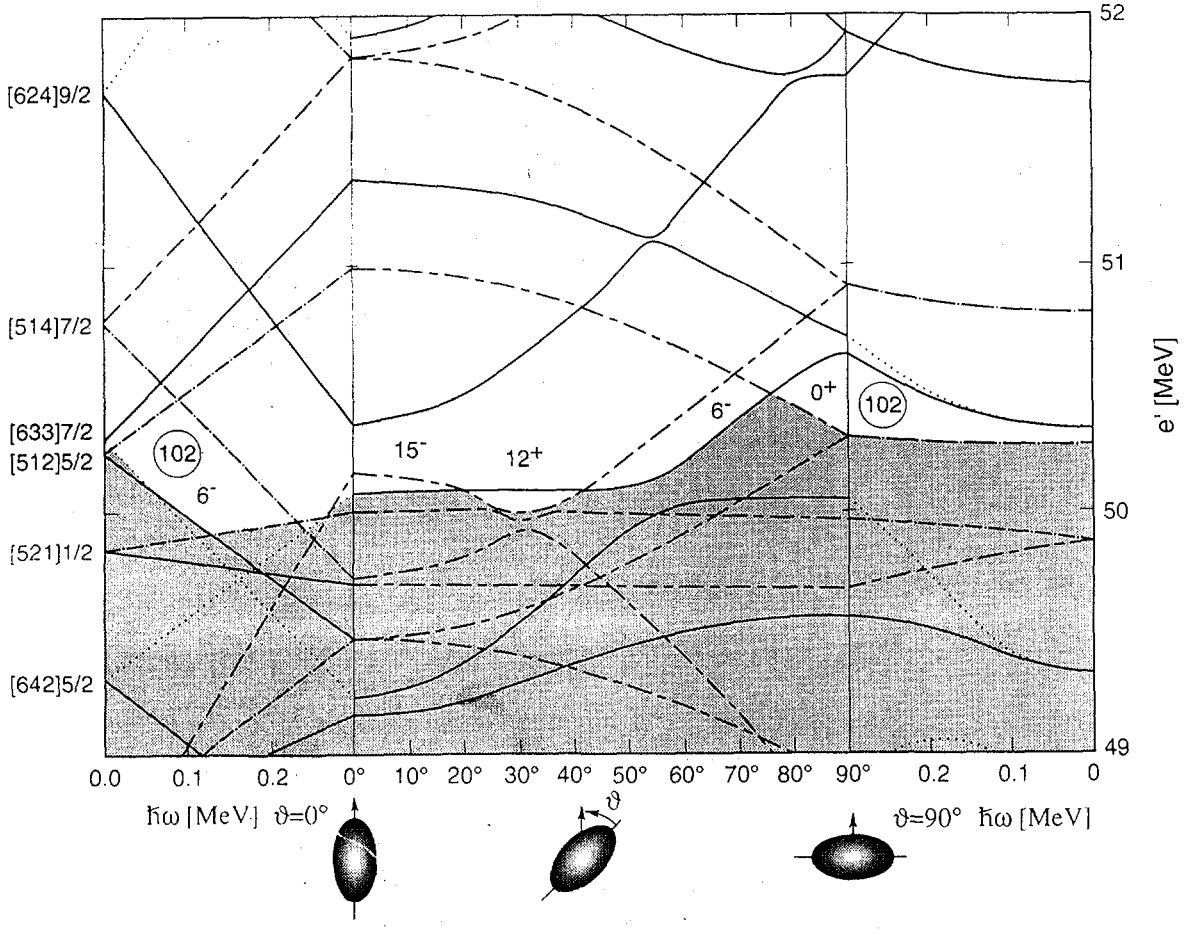

Fig. 2 Single neutron routhians. In the left and right parts the levels are classified with respect to (π, α) using the convention (+,1/2) full, (+,-1/2) dotted, (-,1/2) long dash short dash, (-,-1/2) dash dotted. In the middle full lines indicate positve dashed negative parity. The slopes of the lines are $-i_3, -\omega i_\perp$ and i_1 in the left, middle and right part, respectively. The shaded area indicates the occupied levels for N=102 and I_3^π (rounded to integers) is given. The deformations are $\varepsilon = 0.26$ and $\varepsilon_4 = 0.035$.

In the middle part the rotational axis turns from the 3-axis ($\vartheta = 0^o$) to the collective 1-axis ($\vartheta = 90^o$). Again the Fermi level crosses with other levels resulting in changes of the yrast conf. . Now I_3 is no longer conserved. Nevertheless it is a good way to characterize the conf.s. The yrast sequence is 15^-, 12^+, 6^- and 0^+, where I_3 is *rounded to to the next integer* . In the right part the nucleus rotates about the collective 1-axis where $\hbar\omega$ decreases from $0.3MeV$ back to 0. The yrast conf. has always 0^+ and has the structure of the neutron s-conf. (Although $I_3 = 0$ exactly, it is not a good quantum number.)

Obviously there exist several minima of $E'(\omega, \vartheta)$ with respect to ϑ. They are easily found by minimizing the routhians of the p-h confs. generated from the levels connected diabatically through the crossings . The physical interpretation is that each minimum at $\vartheta > 0$ represents a rotational band. If $\vartheta = 90^O$ it is a PAC solution with good signature restricting the spin of the $\Delta I = 2$ band to $I = \alpha + 2n$. If $\vartheta < 90^o$ the minimum is a TAC solution corresponding to a $\Delta I = 1$ band. [1]

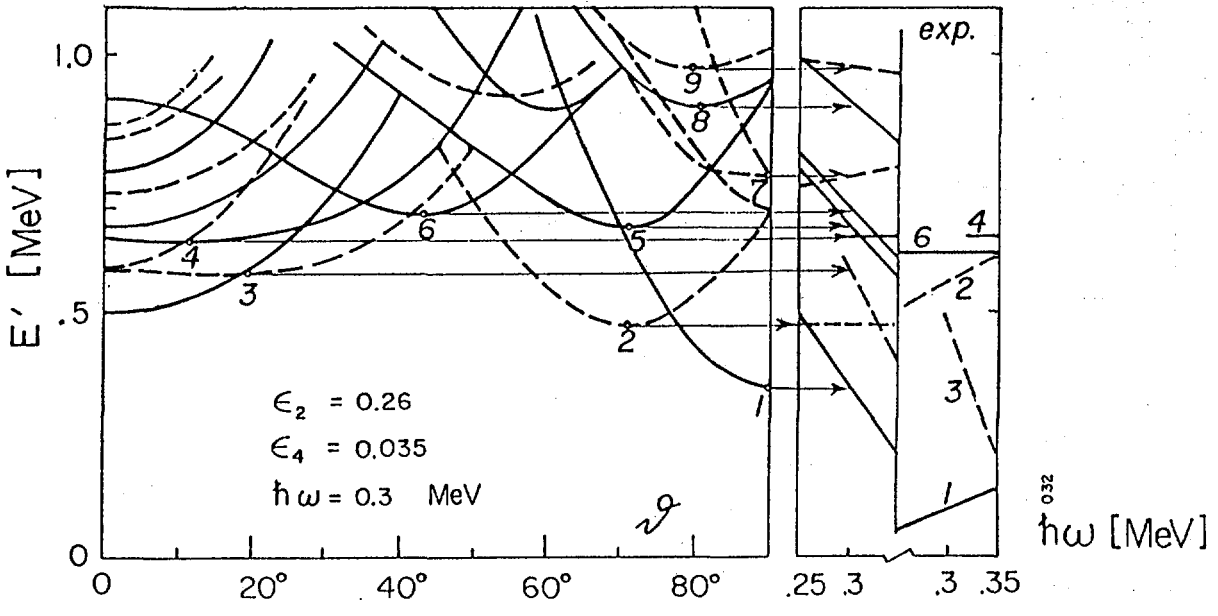

Fig. 3 Total routhians in ^{174}Hf as functions of the tilting angle ϑ (left) and the excitation spectrum as function of the frequency ω (right). Full lines indicate positve dashed negative parity. The energy zero is chosen such that the calculated band 4 agrees with the experimental one. All slopes are reduced by $I = 16\hbar$. The data is from N. Gjorup et al. [4].

Fig. 3 shows the lowest minima in ^{174}Hf obtained by combining the neutron

[1] As for any symmetry breaking, the restoration of the signature for $\vartheta \to 90^O$ cannot completely be described by the meanfield approach used here. A more elaborate discussion of this question is given in ref. [2]

conf.s generated from the levels in fig. 2 with the lowest proton conf.s. For $\hbar\omega \geq 0.3MeV$ the neutron excitatation spectrum is qualitatively reproduced assuming zero pairing (as in fig. 2). However one must include the paired g-conf. into the proton spectrum, since it is still the lowest one. [2] In addition to it only the 8^- proton conf. becoming the $9/2[514], 7/2[404]^{-1}$ at $\vartheta = 0$ comes into the play. Let us charcterize of the equilibrium conf.s by $(I_3^\pi)_\pi (I_3^\pi)_\nu$. The enumerated minima have the structure: $1: 0^+0^+$, $2: 0^+6^-$, $3: 8^-12^+$, $4: 8^-10^-$, $5: 0^+7^+$, $6: 8^-6^-$, $7: 0^+0^-$, $8: 0^+3^+$, $9: 0^+3^-$.

The minima at $\vartheta = 0$ do not belong to a band since the wavefunction does not depend on ω and consequently no angular momentum is gained if ω grows. The band starts at the frequency where the curvature becomes zero and the minimum moves to positive values of ϑ. This defines the bandhead.

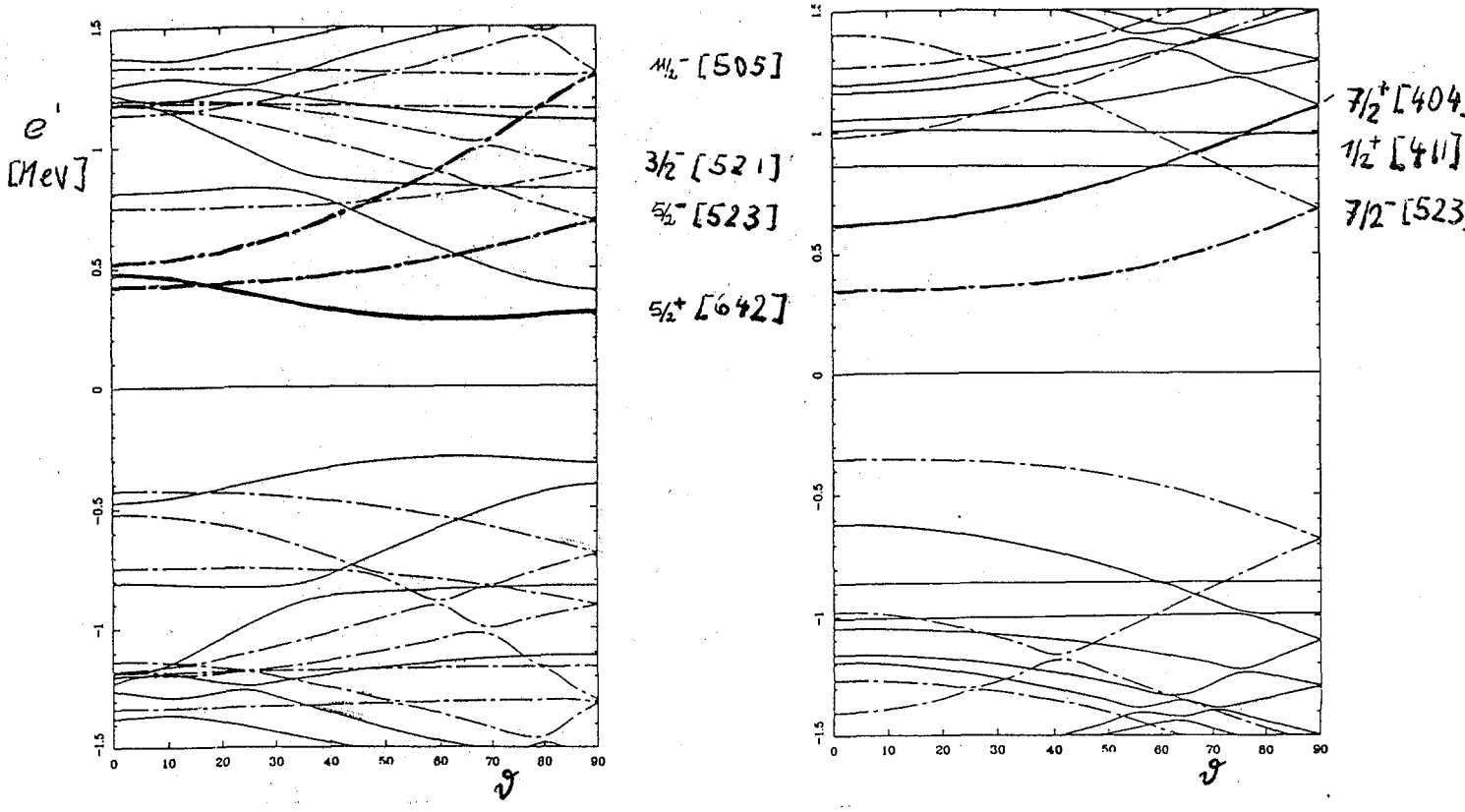

Fig. 4 Quasiparticle routhians for N=95 (left) and Z=68 (right). Full lines correspond to positive dashed dotted to negative parity. The parameters are $\hbar\omega = 0.15MeV$, $\varepsilon = 0.252$, $\varepsilon_4 = 0$, $\Delta_\nu = 0.80MeV$ and $\Delta_\pi = 0.87MeV$.

[2] It is calculated with $\Delta = 0.8\Delta_{eo}$ fixing the energy zero by identifying the s-conf. with the unpaired 0^+ yrast conf. at $\vartheta = 90°$.

Fig.4 shows the quasiparticle levels as functions of the tilting angle for strong pairing. The parameters are appropriate for ^{163}Er. At the relatively low frequency of $\hbar\omega = 0.15MeV$ the 0^+ g-conf. is always lowest. The spectrum in the N=95 Z=68 system is generated by putting 1,3, ... quasinuetrons (qn) on the neutron and 0, 2, ... quasiprotons (qp) on the proton levels. Again we construct diabatic confs., which we minimize with respect to ϑ. The routhians resulting from the minimizations at $\hbar\omega = 0.15$ and $0.30MeV$ are given by the arrows in fig. 5 , which point into the direction of the rotational axis. It is seen how ϑ approaches 90^o along a band. The structure of the lowest configurations is:

- Band 1 PAC, 0qp 1qn on $\alpha = 1/2,\ \ i_{13/2}$
- Band 2 PAC, 0qp 1qn on $\alpha = -1/2,\ \ i_{13/2}$
- Band 3 TAC, 0qp 1qn on $5/2^-[523]$
- Band 4 TAC, 0qp 1qn on $11/2^-[505]$
- Band 5 TAC, 2qp on $7/2^-[523]$, $7/2^-[404]$, 1qn on the lowest $i_{13/2}$
- Band 5 TAC, 2qp on $7/2^-[523]$, $7/2^-[404]$, 1qn on $5/2^-[523]$

4. Experimental routhians

The canonical relations imply how to obtain experimental frquencies and routhians:

$$\hbar\omega(\bar{I}+1/2) = (E(I+\Delta I) - E(I))/\Delta I,\ \ \bar{I} = I + \Delta I/2 \tag{11}$$

$$E'(\bar{I}+1/2) = \frac{1}{2}(E(I+\Delta I) + E(I)) - \omega(\bar{I}+1/2)(\bar{I}+1/2) \tag{12}$$

One may always use $\Delta I = 2$. For well developed TAC bands with no signature splitting $\Delta I = 1$ is better since the discrete datapoints are twice as dense and ω is just equal to the transition energy. Note, the procedure differs from the standart PA CSM [1]: There, the component ω_1 is calculated, here we determine the total ω. Fig. 5 shows the experimental routians $E'(\omega)$ obtained from the recent ^{163}Er data measured with the NORDBALL [3].

The excitation spectrum at a fixed ω can directly be compared with the $E'(\omega)$ calculated for the different minima relative to the lowest minimum. This is done in fig. 5 and the right part of fig.3, which is based on a plot similar to fig. 5 calculated from the recent NORDBALL data on ^{174}Hf [4] (c. f. abstract B3). In addition to the positions the slopes can also be calculated. According to eq. (7) the negative slope is the total spin $I + 1/2 = \sqrt{I_1^2 + I_3^2}$. Making the assignments to the experimental bands we use the parity, the ΔI characteristics (1 for TAC,

2 for PAC), the positions E', the slopes I, and the bandhead spins. (The last are often close to I_3., However, as discussed below, this needs not to be the case if easily alignable quasiparticles like $i_{13/2}$ are involved .) Both for ^{163}Er and ^{174}Hf the calculations account fairly well for the observed spectra. In particular the bandhead frequencies of bands 3 and 4 in ^{174}Hf , which happen to start inside the calculated window, are predicted right. The strongest disagreement occurs for the PAC band 1 in ^{174}Hf , which is the combination $g_\pi s_\nu$. This is not surprising since we assume zero pairing for the s_ν-conf..

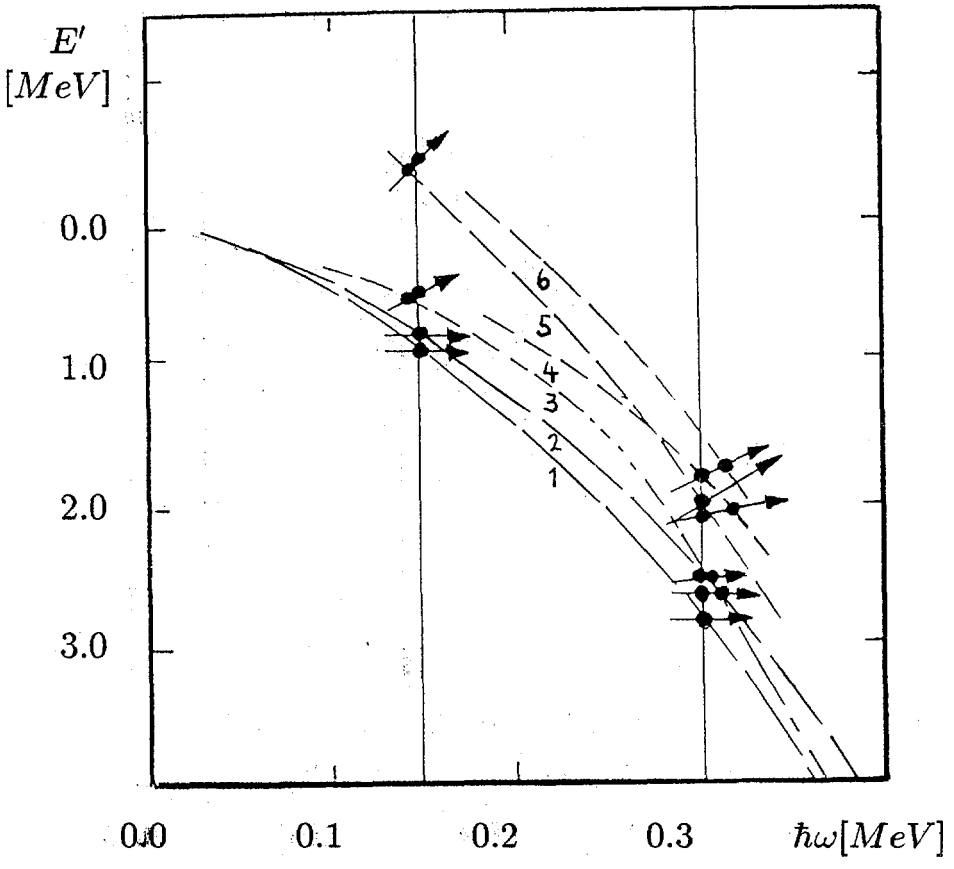

Fig. 5 Experimental routhians in ^{163}Er as calculated by eqs. (11) and (12). The data points lie at the spaces between the lines. Bands 1 and 2 are $\pi = +$ PAC bands. The other are $\pi = -$ TAC bands. The data is from A. Broksted et al. [3]. The arrows represent the results of calculations at $\hbar\omega = 0.15$ and $0.30 MeV$. The dot at the vertical line gives the excitation energy. The energy zero is chosen such that the calculated band 1 agrees with the experimental one. The dot at the intersection with the experimental curve indicates the band the arrow is assigned to. The angle between the arrow and the vertical line is the tilting angle ϑ.

It should also be kept in mind that the scale in the right part of fig. 3 is very blown up. The differences in slope cover only $4\hbar$. Note the TAC band 3 in ^{174}Hf , which both in the calculations and in experiment becomes yrast slightly above $\hbar\omega = 0.35MeV$ [4].

5. Response of the Particles to Tilting

If the excited quasiparticles are strongly coupled to the deformed field, the tilted cranking becomes the semiclassical version of the well known rotational model for bands with finite K [5] . The levels $11/2^-[505]$, $7/2^+[404]$, $7/2^-[523]$ are examples. Their routhians change with the strong coupling function $-Kcos\vartheta$ since the quasiparticle angular momentum is aligned with the deformation axis (DAL). The progess achieved by our method consist in the equally simple description of confs. that contain quasiparticles reacting sensitivly to the inertial forces. The $i_{13/2}$ qn are the well known example in the rare earth region. In fig. 4 the second $\pi = +$ level has a its minimum at $\vartheta = 90°$, i. e. it is rotational aligned (RAL) although it is based on the $5/2^+[642]$ state at zero ω. The lowest $\pi = +$ level has its minimum at about $60°$ meaning that its angular momentum vector points in this direction. It is an example of the Fermialigned coupling (FAL) suggested in ref. [6]. The 1qn conf. 1 is a PAC band since the collective rotation of the vacuum (core) drives strongly towards $90°$. In band 5 the same qn is combined with the 2 DAL qps resulting in a TAC solution which has quasiparticle angular momentum components along *both* the 1- and the 3-axes. This is demonstrated in a dramatic way by the fact that band 5 has a large value of ϑ already at the bandhead (c. f. fig. 5). It is an example of a band that does not start with $I = K$ as expected for strong coupling. A further combination of FAL and DAL quasiparticles are the the t-bands [7] becoming yrast in N=105, Z=74,76 nuclei (c. f. abstract B12). The M1-transition rates depend sensitivly on the orientation of the quasiparticle angular momentum [2]. They may be used to explore the geometry of the angular momentum coupling.

Another conspicuous feature is the complete decoupling of the pseudospin seen for the $\tilde{\Lambda} = 0$ states $1/2^-[521]$ in fig. 2 and $1/2^+[411]$ in fig. 4. In both cases the trajectories are horizontal , i. e. $i_\perp = 0$ and $\vec{s}$ follows $\vec{I}$ when it moves towards $90°$ along the band. The consequences of this behaviour remain to be explored.

6. Summary

Tilted Cranking is a microscopic theory which treats the alignment of quasiparticle angular momentum with both the rotational and symmetry axis on equal footing. Compared with the standart CSM treatment of K [1] it *calculates* I_3 instead of making assumptions. Experimental routhians are defined which depend *only* on the experimental energies. High K- bands lying low above the yrast line have also low lying routhians. The disadvantage compared to the standart CSM

is that each conf. has a different tilting angle (selfconsistency in orientation) and, hence, one quasiparticle diagram is not enough to classify the excitation spectrum. We demonstrate that the theory quantitatively accounts for the experimental excitation spectrum using some low band as a reference. Allowing for selfconsistency in the other important dergrees of freedom (Δ, ε, γ) one may also calculate the total routhians. In addition to energies the theory provides the electromagnetic as well as other intraband transition matrixelents. New structures are found combining quasiparticles that are strongly coupled to the deformed potential with ones reacting sensitivly to the inertial forces.

References

[1] Z. Szymanski, Fast Nuclear Rotation, Clarendon, Oxford 1983, p. 29 ff.

[2] S. Frauendorf,T. Bengtsson, Proc. of the Int. Symp. on Future Directions in Nuclear Physics, Strasbourg 1991, World Sci. Publ. Singapore

[3] A. Broksted and the the NORDBALL collaboration to be published

[4] N. Gjorup et al. Abstract B3 to this conference and to be published

[5] A. Bohr, B. Mottelson Nuclear Structure II, Benjamin, New York 1975 p. 1

[6] S. Frauendorf, Phys. Scr. **24** (1981) 349

[7] S. Frauendorf, Preprint NBI-92-04 and subm. Phys. Let.

Assignment of Nilsson Orbitals at Superdeformation – Identical Bands.

INGEMAR RAGNARSSON

Dept. of Math. Physics, Lund Inst. of Tech., P.O. Box 118, S-221 00 LUND, Sweden

For the superdeformed (SD) bands observed in the Dy/Gd region of nuclei, energies of neighbouring nuclei are compared in the form of effective alignments of the valence particles. The effective alignment is obtained if the transition energies E_γ in the SD bands of an A and $(A+1)$ nucleus, respectively are drawn as I vs. E_γ and the difference at constant E_γ is taken[1]. The method has the "disadvantage" that we must know or guess relative spins but once a consistent scheme is constructed, it also includes a prediction of relative spins. The formalism is useful if relative differences are mainly caused by the alignment of the particle which is added when going from the A to the $(A+1)$ system while changes in shape, size, pairing, etc. are of minor importance. In this case, the effective alignments give a direct image of the Nilsson orbitals as illustrated for $^{146-149}$Gd in the figure. It is evident that the alignment process shows very similar features in the experimental and theortical case. This makes us believe that we do understand which Nilsson orbitals are active in these Gd isotopes. The orbitals are those with asymptotic quantum numbers [651 1/2] and [642 5/2] where a bandcrossing between the branches with signature $\alpha = -1/2$ is one of the typical features which lays a ground for the interpretation.

The near-identical transition energies observed in SD bands in neighbouring odd-proton and even-proton nuclei in the Dy/Tb/Gd region are investigated using the same formalism. The analysis supports previous suggestions that a proton in the [301 1/2], $\alpha = -1/2$ orbital is being removed. Thus, it seems as if the change in alignment with increasing rotational frequency is compensated by deformation changes (and changes in the size of the nucleus) resulting in an effective alignment which *appears* independent of frequency. The inclusion of ε_4 deformations are quite important when reaching this conclusion. The possibility to populate the unfavoured signature of the [301 1/2] band is pointed out as a challenge for the detectors just coming into operation.

With our present understanding, one possibility is to fit the observed bands with some smooth function and extrapolate them the zero frequency. Then, from experimental data alone, it would be possible to construct a s.p. diagram of the active Nilsson orbitals.

[1] I. Ragnarsson, Phys. Lett. B264 (1991) 5.

[2] B. Haas et al., to be publ.; V.P. Janzen et al., Proc. Int. Conf. on High-Spin Physics and Gamma-Soft Nuclei, Pittsburgh 1990 (World Scientific, 1991) p. 225

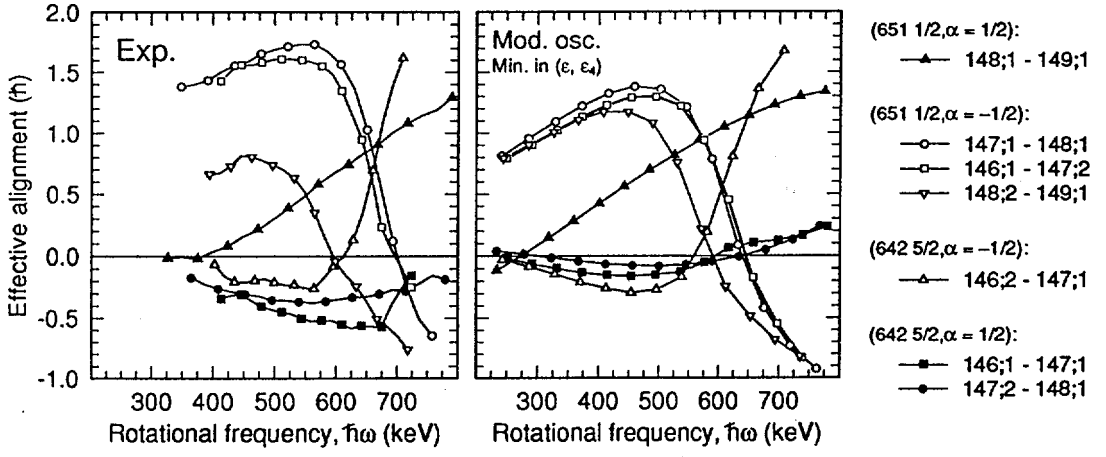

Effective alignments of neutron orbitals as obtained from differences in experimental and calculated (Nilsson-Strutinsky cranking model) transition energies, respectively. Configurations in neighbouring nuclei which are identical except that they have one specific orbital either empty or occupied are compared. The different bands and Nilsson orbitals assigned to them are given to the right where, in accordance with experimental classification [2], the SD "yrast band" is labelled by 1 and the second band by 2.

IDENTICAL BANDS IN (EVEN, ODD) NUCLEI AS EVIDENCE FOR SPECTATOR NUCLEONS

N.C. Schmeing

AECL Research, Chalk River Laboratories, Chalk River, Ontario, Canada K0J 1J0

1. Introduction

Isospectral bands in several (even, odd) pairs of nuclei in the mass 150 region, *e.g.* (^{152}Dy, $^{151}Tb^*$) [1], have properties different from those of most of the known "identical" bands. Firstly, their E_γ spectra are identical, not showing the shift in energy associated with the different nuclear spins I allowed for odd and even nuclei, which is $\pm 1/4$ of the nearly constant spacing between successive E_γ's in the two spectra [2]. By contrast, the pairs (^{152}Dy,^{153}Dy bands 2 or 3) [3] show the expected shift. Further, these (even, odd) pairs are much better isospectral partners than usually seen in the mass 190 region, where there is a "family" of (relatively) identical bands [4]. This lack of a shift has been explained [4] as arising from an aligned spin of 1/2 in the relevant orbital, *i.e.* that of the additional particle in the heavier nucleus. In the particle-rotor model, the shift would be exactly cancelled if the relevant orbital were the [301]1/2, and if it had a decoupling parameter of $a = 1$. To have the energy shift so precisely removed would be a considerable coincidence. It seems for us compelling grounds to investigate the possibility that the relevant orbital is in some way a spectator to the rotation.

The starting point of this work was to formulate conditions for an orbital that would make no direct contribution to the rotational energy of the nucleus. We give here our derivation of a model for such a case, a calculation to show that the energetics of the model are favourable, and finally an indication that this model is compatible with the absence of changes in pairing and deformation large enough to obscure the isospectral effect.

Although the ideas in our approach are well within quantum mechanical orthodoxy, some are novel. So at the outset we will sketch our physical picture. A superdeformed, fast-rotating nucleus executes nearly two-dimensional rotation about an axis; the collective zero-point motion is small. The time-averaged shape of the semi-classical rotating nucleus is close to that of the wave function Ψ_I^I with maximal eigenvalue of spin projection on the quantization axis. The form of the wave function for the nucleus does not support the semi-classical idea of a single, deformed rotating shape with its axis at some orientation Ω in the laboratory system. Rather, the certainty in spin I of the nucleus is accompanied by uncertainty in Ω. There is an amplitude for all orientations Ω, given by the Wigner $\mathcal{D}$-functions. In the laboratory wave function, the prolate intrinsic shape appears as a many-body correlation, like α-clustering.

Consider the nucleons of lowest energy in this rotating nucleus. They have small numbers N of stretched-radial nodes and small orbital angular momentum, with little or no angular momentum barrier. Their mean radius is much smaller than that of the less-bound particles. When their wave functions are calculated in the cranked shell model, they contribute to the prolate deformation of the nucleus. However, these mostbound nucleons interact with one another and all other nucleons in a manner prescribed by the nucleon-nucleon interaction and the location of the other particles. For the latter, all amplitudes in the laboratory wavefunction have physical effect. The effect of amplitudes at various Ω is to diminish the prolate deformation of the field on these particles. Our calculations indicate that a few, perhaps $A/2$, nucleons in the centre of the nucleus condense out of the prolate shape into an oblate shape symmetric about the rotation axis. They lower their kinetic energy by being confined to a larger, oblate volume and they win energy of attraction from components of the laboratory wave function at varying Ω.

In the spectroscopy of normally deformed nuclei this effect would be irrelevant. At 2 to 1 axis ratio, the nonrotating core produces an extruder with motion along the axis of rotation, near the

physical and Fermi surface. A particle in this orbital would not affect the rotational energy of the nucleus and could be removed at little energetic expense.

The derivation that follows expresses these ideas more exactly. We calculate the energy gain from the inert core in an appropriate mean field formulation.

2. A Factored Model

To construct a model for a superdeformed nucleus with a nonrotating core, we take an even reference nucleus of mass A with a core, plus valence particles rotating with respect to the core with a high quantized angular momentum R. This implies that the wave function factors into parts Φ^0_A for the core and $\Psi^{\beta R}_{AR}$ for the valence particles. Assuming independent motion for the core particles, Φ^0_A is a Slater determinant. The factor $\Psi^{\beta R}_{AR}$ is *e.g.* projected from a deformed intrinsic wave function Φ^β_A for the valence particles. The quantization axis chosen for maximal projection R gives a product form for yrast states of the A+1 nucleus.

With antisymmetry implied throughout, the wave function is

$$\Psi^R_{AR} = \Phi^o_A \otimes P^R_R \Phi^\beta_A = \Phi^0_A \otimes \Psi^{\beta R}_{AR}.$$

With $\mathcal{D}$ and $\mathcal{R}$ the Wigner functions and rotation operators, respectively,

$$P^R_M = \sum_K \int d\Omega \, \mathcal{D}^{R*}_{MK}(\Omega)\mathcal{R}(\Omega)$$

is the usual angular momentum projection operator [5]. Without specifying a particular hamiltonian H_A, we may assume that there exists a model, such as the cranked shell model [6], for the deformed reference nucleus, and that we have solutions for Ψ^R_{AR} and the moment of inertia $\mathcal{J}_A$. In general, a particle added to the deformed factor Φ^β_A of the nucleus will result in a new nucleus of mass A+1 with a different moment of inertia $\mathcal{J}_{A+1}$, varying as circa $A^{5/3}$. This is not the case for a particle added to the core in a nonrotating orbital $|k>$. We make the perturbation approximation that the nonrotating particle does not affect the motion of the reference nucleus. The binding energy of the last particle is obtained from: $\Delta H_k = H_{A+1} - H_A = t_k + v_k$; H_{A+1} and H_A are the Hamiltonians for the mass A+1 and mass A systems, respectively; t_k is the kinetic energy of the particle in orbital $|k>$; and the field v_k is the potential in which it moves.

A nonrotating particle does not move with the intrinsic frame of the rotating nucleus, but in the mean field resulting from the other core particles and from the density distribution associated with the angular momentum eigenfunction for the rotating particles. To see this, note that the factor $\Phi^0 \equiv \Phi^0_A$ is a determinant of single-particle wave functions for the core $\Phi^0 = \Pi\phi_i$. From a two-body interaction $V(k',k)$ between particles k' and k one defines the mean field $v(k)$ acting on a particle k in the nonrotating core via:

$$< \phi_k|v(k)|\phi_k > = \sum_{k' \neq k} < \Psi^R_R|V(k',k)|\Psi^R_R > .$$

Separating terms from nonrotating (i) and rotating (j) particles,

$$\Psi^{R*}_R \sum_{k' \neq k} V(k',k)\Psi^R_R = \phi^*_k\phi_k \sum_{j,i \neq k} (\Pi_{ik}\phi^*_i\phi_i)\Psi^{R\beta*}_R \Psi^{R\beta}_R(j_1, \ldots j_n)[V(i,k) + V(j,k)]$$

Integrating over all coordinates except those of the particle k, one obtains

$$v(k) = \sum_{i \neq k} < \phi_i|V(i,k)|\phi_i > + \sum_j < \Psi^{R\beta}_R|V(j,k)|\Psi^{R\beta}_R > .$$

Thus $v(k)$ is the two-body interaction folded with the density distribution of the core (first term) plus the R eigenfunction for rotating particles (second term), which proves the contention. This results because the single particle wave functions of the nonrotating particles enter the wave function multiplicatively as factors, *i.e.* because these particles execute independent particle motion in the dynamical field of the rotor of eigenfunction R, cf. [7,8].

For a nucleus with prolate intrinsic shape, the field v_k is thus primarily an oblate, time reversal invariant field v_0 symmetric about the quantization axis. Setting $h_k = t_k + v_0$, one obtains $H_{A+1} = H_A + h_k$, a model hamiltonian for a nucleus of rotational angular momentum R and a nonrotating particle in orbital $|k>$. The term H_A acts only on the reference nucleus, h_k on the nonrotating particle. The usual Coriolis term does not appear because the mean field v_0 does not rotate. We consider here only the maximally aligned yrast state, which is experimentally observed. An eigenfunction ϕ_k of h_k will have angular momentum quantized along the symmetry axis of the nuclear density, i.e., along the quantization axis of the reference nucleus. The wave function of the nucleus of mass A+1 then is $\Psi_{A+1,R+k} = \phi_k \otimes \Psi^R_{A,R}$. (The other possible wave function $\Psi_{A+1,R-k}$ is degenerate in energy under H_{A+1}.) The expectation value of H_{A+1} in the A+1 system is then $E_A + \epsilon_k$, where $\epsilon_k =< \phi_k|h_k|\phi_k >$ is independent of R. The transition energy between states of rotor angular momentum $R+1$ and $R-1$ is thus the same in the mass A and mass A+1 systems and given by $E_{\gamma,A} = (4R+2)/2\mathcal{J}_A$. This was the intent of the construction: if a particle is added to a mass A nucleus in a nonrotating orbital, without changing the configuration of the rotating particles, the resulting mass A+1 has the same γ-spectrum.

The derivation has an interesting implication for any closed spherical j-subshell below the Fermi surface of a rotating nucleus. For an intrinsically prolate nucleus these nucleons move in the oblate potential v_0. Thus the core Φ^0_A consisting of the lower, occupied j-subshells may be polarized into an oblate shape, with its axis the same as the quantization axis for the rotation. In this perturbation approximation the field v_0 acts as an external dynamical field with cylindrical symmetry imposed on the core particles. So Φ^0_A and Ψ^R_{AR} are eigenfunctions of angular momentum component with eigenvalues 0 and R, respectively. However, Φ^0_A and thus Ψ^R_{AR} are not eigenfunctions of total angular momentum.

This symmetry can be restored by a projection $\Psi^{\mathrm{proj}\ J}_{A\ M} = P^J_M\{\Phi^0_A \otimes P^R_R\ \Phi^B_A\}$. It is crucial that the core couples to the valence rotor as a whole. For large A and R and large deformations, energy considerations should not be much affected by this symmetry restoration, see *e.g.* [5]. It is usual to calculate in the particle-rotor and cranked shell models in a dynamical intrinsic system with wave functions which are not eigenfunctions of angular momentum. Accordingly, the total angular momentum to which Ψ^R_{AR} (respectively $\Psi_{A+1,R+k}$) corresponds is R (respectively $R+k$), because that is the maximum component of angular momentum along the quantization axis.

How energetically favourable such a polarized core is must be determined by minimizing the energy of the nucleus. In contrast to the nonrotating core, the applicable field for the rotating nucleons is the mean field in the intrinsic frame. (The point is, when calculating matrix elements of a two-body operator in a large A-body system there are appreciable contributions only where the overlap of the remaining A-2 particles is near unity.) It is consistent to regard collective rotation as an expression of many-body correlations, and nonrotating particles as without those correlations. One must add contributions to the interaction energy from the nonrotating particles in their oblate mean field, and contributions from rotating particles in the prolate intrinsic field.

3. Calculation

We have applied this model to the identical bands in ^{152}Dy and $^{151}Tb^*$ using programs described in [9]. Nazarewicz, Wyss, and Johnson [9] find that ^{152}Dy is stably superdeformed at $\beta_2 = 0.62, \beta_4 = 0.12, \gamma = 1^o$. Previous approaches [2] interpret $^{151}Tb^*$ as the ^{152}Dy con-

figuration with a [301]1/2 proton hole. In our model the core wave functions are eigenfunctions of the single-particle hamiltonian h_k. For the oblate potential v_0, we required that the axis ratio r_0 of long to short axes for v_0 be the same as the axis ratio r_p of long to short axes found for the optimal prolate potential [9] for ^{152}Dy, ignoring the β_4 deformation. With $r_0 = (1 + \beta_0(5/16\pi)^{1/2})/(1 - 2\beta_0(5/16\pi)^{1/2})$ and $r_p = (1 + 2\beta_p(5/16\pi)^{1/2})/(1 - \beta_p(5/16\pi)^{1/2})$, the β_2 deformation parameter β_p for the prolate intrinsic deformation and β_0 for the oblate field deformation are then related by: $\beta_0 = \beta_p/(1 + (5/16\pi)^{1/2}\beta_p)$. Corresponding to $\beta_p = 0.62$ is $\beta_0 = -0.5186$. Other parameters of the deformed Woods-Saxon potential were the universal parameters generated by the code. We calculated single-particle proton and neutron energies at β_p and β_o, with rotational frequency $\omega = 0$ because the field v_0 does not rotate.

The β-dependence of the energy of single-particle proton and neutron orbitals in ^{152}Dy at $\omega = 0$ has been calculated. At the oblate deformation $\beta_0 = -0.5186$ the orbitals with asymptotic quantum number $N \leq 3$ are all below the $Z = 66$ or $N = 86$ Fermi surface except the proton orbital [330]1/2. For both protons and neutrons, the sum E_0 of the single-particle energies of all $N \leq 3$ orbitals at β_0 is lower than the sum E_p at β_p. For protons it is $E_o = -353.77$ MeV *vs.* $E_p = -347.62$ MeV; for neutrons, $E_o = -530.90$ MeV *vs.* $E_p = -523.81$ MeV. Thus at $\omega = 0$ it would be energetically favorable to replace the $N \leq 3$ prolate orbitals by an $N \leq 3$ oblate core in ^{152}Dy. We propose that the hole in this core which gives the identical band in $^{151}Tb^*$ is in the [330]1/2 orbital near the Fermi surface. The remaining $N \geq 4$ particles would be in the orbitals calculated in [9]. Nonorthogonality of the projected wave functions from the prolate intrinsic basis and the oblate core wave functions may require small modifications in the radial dependence of the orbitals. However, this would affect ^{152}Dy and $^{151}Tb^*$ in the same way. The same orbital responsible for the (^{152}Dy,$^{151}Tb^*$) identical bands is thought to be responsible for several other [2] bands in the region, *e.g.* (^{151}Tb,$^{150}Gd^*$) and (^{150}Tb,$^{149}Gd^{**}$).

Beside making no direct contribution to the rotational energy, a nucleon in the proposed core orbital should have little effect on the motion of the rotating nucleons. The prolate deformation is stable against this nucleon because it does not follow the prolate rotating shape. Effects of mass are not reflected in the rotational spectra, because its interaction with the other nucleons depends on the laboratory frame densities and thus is almost independent of nuclear spin. Perhaps least affected is pairing, because such an orbital cannot block pairing in orbitals of higher asymptotic quantum number near the Fermi surface.

The author acknowledges with thanks the computer codes from R. Wyss, W. Nazarewicz and J. Dudek.

References

1. T. Byrski, F.A. Beck and D. Curien, *Phys. Rev. Lett.* **64** 1650 (1990).
2. W. Nazarewicz, P.J. Twin, P. Fallon and J.D. Garrett, *Phys. Rev. Lett.* **64** 1654 (1990).
3. J.K. Johansson *et al.*, *Phys. Rev. Lett.* **63** 2200 (1989).
4. F.S. Stephens, *Nucl. Phys.* **a520** 91c (1990).
5. F.M.H. Villars and N.C. Schmeing-Rogerson, *Ann. Phys.* **63** 443 (1970).
6. P. Ring and P. Schuck, *The Nuclear Many-Body Problem* (New York: Springer) (1980).
7. Contributed talk by N.C. Schmeing, on "A Factored Model for Identical Bands", summarized by D. Bes in *Strasbourg Workshop on Future Directions in Nuclear Physics with* 4π *Gamma Detection* (March 1991) to be published.
8. R.D. Amado, R. Bijker, F. Cannata, and J.P. Dedonder, *Phys. Rev. Lett.* **67** *2777* (1991).
9. W. Nazarewicz, R. Wyss and A. Johnson, *Nucl. Phys.* A **503** 285 (1989).

INTERNATIONAL CONFERENCE ON NUCLEAR STRUCTURE AT HIGH ANGULAR MOMENTUM

Ottawa

Session 8: Superdeformation in Nuclei (III)

SEARCH FOR SUPERDEFORMATION IN ^{144,145}Gd

T. Rzaca-Urban[a,b,1], R. M. Lieder[a], K. Strähle[a], S. Utzelmann[a], W. Gast[a], A. Georgiev[a,2], D. Kutchin[a], G. Martí[a,3], H. Schnare[a], K. Spohr[a,c], P. von Brentano[b], J. Eberth[b], M. Eschenauer[b], S. Freund[b], E. Ott[b], J. Theuerkauf[b], H. Wolters[b], K.O. Zell[b], K.H. Maier[c], H. Grave[c], C. Bach[c], J. Heese[c], H. Kluge[c], M. Schramm[c] and R. Schubarth[c]

[a] *Institut für Kernphysik, Forschungzentrum Jülich, Germany.*
[b] *Institut für Kernphysik, Universität Köln, Germany.*
[c] *Hahn-Meitner-Institut, Berlin, Germany.*

I Introduction

Theoretical calculations using the anharmonic oscillator-potential or the Woods-Saxon potential suggested that the best candidates for observing superdeformation ($\beta \approx 0.6$) occur around the mass A=150 region [1], [2]. Extensive experimental work followed these predictions and a number of nuclei in this region have been found to possess rotational bands characterised by a high moment of inertia and large quadrupole deformation ($\beta_2 \approx 0.6$). The neutron dependence of superdeformed (SD) bands has been studied very well for the chain of the GD isotopes. Discrete SD bands are known in $^{146-150}$Gd. In one of the SD bands in each of the nuclei ^{146,147,148}Gd a crossing has been established [3]. Furthermore, degenerate and average SD bands have been observed in these nuclei but proposed three diffrent configuration assignments cannot explain all experimental results [3]. Therefore it is very interesting to extend the systematics of SD bands in this region by searching for such bands in nuclei lighter than ^{146}Gd. The calculations predict that nuclei with neutron number N=80 (many SD bands has been found for Z=80) will be good candidates for possessing similar SD bands with deformation between 3:2 and 2:1 ($\beta_2 \approx 0.5$). There have been several attempts to find superdeformed structures in ^{144,145}Gd but to date without success [4], [5]. The purpose of the present experiments was to search for SD bands in these nuclei.

II Experimental methods

Two experiments have been performed to study these neutron deficient GD nuclei. The high-spin states of ^{144}Gd, ^{145}Gd were populated by the reactions ^{108}Pd(^{40}Ar,4n) at a beam energy of 182 MeV and ^{110}Pd(^{40}Ar,4n) at a beam energy of 189 MeV, respectively. The beam was delivered by the VICKSI accelerator of the HMI Berlin. The γ-rays were

[1] Permanent address: Warsaw University, The Institut of Experimental Physics,Poland
[2] Permanent address: Institute of Nuclear Research and Nuclear Energy, Sofia, Bulgaria
[3] Permanent address: Departamento de Fisca, CNEA, Av. del Libertador 8250 (1429) Bs. As. Argentina

measured with the OSIRIS spectrometer which consists of twelve Compton-suppressed Ge detectors and an inner ball of 48 BGO scintillators acting as a γ-ray multiplicity and sum energy filter. In both cases we used two-selfsupporting Pd foils with a thickness of $\approx$0.6 mm between them. For each event it was required that at least two Ge detectors and the inner ball had fired. We recorded γ-ray energies and times with respect to the beam burst for the Ge detectors and the fold and sum energy for inner ball.

III Experimental results

1. ^{110}Pd + ^{40}Ar reaction

In the analysis only events for which at least 17 detectors of the inner ball fired in prompt coincidence with the Ge detectors were considered. This condition enhances the relative yield of the highest-spin states by selecting the events with high γ-ray multiplicity. The final γ-γ coincidence matrix contained 10^8 events of which 47% were in the 5n reaction channel (^{145}Gd). The remaining events belong mainly to the 4n (^{146}GD - 30%), p5n(^{144}Eu - 8%), α4n(^{142}Sm - 12%) and α5n (^{141}Sm - 2%) channels. The analysis of the data revealed the presence of two bands of 8 coincident transitions with an average energy difference of 58 keV and 56 keV,respectively ie.consistent with the spacing expected for the superdeformed shape. They extend over an energy range from about 900 to 1300 keV. These bands

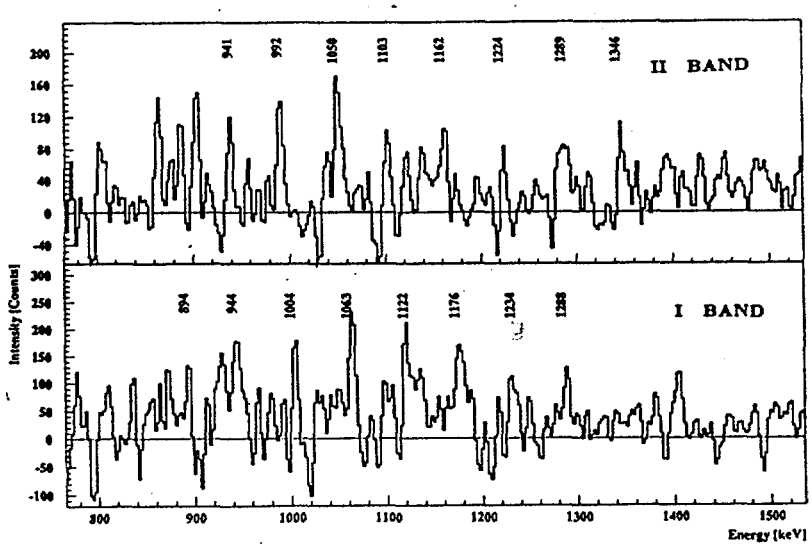

Figure 1: Summed coincidence γ-ray spectra for the two SD sequences observed in ^{110}Pd + ^{40}Ar reaction.

labelled I and II are shown in fig.1. The spectra were obtained by summing coincidence

gates on selected transitions. The two bands presented here are very weak and most of the transitions are contaminated by other lines of stronger intensity. Nevertheless the coincidence relationships between the various transitions in both bands have been verified from the analysis of coincidence spectra obtained from individual gating as well as from the observation of a regular grid pattern being expected in 2-dimensional γ-γ matrices for bands consisting of equally spaced transitions. We assign SD band I to ^{145}Gd because the spectra show the low-lying transitions in ^{145}Gd of 924, 1151, 1025, 1077, 778 keV but no transitions from other nuclei. For the SD band II convincing and exclusive coincidence relationships with low-lying transitions in ^{145}Gd could not be established from these data. The strongest line in the spectrum of 903 keV we could not place in any known nucleus populated in this reaction. A band with similar energies for the 1103 keV to 1288 keV transitons of SD band II has been identified recently in ^{142}Sm by Hackman et al. [6]. However below 1103 keV our transition energies differ from those reported by Hackeman at al. [6] indicating that two SD bands of transitions which are partly energetically degenerate might exist in different nuclei. The known SD bands in ^{146}Gd [3] were not seen in the data although all low-lying lines in ^{146}Gd were observed.

2. ^{108}Pd + ^{40}Ar reaction

In the analysis of this data set we have cut off all events which have a fold $\leq$18 or low sum energy. Only prompt events in a time window of 18 ns were accepted to reduce the background due to neutrons and isomeric decays. The resulting γ-γ correlation matrix contained 50x10^6 events of which 33% were in the 4n reaction channel (^{144}Gd). The remaining events belong mainly to the 3n(^{145}Gd), p3n(^{144}Eu), 5n(^{143}Gd), p4n(^{143}Eu), α2n(^{142}Sm), α3n(^{141}Sm) and α4n(^{140}Sm) channels. Searches for regularly spaced coincident transitions characteristic of superdeformed bands were made both by gating channel by channel and by using an automated search program which makes use of the regularity in the energies of coincident transitions. Two different weakly populated rotational bands have been identified. Most of the individual members of each of the band are masked by very strong cascades of transitions beteewn low-lying states. Fig.2 shows the resulting spectra for the two bands obtained by adding several coincidence spectra obtained by individual gating. Both of them are very weak with intensities of only $< 0.5\%$ of the 4n reaction channel. We assign tentatively these new bands to ^{144}Gd because the transitions in the bands are in coincidence with few low-lying transitions in ^{144}Gd. Strong contaminant transitions in ^{145}Gd and ^{143}Eu preclude a definitive assignment, although the known SD bands in ^{143}Eu [7] and ^{145}GD were not seen in the data.

IV Conclusions

One of open question regarding the A$\approx$150 SD region concerns the limits in both N and Z for which SD structures can be observed. From our new measurements on ^{144,145}Gd it is apparent that the SD bands observed in these nuclei are more weakly populated

than those in the heavier Gd isotopes. The observed decrease in the SD band population strength with decreasing nutron number for ^{144,145}Gd agrees very well with the data for

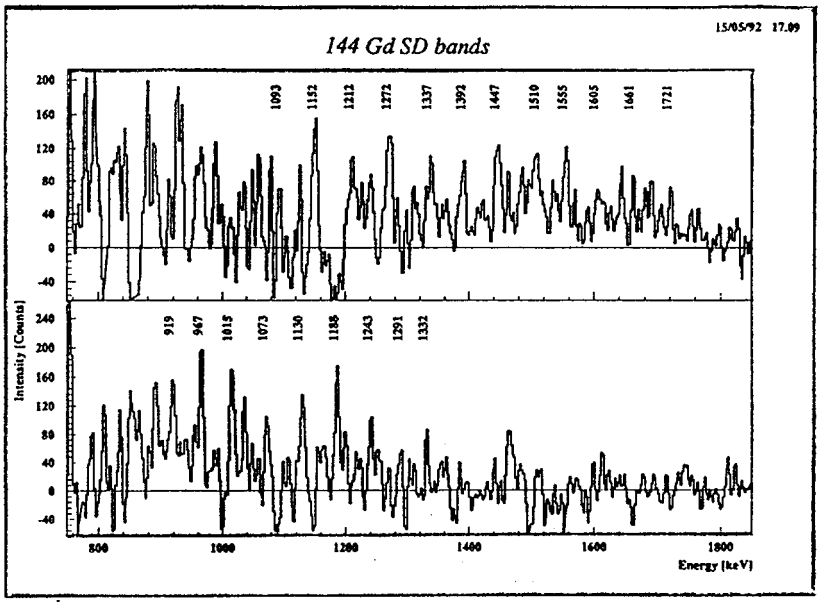

Figure 2: Summed coincidence γ-ray spectra for the two SD sequences observed in ^{108}Pd + ^{40}Ar reaction.

$^{146-149}$Gd obtained by Janzen et.al [8]. The latter results were obtained for roughly the same entry conditions. It was shown that the intensities of the bands varied from isotope to isotope. The intensities of the odd gadolinium isotopes appeared to be systematically higher than those in the neighbouring even ones. Moreover, the intensities of both even and odd isotopes tend to decrease almost linearly as the neutron number decreases. These results suggest that the lower limit of the SD region for Z=64 nuclei occurs at N$\approx$80. Due to the weak population of the γ-ray cascades under discussion and to many different exit channels for the reactions utilized, information concerning a possible band crossing behaviour in ^{144,145}Gd could not be obtained. Additional experimental information on SD bands in this region is needed.

References:

1. J. Dudek et al. Phys. Rev. Lett.,59(1987)1405
2. R.R. Chasman Phys. Lett.,B219(1989)227
3. R.M. Lieder et al. Prog.Part.Nucl.Phys. Vol 28,pp 225,1992
4. J.P. Vivien et al. Phys.Rev. C35(1987)348
5. Y. Schutz et al. Phys.Rev. C35(1987)348
6. G.S. Hackman et al. contribution to this conference
7. A. Atac et al. contribution to this conference
8. V. Janzen et al. Proc.Int.Conf. on High Spin Physics and Gamma-Soft Nuclei 1991

SEARCH FOR LOW SPIN SUPERDEFORMED STATES BY TRANSFER REACTIONS

J.Blons, D.Goutte, A.Leprêtre, R.Lucas, V.Méot, D.Paya and X.H.Phan
DAPNIA SPhN CE Saclay 91191 Gif sur Yvette, FRANCE

G.Barreau, T.P.Doan and G.Pedemay
CENBG, 33175 Gradignan, FRANCE

J.A.Becker and M.A.Stoyer
LLNL, Livermore, CA 94550 U.S.A.

Abstract

We present a specific experimental technique aiming to observe superdeformed isomeric states. Preliminary results on two proton transfer reaction on platinum targets leading to ^{194}Hg are shown.

All the recently discovered superdeformed (SD) rotational bands have in common to vanish before reaching the band head - the so-called isomeric state - but this is not a general feature. One has to remember that such isomeric states have been known for almost thirty years in the actinide region where nuclei decay by spontaneous fission, hence the name of fission isomers for these SD states. Thirty five nuclei are already known to present such an isomerism. The underlying physics can be expressed in the same way as for the SD rotational bands observed in the non-fissile nuclei, a stability of the nucleus at large deformation due to a double humped barrier in the potential energy surface.

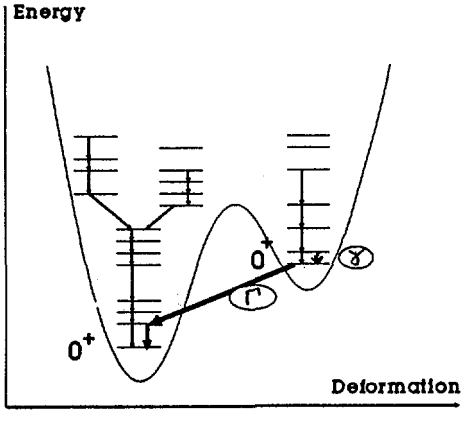

Figure 1 : Potential energy surface exhibiting a second well and an isomeric state. The measurement of "γ" or "Γ" will allow to study this isomeric state.

The question we want to address is to know wether such isomeric states exist in both SD regions, for fissile and non-fissile nuclei.
In the non-fissile regions, one could think about a superdeformation appearing only at high rotational frequencies stabilizing the deformation. In fact, on the basis of theoretical approaches describing SD states, this is the case in certain regions and not in others. For instance, microscopical HFB calculations (Ref Del89 and Bon90) are exhibiting a second well at high spin which disappears for spins lower than 20 ħ in the A = 150 region while it remains deep until the O^+ state in the A = 190 region.

The aim of the program we undertake at the Saclay Superconducting Postaccelerated Tandem is to reach and to study such isomeric states.

The experimental procedure.

All the SD bands observed up to now, have been populated by HI fusion-evaporation reactions, which means that the nucleus is formed at high excitation energy and at high spin.
From these high spin states, the compound nucleus decays within the SD band down to spin values about 20$\hbar$ (A=150 region) or 8$\hbar$ (A=190 region). During this cascade the transition intensity keeps constant until the end where the band depopulates very suddenly in a few transitions.
The idea of this program is to populate such SD bands by a different mechanism, namely few nucleons transfer reactions which should allow to feed the SD band at much lower spin and lower energy, hoping so to keep some intensity in the band until the shape isomeric state. In addition to that, such a technique allows to determine the excitation energy of the formed nucleus and consequently to obtain the position of the band which could not be measured so far.
Finally, such reactions allow to reach nuclei that HI fusion evaporation reactions cannot form as, for instance, neutron rich isotopes.

We bombard a target with a heavy ion beam, detect and identify the ejectile in a spectrometer and observe the gamma decays in a Germanium array surrounding the target.

Two ways for the observation of these isomeric states have been considered :

*the detection of a prompt coïncidence between the ejectile and a gamma ray connecting SD states ("γ" in figure 1)

*the detection of a delayed coincidence between the ejectile and the transition connecting this isomeric state to the normal states of the first well ("I" in figure 1).

The experimental set-up

The Superconducting Postaccelarated Tandem at Saclay delivers light to medium mass ions up to 10 MeV per nucleon. The beam pulse is 800 ps wide with a repetition rate of 13.5 MHz.

The particle detection system has in charge to :

*recognize precisely the ejectile ($\Delta N=1$, $\Delta Z=1$)

*measure its energy

*give a time start for the gamma-particle coïncidence

The ejected particles are analyzed in a QDDD spectrometer. A gas counter placed in the focal plane measures the energy loss (ΔE) of the particle as well as its position. Behind this chamber, the particles are stopped in a large plastic scintillator. The photolight is detected at both ends by phototubes connected to a mean timer system giving a very good time determination. The residual energy collected in this scintillator associated with the ΔE allows a precise particle identification (Fig. 2).

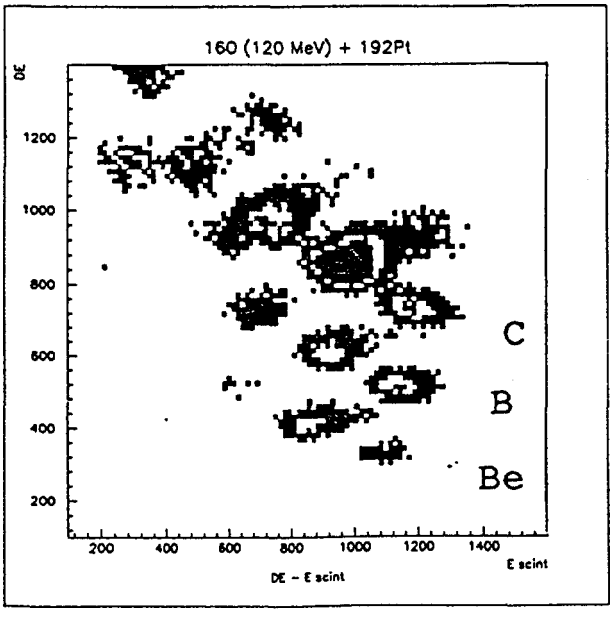

Figure 2 : E-ΔE map measured in the QDDD spectrometer focal plane

The gamma detector is composed of six triple-telescopes BGO Compton suppressed, surrounding the target. Each telescope is built with three germanium crystals: a planar with a 10% efficiency (to detect very small gamma energies down to X-rays) and two coaxials of 25% efficiency. These detectors can be used in various modes : in single mode where the first and last germaniums are used in anti-coïncidence with the central one, and in sum mode where the three energies are added.
The time coïncidence between the ejected particles and the gamma rays is shown in figure 3. With a specified particle the overall resolution reaches 15 ns (FWHM).
This coïncidence leads to a very drastic background rejection, typically a factor of 50 at 500 KeV.

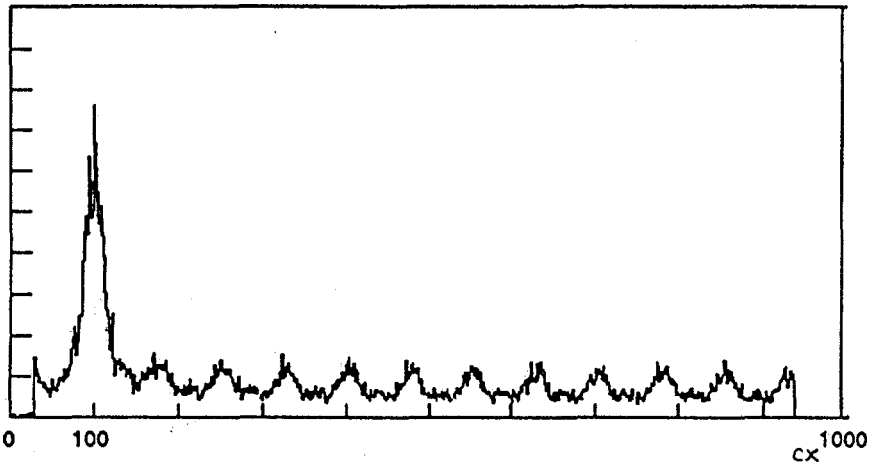

Figure 3 : Particle-gamma coïncidence timing.

Preliminary results

As a first guess we wanted to test if this reaction mechanism, namely few particles transfer reaction, populates SD states since neither shape isomer nor SD bands have been observed in such a way.
In order to do so, we first tried to observe the well known SD band in ^{194}Hg (Ref. Bea90)
We used the following reaction : ^{192}Pt(^{16}O,^{14}C)^{194}Hg at a beam energy of 120MeV. The QDDD spectrometer was positionned at 30°, and the target supplied by the LLNL had the following isotopical composition : ^{192}Pt : 57%, ^{194}Pt : 24%, ^{196}Pt : 8%.
With an average beam current of 20 nA we measured 10 particle gamma coïncidences per second. The highest spin state we were able to populate is 12^+.
Figure 4 shows the low part (E<1 MeV) of the six telescopes added up gamma spectra in coïncidence with ^{14}C. Part A corresponds to the full range of excitation energy of ^{194}Hg. In part B, at low excitation energy, we observe the ^{194}Hg spectrum and in part C, at high excitation energy, the ^{193}Hg shows up mainly because of a one neutron evaporation.
This demonstrates clearly that the direct transfer is not the only way to reach the nucleus of interest; transfer plus one neutron evaporation can be considered. Even more complicated reactions can be used : for instance, we also test the following reaction ^{194}Pt(16O,15C)^{194}Hg + n. In this case the counting rate is only two times smaller than in the direct two protons transfer reaction. Depending on the energy and spin one wants to reach, one or the other of these mechanisms has to be selected.

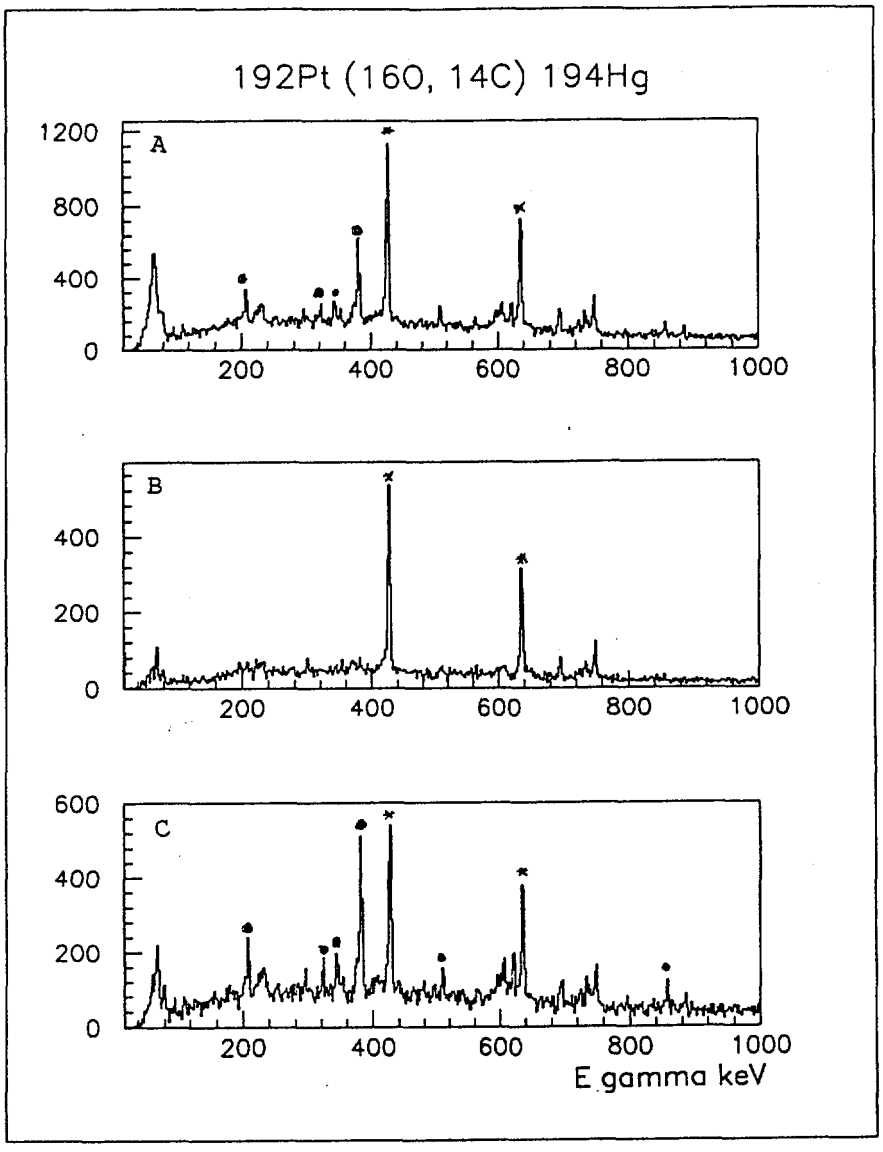

Figure 4: Gamma spectrum in coïncidence with the ejectile. Part A for the whole excitation energy range (E* =6 to 16 MeV). Part B for 6<E*<10 MeV. Part C for 10<E*<16 MeV.
(o = ^{193}Hg, x = ^{194}Hg)

The following spectrum (figure 5) is the sum of all the detectors without any background subtraction. The places where the SD transitions are expected to show up are indicated by arrows. Up to now there is no clear indication of SD tansitions. A complete analysis is in progress.

The future

The second type of procedure consists in observing the gamma transitions connecting these isomeric states to the first well. In fact, this was done a long time ago in the actinide region (Rus73) but again not with heavy ion transfer reactions.

We will, first try to see these transitions in ^{236}U and ^{238}U by neutron transfer reactions.

Following these different preliminary experiments, our program could develop in one of these two directions ("γ" or "Γ" of figure 1) to explore other nuclei which could not be formed by HI fusion evaporation reactions. We want, for instance to study the ^{210}Po with the following reaction : $^{209}Bi(^{12}C,^{11}B)^{210}Po$, as Po isotopes are predicted to present a well defined isomeric state at a quite high excitation energy (from 5 to 10 MeV) (Gir91, Pas90).

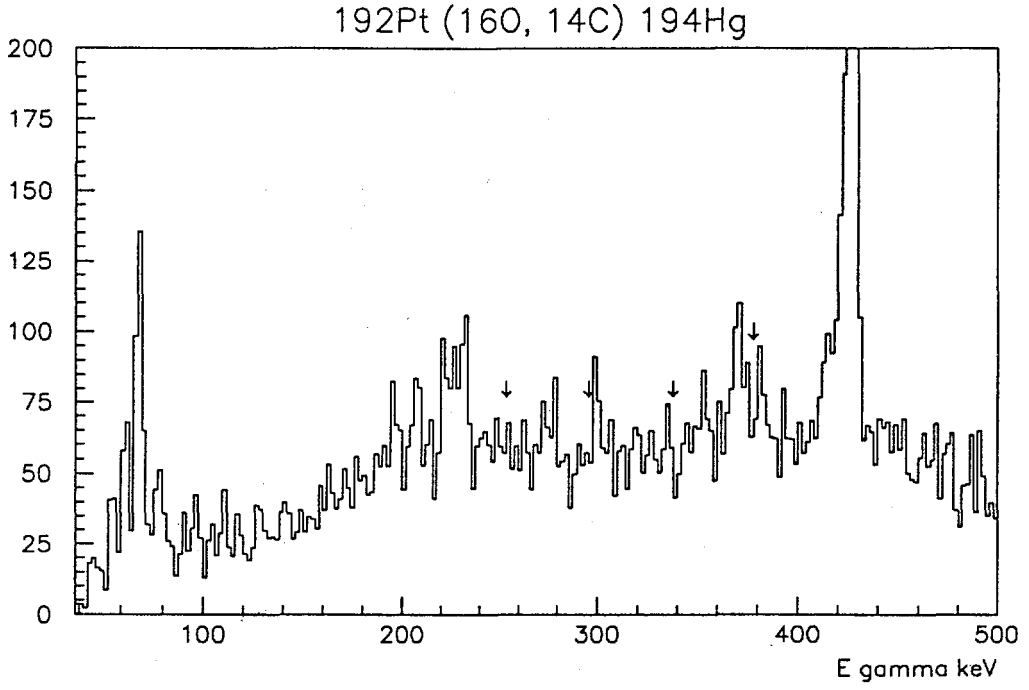

Figure 5 : Gamma spectrum showing the energies where SD transitions were seen (Ref Bea90)

Preliminary conclusion

The experimental set up is now working and the technical feasibility is demonstrated. Depending on the results of the first exploratory experiments we will conclude on the possibility of studying SD states by transfer reaction.

REFERENCES

Bea90	C.W.Beausang et al. Z. Phys. A, 335(1990)325
Bon90	P.Bonche et al., Nucl.Phys. A510(1990)466
Del89	J-P.Delaroche et al. Phys.Lett, B232(1989)145
Gir91	M.Girod, private communication
Pas90	V.Pashkevich Workshop on Microscopic Theories of Superdeformation May1990, Lyon, FRANCE
Rus73	P.A.Russo et al. Physics and Chemistry of Fission 1973 Rochester August 1973, page 271 IAEA Editor

A Superdeformed Band in ^{142}Sm

G.Hackman, S.M.Mullins, J.A.Kuehner, D.Prévost, J.C.Waddington
Dept. of Physics and Astronomy, McMaster University, Hamilton, ON L8S 4M1, Canada

A.Galindo-Uribarri, V.P.Janzen[1], D.C.Radford, N.Schmeing, D.Ward
AECL Research, Chalk River Laboratories, Chalk River, ON K0J 1J0, Canada

Abstract

Observation of γ-γ coincidences from the reaction ^{124}Sn(^{24}Mg,6n)^{142}Sm at 145 MeV indicates the existence of a rotational band with dynamic moment of inertia $\mathcal{J}^{(2)}$ similar to that of the superdeformed band in the isotone ^{143}Eu. This result is consistent with calculations predicting superdeformed structures in $N = 80$, $Z \sim 64$ nuclei.

Many nuclei in the mass regions $A \sim 135$ and $A \sim 150$ exhibit large quadrupole deformation at high spins. Calculations[1] predicted that a link between these islands of superdeformed stability would be observed in $N = 80$, $Z \sim 64$ nuclei as high-spin rotational bands with quadrupole deformation $\beta_2 \simeq 0.5$. The first of these bands was found in ^{143}Eu[2, 3][2]. Recently two bands were reported as candidates for superdeformation in ^{144}Gd[4].

A beam of ^{24}Mg at 145 MeV, provided by the TASCC facility at AECL Chalk River Laboratories, was directed upon two stacked self-supporting $\sim 400 \mu g/cm^2$ ^{124}Sn targets, and the γ rays were observed with the 8π spectrometer. The dominant reaction channels were fusion–evaporation by the 6n reaction to ^{142}Sm[5] and 7n to ^{141}Sm[6]. It was estimated that the 6n reaction would populate ^{142}Sm with an excitation energy of 40 MeV and a maximum angular momentum of $69\hbar$. Events were filtered off-line using a minimum H cut equivalent to a total γ energy of $\simeq$ 21 MeV. The γ–γ matrix contains 137 million events, of which the ratio of ^{142}Sm to ^{141}Sm is $\sim$ 12 : 1. Events leading to ^{142}Pm via p5n were limited to $< 0.5\%$ of the ^{142}Sm channel.

A series of at least twelve γ ray transitions from 800 to 1477 keV with a spacing of $\simeq$ 62 keV were observed in mutual concidence. The spacing of the transitions is similar to that of the band in ^{143}Eu, and is consistent with the decay of a deformed nucleus with $\beta_2 \simeq 0.5$. A sum of gates yields the spectrum in Figure 1, shown in comparison with the total projection spectrum. The BANDAID[7] code indicates

[1]Also McMaster University.

[2]Note: This band was previously assigned to ^{142}Eu in [2]; see [3] for clarification.

an additional transition at 1525 keV . Further band members at lower energy would be masked by strong lines coming from non-collective transitions in ^{142}Sm. The relative intensities of the band members are plotted in Figure 2. Of all events in the ^{142}Sm channel, 0.7% pass through the superdeformed band.

A plot of the $\mathcal{J}^{(2)}$ dynamic moment of inertia versus rotational frequency is shown in Figure 3, and compared to the $\mathcal{J}^{(2)}$ for the ^{143}Eu superdeformed band. The $\mathcal{J}^{(2)}$s are similar at lower rotational frequencies, but whereas the ^{143}Eu $\mathcal{J}^{(2)}$ remains constant, it decreases with increasing $\hbar\omega$ in ^{142}Sm.

Total Routhian Surface (TRS) plots[3] at selected spins for ^{142}Sm and ^{143}Eu are shown in Figure 4. For even-even nuclei like ^{142}Sm, the natural parity and signature (π,α) assignments are (+,0) or (−,1). However, the TRS plots predict that the superdeformed minimum for (π,α) = (−,0) is deeper and more localized. The ^{142}Sm $\beta_2 \simeq$ 0.5 minimum for the (π,α) = (−,0) configuration is calculated to be yrast for $I > 50\hbar$, whereas the ^{143}Eu superdeformed minimum is yrast at $I > 35\hbar$. Total energy plots by Werner and Dudek[8] suggest that superdeformed ^{142}Sm is yrast for $I > 60\hbar$.

Recently the reaction ^{124}Sn(^{23}Na,6n)^{141}Pm at 135 MeV was used to further investigate the $N = 80$ chain. Analysis is in progress.

Dr. R.A.Wyss is thanked for supplying the mesh for the TRS plots. The crew and staff at TASCC are thanked for supplying the beam. This work was supported by the Natural Sciences and Engineering Research Council of Canada (NSERC).

References

[1] W.Nazarewicz, R.Wyss, and A.Johnson, *Nucl.Phys* **A503** 285 (1989)

[2] S.M.Mullins, R.A.Wyss, P.Fallon, T.Byrski, D.Curien, S.A.Forbes, Y-J.He, M.S.Metcalfe, P.J.Nolan, E.S.Paul, R.J.Poynter, P.H.Regan and R.Wadsworth, *Phys.Rev.Lett.* **66** 1677 (1991)

[3] A.Ataç *et al*, contribution at the Erice summer school, Sicily, 1991, to be published in *Prog.Nucl.Part.Phys.* **Vol.28**, and elsewhere in these proceedings

[4] K.Strahle *et al*, elsewhere in these proceedings

[5] M.Lach, J.Styczen, R.Julin, M.Piiparien, H.Buescher, P.Kleinheinz, and J.Blomqvist, *Z.Phys.* **A319** 235 (1984), and *Nucl.Data Sheets* **63** 701 (1991)

[6] M.A.Cardona, G.de Angelis, D.Bazzacco, M.De Poli, and S.Lunardi, *Z.Phys.* **A340** 345 (1991)

[7] J.A.Kuehner, BANDAID code, unpublished

[8] T.R.Werner and J.Dudek, *Atomic Data and Nuclear Data Tables* **50** 179 (1992)

[3] Details of the code are in [1].

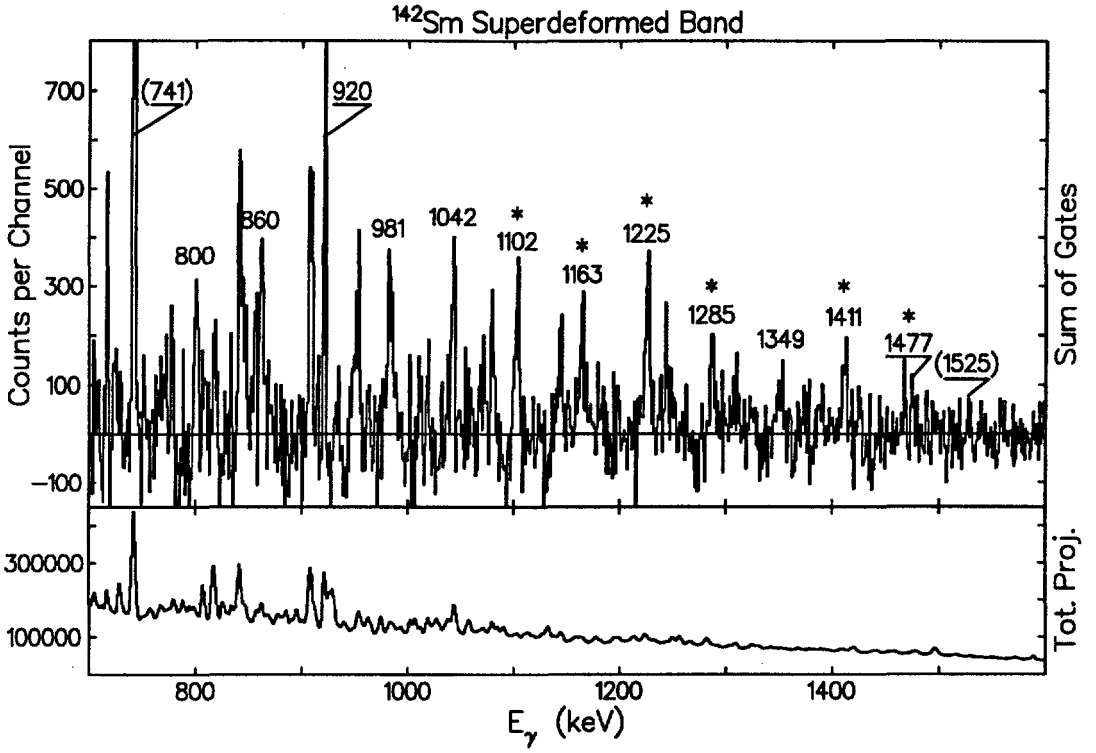

Figure 1. Sum of gates and total projection spectra. Labelled peaks are band members. Those marked with a * were included in the sum of gates. The 1525 is tentative, the 741 and 920 are contaminated by transitions in the noncollective regime.

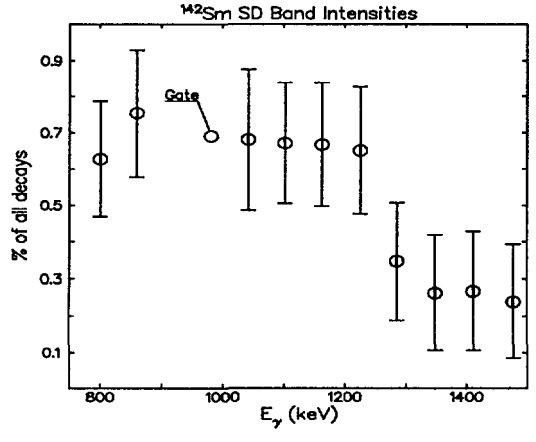

Figure 2. Intensities relative to ^{142}Sm channel, derived from the 981 keV gate. The 920 keV transition is omitted as it is heavily contaminated.

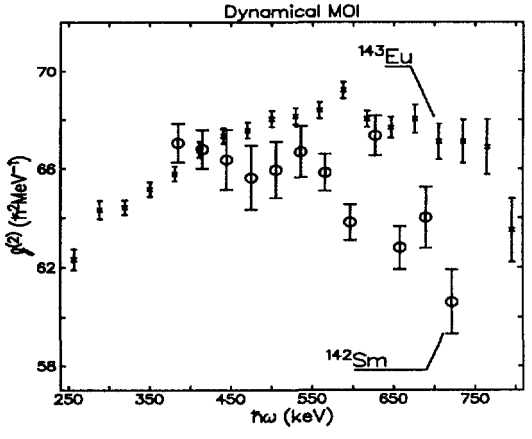

Figure 3. $\mathcal{J}^{(2)}$ dynamic moments of inertia for ^{142}Sm and ^{143}Eu.

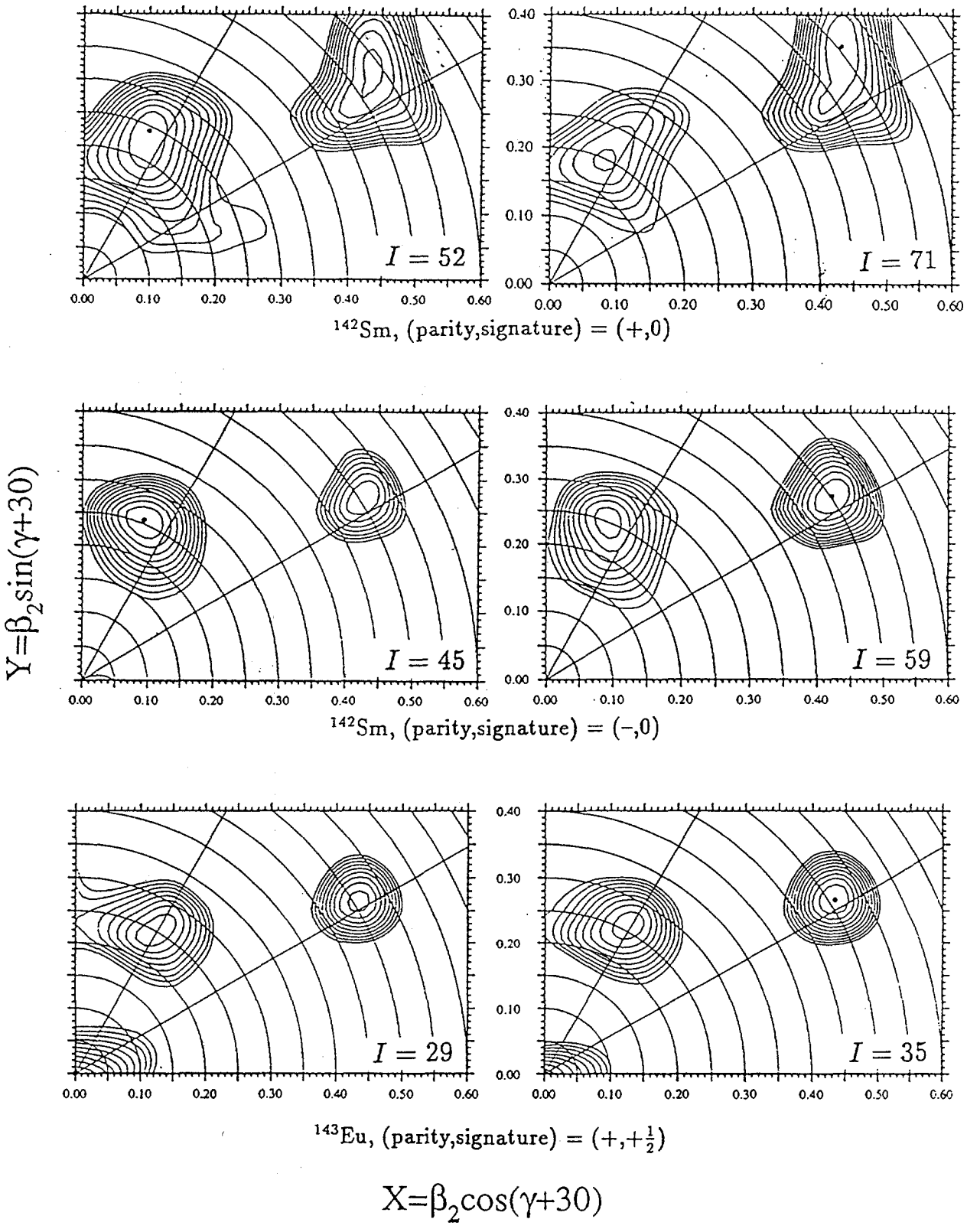

Figure 4. Total Routhian Surface (TRS) plots.

DOUBLE BLOCKING IN THE SUPERDEFORMED ^{192}Tl NUCLEUS

Y. Liang[1], M.P. Carpenter[1], R.V.F. Janssens[1], I. Ahmad[1], R. Henry[1], T.L. Khoo[1], T. Lauritsen[1], F. Soramel[1,2], S. Pilotte[3], J.M. Lewis[4], L.L. Riedinger[4], C.-H. Yu[4], U. Garg[5], W. Reviol[5], I.G. Bearden[6]

[1]Argonne National Laboratory, Argonne, IL 60439, USA. [2]On leave from Padova University, I-35131 Padova, Italy. [3]University of Ottawa, Canada, K1N 6N5. [4]University of Tennessee, Knoxville, TN 37831, USA. [5]University of Notre Dame, Notre Dame, IN 46556, USA. [6]Purdue University, West Lafayette, IN 47907, USA.

Abstract: Six superdeformed bands have been found in the nucleus ^{192}Tl. For two of the bands, the dynamic moment of inertia $J^{(2)}$ is found to be constant with the rotational frequency $\hbar\omega$. This result can be understood in terms of Pauli blocking of quasiparticle alignments in intruder orbitals, and represents the first experimental evidence that the alignment of these intruders is responsible for the smooth rise in $J^{(2)}$ seen in other superdeformed nuclei of this mass region.

One of the most intriguing aspects of superdeformed (SD) nuclei in the A = 190 regions is that the vast majority of SD bands displays a smooth pronounced increase of $J^{(2)}$ as a function of the rotational frequency $\hbar\omega$. The occupation of specific high-N intruders cannot account for this rise[1-4]. An explanation in terms of changes in deformation with $\hbar\omega$ has been ruled out from the available lifetime measurements[5]. It has been suggested that the combined quasiparticle alignments of a pair of N = 6 ($i_{13/2}$) protons and a pair of N = 7 ($j_{15/2}$) neutrons, and the resulting changes in pairing play an essential role in such a rise[3-7]. Experimental evidence for this alignment picture is at present circumstantial. Clearly, the study of the behavior of $J^{(2)}$ in the SD bands of an odd-odd nucleus should be particularly revealing. If both the odd proton and the odd neutron occupy the high-N intruder orbitals, the alignments should be blocked and, as a result, the moments of inertia should be constant with frequency. Here, we report on a study of ^{192}Tl where six SD bands have been located. Two of these bands are characterized by constant moments of inertia, thereby providing the first strong evidence that the alignment of quasiparticles occupying the high-N intruder orbitals indeed plays an essential role in the evolution of $J^{(2)}$ with $\hbar\omega$.

The states in ^{192}Tl were populated with the ^{160}Gd(^{37}Cl, 5n) reaction at beam energies of 178 and 181 MeV. The γ-γ coincidence data were recorded using the Argonne-Notre Dame BGO γ-ray facility consisting of 12 Compton-suppressed Ge detectors and an inner array of 50 BGO elements. A detailed analysis of the data revealed the presence of six superdeformed bands in ^{192}Tl[7]. Fig. 1 presents spectra for these bands. The bands are very weak and in some cases difficult to discriminate from contaminants, the coincidence relationships between the γ rays were also studied carefully by observations of regular grid patterns in the two dimensional γ-γ matrix using the code BANDAID[9,10]. For a few clean γ rays, multipolarity information obtained from angle-sorted matrices[11] indicates that the

transitions involved are of stretched E2 character. As some of the γ rays discussed here are close in energy to SD transitions in ^{191}Tl[12], care was taken to ensure that the assignment into ^{192}Tl is correct by checking that (1) the relative variation of the γ-ray intensities between the beam energies and (2) the fold distributions at each beam energy follow the pattern exhibited by the ^{192}Tl transitions. Finally, in analogy with the neighboring ^{191,193,194}Tl isotopes[12,13,14], these six bands can be grouped into three strongly coupled signature pairs (bands 1-2, 3-4, 5-6).

The dynamic moments of inertia for the six bands are presented as a function of the rotational frequency $\hbar\omega$ in fig. 2. From this figure, several observations can be made. First, it is clear that $J^{(2)}$ remains constant with $\hbar\omega$ for bands 3 and 4 (fig. 2a), while the other four SD bands display the more typical rise with $\hbar\omega$ (fig. 2b). Second, a comparison between the $J^{(2)}$ values for bands 3 and 4 and those of the odd-even neighboring nuclei ^{191}Hg (band 1)[4] and ^{191}Tl[12] (fig. 2a) indicates that, at the lowest frequencies, the value of $J^{(2)}$ is lower in the odd-even neighbors than in the two new SD bands. In order to understand these results, we have performed cranked shell model calculations with the Warsaw-Lund code which uses a Wood-Saxon potential[15] with the universal parameters given in ref. 16. While specific results depend on the deformation and the pairing gaps used, the following general conclusions can be drawn: (i) An alignment of an N=7 neutron pair, which is calculated to occur in ^{191}Tl (and ^{192}Hg) within $0.15< \hbar\omega <0.3$ MeV is blocked in ^{192}Tl (and ^{191}Hg) when the odd neutron occupies the second $j_{15/2}$ orbital involved. (ii) An alignment of a pair of N=6 protons is calculated to occur between $0.25< \hbar\omega <0.4$ MeV in ^{191}Hg (and ^{192}Hg). This alignment is also blocked in ^{192}Tl (and ^{191}Tl) when the proton occupies the third intruder $i_{13/2}$ orbital. (iii) At low values of $\hbar\omega$, our calculations show that the occupation of both the $\pi i_{13/2}$ and $\nu j_{15/2}$ orbitals will result in an additional contribution to $J^{(2)}$ with respect to the odd-even neighboring nuclei. The calculated value (107 $\hbar^2 MeV^{-1}$) for the double-blocked configuration discussed above, is also shown in fig. 2a, and agrees well with the data. On the basis of this discussion, we propose that bands 3 and 4 correspond to a configuration built on the favored (r=i) signature of the $\nu j_{15/2}$ orbital coupled to the two signatures (r=$\pm$i) of the $\pi i_{13/2}$ orbital, i.e., $\pi i_{13/2}(r=\pm i)\otimes\nu j_{15/2}(r=i)$. (It has been shown in ref. 4 that the unfavored (r=$-$i) signature of $\nu j_{15/2}$ orbital is located too high in energy to be observed experimentally.) In fact, the data on bands 3 and 4 represent the first case where constant values of $J^{(2)}$ have been observed in SD bands near A = 190.

The discussion above also serves as a starting point for the interpretation of the four other SD bands in ^{192}Tl. From fig. 2b it is apparent that the four bands all exhibit a rise in $J^{(2)}$ with $\hbar\omega$. Furthermore, this rise is similar to that seen over the same frequency range in the odd-even neighbors and is significantly smaller than that observed in the even-even ^{192,190}Hg nuclei. This suggests that only one pair of high-N intruders is aligning in these four ^{192}Tl bands. (This argument is also consistent with the observation that the $J^{(2)}$ values at the lowest frequencies are smaller here than in bands 3 and 4, as discussed above.) The

question then remains whether it is possible to identify the odd intruder particle as a proton or a neutron.

We propose that the four bands are associated with the intruder $\pi i_{13/2}[642]5/2$ configuration coupled to the lowest neutron excitation identified in ^{191}Hg (bands 2 and 3 in ref. 4) , i.e. the $\nu i_{11/2}[642]3/2$ orbital. This assignment is based on the following considerations. (1) Both pairs of SD bands show increasing signature splitting as a function of $\hbar\omega$ as expected for the $\pi i_{13/2}[642]5/2$ and $\nu i_{11/2}[642]3/2$ orbitals, and these splittings have been observed experimentally in the SD bands of ^{191,193}Tl[12,13] and ^{191}Hg[4]. (2) Recently, Stephens et al.[17] have proposed to compare SD bands near A = 190 by examining the evolution with $\hbar\omega$ of the incremental alignment Δi. Striking patterns of incremental alignment values cluster around Δ i = 1, +0.5, 0 over a wide $\hbar\omega$ range have been shown to occur, particularly when the SD bands being compared are characterized by configurations involving the same number of high-N intruder orbitals[1,13,14,18]. We have computed Δi values for the ^{192}Tl SD bands using ^{190,191,192}Hg and ^{191,193}Tl as possible references. Only when one of the ^{191}Tl SD bands[12] is the reference does Δi exhibit behavior of this type. We obtained Δi (band 2) $\simeq$ 0 relative to band 1 of ^{191}Tl, and Δi (band 5) $\simeq$ 1 relative to band 2 of ^{191}Tl over the entire $\hbar\omega$ range, respectively. This suggests that bands 2 and 5 share the same $\pi i_{13/2}$ (r=$\pm$i) intruder content as ^{191}Tl. Furthermore, the signature partners (band 1 and 6 respectively) show smoothly decreasing values of Δi with $\hbar\omega$ in analogy to that seen in SD bands associated with the $\nu i_{11/2}[642]3/2$ orbital in ^{191}Hg[4]. Thus, one of the two pairs of bands (1-2 or 5-6) corresponds to $\pi i_{13/2}[642]5/2$(r=i)$\otimes\nu i_{11/2}[642]3/2$(r=$\pm i$) configuration while the other is associated with the unfavored (r=$-$i) $\pi i_{13/2}$ partner coupled to the same neutron configuration. Unfortunately, the available data do not provide an unambiguous way to determine which of the pairs should be associated with the r=+i or the r=$-$i proton configuration.

It is worth pointing out that a similar classification can be proposed for the SD bands in ^{194}Tl of ref. 14. A pair of SD bands labeled as bands 3a & 3b in ref. 14, has a higher $J^{(2)}$ at low $\hbar\omega$ and displays a smaller rise with $\hbar\omega$. This pair is most likely associated with a configuration where the two odd particles occupy high-N intruder orbitals. The small rise in $J^{(2)}$ would then have to be the result of second order effects (such as small changes in deformation with $\hbar\omega$ and/or small changes in higher order pairing corrections....) The two other signature partner pairs (marked 1a & 1b and 2a & 2b in ref. 14) can then be understood as being based on the intruder proton configuration coupled to neutron excitations observed in the ^{193}Hg SD bands.

In conclusion, six SD bands have been found in ^{192}Tl. Two of these bands are characterized by a dynamic moment of inertia $J^{(2)}$ which remains constant with rotational frequency. This result can be understood within the framework of cranked shell model calculations with pairing as being due to Pauli blocking of high-N intruder orbitals. This is the first evidence that pairing is indeed carried to a large extent by these intruder orbitals in the SD nuclei near A = 190. Configurations have been proposed for all six SD bands. They involve proton

and neutron excitations which have been observed in the odd-even neighboring SD nuclei ^{191}Tl and ^{191}Hg.

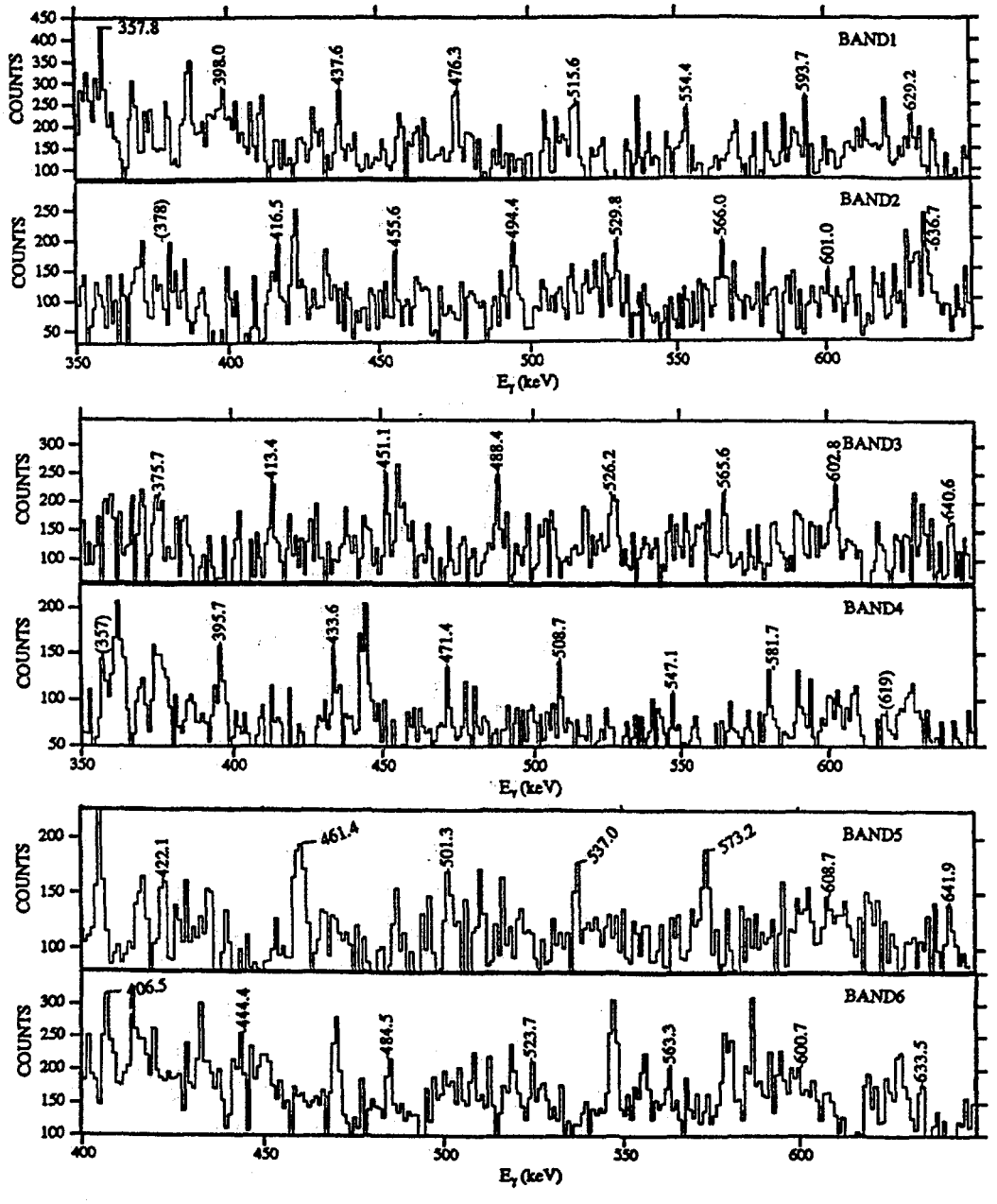

Figure 1: *γ-ray spectra obtained for the six SD bands in ^{192}Tl by summing cleanest coincidence gates. The SD band energies are indicated. The errors are on the order of 0.5 keV for the strongest transitions and up to 1 keV for the weakest γ rays. Transitions for which the placement is not certain are given in parenthesis. Several contaminants are also present in the spectra.*

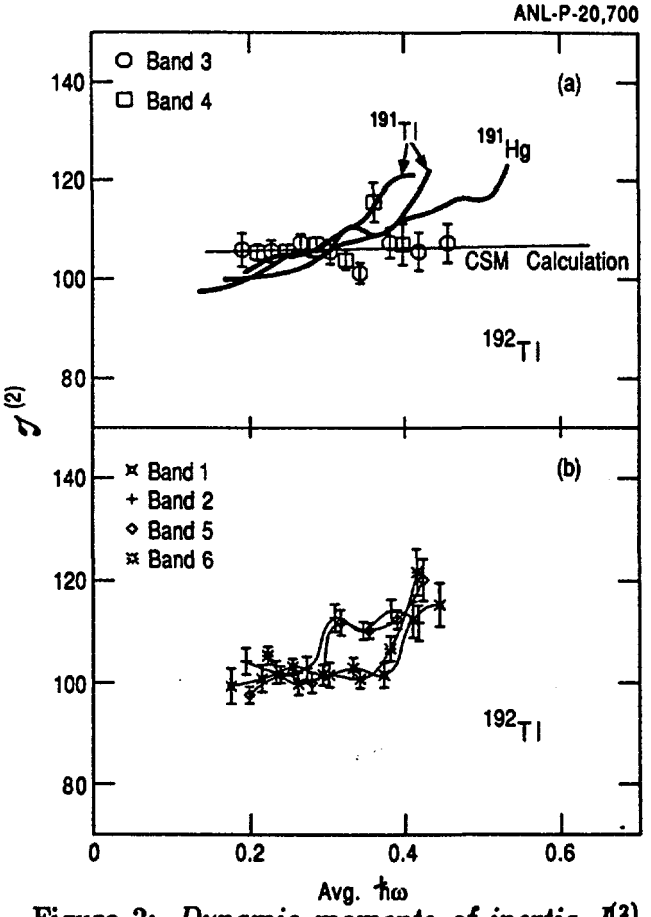

Figure 2: *Dynamic moments of inertia $\mathcal{J}^{(2)}$ for the six SD bands in ^{192}Tl. (a): the $\mathcal{J}^{(2)}$ values for bands 3 and 4 are compared with those of the two SD bands in ^{191}Tl[11] and with the first SD band in ^{191}Hg[4] (thick lines). The result of a cranked shell model calculation discussed in the text is given as the thin line. (b): dynamic moments of inertia for bands 1, 2, 5 and 6. The lines joining the points have been drawn to guide the eye.*

This work was supported by the Department of Energy, Nuclear Physics Division, under contracts W-31-109-ENG-38, DE-FG05-87ER40361 and by the National Science Foundation under grant PHY91-00688.

REFERENCES:

1. The topic has recently been reviewed by R.V.F. Janssens and T.L. Khoo, Ann. Rev. Nucl. Part. Sci. **41**, 321 (1991)
2. E.F. Moore et al., Phys. Rev. Lett. **63**, 360 (1989)
3. D. Ye et al., Phys. Rev. **C41**, R13 (1990)
4. M.P. Carpenter et al., Phys. Lett. **B240**, 44 (1990)
5. E.F. Moore et al., Phys. Rev. Lett. **64**, 3127 (1990)
6. M.A. Riley et al., Nucl. Phys. **A512**, 178 (1990)
7. R.R. Chasman, Phys. Lett. **B242**, (1990) 317
8. Y. Liang et al., to be published.
9. J.A. Kuehner, to be published
10. J.K. Johansson et al., Phys. Rev. Lett. **63**, 2200 (1989)
11. The technique is described in detail for the set-up in use here in M.W. Drigert et al., Nucl. Phys. **A530**, 452 (1991)
12. S. Pilotte et al., to be published
13. P. B. Fernandez et al., Nucl. Phys. **A517** 386 (1990)
14. F. Azaiez et al., Phys. Rev. Lett. **66**, 1030 (1991)
15. W. Nazarewicz, J. Dudek, R. Bengtsson, T. Bengtsson and I. Ragnarsson, Nucl. Phys. **A435**, 397 (1985).
16. J. Dudek, Z. Szymanski and T. Werner, Phys. Rev. **C23**, 929 (1981)
17. F. S. Stephens et al. Phys. Rev. Lett. **64**, 2623 (1990)
18. W. Satuła et al., Nucl. Phys. **A529**, 289 (1991)

INTERNATIONAL CONFERENCE ON NUCLEAR STRUCTURE AT HIGH ANGULAR MOMENTUM

Ottawa

Special Sessions on Nuclear Data Compilation

NUCLEAR DATA FOR THE HIGH-SPIN COMMUNITY

R.B. Firestone[†] and B. Singh[‡†]

[†] Isotopes Project, Lawrence Berkeley Laboratory, Berkeley, CA 94720
[‡] Tandem Accelerator Laboratory, McMaster University, Hamilton, Ontario L8S 4K1

The Isotopes Project is developing the Evaluated High-Spin Data File (EHSDF). This database is intended to help satisfy the needs of the high-spin community for up-to-date information. The EHSDF database is envisioned as a subset to the Evaluated Nuclear Structure Data File (ENSDF). ENSDF currently contains data on over 2700 rotational bands for nuclei with $45 \leq A \leq 254$. The database includes levels, transitions, and related information such as reduced transition probabilities, band parameters, and nuclear moments. Although the ENSDF database is not entirely up-to-date, it provides an excellent starting point for developing this new, more complete database. The Isotopes Project plans to assign one scientist to the task of updating the EHSDF database, standardizing the rotational band designations, and coordinating with the high-spin community to assure that its needs are met. We plan to compile all high-spin data within less than one-year of publication. A special effort will be extended, in collaboration with the high-spin research community, to obtain pre-publication information. Several high-spin databases, with varying degrees of completeness, have been compiled at other laboratories. We hope to bring those databases together with EHSDF to form a more complete file which can then be supported by the U.S. and international nuclear data programs. In addition, we will provide a repository where new, unpublished high-spin data can be collected. Researchers will be encouraged to FAX new information to the Isotopes Project computers where it can be distributed by FAX or E-mail to other researchers through our on-line services. The participation of members of the high-spin community in both developing the EHSDF file and providing data will be encouraged and greatly appreciated.

Access to the EHSDF database will be available through the Electronic *Table of Isotopes* (ETOI), described below. A prototype version of this computer program is available, on-line, at LBL. With this system users can search on level properties including rotational band information. Guest accounts for using the ETOI and other LBL databases can be obtained by contacting the Isotopes Project. A sample interactive session with the ETOI is given in the Appendix. In addition, a looseleaf collection of rotational band drawings, generated for the 8th edition of the *Table of Isotopes*, will be maintained and updated at LBL.

The Isotopes Project has been asked by the U.S. Department of Energy to develop an electronic nuclear data publication system to replace the *Nuclear Data Sheets*. Our goal is to provide flexible access to the ENSDF file tailored to a variety of potential users including the high-spin community. A variety of publications, databases, and computer software are planned at this time. The following products are currently under development.

• 8th Edition of the *Table of Isotopes*

Publication of adopted and decay data from the Evaluated Nuclear Structure Data File (ENSDF). This edition will contain decay scheme drawings, rotational band figures, abbreviated mass-chain decay-scheme drawings, tabular data, and appendices. It will be available as a bound volume (1993) or on computer media as PostScript files. Computer files will be continually updated and new editions will be published at about 5-year intervals.

• Electronic *Table of Isotopes*

A computer program providing easy access to ENSDF data on PC, Macintosh, and workstation computers. *Chart of the Nuclides* and *Periodic Table* graphical interfaces will provide "point and shoot" selection of data and "pull-down menus" to select ranges of level or transition properties for database searches. Data may be viewed in tabular or graphical (decay scheme) form, saved on disk, or printed. The ETOI program will provide application utilities for the calculation of conversion coefficients, log*ft*, Nilsson states, etc.; appendices on subjects such as the interaction of radiation with matter and nuclear structure; a nuclear structure reference library; and additional

databases of atomic masses, atomic properties, nuclear moments, and many other topics. A preliminary version of the ETOI will be available in 1992 and the first complete version is expected to be completed in 1994.

• Data Bases

In support of the projects outlined above, the Isotopes Project plans provide up-to-date databases for radioactive decay, high-spin, and ground-state/isomer properties. These databases will be evaluated at LBL in collaboration with associated research communities and are expected to become subset databases of ENSDF. Specialized publications from these databases will be developed.

• Nuclear Charts

Standard nuclear charts providing ground-state and isomer properties will be available in both color and black/white versions. Also, the computer code CHARTIST will be provided for preparation of user-designed charts. Several standard charts are currently available, and a preliminary version of CHARTIST has been released. This program was used for the preparation of charts published in *The IsoSpin Laboratory (ISL) Research Opportunities with Radioactive Nuclear Beams* report (LALP 91-51). A nuclear chart computer program, MacNuclide, developed in collaboration with C.A. Stone at San Jose State University, will be distributed in 1992. Similar chart programs are planned for use on IBM/PC and workstation computers.

• Nuclear Wallet Cards

A pocket-sized summary of ground-state and isomer data and other useful information. This publication was published at LBL in 1978 and subsequently by BNL in 1985 and 1990. It will be published yearly beginning in 1993.

• Nuclear CD-ROM

The Evaluated Nuclear Data File (ENDF), ENSDF, their manuals, the 8th edition of the *Table of Isotopes*, and Nuclear Structure References (NSR) will be available on CD-ROM. In addition, a broad selection of application software will be included on the disk. This computer medium offers one of the best, low-priced methods for the distribution of large databases. A demonstration CD-ROM with nearly 200MB of information has been prepared, and a test release of the Nuclear CD-ROM is expected planned for late 1992.

• FAX Data Services

Access to nuclear data will be available by FAX in 1993. Tabular data and level scheme drawings will be provided by sending a standard form to the Isotopes Project, by FAX, containing the desired data request. This request will be processed immediately and the desired information supplied by return FAX.

• On-line Data Services

The products described above will also be available on-line from the Isotopes Project computers. They will be accessible through networks and by computer links. In addition there will be a data registry service to provide users with automatic updates of desired information as it is entered into the system. A local on-line system has been in operation a LBL for about 6 years and currently provides access to ENSDF, ETOI, and several nuclear physics utility codes.

APPENDIX

SAMPLE INTERACTIVE SESSION WITH THE ELECTRONIC *TABLE OF ISOTOPES*

The following is a sample interactive session with the Electronic *Table of Isotopes*. Lines beginning with $ indicate the dialogue between the user and the program. This session was run on a VAXstation 3100 workstation where the computer response time was negligible. The retrieved band names and data are written as entered into ENSDF without necessary translation.

ELECTRONIC TABLE OF ISOTOPES

The Electronic Table of Isotopes supports on-line retrieval of nuclear data from a database derived primarily from the Evaluated Nuclear Structure Data File ENSDF which is maintained at the National Nuclear Data Center at Brookhaven National Laboratory. Data may be selected on the basis of nuclear properties such as A, Z, N, level energy, spin/parity, and half-life. Information is displayed in energy-ordered level tables and can be organized by rotational bands, reaction types, radioactive parents, and nuclear moments.

Comments about the Electronic Table of Isotopes may be sent by E-mail to RBF@LBL, FAX to (510)486-5757, telephone to (510)486-7646.

Enter carriage return to continue

Electronic Table of Isotopes (TOI) Version 0.2

Example 1: Search for all Even-A Dysprosium K=0 bands.

TOI Option Menu

```
------------------------------------------------------------------------
Level Search Options:
  (I)sotope name AAAZZ          (E)Energy range   0.0-99999.9 keV
  (A)Range of A  1-266          (J)Spin/parity
  (Z)Range of Z  0-109          (T)t1/2 range
  (N)Range of N  0-160          (#)Level sequence:  Level  1 + 999 levels
  (X)Reset to default seatch parameters
Display options:
  (1)Show Levels *
  (2)Show Levels and Gammas
  (3)Show secondary data
  (4)Write external file.  File:
  (5)Paginate output
------------------------------------------------------------------------
$ Enter option, (S)earch, (M)enu, (Q)uit, or (H)elp: Z
$    Enter Range Z-min, Z-max (or odd, even): 66 66
$ Enter option, (S)earch, (M)enu, (Q)uit, or (H)elp: A
$    Enter Range A-min, A-max (or odd, even): EVEN
$ Enter option, (S)earch, (M)enu, (Q)uit, or (H)elp: 2
$ Enter option, (S)earch, (M)enu, (Q)uit, or (H)elp: 3
$ Enter option, (S)earch, (M)enu, (Q)uit, or (H)elp: 5
$ Enter option, (S)earch, (M)enu, (Q)uit, or (H)elp: S
```

The following search types are available

(L)evel data
(R)otational Band data
(C)ross-referenced Reaction Data
(U)Magnetic moments
(D)ecay data

$ Enter selection, (M)enu, or (Q)uit: R

$ Enter search string (carriage return for all bands): K=0

1. 154DY K=0+ ground-state band.
2. 154DY K=0+ B-vibrational band.
3. 154DY K=0+ band.
4. 156DY K=0+ ground-state band, A=24.16 B=-0.197
5. 156DY K=0+ B-vibrational band, A=27.55 B=-0.346
6. 156DY K=0- band, A=6.956 B=0.0425
7. 156DY K=0+ band, A=12.88
8. 158DY K=0 BETA-VIBRATIONAL BAND
9. 160DY K=0+ GS BAND
10. 162DY K=0+ ground-state band; A=13.51, B=0.011
11. 162DY K=0- octupole-vibrational band including
12. 162DY K=0+ band; A=8.93, B=-0.0083
13. 162DY K=0+ band; A=11.31
14. 164DY K=0+; A=12.284, B=-0.0086
15. 164DY K=0-; A=8.28 IF B=0.
16. 164DY K=0+; A=9.4, B=0.12.
17. 164DY K=0+; A=12.2, B=0.08
18. 166DY K=0+; A=12.80, B=-0.0063
19. 166DY K=0+; A=9.8 IF B=0

$ Enter Band selection number, (L)ist, or (S)earch Menu: 1

154DY: K=0+ ground-state band.

E(Level)	JPI	t1/2	Levels in 154DY
0.0	0+	3.0E+6 y 15	
%α= 100			
334.58 8	2+	27.1 ps 23	
γ 334.6 1 (100) E2			
BE2W= 97 8			
747.01 11	4+	6.0 ps 7	
γ 412.4 1 (100) E2			
BE2W= 156 18			
1224.09 14	6+	2.31 ps 25	
γ 477.1 1 (100) E2			
BE2W= 199 21			
1747.83 16	8+	1.34 ps 24	
γ 523.8 1 (100) E2			
BE2W= 215 38			
2305.1 4	10+	1.2 ps 3	
γ 557.3 3 (100) E2			
BE2W= 179 45			
2894.3 6	12+	0.93 ps 19	
γ 589.2 5 E2			
BE2W= 173 35			
3510.2 7	14+	0.64 ps 15	
γ 616.0 4 E2			
BE2W= 200 46			
4174.6	16+		
γ 664.4			
4870.3	(18+)		
γ 695.6			

Example 2: Search for all superdeformed bands in database (defaults were reset).

The following search types are available

(L)evel data
(R)otational Band data
(C)ross-referenced Reaction Data
(U)Magnetic moments
(D)ecay data

$ Enter selection, (M)enu, or (Q)uit: R

$ Enter search string (carriage return for all bands): super

1. 104PD SUPERDEFORMED DELTA J=2 BAND BUILT ON A (24) LEVEL, SEE 88MA3
2. 152DY SUPERDEFORMED ROTATIONAL BAND
3. 164ER EVEN-SPIN YRAST SUPERBAND.
4. 165YB 5/2(523)+SUPERBAND
5. 165YB 5/2(642)+SUPERBAND
6. 166YB SUPER BAND
7. 166HF SUPER BAND

$ Enter Band selection number, (L)ist, or (S)earch Menu: 2

152DY: SUPERDEFORMED ROTATIONAL BAND

E(Level)	JPI	t1/2	Levels in 152DY
X	(22)		
3464+X	(32)	14 fs	
	γ 783.5 3 (100) E2		
	BE2W=2827		
4293+X	(34)	10 fs	
	γ 829.2 2 (100) E2		
	BE2W=2982		
5169+X	(36)	8 fs	
	γ 876.2 2 (100) E2		
	BE2W=2831		
6092+X	(38)	6.3 fs	
	γ 923.1 2 (100) E2		
	BE2W=2771		
7062+X	(40)	4.8 fs	
	γ 970.0 2 (100) E2		
	BE2W=2840		
8079+X	(42)	3.9 fs	
	γ 1017.0 2 (100) E2		
	BE2W=2760		
9143+X	(44)	3.1 fs	
	γ 1064.8 2 (100) E2		
	BE2W=2760		
10255+X	(46)	2.5 fs	
	γ 1112.7 3 (100) E2		
	BE2W=2747		
11416+X	(48)	2.0 fs	
	γ 1160.8 3 (100) E2		
	BE2W=2780		
12625+X	(50)	1.6 fs	
	γ 1208.7 3 (100) E2		
	BE2W=2839		
13881+X	(52)	1.3 fs	
	γ 1256.6 3 (100) E2		
	BE2W=2878		
15186+X	(54)	1.1 fs	
	γ 1304.7 3 (100) E2		
	BE2W=2819		
16539+X	(56)	0.9 fs	
	γ 1353.0 3 (100) E2		
	BE2W=2873		
17940+X	(58)	0.8 fs	
	γ 1401.7 4 (100) E2		
	BE2W=2709		
19389+X	(60)	0.6 fs	
	γ 1449.4 6 (100) E2		
	BE2W=3056		

INTERNATIONAL CONFERENCE ON NUCLEAR STRUCTURE AT HIGH ANGULAR MOMENTUM

Ottawa

SESSION 9: NUCLEAR SPECTROSCOPY (II)

NON-COLLECTIVE OBLATE STATES IN IODINE ISOTOPES AT HIGH SPIN

E.S. Paul[1], I. Ali[1], M.A. Bentley[2], A.M. Bruce[2], R.M. Clark[3], D.M. Cullen[1], P. Fallon[1] S.A. Forbes[1], D.B. Fossan[4], F. Hanna[1], J.R. Hughes[4], D.R. LaFosse[4], Y. Liang[5], R. Ma[6], P.J. Nolan[1], P.H. Regan[3], J. Simpson[2], H. Timmers[1], P. Vaska[4], R. Wadsworth[3], and M.P. Waring[4]

[1] *Oliver Lodge Laboratory, University of Liverpool, Liverpool L69 3BX, UK*
[2] *SERC Daresbury Laboratory, Daresbury, Warrington WA4 4AD, UK*
[3] *Department of Physics, University of York, Heslington, York YO1 5DD, UK*
[4] *Department of Physics, SUNY at Stony Brook, NY 11794, USA*
[5] *Argonne National Laboratory, 9700 S. Cass Ave., Argonne, IL 60439, USA*
[6] *Medical Department, Brookhaven National Laboratory, Upton, NY 11973, USA*

ABSTRACT

Competition between single-particle and collective modes of excitation has been observed in the odd-A $^{113-119}$I isotopes at high spin. The maximally-aligned $\pi[h_{11/2}\ g^2_{7/2}]_{23/2^-} \otimes \nu[h^2_{11/2}]_{10^+}$ non-collective $43/2^-$ configuration at γ=+60° is seen at similar excitation energies in these nuclei.

INTRODUCTION

Although iodine (Z=53) lies just above the Z=50 shell gap, the neutron-deficient isotopes exhibit well developed rotational structures. The dominant features observed in the odd-A nuclei are associated with the $[550]1/2^-$ "intruder" orbital from the bottom of the $\pi h_{11/2}$ subshell and the $[404]9/2^+$ "extruder" orbital (proton hole) from the top of the $\pi g_{9/2}$ subshell originating from below the shell gap. The occupancy of these orbitals is able to stabilise a sizeable prolate quadrupole deformation $\beta_2 \sim 0.25$.

At higher spin, competition between single-particle and collective degrees of freedom is the important factor that determines the nuclear structure. Indeed, non-collective "band termination" oblate states ($\gamma = +60°$, Lund convention) have been predicted to become yrast at spins around $24\hbar$ in xenon (Z=54) isotopes [1]. In these states the nuclear angular momentum is generated more efficiently by the alignment of valence particles outside closed shells rather than by the collective rotation of the whole nucleus. The valence nucleons reside in equatorial orbits which leads to an oblate density distribution about the spin axis, and consequently an oblate nuclear shape. Thus, at high spin the rotational level structure gives way to a more complex single-particle structure. Such effects were originally observed in ^{118,122}Xe [2,3] and the odd-A ^{121}I isotope [4,5]. New data is now available for

the lighter $^{113-119}$I isotopes which show similar effects.

EXPERIMENTS

Standard γ-ray spectroscopy experiments were performed at Daresbury, UK, and Stony Brook, USA. The following reactions were used: ^{58}Ni(^{58}Ni,3p)^{113}I (Eurogam26), ^{92}Mo(^{27}Al,2p2n)^{115}I (TESSA3), ^{94}Mo(^{27}Al,2p2n)^{117}I (SUNY), and ^{96}Zr(^{28}Si,p4n)^{119}I (TESSA3). Charged-particle–γ coincidences have also been measured for the ^{58}Ni + ^{58}Ni reaction at Chalk River to assist in the identification of ^{113}I [6].

RESULTS: ^{119}I

As an example, the high-spin level scheme of ^{119}I is presented in Fig. 1. The rotational band structure shown to the left is based on the prolate [550]1/2$^-$ intruder orbital from the bottom of the $\pi h_{11/2}$ subshell. The band undergoes an alignment between spins 39/2 and 51/2 which is attributed to $h_{11/2}$ neutrons and the rotational $\pi h_{11/2} \otimes [\nu h^2_{11/2}]$ band continues up to $I^\pi = 63/2^-$. The states shown to the right in Fig. 1 with spins between 39/2 and 49/2 are interpreted as non-collective oblate states where the nuclear angular momentum is generated from the sum of single particle spins of aligned valence nucleons rather than the collective rotation of the nucleus.

Fig. 2 shows the energy levels of ^{119}I minus a rigid-rotor reference plotted as a function of spin. The solid circles represent the rotational yrast band and show its evolution from the $\pi h_{11/2}$ configuration at low spin to the $\pi h_{11/2} \otimes [\nu h^2_{11/2}]$ configuration at high spin. The open circles represent the non-collective oblate states. Three states exist at 43/2$^-$ with the non-collective state lying lowest in energy. The other two states can be associated with rotational $\pi h_{11/2}$ and $\pi h_{11/2} \otimes [\nu h^2_{11/2}]$ configurations, respectively. The 45/2 non-collective state is also favoured compared to the rotational band. However, the 47/2 and 49/2 non-collective states exist at higher energy where the collective $\pi h_{11/2} \otimes [\nu h^2_{11/2}]$ configuration becomes yrast.

STRUCTURE OF THE OBLATE STATES

Both CSM (see Fig. 3) and TRS calculations suggest a maximally-aligned $\pi[h_{11/2}\, g^2_{7/2}]_{23/2^-} \otimes \nu[h^2_{11/2}]_{10^+}$ configuration at $\gamma = +60°$ for the favoured 43/2$^-$ state, shown to the right in Fig. 1. Several other states are seen above this non-collective 43/2$^-$ state in ^{119}I, while a lower 39/2$^-$ state is also seen. This latter state, which is yrast in ^{121}I, has been interpreted as involving the $h_{11/2}$ neutrons coupled to 8$^+$ rather than the maximum 10$^+$ [4]. The states above 43/2$^-$ are probably also built on non-collective configurations since they are connected by dipole transitions rather than electric quadrupoles expected for collective nuclear rotation. These higher non-collective states would involve the breaking of the $^{114}_{50}$Sn$_{64}$ core. Since the N=64 shell gap is much smaller than the Z=50 shell gap and rapidly disappears with increasing (oblate) quadrupole deformation, it is easier to

align further neutron pairs. Indeed, cranked shell model calculations have been performed and suggest the involvement of positive-parity neutrons. Hence, the higher non-collective states may be interpreted as seven aligned valence nucleons outside a ^{112}Sn core. The 45/2 and 47/2 states can be explained by promoting a neutron from the $\nu g_{7/2}$ subshell into the $\nu s_{1/2}$ subshell; the configurations are $\pi[h_{11/2} \otimes g^2_{7/2}]_{23/2^-} \otimes \nu[h^2_{11/2} \otimes g^{-1}_{7/2} \otimes s_{1/2}]_{11^+,12^+}$, respectively. Similarly, a $\pi[h_{11/2} \otimes g^2_{7/2}]_{23/2^-} \otimes \nu[h^2_{11/2} \otimes g^{-1}_{7/2} \otimes d_{3/2}]_{13^+}$ configuration could explain the non-collective 49/2 state. As can be seen in Fig. 2, these non-collective states compete with the rotational states associated with the $\pi h_{11/2} \otimes [\nu h^2_{11/2}]$ configuration which are strongly favoured at high spin.

IODINE SYSTEMATICS

The systematics of the rotational $h_{11/2}$ bands and non-collective oblate states in odd-A $^{113-121}$I are shown in Fig. 4. The maximally-aligned $43/2^-$ state is seen at similar excitation energies in all isotopes. In addition, a non-collective $39/2^-$ state is observed in $^{117-121}$I. The $39/2^-$ state is especially favoured in ^{121}I, lying only 392 keV above the rotational $35/2^-$ state [4]. In $^{117-119}$I the non-collective $39/2^-$ state lies slightly above the rotational $39/2^-$ state, but is not seen in the lightest isotopes. There is also evidence for band termination in doubly-odd ^{116}I, which was obtained as a by-product of the ^{115}I data. The rotational structure breaks down at spin $I \sim 23$, as expected for a structure related to the $43/2^-$ states in the odd-A iodine isotopes.

CONCLUSIONS

While evidence for non-collective oblate states has been found in the neutron-deficient iodine (Z=53) isotopes, no such states have been identified in neighbouring odd-Z antimony (Z=51) or caesium (Z=55) isotopes. For example, $\pi[550]1/2^-$ bands in the $^{111-115}$Sb nuclei maintain their collective character to much higher spins than observed in the iodine nuclei. Furthermore, non-collective oblate states have been identified in xenon (Z=54) isotopes while searches in barium (Z=56) isotopes have proven unsuccessful. These observations may be related to extra oblate stability caused by an oblate shell gap which occurs for Z=54 in calculations based on a Woods-Saxon single-particle potential.

The CSM calculations of Fig. 3 indicate a deep minimum at $\gamma = -120°$ associated with a $g_{9/2}$ proton. Therefore, non-collective prolate band termination may also be possible involving configurations of the type $\pi g_{9/2} \otimes [\nu g^2_{7/2}]$ or $\pi g_{9/2} \otimes [\nu g_{7/2} h_{11/2}]$. Such prolate termination states may be observed at high spin in the collective oblate ($\gamma = -60°$) structures recently established in several odd-A iodine isotopes [7].

[1] R. Wyss Ph D thesis, Manne Siegbahn Institute of Physics, Stockholm (1990)
[2] S. Juutinen et al., Z. Phys **A338**, 365 (1991)
[3] J. Simpson et al., Phys. Lett. **262B**, 388 (1991)
[4] Y. Liang et al., Phys. Rev. C **44**, R578 (1991)

[5] Y. Liang et al., Phys. Rev. C **45**, 1041 (1992)
[6] V.P. Janzen et al., private communication
[7] Y. Liang et al., Phys. Rev. Lett. **64**, 29 (1990)

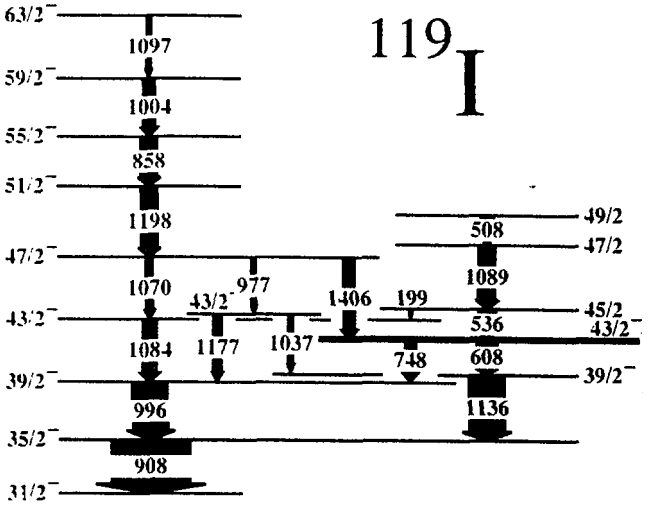

Fig. 1 *Partial level scheme of* ^{119}I *above* $I^{\pi} = 31/2^{-}$. *The non-collective yrast* $43/2^{-}$ *state is indicated by the thicker level.*

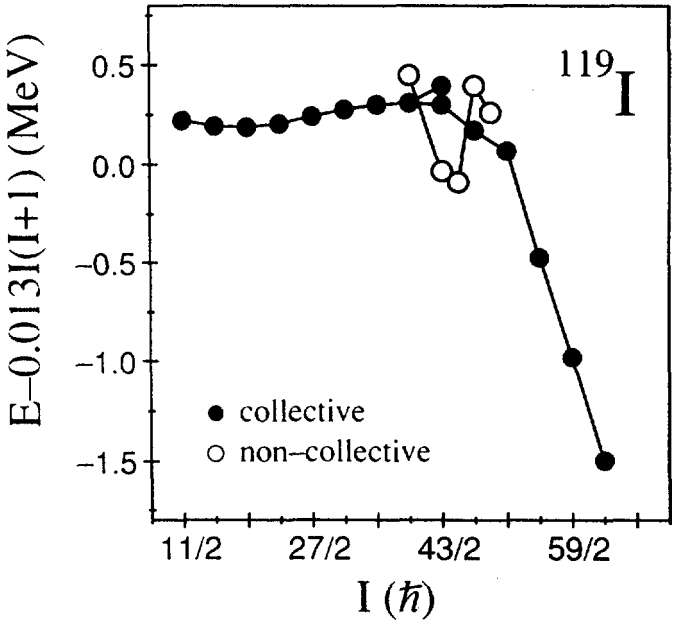

Fig. 2 *Energies of the states in* ^{119}I *minus the energy of a rigid-rotor plotted as a function of spin.*

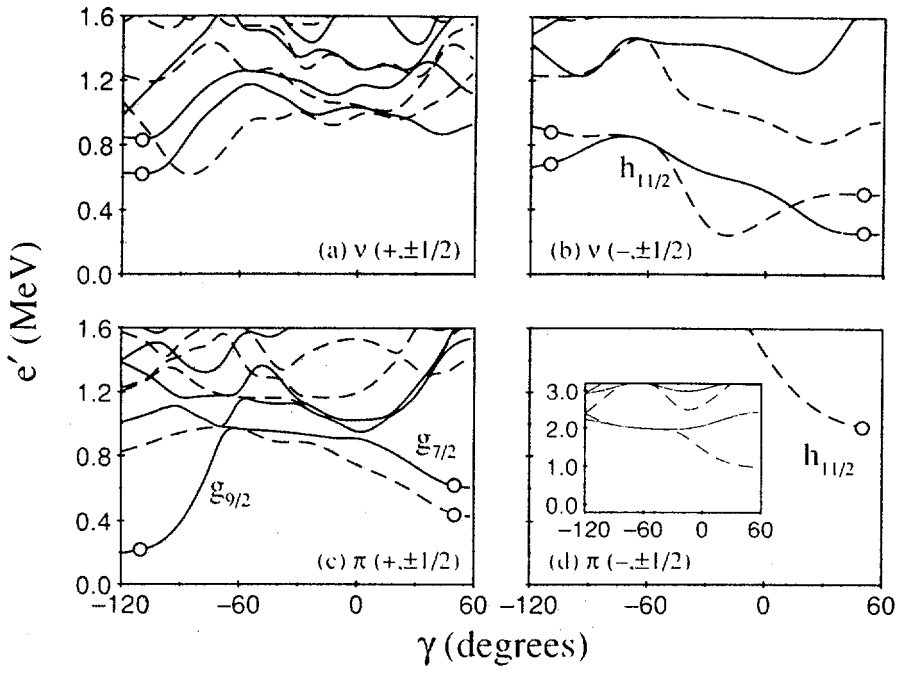

Fig. 3 *CSM single-quasiparticle levels for neutrons (a and b) and protons (c and d). Full lines indicate levels with parity and signature* $(\pi, \alpha) = (\pm, +1/2)$*; dashed lines indicate levels with* $(\pm, -1/2)$*. The oblate* $43/2^-$ *configuration at* $\gamma = +60°$ *is indicated by the open circles. Non-collective prolate configurations are similarly indicated at* $\gamma = -120°$*.*

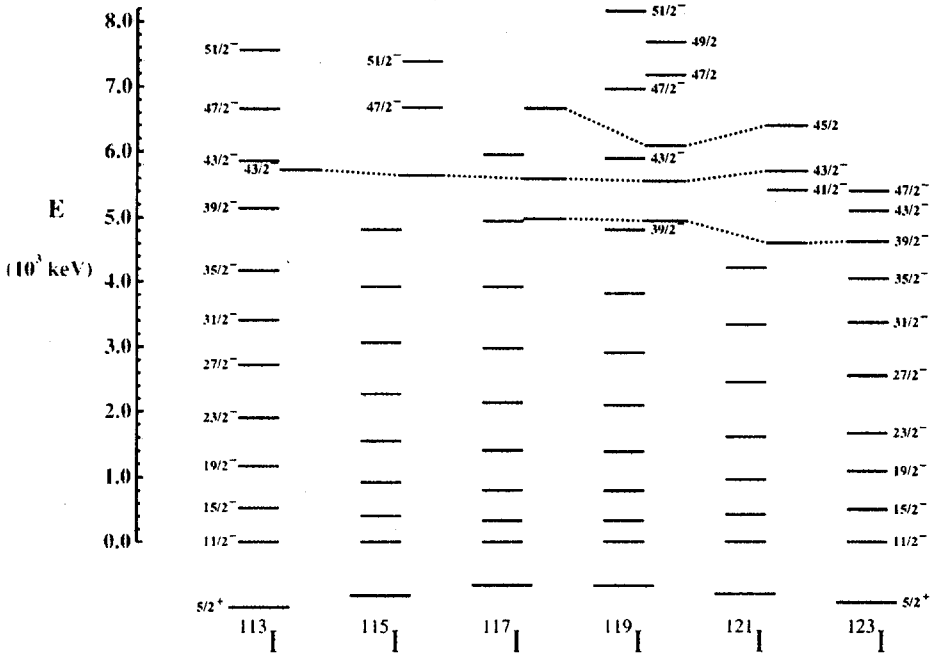

Fig. 4 *Systematics of the rotational yrast bands and non-collective oblate states in the odd-A* $^{113-121}I$ *isotopes.*

Two- to One-Phonon E3 Transition Strength in ^{148}Gd

M. Piiparinen[1,2], P. Kleinheinz[3], J. Blomqvist[4], A. Virtanen[2], A. Ataç[1], D. Müller[2], J. Nyberg[1], T. Ramsøy[1], G. Sletten[1]

[1] *Niels Bohr Institute, Tandem Accelerator Laboratory, Roskilde, Denmark*
[2] *Department of Physics, University of Jyväskylä, Jyväskylä, Finland*
[3] *Institut für Kernphysik, Forschungszentrum Jülich, Jülich, Germany*
[4] *Manne Siegbahn Institute, Stockholm, Sweden*

Abstract: *In a plunger experiment the mean life of the $(\nu f_6^2 \times 3^- \times 3^-)12^+$ state at 3.981 MeV in $^{148}_{64}Gd_{84}$ was measured as τ=83(10)ps, giving 77(11)B_W for the 1286 keV $12^+ \rightarrow 9^-$ E3 transition rate, which confirms the double-octupole character of the 12^+ state. The observed deviations in energy and transition rate from harmonic vibration are shown to be caused by the exclusion principle acting between nucleons in the two phonons and are related to the dominant contributions to the ^{148}Gd octupole phonon of the low-lying $\Delta\ell=\Delta j=3$ proton- and neutron in-shell 3^- excitations which are of vital significance for the octupole mode in open-shell nuclei.*

The statement from 1975 *"Although, at present, there is only little evidence concerning anharmonic effects in the octupole mode, these effects are potentially of considerable interest"* [1] can also form an adequate summary of the present situation. Although some experimental data have been obtained [2–10] in the intervening years, the evidence is still fragmentary, and no clear picture of the degree of harmonicity of nuclear octupole vibrations has emerged.

In the radium ($Z \sim 88$, $N \sim 134$) and barium ($Z \sim 56$, $N \sim 90$) regions the existence of low $K^\pi=0^-$ bands in even-even nuclei, and other evidence, suggest [11] that these quadrupole-deformed nuclei are soft with respect to octupole shape changes. On the other hand, in spherical doubly-closed-shell regions around ^{56}Ni, ^{100}Sn, ^{132}Sn and ^{208}Pb one expects that the octupole vibrations are nearly harmonic, since the 3^- phonon is built from a large number of particle-hole excitations between well separated single-particle orbits. This contrasts with the situation for the 2^+ quadrupole mode in open-shell nuclei, where the phonon is built from a few low-energy excitations within a major shell. The quantitative analysis of the quadrupole mode within the framework of the interacting boson model shows that the interactions in general produce large anharmonic effects.

Quantitative information about anharmonic characteristics can most directly be derived from the properties of two-phonon states, such as energies and transition rates. For the octupole mode in the harmonic limit the two-phonon states should form a degenerate 0^+, 2^+, 4^+, 6^+ multiplet at twice the energy of the one-phonon state, and the $E3$ transition rates to the one-phonon state should be twice that from the one- to zero-phonon state.

Attempts to identify two-phonon octupole excitations in nuclei have proven to be exceedingly difficult. One reason for this is that in deexcitation of the two-phonon states unspecific low-multipolarity radiation can dominate such that the configuration-specific $E3$ transitions cannot be observed. Some time ago the first case of a two-phonon octupole state in an even-even nucleus was identified [7,10] in $^{148}Gd_{84}$ through observation of a $12^+ \rightarrow 9^- \rightarrow 6^+$ stretched double $E3$ cascade, where the 6^+ basis state is the maximum-spin coupling of the two valence neutrons in the $f_{7/2}$ orbit. The experimental energy ratio $(E_{12^+} - E_{6^+})/(E_{9^-} - E_{6^+}) = 2.45$ deviates considerably from the harmonic value of 2. A major reason for this deviation has been traced [7] to the effect of Pauli blocking on the large proton $h_{11/2}d_{5/2}^{-1}$ component in the phonon.

From the 17 ns half life measured in these experiments for the 9^- level, significant collectivity of the $9^- \rightarrow 6^+$ one- to zero-phonon transition was established, but the $12^+ \rightarrow 9^-$ two- to one-phonon $E3$ strength could not be determined since 97% of the 12^+ level decay proceeds through an $E1$ transition, which suggested a level half life of about 100 ps. We have now determined this half life in a plunger experiment using the Nordball multi-detector array at the Niels Bohr Institute Tandem accelerator.

The measurement is quite difficult since several ^{148}Gd levels above the 12^+ double-octupole state have life times of comparable magnitude. In fact an earlier attempt [10] to measure the 12^+ half life using the (^{28}Si,4n) reaction failed due to this reason since here the major population intensity proceeded through the 6.835 MeV 1.5 ns 20^- isomer. In order to optimize the side feeding close to the 12^+ state the present experiment was carried out using the ^{133}Cs(^{19}F,4n) reaction with a 73.5 MeV ^{19}F beam. At the target this beam energy gave an average reaction energy of 70 MeV which is essentially at the Coulomb barrier. The schematic ^{148}Gd level scheme of Fig. 1 gives the feeding intensity distribution in the present measurements. The target was prepared by evaporating a 1.3 mg/cm^2 thick layer of undissociated natural CsJ on an 800 μg/cm^2 gold backing, and a 6 mg/cm^2 gold foil was used as a stopper. Both were stretched in normal plunger manner. Data were taken at 10 distances ranging from 20 to 3000 μm.

The γ-ray spectra were measured with the Nordball array consisting of 20 Compton-suppressed Ge-detectors positioned in four conical rings of five detectors each, viewing the target at 37° and 79° to the beam direction in the forward and backward hemisphere. The plunger spectra were recorded in the two 37° detector rings; for coincidence gating all 20 Nordball detectors were used. Setting gates on the nine intense ^{148}Gd transitions emitted in decay of the 17 ns 9^- isomer gave highly clean spectra for the ^{148}Gd γ-rays in the region of interest, free from transitions in ^{142}Sm and other reaction channels. These ^{148}Gd data were then analysed in the standard manner of singles plunger data where in a global fit the decay-time results measured for all individual transitions are compared with the respective theoretical function for the pertinent portion of the decay chain. The experiment gave individual decay-time data for the seven stronger transitions underlined in Fig. 1 which, together with measured intensities, were the principal input data for the fit. Additional decay branches [10] involve transitions that are too weak to obtain meaningful timing data, but their measured intensities together with the associated decay properties were included in the experimental decay chain. In the analysis the side feeding intensity to each level was represented by two components with different effective feeding times which were fitted as free parameters. As an example, the Fig. 2 shows the fit to the decay time data for the 279 keV $12^+ \rightarrow 11^-$ transition. The data sets of the two independent measurements from the forward and backward detector rings were analysed separately and gave the results $\tau_{143°}(12^+, 3.981\ \text{MeV}) = 85.0(49)$ ps, with $\chi^2 = 3.6$, and $\tau_{37°}(12^+, 3.981\ \text{MeV}) = 82.1(42)$ ps, with $\chi^2 = 2.8$, where the statistical errors are quoted. A characteristic property of the fit to the data are slow side-feeding components for most of the levels. This is in accord with other plunger studies [12], where also side-feeding times comparable to the typical level half lives under study are found. We investigated the stability of the fit against variations of the side-feeding times which probably represent the largest contribution to the systematic error. From the two above determinations we adopt

$$\tau(12^+, 3.981\text{MeV}) = 83(10)\ \text{ps}$$

where the increased error covers our estimated systematic uncertainties.

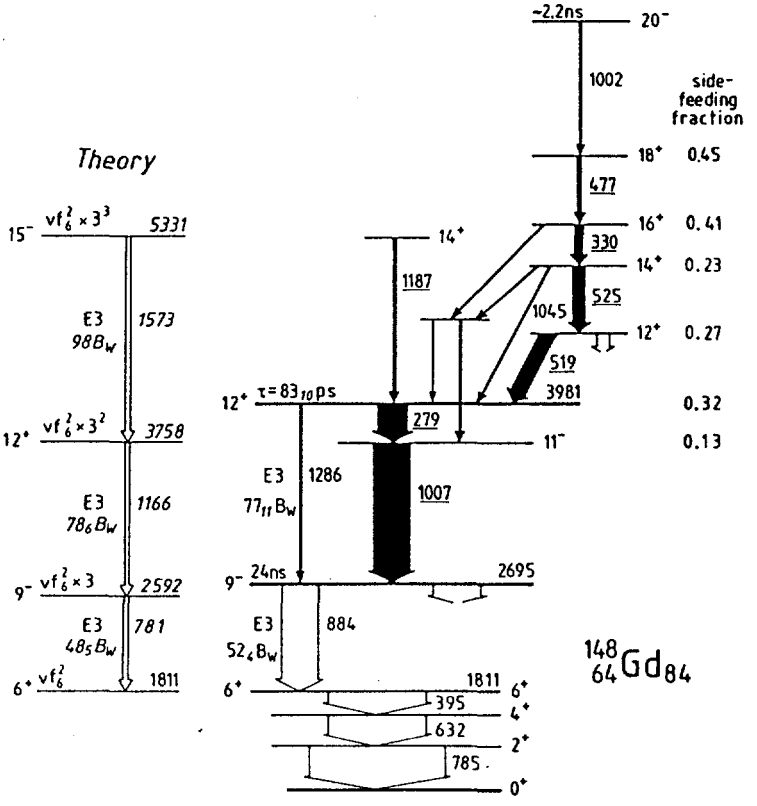

Fig. 1. *Schematic partial level scheme of ^{148}Gd as observed in the present experiments. The filled γ-transitions were included in the decay time fit, individual timing data were obtained for the underlined γ's. Transitions without energies are symbolic and represent the inclusion in the fit of complex known weak branches. The theoretical results of a parameter-free calculation are from Ref.[10].*

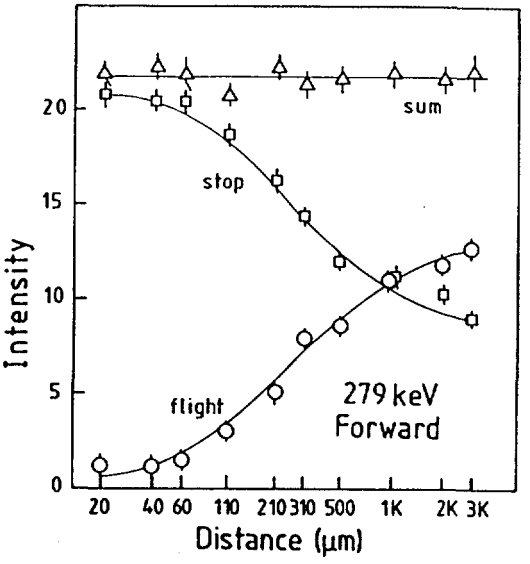

Fig. 2. *Decay time fit to the plunger data for the 279 keV 12^+ to 11^- transition measured in the 5 forward detectors at 37° to the beam direction.*

The important 1286 keV $E3$ to 279 kev $E1$ intensity ratio was not well determined from the previous experiments [10,13]. We therefore made a separate measurement with a backed target to stop the recoiling nuclei, and using 76 MeV beam energy which significantly increased the ^{148}Gd production cross section. From these data we extract the 1286 keV $E3$ decay branch as 2.8(2)%. Also for the 884 keV $E3$ decay branch from the 2.695 MeV 9^- level these new data gave a more accurate value, of 39(3)%, giving the one- to zero-phonon transition rate as

$$B(E3, 9^- \rightarrow 6^+, 884 \text{ keV}) = 68(5) \cdot 10^3 \text{ e}^2\text{fm}^6 = 52(4)\ B_W.$$

For the two- to one-phonon $E3$ strength we obtain

$$B(E3, 12^+ \rightarrow 9^-, 1286 \text{ keV}) = 100(14) \cdot 10^3 \text{ e}^2\text{fm}^6 = 77(11)\ B_W.$$

This is the fastest observed nuclear $E3$ transition. It firmly characterises the 3.981 MeV 12^+ state of ^{148}Gd as a two-phonon octupole excitation.

The ^{148}Gd 12^+ two-phonon state deviates markedly from harmonic vibration where it should have twice the energy and double the $E3$ strength of the one-phonon state. While the energy of the 12^+ state was already known to be considerably higher than the harmonic value, we have now established that also the transition rate, $B(E3, 12^+ \rightarrow 9^-)/B(E3, 9^- \rightarrow 6^+) = 1.48(24)$, deviates significantly from harmonicity.

Such double-phonon anharmonicities have been a subject of intense theoretical discussion. One simple physical phenomenon that can contribute to the anharmonicity is the coupling of the two phonons through their multipole moments, in particular the quadrupole moments [14]. This interaction lowers the energy of the two-phonon $(3^- \times 3^-)6^+$ coupling. The effect was so far only discussed for ^{208}Pb, where the 3^- quadrupole moment has been measured [15], but here the 6^+ two-phonon energy is still unclear. Other elementary contributions to the anharmonicity are of quantal nature. One particular effect [6] effect can be viewed as a correction for the Pauli principle acting between the particles or holes in different phonons. As we will show this effect is dominant in the $(\nu f_6^2 \times 3^- \times 3^-)12^+$ two-phonon state in ^{148}Gd.

As mentioned above the octupole vibration is expected to be nearly harmonic in a doubly magic nucleus like ^{208}Pb. The situation is different in a nucleus like ^{146}Gd, where the neutron number is still magic, while the proton Fermi surface at Z=64 lies between the $\pi d_{5/2}$ and $\pi h_{11/2}$ orbitals which are connected by a large Y_3 matrix element. This orbital pair will give rise to one very low-lying 3^- particle-hole excitation in addition to the large number of ph-excitations at higher energy where one nucleon is lifted across a major shell gap. Consequently the ^{146}Gd 3^- phonon will have a prominent component of this specific $\pi h_{11/2}\pi d_{5/2}^{-1}$ particle-hole excitation. This additional component in the octupole wave function increases the collectivity, but also makes the vibration anharmonic via the aforementioned effect of the exclusion principle.

Such low-lying 3^- excitations are formed by antialigned coupling of the special orbital pairs with j=ℓ+$\frac{1}{2}$ and $\triangle\ell$=3 that lie close in energy within the same major shell, namely $g_{9/2} - j_{15/2}, f_{7/2} - i_{13/2}, d_{5/2} - h_{11/2}$, and $p_{3/2} - g_{9/2}$. They can not contribute to the 3^- phonon in doubly magic nuclei since they here always occur on the same side of the Fermi surface. But these in-shell excitations are of crucial significance for the octupole mode in single-closed shell and open shell nuclei.

In ^{148}Gd the $\nu f_{7/2} \rightarrow \nu i_{13/2}$ excitation also contributes in a similar manner to the octupole vibration, resulting in the $(\nu f_6^2 \times 3^-)9^-$ one-phonon energy of 884 keV and the $E3$ transition rate of $52(4)B_W$, compared to 1579 keV and $37(2)B_W$ of the 3^- state in ^{146}Gd. In a previous theoretical analysis [10] of the 12^+ double-octupole state in ^{148}Gd we have handled the Pauli principle for the protons in perturbation theory, while the contribution of the two valence neutrons to the octupole collectivity was calculated explicitly. These theoretical results are shown to the left in Fig. 1 and are in good agreement with experiment for both the energies and the transition rates. We therefore conclude that the principal cause of the anharmonicity in this case is correctly identified.

The contribution of the $\nu f_{7/2} \rightarrow \nu i_{13/2}$ transition to the octupole collectivity should increase towards higher neutron number, which is observed in the N=88 nucleus ^{152}Gd where the strength of the 3^- is 52 B_W compared to 42 B_W in ^{148}Gd [10,16]. At N=90 where the $f_{7/2}$ shell should be completed the nuclei have acquired static quadrupole deformation, and the associated rearrangement of the single particle energies shifts the maximum octupole collectivity to the nuclei around $^{146}_{56}$Ba$_{90}$ and induces an octupole component in the nuclear

shape. Originally such reflection asymmetric shapes have been found in the actinide nuclei [11] in the vicinity of $^{222}_{88}Ra_{134}$, where they result from the filling of the $\pi f_{7/2} - \pi i_{13/2}$ and $\nu g_{9/2} - \nu j_{15/2}$ orbital pairs.

The prominent role of the $\pi d_{5/2} \rightarrow \pi h_{11/2}$ 3^- excitation in the N=82 isotones has early become evident from the regular variation of the properties of the octupole phonon [16] which has lowest energy and maximum transition rate in Gd. There are three other regions of single closed shell nuclei where similar data [16] on the octupole vibration exist. They are the Z=50 nuclei around ^{114}Sn exploiting the $\nu d_{5/2} \rightarrow \nu h_{11/2}$ excitation, the N=50 nuclei around ^{90}Zr with $\pi p_{3/2} \rightarrow \pi g_{9/2}$, and the Z=28 isotopes close to ^{66}Ni with the $\nu p_{3/2} \rightarrow \nu g_{9/2}$ excitation. The strongest 3^- one-phonon strength, $66(9)B_W$, has recently been measured [17] in ^{96}Zr. In this spherical nucleus the $\pi p_{3/2} \rightarrow \pi g_{9/2}$ as well as the $\nu d_{5/2} \rightarrow \nu h_{11/2}$ excitations are fully contributing to the collectivity of the octupole phonon. In all these nuclei one can expect that substantial anharmonicity of the octupole vibration is brought about by the effect of the Pauli principle, causing a positive contribution to the energy shift for the two-phonon 6^+ coupling as discussed above for the Gd region.

In summary, we have measured the $12^+ \rightarrow 9^-$ $E3$ transition rate in ^{148}Gd as $77(11)B_W$. This result confirms the identification of the 3.981 MeV 12^+ state as the $\nu f_6^2 \times 3^- \times 3^-$ two-phonon octupole excitation. This is the first two- to one-phonon $E3$ transition rate measured in an even nucleus. Theoretical analysis shows that the observed anharmonicities in energy and transition strength are due to the effect of the Pauli principle acting between nucleons in different phonons.

This work was partially supported by the Academy of Finland and Swedish Natural Science Research Council.

References

1. A. Bohr, B.R. Mottelson: *Nuclear Structure*, Vol.II, (W.A. Benjamin, MA, 1975), p. 567
2. P.R. Christensen *et al.*: unpublished, quoted in S. Landowne *et al.*: Phys. Lett. **B70** (1977) 292
3. M.A.J. Mariscotti *et al.*: Nucl. Phys. **A407** (1983) 98
4. R. Julin *et al.*: Phys. Rev. **C36** (1987) 1129
5. H. Wollersheim *et al.*: Z. Phys. **A341** (1992) 137, and M. Schramm *et al.*: Z. Phys. A (1992)(in press)
6. P. Kleinheinz, *et al.*: Phys. Rev. Lett. **48** (1982) 1457
7. S. Lunardi, *et al.*: Phys. Rev. Lett. **53** (1984) 1531
8. G. Molnar *et al.*: Nucl. Phys. **A500** (1989) 43, and D.F. Kusnetzov *et al.*: Phys. Lett. **B228** (1989) 11
9. R.A. Gatemby *et al.*: Phys. Rev. **C41** (1990) R414
10. M. Piiparinen *et al.*: Z. Phys. **A337** (1990) 387
11. S.G. Rohoziński, *et al.*: Rep. Prog. Phys. **51** (1988) 541
12. S. Harissopulos *et al.*: Nucl. Phys. **A467** (1987) 528
13. M.W. Drigert et al: Nucl. Phys. **A515** (1990) 466
14. J. Blomqvist: Phys. Lett. **B33** (1970) 541
15. R.H. Spear *et al.*: Phys. Lett. **B128** (1983) 29
16. R.H. Spear: At. Data Nucl. Data Tables **42** (1989) 55
17. H. Ohm *et al.*: Phys. Lett. **B241** (1990) 471, and H. Mach *et al.*: Phys. Rev. **C42** (1990) R811

High-Spin Spectroscopy of ^{168}Yb and the Reduction of Pairing Correlations

J.R.B.Oliveira[a], F.S.Stephens, M.A.Deleplanque, R.M.Diamond, J.E.Draper[b], E.Rubel[b], C.Duyar[b], J.A.Becker[c], E.A.Henry[c], N.Roy[c], C.W.Beausang[d]

Nuclear Science Division, Lawrence Berkeley Laboratory, 1 Cyclotron Rd., Berkeley, CA 94720

and

S.Frauendorf

Institut fur Kern und Hadronen Physik, FZ- Rossendorf, PF.19 0-8051 Dresden,Germany;

The high-spin states of ^{168}Yb have been investigated by means of in-beam gamma-ray spectroscopy with the High Energy Resolution Array (HERA) at the 88-inch cyclotron of the Lawrence Berkeley Laboratory. The ^{168}Yb nucleus was produced in the reaction ^{124}Sn(^{48}Ca,4n) at 210 MeV. A gamma-gamma coincidence matrix was histogrammed containing 315 million counts, with requirements of fold >17 and sum energy >13 MeV in the inner-ball detectors. The level scheme based on the present work is presented in figure 1. Five bands previously reported by Bacelar *et al.* [1] were confirmed (1 to 5 in fig. 1) and extended by one or two higher-lying transitions. In addition, four new bands (6-9, fig. 1), two extending up to $I \approx 40\hbar$, were observed.

It is well known that at high rotational frequencies ω the Coriolis anti-pairing and the blocking effects that appear with the first crossings in each band should considerably reduce the strength of the static pairing field for the neutrons. Evidence for that is the close resemblance between the experimental Routhians and particle-hole calculations for the neutron configurations in the mass-168 region at very high ω, in particular the absence of band crossings characteristic of a strong pairing field[1,2].

In order to provide a suitable description for the whole frequency interval from the strong pairing phase below the first crossings to the weak pairing phase at the highest ω values observed experimentally, we assumed a schematic frequency dependence of the pairing-gap parameter $\Delta(\omega)$ in an otherwise conventional Cranked Shell Model quasiparticle calculation. Figure 2a shows the result of such a calculation for ^{168}Yb. The Routhians of the lower lying configurations are shown relative to the lowest $(\pi,\alpha) = (-,1)$ configuration. At the top of the figure we provide a scale for Δ. Up to ω=0.25 MeV, where the first crossing occurs in the calculation, Δ is assumed to be large and constant (0.8 MeV). It decreases linearly down to zero between ω=0.25 and ω=0.5 MeV, staying constant thereafter. In the weak (or absent) pairing region, where occupation probabilities are close to one or zero the quasiparticle formalism presents a problem: since it does not distinguish between particles and holes, spurious particle-particle and hole-hole excitations (which change the total number of neutrons by +2 or -2 respectively) appear at high ω, as well as the number-conserving particle-hole excitations. These spurious states have to be eliminated. On the contrary, at low ω all low lying states are physical, since the occupation probability of all states close to the Fermi surface is around 0.5. The crossings of the spurious states with the physical ones break the latter into separate pieces which have to be reconnected by hand in their order of appearance. In figure 2a some of these spurious states with $(\pi,\alpha) = (+,0)$ are indicated in thin solid lines. The spurious states of other (π,α) are not shown for simplicity.

Figure 2b shows the experimental Routhians for ^{168}Yb. Only the bands which extend to very high spin, and which we assign to neutron configurations have been included. The reference band is again the (-,1) band (2) which is yrast at high ω. The choice of this reference is very convenient since it is well defined in the whole frequency interval in which we are interested. No extrapolations have to be made, and the figure can be directly compared to the calculated excitation energies of fig. 2a. The corresponding bands can be identified by the numbers included in fig. 2a. This comparison shows that indeed we can provide a good description of the experimental data by means of the schematic treatment of Δ assumed in the calculations of fig 2a. There is only one low lying configuration which is not observed experimentally (the lowest (-,0) configuration). An assignment of this configuration to band 6 is not completely excluded. The transitions that connect band 6 to the ground state band were not observed, therefore there is a certain freedom of choice in terms of excitation energy and spin for that band, but the ones shown in fig 1 are the most probable according to the available experimental evidence (coincidences and intensities), and result in an unusually high alignment for this band. This is more consistent with a proton configuration which still has strong pairing. For this reason band 6 was left out of fig 2b.

Figure 3 (a-f) shows a comparison of the experimental data for some neighboring nuclei with the calculations done with a frequency dependence of Δ similar to that in fig 2a. There is a close correspondence, indicating that such a schematic treatment can provide a good description for the intermediate and high-spin data from that mass region.

FIGURE CAPTIONS:

Figure 1 - The level scheme of ^{168}Yb. The different bands are numbered for further reference.

Figure 2 - Band structure of ^{168}Yb. The Routhians are plotted relative to the lowest (-,1) configuration (band 2). The solid, dashed, dot-dashed and dotted lines correspond to (π,α) = (+,0), (+,1), (-,0) and (-,1), respectively. **(a)** Calculation with decreasing pairing gap (Δ). The physical states are indicated by thick lines. Some spurious states of (+,0) are also shown as thin lines. On the insert at the bottom right, the particle-hole excitations of the (-,1) core (band 2) are shown (in this case the solid, dashed, dot-dashed and dotted lines correspond to (π,α) = (+,1/2), (+,-1/2), (-,1/2) and (-,-1/2), respectively). They are strictly valid only above ω=0.5 MeV where Δ=0. **(b)** Experimental Routhians. The experimental points are indicated by the numbers and correspond to the quadrupole transitions in figure 1.

Figure 3 - Comparison between experimental data on the left for (A) ^{166}Yb, (C) ^{167}Yb and (E) ^{169}Yb, and the corresponding calculation with decreasing Δ (B, D, F) on the right. The line conventions are the same as in figure 2a and insert for the even-N and odd-N, respectively.

---

[a] *Universidade de Sao Paulo, S. Paulo, SP, Brazil*

[b] *University of California, Davis, CA, 95616*

[c] *Lawrence Livermore National Laboratory, Livermore, CA 94550*

[d] *University of Liverpool, Liverpool L69 3BX, United Kingdom*

[1] J.C.Bacelar *et al.* Nucl.Phys. **A442**(1985)509

[2] S.Frauendorf Nucl.Phys. **A409**(1983)243

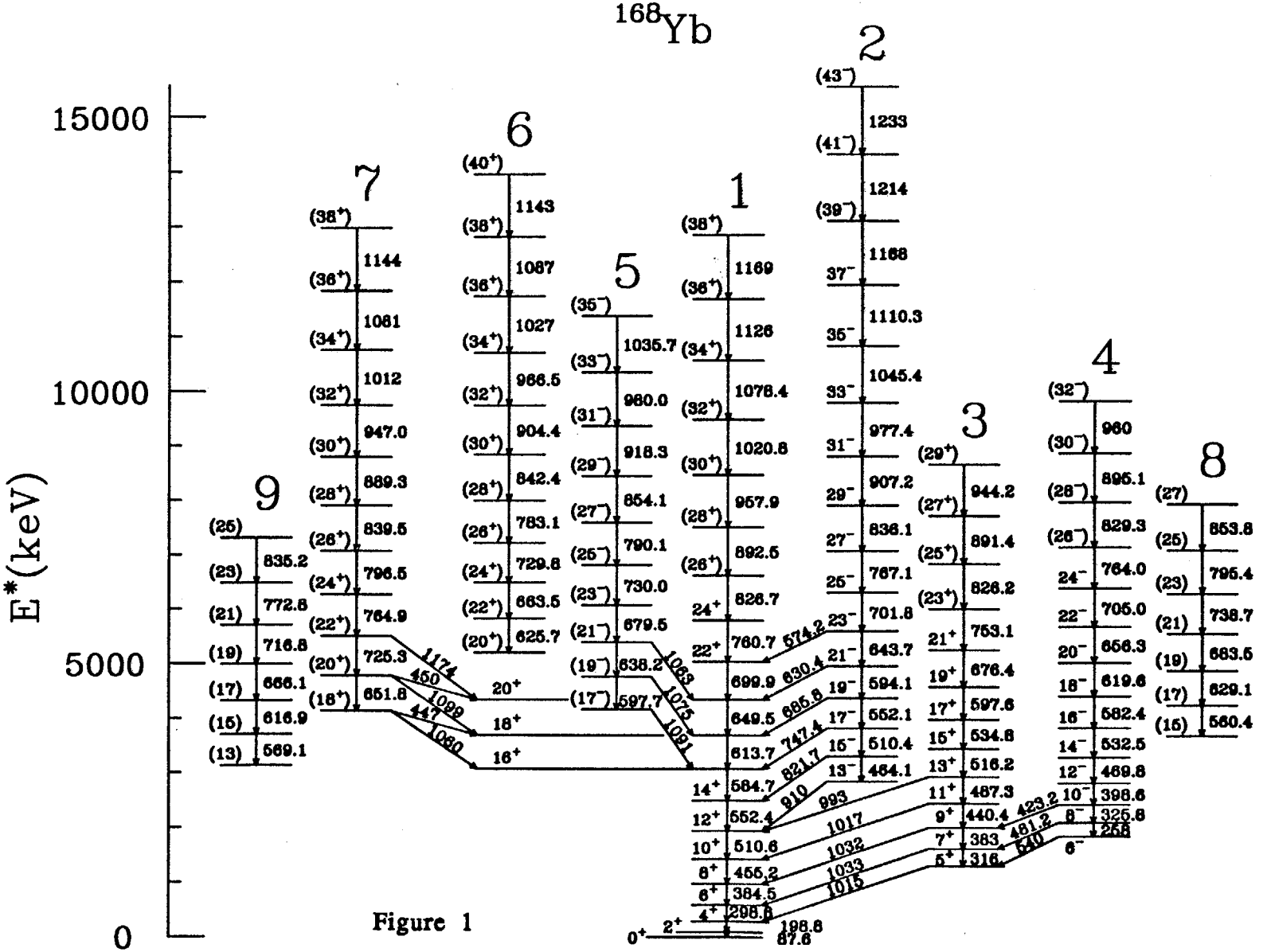
168Yb
E*(keV)
15000
10000
5000
0
1
2
3
4
5
6
7
8
9
(43⁻)
1233
(41⁻)
1214
(39⁻)
1168
37⁻
1110.3
35⁻
1045.4
33⁻
977.4
31⁻
907.2
29⁻
836.1
27⁻
767.1
25⁻
701.8
23⁻
643.7
21⁻
594.1
19⁻
552.1
17⁻
510.4
15⁻
464.1
13⁻
(38⁺)
1169
(36⁺)
1126
(34⁺)
1078.4
(32⁺)
1020.8
(30⁺)
957.9
(28⁺)
892.5
(26⁺)
826.7
24⁺
760.7
22⁺
699.9
649.5
613.7
14⁺
584.7
12⁺
552.4
10⁺
510.6
8⁺
455.2
6⁺
384.5
4⁺
298.6
2⁺
198.6
0⁺
87.6
574.2
630.4
685.8
747.4
821.7
910
993
1017
1032
1033
1015
(29⁺)
944.2
(27⁺)
891.4
(25⁺)
826.2
(23⁺)
753.1
21⁺
676.4
19⁺
597.6
17⁺
534.8
15⁺
516.2
13⁺
487.3
11⁺
440.4
9⁺
383.
7⁺
316.
5⁺
423.2
461.2
540
(32⁻)
960
(30⁻)
895.1
(28⁻)
829.3
(26⁻)
764.0
24⁻
705.0
22⁻
656.3
20⁻
619.6
18⁻
582.4
16⁻
532.5
14⁻
469.8
12⁻
398.6
10⁻
326.8
8⁻
258
6⁻
(27)
853.8
(25)
795.4
(23)
738.7
(21)
683.5
(19)
629.1
(17)
560.4
(15)
(40⁺)
1143
(38⁺)
1087
(36⁺)
1027
(34⁺)
966.5
(32⁺)
904.4
(30⁺)
842.4
(28⁺)
783.1
(26⁺)
729.8
(24⁺)
683.5
(22⁺)
625.7
(20⁺)
20⁺
18⁺
16⁺
(35⁻)
1035.7
(33⁻)
980.0
(31⁻)
918.3
(29⁻)
854.1
(27⁻)
790.1
(25⁻)
730.0
(23⁻)
679.5
(21⁻)
638.2
(19⁻)
597.7
(17⁻)
1068
1075
1081
(38⁺)
1144
(36⁺)
1081
(34⁺)
1012
(32⁺)
947.0
(30⁺)
889.3
(28⁺)
839.5
(26⁺)
796.5
(24⁺)
764.9
(22⁺)
725.3
(20⁺)
651.8
(18⁺)
1174
450
1089
447
1060
(25)
835.2
(23)
772.8
(21)
716.8
(19)
666.1
(17)
616.9
(15)
569.1
(13)

Figure 1

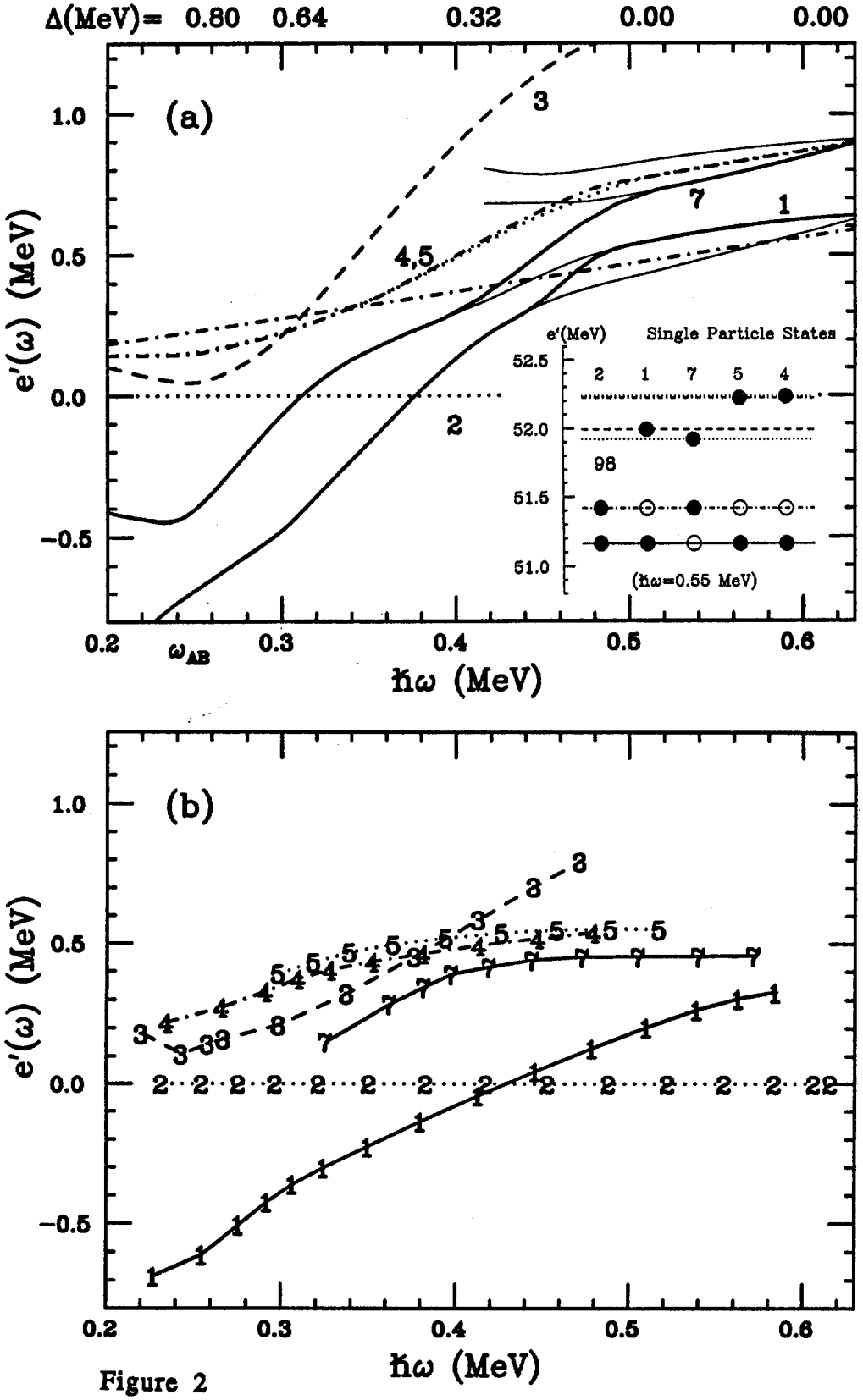
Δ(MeV)= 0.80 0.64 0.32 0.00 0.00
(a)
e'(ω) (MeV)
ħω (MeV)
ω_AB
e'(MeV) Single Particle States
(ħω=0.55 MeV)
(b)
e'(ω) (MeV)
ħω (MeV)

Figure 2

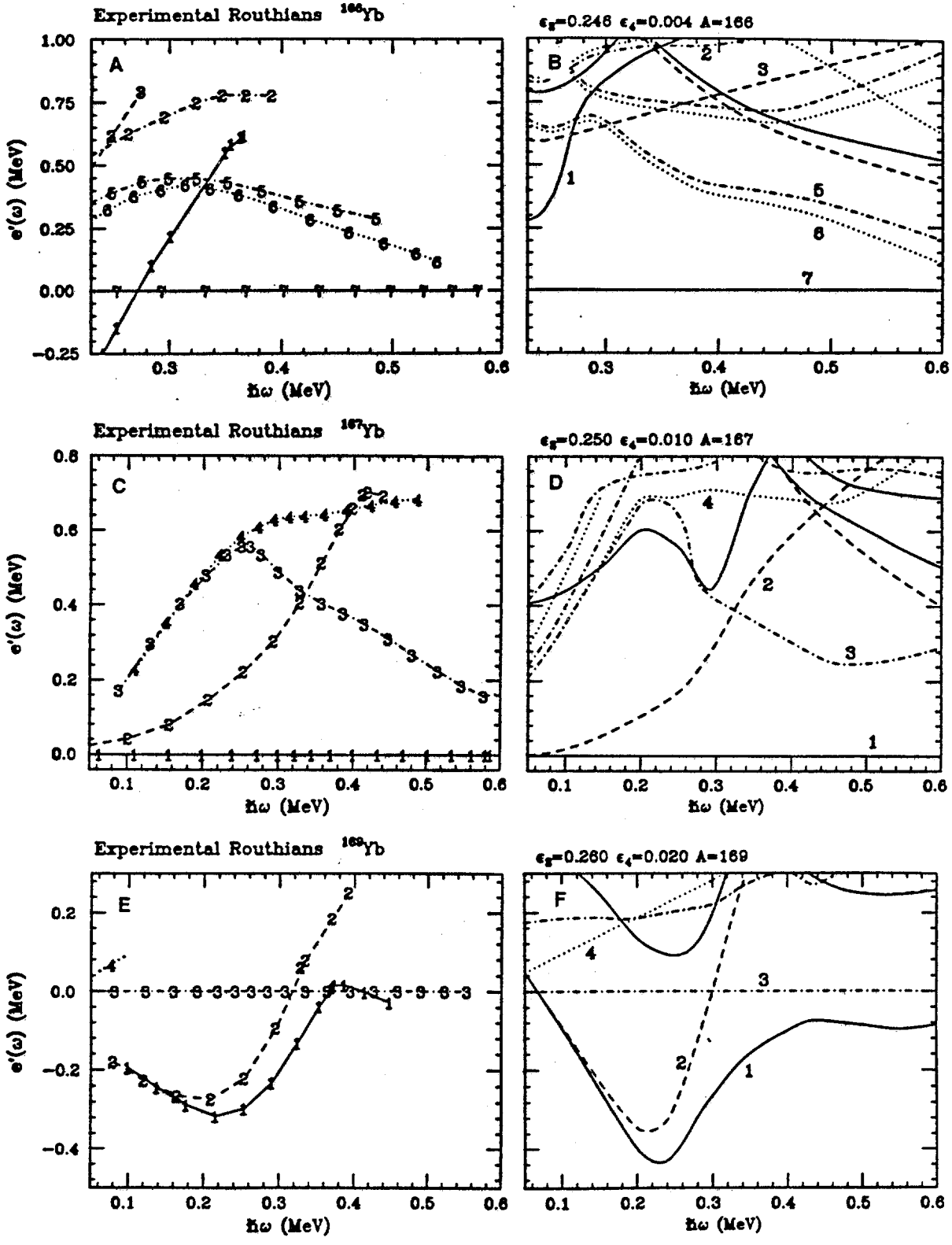
Experimental Routhians ^{166}Yb
ϵ_2=0.246 ϵ_4=0.004 A=166
A
B
Experimental Routhians ^{167}Yb
ϵ_2=0.250 ϵ_4=0.010 A=167
C
D
Experimental Routhians ^{169}Yb
ϵ_2=0.260 ϵ_4=0.020 A=169
E
F
e'(ω) (MeV)
ħω (MeV)

Figure 3

Electromagnetic Properties of ^{181}Ir: Evidence of β-stretching?

U. Garg and W. Reviol
Department of Physics, University of Notre Dame, Notre Dame, IN 46556, USA

P. Semmes
Department of Physics, Tennessee Technological University, Cookeville, TN 38505, USA

Nuclei with many valence protons and neutrons exhibit rotational features characteristic of a deformed nuclear shape, while those closer to the "magic numbers" have softer shapes and are more transitional in nature. In some cases, a delicate balance may exist between different shapes in the same nucleus, and the most favored shape depends sensitively on the angular momentum and/or a particular nuclear configuration. Such shape coexistence is well established in the low energy spectra of many nuclei in the A≈180 region, and typically involves a competition between prolate and oblate shapes ([HIW 83], [HHZ 85]). For the neutron deficient Ir isotopes, there have been predictions of coexistence between different prolate configurations at low to moderate spins ([NRG 90], [Be 90], [WSN 90], [Wy 90]), perhaps accompanied by a shape transition in the yrast band as the spin increases; some triaxial configurations have also been predicted at low energy and low spin ([Be 90]).

Experimentally, a number of rotational structures have been observed in $^{173\text{-}181}$Ir ([JAH 91], [CFW 91], [DFB 91], [[DFK 91], RJY 90], [Ji 91], [KGC 90] and [KGF 92]). In most cases, two decoupled bands are known, assigned as $\pi i_{13/2}$ and $\pi h_{9/2}$ bands, as well as two strong coupled sequences, assigned as $h_{11/2}$ and $[402]5/2^+$ bands. One puzzle, systematically present in this data, is that the $i_{13/2}$, $h_{11/2}$ and $[402]5/2^+$ bands all show smooth, gradual alignment increases with respect to a reference derived from the $h_{9/2}$ band. Some evidence has been presented for configuration-dependent deformations from the systematics of the $vi_{13/2}$ crossing frequencies and from the complex alignment patterns ([LJY 90]). In Refs. [CFW 91] and [JAH 91], clear irregularities in the energy spectra of the $h_{11/2}$ band at the lowest observed spins in ^{173,175}Ir were attributed to a transition from a less-deformed prolate shape (with $\beta_2 \approx 0.16$) to a more-deformed shape ($\beta_2 \approx 0.25$), and this interpretation is supported by TRS calculations. Phenomenological 3-band mixing calculations ([DFB 91], [DFK 91]) seem to reproduce both the alignments (level spacings) and the electromagnetic transition rates [B(M1;I→I-1)/B(E2;I→I-2) ratios] if the three bands are identified as corresponding to, respectively, the less-deformed and more-deformed prolate 1-quasiparticle structures and a 3-quasiparticle configuration containing a rotation-aligned pair of $i_{13/2}$ neutrons. These calculations suggest that the shape mixing is also important for the heavier isotopes, ^{179,181}Ir, even though the strong irregularities found in the level structures of ^{173,175}Ir are not present in these nuclei. Although some parameters are constrained in such an analysis, the peculiarities in the level spacings alone cannot identify the nature of the different configurations. Furthermore, these calculations used a semiclassical estimate for the M1 and E2 transition rates of the unperturbed (single shape) bands,

rather than calculating these quantities directly from particle-rotor wavefunctions. Finally, it should be noted that the spins have not been experimentally determined for Ir isotopes with A < 181, but, instead, have been *assigned* through model-dependent arguments and/or on the basis of systematics.

We have calculated the B(M1)/B(E2) ratios in ^{181}Ir within a shape-fixed particle + rotor model, in order to investigate how sensitive these may be to the nuclear shapes under consideration, and whether or not there is evidence of shape coexistence (or beta stretching) in the electromagnetic data alone. The model calculations employed the same Woods-Saxon potential that has been used previously for TRS and bandhead calculations ([Wy 90], [Be 90], [NRG 90] and [CFW 91]), and all parameters have been taken at their standard values, without any adjustments. To the extent possible with present models, these calculations should represent predictions for the B(M1)/B(E2) ratios at the deformations expected from the TRS and bandhead calculations. A comparison with the ^{181}Ir data is stimulated by the fact that this is the lightest-mass Ir nucleus for which the spins and parities are firmly established experimentally; we find that the electromagnetic transition rates in this nucleus are well reproduced under the assumption of a single, fixed shape.

The particle-rotor model employed here is essentially the "Lund version", originally described in [LLR 78], but with an extension to incorporate the Woods-Saxon potential [Le 83]. A more complete description of the model and the associated computer codes can be found in [Se 91].

Two separate calculations have been performed: one for the less-deformed prolate shape (β_2 = 0.19, γ = 0°, β_4 = –0.004), and the other for the more-deformed shape (β_2 = 0.24, γ = 0°, β_4 = –0.004). The moments of inertia were estimated from Grodzins' relation, giving core 2^+ energies of 0.183 and 0.119 MeV, respectively, and the proton Fermi level and pairing gap were obtained from a standard BCS calculation on the adiabatic single-particle states. The model space included about 10 Nilsson orbitals near the Fermi level, sufficient to ensure numerical convergence, and no Coriolis attenuation was introduced. The effective g_s factor for the odd proton was taken at 70% of the free-nucleon value, and the core-value, g_R, was taken as Z/A. The intrinsic core E2 moments were calculated from the macroscopic shape parameters. Since this model is restricted to a constant moment of inertia, it cannot reproduce the details of the experimental alignments; however, reasonable adjustments in the moment of inertia do not affect the main results of this study (also, a particle-rotor calculation with a variable moment of inertia (VMI) for ^{179}Ir is described in [Ji 91] with similar results).

The results of our calculations for the B(M1)/B(E2) ratios for the $9/2^-$[514] and $5/2^+$[402] bands are summarized and compared with experimental results in Figs. 1 and 2, respectively. The solid lines in the figures represent calculations for the more-deformed (β_2 = 0.24) case whereas the dot-dashed lines represent the less-deformed (β_2 = 0.19) case. The agreement between the data and the calculations for the more-deformed case is remarkably good. The less-deformed case, on the other hand, appears to fail ignominiously to reproduce the measured B(M1)/B(E2) ratios, suggesting that any mixing with the less-deformed shape must be, at best, rather small, especially at low spins.

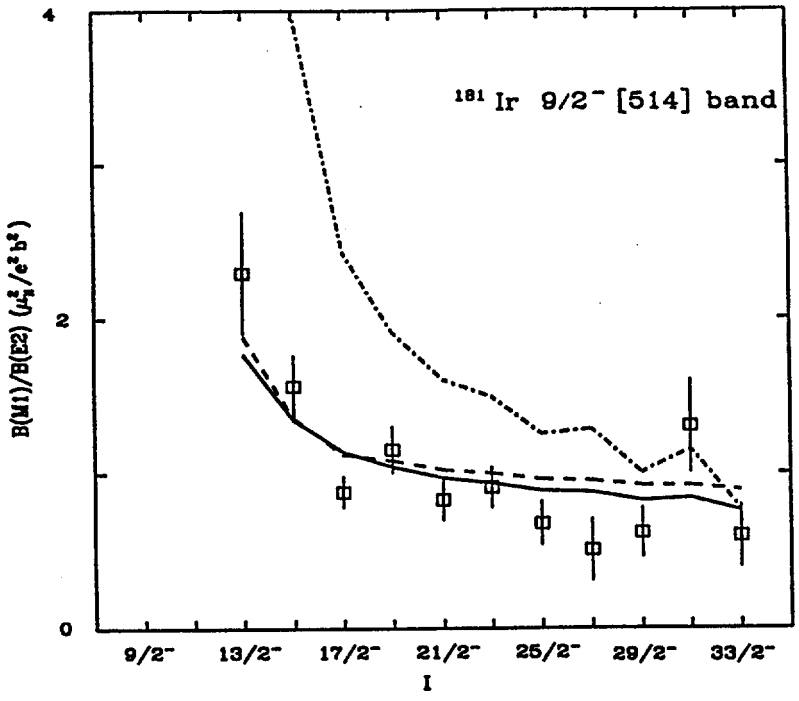

Fig. 1. B(M1)/B(E2) ratios for the [514]9/2⁻ band in ^{181}Ir. The solid line corresponds to the "more-deformed" case and the dot-dashed line to the "less-deformed" case. The dashed line represents the ratios calculated with a larger moment of inertia parameter for the "more-deformed" case (see text). The experimental data are from [KGF 92].

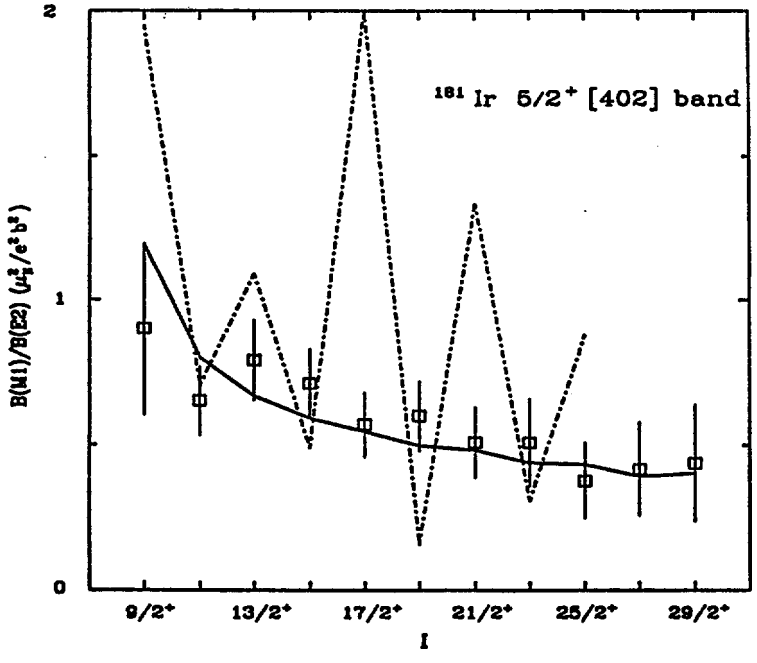

Fig. 2. Same as Fig. 1 except for the [402]5/2⁺ band.

Further support for the single, more-deformed, shape for ^{181}Ir comes from the calculated low-energy level structures for the two cases mentioned above. These are shown in Figs. 3 and 4 for the negative and positive parity states, respectively. Again, while the level-ordering and relative positions of various levels obtained for the more-deformed case are in qualitative agreement with the experimental levels

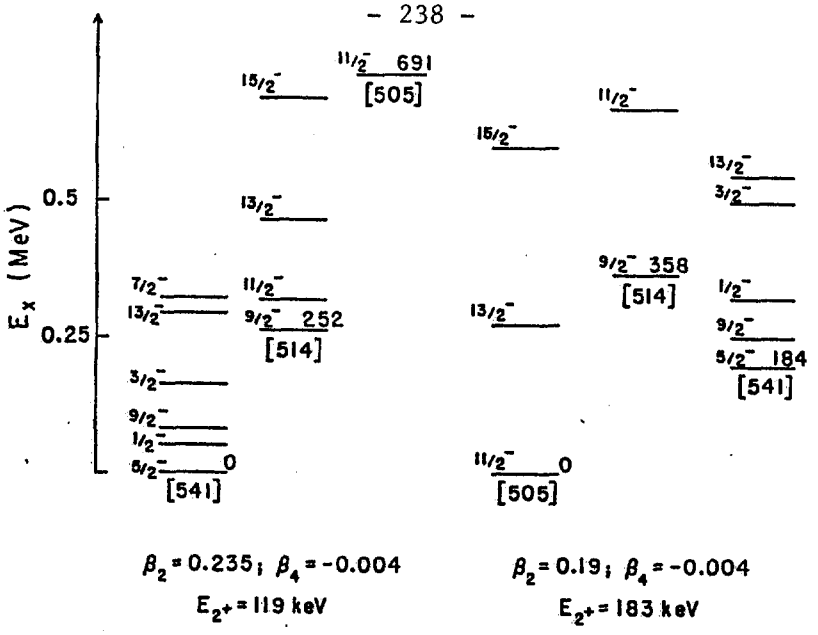

Fig. 3. Low-lying, negative parity level-structure of ^{181}Ir obtained from our calculations. The "more-deformed" and "less-deformed" cases are to the left and right, respectively.

[KGF 92], the calculations for the less-deformed case lead to a level structure markedly different from the observed one. We further note that the M1-E2 mixing ratios obtained in our calculations are also consistent

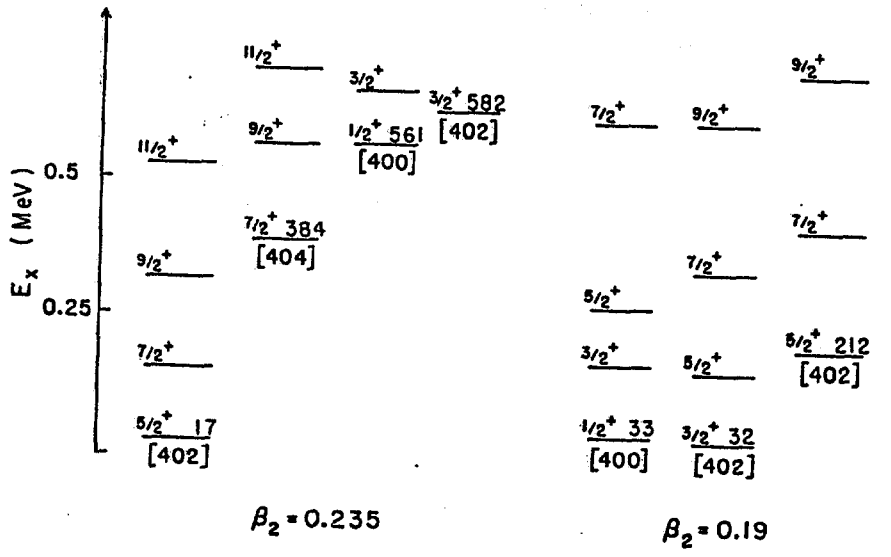

Fig. 4. Same as Fig. 3 for the positive parity levels.

with the experimental values, where available.

As mentioned before, our calculations employ a fixed moment of inertia. However, changes in the moment of inertia parameter do not significantly alter the final results for the B(M1)/B(E2) ratios. The results of calculations with a different moment of inertia parameter for the more-deformed case (corresponding to an energy of 80 keV for the 2^+ state, chosen so as to roughly reproduce the $25/2^- \rightarrow 21/2^-$ transition energy) are also shown in Fig. 1 as the dashed line--the results are substantially similar to those for the moment of inertia parameter originally employed.

We wish to reemphasize that this model does not purport to--and cannot--reproduce the finer details in the observed alignments which originally led to the suggestions of band-mixing and β-stretching. It is, nevertheless, remarkable how well the available electromagnetic transition probabilities data for the one nucleus in this region where the spins and parities of nuclear levels have been experimentally determined, *viz.* ^{181}Ir, can be reproduced within the framework of a simple particle + rotor model with a single, fixed shape. Our results provide a benchmark against which the experimental and theoretical results for other Ir isotopes can be tested. Whether a more realistic calculation of the electromagnetic properties with shape-mixing included would simultaneously explain the observed alignments and the electromagnetic transition rates still remains an open question, however.

This work was initiated during the Hands-On Nuclear Structure Theory Workshop, held at the Joint Institute of Heavy Ion Research, Oak Ridge, August 5-16, 1991. UG and WR wish to thank the organizers for the stimulating environment and superb training afforded by the Workshop. Partial financial support for this work has been provided by the National Science Foundation (Grant number PHY91-00688) and the Department of Energy (Contract number DE-FG05-92ER40694).

REFERENCES

[Be 90] R. Bengtsson, Nucl. Phys. **A520** (1990) 201c.

[CFW 91] B. Cederwall, B. Fant, R. Wyss, A. Johnson, J. Nyberg, J. Simpson, A. M. Bruce and J. N. Mo, Phys. Rev. **C43** (1991) R2031.

[DFB 91] G. Dracoulis, B. Fabricius, A. P. Byrne, A. E. Stuchberry, A. M. Baxter, K. P. Lieb, K. J. Schiffer and T. Kibedi, Phys. Lett. **257B** (1991) 21.

[DFK 91] G. Dracoulis, B. Fabricius, T. Kibedi, A. M. Baxter, A. P. Byrne, K. P. Lieb and A. E. Stuchbery, Nucl. Phys. **A534** (1991) 173.

[HHZ 85] J. H. Hamilton, P. G. Hansen and E. F. Zganjar, Reports on Progress in Physics **48** (1985) 631.

[HIW 83] K. Heyde, P. Van Isacker, M. Waroquier, J. L. Wood and R. A. Meyer, Physics Reports **102** (1983) 291.

[JAH 91] S. Juutinen, P. Ahonen, J. Hattula, R. Julin, A. Pakkanen, A. Virtanen, J. Simpson, R. Chapman, D. Clarke, F. Khazaie, J. Lisle and J. N. Mo, Nucl. Phys. **A526** (1991) 346.

[Ji 91] H.-Q. Jin, Ph. D. Thesis, University of Tennessee, 1991, and to be published.

[KGC 90] R. Kaczarowski, U. Garg, A. Chaudhury, E. G. Funk, J. W. Mihelich, D. Frekers, R. V. F. Janssens and T. L. Khoo, Phys. Rev. **C41** (1990) 2069.

[KGF 92] R. Kaczarowski, U. Garg, R. G. Funk and J. W. Mihelich, Phys. Rev. **C45** (1992) 103

[Le 83] G. Leander, unpublished.

[LLR 78] S. E. Larsson, G. Leander and I. Ragnarsson, Nucl. Phys. **A307** (1978) 189.

[NRG 90] W. Nazarewicz, M. A. Riley and J. D. Garrett, Nucl. Phys. **A512** (1990) 61.

[RJY 90] L. L. Riedinger, H. -Q. Jin and C. -H. Yu, Nucl. Phys. **A520** (1990) 201c.

[Se 91] P. Semmes, "The Particle + Triaxial Rotor Model: A User's Guide" distributed at the Hands-On Nuclear Theory Workshop, Oak Ridge, Aug. 5-16, 1991.

[WSN 90] R. Wyss, W. Satula, W. Nazarewicz and A. Johnson, Nucl. Phys. **A511** (1990) 324.

[Wy 90] R. Wyss, private communication, and to be published.

Spectroscopy of ^{96}Ru and ^{98}Ru: Structures of Varied Character at N ≥ 52

W. Reviol, U. Garg, A. Aprahamian, B.F. Davis, M.C. Herr, S. Naguleswaran, J.C. Walpe, D. Ye
University of Notre Dame, Notre Dame, IN 46556, USA

I.Ahmad, M.P. Carpenter, R.V.F. Janssens, T.L. Khoo, T. Lauritsen and Y. Liang
Argonne National Laboratory, Argonne, IL 60429, USA

In the neutron-rich A ≥ 100 nuclei (*e.g.* the Ru isotops with N ≥ 56), collective rotational structures based on $\nu h_{11/2}$ intruder states are well established[1,2]. Also, Nilsson-levels from the lower-lying $\nu g_{7/2}$ orbital could drive these and slightly lighter nuclei from a spherical to a deformed shape; such structures, however, have not been observed so far. In order to search for the onset of deformation above the N = 50 closed shell, we have studied the nuclei $^{96\text{-}98}$Ru (N ≥ 52) up to high spins where γ-softness and shape coexistence is predicted. The Ru nuclei are very suitable for this investigation. Since they are located between the Z = 40 subshell (Zr) and the Z = 50 shell closure, a abrupt change from a spherical to a deformed shape as in the isotopic chain of Zr nuclei[3,4] is unlikely and a rather smooth, transitional behavior as a function of neutron number is expected. Furthermore, the Z > 40 systems offer energetically favored deformed $\pi h_{9/2}$ configurations[4] and these intruder proton orbitals are also expected to be observed at high excitation energies and spins. Here we report the results of our investigation on the even-A nuclei – ^{96}Ru and ^{98}Ru.

The ^{96,98}Ru nuclei were produced with the ^{65}Cu(^{36}S,pxn) reactions using 135 and 142 MeV beams from the Argonne Tandem Linac Accelerator System. At these energies the final nuclei were populated at an angular momentum of about 44 $\hbar$ and an excitation energy of about 33 MeV. The recoiling nuclei were stopped in a thick Au backing on the ^{65}Cu target, and the γ-decays were measured with the Argonne-Notre Dame γ-ray facility which comprises 12 CSG's and a 50 element BGO array. Approximately 135 million events with array multiplicity K ≥ 4 were recorded. The coincidence data associated with high multiplicities (K ≥ 8 and K ≥ 15) have been used to construct level schemes of ^{96}Ru and ^{98}Ru, shown in Figs. 1 and 2, respectively. In each case, the previous known level scheme[5] has been extended significantly (up to $E_x \sim 10$ MeV and $I \sim 20\ \hbar$). The proposed spin assignments have been deduced from DCO ratios. However, most of these as also all parity assignments should be treated as prelimnary.

Two independent level structures have been established in both nuclei. In ^{96}Ru most of the intensity feeds through the level sequence on the left half of the scheme. This structure seems to be the continuation of the positive-parity yrast states at low spin and, based on the observed level spacings, is tentatively described as vibrational-like. The other relevant sequence, placed on the right-hand side, consists of five stretched E2 transitions and feeds into the known $9^{(-)}$ state.[5] The

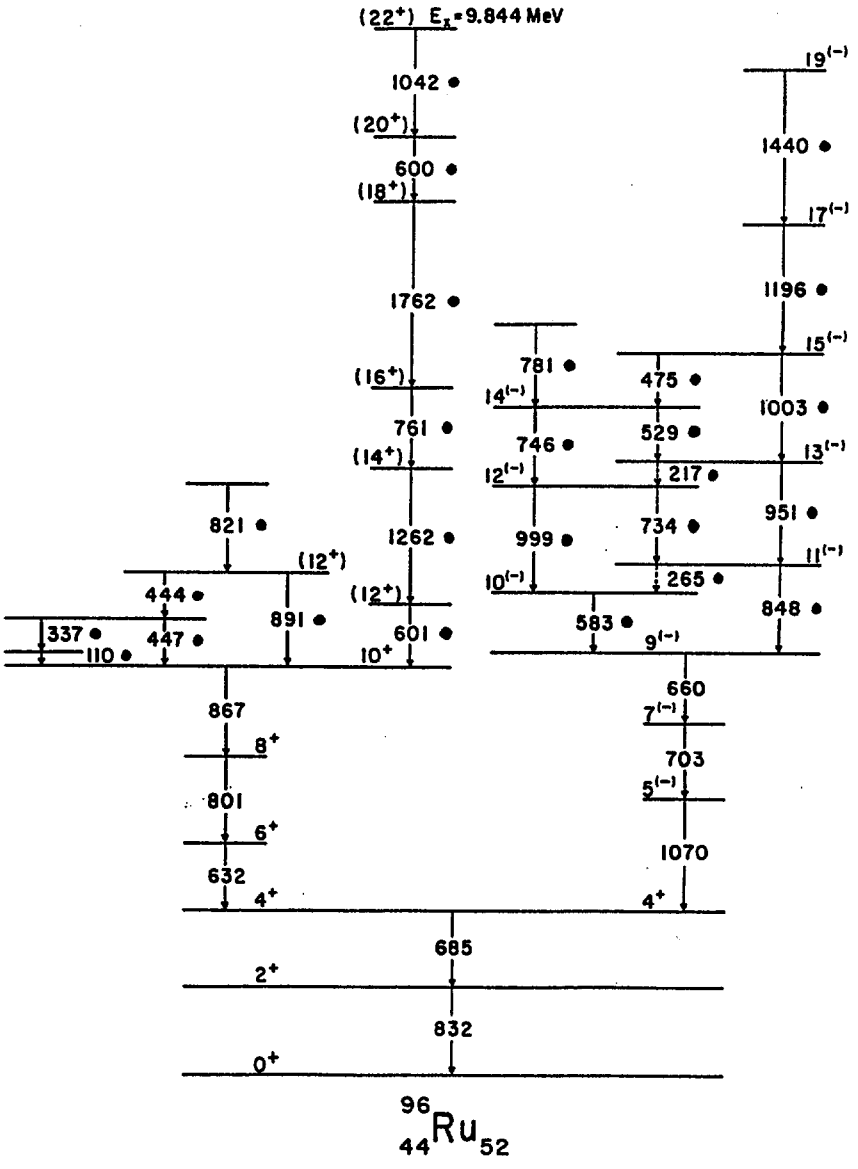

Fig. 1: Partial level scheme of ^{96}Ru involving the strongest γ-transitions for K ≥ 8. Newly-observed transitions are marked with a dot. The spin- and parity assignments, given in parenthesis, are prelimnary.

regularity of the energy spacings, together with the fact that the E2 transitions are relatively strong compared to the parallel dipole transitions observed in some cases, is suggestive of a rotational-like sequence. A prelimnary lineshape analysis (DSAM) for these E2 transitions, on the other hand, shows that their decay (feeding + lifetime) is slower than the stopping process of the recoils in the target backing (~ 1.2 ps), providing a lower limit of the lifetimes that is still compatible with a weak deformation ($\beta_2 < 0.09$). The situation in ^{98}Ru is very similar: In this case too, we observe a strong vibrational-like sequence shown on the left-hand side of Fig. 2. Since the 724 keV γ-ray

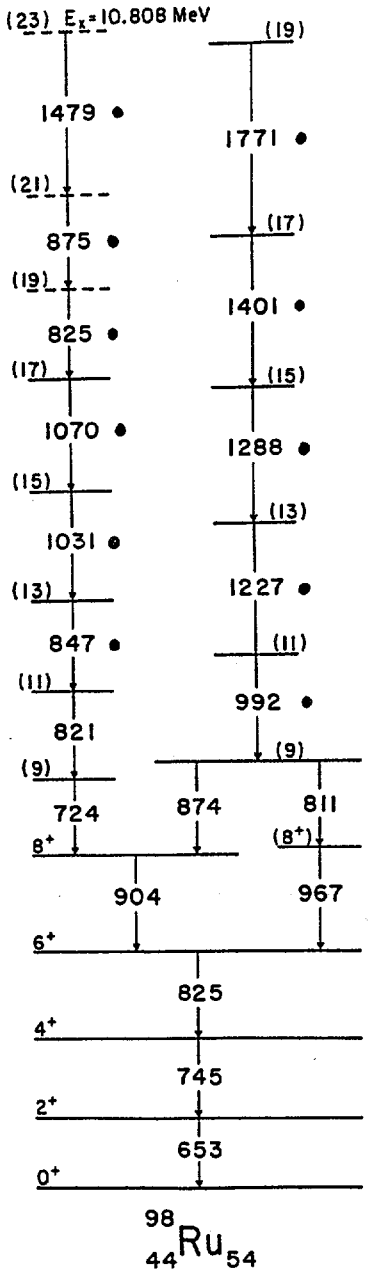

Fig. 2: Partial level scheme of ^{98}Ru from the strongest gamma-transitions for K ≥ 15. Symbols have the same meanings as in Fig. 1. Dashed levels indicate ambiguities in the ordering of transitions.

placed on the bottom of this sequence (I ≥ 8) is not a stretched E2 transition the prelimnary spin assignments differ from the analogous sequence in ^{96}Ru. Above the 8$^+$ state in ^{98}Ru, and parallel to the main level structure, we observe a regular sequence of transitions, most likely of E2 character, with features similar to the analogous sequence in ^{96}Ru discussed above.

The data also contain some evidence for a weak sequence of γ-transitions with very regular energy spacings ($\Delta E_\gamma \sim 60$ keV) shown in Fig. 3. Because of coincidences with known transitions in ^{96}Ru, the sequence is assigned to this nucleus, and it is probably linked with states above the $14^{(-)}$ level (Fig. 1). Linking transitions to the known levels, however, have not been found and the excitation energy of this newly-observed sequence is therefore unknown. The DCO ratios obtainable for some of the weak transitions indicate stretched dipole transitions with some quadrupole admixture, suggesting an M1 multipolarity. An E1 assignment for these transitions is ruled out from lifetime considerations. The intensities corrected for M1 conversion allow to order at least the five lowest dipole transitions with increasing energy; the situation for the higher transitions in the spectrum is, however, complicated by the fact that they are doublets.

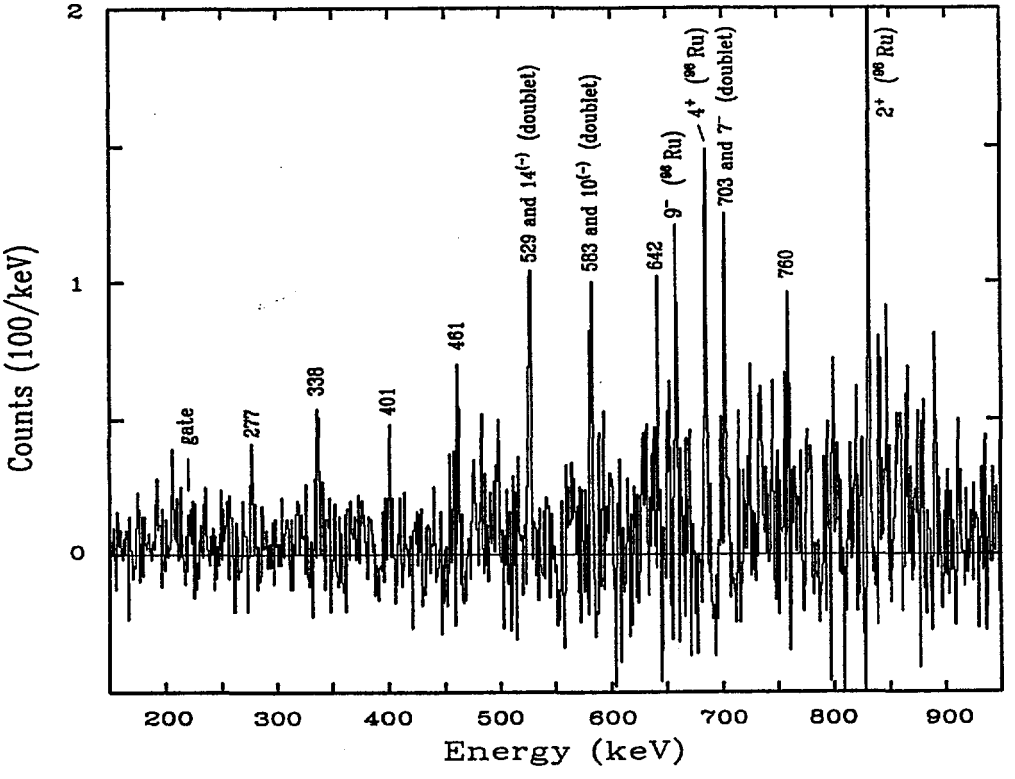

Fig. 3: Weak sequence of dipole transitions observed in ^{96}Ru. The new transitions are labeled by their energies in keV. Known transitions in ^{96}Ru are labeled by their initial state.

TRS calculations by Wyss *et al.* [6] predict the existence of deformed neutron configurations with negative parity ($\nu h_{11/2}$) in ^{96,97,98}Ru. They have a near-prolate shape ($\gamma \sim 0^o$) but the expected deformation is small ($\beta_2 < 0.13$) and the local minima in the total routhian surface are shallow. The addition of aligned $g_{9/2}$ protons which, according to the calculations, are not strong

enough to drive the spherical configurations to a stable deformation, can nevertheless stabilize the already deformed minimum. The best case for this $(\nu h_{11/2}) \otimes (\pi g_{9/2})^2$ configuration is expected to be in ^{97}Ru where a relatively low-lying prolate minimum appears at $\hbar\omega > 0.38$ MeV. A similar configuration is likely to be associated with the E2 sequences observed in the even-A nuclei.

The regular dipole sequence in ^{96}Ru might also be seen as possible indication for collective rotation at $N \geq 52$. This structure appears to be similar to the high-K oblate bands recently observed in the Iodine[7] and Lead nuclei.[8] In analogy with those results, this structure would be associated with the ν[505]11/2 and ν[413]7/2 orbitals which tend to drive the nucleus to an oblate shape ($\gamma = -60^o$).[4] This suggestion is also partially supported by the corresponding TRS calculations indicating a weakly deformed ($\beta_2 < 0.10$) oblate and very soft shape. The dynamic moments of inertia for this structure are on the average quite small ($\sim 18\ \hbar^2\ \mathrm{MeV}^{-1}$) and comparable to those of oblate collective E2 bands in neighboring nuclei (*e.g.* ^{82}Sr (ref. 9)).

To summarize, we have observed in ^{96}Ru and ^{98}Ru regular E2 sequences reminiscent of collective rotation. In addition, we find evidence for a weak, very regular band of, presumably, M1 transitions in ^{96}Ru. These sequences coexist with the dominant single-particle structures above 8 $\hbar$. Additional lifetime measurements (RDM) would be desirable in order to verify the collective nature of the E2 sequences. Evidence for collective rotation at $N \geq 52$ might also come from the odd-A isotope ^{97}Ru, for which the analysis is in progress.

This work has been supported in part by the National Science Foundation (grant no. PHY91-00688) and the Department of Energy (contract W-31-109-ENG-38). M.C. Herr was a participant in the REU program at the University of Notre Dame.

---

1 M.J. A. de Voigt *et al.*, Nucl. Phys. A 270 (1976) 141
2 D.R. Haenni *et al.*, Phys. Rev. C 33 (1986) 1543
3 F.K. Wohn *et al.*, Nucl. Phys. A 507 (1990) 141c
4 W. Nazarewicz, in: *High Spin Physics and Gamma-Soft Nuclei*, J.X. Saladin, R.A. Sorensen, and C.M. Vincent, eds. (World Scientific, 1991) p. 409, and private communication
5 C.M. Lederer *et al.*, Nucl. Phys. A 169 (1971) 449
6 R. Wyss *et al.*, private communication
7 Y. Liang *et al.*, Phys. Rev. Lett. 64 (1990) 29
8 R.M. Clark *et al.*, Phys. Lett. B 275 (1992) 247; G. Baldsiefen *et al.*, ibid., p. 252
9 C. Baktash *et al.*, Phys. Lett. B 255 (1991) 174

High spin γ-ray spectroscopy of ^{121,122}Xe

Shape diversity and band-termination

H. Timmers[a,b], J. Simpson[c], M.A. Riley[a1],
T .Bengtsson[d2], M.A. Bentley[c], F. Hanna[a], S.M. Mullins[a3], J.F. Sharpey-Schafer[a], R. Wyss[e]
J.R. Hughes[b], D.B. Fossan[b], Y. Liang[b], R. Ma[b], N. Xu[b]

[a] *Oliver Lodge Laboratory, University of Liverpool, PO 147, Liverpool L69 3BX, UK*
[b] *Department of Physics, SUNY at Stony Brook, NY 11794, USA*
[c] *SERC Daresbury Laboratory, Daresbury, Warrington WA4 4AD, UK*
[d] *Dep. of Math. Phys.,Lund Institute of Technology, Box118, S-22100 Lund, Sweden*
[e] *Institute for Heavy Ion Research, ORNL, P.O. 2008, Oak Ridge, TN 37831, USA*

The recent discovery of band-terminating high spin single particle states in the A=120 mass region in ^{122}Xe [Si91], ^{118}Xe [Ju91], ^{121}I [Li91] and the lighter odd-even iodines $^{113-119}$I [Pa91a], [Pa91b] motivates a comprehensive investigation of the nuclei in this region.

In order to study the nuclei ^{121,122}Xe the following two experiments have been performed. States in ^{121}Xe have been populated employing the reaction ^{108}Pd(^{16}O,3n)^{121}Xe at a beam energy of 65 MeV. The ^{16}O beam was provided by the FN Tandem/LINAC at SUNY, Stony Brook. Coincident γ-rays following the neutron evaporation were detected by an array of six Compton-suppressed Ge-detectors. In the γ-γ coincidence matrix events in ^{121}Xe were enhanced by applying the multiplicity and total energy information from the 14 element BGO calorimeter.

Furthermore an experiment was carried out at the NSF at Daresbury, UK. Employing the TESSA3 γ-ray spectrometer, which comprises 16 Compton-suppressed Ge-detectors and a 50-element BGO inner ball, γ-γ coincidence data from the fusion evaporation reaction ^{96}Zr(^{30}Si,4n/5n)^{122}Xe/^{121}Xe were detected at a beam energy of 135 MeV. Both gold-backed and self-supported Zirconium targets were used. The average angular momentum brought into the residual nuclei ^{122}Xe and ^{121}Xe in this reaction was 60 $\hbar$ and 46 $\hbar$, respectively.

The level structure of ^{121}Xe and ^{122}Xe has been extended to higher spins, 47/2 $\hbar$ and 31(32) $\hbar$, respectively, see figure 1. In ^{121}Xe a coupled band has been established feeding the $19/2^-$ level of the yrast band [Hu92]. In ^{122}Xe newly discovered decays together with previously known transitions [Ha87] have been linked together forming a structure which is suggested to be a sequence of stretched E2 quadrupole transitions connecting states of positive parity. While in ^{121}Xe even at highest spins this phenomenon was not observed at all, a break up of the rotational feature has been detected at the highest spins in several bands in ^{122}Xe, leading to irregular level structures [Si91].

The structure of ^{122}Xe has been analysed [Ti91] (see also [Ha87]) in the framework of the Cranked Shell Model CSM. While the back-bend in the yrast band of ^{122}Xe can clearly be assigned as a $h_{11/2}$

[1] Present address: Dep. of Physics, FSU, Tallahassee, FL 32306, USA
[2] Present address: ABB Corporate Research, Laboratory for Electrical Insulation, S-721 78 Västeras, Sweden
[3] Present address: Dep. of Physics, McMaster University, Hamilton, Canada

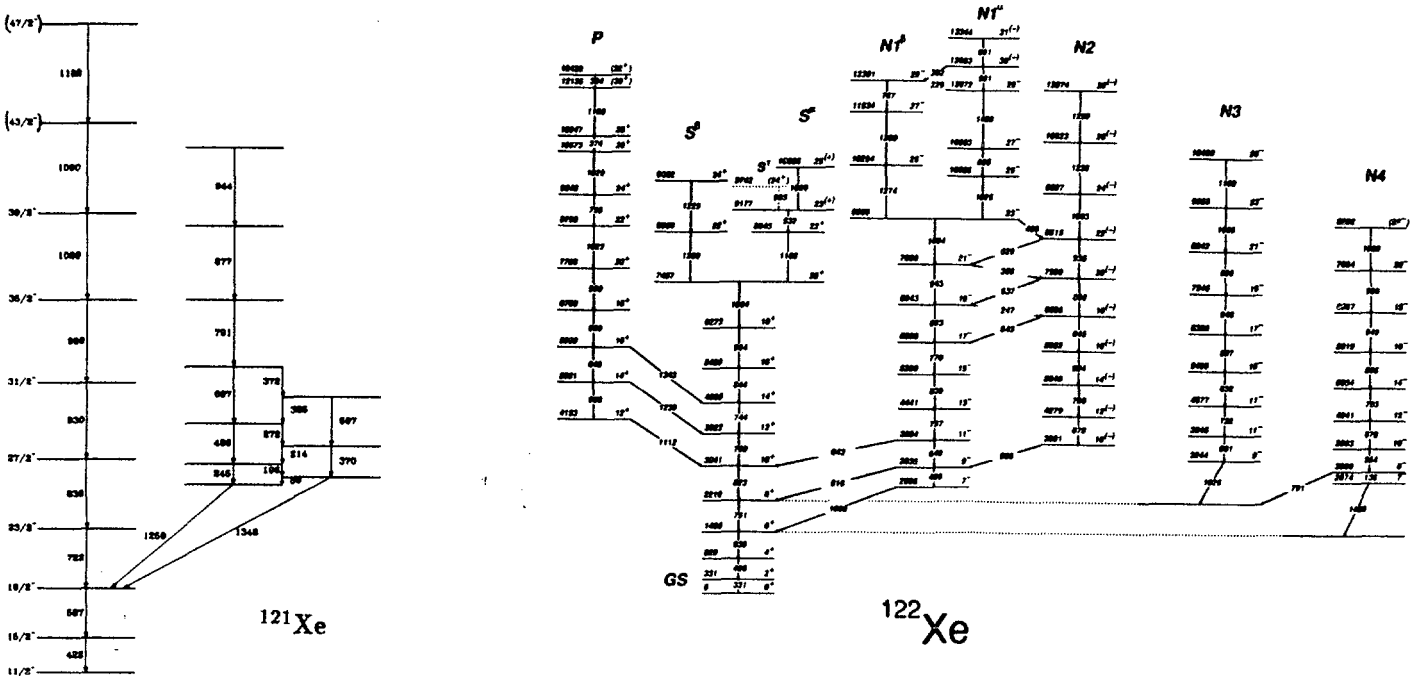

Figure 1: *Partial level schemes of* ^{121}Xe *and* ^{122}Xe

two quasi-neutron alignment, the configuration of the new, probably positive parity side band is not clear. A four quasi-neutron or a two quasi-proton configuration of $h_{11/2}$ nucleons might be considered for this structure.

From CSM calculations with fixed deformation and pairing, the four decoupled negative parity bands, see figure 2, in ^{122}Xe are suggested to be two quasi-proton and quasi-neutron excitations of $h_{11/2}$ and $g_{7/2}d_{5/2}$ quasi-nucleons with the energetically favoured signature pair corresponding to two quasi-proton excitations. This is not supported by CSM calculations with self-consistent deformation and pairing which have been carried out in addition [Be91], [Wy91], and suggest two quasi-neutron configurations for the favoured signature partners.

A conclusive picture, however, could be obtained at high spin where the fast rotation destroys the pairing interaction and the irregular level structure is reproduced by the latter calculations as oblate single particle configurations. The transition to high spin single particle structures occurs in three bands in ^{122}Xe above spin 20 $\hbar$, 22 $\hbar$ and 23 $\hbar$, respectively. These states show both quadrupole and dipole decays. Parallel to the single particle states the rotational sequences continue and lead to a competition between the rotational and single particle states, with the rotational sequences, however, becoming increasingly unfavoured.

At low spin the nucleus ^{122}Xe, which has a prolate ($\beta_2 \approx 0.2$) ground state deformation, generates its angular momentum by a collective rotation of all nucleons about an axis perpendicular to its symmetry axis, while at high spins the Coriolis and centrifugal forces become more and more important. They force the four valence neutrons and four valence protons outside the $^{114}_{50}Sn_{64}$ core to occupy equatorial orbits around the rotation axis, thus aligning the single particle spin of the valence nucleons with the rotation. The nucleus undergoes a shape change from prolate to oblate deformation with axial symmetry about the rotation axis. Quantum-mechanically this symmetry does not allow collective rotation, but the large spin projections of the aligned valence nucleons guarantee angular momentum conservation. Similar phase transitions from prolate collective rotation to oblate single particle alignment had previously been observed in the mass A=160 region, see e.g. [Ri86]. The phase transitions in three bands in ^{122}Xe are illustrated in figure 2 where the excitation energies minus a

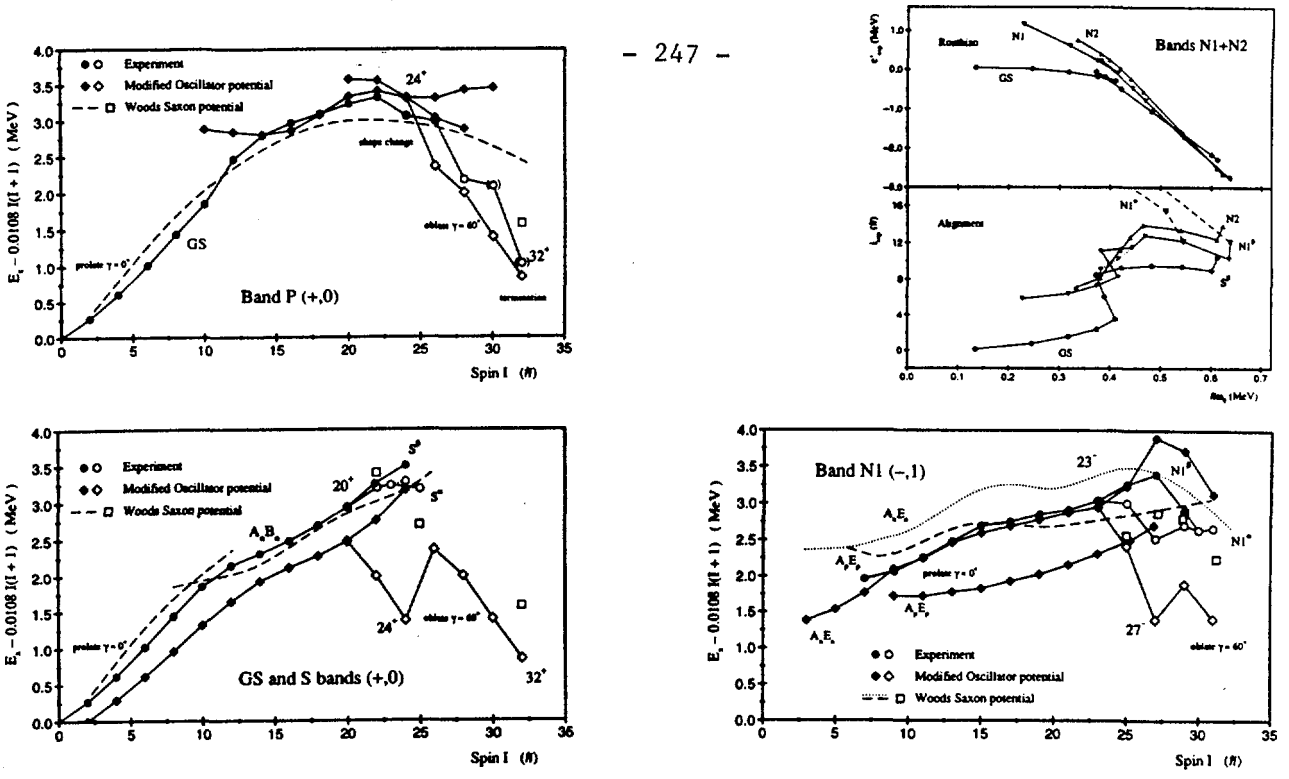

Figure 2: *The excitation energy minus a rigid rotor reference plotted versus spin for the three bands in ^{122}Xe which undergo a high spin phase transition. In addition the theoretical predictions are shown. Furthermore the experimental Routhians and the alignment are displayed for the lowest energy negative parity signature partners with the Stockholm band as a reference.*

rigid rotor reference are plotted versus spin.

The positive parity high spin structure in ^{122}Xe displays three[4] 22^+ positive parity states of different character. This is reproduced by TRS calculations [Be91], see figure 3, which predict for this spin two shapes with predominantly prolate collective characteristic ($\epsilon \approx 0.2, \gamma \approx -30^o$ and $\epsilon \approx 0.3, \gamma \approx 0^o$) and a favoured oblate single particle state ($\epsilon \approx 0.22, \gamma \approx 60^o$).

The generation of angular momentum by aligning the spin of valence nucleons is restricted because of their limited number. Thus the full alignment of the valence nucleons leads to a band-terminating state. This is predicted for ^{122}Xe to be the $\pi[(h_{11/2})^2(g_{7/2}d_{5/2})]_{16^+} \otimes \nu[(h_{11/2})^4]_{16^+}$ configuration with $I^\pi = 32^+$. Although this state has not firmly been established as yet, assuming the suggested spin and parity assignments of the positive parity side band in ^{122}Xe are correct, it could correspond to the $(32^{(+)})$ level in this band [Ti91]. However, partially aligned favoured single particle configurations, which are predicted by Modified Oscillator calculations for 27^- and 31^- states [Be91] are identified with single particle levels on top of the lowest energy negative parity band in this nucleus, see for details [Si91].

It is of great interest to fully establish and assign the high spin single particle structures in ^{122}Xe, since the knowledge of excitation energies for these configurations allows a valuable check of the predictions of the single particle mean-field model. This is important because in this region at low spins the nuclear structure is dominated by collective excitations and pairing interactions. The very fast rotation, however, breaks the pairing interactions and at the same time forces the nucleus to the alignment of symmetry and rotation axis. This does not allow collective rotation and leads to pure single particle excitations. The investigation of the high spin single particle states in the A=160 nuclei has already led to a revision of the standard parameters in the Modified Oscillator model.

In order to map out the high spin single particle structure in ^{122}Xe an experiment has been proposed

[4] If the assignment of the excited positive parity band is correct.

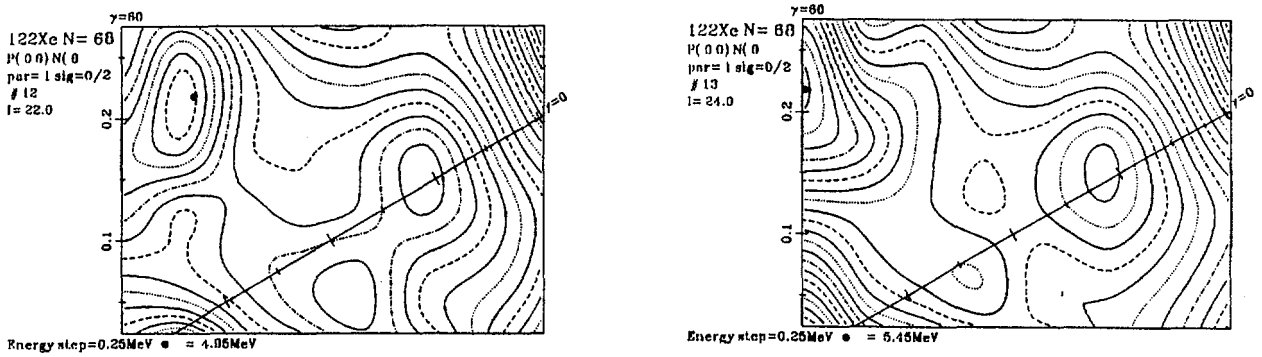

Figure 3: *The results of the Modified Oscillator TRS calculations for $I^{\pi} = 22^{+}$ and 24^{+} in ^{122}Xe. At spin 22^{+} two collective prolate shapes are predicted which compete with a favoured single particle configuration with oblate character.*

by the author *et al* using the same reaction as previously but employing the new EUROGAM detector array comprising up to 70 Compton-suppressed Ge-detectors. This experiment has been accepted and will be performed in summer 1992. The data to be obtained in this experiment will permit high statistics intensity measurements in order to detect the multitude of decay paths which develop in connection with the single particle structures on the very top of the rotational bands in ^{122}Xe.

In addition this experiment will produce high spin γ-γ coincidence data on ^{121}I through the reaction channel ^{96}Zr(^{30}Si,p4n). This nucleus at high spin also undergoes a phase transition from prolate collective to oblate single particle excitation [Li91]. Furthermore it is predicted [Na91], that the oblate collective band in this nucleus terminates in prolate single particle configurations at $\gamma = -120^{o}$. This would be the first observation of oblate and prolate band-terminations in the same nucleus.

The experiment also should allow to detect states even beyond the fully aligned band-terminations. This is of interest since in order to generate even higher angular momenta the fully alignment of the valence nucleons requires either the break of the closed $^{114}_{50}Sn_{64}$ core or a shape change back to collectivity. The latter phenomenon has recently been discovered in ^{119}I [Pa91a].

There is a very important indication of band-termination which as yet has not been detected in the mass A=120 region. Because of their single particle character terminating states should show increased lifetimes compared to their collective competitors. This was observed for the terminating states in the mass A=160 region which appear as stopped peaks in backed target data, while the corresponding collective states show strong Doppler-broadening because they decay already during the slowing down process of the residual nucleus. In the ^{122}Xe data no difference in broadening between the single particle and collective high spin decays can be seen indicating, that the lifetimes of both are considerably longer than the slowing down time in the gold-backing, which is 10^{-12} sec. In order to reveal the lifetimes of the high spin single particle states in ^{122}Xe and ^{121}I plunger measurements are planed.

References

[Be91] private communication

[Ha87] J. Hattula *et al.*; J. Phys. G. Nucl. Phys.**13** (1985):57

[Hu92] J.R. Hughes, private communication

[Ju91] S. Jutinnen *et al.*; Z. Phys. **A338** (1991): 365

[Li91] Y. Liang *et al.*; Phys. Rev. **C44** (1991): R578

[Na91] W. Nazarewicz, private communication

[Pa91a] E.S. Paul *et al.*; Shape coexistence in ^{119}I at high spin, submitted (1991)

[Pa91b] E.S. Paul *et al.*; Collective and non-collective high-spin states in ^{115}I, submitted (1991)

[Ri86] M.A. Riley *et al.*; Phys. Lett. **B177** (1986):15

[Si91] J. Simpson, H. Timmers *et al.*; Phys. Lett. **B262** (1991): 388

[Ti91] H. Timmers; Diplomarbeit, LM Universität München (1991)

[Wy91] R. Wyss, private communication

An $i_{13/2}$ Neutron Intruder Band in ^{141}Gd

S.M.Mullins[†], H.R.Andrews[‡], G.C.Ball[‡], T.E.Drake[§], D.B.Fossan[¶], A.Galindo-Uribarri[‡], V.P.Janzen[‡,†], D.Lafosse[¶], A.Omar[†], L.Persson[†], D.Prévost[†], D.C.Radford[‡], P.Vaska[¶], J.C.Waddington[†], R.Wadsworth[ϒ], D.Ward[‡] and M.Waring[¶]

[†] *Dept. of Physics and Astronomy, McMaster University, Hamilton, ON L8S 4M1, Canada*
[‡] *AECL Research, Chalk River Laboratories, Chalk River, ON K0J 1J0, Canada*
[§] *Department of Physics, University of Toronto, Toronto, ON M5S 1A7, Canada*
[¶] *Department of Physics, SUNY at Stony Brook, New York, NY 11794 USA*
[ϒ] *Department of Physics, University of York, Heslington, York YO1 5DD UK*

Abstract

The nucleus ^{141}Gd has been investigated at high spins for the first time following the reactions ^{112}Sn(^{32}S,2*pn*)^{141}Gd at 155 MeV and ^{112}Sn(^{33}S,2*p*2*n*)^{141}Gd at 170 MeV. The methods of in-beam γ-ray spectroscopy were used to establish a number of different structures, including a band which has been assigned as being based on the $\nu i_{13/2}[660]\frac{1}{2}^+$ Nilsson intruder orbital. This is the heaviest nucleus thusfar in which this type of intruder band has been identified.

High spin rotational bands, built on states of large quadrupole deformation, have been extensively studied in the mass regions centered around A $\simeq$ 135 and A $\simeq$ 150. Comparison of experiment with theory shows that the properties of the bands in the lighter region are consistent with the occupancy of one or two $i_{13/2}$ neutron orbitals intruding from the N = 6 oscillator shell. These strongly deformed bands ($\beta_2 \simeq$ 0.3–0.4) show large variations in the $\mathcal{J}^{(2)}$ dynamic moment of inertia, indicating that the single particle configuration is the dominant aspect in determining their structure. The high-N intruders in the heavier region are $i_{13/2}(N = 6)$ proton orbitals and $j_{15/2}(N = 7)$ neutron orbitals. These drive to superdeformed shapes ($\beta_2 \simeq 0.6$) which gain added stability from large energy gaps in the single-particle level spectrum.

A question of considerable interest is whether similar bands exist in intermediate mass nuclei, bridging the two regions. The discovery of superdeformation ($\beta_2 \simeq 0.5$) in ^{143}Eu[1] [1] and ^{142}Sm [3] has shown this to be the case. Gadolinium-141 was chosen here since Total Routhian Surface (TRS) calculations predict the possibility of observing two highly deformed shapes, one being similar to the A $\simeq$ 135 bands, and one with a deformation similar to ^{143}Eu.

The nucleus ^{141}Gd has been previously studied by β^+decay [4], but no in-beam γ-spectroscopy has been carried out. Hence, an initial experiment was undertaken to identify transitions belonging to ^{141}Gd.

[1]Note: This band was previously assigned to ^{142}Eu in [1]; see [2] for clarification.

Charged particle-γ-γ coincidences were measured following the $^{32}S + ^{112}Sn$ reaction at 155 MeV, the beam being provided by the upgraded MP tandem accelerator of the TASCC facility at AECL, Chalk River Laboratories. A single $\sim 500 \mu g/cm^2$ target foil enriched to $\sim$98% in ^{112}Sn was used, since a double foil would have severely reduced the efficiency for detecting the charged particles. States in ^{141}Gd were populated via the $2pn$ exit channel, the major competitors being ^{140}Gd [5] ($2p2n$), ^{141}Eu [6] ($3p$) and ^{138}Sm [7] ($\alpha 2p$). The γ-rays were detected by the 8π spectrometer, while charged particles were detected using the ALF-miniball [8] located inside the 8π. The data were written event-by-event onto magnetic tape for subsequent analysis.

In the replay of the data, the contribution from ^{140}Gd was greatly reduced by using the BGO-ball to select exit channels in which only three particles were evaporated. The charged particle identification and multiplicity from the ALF-miniball were then used to assign transitions to ^{141}Gd.

A second experiment was undertaken using the reaction $^{112}Sn(^{33}S,2p2n)^{141}Gd$ at 170 MeV, this time without the ALF-miniball, the aim being to bring in more angular momentum ($l_{max} \sim 65\hbar$ compared to about $55\hbar$ in the first experiment).

Having assigned transitions to ^{141}Gd, a level scheme was constructed using standard techniques, together with the codes MATFIT, LF8R and ESCL8R. This was done on the basis of the coincidence intensities through a least squares fit to the proposed level scheme shown in figure 1. The J^π values were inferred from Directional Correlation from Oriented states (DCO) analysis. The cascade labelled '1' in figure 1 has a mean DCO ratio between band members of (1.9±0.2) which is consistent with a cascade of stretched E2 transitions. The DCO ratio of the 603 keV transition is (1.1±0.1) and hence it has been placed as a stretched $\Delta J = 1$ feed-out transition from the bottom of the band. Assuming it is an electric dipole (E1) transition, it decays from a level with $J^\pi = \frac{13}{2}^+$. If this is the bandhead, then the only candidate is the $[660]\frac{1}{2}^+$ Nilsson state coming from the $i_{13/2}$ spherical multiplet. This orbital is responsible for the highly deformed bands found in the A = 130–140 region, including examples which are closely related to ^{141}Gd, namely the isotope ^{139}Gd [9] and the isotone ^{137}Nd [10].

Some Total Routhian Surfaces for ^{141}Gd are shown in figure 2 for the lowest $(\pi,\alpha) = (+,+\frac{1}{2})$ configuration. The yrast minimum starts as triaxial ($\beta_2 \simeq 0.27$, $\gamma \simeq 15°$), and then a 'superdeformed' prolate shape ($\beta_2 \simeq 0.5$, $\gamma \simeq 0°$) develops. This suggests that superdeformation may occur in ^{141}Gd. No evidence, however, could be found for a superdeformed band in ^{141}Gd. The triaxial minimum is similar to one seen in the TRS for ^{137}Nd [11], though in this case it evolves from a γ-soft prolate shape which is yrast at lower spins. Cranked Shell Model (CSM) calculations for the triaxial shape are shown in figure 3, where the $i_{13/2}$ $(\pi,\alpha) = (+,+\frac{1}{2})$ routhian is seen to be yrast beyond $\hbar\omega \simeq 0.25$ MeV. Hence, the assignment of the bandhead as $\nu i_{13/2}$ is consistent with the predictions of the CSM and TRS calculations.

In conclusion, the nucleus ^{141}Gd has been studied for the first time using in-beam γ-spectroscopy following heavy-ion induced reactions. The newly identified γ-ray transitions have been arranged into a decay scheme. A number of different level structures have been

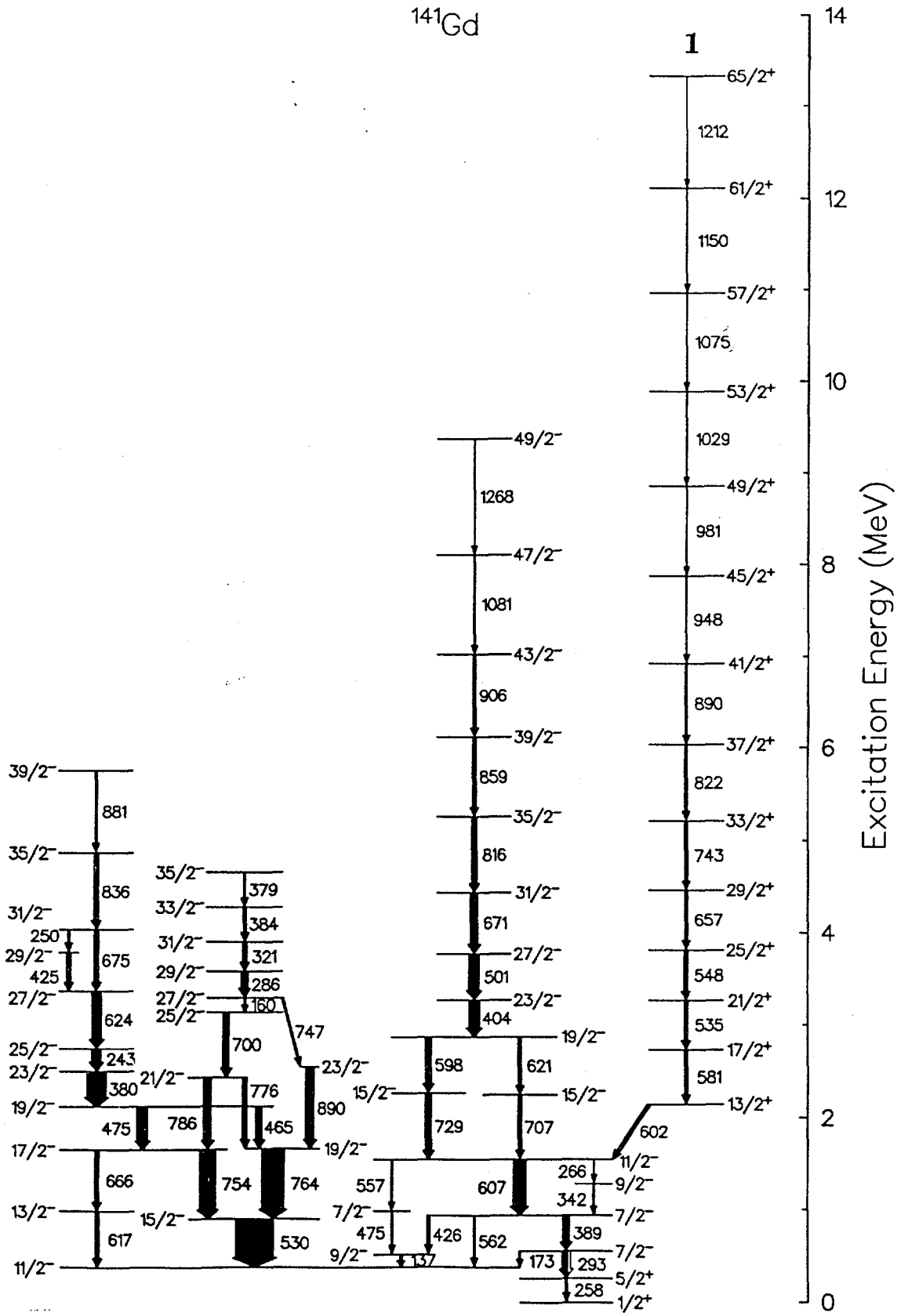

Figure 1.
Partial decay scheme for ^{141}Gd. The width of each arrow is proportional to the intensity of the respective transition.

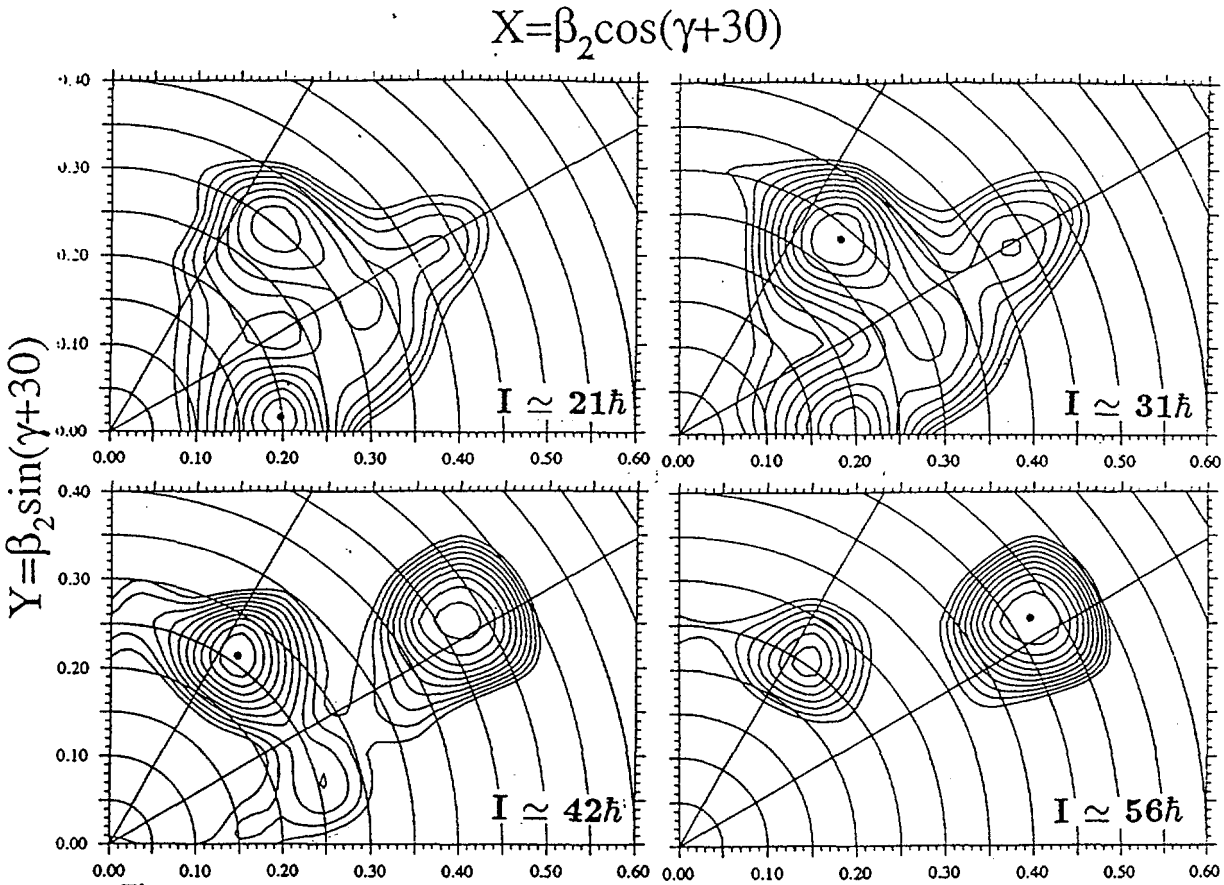

Figure 2.
Total Routhian Surface (TRS) calculations for ^{141}Gd, showing energy contours for the $(\pi,\alpha) = (+,+1/2)$ configuration.

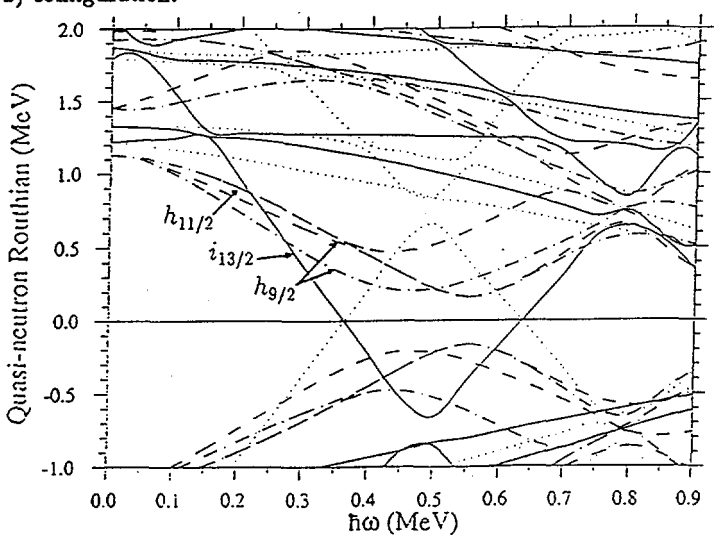

Figure 3.
Cranked Shell Model (CSM) calculations for ^{141}Gd, showing quasineutron routhians. The input parameters were $\beta_2 = 0.27$, $\gamma = 15°$, $\beta_4 = 0.01$, $\Delta_n = 1.02$ MeV.

found, including a rotational cascade which has been assigned as an $i_{13/2}$ neutron intruder band. This is the heaviest light rare earth nucleus in which this type of band has been isolated and is the first case to be clearly identified down to the $\frac{13}{2}^+$ bandhead.

This work was supported by the Natural Sciences and Engineering Research Council of Canada, AECL Research and by NATO under grant number CRG910182.

References

[1] S.M.Mullins *et al*, *Phys.Rev.Lett.* **66** 1677 (1991)

[2] A.Ataç *et al*, these proceedings

[3] G.Hackman *et al*, these proceedings

[4] J.Gilat, J.M.Nitschke, P.A.Wilmarth and R.B.Firestone, *Phys.Rev* **C40** 2249 (1989)

[5] C.J.Lister *et al*, *Phys.Rev.Lett.* **55** 810 (1985)

[6] N.Xu, C.W.Beausang, J.R.Hughes, Y.Liang, R.Ma, E.S.Paul, W.F.Piel Jr., S.Shi and D.B.Fossan, *Phys.Rev.* **C 43** 2189 (1991)

[7] S.Lunardi, F.Scarlassara, F.Soramel, S.Beghini, M.Morando and C.Signorini, *Z.Phys* **A321** 177 (1985)

[8] A.Galindo-Uribarri, in *Prog.Part.Nucl.Phys* **Vol 28** 463 (1992) (Pergamon Press).

[9] R.Ma *et al*, *J.Phys.G:Nucl.Part.Phys.* **16** 1233 (1990)

[10] R.Wadsworth *et al*, *J.Phys.G* **13** L207 (1990)

[11] S.M.Mullins *et al Phys.Rev.C* in press

High spin level structure of $^{143}_{63}Eu_{80}$

M. Piiparinen[1*], A. Ataç[1], G. de Angelis[2], S. Forbes[3], N. Gjørup[1], G. Hageman[1], B. Herskind[1], F. Ingebretsen[4], H. Jensen[1], D. Jerrestam[5], H. Kusakari[1], R. Lieder[1], G.M. Marti[6], S. Mullins[3], J. Nyberg[1], A. Santonocito[1], H. Schnare[6], G. Sletten[1], K. Strähle[6], M. Sugawara[1], P.O. Tjøm[4], A. Virtanen[1], R. Wadsworth[3]

[1] *Niels Bohr Institute, Tandem Accelerator Laboratory, Roskilde, Denmark*
[2] *Laboratori Nazionali di Legnaro, Legnaro, Italy*
[3] *Oliver Lodge Laboratory, University of Liverpool, Liverpool, U.K.*
[4] *Department of Physics, University of Oslo, Oslo, Norway*
[5] *Studsvik Science Laboratory, Nyköping, Sweden*
[6] *Institut für Kernphysik, Forschungszentrum Jülich, Jülich, Germany*

Abstract: *The level scheme of ^{143}Eu has been extended to I=75/2 in an experiment with the NORDBALL Compton-suppressed Ge detector array and the $^{110}Pd(^{37}Cl,4n)$ reaction. Most of the scheme shows irregular structure of multiparticle excitations. A strongly populated straight cascade of more than 10 stretched E2 transitions suggests the onset of collectivity.*

We have performed a high statistics experiment [1] in the nucleus ^{143}Eu where a superdeformed (SD) band was recently reported [2]. The experiment was primarily devoted to a search for the connection between the SD band and the normal yrast structure. For that it is necessary to know also the normal level scheme in the region where the SD band feeds in. Here we report our results on the ^{143}Eu yrast scheme, previously known [3] to spin 35/2, which we have extended up to spin 75/2 and 15.6 MeV excitation.

The experiment was carried out with the NORDBALL detector array at the Niels Bohr Institute Tandem accelerator laboratory, employing 19 Compton-suppressed Ge detectors and one LEP spectrometer, together with the BaF_2 calorimeter for multiplicity and sum energy measurement. We used the ^{110}Pd(^{37}Cl,4n) reaction at 160 MeV bombarding energy. The target was either a stack of 2 or 3 selfsupporting ^{110}Pd foils with a total thickness of 1.2 mg/cm^2 or a 0.9 mg/cm^2 layer of ^{110}Pd sputtered on an 11 mg/cm^2 Au backing. In each case 98.6 % enriched ^{110}Pd material was used. About 10^9 triple coincidence events were collected in the thin target experiment and 5×10^8 doubles with the Au-backed target. In about 30 % of the compound nucleus formations the reaction led to ^{143}Eu through the 4n channel.

From comprehensive coincidence data more than 170 transitions have been placed in the ^{143}Eu level scheme of Fig. 1 which shows a very complex and irregular structure. This is typical for a spherical or slightly oblate nucleus where multiparticle excitations dominate. The complex scheme with numerous cross connections, all of them established by observed coincidence relations, provide many checks for the transition placements and orderings. Still there are many cascades in the ^{143}Eu level scheme without connections to the intermediate levels and the transition orderings cannot always be established unambiguously. The intensity unbalance on several levels and many additional coincidence relations indicate that there are still numerous cross connections which have not been observed.

The SD band in ^{143}Eu has been observed [4] in coincidence with all reasonably strong γ rays in the right part of the level scheme of Fig. 1 below the I=35/2 level at 4949 keV.

*Permanent address: Dept. of Physics, Univ. of Jyväskylä, Jyväskylä, Finland

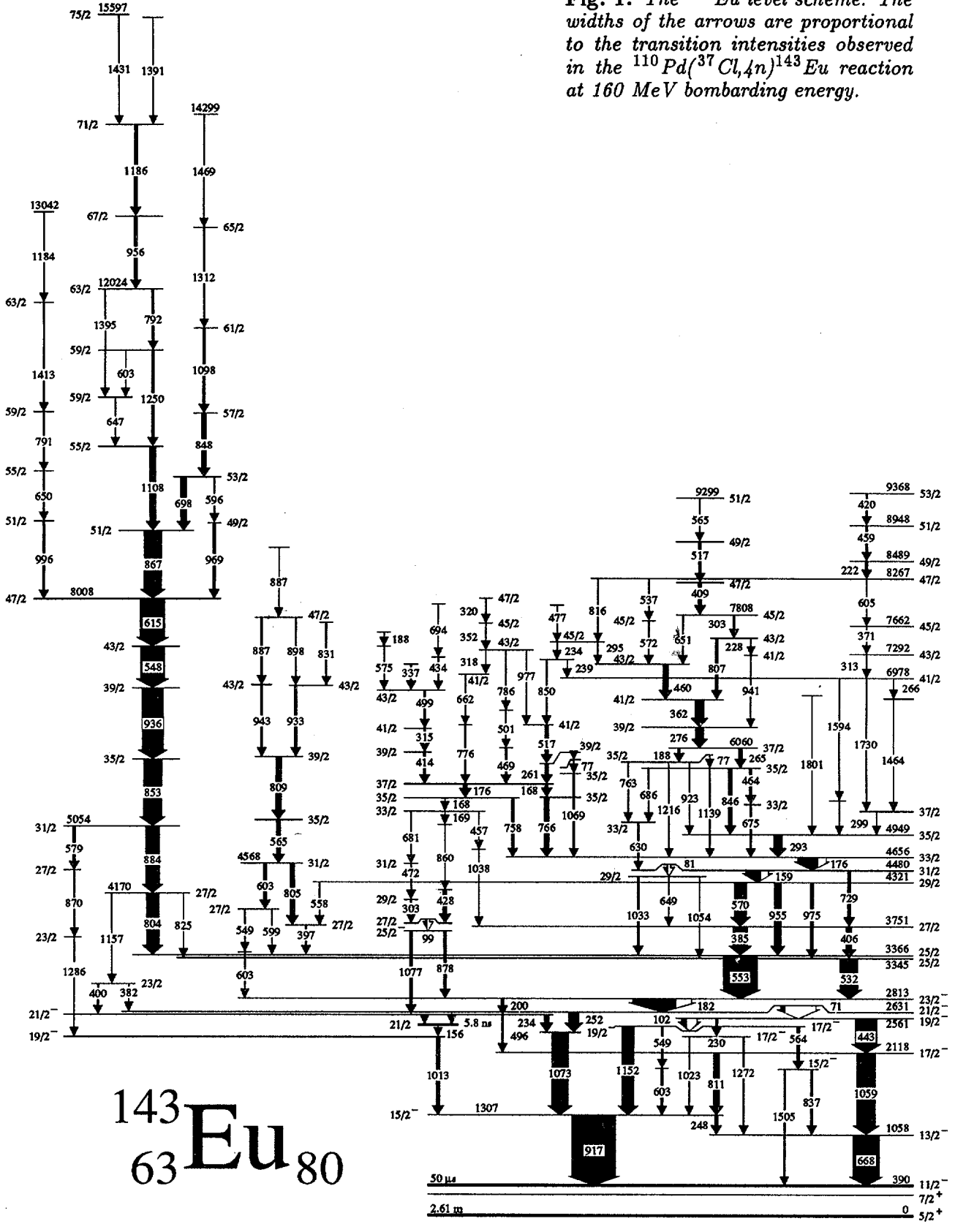

Fig. 1. *The ^{143}Eu level scheme. The widths of the arrows are proportional to the transition intensities observed in the $^{110}Pd(^{37}Cl,4n)^{143}Eu$ reaction at 160 MeV bombarding energy.*

The strongly fragmented decay from the SD band feeds mostly the $33/2 - 39/2$ spin interval. This region of the level scheme is particularly complex and the detailed knowledge of this structure was found to be vitally important for establishing the connection between the SD band and the normal yrast structure which in ^{143}Eu was done [4] for the first time. An interesting feature of the ^{143}Eu level scheme is the existence of several high energy 1.5 – 1.8 MeV $E2$ transitions, shown to the right in Fig. 1. In a shell model nucleus this is usually an indication of breaking the core and lifting a particle across the shell gap to a higher-lying high-j orbital. The other levels with comparable spins have probably both quite different multiparticle configurations and shapes which govern their decay properties. A competition between spherical and oblate structures have been observed [5,6] to cause very complex decay schemes in this mass region.

In the new ^{143}Eu level scheme a striking observation is a very strongly populated straight cascade of more than 10 stretched $E2$ transitions starting from a I=27/2 level at an excitation energy of 4.2 MeV. These transitions with energies between 550 and 1250 keV form an irregular sequence, not resembling any rotational band. The transition intensities in the lower half of the cascade are clearly increasing with increasing level energy, as can be seen in Fig. 1. However, the transition ordering is rather firm and some intensity is decaying out of the cascade through a large number of weak pathways which have not been established.

Almost all the γ transitions of the ^{143}Eu level scheme appeared as sharp spectral lines in the backed target experiment indicating that they were emitted from stopped recoil nuclei. However, at the top of the scheme, especially in the above mentioned $E2$ cascade the effective lifetimes are in the order of or shorter than ps since the lines start to get Doppler broadened and the highest transitions could be obtained only from the thin target data. The appearance of such a long $E2$ cascade which is very unusual in a spherical nucleus and the fact that at least the upper part of it is fast $E2$'s apparently indicates some kind of increase of collectivity of the nucleus.

The nucleus ^{143}Eu forms an interesting battle ground where in the same excitation energy region several very different modes are competing. Superdeformed levels are observed [4] down to $I \simeq 35/2$ at 8.6 MeV, to the same energy range where most of the scheme is dominated by spherical or oblate states favouring dipole radiation. However, several parallel high-energy $E2$ transitions have also been recorded and a long $E2$ cascade dominates the highest part of the "normal" (not superdeformed) level scheme.

This work was partially supported by the Academy of Finland and Swedish Natural Science Research Council.

References

1. A. Ataç, *et al.*: Int. Conf. on Progress in Particle and Nuclear Physics, A. Faessler (Ed.). Pergamon Press, UK, 1991, Erice Vol. 28
2. S.M. Mullins *et al.*: Phys. Rev. Lett. **66**, 1677 (1991) (originally the SD band was assigned to ^{142}Eu but our data unambiguously indicate reassignment to ^{143}Eu)
3. M. Müller-Veggian *et al.*: Z. Phys. **A330**, 343 (1988)
4. A. Ataç, *et al.*: separate contribution to these proceedings and to be published
5. O. Bakander, *et al.*: Nucl. Phys. **A389**, 93 (1982)
6. M. Piiparinen, *et al.*: Phys. Lett. **B194**, 468 (1987)

INTERNATIONAL CONFERENCE ON NUCLEAR STRUCTURE AT HIGH ANGULAR MOMENTUM

Ottawa

SESSION 10: NUCLEAR THEORY (II)

EXOTIC NUCLEAR SHAPES - AXIAL AND NONAXIAL OCTUPOLES AT NORMAL AND AT SUPER-DEFORMATION

J. Skalski[1,2], P.-H. Heenen[2], P. Bonche[3], H. Flocard[4] and J. Meyer[5]

(1) Soltan Institute for Nuclear Studies, PL- 00 681, Warsaw, Poland
(2) SPhNT U.L.B - C.P. 229 - 1050 Brussels, Belgium
(3) SPhT CEN Saclay - 91191 Gif sur Yvette Cedex, France
(4) DPhT [6], IPN - 91406 Orsay Cedex, France
(5) IPNL, IN2P3-CNRS / Université C. Bernard Lyon 1, 69622 Villeurbanne Cedex, France

ABSTRACT

We have studied collective octupole dynamics including nonaxial components of the octupole mean field, mainly at superdeformed shape in the Hg-Pb region. Both the Strutinsky method combined with cranking and the generator coordinate method within the selfconsistent Hartree-Fock basis suggest the existence of collective octupole excitations at the superdeformed minima. GCM calculations point out to the E1 transitions as their most prominent experimental manifestation. We also comment on the nonaxial octupole components influence on octupole dynamics in traditional octupole region of Ra-Th nuclei.

1. Introduction

It is rather obvious that a thorough study of octupole dynamics in atomic nuclei requires inclusion of nonaxial components of octupole tensor. Nonaxial octupole modes have been studied within the RPA already in the seventies [1], but the deformed shell model approach has not been attempted until recently, mainly because of difficulties acompanying the introduction of nonaxial octupole components into the nuclear mean field. First, such deformations destroy mean field symmmetries, which makes calculations more time-consuming.[7] Second, there is a problem of the proper parametrization of octupole deformation and of a practical way of dealing with the seven parameter shape family.

A new impulse to study these exotic nuclear shapes came from the rising interest in nuclear structure at super-deformed (SD) shapes, expected to show new features, different from those at normal deformations. Indeed, theoretical studies have shown that SD minima are more sensitive to the axial octupole deformation than normally deformed ground states [2-7]. It has also been noticed that the structure of single-particle levels at deformations corresponding to the ellipsoid axes ratio 2:1 opens the possibility for the existence of low energy non-axial octupole excitations [8]. The SD shapes with non-axial octupole components have been studied in [9-12] within the Strutinsky method. Octupole excitation energies at SD minima were calculated within a simplified RPA approach in [13-16]. The most unexpected results were obtained in [11], where secondary SD minima with very large nonaxial octupole deformation β_{31} (banana-like shape) have been found at high spin in many nuclei from the Pb-Hg region.

Experiments [17, 18] point also to octupole correlations as a possible explanation of SD bands deexcitation patterns. In particular, ref. [18] has given a clear evidence for the existence of regular dipole transitions connecting two SD bands in ^{193}Hg. Recently,

[6] Unité de recherches des Universités Paris XI et Paris VI associée au C.N.R.S..

[7] for quite general octupole deformation, one reaches an extreme situation when even the only granted Kramers degeneracy cannot be practically used.

arguments have been presented suggesting the M1 character of these dipole transitions [19, 20], thus challenging the initial octupole correlations interpretation. This uncertainity on the experimental side adds even more interest to the study of possible octupole excitations in SD nuclei.

In this contribution we discuss results of the study of octupole correlations including nonaxial octupole shapes, mainly in SD nuclei from the Hg-Pb region. First, we describe results obtained within the Strutinsky method combined with cranking, concerning the rotation-dependent octupole stiffness of the SD minima, partly published in [12]. Then we describe recent fully microscopic calculations of octupole excitation properties at SD shape, performed within the generator coordinate method (GCM) based on the selfconsistent Hartree-Fock plus BCS (HFBCS) theory [21]. Finally, we present some preliminary results obtained within the Strutinsky method for octupole deformed Ra-Th nuclei, concerning the effect of mixing of the axial and μ=1 octupole deformations.

2. Mean-field symmetries and macroscopic considerations

We parametrize the nuclear shape using deformation parameters $\beta_{\lambda\mu}$ defined by the equation of the nuclear surface:

$$R(\theta,\phi) = R_0 c(\beta)(1 + \sum_{\lambda\mu} \beta_{\lambda\mu} Y_{\lambda\mu(c)}(\theta,\phi)), \tag{1}$$

where octupole deformations are introduced by means of real orthonormal spherical harmonics:

$$\begin{aligned} Y_{30}(\theta) &= (\tfrac{7}{16\pi})^{\frac{1}{2}}(5\cos^3\theta - 3\cos\theta), \\ Y_{31c}(\theta,\phi) &= -(\tfrac{21}{32\pi})^{\frac{1}{2}}\sin\theta(5\cos^2\theta - 1)\cos\phi, \\ Y_{32c}(\theta,\phi) &= (\tfrac{105}{16\pi})^{\frac{1}{2}}\sin^2\theta\cos\theta\cos 2\phi, \\ Y_{33c}(\theta,\phi) &= -(\tfrac{35}{32\pi})^{\frac{1}{2}} sin^3\theta cos 3\phi, \end{aligned} \tag{2}$$

instead of the usual complex ones.

Allowing only the four deformations of eq.2, we assure one reflection symmetry plane of the considered octupole shape (simplex symmetry). In the following we consider even more specific shapes, with only one nonvanishing octupole component superposed with the SD quadrupole-hexadecapole shape. Such shapes have two reflection symmetry planes. Mean fields containing Y_{30}, Y_{31c}, Y_{32c}, and Y_{33c} terms have symmetry groups $C_{\infty v}$, C_{2v}, D_{2d} and D_{3h}, respectively. Single nucleon levels in potentials with the corresponding symmetries fall into classes according to irreducible representations (irreps) of the corresponding double groups. The $C_{\infty v}$ case is well known as it corresponds to the axial symmetry. The groups C_{2v}, D_{2d} and D_{3h} have one 2-D, two 2-D, and three 2-D nonequivalent spinor irreps, respectively [22]. Thus, in all cases that we consider we deal only with the Kramers degeneracy in general. In a potential with Y_{31c} deformation all s.p. levels interact so this is the case where we should not expect a pronounced shell structure. For SD shapes with Y_{32c} and Y_{33c} deformations we have 2 and 3 mutually noninteracting groups of levels (s.p. hamiltonian blocks), respectively [1]. In particular, axial, good parity states with positive Ω may be classified according to D_{2d} symmetry into two groups: $1/2^+, 3/2^-, 5/2^-, 7/2^+, 9/2^+, 11/2^-, ...$, and $1/2^-, 3/2^+, 5/2^+, 7/2^-, 9/2^-, 11/2^+, ...$, while according to D_{3h} symmetry they fall into three groups: $1/2^+, 5/2^-, 7/2^-, 11/2^+, 13/2^+, ...$, $1/2^-, 5/2^+, 7/2^+, 11/2^-, 13/2^-, ...$, and $3/2^\pm, 9/2^\pm, 15/2^\pm, ...$ This makes some shell effects more likely. We note that simultaneous admission of octupole distortions with $\mu = 0$, 2 or $\mu = 1$, 3 reduces the symmetry group to C_{2v}.

[1] and extra Kramers degeneracy

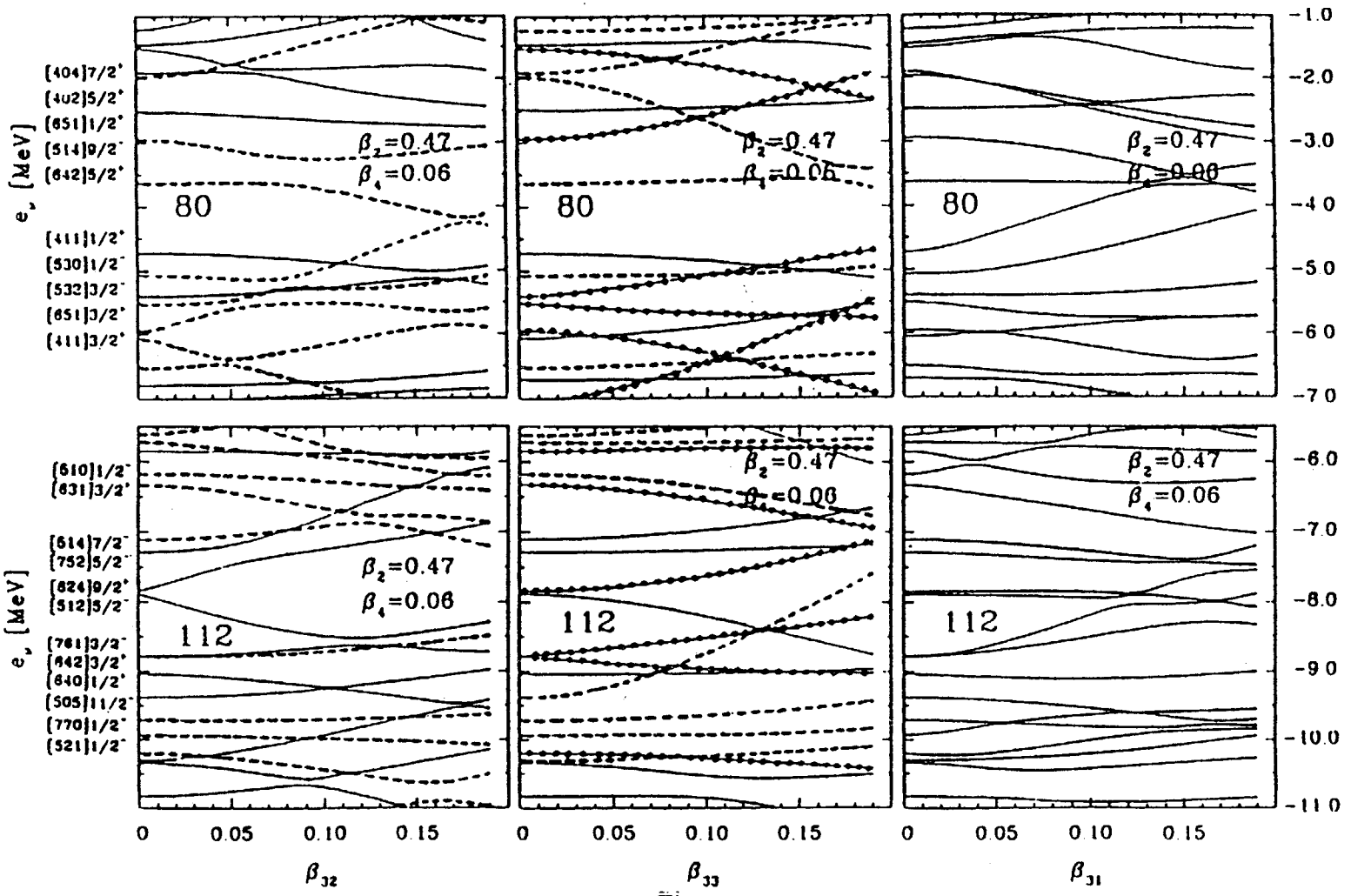

Figure 1

The neutron (bottom) and proton (top) Woods-Saxon levels in ^{192}Hg as a function of the octupole deformations β_{32}, β_{33} and β_{31} (from left to right) near the SD minimum. Solid, dashed (and solid dotted) lines are used to make distinction between levels belonging to two (three) inequivalent irreps of the D_{2d} (D_{3h}) group. The asymptotic Nilsson labels at the axially symmetric SD minimum are displayed to the left.

These remarks are illustrated in Fig. 1, where s.p. levels in ^{192}Hg are shown as a function of $\beta_{3\mu}$, μ=1,2,3, near the SD minimum. They have been obtained using the Woods-Saxon potential of [23], on which the microscopic part of our routhian calculations is based. In the μ=1 case, there are many avoided crossings and both SD gaps, at N=112 and at Z=80, close rather quickly with increasing β_{31}. A pronounced octupole-related shell effect occurs only for β_{32} deformation and N=114. It results from the strong Y_{32c} coupling of the neutron [512]5/2$^-$ and [624]9/2$^+$ states (using Nilsson asymptotic labels) which are nearly degenerated with the N=114 Fermi level at the SD minimum. We shall discuss its consequences later. The corresponding proton spectrum preserves the Z=80 gap up to $\beta_{32} \approx 0.10$. The Z=80 gap is even more stable with respect to the β_{33} deformation, but the resulting shell effect is cancelled by the neutron levels behaviour.

The macroscopic energy must be included in our Strutinsky calculations in order to account for the bulk nuclear deformation energy. In the quadrupole prolate field, the macroscopic energy sets the hierarchy for octupole deformations of different μ, favouring smaller μ. The "Yukawa-plus-exponential" energy [24], employed in this calculation, increases roughly by 100 keV per step in μ at $\beta_{3\mu}$ =0.08 and by 300 keV per step in μ at $\beta_{3\mu}$ =0.16 and fixed $\beta_2 \approx 0.5$, typical of SD minima in Hg-Pb region. Thus, at $\beta_{3\mu}$=0.16, the deformation Y_{33c} is hindered by the macroscopic energy roughly by 1.2 MeV as compared to Y_{30}. We have also checked, that for large deformations $\beta_{3\mu} \approx 0.5$, and β_2 typical of SD or smaller, the macroscopic energy is 10-15 MeV larger than at the $\beta_{3\mu}$=0 point. Thus, the macroscopic energy contribution seems to hinder large octupole deformations.

The Y_{31c} deformation differs from the three others of eq.2 in this respect that it breaks the axial symmmetry of the rigid body inertia tensor. In this case, various choices of the cranking axis, perpendicular to the elongation axis, are not equivalent. As we have found in calculations, related differences are small as compared to the effects we want to discuss. The rigid body moment of inertia at SD shape is not sensitive to octupole distortions: it is larger at $\beta_{3\mu}$ =0.16 than at β_3 =0 by 1.5 %, 1.4 %, 0.4 %, and 0.05 % for μ =0, 1, 2, 3, respectively.

3. Cranked Strutinsky method results

In [12], the total routhians, $E^\omega(\omega,\beta)$, of selected even Hg and Pb nuclei have been calculated for rotational frequencies $\hbar\omega$ =0 (0.05) 0.55 MeV at $\beta_{3\mu}$ =0 (0.04) 0.16, μ =0, 1, 2, 3, and fixed β_2 and β_4 deformations, corresponding to SD minima [6]. Pairing has been treated within the BCS method at ω =0 and at ω >0 it has been parametrized as in [25], using $\hbar\omega_c$ =0.45 MeV for neutrons and $\hbar\omega_c$ =0.50 MeV for protons. In order to present results in a compact form we have chosen the octupole stiffness of the routhian at fixed ω, defined as $C^\omega_{3\mu}=\frac{\partial^2 E^\omega}{\partial\beta^2_{3\mu}}$. Actually, it has been calculated from the relation: $E^\omega(\omega,\beta_{3\mu}=0.04) - E^\omega(\omega,\beta_{3\mu}=0) = \frac{1}{2}C^\omega_{3\mu}\beta^2_{3\mu}$. This choice has its drawbacks since $C^\omega_{3\mu}$ is a local quantity, depending on assumed β_2 and β_4 values. Especially C^ω_{30} shows large sensitivity to the assumed SD minimum deformations. On the other hand, these deformations show very small variation with ω [6] and related effects will be small as far as general features of the octupole stiffness are concerned.

The calculated values of $C^\omega_{3\mu}$ are shown in fig. 2 (results of cranking around x-axis are given for Y_{31c} deformation). The softest are: the axial mode, favoured by the macroscopic energy and by the shell correction [1], and the μ=2 mode, especially for N=114, in close relation to the shell effect visible in fig.1. As expected from fig.1, the μ=1,3 modes are disfavoured

[1] at the SD shape in the Hg-Pb region the μ = 0 octupole-driving shell effect comes from neutrons (N≈112), while protons (Z≈80) counteract this tendency [3, 5, 6]

by the shell correction (1.5-1.8 MeV increase from β_{31}=0 to β_{31}=0.16). According to the $C^{\omega}_{3\mu}$ values at ω=0 the stiffness increases in the following order: μ=0, 2, 3, 1, the last one being at least two times larger than the first.

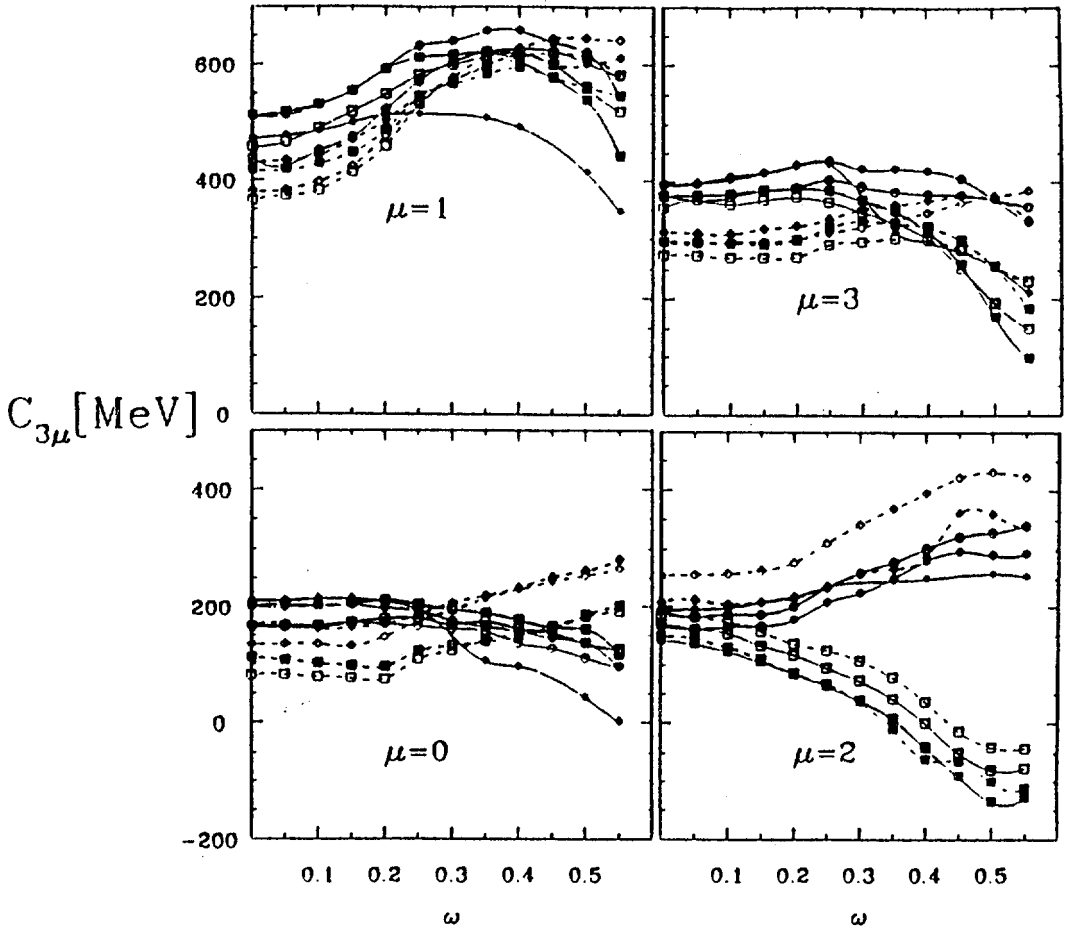

Figure 2

The routhian stiffness, $C^{\omega}_{3\mu}$, against the four components of the octupole deformation at the SD minimum as a function of the rotational frequency ω for ^{192}Hg (open circles), ^{194}Hg (open squares), ^{196}Hg (open diamonds), ^{192}Pb (stars), ^{194}Pb (full circles), ^{196}Pb (full squares) and ^{198}Pb (full diamonds). Points resulting from calculations at β_2 =0.47, β_4 =0.06 are connected by solid lines and those obtained at β_2 =0.47, β_4 =0.04 are connected by dashed lines (from [12]).

The main features of the ω dependence of the stiffness coeficients are: the softening of the μ=2 mode for N=114 and the increase of the μ=1 stiffness with ω (up to $\hbar\omega$=0.3). Both result from the pairing effect on the moment of inertia, directly correlated with the neutron and proton level densities in fig.1. In particular, the gap opening for N=114 with increasing β_{32} causes a reduction of Δ_n while the N=112 gap closing vs. β_{31} causes an increase of Δ_n. The former effect gives rise to the routhian minimum at β_{32} ≈0.04 for ω=0.4, and negative C^{ω}_{32} values in fig.2.

Routhian plots vs. $\beta_{3\mu}$ for some nuclei are shown in fig.3. One can see there that the axial mode is globally the softest one. The depth of the β_{32} minimum in ^{194}Hg is so small that the corresponding routhian reminds rather a wide well centered still at β_{32}=0. The routhians of ^{192}Hg, displayed in fig.3, are typical for studied Hg-Pb nuclei, the N=114 systems being

rather exceptional. Interestingly enough, this picture is also characteristic for SD nuclei around ^{152}Dy, for which we performed similar calculations ($\hbar\omega_c$=0.6 MeV for neutrons and 0.7 MeV for protons). This can be seen by comparing the routhian plot of ^{152}Dy, also shown in fig.3, to that of ^{192}Hg. Note that for ^{152}Dy, the difference between the two possible Y_{31c} cranking modes, around x and y axes, becomes visible in the routhian plot.

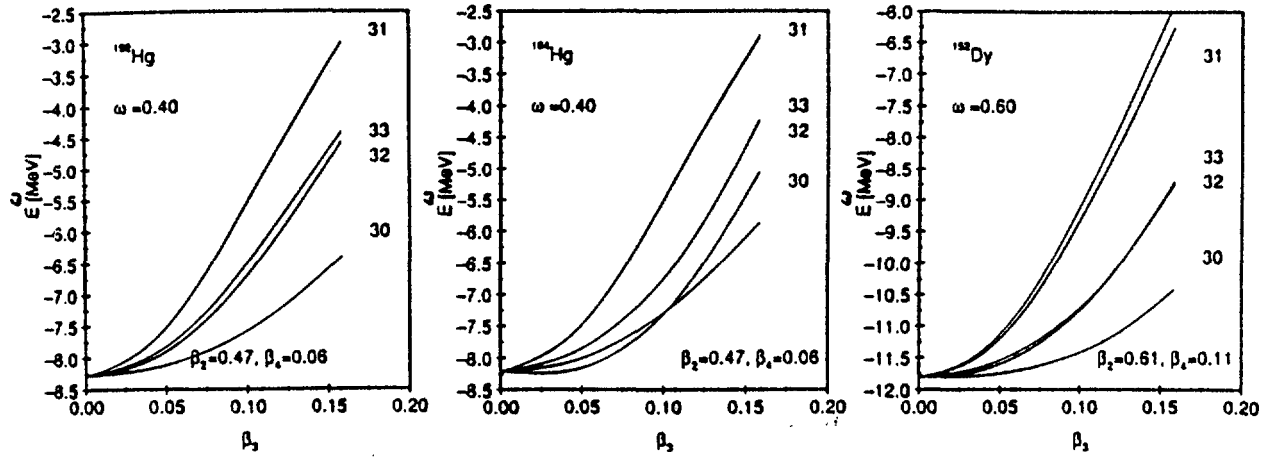

Figure 3

The routhians $E^{\omega}(\beta_{3\mu})$ for ^{192}Hg, ^{194}Hg and ^{152}Dy, calculated at $\hbar\omega$=0.4 MeV (Hg, I≈45$\hbar$) and $\hbar\omega$=0.6 MeV (Dy, I≈58$\hbar$). Curves are labelled by the corresponding μ; in β_{31}-deformed ^{152}Dy the y-axis cranking is favoured.

We have estimated octupole vibration energies at the SD minimum and spin zero by calculating the inertia parameters $B_{\mu\mu}$ [1] within the cranking approximation [26] and using the simple formula: $\hbar\omega_{3\mu} = \sqrt{C_{3\mu}(\omega=0)/B^{cf.f}_{\mu\mu}}$. We obtained the following esimates for $\hbar\omega_{3\mu}$: 1.4-1.6 MeV for μ=0, 2.0-2.3 MeV for μ=1, 1.07-1.4 MeV for μ=2, and 2.4-2.5 MeV for μ=3 [12]. In order to have some reference, we estimated in a similar way the $\hbar\omega_{30}$ frequency at the normal deformation in the same nuclei [12] and obtained $\hbar\omega_{30}$ values increasing with neutron number N, from 2.0 to 2.4 MeV (from 2.1 to 2.7 MeV), for Hg(Pb) isotopes. These values are consistent with experimental systematics [27].

4. GCM results

Recently, we have extended the octupole GCM calculations by introducing non-axial μ=1 and 2 octupole moment components into the analysis of the octupole collectivity, in addition to the axial μ=0 mode [2]. This work [21] is based on previous HFBCS [28, 29] and GCM studies in the Hg-Pb region [30, 31, 7]. A possible coupling to the quadrupole motion is neglected here which is partly justified by the results of [7] and those of a forthcoming study [32]. Rotation being not included, our results describe octupole vibrations built on the lowest SD $I^{\pi} = 0^+$ state. One can try to deduce from them excitation energies and other properties of an octupole-excited SD band at not too large angular momenta.

We have used mainly the SkM* Skyrme effective interaction [33], already employed in the HFBCS description of the SD nuclei in the mercury-lead region [28]. This version of the

[1] note that off-diagonal masses $B_{\mu\nu}$ strictly vanish at the axially symmetric deformation.
[2] We postponed the inclusion of the μ=3 mode as it has been found much less collective in all studies [13, 14, 15, 10, 12].

Skyrme force is believed to be appropriate for SD nuclei since it has improved surface tension properties leading to a reasonable description of fission barriers. Nevertheless, we have also performed a comparison with the Skyrme force SIII which is not excluded as an alternative for the considered nuclei [30, 34].

We constructed HFBCS states for three nuclei: ^{192}Hg, ^{194}Hg and ^{194}Pb using the Skyrme SkM* effective force and the monopole pairing interaction included within the BCS formalism with constant pairing strengths: G_n=16.5/(11+N) and G_p=17.5/(11+Z) (see e.g. [28]). The quadrupole moments were kept independent of octupole deformations and fixed at the values q=42b, 42b and 46b, respectively, which correspond to the reflection-symmetric SD minima. For each nucleus we generated three sets of states with octupole moments $q_{30} =< r^3 Y_{30} >$, $q_{31} = \frac{1}{2} < r^3(Y_{31} - Y_{3-1}) >$ and $q_{32} = \frac{1}{2} < r^3(Y_{32} + Y_{3-2}) >$ increasing in steps of 1000 fm^3, 1000 fm^3 and 500 fm^3, respectively. For the purpose of the GCM calculation it was enough to include the maximal octupole moments of 6000 fm^3, 5000 fm^3 and 2500 fm^3 for μ=0,1 and 2, respectively. For the nucleus ^{194}Hg we have performed also the analogous calculations using the effective force SIII.

Using the same effective force and the deformed HFBCS states we have calculated the norm and energy overlaps and solved GCM problem as described in [30]. The GCM states $| \Psi_k)$ which result from the diagonalization of the hamiltonian can be written in the form of an expansion on the nonorthogonal basis of HFBCS states $| \Phi(q_{3\mu}))$ corresponding to different octupole moments $q_{3\mu}$:

$$| \Psi_k) = \sum_{q_{3\mu}} f(q_{3\mu}) \, | \Phi(q_{3\mu})). \tag{3}$$

The collective wave function in the generating coordinate, $g(q_{3\mu})$, is related to $f(q_{3\mu})$ of eq. 3 via the square root of the norm overlap matrix [30].

Since spatial reflection is a symmetry of the hamiltonian we obtain positive and negative parity GCM solutions. The lowest positive parity GCM solution represents the intrinsic state of the SD g.s. band while the lowest negative parity GCM state corresponds to the intrinsic configuration of the first excited octupole state with $| K |= \mu$ in the SD well. The difference of their energies is the excitation energy of the lowest octupole excitation with given μ. Reduced transition probabilities from the SD g.s. to the excited state have been calculated using formulas based on the rotational collective model [35]:

$$\begin{aligned} B(E1; K=0, I=0 \rightarrow K=\mu, I=1) &= a\tfrac{3}{4\pi} \, | \langle g.s. \, | \, \hat{D} \, | \, (\mu)_1 \rangle \, |^2, \\ B(E3; K=0, I=0 \rightarrow K=\mu, I=3) &= a \, | \langle g.s. \, | \, \textstyle\sum_p r^3 Y_{3\mu}(p) \, | \, (\mu)_1 \rangle \, |^2, \end{aligned} \tag{4}$$

where $\hat{D}$ is the dipole moment operator, $| \, (\mu)_1 \rangle$ is the lowest negative parity intrinsic GCM excitation, and the factor a=1 for μ=0 and a=2 for μ=1,2 (there are no $E1$ transitions associated with the μ=2 octupole deformation).

Near the SD minima, the HFBCS energy is an increasing function of the three considered octupole deformations. This is visible in fig. 4a, where this energy for ^{192}Hg is plotted as a function of each $\beta_{3\mu}$, μ=0, 1, 2 [1]. The energy vs. deformation curves do not display secondary octupole minima. This was checked especially for β_{31} deformation, which has been studied over a very large range extending up to β_{31}=0.43, i.e. still larger than shown in fig. 4. We obtained for this extreme value of β_{31} the energy 15.5 MeV above the SD minimum. Although the moment of inertia increases with the octupole moment q_{31} (up to 5% at the largest q_{31}) we believe that the corresponding effect on the routhian associated with rotation will not be sufficient to create a well in the steeply increasing Hartee-Fock energy (taking a

[1] $q_{3\mu} = b_\mu \beta_{3\mu}$, where for ^{192}Hg, b_μ=21100, 13880 and 10760 fm^3 for μ=0,1,2, respectively [21]

typical value of the moment of inertia at SD shape, $\mathcal{J}$=100 $\hbar^2$/MeV, the rotational energy I(I+1)/2$\mathcal{J}$ at spin I=30 amounts only to 4.65 MeV). Therefore, our results do not support those of [11] concerning the existence of banana-like minima. A comparison of the energy variations for different $\beta_{3\mu}$ shows that the octupole stiffness grows with μ: at $\beta_{3\mu} \approx 0.14$ the μ=1 curve is 0.6 MeV above that for μ=0 and 0.73 MeV below that for μ=2. We find the same result for other nuclei and small deformations. For larger deformations, it can happen that μ=0 and 1 energies cross, the latter becoming the lowest one.

In fig. 4 a we also show the energies of the parity-projected HFBCS states E^+ and E^-. The lowering of the E^+ curve with respect to the HFBCS curve shows the gain in energy due to mixing of states with $q_{3\mu}$ and $-q_{3\mu}$. The GCM energies are indicated in fig. 4 by the ordinates of the horizontal bars drawn below the minima of the corresponding projected energy curve. The total SD g.s. octupole correlation energy obtained in GCM, given by the difference between the HFBCS curve minimum and the lower horizontal bar, decreases with μ, taking the values of 1.68, 1.57 and 1.25 MeV for μ=0, 1, 2, respectively. In fig. 4b we show the collective probability densities $g^2(q_{3\mu})$ of the SD g.s. and the lowest octupole excited state for each of the three modes. As expected from the deformation energy curves, the SD g.s. density is always peaked at $\beta_{3\mu}$=0. On the other hand, the extension of the density of the octupole state which measures the amplitude of dynamical octupole correlations is related to the E1 and E3 transition matrix elements.

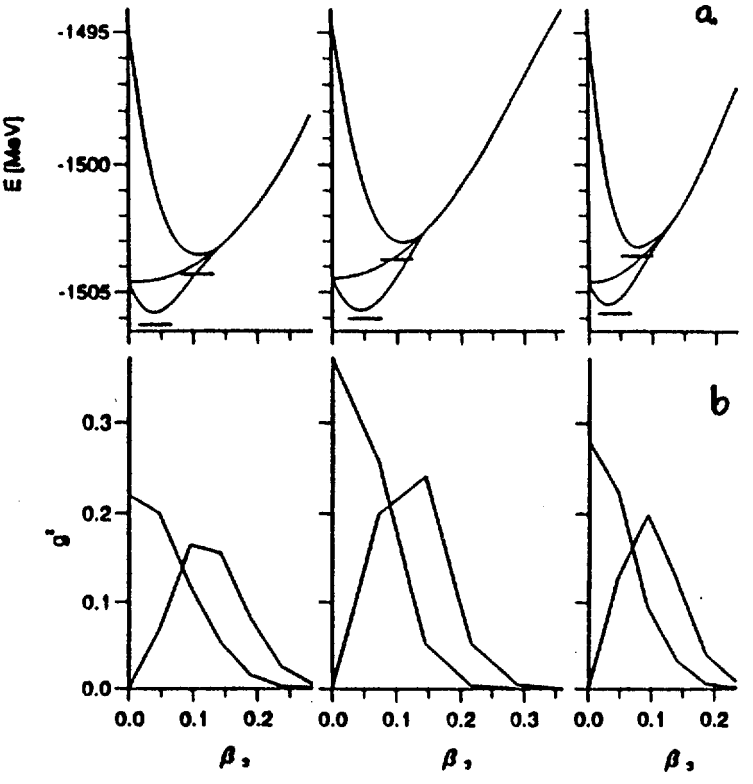

Figure 4

a) The HFBCS energy and the energies of the parity-projected states of ^{192}Hg as functions of the octupole deformations $\beta_{3\mu}$ around the SD minimum (μ=0,1,2 from left to right). The horizontal bars show the GCM energies of the SD ground- and the first excited states. b) The GCM probability densities of the SD ground- and the first excited states for three octupole modes μ=0,1,2 (from left to right).

The GCM results are summarized in table 1. For all nuclei the energy of the axial mode is the lowest one which is consistent with the HFBCS energy behaviour. The μ=2 energy is lower than that of μ=1 indicating that collective mass effect favours the μ=2 mode over the μ=1 and compensates the energy difference shown in fig. 2a. The obtained octupole transitions rates B(E3) of the order of 20 to 40 B(E3)$_{sp}$ (B(E3)$_{sp}$=0.42 A^2 e^{2}fm^6) show that octupole excitations at SD shape are indeed collective although these transition probabilities are not dramatically large [1]. The largest B(E3) occur for μ=0, the least collective (roughly two times smaller) are those for μ=1. The calculated transition dipole moments are largest

[1] for comparison: the measured B(E3) value in ^{208}Pb is 34(5) B(E3)$_{sp}$ [36]

also for the μ=0 mode and two times smaller for the μ=1 mode. In fact they are larger than the largest octupole-induced transition dipole moments measured up to now [37]. Assuming no dipole moment reduction due to rotation and a Clebsch-Gordan coefficient $1/\sqrt{2}$ (roughly appropriate for large angular momentum) we obtain $B(E1)$ = 7 10^{-2} e^2fm^2 from SD g.s. band to octupole-excited opposite parity SD band in ^{194}Pb. Such transitions should be detectable even in competition with SD $E2$ transitions. In table 1 we give also results obtained for the nucleus ^{194}Hg with the Skyrme force SIII and the same pairing strengths as in the calculation with SkM*. Compared with preceding results transition rates are moderately affected. The major difference is a lowering of the μ=2 mode by 0.45 MeV which becomes the lowest octupole excitation at the SD shape in this nucleus. The HF-BCS energy curve for μ=2 is softer with SIII interaction than it is with SkM*. In fig. 5 we show the ^{194}Hg neutron levels vs. β_{32} deformation obtained for both interactions (q =42 b). From the asymptotic Nilsson labels at β_{32}=0 one sees that the two effective forces predict different levels ordering. In particular, there is no visible N=112 gap in the SkM* spectrum, in contrast with the SIII spectrum. In spite of differences, both spectra display a gap at N=114 which arises with increasing β_{32}, quite similar to the one obtained in the Woods-Saxon potential, fig.1. Its origin is exactly the same as discussed there. The enhancement of the μ=2 octupole correlations in N=114 SD systems is, however, stronger for SIII force which is not clear from fig. 5. An additional check of this shell effect strength dependence on the interaction is provided by neutron pairing gaps which, as is well known, are anticorrelated with shell correction: although at the SD minimum Δ_n are similar (0.87 and 0.95 MeV), at β_{32} ≈0.14

Nucleus	E [MeV]	D [e fm]	B(E3) [B(E3)$_{sp}$]
^{194}Pb	1.94	0.76	37.2
SkM*	2.55	−0.27	16.7
	2.32	-	23.5
^{194}Hg	2.10	0.54	30.4
SkM*	2.20	−0.24	16.6
	2.16	-	22.5
^{194}Hg	2.22	0.46	29.4
SIII	2.40	−0.19	14.8
	1.71	-	22.5
^{192}Hg	1.95	0.63	33.7
SkM*	2.30	−0.27	17.3
	2.23	-	21.9

Table 1

For each nucleus and the forces indicated in the first column, the GCM excitation energy, transition dipole moment and $B(E3; K = 0, I = 0 \rightarrow K = \mu, I = 3)$ value of μ=0,1,2 octupole modes (from top to bottom) at the SD minimum are given.

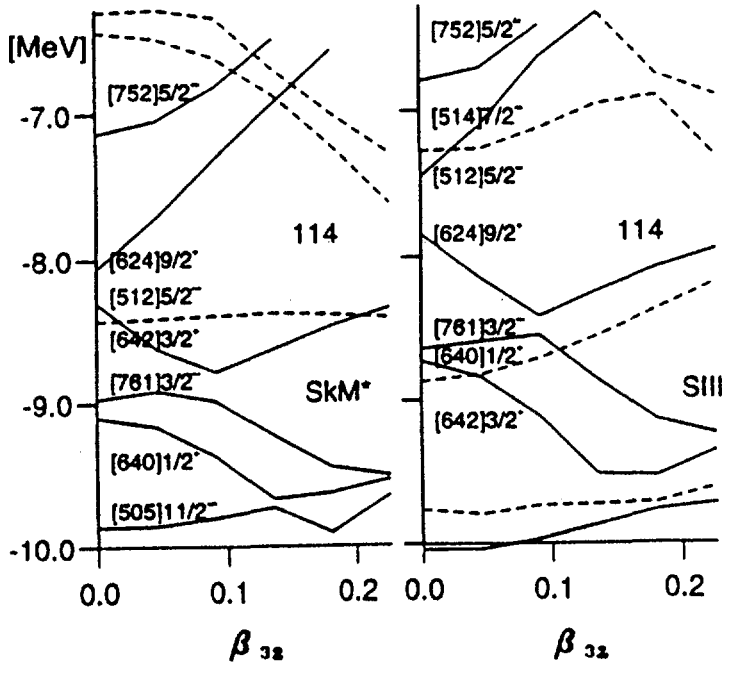

Figure 5

Comparison between the s.p. neutron levels vs. β_{32} for ^{194}Hg obtained with SkM* and SIII effective forces. Solid (dashed) lines are used to make distinction between levels belonging to two inequivalent irreps of the mean field symmetry group D_{2d}.

we find that Δ_n=0.92 MeV with the SkM* and only 0.66MeV for SIII.

Finally, an extended GCM calculation in which we have investigated the possible mixing of K =0 and 2 octupole modes shows that these modes are to a large extent uncoupled. In particular, the SD g.s. correlation energies induced by them are (almost) additive, and excitation energies are unchanged by the mixing. The only noticeable effect of the coupling of μ =0 and 2 modes is a moderate reduction of the $E1$ and $E3$ transition probabilities.

5. β_{31} deformation in Ra-Th region

A shape with combined β_{30} and β_{31} deformations breaks one of the plane reflection symmetries assumed hitherto. The remaining one allows to identify the Kramers degenerated s.p. orbits as simplex partners. The dynamical coupling between these two modes is very interesting physically since both β_{30} and β_{31} can have effect on the intrinsic dipole moments and E1 transitions. Due to Coriolis coupling, mixing octupole excitations with different K, the E1 transition from the g.s. to the lowest octupole state with $I^\pi=1^-$ will have the matrix element:

$$B(E1, I^\pi = 0^+ \rightarrow I^\pi = 1^-) = | a\langle \mu = 0 \mid \mathcal{M}(\Delta K = 0) \mid g.s.\rangle + b\sqrt{2}\langle \mu = 1 \mid \mathcal{M}(\Delta K = 1) \mid g.s.\rangle |^2, \qquad (5)$$

where a and b are the mixing amplitudes [1] These amplitudes are related to both the collectivity of μ=0,1 modes and the Coriolis coupling strength. As a preliminary result in this context, we show in fig.6 the Strutinsky energy map in the β_{30}, β_{31} plane for ^{222}Ra. The β_2 and β_4 deformations were fixed at equilibrium values of [38], and β_5 was related linearly to β_{30} as to interpolate between zero and the value at the reflection asymmetric minimum. As seen in fig.6, the β_{31} stiffness is quite small along the β_{30}=0 axis and increases near the β_{30} ≈0.09 minimum. Since the g.s. density will be large near the origin (β_{30} ≈0) one can expect sizable $\mathcal{M}(\Delta K = 1)$ contribution, provided the static μ=1 dipole moment is not hindered. The softness with respect to the octupole μ=1 mode near β_{30}=0 appears to be quite common for "octupole" Ra-Th nuclei.

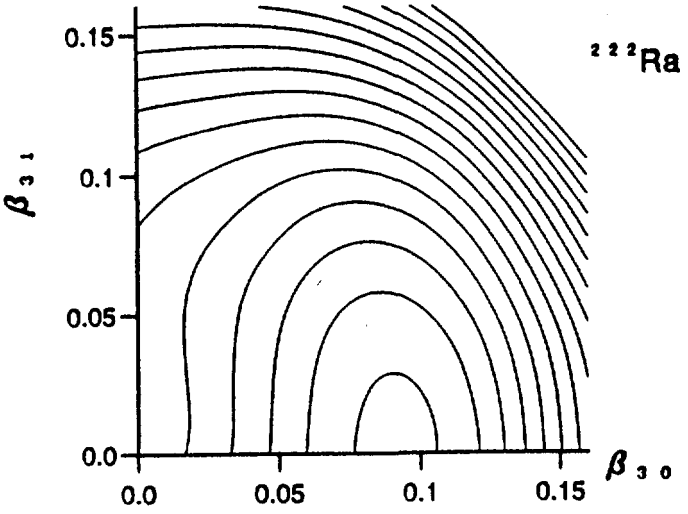

Figure 6

The Strutinsky energy map, E(β_{30}, β_{31}), for ^{222}Ra; the contour lines spacing is 200 keV.

6. Summary

The results obtained within the cranked Woods-Saxon model indicate that the μ=0 and 2 octupole modes are favoured in SD Hg and Pb nuclei ($\hbar\omega_{3\mu}$ from 1.1 to 1.6 MeV at I=0) while the μ=1 and 3 modes are unfavoured ($\hbar\omega_{3\mu}$ from 2.0 to 2.5 MeV at I=0), the former by the stiffness, the latter by the inertia. Typical order of increasing stiffness coefficients: μ=0, 2 and 3, 1 is obtained also for SD nuclei in the ^{152}Dy region.

GCM calculations using the Skyrme effective interaction SkM* predict the existence of collective octupole K =0,1,2 excitations with energies in the range 1.9-2.5 MeV, B(E3)

[1] For simplicity, less imortant couplings to other 2q.p. configurations and modifications of eq. 5 for higher I are neglected.

values of 15 to 37 single particle units and unusually large B(E1) transition rates up to 0.02 W.u. Excitation energies are lowest for K =0 and highest for K =1.

Compared to the RPA calculations [14], the GCM K =1,2 energies for ^{192}Hg are higher and the $B(E3)$ values are three times smaller, whith similar K dependence. GCM K =0,2 energies are also higher than estimates given in sect. 3, and the stiffnes of the K=1 mode is smaller than within the Woods-Saxon model. With another interaction SIII, the results are more favourable for the K =2 mode. With both effective forces, there is a steep increase of the energy with respect to the β_{31} octupole deformation. This result does not support the prediction of secondary banana-like minima corresponding to large values of this deformation given in [11].

Acknowledgements

One of the authors (J.S.) expresses his thanks to the DThNPMP staff at ULB for the hospitality extended to him during his stay there. We thank J.Dobaczewski for useful discussions. Partial support of the Université Libre de Bruxelles in computation is also acknowledged.

REFERENCES

1. K. Neergård and P. Vogel, Nucl. Phys. A 145 (1970) 33
2. J.Dudek, in "The Variety of Nuclear Shapes", ed. J.Garret et al., (World Scientific, Singapore, 1987), p. 195
3. J.Dudek, T.Werner and Z.Szymański, Phys. Lett. 248 B (1990) 235
4. S.Åberg, Nucl. Phys. A 520 (1990) 35c
5. J.Holler and S.Åberg, Z. Phys. A336 (1990) 363
6. W.Satula, S.Ćwiok, W.Nazarewicz, R.Wyss and A.Johnson, Nucl. Phys. A 529 (1991) 289
7. P.Bonche, S.J.Krieger, M.S.Weiss, J.Dobaczewski, H.Flocard and P.-H.Heenen, Phys. Rev. Lett. 66 (1991) 876
8. J.Dobaczewski and W. Nazarewicz, Phys. Rev. Lett. 68 (1992) 154
9. J.Dudek, in "High Spin Physics and Gamma-Soft Nuclei", ed. J.X.Saladin, R.A.Sorensen and C.M.Vincent, (World Scientific, Singapore, 1991) p. 146
10. X. Li, J. Dudek and P. Romain, Phys. Lett. 271 B (1991) 281
11. R. Chasman, Phys. Lett. 266 B (1991) 243
12. J. Skalski, Phys. Lett. 274 B (1992) 1
13. S.Mizutori, Y.R.Shimizu and K.Matsuyanagi, Prog. Theor. Phys. 83 (1990) 666
14. S.Mizutori, Y.R.Shimizu and K.Matsuyanagi, Prog. Theor. Phys. 85 (1991) 559
15. S.Mizutori, Y.R.Shimizu and K.Matsuyanagi, Prog. Theor. Phys. 86 (1991) 131
16. K. Matsuyanagi, these proceedings
17. K.Zuber et al., Phys. Lett. 254 B (1991) 308
18. D.M.Cullen et al., Phys. Rev. Lett. 65 (1990) 1547
19. P. Walker, Phys. Rev. Lett. 67 (1991) 1174
20. P. B. Semmes, I. Ragnarsson and S. Åberg, Phys. Rev. Lett. 68 (1992) 460
21. J. Skalski, P.-H. Heenen, P. Bonche, H. Flocard and J. Meyer, submitted to Nucl. Phys. A
22. J.P.Elliot and P.G.Dawber, "Symmetry in Physics", (Macmillan Press, London, 1979)
23. J.Skalski, Phys. Rev. C 43 (1991) 140
24. H.J.Krappe, J.R.Nix and A.J.Sierk, Phys. Rev. C20 (1979) 992
25. W.Nazarewicz, R.Wyss and A.Johnson, Nucl. Phys. A 503 (1989) 285
26. M. Brack, J. Damgaard, A.S. Jensen, H.C. Pauli, V.M. Strutinsky and C.Y. Wong, Rev. Mod. Phys. 44 (1972)

320

27. C.S.Lim, W.N.Catford and R.H.Spear, Nucl. Phys. A 522 (1991) 635
28. P. Bonche, S. J. Krieger, P. Quentin, M. S. Weiss, J. Meyer, M. Meyer, N. Redon, H. Flocard and P.-H. Heenen, Nucl. Phys. A 500 (1989) 308
29. S. J. Krieger, P. Bonche, M. S. Weiss, J. Meyer, H. Flocard and P.-H. Heenen, Nucl. Phys. A, in press.
30. P. Bonche, J. Dobaczewski, H. Flocard, P.-H. Heenen and J. Meyer, Nucl. Phys. A 510 (1990) 466
31. P. Bonche, J. Dobaczewski, H. Flocard, P.-H. Heenen, S. J. Krieger, J. Meyer and M. S. Weiss, Nucl. Phys. A 519 (1990) 509
32. J. Meyer , P. Bonche , J. Dobaczewski, H. Flocard and P.-H. Heenen, to be published
33. J. Bartel, P. Quentin, M. Brack, C. Guet and H. B. Håkansson, Nucl. Phys. A 386 (1982) 79
34. M. Meyer, N. Redon, P. Quentin and J. Libert, Phys. Rev. C 45 (1992) 233
35. A. Bohr, B. Mottelson, Nuclear Structure, Vol. 2 (Benjamin, Reading, 1975)
36. R. H. Spear, At. Data and Nucl. Data Tables 42 (1989) 55
37. P. A. Butler and W. Nazarewicz, Nucl. Phys. A 533 (1991) 249
38. A. Sobiczewski, Z. Patyk, S. Ćwiok and P. Rozmej, Nucl. Phys. A 485 (1988) 16

Symmetry-breaking and High-spin States

F. C. Khanna
Theoretical Physics Institute, Department of Physics
University of Alberta
Edmonton, Alberta, Canada, T6G 2J1
and
TRIUMF, 4004 Wesbrook Mall, Vancouver, BC, Canada, V6T 2A3

Spontaneous symmetry breaking in nuclear matter would require Nambu-Goldstone bosons in the system. A model calculation gives the nature of these excitations. In finite nuclei the excitations will be a mixture of rotational, surface vibrations and pseudo-Goldstone bosons. A search for such excitations would be fruitful.

I take this opportunity to present to you some new ideas that we have been exploring about collective excitations in nuclei. It can be argued that presence of a universal phenomenon in systems must signal an underlying symmetry property and the excitations may be traced to dynamical properties of the system. For the case of nuclei, it is well-known that deformation of nuclei is a universal phenomenon even though there are a variety of shapes. Finite nuclei may have excitations that relate to the overall rotation of the nucleus about a symmetry axis. In addition, the surface of finite nuclei has vibrations. It is well-known that rotations and vibrations interact leading to a complex set of excitations. We would like to concentrate on the intrinsic dynamical features that do not depend on the geometrical effects of finite nuclei. Therefore, we would like to concentrate on large nuclei or nuclear matter to identify the nature and properties of the collective excitations.

It is appropriate to indicate two features[1] of the superdeformed bands in neighboring nuclei.

(a) Transition energies in neighboring nuclei are found to be equal to better than 3 parts in 1000.

(b) The transition quadrupole moments are constant.

Such properties of neighboring nuclei suggest that there may be a deeper meaning to the character of the excited states.

Traditional models[2] based on potential models, moment of inertia etc. do provide an overall picture of the excitation spectrum but fail to provide an adequate explanation for the constancy of transition energies to a few parts in 1000. In fact it is fair to state such level of accuracy in energy calculation is perhaps unattainable within a potential model. Explanation must be sought at a deeper level. Symmetry of the Hamiltonian may be playing an important role and explicit nature and properties of the model Hamiltonian and/or the wavefunctions may be unimportant.

Spontaneous-symmetry breaking[3]

In the present problem the wavefunction of the ground state is not rotationally invariant while the Hamiltonian of the system is rotationally invariant. This appears strange but situations of similar nature are common in physics. A celebrated example is a ferromagnet where the spins of electrons are lined up i.e. a direction in space is defined, while the Hamiltonian is rotationally invariant and has no such property. As we are well-aware the spin-1/2 is defined by the three operators, σ_x, σ_y and σ_z with a well-known algebra (SU(2)). The consequence of spontaneous-breaking of SU(2) symmetry is the spin waves, collective excitations in the ferromagnet. In field theoretic language such excitations are called Nambu-Goldstone (N-G) modes with the property that in the limit of momentum $k \rightarrow 0$, the energy, ω_k, of the mode goes to zero. This is to be contrasted with the relativistic field theory where the spontaneous symmetry breaking leads to N-G excitations with zero-mass. In non-relativistic field theory mass is a parameter that relates energy and momentum ($E = p^2/2m$) while in a relativistic field theory mass is an invariant ($m^2 = E^2 - p^2$).

Consider a many-body system in the framework of the quantum field theory. Assume that a system with an infinite number of particles is invariant with respect to a symmetry group G. If this symmetry is spontaneously broken such that the rotation group, R(3), is preserved, then the N-G bosons will have good angular momentum. The choice of the initial symmetry group G is dictated by the dynamical properties of the system. Here we take an example that is well-known in nuclear physics. We consider a Hamiltonian that is invariant with respect to the Elliott U(3)

group[4]. This will help us to establish the type of excitations that may be present in an infinite nuclear system with this symmetry property. We assume that the U(3)-symmetry is spontaneously broken to a stability group, R(3), that preserves the rotational symmetry. This will give rise to N-G bosons with definite angular momentum.

The generators of the U(3) group are

$$T^o_o = \frac{1}{2\sqrt{3}} (x^2 - \nabla^2_x)$$

$$T^1_q = \frac{1}{\sqrt{2}} (x \otimes \nabla_x)^1_q$$

$$T^2_q = \frac{1}{\sqrt{6}} \sqrt{\frac{4\pi}{5}} \left[x^2 y_{2q}(\theta_x,\phi_x) + \nabla^2 y_{2q}(\theta_\nabla,\phi_\nabla)\right]$$

The three operators T^1_q form the rotation group, R(3). Given a Lagrangian it is easy to write the Noether theorem

$$\frac{d}{dt} N^k_q(t) = 0$$

where

$$N^k_q(t) = \int d^3x\, \phi^*(x)\, T^k_q(x,\nabla)\, \phi(x)$$

with $\phi(x)$ being the nucleon field (assume it to be a scalar field for simplicity). The invariance of the Hamiltonian under the U(3) group implies that

$$[H(t), N^k_q(t)] = 0 \ .$$

Classically the vacuum is defined to be a state with no particles and is supposed to be invariant under the symmetry group i.e. $N^k_q \mid 0 > = 0$. However it is established that for a system with infinite degrees of freedom, the vacuum may be complicated and contain a condensate of particles with non-trivial quantum numbers. Then it is possible to have $N^k_q \mid 0 > \neq 0$ for certain (k,q). In such a case the U(3) symmetry is spontaneously broken and the nuclear spectrum does not exhibit the U(3) symmetry. Then the Goldstone theorem states that the dynamical symmetry is rearranged such that N-G bosons should appear.

A simple realization of the N-G bosons is in terms of pairing of nucleons. Unlike the case of superconductivity, spontaneously-broken U(1) symmetry, where the pairing is in momentum space, the nuclear system may be considered to have pairing in the angular momentum space. It is easy to show[5] that there are six N-G bosons that may be expressed as spin zero and spin 2 N-G bosons, a consequence of R(3) symmetry. A gap equation may be obtained. It should be stressed that unlike the case of superconductivity, where the N-G boson is eaten up by the gauge field due to the long-range interaction, the N-G bosons for an infinite nuclear system would appear as excitation modes with appropriate dispersion relation such that $\lim_{p\to 0} E\to 0$ but these will be zero-energy excitations.

N-G modes in many-body systems

Spontaneous symmetry breaking and appearance of N-G excitations is a common feature in physics. Many of the familiar many-body systems have boson excitations that may be traced to the breaking of symmetry. It is obvious that in systems with the ground state having a lower symmetry than the Hamiltonian there is a re-arrangement of the symmetry. The presence of N -G boson along with the ground state has the right symmetry. The pion being the N-G boson of spontaneous chiral-symmetry breaking is a well-known example in particle physics. The present example and the spontaneous breaking of SU(4) symmetry in nuclear matter provides a complete picture for the presence of strong excitation modes in many-body systems.

System	Symmetry	N-G bosons
Crystals	Translation	Phonons
Superconductivity	U(1)	No Goldstone boson
Ferromagnet	SU(2)	Spin waves
Paramagnet	SU(2)	Paramagnon
Nuclear matter	SU(4)	Isobaric analog states Gamow-Teller states Isovector-spin and Isoscalar-spin
	U(3)	L=0 and L=2 bosons
QCD	Chiral	Pion

Finite nuclear system

Transition to finite nuclear system may not be entirely continuous. The appearance of a surface remains a question that cannot be easily answered. However we are well aware of the fact that there are explicit symmetry-breaking terms in the Hamiltonian, spin-orbit, tensor etc. interactions that would lead to endowing the N-G bosons with a finite mass. This is similar to the situation in QCD where pion acquires a finite mass due to explicit chiral-symmetry breaking ; thus becoming a pseudo-Goldstone boson. The N-G bosons in nuclear matter will acquire a similar status. The size of the nucleus leads to a mass of a few MeV for the N-G bosons.

High-spin states in nuclei

For a finite nuclear system there will be rotational excitations and surface vibrations in addition to the anticipated remnants of the N-G bosons arising from the spontaneous breakdown of SU(3) symmetry. The spectrum will be complex and the three excitation modes will interact. Since there are N-G bosons with spin 2, these will have their own quadrupole moment and could play an important role in electric quadrupole transitions. It may be a wild conjecture that the constancy of energy in neighboring nuclei may be an indication of N-G bosons leading to the decay of excited states. At this time we do not have numerics to establish the nature of N-G bosons and their contribution to the collective excitation spectrum of the high-spin states in finite but large nuclei. The idea is highly appealing and may have some relevance to the structure of high-spin states in nuclei.

Conclusions

An idea has been presented about the possibility of N-G excitation modes related to the spontaneous-symmetry breaking in nuclear matter. Such excitations have a dynamical origin. The nature of the N-G modes may be expressed as paired nucleons with total spin of 0 and 2. At present we are attempting to deduce non-perturbative consequences of the dynamical symmetry re-arrangement. These should point to specific experimental verifications of these ideas. In the meanwhile, it will be useful to consider specific deviations from rotational and vibrational spectra

as indication for a dynamical feature that may have roots in the overall symmetry of the system. Detailed calculations are in progress.

It should be stressed that the choice of the dynamical symmetry is arbitrary. In finite nuclei it may be desirable to choose a larger group. However the general arguments about the presence of N-G bosons in the presence of spontaneous symmetry breaking remains valid. Even though the example of SU(3) symmetry considers scalar nucleons, the general conclusions are independent of the spin of the particles. It is useful to remark that superconductivity considered as a spontaneously broken U(1)-symmetry would lead to similar features both for fermi as well as boson many particle systems.

It is a pleasure to thank Prof. H. Umezawa and Dr. X.Q. Zhu for suggestions and discussion. The resarch is supported in part by Natural Sciences and Engineering Research Council of Canada.

Referemces

1. R.V.F. Janssens and T.L. Khoo, Ann. Rev. Nucl. Sci. **41**, 321 (1991).
2. See Review Articles in these proceedings.
3. H. Umezawa, H. Matsumoto and M. Tachiki, Thermo Field Dynamics and Condensed States (North Holland, Amsterdam, 1982).
4 J.P. Elliott, Proc. R. Soc. (London) Ser. A **245**, 128 (1958); **245,** 562 (1958).
5 X.Q. Zhu, F.C. Khanna and H. Umezawa, Phys. Rev. C **43** , 2891 (1991).

NUCLEAR WOBBLING MOTION AND PROPERTIES OF E2-TRANSITIONS

Yoshifumi R. Shimizu and Masayuki Matsuzaki*)

Department of Physics, Kyushu University 33, Fukuoka 812, Japan
*) Department of Physics, Fukuoka University of Education,
Munakata, Fukuoka 811-41, Japan

Abstract

The nuclear wobbling motion associated with the static triaxial deformation are discussed based on a microscopic theory. Properties of the $E2$-transitions between the one-phonon wobbling band and the yrast (vacuum) band are studied and their characteristic features are suggested.

1. Nuclear Wobbling Motion and E2-transition

The nuclear wobbling motion is a new elementary mode of excitations which is predicted to appear at high-spin states[1] by analogy with the classical motion of the asymmetric top. The lowest energy motion of the classical top is a uniform rotation around a certain principal axis, which corresponds to the yrast states, and the excited motion is such that the angular momentum vector in the body-fixed frame fluctuates, i.e., "wobbles" or "precesses", around the main rotation axis. Note that the static triaxial deformation is necessary for such a three-dimensional non-uniform rotation to be realized. Recent measurements of detailed properties of the electromagnetic(EM) transitions rates revealed that the triaxial degrees of freedom, either of static or of dynamic (vibrational) nature, do play an important role at high-spin states. It is, therefore, interesting to ask how it appears at this stage.

A band structure expected for *the triaxial rigid-rotor* at high-spins is shown schematically in Fig.1. States are classified into two sequences, the "horizontal" and "vertical" excitations, and their slopes are connected to the largest and the smallest moment of inertia, respectively. Members of the horizontal sequence are connected by the stretched ($\Delta I = \pm 2$) $E2$-transitions which is characteristic to the usual collective rotation around the axis of largest moment of inertia. The vertical sequence is generated by superimposing the rotation around the axes other than the main rotation and can be regarded as multipole excitations of the $\Delta I = \pm 1$ (signature $\alpha = 1$) "wobbling phonon".

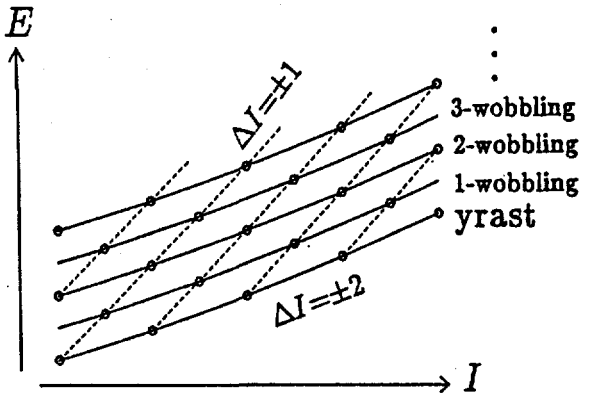

Fig.1. A schematic figure of the band structure expected from the triaxial rigid-rotor.

Study of such a genuine three-dimensional rotational motion is important because it is related to fundamental questions: In what extent the nucleus behaves as a "rotor"?, or how

the "intrinsic" (body-fixed) frame is defined? The definition is highly non-trivial in the case of general rotations around three spatial axes since the underlying nucleonic motions and, therefore, the selfconsistent deformation are strongly affected by the rotational motion in the many-body system like atomic nuclei. The dynamical fluctuations of the angular momentum vector in the intrinsic frame is, in general, a large amplitude motion. Such a general case has been studied in Refs.[2,3] by using the time-dependent variational method with a proper definition of the intrinsic frame. Unfortunately the results of Refs.[2,3] are rather complicated and it is difficult to understand the essential property of the wobbling motion. In the yrast region such a genuine three-dimensional rotational motion is expected to be of small amplitude, and a fully microscopic treatment is possible within the random phase approximation (RPA).[4] Then the wobbling mode is described as a kind of "vibration", or the wobbling phonon, i.e., the quantized precession of the angular momentum vector. Here we discuss such a relatively simple case and concentrate on the 1-wobbling band in Fig.1.

Since various kinds of rotational bands, both of collective and of single-particle nature, are observed, it is difficult to identify the wobbling band among them only from the energy spectra. The information of the electromagnetic transitions, especially the $B(E2)$ which sensitively reflects the collective properties, is important in this respect. For the general band structure shown in Fig.1, the $B(E2)_{\Delta I=\pm 2}$ of the horizontal transitions are related to the static deformation around the main rotation-axis, or the cranking-axis (x-axis), as usual. The $B(E2)_{\Delta I=\pm 1}$ of the vertical transitions are determined by the electro-magnetic properties of the wobbling phonon and reflect the effect of dynamical fluctuations of the angular momentum vector.

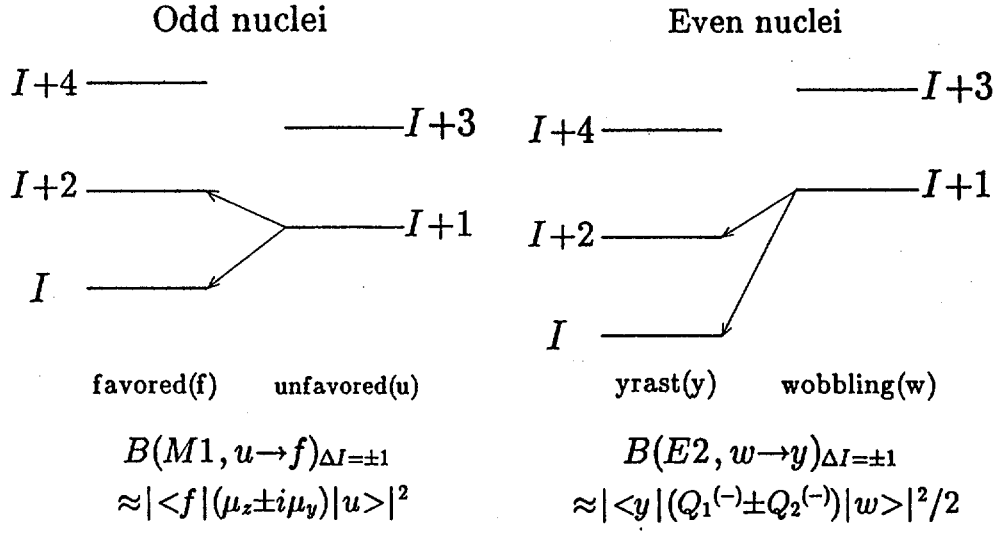

Fig.2. An analogy between the $\Delta I = \pm 1$ $M1$-transitions for the quasiparticle band and the $\Delta I = \pm 1$ $E2$-transitions for the wobbling band.

Within the lowest order approximation in the $1/I$-expansion,[4] $E2$-transition rate is expressed as

$$B(E2; i \to f)_{\Delta I=\pm 1} \approx |\langle f|(Q_1^{(-)} \pm Q_2^{(-)})|i\rangle|^2/2, \tag{1}$$

where $Q_K^{(-)}$ $(K = 1, 2)$ is the signature-coupled quadrupole operator (quantized with respect to the z-axis). Now the analogy to the case of interband $M1$-transitions between the favoured and unfavoured quasiparticle bands in odd nuclei, are quite obvious: The effects of the rotation and the triaxial deformation make both the K=1 and 2 components of quadrupole transitions non-vanishing (K-mixing) and may cause characteristic staggering in $\Delta I = \pm 1$ $E2$-transitions between the yrast and the wobbling band, see Fig.2.

2. A Microscopic Treatment

It is interesting to see how the rotor-picture appears from the microscopic viewpoint.[4] The starting point of the microscopic description of the wobbling motion is the cranked mean-field approximation followed by the time-dependent Hartree-Bogoliubov (TDHB) method in the uniform-rotating(UR) frame In the small amplitude limit (RPA) the signature $\alpha = 0$ (even-I transfer) and $\alpha = 1$ (odd-I transfer) modes decouple and the wobbling motion belongs to the latter.

Assuming the quadrupole-field as a main deformation component, the time-dependent single-particle hamiltonian in the presence of the wobbling motion is written as

$$h_{UR}(t) = h_{def} - \Omega J_x - \kappa_y \mathcal{Q}_y(t) Q_y - \kappa_z \mathcal{Q}_z(t) Q_z. \tag{2}$$

Here Ω is the cranking frequency, the Q_i $(i = y, z)$ is a non-diagonal component of the quadrupole tensor, $Q_i = \sum_{a=1}^{A} (x_j x_k)_a$ $(i, j, k$=cyclic), and $\mathcal{Q}_i(t)$ is its expectation value with respect to the corresponding UR-frame TDHB state. Note that the deformation fields in eq.(2), $Q_y \propto Q_{K=1}^{(-)}$ and $iQ_z \propto Q_{K=2}^{(-)}$ (cf. eq.(1)), so that they correspond to the dynamical fluctuation of the triaxiality. If $\mathcal{Q}_i(t) \ll \alpha_i$, with α_i being the static deformation, i.e., the expectation value of the diagonal component, $\alpha_i \equiv \langle \sum_{a=1}^{A} (x_j^2 - x_k^2)_a \rangle$, it is possible to make a time-dependent coordinate transformation to the body-fixed or the principal-axis(PA) frame which is introduced in such a way as the shape fluctuation disappears, $\mathcal{Q}_i^{PA}(t) = 0$.[2,4] Then the three-dimensional nature of the rotation shows up in this new coordinate frame and the TDHB hamiltonian now takes the form,

$$h_{PA}(t) = h_{def} - \Omega J_x - \Omega_y(t) J_y - \Omega_z(t) J_z . \text{eq.}(3)$$

Namely, the angular frequency vector, $\Omega(t)$, or the angular momentum vector, $\langle \mathbf{J} \rangle_{PA}(t)$, wobbles around the cranking x-axis (note $\Omega_x(t) \approx \Omega$ and $\langle J_x \rangle_{PA}(t) \approx \langle J_x \rangle = I$ in the RPA order). After the quantization the time-dependences of the physical quantities can be expressed as linear combinations of those corresponding to the RPA normal-modes.

Then the moment of inertia around the axes perpendicular to the cranking axis, $\mathcal{J}_i^{eff} \equiv \langle J_i \rangle_{PA}^{(n)} / \Omega_i^{(n)}$ $(i = y, z)$, for each n-th wobbling phonon state can be calculated[4] full-microscopically without any macroscopic assumptions. Moreover, it can be shown that the RPA-eigen value equation (and also the expressions of E2-transition matrix elements) in the UR-frame is transformed to the well-known "wobbling equation"[1] in terms of there moments of inertia, $\mathcal{J}_x \equiv \langle J_x \rangle / \Omega$, $\mathcal{J}_y^{eff}$ and $\mathcal{J}_z^{eff}$ (and the static deformations, α_x, α_y and α_z). Note that any physical observables in the PA-frame can be obtained uniquely from the RPA-phonon amplitudes which are calculated in a usual manner in the UR-frame.

An example of calculations for the wobbling mode excited on top of the s-band of ^{182}Os are shown in Fig.3, in which staggering between $\Delta I = +1$ and $\Delta I = -1$ $B(E2)$ is apparent. Note that this characteristic feature of the transition amplitude are connected to the dynamical fluctuation of the angular momentum vector in the PA-frame, or $(\mathcal{J}_x, \mathcal{J}_y^{eff}, \mathcal{J}_z^{eff})$, as is discussed above. The microscopic calculation predicts[5] that these moments of inertia change from "axially symmetric like" to "triaxial like" even though the mean-field parameters are kept constant. Furthermore, the predicted dependence of these inertia on the triaxiality parameter is quite different from one expected in the macroscopic models like the rigid-body or the irrotational-flow.[6]

3. Discussions

In this conference an interesting possibility of the "tilted cranking" bands is discussed,[7] where the direction of the angular momentum vector in the intrinsic frame deviates from the

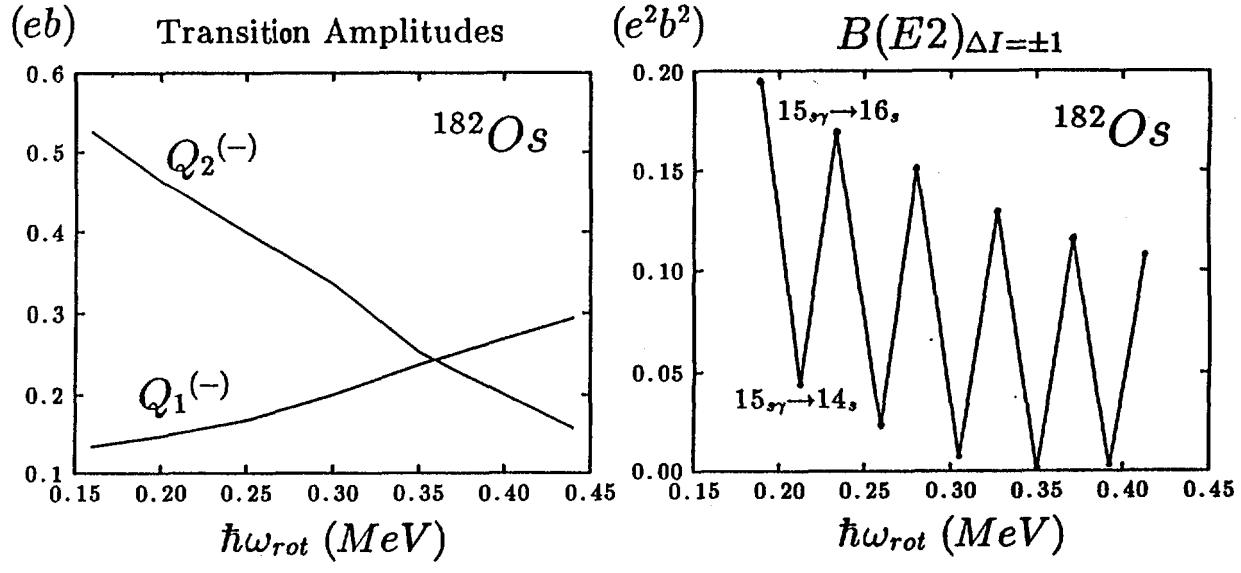

Fig.3. An example of the microscopic RPA calculation for the wobbling mode excited on top of *the s-band* of ^{182}Os. The transition amplitudes (left panel) and $B(E2)_{\Delta I=\pm 1}$ (right panel) are shown as functions of the rotational frequency. The calculational procedure is the same as Ref.[5] but with using the RPA equation where the Nambu-Goldstone mode is explicitly decoupled.

principal axes but still the rotation is uniform, i.e., $\Omega \parallel \langle \mathbf{J} \rangle_{PA}$. Such a motion is not allowed in the classical-top, thus, is not the same thing as the wobbling motion. It is, however, similar to the wobbling in the sense that both reflect the three-dimensional nature of the nuclear rotational motion. In fact the strong coupling bands based on the high-K isomers systematically observed in the $Hf-W$ region can be regard as a special case of the wobbling motion, called the "precession",[8] i.e., the case where only the vertical sequences in Fig.1 are present (the horizontal sequences correspond to the rotation around the symmetry-axis and are forbidden in the quantal systems).

At least up to now, there are no definite experimental data which indicate the existence of the nuclear wobbling motions. In order to identify the wobbling band we suggest to look for the continuation of odd-I sequence ($\alpha = 1$) of the γ-band after the back-bending, i.e., excited on top of the s-band where sizable static triaxiality is sometimes predicted, in even-even nuclei according to our theoretical calculations.[5,9] This is because the wobbling mode is closely related to the dynamical fluctuation of triaxiality as is discussed in §2. In this respect the band in ^{182}Os[10] may be a possible candidate, for which the calculation in Fig.3 has been done.[5] Recently it is predicted[11] that the coupling of the wobbling mode to the quasiparticle orbits leads the signature-inversion of routhians in odd $\gamma < 0$ nuclei, which is observed in e.g. ^{167}Tm and is difficult to explain in the simple cranking model. This an example which indicates an importance of the wobbling motion in odd nuclei.

The characteristic staggering of $B(E2)_{\Delta I=\pm 1}$ as is shown in Fig.3 may be an important factor for the identification. This staggering is rather general and has been observed in the γ-vibrational bands at low-spin[1] though the staggering is not so pronounced because $Q_1^{(-)} \ll Q_2^{(-)}$ in this case (cf. eq.(1)). There is a definite phase rule between the RPA amplitudes of $Q_2^{(-)}$ and $Q_1^{(-)}$ for the triaxial deformation[5] and, for example, $B(E2)_{\Delta I=+1} >$ $(<)$ $B(E2)_{\Delta I=-1}$ for $0 > \gamma > -60°$ ($\gamma > 0$) so that the way of staggering depends on the sign of γ. Although such transitions are too weak and their measurements are not yet available, we hope that the new generation 4π crystal ball spectrometers make it possible in near future.

References

1. Å. Bohr and B. R. Mottelson, *Nuclear Structure*, Vol. II, (Benjamin, New York, 1975).
2. A. K. Kerman and N. Onishi, Nucl. Phys. **A361** (1981), 179.
3. N. Onishi, Nucl. Phys. **A456** (1986), 390.
4. E. R. Marshalek, Nucl. Phys. **A275** (1977), 416; **A331** (1979), 429.
5. M. Matsuzaki, Nucl. Phys. **A509** (1990), 269.
6. Y. R. Shimizu, T. Kisaka and M. Matsuzaki, *Soryushiron Kenkyu* (Kyoto) **81** (1990), No. 61, F182.
7. S. Frauendorf, talk in this conference.
8. C. G. Andersson et. al., Nucl. Phys. **A361** (1981), 147.
9. Y. R. Shimizu and K. Matsuyanagi, Prog. Theor. Phys. **70** (1983), 144; **72** (1984), 799.
10. P. Chowdhury et. al., NBITAL Annual Report (1988).
11. M. Matsuzaki, "Signature Inversion Driven by Wobbling Motion in Negative-Gamma Nuclei", preprint (1992).

The Spin-Orbit Interaction and SU(3) generators in Superdeformation

K. Sugawara-Tanabe and A. Arima†

School of Social Information, Otsuma Women's University, Tokyo 206 Japan

†*Department of Physics, University of Tokyo, Tokyo 113 Japan*

When we look at the Nilsson diagram, we find the degeneracy of the two levels with asymptotic quantum number $[N, n_z = N, \Lambda = 0]\frac{1}{2}$ and $[N-1, n_z = N-2, \Lambda = 1]\frac{1}{2}$ at large deformation. The former level belongs to the unique parity levels with $\Omega = \frac{1}{2}$, and the latter level to the pseudo-spin family, as $[\tilde{N}-2, \tilde{N}-2, \tilde{0}]\frac{1}{2}$ in the pseudo-spin[1,2] representation. We will name this pair levels as different parity-pair (P-P) levels from now on. The P-P levels become nearly degenerate around the fermi surface in superdeformed shape for $A \sim 150$ and $A \sim 190$ region, but not $A \sim 130$ region. We propose the idea that this P-P levels are responsible for the quantization of alignment[3]. At first we will comment on the energy levels of P-P levels. We adopt the Nilsson Hamiltonian[4] in a deformed axially symmetric oscillator potential with a rational ratio $a : b$ between the frequencies $\omega_\perp$ and ω_z.

$$\begin{aligned} H &= -\frac{\hbar^2}{2M}\mathbf{P}^2 + \frac{M}{2}(\omega_\perp^2(x^2+y^2) + \omega_z^2 z^2) + \xi_{ll}(\mathbf{l}^2 - <\mathbf{l}^2>_N) + \xi_{ls}\mathbf{ls}, \\ &\equiv H_0 + \xi_{ll}(\mathbf{l}^2 - <\mathbf{l}^2>_N) + \xi_{ls}\mathbf{ls}, \end{aligned} \tag{1}$$

The energy eigenvalues of H_0 is described by the shell quantum number $N_{sh} = an_\perp + bn_z$, In the superdeformed shape where $a : b = 2 : 1$, our P-P levels belong to the same $N_{sh} = 2n_\perp + n_z = N$ with the same shell energy $\hbar\omega_{sh}(N_{sh} + 3/2)$, which proves P-P levels are almost degenerate in the energy diagram. Including the residual $\mathbf{l}^2$ and ls interactions in (1) in the first and second order perturbation, and also the Coriolis coupling term $\hbar\omega_{rot}J_x$, we calculated the energy difference between P-P levels and found it is small.

Now we will evaluate the amount of the ls interaction using the wave function obtained numerically by the exact diagonalization of total H. Using the eigenvector obtained from $H\,|\sigma, \Omega> = E(\sigma,\Omega)\,|\sigma, \Omega>$, we calculated the expectation values of spin-orbit force, i.e. $<\sigma, \Omega\,|\mathbf{ls}|\,\sigma, \Omega>$. Fig.1 shows these values for the P-P levels both for $A = 192$ and 152 cases. We see the decrease of $<\sigma, \Omega|\mathbf{ls}|\sigma, \Omega>$ according with the increasing deformation for P-P levels both for Dy and Hg cases. Most of the cases in the figure come to 0 or $\frac{1}{2}$ around $\delta \sim 0.6$. This results indicate

ls interaction is negligible in P-P levels. This is characteristic only for P-P levels and not common for all the other single-particle levels. In comparison we show the values of the $<\sigma, \Omega|\mathrm{ls}|\sigma, \Omega>$ for all the other levels with $\Omega = \frac{1}{2}$ except for P-P levels and those with $\Omega = \frac{3}{2}$ in $N = 7$ shell for Hg case in Fig.2. In Fig.3 we show the values of alignment for P-P levels, i.e. $<<\sigma, \frac{1}{2}|J_x|\sigma, \frac{1}{2}>>$ where $|\sigma, \frac{1}{2}>>= \frac{1}{2}(|\sigma, \frac{1}{2}> + T|\sigma, \frac{1}{2}>)$ with time reversal operator T. The horizontal lines in the figure denote the values of $\pm\frac{1}{2}$. The alignment around $\delta \sim 0.6$ comes to $\pm\frac{1}{2}$.

These phenomena are explained by the nature of the axially symmetric deformed field which is proportional to δY_{20}. The matrix element of $<j' = l - 2 \pm \frac{1}{2}|Y_{20}|j = l \pm \frac{1}{2}>$ is comparable order to the diagonal element $<j' = l \pm \frac{1}{2}|Y_{20}|j = l \pm \frac{1}{2}>$, and the matrix element between spin-orbit partners $<j' = l - \frac{1}{2}|Y_{20}|j = l + \frac{1}{2}>$ is usually much smaller than the diagonal one. Thus the coupling among $j = l + \frac{1}{2}$ family or that among $j = l - \frac{1}{2}$ is strongly enhanced. However the matrix element between spin-orbit partners of the spherical basis with small value of l becomes non-negligible order but almost comparable order to the diagonal element. This causes the mixing between the spin-orbit partners with large l value. The matrix elements of H which should be diagonalized in the subspace of $\Omega = \frac{1}{2}$ at $\delta = 0.6$ can be approximated as the following symmetric matrix. Here the rows and columns correspond to $s1/2$, $d3/2$, $d5/2$, $g7/2$ and $g9/2$ with $\Omega = \frac{1}{2}$ in order.

$$\begin{pmatrix} 0 & -1 & -1 & 0 & 0 \\ -1 & -1 & 0 & -1 & 0 \\ -1 & 0 & -1 & 0 & -1 \\ 0 & -1 & 0 & -1 & 0 \\ 0 & 0 & -1 & 0 & -1 \end{pmatrix} \tag{2}$$

The eigenfunction of this matrix shows complete mixing between $d3/2$ and $d5/2$ or $g7/2$ and $g9/2$. This is why the small spin-orbit interaction is found in P-P levels at superdeformation.

Since the residual ls interaction is small for P-P levels, we can limit our discussion to H_0 in (1) for P-P levels. As an analogy to Holstein-Primakoff transformation in spin operators, we can construct the new boson operator d, which is commutable with H_0, from the harmonic oscilator bosons, c_i and $c_i^\dagger$ with $i = x, y$ and z.

$$d = \frac{1}{\sqrt{2 + 2c_z^\dagger c_z}} c_z c_z, \quad d^\dagger = c_z^\dagger c_z^\dagger \frac{1}{\sqrt{2 + 2c_z^\dagger c_z}}, \tag{3}$$

or

$$d = \frac{1}{\sqrt{4 + 2c_z^\dagger c_z}} c_z c_z, \quad d^\dagger = c_z^\dagger c_z^\dagger \frac{1}{\sqrt{4 + 2c_z^\dagger c_z}}. \tag{4}$$

Eq.(3) corresponds to N_{sh} = even and $d^\dagger d = c_z^\dagger c_z/2$, while (4) to N_{sh} = odd and $d^\dagger d = (c_z^\dagger c_z - 1)/2$. For N_{sh} = even (odd) case, $N_{sh}/2 - n_d$ = even ($(N_{sh}-1)/2 - n_d$ = odd) corresponds to positive (negative) parity level and odd (even) to negative (positive) parity level, respectively. Here n_d corresponds to the eigenvalue of $d^\dagger d$. So long as we are treating a fixed N_{sh}, both of (3) and (4) do not mix each other. Eqs. (3) and (4) are the same as the ladder operator introduced by ref.[5].

Elliot[6] has found the quadrupole group operator which is commutable with the spherical Hamiltonian whithin the approximation to cut $\pm 2\hbar\omega_0$ excitation. According to this recipe developed in the spherical case, we replace $x \rightarrow x\sqrt{M\omega_\perp}$, $z \rightarrow z\sqrt{M\omega_z}$ and $p_x \rightarrow p_x/\sqrt{M\omega_\perp}$, $p_z \rightarrow p_z/\sqrt{M\omega_\perp}$. Then replacing c_z, $c_z^\dagger$ by d, $d^\dagger$, we get the new set of operators $\tilde{Q}$ and $\tilde{\ell}$ for our new SU(3) group. The oscillator Hamiltonian H_0 is invariant not only with respect to rotations but also with respect to the group SU(3) described by this eight infinitesimal group operators $\tilde{\ell}_q$ and $\tilde{Q}_q$. The commutation relations among these operators are the same as in [6]. In contrast to the Elliot's case which corresponds to cut $\pm 2\hbar\omega_0$ excitation, our SU(3) equation neglects $\pm 2\hbar\omega_{sh}$ excitation. The irreducible representation for the group SU(3) is labelled by the symbols (λ, μ), as in [6] or in [5].

Since these P-P levels are locating near the fermi surface of ^{192}Hg and ^{152}Dy (i.e. reference system in the discussion of the quantization of alignment), we can use real spin " s " instead of the pseudo-spin " $\tilde{s}$ ". This real spin can explain the quantization of alignment in unit of $\frac{1}{2}$. As both positive and negative parity levels are degenerate in P-P levels and the parity mixing is usually very small, it can explain the existence of the twin bands. Thus we propose this P-P levels are the candidate for the excited superdeformed bands and the quantization of alignment.

References

[1] A. Arima, M. Harvey and K. Shimizu, Phys. Lett. **30B**(1969)517.

[2] K.T. Hecht and A. Adler, Nucl. Phys. **A137**(1969)129.

[3] F.S. Stephens et al, Phys. Rev. Lett. **64**(1990)1654.

[4] S.G. Nilsson, Dan Mat. Fys. Medd. **29**, no.16(1955).

[5] W. Nazarewitch and J. Dobaczewski, Phys.Rev.Lett. **68**(1992)154.

[6] J.P. Elliot, Proc. Roy. Soc. **A245**(1958)128; 562.

Figure captions.

Fig.1 : The expectation values of ls by the eigenstate $|\sigma, \Omega = \frac{1}{2} >$ for the P-P levels. The longitudinal axis is in units of $\hbar$. In each figures the P-P levels are labelled by the asymptotic quantum numbers $[N, n_z, \Lambda]\Omega$.

Fig.2 : The expectation values of ls by the states $|\sigma, \Omega = \frac{3}{2} >$, and by the state $|\sigma, \Omega = \frac{1}{2} >$ except for $[770]\frac{1}{2}$ and $[761]\frac{1}{2}$ in $N = 7$ shell for $A = 192$ as a function of deformation δ.

Fig.3 : The alignment for the P-P levels as a function of the deformation. The longitudinal axis is for $<< \sigma\Omega|J_x|\sigma, \Omega >>$ in unit of $\hbar$ and the horizontal axis is for δ. The symbols correspond to the same quantities as in Fig.1. The time-reversal phase is chosen to be $T|n, l, j, \Omega) = (-)^{l+j-\Omega}|n, l, j, -\Omega)$. The horizontal lines is drawn at the value of $\pm\frac{1}{2}$.

Fig.2

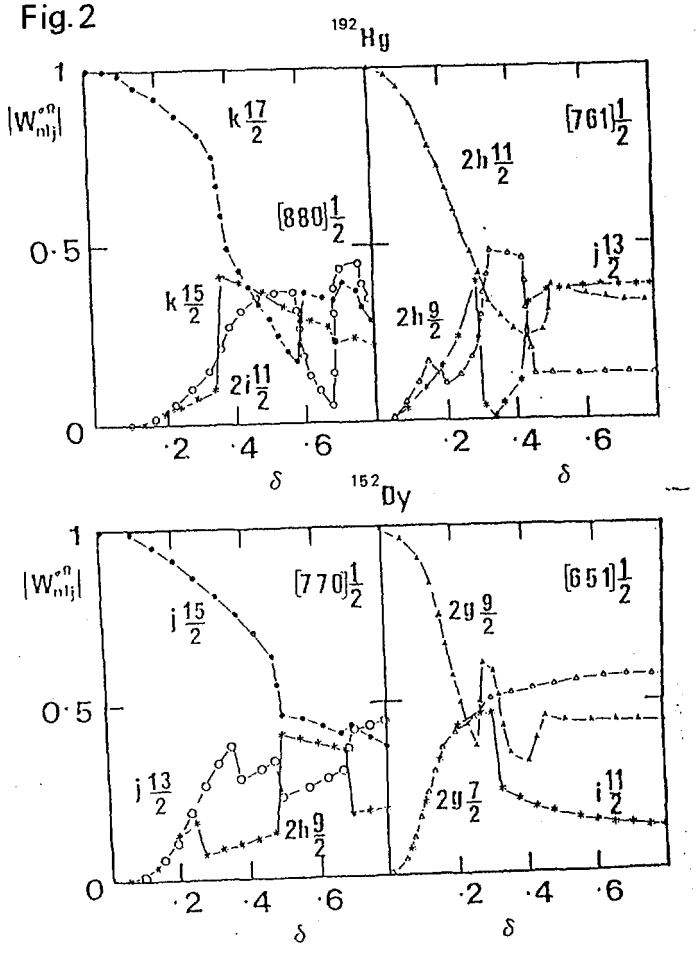

Fig.1

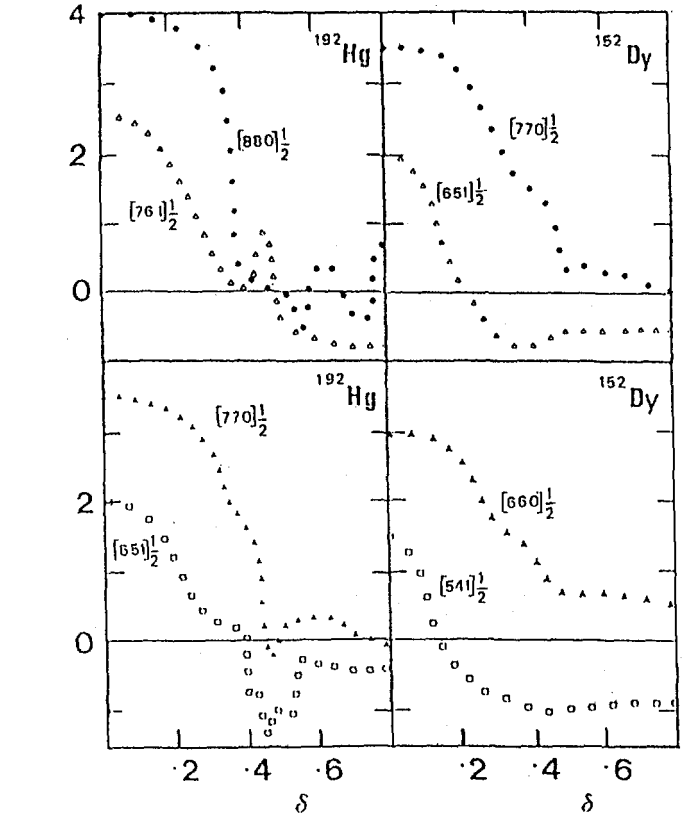

Fig.3

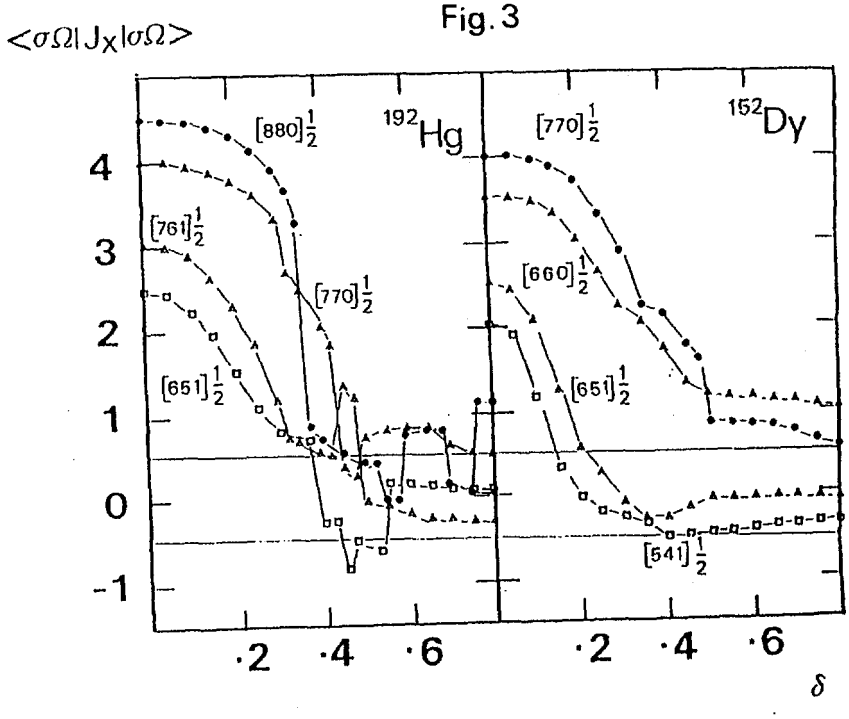

Vortex Excitations and Identical Superdeformed Bands

J.C. Waddington and R.K. Bhaduri,
Department of Physics and Astronomy,
McMaster University, Hamilton, Ontario, Canada L8S 4M1.

Striking relationships exist amongst the transition energies of the identical superdeformed bands (SDB). In this paper we investigate the possibility that all of the identical bands in both the mass 150 and 190 regions are related. The especially stable double closed shell nucleus ^{152}Dy at high spin is taken as a reference. It will be argued that as particles are added to ^{152}Dy, a superfluid is formed which does not take part in the collective rotation and does not contribute to either the moment of inertia or the spin. As the rotational frequency, ω, is increased, however, we propose the quantized vortices are formed in the superfluid, in much the same way as in superfluid ^{4}He. These vortices increase in number with increasing ω and contribute to the total angular momentum. Analogies to the quantum Hall effect will be made.

At the highest spin observed in ^{152}Dy the dynamic moment of inertia, $^{(2)}\Im$, reaches a constant value of 83.2 $\hbar^2$MeV^{-1}. This is the value expected for a rigid ellipsoid with a 2:1 axis ratio, if one assumes that the radius parameter r_0=1.13fm. A number of so-called identical bands are known to be based on this band. For ^{153}Dy, two excited SDB's were observed which not only have a moment of inertia which is identical to that of ^{152}Dy, but the transition energies are shifted by ±1/4 of a rotational spacing. It is as if the spin 1/2 of the last neutron has been added directly to the angular momentum of the core, but that the mass of this last particle has not contributed to the moment of inertia.

Many attempts have been made at explaining these and other identical bands with somewhat limited success. The moments of inertia of the mass 190 SDB's are very different than those in the mass 150 nuclei. These A~190 moments are generally similar to each other, but increase throughout the entire observed range of frequencies. In figure 1 the gamma ray differences are plotted against assumed spins for ^{152}Dy and ^{192}Hg. A constant value of 48.1 keV is maintained over the highest 9 transitions in ^{152}Dy. Shown on the same graph is a straight line with the same intercept drawn through the data for ^{192}Hg. The reason that the moment of inertia for ^{192}Hg at low spin is similar to the near rigid value for ^{152}Dy is uncertain, but it appears as if the extra particles that have been added in going from Dy to Hg are in some superfluid state that does not take part in the collective rotation.

Why does the moment of inertia not change for some bands as particles are added to ^{152}Dy or ^{192}Hg? The quantum Hall effect might provide a clue. In some two-dimensional solids a constancy of the cross-conductivity is observed under the application of a strong magnetic field. This is related to the existence of a specially stable "closed shell" state of the system. We see a parallel here to the stability of ^{152}Dy under strong rotation. For the fractional quantum Hall effect, quasiparticles obeying fractional statistics are invoked[1,2]. The quasiparticles of this theory are vortices which cause an excess or deficit of the fluid particles. Thouless's[3] approach shows that the constancy of the cross-conductivity in the quantum Hall effect is of topological origin. The excitations in condensed matter in some circumstances may be a spin 1/2 neutral particle (a spinon) and a charged spinless particle. We are investigating the possibility that the identical SDBs arise from an equivalent picture under the strong rotation of the specially stable ^{152}Dy. The rotation renders the three-dimensional space topologically nontrivial in this case.

An empirical fit can be made to the data for ^{192}Hg with this idea in mind. If it is assumed that the rotational energy for this

nucleus is given by

$$E = \frac{(I-j)(I-j+1)}{2\Im_c}$$

an excellent fit to the transition energies is obtained with $\Im_c$ taken as the value for ^{152}Dy and the aligned spin, j, proportional to I^2. The proportionality constant is such that at spin 48 (the highest spin observed) $j=4\hbar$. The results of this fit are shown in figures 2 and 3. (Somewhat better fits can be obtained if one does not require the moment of inertia $\Im_c$ to be that of the core ^{152}Dy).

This formulation suggests that the total angular momentum $\vec{I}$ is made up of the collective rotation $\vec{R}$ and an additional part with the very unusual I^2 spin dependence. We suggest that as ω increases, quantized vortices are formed in the superfluid, much the same way as in superfluid ^{4}He. These vortices increase in number with increasing ω and contribute to the total angular momentum. These two dimensional vortices in the nuclear superfluid might have spin 1/2 and be aligned along the axis of rotation. A simple density of states argument shows that the number of these vortices is proportioned to the rotational energy, i.e. proportional to the square of the angular momentum, as is observed.

1) R.B. Laughlin, PRL 50 (1983) 1395
2) B.I. Halperin, PRL 52 (1984) 1583
3) D.J. Thouless et al, PRL 49 (1982) 405

Captions

Figure 1 : The difference in gamma ray energies for ^{152}Dy and ^{192}Hg plotted versus assumed spin. ^{192}Hg has an alignment proportional to I^2.

Figure 2 : A comparison of the differences in gamma ray energies, calculated and experimental.

Figure 3 : The difference between the calculated and experimental gamma ray energies.

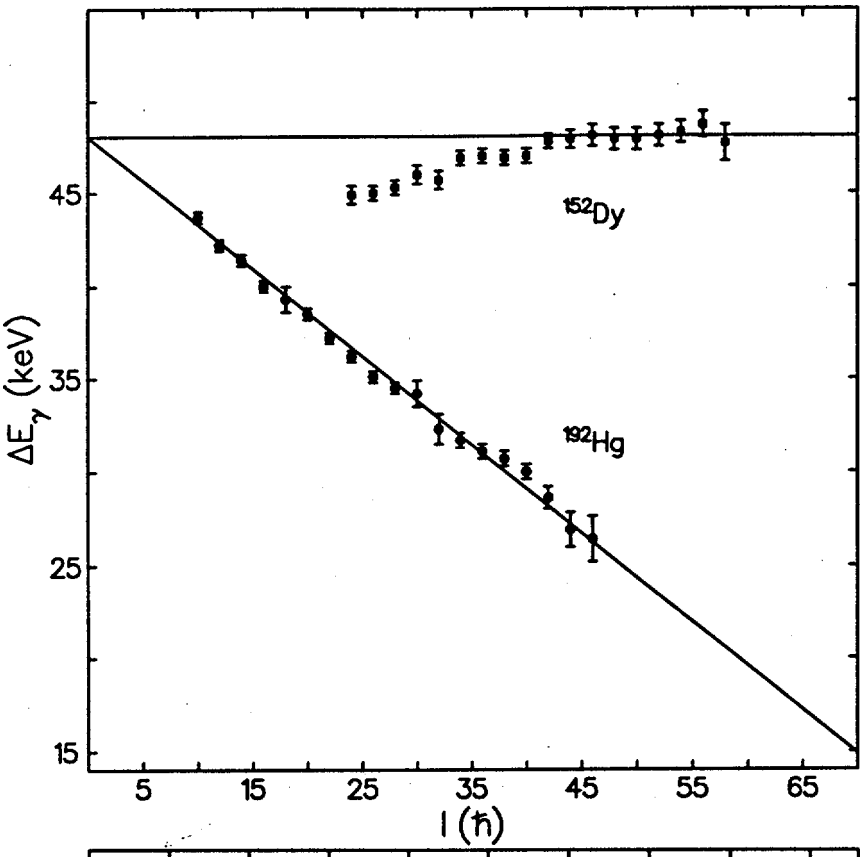
45
35
25
15
ΔE_γ (keV)
^{152}Dy
^{192}Hg
5
15
25
35
45
55
65
I (ħ)

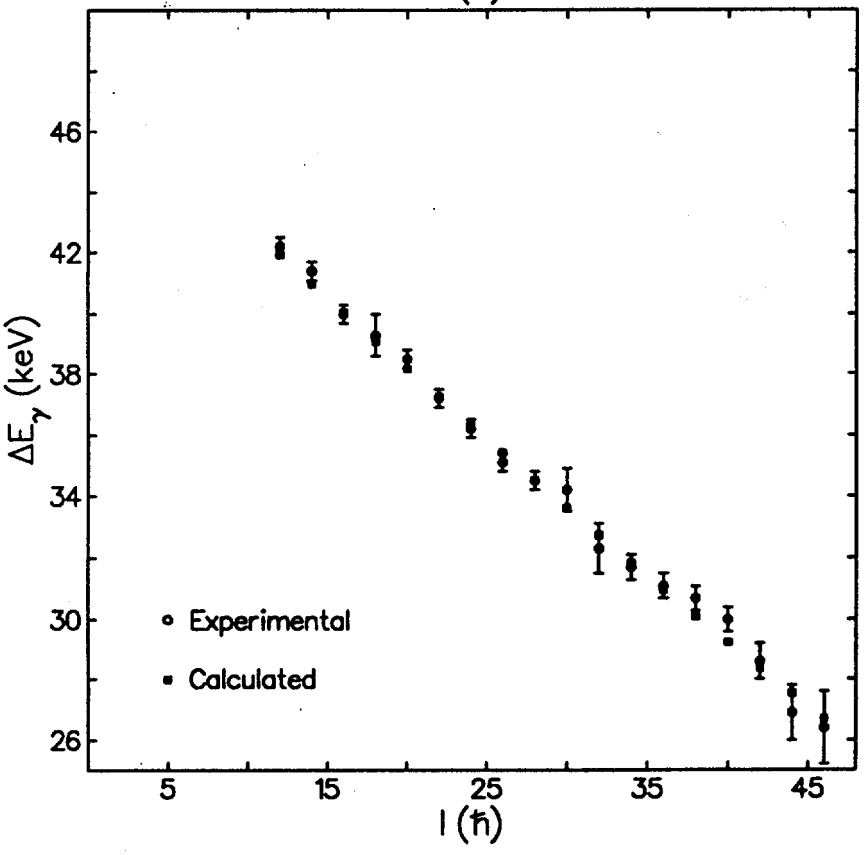
46
42
38
34
30
26
ΔE_γ (keV)
Experimental
Calculated
5
15
25
35
45
I (ħ)

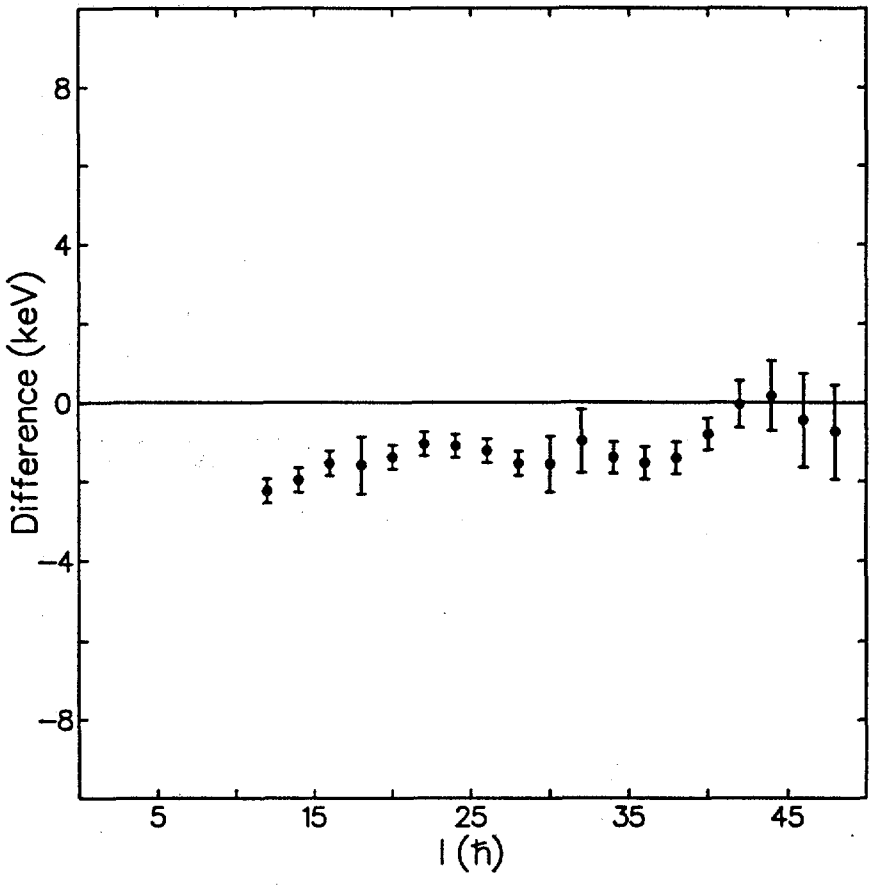
8
4
0
−4
−8
Difference (keV)
5
15
25
35
45
I (ħ)

INTERNATIONAL CONFERENCE ON NUCLEAR STRUCTURE AT HIGH ANGULAR MOMENTUM

Ottawa

SESSION 11: EXOTIC SHAPES, CLUSTERS, ETC.

Shape Coexistence, Lanczos Techniques, and Large-Basis Shell-Model Calculations

W.C. Haxton
Department of Physics, FM-15 and Institute for Nuclear Theory, HN-12
University of Washington, Seattle, Washington 98195

Abstract

I discuss numerical many-body techniques based on the Lanczos algorithm and their applications to nuclear structure problems. Examples include shape coexistence, inclusive response functions, and weak interaction rates in $^{16}0$; weak-coupling descriptions of the 0^+ bands in isotopes of Ge and Se; and the evaluation of the nuclear Green's functions that arise in two-neutrino $\beta\beta$ decay and in nuclear anapole and electric dipole moment calculations.

As most of my nuclear structure studies have involved light nuclei and relatively low spin, my presence on the program of this high spin conference is a bit amusing. Despite the incongruity, some of the issues my collaborators and I have addressed are also central to this conference: shape coexistence, band mixing, and deformation. We have tried to describe such phenomena in light- and medium-mass nuclei from the starting point of a g-matrix derived directly from the NN interaction. Our tools are a set of powerful algorithms based on the work of Lanczos.[1] Some of the techniques we use might be equally effective for heavy nuclei and high spin, particularly when the spin is close to the limiting value in the chosen shell model space.

The basic tool, the Lanczos algorithm, allows one to find the extremum (lowest and highest) eigenvalues and associated eigenvectors of a very large matrix iteratively. With standard workstations, matrices of dimension $\sim 10^6$ by 10^6 can be treated in this way. In contrast, standard methods for fully diagonalizing matrices are usually limited to about $\sim 10^3$ by 10^3. An even more powerful aspect of this algorithm, due to its connections with the method of moments, is that it can be used to generate inclusive response functions and Green's functions iteratively. Thus the Lanczos algorithm has proven useful in a wide variety of problems, including the nuclear shell model, atomic and molecular structure, spin-lattice problems in condensed matter physics, and Hamiltonian lattice gauge theory.

Consider a Hamiltonian H, defined over a finite Hilbert space of dimension N, and a starting normalized vector $|v_1\rangle$ in that space. We begin to construct a basis for representing H by

$$H|v_1\rangle = \alpha_1|v_1\rangle + \beta_1|v_2\rangle$$

where $|v_2\rangle$ is a normalized vector representing that part of $H|v_1\rangle$ orthogonal to $|v_1\rangle$. Proceeding

$$H|v_2\rangle = \beta_1|v_1\rangle + \alpha_2|v_2\rangle + \beta_2|v_3\rangle$$
$$H|v_3\rangle = \beta_2|v_2\rangle + \alpha_3|v_3\rangle + \beta_3|v_4\rangle$$

and so on. Note that the term $\beta_1|v_1\rangle$ must appear in the first line above because H is Hermitian. Also note that $|v_1\rangle$ does not appear in the second line above because everything that connects to $H|v_1\rangle$ other than $|v_1\rangle$ is defined as $|v_2\rangle$. Similarly, $H|v_4\rangle$ will contain nothing proportional to $|v_1\rangle$ or $|v_2\rangle$. Thus H has been cast in a tridiagonal form

$$H = \begin{pmatrix} \alpha_1 & \beta_1 & 0 & 0 & \\ \beta_1 & \alpha_2 & \beta_2 & 0 & \cdots \\ 0 & \beta_2 & \alpha_3 & \beta_3 & \\ 0 & 0 & \beta_3 & \alpha_4 & \\ & \vdots & & & \end{pmatrix} \tag{1}$$

If this procedure is continued for N steps, the full H would then be in tridiagonal form. However the power of the algorithm derives from the information in the tridiagonal Lanczos matrix when the procedure is truncated after n iterations, $n \ll N$. If $\{\psi_{E_i}, i = 1, \ldots N\}$ are the exact eigenfunctions of H, then

$$\langle v_1|H^\lambda|v_1\rangle = \sum_{i=1}^{N} |\langle v_1|\psi_{E_i}\rangle|^2 E_i^\lambda \equiv \sum_{i=1}^{N} f(E_i)E_i^\lambda$$

The distribution $\{f(E_i), i = 1, N\}$ can be thought of a set of N weights f and measures E_i (the eigenvalues) characterizing the distribution of $|v_1\rangle$ in energy, i.e., the f's determine a complete set of moments. The truncated Lanczos matrix, when diagonalized, provides the information needed to construct a distribution $\{g(\tilde{E}_i), i = 1, \ldots, n\}$ which has the same 2n-1 lowest moments in E as the exact distribution $\{f(E_i)\}$. That is, the Lanczos algorithm provides, at each iteration, a solution to the classical moments problem.[2] As Whitehead has emphasized[2,3], the speed and numerical stability of this moments algorithm is a very special property of Lanczos, and leads to marvelous procedures for evaluating total response functions and Green's functions in various many-body applications.

If, as n increases, the Lanczos algorithm continues to accurately characterize the (2n - 1) lowest moments, clearly it must describe the extremum eigenvalues very faithfully: these are given enormous weight for large powers of H because they lie so far from the centroid of the distribution $\{f(E_i)\}$ in E. Thus a second important property of Lanczos is that some of the $\tilde{E}_i$ in the distribution $\{g(\tilde{E}_i)\}$ must quickly converge to the exact extremum eigenvalues of the matrix H. That is, we can use Lanczos as an efficient matrix diagonalization scheme provided we are interested in extremum eigenvalues.

Thus one concludes that the Lanczos algorithm is almost always adequate for physical applications. For instance, in nuclear physics we tend either to study familiar, low-lying excitations (for which the Lanczos algorithm can provide the eigenvalues and eigenfunctions) or total nuclear responses (which Lanczos can characterize by its moments, even if all of the contributing discrete states cannot be determined). In either

case, it is straightforward to use the Lanczos algorithm on matrices of order $10^6 \times 10^6$, a scale that often arises in problems of physical interest.

The shell model code I use is about 10 generations removed from the original parent, the Glasgow code of Rex Whitehead and collaborators[3] that was distributed in the mid-1970's. Although the early revisions John Dubach and I made to the Glasgow code where substantial, the present code remains almost identical to the original in its mathematical outline: Most of the revisions focused on improvements in speed, exportability, and adaptability. We also coupled Glasgow to new codes for generating density matrices for arbitrary one- and two-body operators.

The Glasgow code works in the m-scheme, rather than in subspaces of definite J, in order to exploit the natural connection between Fock-space fermion Slater determinants and computer words: each fermion single-particle state is associated with a bit in a computer word and can be occupied (bit = 1) or unoccupied (0). If the number of single-particle states exceeds the computer word size, more than one word can be used to represent the Slater determinant. Each of the vectors $|v_1\rangle, |v_2\rangle$, etc., forming the basis for Eq. (1) are stored as a list of amplitudes, corresponding to the list of all possible Slater determinants of the chosen total M that exist in the Hilbert space. If H contains only one- and two-body operators, the Lanczos algorithm requires us to evaluate

$$\sum_{\substack{\alpha>\beta \\ \gamma>\delta}} a_\alpha^+ a_\beta^+ a_\delta a_\gamma \langle \alpha\beta|H|\gamma\delta\rangle_A |v_i\rangle$$

where $\langle \alpha\beta|H|\gamma\delta\rangle_A$ are the antisymmetrized two-body matrix elements that must be supplied by the user. One of the clever ideas of the Glasgow code was the realization that efficient bit-manipulation algorithms could be used to evaluate $a_\alpha^+ a_\beta^+ a_\delta a_\gamma$ acting on Slater determinants stored as computer words.

Since only M is fixed, the Lanczos algorithm will generate the extremum eigenvalues and eigenfunctions for all states $J \geq M$. In fact, since angular momentum is not explicitly imposed, the convergence to states of good J is a powerful numerical check. Within the m-scheme one can use time-reversal symmetry (if A = N + Z is even) to select only even or only odd J states, and charge conjugation symmetry (if $N = Z$) to select even isospin states or odd isospin states.

Although most shell model practitioners tend to concentrate on light nuclei, the m-scheme might be interesting from the perspective of high spin. Heavy nuclei often require very large single-particle spaces, but our existing codes permit up to 120 distinct s.p. states. While the full Hilbert space is then enormous, one could choose M to be only slightly smaller than the maximum J that could be formed in this space, thereby eliminating all states with $J < M$ and making the dimensions of the Hilbert space reasonable.

The Glasgow group's review provides an excellent discussion of properties and possible applications of the Lanczos algorithm.[3] A few of the relevant points are:

1) Although spherical single-particle bases are commonly used, there is no requirement to do so. For instance, a Nilsson basis could be adopted.

2) For moderately large shell model problems (N $\sim 10^5$), 200 iterations typically yield 10 fully converged states at the low-energy end of the spectrum.
3) If the space is separable, spurious center-of-mass motion can be removed by adding a (large) multiple of the center-of-mass Hamiltonian H_{cm} to H.
4) Common UNIX workstations with adequate disk space (Gbyte) are suitable for calculations with $N \lesssim 10^6$. We have adapted our code for supercomputers, but have been disappointed with the results: it does not fully vectorize, and the disk-space and memory demands are often troublesome in multi-user environments.

Calvin Johnson and I recently completed a study of the structure of ^{16}0 and of axial-charge transitions that made heavy use of Lanczos techniques.[4] The one-body axial-charge operator $\vec{\sigma}(i)\cdot\vec{p}(i)$ transforms under particle-hole conjugation like the more familiar E1 operator, and thus its matrix elements are suppressed by and very sensitive to 2p2h pairing correlations. One of the most thoroughly studied axial-charge transitions is the $0^+ \leftrightarrow 0^-$ β decay and μ-capture transition in ^{16}0. This transition has been an important test of strong exchange-current corrections. (The two-body axial-charge operator determined from PCAC and current algebra is of the same order, $\frac{v}{c}$, as the one-body term and typically increases transition rates by a factor of two.) The μ-capture transition has been exploited as a test of g_P/g_A and its deviations in nuclei from the Goldberger-Treiman value. In addition, there is a strong connection between the axial-charge β-decay operator and hadronic weak interactions: the parity-nonconserving two-body interaction, when reduced to an effective one-body form, becomes the axial charge. Thus our ability to correctly describe the effects of correlations on the A=16 axial-charge transition is quite relevant to similar shell model studies in ^{14}N, ^{18}F, ^{19}F, and ^{21}Ne, where hadronic PNC measurements have been made.

The structure of ^{16}0 also provides a classic example of shape coexistence. Brown and Green (BG) first pointed out that the $K^\pi = 1/2^+$ and $1/2^-$ Nilsson levels near $A = 16$ were nearly degenerate for large positive β, so that the spherical closed-core 0^+ state could strongly mix with a deformed 4p4h excitation and with a deformed 2p2h excitation of favored symmetry. An extreme weak-coupling calculation, mixing these three states with a $\delta 2\hbar\omega$ interaction $V_{2\hbar\omega}$, yielded wave functions that successfully reproduced many of the observed properties.[5] Johnson and I were interested in whether similar shape coexistence would emerge naturally from a complete microscopic calculation employing a realistic g-matrix.

Finally, the Gamow-Teller distribution for $A = 16$ is an interesting quantity that can be studied by exploiting the moments properties of the Lanczos algorithm. The ^{16}0 GT distribution is entirely a measure of ground-state correlations. Many theoretical calculations fail to reproduce the observed GT strength in the low-energy tail of this distribution.

The Brown and Green work suggested that we focus on $V_{2\hbar\omega}$, ignoring $V_{4\hbar\omega}$ and more exotic terms. It is clear that first-order perturbation theory demands that any calculation that includes $V_{2\hbar\omega}$ must contain the $4\hbar\omega$ basis states: without these, the $2\hbar\omega$ basis states are repelled by the ground state, with no compensating effect from the $4\hbar\omega$ states. [Despite this, most "$2\hbar\omega$" calculations of ^{16}0 and similar nuclei omit $4\hbar\omega$ states, and compensate for this emission by an ill-advised readjustment of $V_{0\hbar\omega}$ that

distorts the mixing of $0\hbar\omega$ and $2\hbar\omega$ states.] The resulting full $4\hbar\omega$ single-particle basis is very large [1s, 1p, 2s1d, 2p1f, 3s2d1g, 3p2f1h], spanning four computer words on 32-bit machines. Since time-reversal and charge-conjugation symmetries can be applied, the basis for the four needed calculations (even and odd J and T) are moderate, N $\sim$ 90,000.

In the spirit of BG, we allowed the N-N residual interaction to operate only in the 1p-2s1d shell, but projected spuriosity by allowing H_{cm} to operate everywhere. Kuo's Reid soft-core bare g-matrix[6] was employed for $V_{2\hbar\omega}$.

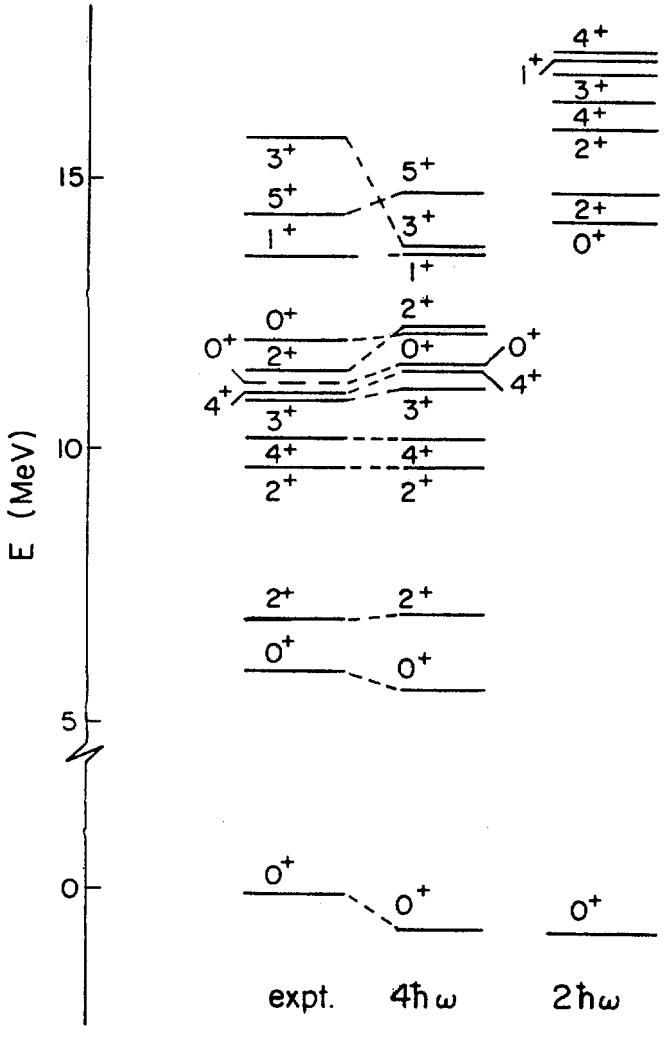

Fig. 1 A comparison of experiment and the $4\hbar\omega$ ^{16}O shell-model spectrum of T=0 states. The spectrum resulting from diagonalizing the same Hamiltonian in a $2\hbar\omega$ space is also shown.

In the second column of Fig. 1, I show the resulting spectrum of $T = 0$ states. The third column shows the effect of removing interactions with the $4\hbar\omega$ states, which

are responsible for about an 8 MeV shift in the positions of states (dominantly) $2\hbar\omega$ in character.

The BG and shell model $0\hbar\omega$, $2\hbar\omega$, and $4\hbar\omega$ probabilities for the first 0^+ states are compared in Table I. They cannot be completely in accord: for instance, the BG spherical state is mixed only among three states, while in the realistic calculation it mixes with a complete set of $2\hbar\omega$ and $4\hbar\omega$ 0^+ states. Yet there is substantial agreement between the schematic and microscopic results. In Table II shell model B(E2) values, calculated with bare charges and with radial wave functions from the Ginocchio potential[7], are compared to experiment. The systematics are very well reproduced. Further technical details relevant to Fig. 1 and Tables I and II are given in Ref. [4].

Often one is interested in the inclusive response of some nucleus, initially in its ground state, to some perturbation. This can be accomplished by applying the Lanczos algorithm to the starting vector

$$|v_1\rangle = \hat{0}|g.s.\rangle$$

where $\hat{0}$ is the operator of interest. In our $^{16}0$ calculation we followed this procedure for

$$\hat{0} = \sum_{i=1}^{A} \vec{\sigma}(i)\tau_{\pm}(i)$$

thereby generating the distribution of B(GT) strength shown in Fig. 2. Relative to a $2\hbar\omega$ shell model calculation, the integrated strength increases by ~50%, and the strength at low excitation energies is strongly enhanced, although not sufficiently to reproduce experiment.

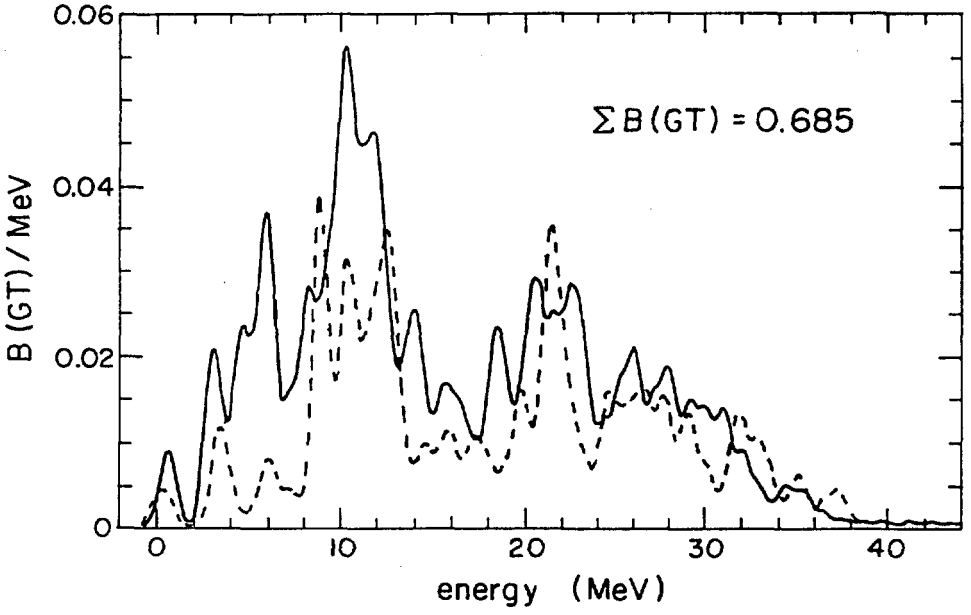

Fig. 2 The $4\hbar\omega$ (solid line) and $2\hbar\omega$ (dotted line) B(GT) specta in $^{16}0$. In each case excitation energies are measured relative to the lowest 1^+1 level.

Table I. Comparison of the shell-model (SM) and Brown-Green (BG) 0p0h, 2p2h, and 4p4h probabilities for the first three 0^+ states in ^{16}O.

Probability	g.s.		0_2^+(6.05 MeV)		0_3^+	
	Bg	SM	BG	SM	BG	SM
0p0h	0.76	0.42	0.07	0.04	0.07	0.03
2p2h	0.22	0.45	0.05	0.05	0.73	0.68
4p4h	0.02	0.13	0.88	0.90	0.10	0.30

Table II. Experimental, shell-model, and schematic-model ^{16}O $B(E2)$ values. Ginocchio potential single-particle wave functions were used in the shell model calculation.

Transition	Expt.	SM	BG[5]
$2_1^+(6.92) \rightarrow 0_1^+(0.0)$	7.4±0.2	4.3	5.3
$2_1^+(6.92) \rightarrow 0_2^+(6.05)$	65±7	53	103
$2_2^+(9.84) \rightarrow 0_1^+(0.0)$	0.074±0.007	0.054	
$2_2^+(9.84) \rightarrow 0_2^+(6.05)$	2.9±0.7	0.68	
$2_3^+(11.52) \rightarrow 0_1^+(0.0)$	3.6±1.2	2.2	3.3
$2_3^+(11.52) \rightarrow 0_2^+(6.05)$	7.4±1.2	4.8	7.7
$4_1^+(10.36) \rightarrow 2_1^+(6.92)$	156±14	63	152
$4_2^+(11.10) \rightarrow 2_1^+(6.92)$	2.4±0.7	5.1	

Even though many 1^+ states exist in ^{16}F/^{16}N, experiment cannot resolve all of these. The distribution shown in Fig. 2 corresponds to our Lanczos distribution $\{g(\tilde{E}_i), i = 1, \ldots n\}$ folded with a resolution function that approximates the resolution achievable in (p, n) mappings of GT strength. The distribution is fully converged (n $\approx$ 200). The important point is that the Lanczos algorithm permits one to effectively extract, from a large matrix, all of the information that is relevant for comparisons to inclusive cross sections.

An interesting extension of the Lanczos shell-model techniques was undertaken

several years ago, motivated by the problem of double beta decay. Double beta decay is an exclusive process, usually involving only the transition to the daughter ground state, $J^\pi = 0^+$. Two transitions of experimental relevance are ^{76}Ge $\rightarrow ^{76}$Se and ^{82}Se $\rightarrow ^{82}$Kr. The canonical spaces for these nuclei, $\{p_{3/2}, p_{1/2}, f_{5/2}, g_{9/2}\}$, lead to matrices that exceed 10^6 and are therefore beyond our capabilities to diagonalize directly.

The procedure we followed for these medium-mass nuclei was p-n weak coupling. Writing $\mathrm{H} = H_p + H_n + H_{pn}$, we treated H_{pn} as a perturbation. H_p and H_n were diagonalized separately, and a weak coupling basis was formed from the resulting wave functions

$$\{\psi_{ij}\} = \{[\psi_p^J(i) \otimes \psi_n^J(j)]_{J_o=0}\}$$

We retained about 50 each of the lowest energy proton and neutron states, coupling them together to form a $J_0 = 0^+$ basis. H_{pn} was then diagonalized in this partial basis, one in which the most favored proton and neutron configurations should be well represented. [To carry this out in the m-scheme requires several clever tricks!]

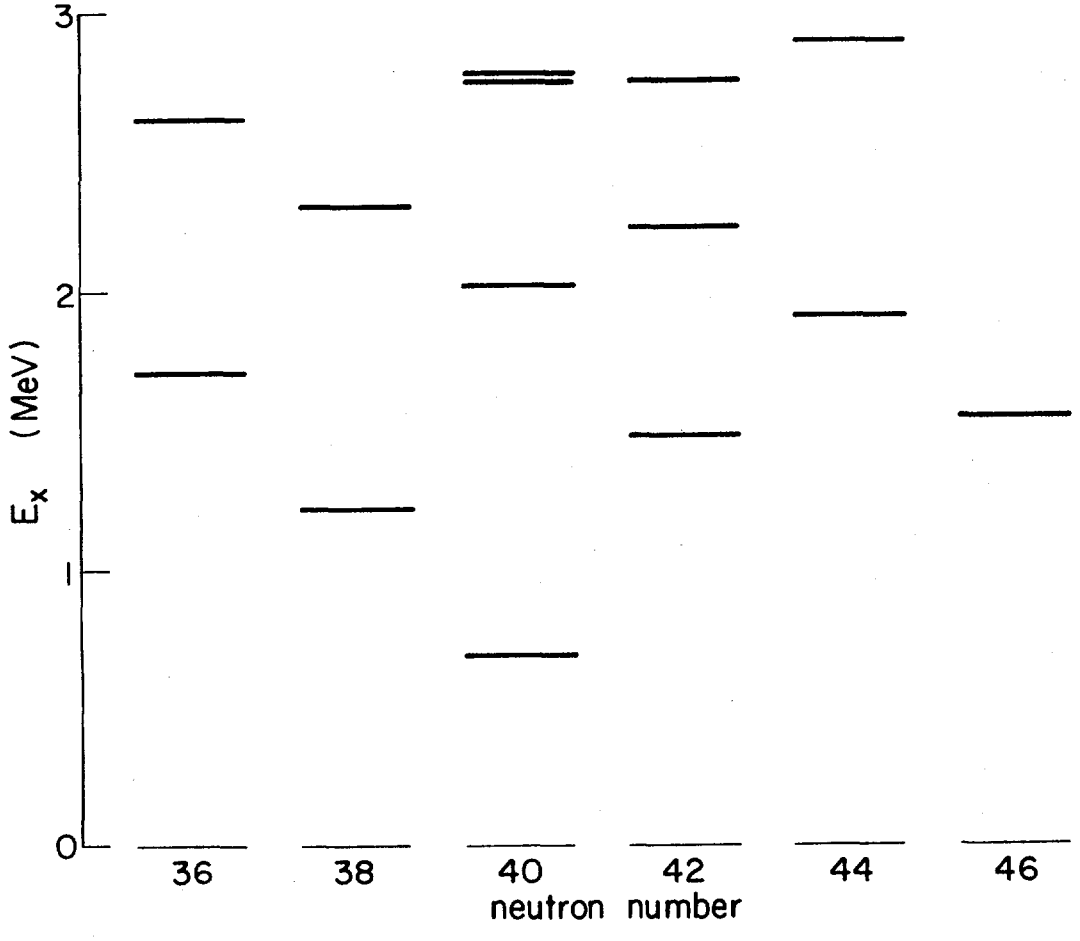

Fig. 3 Excitation energies of the low-lying 0^+ states in the Ge isotopes as a function of neutron number.

Ge and Se isotopes have both been studied as a function of neutron number and

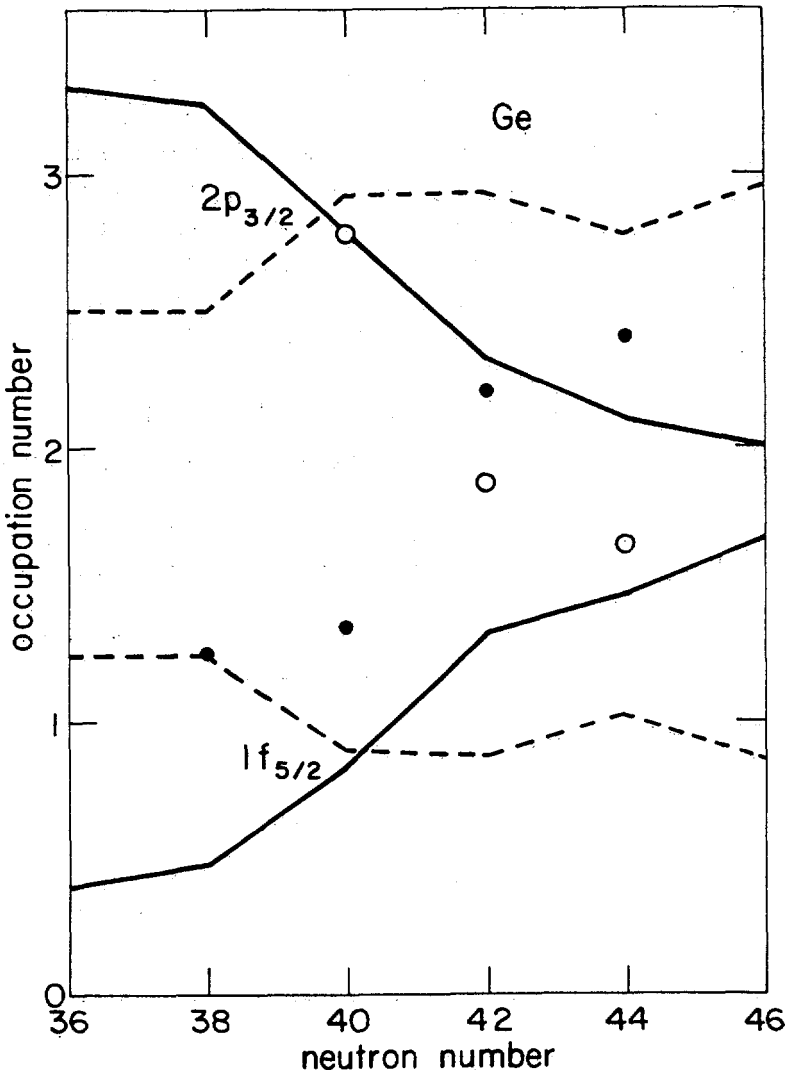

Fig. 4 The solid lines give the weak-coupling predictions for the occupation numbers of the $2p_{3/2}$ and $1f_{5/2}$ subshells for the 0_1^+ ground states of the isotopes of Ge. The dashed lines are the corresponding results for the 0_2^+ states. The solid and empty circles give the experimental $\langle 1f_{5/2} \rangle$ and $\langle 2p_{3/2} + 2p_{1/2} \rangle$ occupation probabilities, respectively, of the ground states.

exhibit some dramatic physics. Fig. 3 shows that the 0_2^+ state plunges with increasing neutron number: perhaps a level crossing of the two lowest bands occurs at neutron number ≈ 40. Fig. 4 shows that the protons occupation numbers correspondingly are undergoing rather sudden changes. One expects that this may reflect the strong interaction between $1f_{5/2}$ (protons) and $1g_{9/2}$ (neutrons), shells with the same nodal structure. As neutrons are added to the $1g_{9/2}$ shell, the protons are polarized: The mixing of three 0^+ bands (spherical, $p^2_{3/2}\ f^2_{5/2}$ (protons) - $p^0_{1/2}\ g^6_{9/2}$ (neutrons), and $p^0_{3/2}\ f^4_{5/2}$ (protons) - $p^0_{1/2}\ g^6_{9/2}$ (neutrons)) is an aspect of this polarization, and must change rapidly with neutron number.

Figs. 3 and 4 show that the weak-coupling shell model with the Kuo (^{56}Ni) g-matrix reproduces most of this complicated physics, and this gave us a great deal of confidence in our $\beta\beta$ decay predictions. The standard model 2ν rates we calculated were later measured and shown to agree to within about 50%.[8] This in turn has boosted the confidence in the Majorana neutrino mass limits we extracted from calculations of 0ν $\beta\beta$ decay nuclear matrix elements.

The final, and perhaps most extraordinary, application of the Lanczos algorithm is in evaluating fully-interacting nuclear Green's functions. For instance, in $\beta\beta$ decay one needs the quantity

$$\langle 0_f^+ | \hat{0}_{GT} \frac{1}{E_0 - H} \hat{0}_{GT} | 0_i^+ \rangle$$

where $\hat{0}_{GT}$ is the GT operator. Defining $|v_1\rangle = \hat{0}_{GT}|0_i^+\rangle$, one can demonstrate

$$\frac{1}{E_0 - H} |v_1\rangle = g_1(E_0)|v_1\rangle + g_2(E_0)|v_2\rangle + \ldots$$

where the $|v_i\rangle$ are the Lanczos vectors and the $g_i(E_0)$ continued fractions formed from the entries in the tridiagonal Lanczos matrix.[9] For example,

$$g_1(E_0) = \cfrac{1}{E_0 - \alpha_1 - \cfrac{\beta_1^2}{E_0 - \alpha_2 - \cfrac{\beta_2^2}{E_0 - \alpha_3 - \beta_3^2}}} \ddots$$

Roger Haydock has extensively explored Lanczos Green's functions methods in condensed matter physics.[10] My experience in various nuclear physics applications has led me to conclude that this is a wonderfully stable and rapidly converging (often ~20 iterations) procedure to evaluate a quantity that is inherently very complex.

In $\beta\beta$ decay we have used this algorithm to complete a full fp-shell calculation of the transition ^{48}Ca $\rightarrow$^{48}Ti (g.s.), thereby respecting all sum rules for the GT operator.[11] Similar calculations for ^{76}Ge $\rightarrow$^{76}Se and ^{82}Se $\rightarrow$^{82}Kr are perhaps a workstation generation away. Other applications where nuclear polarizabilities must be evaluated include anapole moments, electric dipole moments, and $0^+ \rightarrow 0^+$ 2γ transitions.

In conclusion, I hope the description of structure techniques we use in lighter nuclei might suggest some applications to high spin physics. The possibilities seem quite intriguing to me. It would be reassuring if tools could be developed to predict the properties of very high spin states from microscopic calculations based on realistic g-matrices.

References

1. See, for example, J.H. Wilkinson, The Algebraic Eigenvalue Problem (Clarendon Press, Oxford, 1965).
2. R.R. Whitehead, in Moment Methods in Many Fermion Systems, ed. B.J. Dalton, S.M. Grimes, J.P. Vary, and S.A. Williams (Plenum Press, New York, 1980), p. 235.
3. R.R. Whitehead *et al.*, Adv. in Nucl. Phys. **9** (1977) 123.
4. W.C. Haxton and Calvin Johnson, Phys. Rev. Lett. **65** (1990) 1325.
5. G.E. Brown and A. M. Green, Nucl. Phys. **75** (1966) 401.
6. T.T. S. Kuo, private communication.
7. J.N. Ginocchio, Ann. Phys. (N.Y.) **156** (1984) 203; **159** (1985) 467.
8. W.C. Haxton to appear in Proceedings of Neutrino '92 (Granada, 1992).
9. R. Haydock, J. Phys. **A7** (1974) 2120.
10. R. Haydock, in Computational Methods in Classical and Quantum Physics, ed. Hooper (Advance Publications, London, 1976) p. 268.
11. J. Engel, W.C. Haxton, and P. Vogel, in preparation.

FROM SUPERDEFORMATION TO CLUSTERS

R. R. Betts
Physics Division, Argonne National Lab., Argonne, IL 60439

Much of the discussion at this conference has centered on the topic of superdeformed states in nuclei, and their study with the exquisitely precise tool of gamma ray spectroscopy, carried out with state-of-the-art detector arrays. In the usual way in which superdeformed states are populated, via compound nucleus formation and evaporation, gamma decay is the last process to occur in the decay chain. In some other sense, it is also the last to occur in the meaning of least likely. Figure 1 illustrates schematically the

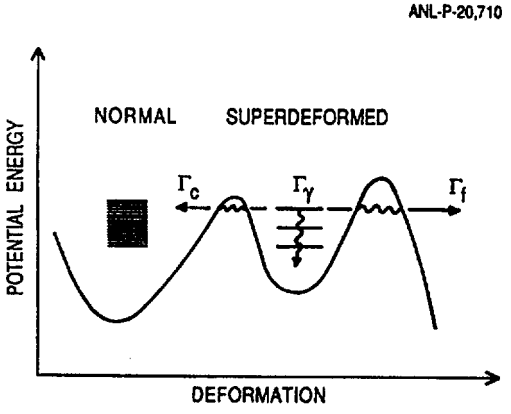

Fig. 1. Schematic representation of the potential energy of a nucleus as a function of deformation. The different contributions to the decay widths of quasi-stable states in the superdeformed minimum are indicated.

potential energy surface of a nucleus as a function of deformation showing the quasi-stable states which exist in the secondary superdeformed minimum at large deformations. Several components contribute to the total decay width of states in this secondary minimum. They are, respectively; Γ_γ, the gamma decay width; Γ_f, the fission or particle decay width and Γ_c, the width for decay into states of normal structure. The natural units which set the scale for each of these components are: for Γ_γ, the Weisskopf unit which, for a 1 MeV E2 transition in a mass 150 nuclei gives $\Gamma_\gamma \simeq 4 \times 10^{-5}$ eV and for Γ_f, the Wigner limit which, roughly, for symmetric breakup gives values of several keV. Thus, we see that, in order for gamma decay of superdeformed states to occur, not only must the gamma decay width be tremendously enhanced by the collective rotation of the system, but the fission decay width must be enormously suppressed by penetration through the outer part of the two-humped fission barrier. This, of course, is obviously the case in those nuclei in which we have been able to observe gamma-decaying states, but there is an implication that a much wider area of study for superdeformation may be available with modes other than gamma decay.

The first evidence for superdeformation came from the observation of isomeric fissioning states in very heavy nuclei. These superdeformed states were populated via the compound nucleus formed in neutron capture, which then couples to the superdeformed minimum through Γ_c, and fissions through Γ_f. The exact details of this process depend on the relative values of Γ_c and Γ_f and on the level densities of normal and superdeformed states. One case which is of interest in the context of the present discussion is, perhaps prophetically, mentioned in Bohr and Mottelson Vol. II[1] corresponding to the situation where $\Gamma_f >> \Gamma_c$ when the total width of the superdeformed states is much larger than the average width of normal states. In this situation; *"The broad type II (superdeformed) state would strongly manifest itself in the hypothetical fission fragment scattering process."* This is the subject of this talk.

Fission fragment scattering may be thought of as the ultimate radioactive beam experiment. The fission fragments from heavy nuclei are produced in highly excited states and therefore any attempt to observe superdeformed states via the inverse of their fission decay might seem fruitless. This is emphasized in Fig. 2,

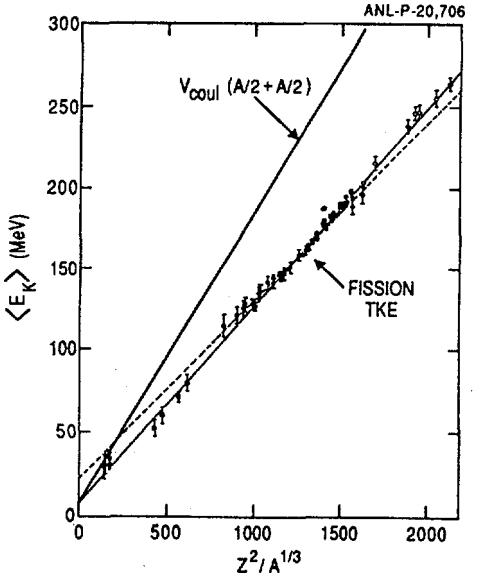

Fig. 2. Systematics of fission fragment kinetic energies compared with the Coulomb barrier for spherical fragments.

which shows the systematics of fission fragment kinetic energies plotted as a function of $Z^2/A^{1/3}$ due to Viola[2], compared with the Coulomb energy for touching spheres of mass A/2. For heavier systems, the difference between the fragment kinetic energies and the spherical Coulomb barrier reflects the large deformations of the fission fragments at scission and underlines the essential impossibility of mimicking the time-reversal fission process through collision processes. For much lighter systems, however, the fragment kinetic energies lie much closer to the spherical Coulomb barrier, reflecting the shape transition predicted by the liquid drop model[3] to a scission point configuration close to two touching

spheres. In these cases, therefore, we expect that scattering processes may indeed be similar to inverse fission of the compound nucleus. This observation opens up the possibility of studying regions of superdeformation predicted to occur for $Z < 40$, $A < 80$ which can be accessed via a variety of scattering channels.

The above ideas provide a useful vehicle for discussion of some features of a wide variety of data on scattering and reactions of light nuclei. One striking example[4] of this is shown in Figs. 3-5. In Fig. 3, the angular distribution of elastic scattering of ^{28}Si +

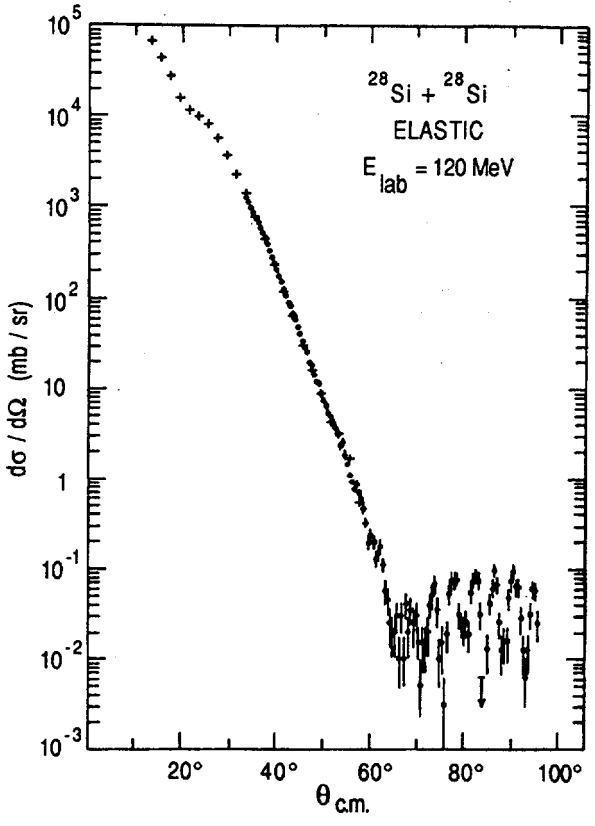

Fig. 3. Angular distribution of elastic scattering of ^{28}Si + ^{28}Si at a bombarding energy of 120 MeV.

^{28}Si at a bombarding energy of roughly twice the Coulomb barrier is shown. At forward angles, the data show a typical transition from Coulomb scattering through nuclear-Coulomb interference to a steep fall-off characteristic of the scattering of strongly absorbing particles. These features are readily described with a variety of optical model calculations. At the largest angles, however, the data show an abrupt transition to a highly oscillatory behavior similar to that of a pure Legendre polynomial squared of order L = 40 which, in this case, is the grazing angular momentum. In the large-angle region, the elastic scattering channel is relatively weak as demonstrated by the spectrum shown in Fig. 4 which shows

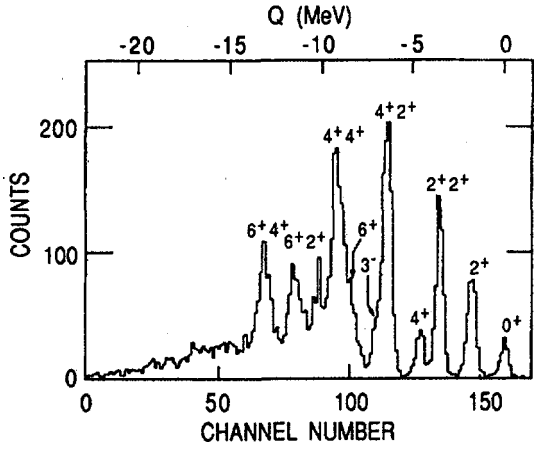

Fig. 4. Spectrum of ^{28}Si + ^{28}Si at large angles measured at a bombarding energy of 120 MeV.

strong excitation of inelastic and mutual inelastic channels. These channels show the same general angular behavior as do the elastics as displayed in Fig. 5. Namely, a forward angle dependence of the

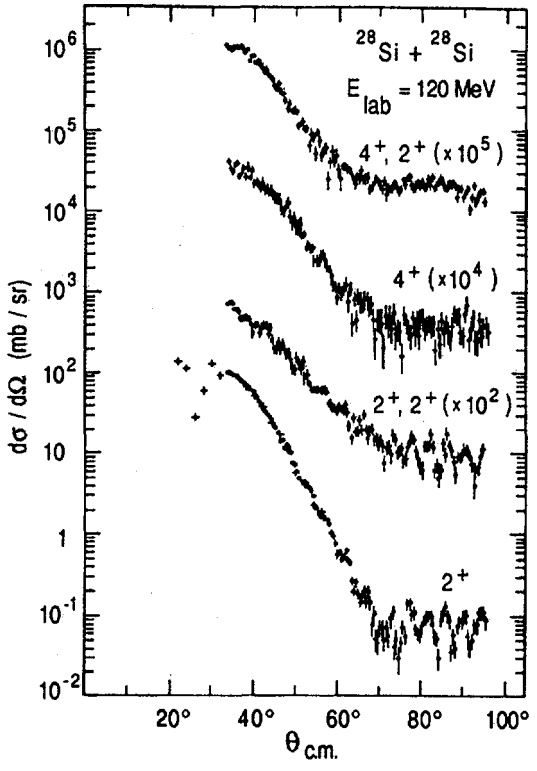

Fig. 5. Angular distributions of inelastic and mutual inelastic scattering of ^{28}Si + ^{28}Si at a bombarding energy of 120 MeV.

cross-section characteristic of Coulomb and nuclear scattering with strong absorption, and a large-angle behavior suggesting the presence of a much longer time-scale process.

The demonstration of the long time-scale involved in the large angle cross-sections comes from the data[5] shown in Fig. 6 which

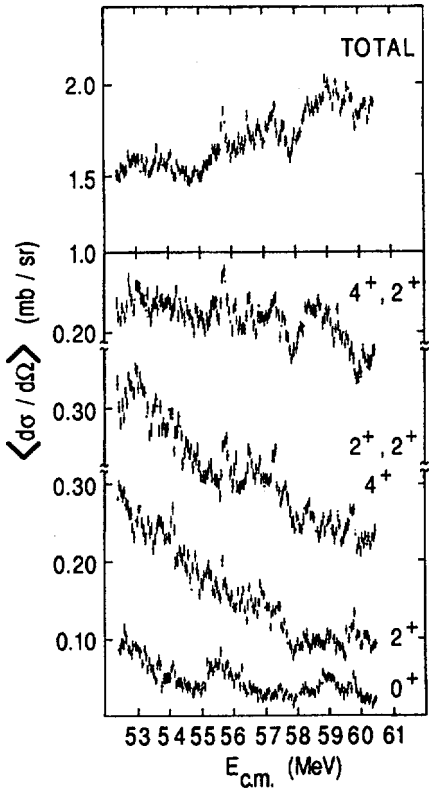

Fig. 6. Excitation functions for elastic and inelastic scattering of ^{28}Si + ^{28}Si showing many correlated structures of width 100-200 keV.

displays the energy dependence of the large angle cross-sections measured in center-of-mass energy steps of 50 keV. The narrow structures observed in this cross-section have been demonstrated[6] to correspond to a complex pattern of isolated resonances in the composite system with angular momenta, obtained from elastic scattering angular distributions[7], ranging from 36-40 $\hbar$. These resonances, which appear with an average spacing of 300 keV lie in a region of excitation energy and angular momentum from which the level density of the compound nucleus, ^{56}Ni, is calculated to be several thousand per MeV. Conversely, their decay widths into the symmetric channel (^{28}Si + ^{28}Si) are on the order of keV whereas the average compound nuclear state has a statistical decay width into these channels of only eV. It is clear therefore, that these resonances correspond to a rather special subset of states stabilized against mixing into the more numerous compound nucleus states by some special symmetry.

Information on the origin of this special stability comes from data[4] for ^{28}Si + ^{30}Si and ^{30}Si + ^{30}Si shown in comparison with ^{28}Si + ^{28}Si in Fig. 7. The addition of neutrons not only results in a

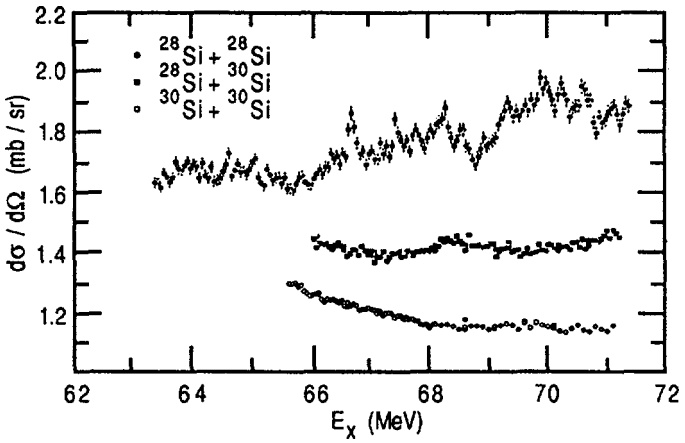

Fig. 7. Total large-angle cross sections for scattering and reactions of $^{28}Si + ^{28}Si$, $^{28}Si + ^{30}Si$ and $^{30}Si + ^{30}Si$ as a function of compound nucleus excitation energy.

disappearance of the prominent narrow structures, but also in a suppression of the total cross-sections by factors of two and four respectively. The general behavior of these cross-sections, as well as the mass distributions are quite consistent with the origin of these processes being fission of the compound nucleus. In which case, the disappearance of the narrow structures may be associated with the disappearance of a shell-stabilized secondary minimum which occurs with the addition of neutrons. These data, therefore, provide evidence for superdeformation in the mass 56 region.

It should be hoped that one could proceed from these observations to a spectroscopy which would then further test the hypothesis. The pattern of resonances is, however, extremely complex and we lack evidence for unifying features of the data such as rotational bands which appear in such a direct way in the gamma-ray studies. For other systems, such as $^{24}Mg + ^{24}Mg$[8] shown in Fig. 8 there is an apparently simpler behavior, with similar groups of

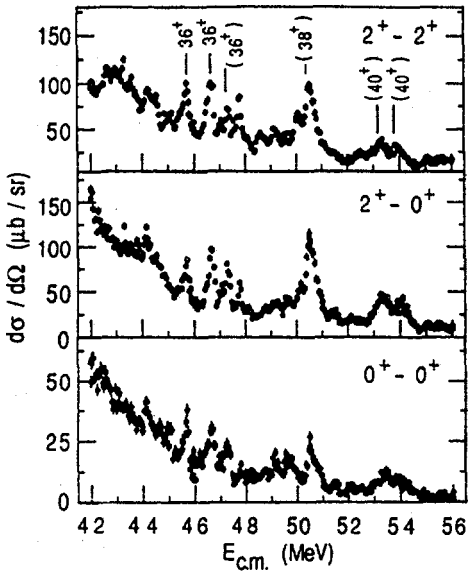

Fig. 8. Excitation functions for elastic and inelastic scattering of $^{24}Mg + ^{24}Mg$.

resonances appearing for each spin[8,9]. It is therefore of interest to look at some models to see if any such features appear in a simple way. In this case, the deformed harmonic oscillator provides a useful starting point which may have some validity in these light nuclei. Note here, that Nilsson-Strutinsky calculations[10] using deformed oscillator shell corrections predict a 3:1 hyperdeformed minimum for ^{48}Cr at angular momenta appropriate to the ^{24}Mg + ^{24}Mg scattering data.

The energy levels of an axially deformed harmonic oscillator are shown in Fig. 9 plotted versus deformation. Shell gaps appear

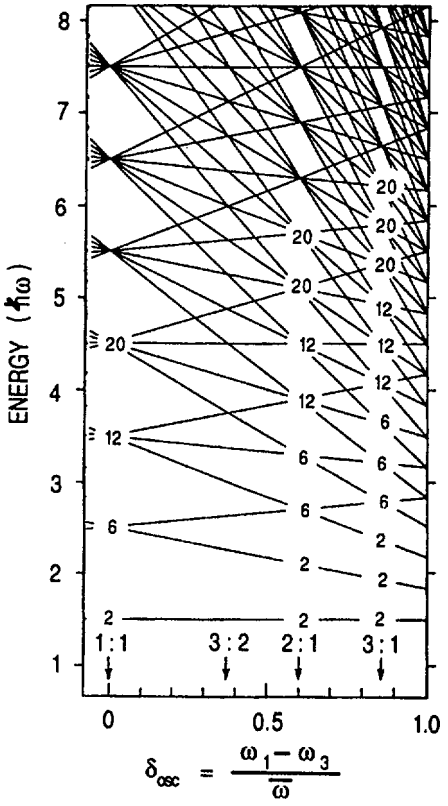

Fig. 9. Energy levels of an axially deformed harmonic oscillator with the degeneracies of the shells which occur at integer ratios of the frequencies.

at deformations corresponding to integer ratios of the frequencies along and perpendicular to the deformation axis. Also shown are the degeneracies of the orbits at these values of the deformation. For 2:1 deformation we see a doubling of the spherical degeneracies, for 3:1 a tripling and so on. It has been shown[11] that these sets of degenerate orbits have the same SU(3) symmetry as do the spherical shells and a decomposition of the deformed oscillator wavefunctions at these deformations into "multi-clusters" has been proposed. These authors were careful to point out that the use of the word "cluster" was not to be taken in the usual sense, as such true clustering would be strongly inhibited by the Pauli principle. A closer look at the details of the wavefunctions, however, reveals a

possible connection between the deformed oscillator and clustering. For example, for the 2:1 shape, the quantum numbers of the degenerate orbits fall into two groups:

Degeneracy	Sphere [N N_3]	2:1	
2	[0,0]	[0,0]	[0,1]
6	[1,0]	[1,0]	[1,1]
	[0,1]	[0,2]	[0,3]
12	[2,0]	[2,0]	[2,1]
	[1,1]	[1,2]	[1,3]
	[0,2]	[0,4]	[0,5]
	[N N_3]	[N $2N_3$]	[N $2N_3$+1]

This connection between the spherical quantum numbers and those at the 2:1 shape is precisely that which comes from the evolution of a two-center shell model into a single center potential, provided that this evolution takes place adiabatically. The origin of this is illustrated schematically in Fig. 10 where the evolution of the

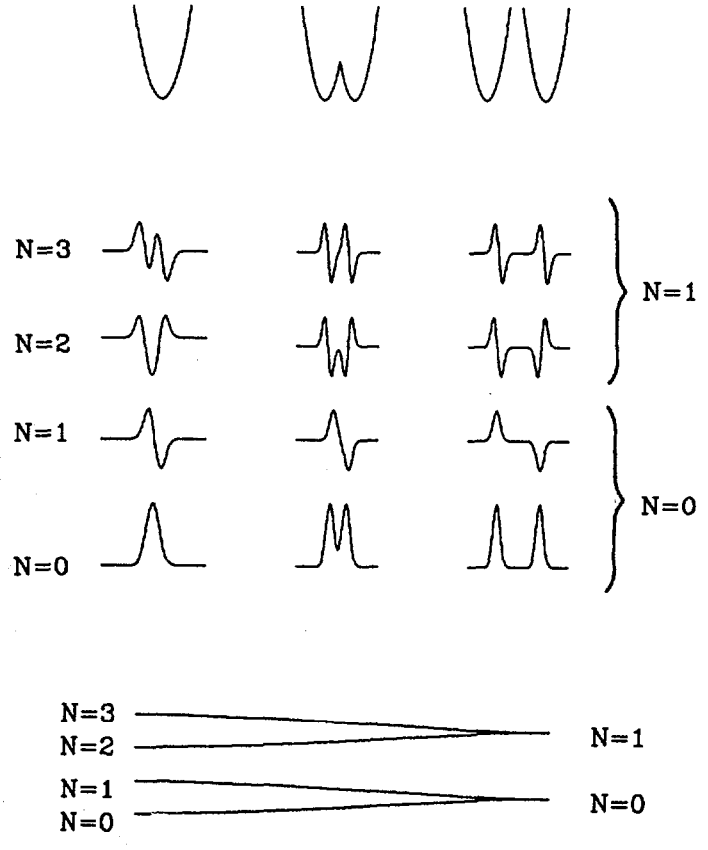

Fig. 10. Evolution of the potential, wavefunctions and energies of a symmetric two center harmonic oscillator.

wavefunctions and energy levels in a two-center model are shown as a function of separation of the two centers. In the symmetric two-center case, the requirement that the wavefunction have good parity results in an initially degenerate pair of states with positive and negative parity which split as the two centers merge. In this way the quantum number N of the single center potential wavefunctions evolves to either 2N or 2N+1, exactly as is the case for the 2:1 oscillator. These ideas may be generalized to the N:1 oscillator and the N-center shell model and also to cases of non-axial symmetry. The general conclusion is that states in the secondary minima created by the degeneracies which occur in the deformed shell model with rational ratios of axes will, if allowed to do so adiabatically, naturally evolve into clusters suggested by the SU(3) symmetries of the deformed shells. Thus, although the overlaps of the deformed wavefunctions with the clusters may not be large, they contain the correct symmetries for the dynamical evolution of the system into many-center states which have complete overlap with the clusters. In this way, the parentage of highly deformed states can be identified and selection rules for their decay determined.

The above discussion provides some new insight into the comparison of the results of a multi-center shell model calculation[12] of six alpha-particles with a Nilsson-Strutinsky calculation[13] of ^{24}Mg. The results of these two calculations are shown in Fig. 11 where the deformed shell model potential energy

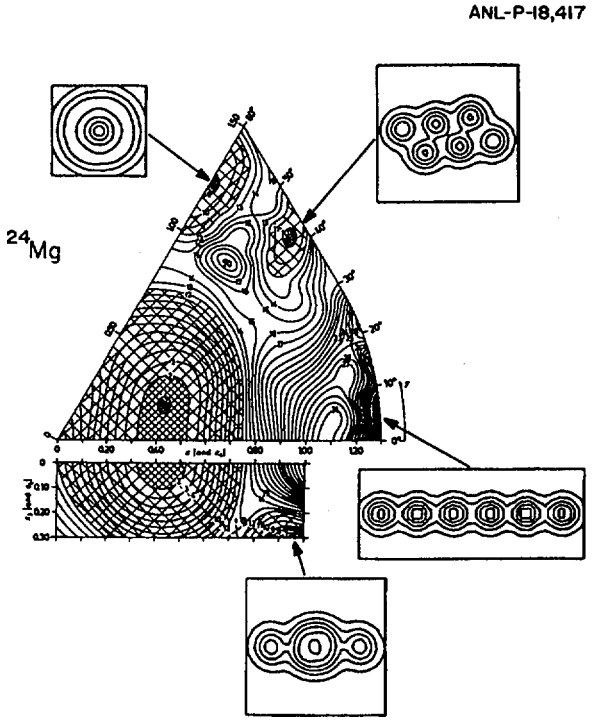

Fig. 11. Comparison between the potential energy surface of ^{24}Mg from a deformed shell model calculation and density contours of cluster states from a multi-center cluster model calculation.

surface is compared with the density contours of quasi-stable configurations of six alpha-particles from the many center shell model calculations. It is possible to make a one-to-one correspondence between the two calculations in a way which gives new order to the variety of resonance phenomena seen in reactions leading to ^{24}Mg. The triaxial minimum ($\epsilon = 1.1$, $\gamma = 40°$) is seen to correspond to a cluster configuration which has the symmetry of two ^{12}C (ground-state) triangles and should therefore be identified with the family of broad resonances seen in $^{12}C + ^{12}C$ elastic and inelastic scattering[14]. The reflection asymmetric minimum ($\epsilon = 1.0$, $\gamma = 0°$, $\epsilon_3 = 0.30$) has a rather complex structure, with overlap with $^{20}Ne + \alpha$, $^{16}O + ^{8}Be$ as well as $^{12}C + ^{12}C$ channel. This configuration is the basis of the original[15] $^{12}C + ^{12}C$ barrier resonances and has also been recently, and elegantly, studied[16] via ^{24}Mg breakup reactions.

In these recent experiments, a beam of ^{24}Mg bombarded a ^{12}C target and ^{12}C fragments were detected and identified at forward angles. From their energies and angles, events corresponding to breakup in which all three participating ^{12}C nuclei are in their ground states were selected and the excitation energy of the ^{24}Mg decaying to two ^{12}C determined. Thus resulting spectrum is shown in Fig. 12. This spectrum is quite similar to the spectrum of

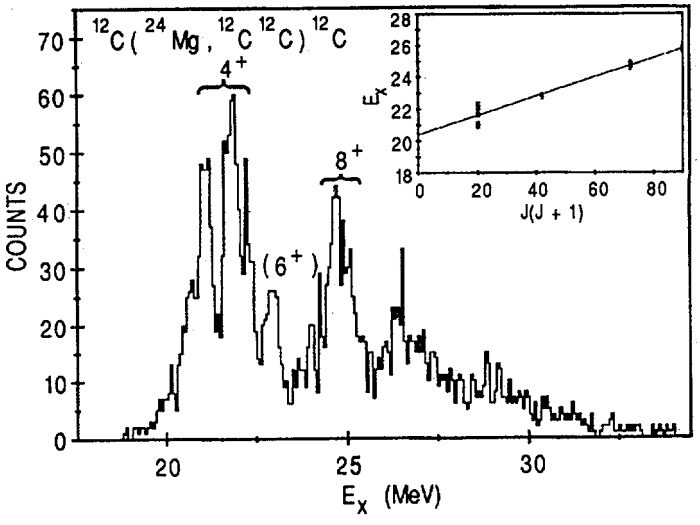

Fig. 12. Excitation energy spectrum of ^{24}Mg states which break up into two ^{12}C (g.s.). The inset shows the rotational band formed by these states.

resonances observed in $^{12}C + ^{12}C$ reactions[17] in the same excitation energy region. From the angular correlations of the two breakup ^{12}C it is possible to deduce the resonance spins[18] which, as shown in the inset, lie quite nicely on a rotational band with a moment of inertia of 60 keV, compared to 94 keV predicted from the multi-center shell model, and 74 keV from the deformed shell model.

Finally, both the deformed shell model and multi-center shell model predict the rather exotic configuration with a 6:1 axis ratio corresponding to a linear chain of alpha-particles to be stable.

Phase space and structural considerations lead us to expect that states of this configuration will split into two three alpha-particle chains which, in the cluster model, correspond to the 7.65 MeV 0_2^+ state in ^{12}C. The 0_2^+ state in ^{12}C is itself unstable to decay into alpha + ^8Be and we therefore expect the ^{24}Mg chain configuration to result in six alpha particles produced in a kinematically correlated fashion via the above sequential route. The detection and characterization of a six particle final state is in itself a formidable challenge. A search for this signature of the chain configuration has been carried out[19], using an array of double-sided silicon strip detectors which allow the simultaneous detection of several particles with good energy and spatial resolution[20]. A beam of ^{12}C was used to bombard a ^{12}C target - the resulting particles were detected on either side of the beam axis with two 5 x 5 cm, 256 quasi-pixel, strip detectors. The resulting excitation spectrum calculated from events in which three alpha-particles hit a single detector is shown in Fig. 13, showing the

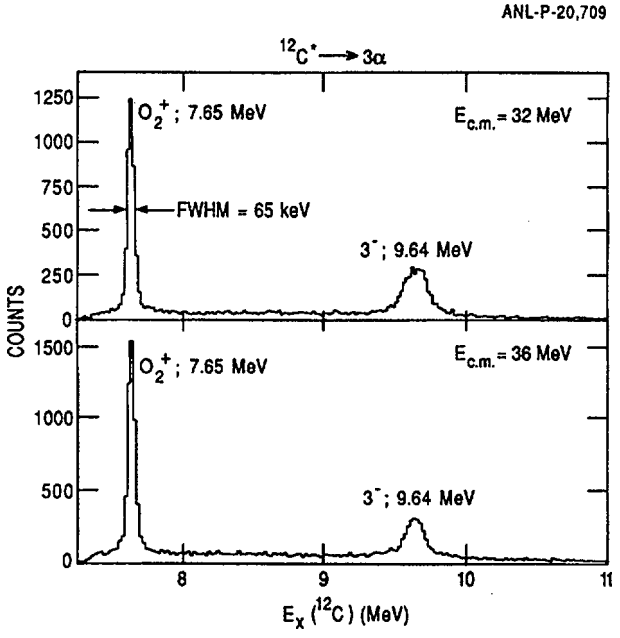

Fig. 13. Excitation spectrum of ^{12}C for events in which three alpha particles are detected in one strip detector.

7.65 MeV 0_2^+ in ^{12}C. For events in which three alpha-particles were detected in each of the strip detectors, the total excitation energy spectrum shown in Fig. 14 clearly shows the double excitation of the 0_2^+ channel, the sought after decay mode of the ^{24}Mg chain. The cross-section for this channel is shown as a function of energy in Fig. 15 and exhibits a pronounced broad structure centered at E_{cm} = 32.5 MeV corresponding to an excitation energy of 46.4 MeV in ^{24}Mg with a width of approximately 5 MeV. Subsequent detailed measurements of the angular distributions over the resonance show that, whereas the structure is not characterized by a single angular momentum and therefore corresponds to a number of overlapping resonances, it does appear to be dominated by angular momenta in the vicinity of 14-16 $\hbar$. Thus, the observed structure lies very close to the predicted crossing of the rotational band based on the chain

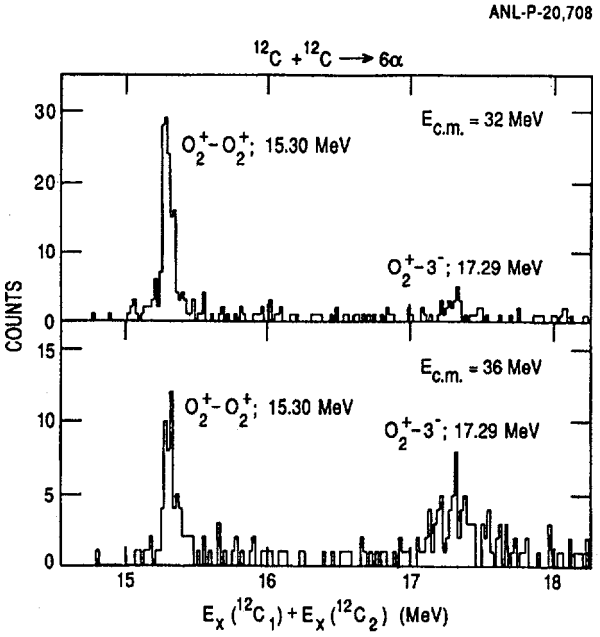

Fig. 14. Total excitation spectrum for events in which six alpha particles are detected, clearly showing the double 0_2^+ excitation.

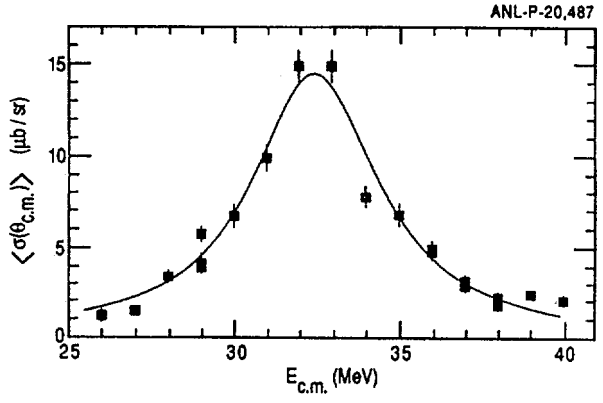

Fig. 15. Cross-section for the double 0_2^+ excitation shown as a function of bombarding energy.

configuration with the ^{12}C + ^{12}C grazing trajectory, as illustrated in Fig. 16. Further experiments and analysis ares clearly necessary to substantiate these suggestions but the data are quite consistent with the observation of these extremely unusual configurations of alpha-particle chains.

In summary, there exists clear evidence for the existence of shell effects at extreme deformations in light nuclei studied via fission and cluster decay. The connection between the deformed shell model and the multi-center shell model can be exploited to give insight into the cluster structure of these extremely deformed states and also give hope for a spectroscopy based on selection rules for cluster decays which come from this connection. A clear handicap is, however, at this stage, our inability to make this spectroscopy more quantitative through calculation of the cluster decay widths. Finally, it is also apparent that the introduction of

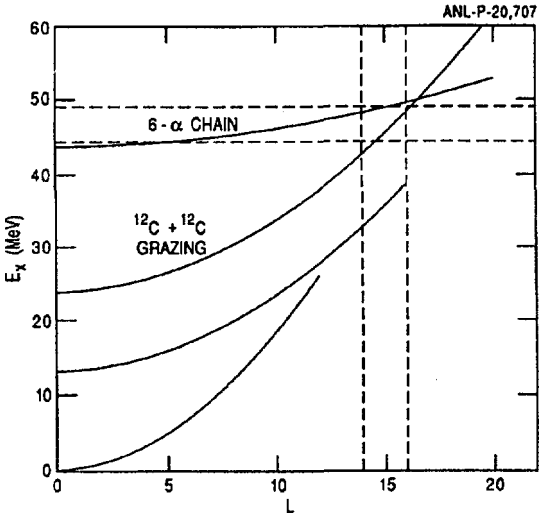

Fig. 16. Plot of excitation energy versus spin for ^{24}Mg showing the predicted location of the six-alpha chain band and its crossing with the $^{12}C + ^{12}C$ grazing trajectory. The location of the broad structure observed in the double 0_2^+ channel is indicated by the dashed lines.

a new generation of high segmentation, high resolution particle arrays has and will have a major impact on this aspect of the study of nuclear structure at extreme deformations.

Collaboration and discussions with Martin Freer and Alan Wuosmaa during the preparation of this talk are gratefully acknowledged. This work is supported by the U.S. Department of Energy, Nuclear Physics Division, under contract W-31-109-ENG-38.

References

1) Nuclear Structure, A. Bohr and B. Mottelson, (Benjamin, New York 1975) vII, p. 627

2) V. E. Viola, K. Kwiatkowski and M. Walker, Phys Rev. C31, 1550 (1985)

3) A. J. Sierk, Phys. Rev. C33, 2039 (1986)

4) R. R. Betts, in Proceedings of Conference on Nuclear Physics with Heavy Ions, Stony Brook 1983, ed. P. Braun-Munzinger (Harwood, New York 1984) p. 347

5) R. R. Betts, B. B. Back and B. G. Glagola, Phys. Rev. Lett. 47, 23 (1981)

6) S. Saini and R. R. Betts, Phys. Rev. C29, 1769 (1984)

7) R. R. Betts, S. B. DiCenzo and J. F. Petersen, Phys. Lett. 100B, 117 (1981)

8) R. W. Zurmühle, P. Kutt, R. R. Betts, S. Saini, F. Haas and Ole Hansen, Phys. Lett. 129B, 384 (1983)

9) A. H. Wuosmaa, R. W. Zurmühle, P. H. Kutt, S. F. Pate and S. Saini, Phys. Rev. C41, 2666 (1990)

10) S. Åberg (private communication)

11) W. Nazarewicz and J. Dobaczewski, Phys. Rev. Lett. 68, 154 (1992)

12) S. Marsh and W. D. M. Rae, Phys. Lett. 180B, 185 (1986)

13) G. Leander and S. E. Larsson, Nucl. Phys. A239, 93 (1975)

14) T. M. Cormier, C. M. Jachcinski, G. M. Berkowitz, P. Braun-Munzinger, P. M. Cormier, M. Gai, J. W. Harris, J. Barrette and H. E. Wegner, Phys. Rev. Lett. 40, 924 (1978)

15) D. A. Bromley, J. A. Kuehner and E. Almquist, Phys. Rev. Lett. 4, 365 (1960)

16) B. R. Fulton, S. J. Bennett, C. A. Ogilvie, J. S. Lilley, D. W. Banes, W. D. M. Rae, S. C. Allcock, R. R. Betts, and A. E. Smith, Phys. Lett. 181B, 233 (1986)

17) K. A. Erb, R. R. Betts, M. H. Hindi, S. K. Korotky, P. P. Tung, M. W. Sachs, S. T. Willett and D. A. Bromley, Phys. Rev. C 22, 507 (1980)

18) B. R. Fulton, S. J. Bennett, M. Freer, J. T. Murgatroyd, G. J. Gyapong, J. S. Jarvis, C. D. Jones, D. L. Watson, J. D. Brown, W. D. M. Rae, A. E. Smith and J. S. Lilley, Phys. Lett. B267, 325 (1991)

19) A. H. Wuosmaa, R. R. Betts, B. B. Back, M. Freer, B. G. Glagola, T. Happ, D. J. Henderson, P. Wilt, and I. G. Bearden, Phys. Rev. Lett. 68, 1295 (1992)

20) A. H. Wuosmaa, P. Wilt, R. R. Betts, B. B. Back, M. Freer, B. G. Glagola, Th. Happ, D. J. Henderson, I. G. Bearden, R. W. Zurmühle, D. P. Balamuth, S. Barrow, D. Benton, Q. Li, Z. Liu and Y. Miao, Nucl. Inst. and Meth. (submitted)

INTERNATIONAL CONFERENCE ON NUCLEAR STRUCTURE AT HIGH ANGULAR MOMENTUM

Ottawa

SESSION 12: SYSTEMATICS OF NUCLEAR STATES

Triaxiality and alternating M1 strengths in f-p-g shell nuclei

S.L. Tabor, T.D. Johnson, J.W. Holcomb,
P.C. Womble, J. Döring, and W. Nazarewicz†
Department of Physics, Florida State University, Tallahassee, FL 32306 USA

The appearance of alternating patterns in B(M1) strengths in f-p-g shell nuclei is surveyed. The M1 alternations in a sequence of N = 41 isotones, in conjunction with particle-rotor model calculations, is shown to provide information about changing γ deformation. In addition to other odd-A nuclei, several odd-odd nuclei are shown to exhibit alternating B(M1) values and signature inversion. Alternations have also been reported in a 4 quasiparticle band in ^{86}Zr, where they have been interpreted in terms of the interacting boson model.

Alternating patterns in the strengths of magnetic dipole transitions between states of opposite signature have been seen in a number of *f-p-g* shell nuclei, both in our laboratory and by other groups. The alternating M1 patterns have been related to signature splitting and the triaxiality parameter γ. They can, thus, provide information on the γ degree of freedom. Generally, the M1 transitions from states of favored signature (relatively lower in energy) to states of unfavored signature (relatively higher in energy) are stronger than those from states of unfavored to favored signature. These alternations are discussed in terms of the B(M1) values, which are directly related to the nuclear matrix elements, after removal of the transition energy dependence from the experimental lifetimes. In fact, the larger B(M1) values correspond to the lower energy transitions.

The purpose of this report is to summarize what is currently known about alternating B(M1) strengths in the *f-p-g* shell, both in terms of experimental measurements and theoretical calculations. Special emphasis will be given to recent work on the N = 41 isotones, which provides perhaps the clearest information on γ values at present.

A few words are appropriate about the conditions required to experimentally observe alternating M1 patterns: First, in order to see Δ I = 1 transitions at all, there must exist and one must observe two signature partner rotational bands. Second, the B(M1) strengths must be large enough to compete successfully with the enhanced E2 decays. Third, in many models the alternations are related to signature splitting, so some amount of signature splitting must be present. However, if the energies of the unfavored states rise too close to or above those of the favored states one unit of spin lower, some of the M1 branches become too weak to observe. The ΔI = 1 / ΔI = 2 branching ratios provide information about alternating M1 values, provided that the E2 strengths and the E2/M1 mixing ratios δ for the ΔI = 1 transitions remain constant or change smoothly. However, measurements of the mixing ratios and of the lifetimes of the states are necessary to determine absolute B(M1) strengths.

1. N = 41 Isotones

Three N = 41 isotones, ^{75}Se, ^{77}Kr and ^{79}Sr, provide a sequence with a varying degree of signature splitting and expected γ deformation, where M1 transitions are observable. The signature splitting in the yrast $g_{9/2}$ band is largest for ^{75}Se (Ref. 1), moderate for ^{77}Kr (Ref. 2) and smallest for ^{79}Sr (Ref. 3), i.e., it decreases with increasing mass. This variation can be seen in the Routhians shown in Fig. 1. The signature splittings decrease at the first band crossing, which occurs in the frequency range of $\omega \approx 0.5$ - 0.6 MeV/$\hbar$, as can be seen from the graphs of aligned angular momentum also shown in Fig. 1.

The behavior of the magnetic dipole transitions in these three isotones is shown in Fig. 2. The one quasiparticle (qp) band in ^{75}Se again shows the largest alternations in B(M1) and the largest absolute values, which approach one Weisskopf unit (W.u.). The B(M1) alternations in ^{77}Kr are significant, but smaller, and remain relatively constant throughout the wide range over which they have been observed. In ^{79}Sr only five B(M1) values are known in the yrast 1 qp band, but they also show a tendency to alternate.

The shapes expected for the lowest 1 qp $\pi = +$ bands in these nuclei also vary in a systematic way, as shown in the total Routhian surfaces (TRS) of Fig. 3. The calculations are described in the references listed above for the individual nuclei. They predict that the β_2 deformation decreases with decreasing mass, while the γ triaxiality parameter increases from near 0° for ^{79}Sr to -10 ° for ^{77}Kr to -60° for ^{75}Se.

Hagemann and Hamamoto[4] have demonstrated a relationship between the alternations in B(M1) strength and the signature splitting of the 1 qp

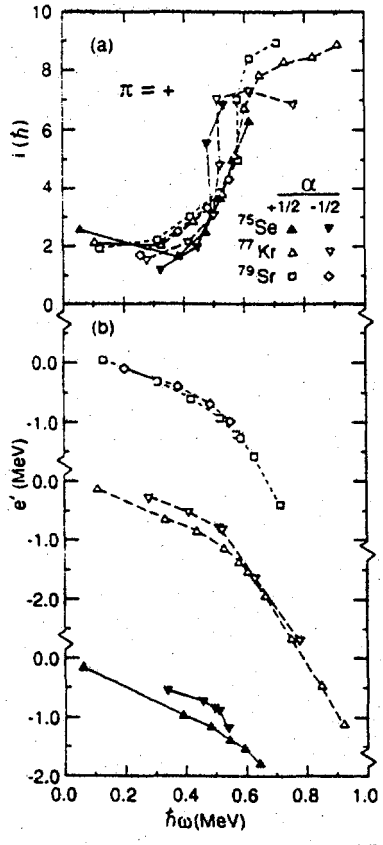

Fig. 1. Aligned angular momenta (i) and Routhians (e') for the lowest $\pi = +$ bands in three N = 41 isotones. The Harris parameters for the reference rotor are $J_0 = 10\ \hbar^2$/MeV and $J_1 = 5\ \hbar^4$/ MeV^3.

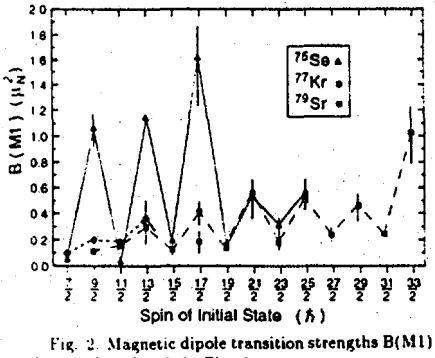

Fig. 2. Magnetic dipole transition strengths B(M1) for the three bands in Fig. 1.

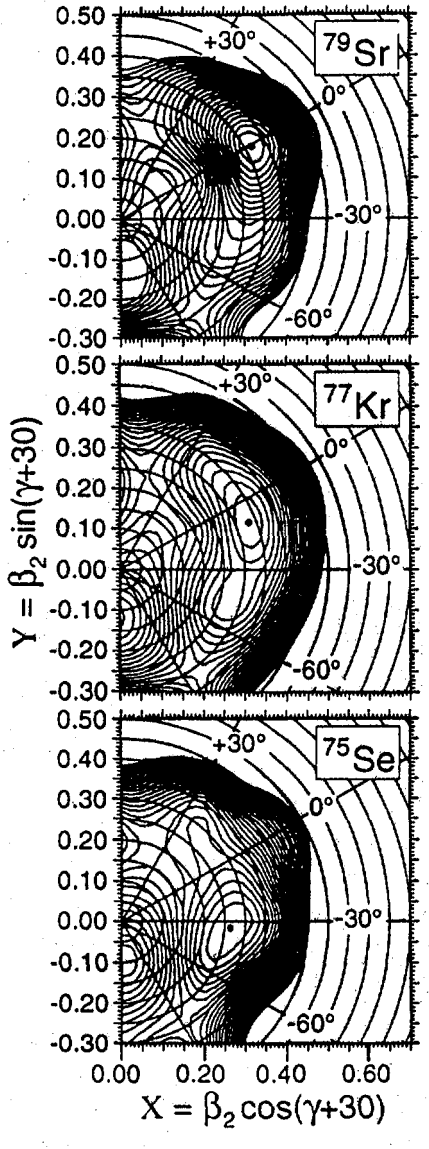

Fig. 3. Total Routhian surfaces (with pairing) in the (β_2,γ) plane for the lowest $\pi = +$ configurations in the indicated nuclei calculated for a rotational frequency ω of 0.3 MeV/$\hbar$. The distance between contour lines is 500 keV.

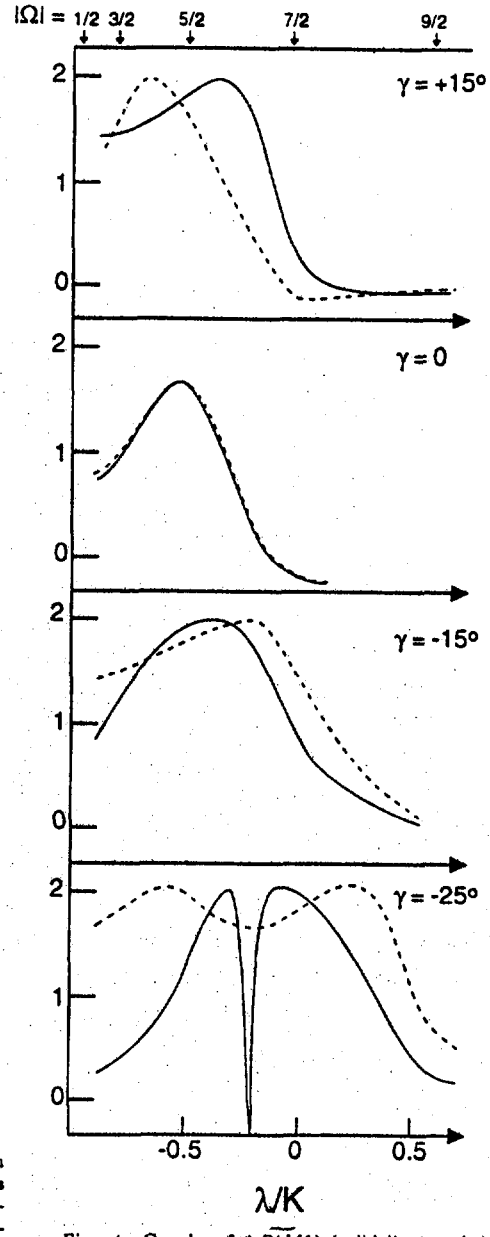

Fig. 4. Graphs of $\Delta\widetilde{B(M1)}$ (solid line) and $\Delta e'$ (dashed line) calculated in the particle-rotor model. The graphs are reproduced from Ref. 4.

Routhians for nuclei with an axially symmetric shape. Defining

$$\Delta\widetilde{B(M1)} \equiv \frac{\Delta B(M1)}{B(M1)_{av}}$$

and

$$\widetilde{\Delta e'} \equiv \frac{4(\Delta e')(\hbar\omega)}{(\Delta e')^2 + (\hbar\omega)^2}$$

they have shown that

$$\Delta\widetilde{B(M1)} = \widetilde{\Delta e'}$$

under these conditions. They have also used particle-rotor model calculations to explore the relation between these quantities for the more general case of triaxial shapes. Their results for several values of the γ parameter are reproduced in Fig. 4. These calculations are based on one quasiparticle in the j = 11/2 shell. When scaled for the present case of j = 9/2, the value of λ/κ for N = 41 is about 0.

The values of the quantities defined above are listed in Table 1 for the three N = 41 isotones and for ^{79}Kr (Ref. 5). Note that these reduced signature splittings in the Routhians and B(M1) values are determined from a sequence of two ΔI = 1 transitions starting from and ending on states of favored signature. In the table the sequence is labeled by the spin of the initial state. The rotational frequency is that corresponding to the ΔI = 2 transition which skips the intermediate state of unfavored signature, and the signature splitting is determined at this frequency by interpolating the Routhians for the unfavored signature. These quantities have been evaluated only below the first band crossing since the theoretical arguments apply only to 1 qp configurations. In fact, even the $17/2^+$ states may not be purely 1 qp, so more attention should be focused on the decay sequences starting from the $13/2^+$ states.

Table 1

Nucleus	I_{init}	$\hbar\omega$	$\widetilde{\Delta e'}$	$\Delta\widetilde{B(M1)}$
^{75}Se	$13/2^+$	0.387	1.96(2)	1.70(18)
^{75}Se	$17/2^+$	0.480	1.85(1)	1.58(13)
^{77}Kr	$13/2^+$	0.328	1.66(7)	0.61(43)
^{77}Kr	$17/2^+$	0.434	1.58(3)	1.09(23)
^{79}Sr	$13/2^+$	0.308	1.20(12)	0.74(35)
^{79}Kr	$13/2^+$	0.400	1.97(1)	1.56(20)
	$17/2^+$	0.504	1.94(1)	1.00(64)

Because the quantities $\widetilde{\Delta e'}$ and $\Delta\widetilde{B(M1)}$ for ^{75}Se are so similar and Hagemann and Hamamoto have shown them to be equal for axial deformation, there appears at first to be a conflict with the predicted maximum triaxial deformation of $\gamma \approx$ -30 °. However, an examination of Fig. 4 shows that for $\frac{\lambda}{\kappa} \approx$ 0 and for γ = 0 °, the calculated values for the two normalized signature splittings are close to 0 and far from the observed values of 1.7 - 2.0. In fact, the curves for γ = -25 ° are close to the experimental values at $\lambda/\kappa \approx 0$, in agreement with the predicted large triaxial deformation. There is similar qualitative agreement between the measured values for ^{77}Kr and the graphs calculated for $\gamma \approx$ -15 °. In the case of ^{79}Sr the experimental values would agree with a γ deformation of -5 to -10 ° better than the predicted 0 °.

In summary, there is a reasonable agreement between the degree of triaxiality predicted for ^{75}Se and ^{77}Kr and the measured normalized signature splittings $\widetilde{\Delta e'}$ and $\Delta\widetilde{B(M1)}$ when compared with the particle-rotor calculations. The measurements suggest somewhat more triaxiality than is predicted for ^{79}Sr.

2. Other odd-A nuclei

Schwengner *et al.*[5] have demonstrated a similar alternation in the M1 strengths in the $g_{9/2}$ band of ^{79}Kr. The band exhibits large signature splittings on the order of 0.5 MeV and B(M1) values which alternate by factors of 2 to 8. Unlike ^{77}Kr the M1 strengths increase but stop alternating in the 3 qp band. The values for $\widetilde{\Delta e'}$ and $\Delta\widetilde{B(M1)}$ are also listed in Table 1. The shape is predicted to be nearly oblate ($\gamma \approx$ -50 °, so none of the previously calculated curves in Fig. 4 would apply to this case. However, the authors used the semiclassical model of Dönau[6] to calculate B(M1) values and obtained good agreement with the measured ones, assuming the predicted nearly oblate shape.

Another Kr isotope may also show alternating B(M1) strengths, but the evidence is less certain. The branching ratios measured in two recent experiments[7,8] suggest an alternating pattern for ^{75}Kr, while the branching and mixing ratios measured by another group[9] do not.

It is difficult to find other clear cases of alternating M1s in odd A nuclei. All of the ones discussed in these two sections have an even Z and odd N.

3. Odd-odd nuclei

There are a number of odd-odd nuclei which exhibit interesting patterns in the signature splittings of both the Routhians and M1 strengths. The bromine isotopes ^{74}Br (Ref. 10) and ^{76}Br (Refs. 11 and 12)

provide good examples. Both splittings can be seen in Fig. 5 for the $k^{\pi} = 4^{+}$ $\pi g_{9/2}$ x $\nu g_{9/2}$ yrast bands. An alternating pattern in the adjacent energy spacings plotted in the lower part of the figure indicates signature splitting in the energies or Routhians. While most odd A nuclei exhibit alternations with a constant phase, there is an abrupt phase reversal in the alternations in these odd-odd Br isotopes. Kreiner and Mariscotti[13] predicted this signature inversion on the basis of two-particle-plus-rotor model calculations where it is attributed to alignment of the two quasiparticles. A clear alternating pattern can also be seen in the B(M1) values, although only 3 points are known for ^{76}Br. Unlike the case of the energies, there appears to be no phase change in the alternations of the M1 values. Perhaps this reflects the greater sensitivity of energies to small components in the wave functions.

The behavior of the yrast band of ^{78}Rb is quite similar[14], as can be seen in Fig. 6. The parity of this band has not been determined. Its yrast nature and its similarity to the Br bands discussed above strongly suggest a $\pi g_{9/2}$ x $\nu g_{9/2}$ configuration with $\pi = +$. The Routhians for the two signatures in the lower part of the figure cross indicating an inversion of the signature splitting. In this case no lifetimes are known, but the branching ratios in the upper part of the figure imply an alternating pattern of M1 strength, assuming a smooth variation of the E2 strengths.

Although odd-odd nuclei have not been studied as well, it seems likely that others will also show alternating B(M1) patterns, since a good fraction of those which are known exhibit the behavior. It may be possible with the proper particle-rotor calculations to determine the γ deformation as well as the residual p-n interaction from the signature splitting in the Routhians and magnetic dipole strengths.

4. Even-even nuclei

Although a lack of signature partners reduces the chances of investigating M1 strengths in even-even nuclei, one interesting example has been reported[15] in a 4 qp band in $^{86}Zr_{46}$. Significant signature splitting is seen in the energies of the two signature partners and the B(M1) strengths exhibit a strong alternating pattern with maximum values approaching one W.u. Because of the proximity of the N = 50 shell closure and B(E2) strengths which do not exceed 20 W.u., the authors analyzed the structure in terms of a version of the interacting boson model (IBM-1) which allows the breaking of bosons to form noncollective fermion pairs. They were able to reproduce the pattern of electromagnetic transition strengths rather well. In

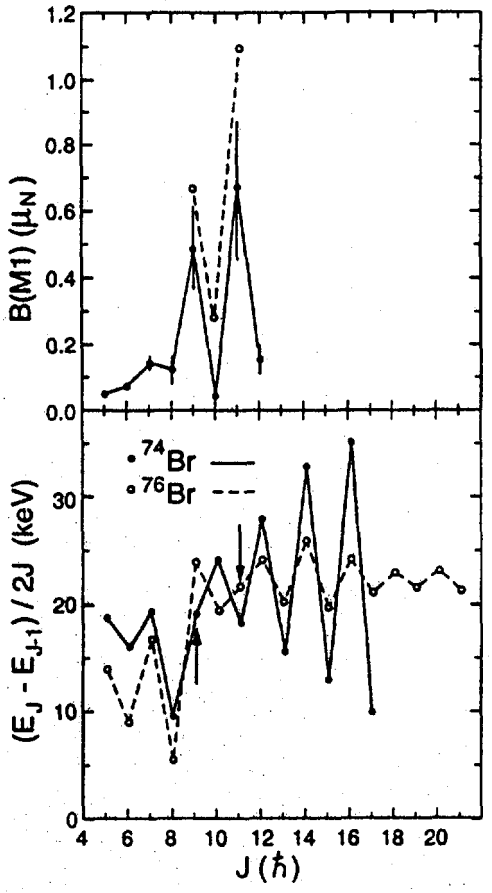

Fig. 5. Graphs of magnetic dipole transition strengths B(M1) and adjacent energy differences for the yrast bands of two odd-odd Br isotopes. The arrows in the lower graph indicate where phase reversals in the signature splittings occur.

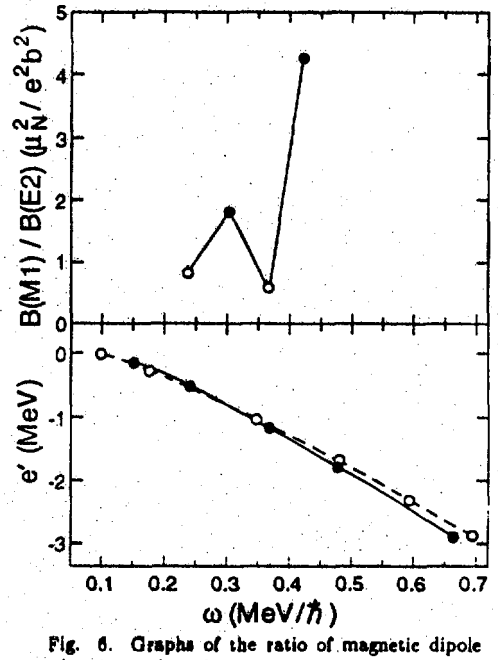

Fig. 6. Graphs of the ratio of magnetic dipole to electric quadrupole transition strength (top) and Routhians (e') for the yrast bands of ^{78}Rb.

this model the alternating M1 strengths arise because the doublets of states with spin (15^+,16^+), (17^+,18^+) and (19^+,20^+) have, in leading order, the same boson structure. M1 transitions are strong within the doublets and vanish to leading order between the doublets.

5. Summary

In a number of *f-p-g* shell nuclei, the magnetic dipole transitions between signature partner states exhibit an alternating behavior. The B(M1) values are stronger for transitions from states of favored signature than those from unfavored signature. In the N = 41 isotones a comparison between the signature splitting in the Routhians and the B(M1) values, in conjunction with particle-rotor model calculations, provides information about the changing γ deformation or triaxiality. In ^{79}Kr such a comparison interpreted in terms of a semiclassical calculation of the B(M1) strengths helped to confirm a predicted near-oblate shape.

Several odd-odd nuclei, including ^{74}Br, ^{76}Br and ^{78}Rb, exhibit alternating M1 strengths, as well as an inversion of the signature splitting in the Routhians. It remains to be seen whether these will also provide information about the triaxiality. The nucleus ^{86}Zr shows that the phenomenon can also be seen in even-even nuclei, where it has been explained in terms of the IBM.

In all these cases, one or more $g_{9/2}$ quasiparticles are involved in the structure. It is not clear whether this is somewhat of a necessary condition for M1 alternations, or whether the high-spin character of the unique parity orbital just makes such bands easier to observe.

It is certainly possible to account for the alternations within existing models. In the particle-rotor and semiclassical models they are related to signature splitting and γ deformation, while in the IBM they arise from similarities and differences in the boson structure of the states. In view of the unity of the empirical observations, one wonders whether there is an underlying unity in the theoretical explanations. *I.e.*, whether the underlying physics is really different, or whether a similar underlying physics is merely described in different languages in the different models.

Acknowledgment

This work was supported in part by the U.S. National Science Foundation.

References

† also at Joint Institute for Heavy Ion Research, Holifield Heavy Ion Research Facility, Oak Ridge, TN 37831; permanent address: Institute of Theoretical Physics, University of Warsaw, ul. Hoza 69, 00-689 Warsaw, Poland.

1. T.D. Johnson, T. Glasmacher, J.W. Holcomb, P.C. Womble, S.L. Tabor and W. Nazarewicz, Phys. Rev. (in press).
2. T.D. Johnson, J.W. Holcomb, P.C. Womble, P.D. Cottle, S.L. Tabor, F.E. Durham, S.G. Buccino and M. Matsuzaki, Phys. Rev. C42, 2418 (1990).
3. J. Heese, K.P. Lieb, S. Ulbig, B. Wörmann, J. Billowes, A.A. Chishti, W. Gelletly, C.J. Lister and B.J. Varley, Phys. Rev. C41, 603 (1990).
4. G.B. Hagemann and I. Hamamoto, Phys. Rev. C40, 2862 (1989).
5. R. Schwengner, J. Döring, L. Funke, G. Winter, A. Johnson and W. Nazarewicz, Nucl. Phys. A509, 550 (1990).
6. F. Dönau, Nucl. Phys. A471, 469 (1987).
7. A.A. Chishti, W. Gelletly, C.J. Lister, J.H. McNeill, B.J. Varley, D.J.G. Love, and O. Skeppstedt, Nucl. Phys. A501, 568 (1989).
8. D.F. Winchell, M.S. Kaplan, J.X. Saladin, H. Takai, J.J. Kolata and J. Dudek, Phys. Rev. C40, 2672 (1989).
9. S. Skoda, J.L. Wood, J. Eberth, J. Busch, M. Liebchen, T. Mylaeus, N. Schmal, R. Sefzig, W. Teichert and M. Wiosna, Z. Phys. A336, 391 (1990).
10. J.W. Holcomb, T.D. Johnson, P.C. Womble, P.D. Cottle, S.L. Tabor, F.E. Durham and S.G. Buccino, Phys. Rev. C43, 470 (1991).
11. S.G. Buccino, F.E. Durham, J.W. Holcomb, T.D. Johnson, P.D. Cottle and S.L. Tabor, Phys. Rev. C41, 2056 (1990).
12. D.F. Winchell, J.X. Saladin, M.S. Kaplan and H. Takai, Phys. Rev. C41, 1264 (1990).
13. A.J. Kreiner and M.A.J. Mariscotti, Phys. Rev. Lett. 43, 1150 (1979).
14. G.C. Hicks, C.J. Gross, U.J. Hüttmeier, Xi-Ting Lu, G. Neuschaefer and S.L. Tabor, Phys. Rev. C30, 549 (1984).
15. P. Chowdhury, C.J. Lister, D. Vretenar, Ch. Winter, V.P. Janzen, H.R. Andrews, D.J. Blumenthal, B. Crowell, T. Drake, P.J. Ennis, A. Galindo-Uribarri, D. Horn, J.K. Johansson, A. Omar, S. Pilotte, D. Prévost, D. Radford, J.C. Waddington and D. Ward, Phys. Rev. Lett. 67, 2950 (1991).

LOW–ENERGY E1 TRANSITIONS AND OCTUPOLE SOFTNESS IN ODD–A DEFORMED NUCLEI

G.B. Hagemann*, I. Hamamoto†, J. Kownacki‡ and W. Satuła†§

In recent yrast spectroscopy relatively strong E1 transitions are often observed in odd-A rare-earth nuclei. The observation of E1 transitions in competition with collective rotational (stretched) E2 transitions with the present day experimental techniques means, that the E1 strengths have to be of the order of (or larger then) $10^{-4}e^2fm^2$. Moreover, the angular momentum dependence of those observed E1 transition strengths do not follow the Alaga rule.

It is known that the low-lying E1 transitions are strongly hindred. The mechanism of hindrance is schematically presented in fig. 1. There are three main reduction factors: **(i)** Small E1 effective charge given by the equation[1)] in the left upper corner of fig. 1. It includes two effects: **a)** The exclusion of the isoscalar part of E1 transition operator which is equivalent to the excitation of the center-of-mass motion. **b)** The shift of major part of the E1 strength of low-energy transitions to the region of higher energy due to repulsive character of the isospin dependent part of the nuclear residual interaction (giant dipole resonance polarizability $\chi \approx -0.7$). **(ii)** Strong hindrance due to shell-structure. The calculated single particle matrix elements of the rY_{10} and $rY_{1\pm1}$ operators for the single-particle energy difference $\Delta\varepsilon_{sp} \leq$2MeV in the modified oscillator potential (A=170, ε=0.25) are usually less than 0.1fm, see two figures in the middle part of fig. 1 . **(iii)** Reduction due to residual pairing interaction. See left lower corner of fig. 1, where the calculated pairing factors for transitions without changing the number of quasiparticels are presented for selected nuclei. The effects described above reduce consecutively the upper limit of the B(E1) values in the following way: **(i)** $\Rightarrow 4\times10^{-2}e^2fm^2 \rightarrow$ **(ii)** $\Rightarrow 10^{-4}e^2fm^2 \rightarrow$ **(iii)** $\Rightarrow 10^{-5}e^2fm^2$, see fig. 1. Usually, the calculated B(E1) values are much smaller than $10^{-5}e^2fm^2$.

The rotational perturbation the of wave function may induce a drastic change in the angular momentum dependence of the B(E1) values. It is, however, not possible that the rotational perturbation will increase the B(E1) values to the order of $10^{-4}e^2fm^2$. To illustrate this effect we present the results of calculations for ^{169}Lu, see fig. 2. Using the model of one-quasiparticle coupled to a rotor with reasonable values of the Coriolis reduction factor, quadrupole deformation and pair-correlation parameter, first, we try to reproduce satisfactorily the observed level scheme in the angular momentum region before the lowest band crossing. Then, using the resulting wave

*The Niels Bohr Institute,University of Copenhagen,Denmark
†Department of Mathematical Physics, University of Lund, Sweden
‡Institute of Experimental Physics, Warsaw University, Poland
§Institute of Theoretical Physics, Warsaw University, Poland

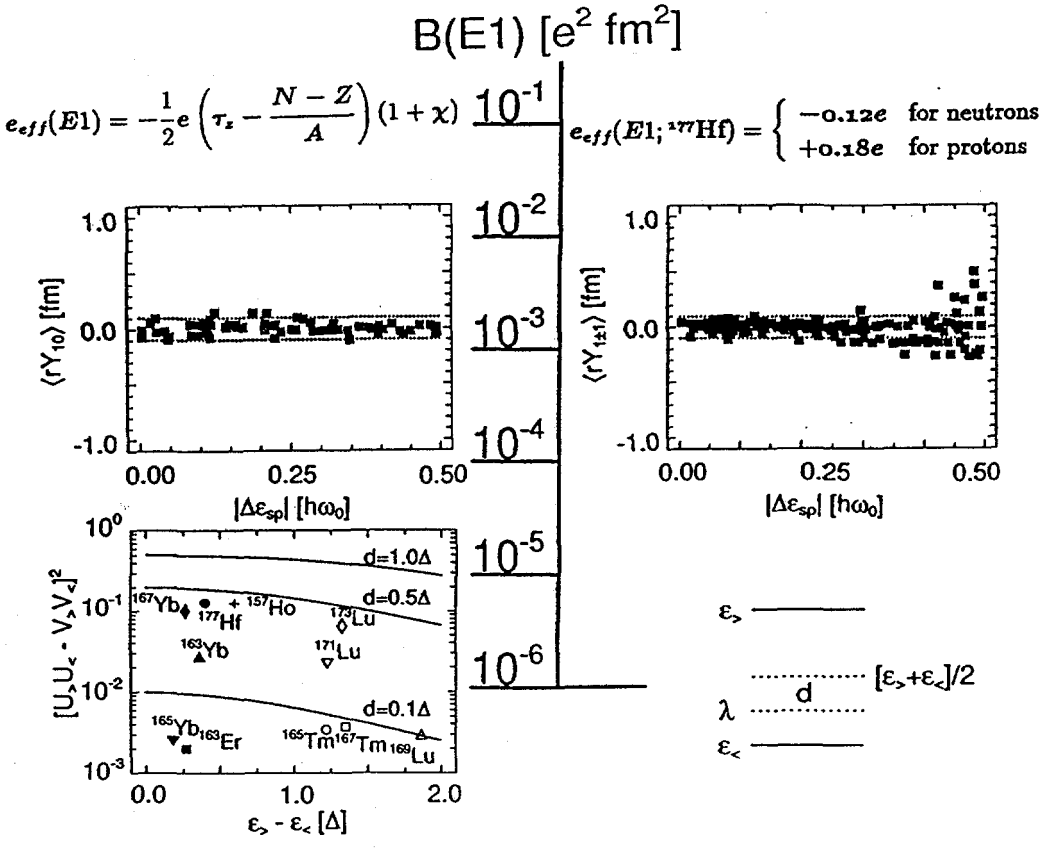

Fig. 1. Schematic illustration of hindrance mechanisms for E1 transitions. The details are described in the text.

functions, we calculate B(E1) values. The values obtained by using $e_{eff}(E1) = 0.2e$ are plotted in fig. 2. As is seen from the figure, the resulting B(E1)$\leq 10^{-5}e^2fm^2$ i.e. they are much smaller than the experimental values, see fig. 3 for comparison.

Thus, following the model in ref.[3] we analyze available data by introducing the parameters b_ν, which effectively take into account the contribution from octupole softness to the E1 transition strength. The first order perturbation treatment of the particle-octupole-vibration coupling leads to an effective E1 transition operator:

$$\mathcal{O}(E1,\nu) = e_{eff}(E1) r Y_{1\nu} + e b_\nu r^3 Y_{3\nu} \tag{1}$$

where

$$e b_\nu = \sum_{i,\tau} \chi_3(\tau) \left(\frac{-2}{\hbar\omega_i}\right) \langle i,\tau | r^3 Y^*_{3\nu} | 0\rangle \langle 0 | \mathcal{O}(E1,\nu) | i,\tau\rangle, \quad \chi_3(\tau) = \kappa_0 + \tau\kappa_1 \tag{2}$$

Here, $|i\rangle$ denotes all possible $K^\pi=0^-$ (or 1^-) RPA excitation modes, $\tau = \pm 1$ for like (unlike) particles and $\kappa_0(\kappa_1)$ denotes the isoscalar (isovector) coupling constant for the bare octupole-octupole interaction.

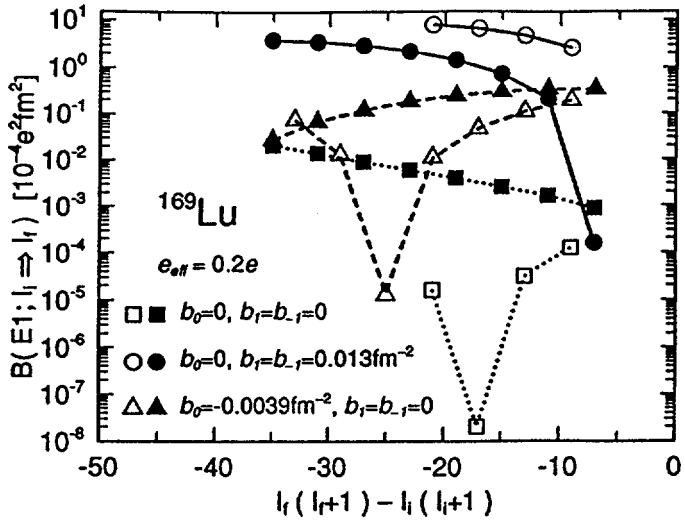

Fig. 2. Calculated values of B(E1) transitions from the [411 1/2] to the [541 1/2] band in ^{169}Lu. Dotted lines represent the results without octupole phonon polarization. The remaining curves exemplify the I dependence of B(E1) values coming from calculations including either only b_0 or only b_1 octupole phonon polarization effects.

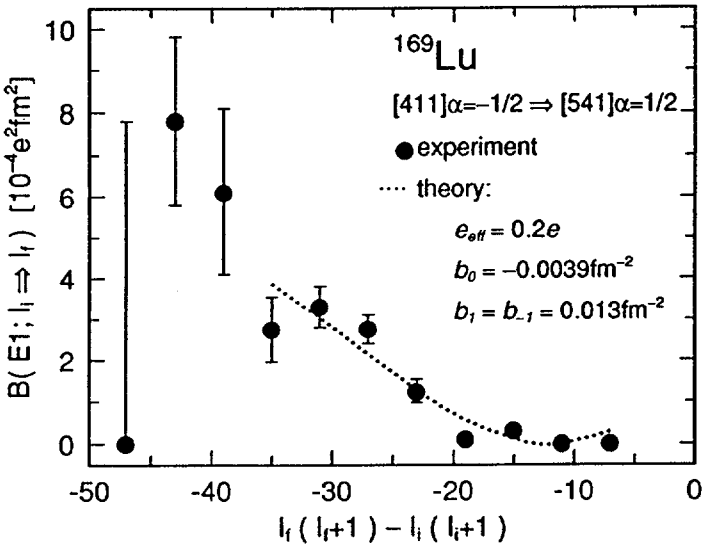

Fig. 3. Experimental values[2] of B(E1) for transitions in ^{169}Lu. The B(E1) values were obtained from E2/E1 branching ratio measurement, assuming $Q_t^2 = 50b^2$. The dotted line represents a theoretical fit to the experimental data (below the first band crossing i.e. below I=35/2) obtained in the present model including the effects of octupole phonon polarization (see text for details).

First, we determine the values of b_0 and b_1 which are needed to reproduce the observed B(E1) values. An example of such calculations is presented in fig. 3. For comparison, in fig. 2 we show B(E1) values calculated by introducing either only b_0

or only b_1. Note, that these two curves show different spin dependence. Thus, we can uniquely determine the parameters b_0 and b_1 for this nucleus.

In table 1 the values of b_ν parameters, which are needed to reproduce available B(E1) values measured in several nuclei, are given. We observe that: **a)** The b_0 values and/or b_1 values needed are of the order of 10^{-2}fm^{-2}. **b)** The b_ν values depend on the nucleus and are sensitive to a particular pair of involved bands.

Nucleus	$[Nn_z\Lambda\,\Omega]^{(i)} \rightarrow [Nn_z\Lambda\,\Omega]^{(f)}$	e_{eff}	b_0 [fm^{-2}]	b_1 [fm^{-2}]
$^{165}_{69}\text{Tm}_{96}$	[411 1/2]→[541 1/2]	0.2e	−0.0054	0.018
$^{169}_{71}\text{Lu}_{98}$	[411 1/2]→[541 1/2]	0.2e	−0.0039	0.013
	[514 9/2]→[404 7/2]	0.2e	0.01	0.01
$^{177}_{72}\text{Hf}_{105}$	[624 9/2]→[514 7/2]	−0.15e	0.0102	0.0006

Table 1. Examples of b_0 and b_1 parameters needed to reproduce the experimental data.

Next, we try to investigate whether the magnitudes of the obtained b_ν parameters can be reasonably understood in terms of a microscopic model. In the estimate of the expression (2) the RPA modes have to be free from the excitation of the "spurious" center-of-mass motion and contain the isoscalar as well as the isovector octupole correlation. Moreover, noting that the effective charge has a different sign for protons and neutrons, the final b_ν value is a result of the subtle cancellation between a relatively large contribution from protons and that from neutrons. Considering the accuracy of the possible theoretical estimate available at present we feel that presumably nobody can estimate the absolute magnitudes of b_ν values in quite a reliable way. Therefore, in the following we try to estimate the difference of b_ν values for the two sets of E1 transitions between the two pairs of bands in the same nucleus ^{169}Lu, see table 1. The difference comes from the blocking effect due to the presence of the odd quasiparticle. The blocking effect depend on the orbitals involved in the E1 transitions and it may be estimated in a relatively reliable way.

First of all, as is illustrated in fig. 4, we replace the RPA excitation modes "i" in eq. (2), which are expressed by wavy lines in fig. 4, by $\Delta N = 1$ 2qp excitations "j", which are represented by bubbles. Correspondingly, the bare octupole-octupole interaction should be replaced by a renormalized one. It is expressed by double-lines in fig. 4. Thus the RPA excitation modes in eq. (2) are now replaced by 2qp excitations, while the polarizability χ (see the expression in fig. 1) is set to zero.

In fig. 5 we show the calculated contributions (besides the renormalized coupling constant) to the expressions for the b_ν parameters. We note that all lower-lying 2qp excitations have a definite sign and that only a few 2qp states (with specific asymptotic quantum numbers) contriubute appreciably. Moreover, the contributions from protons and neutrons cancel each other. The detailed analysis of the contributions in terms of both asymptotic quantum numbers of one-particle orbitals and

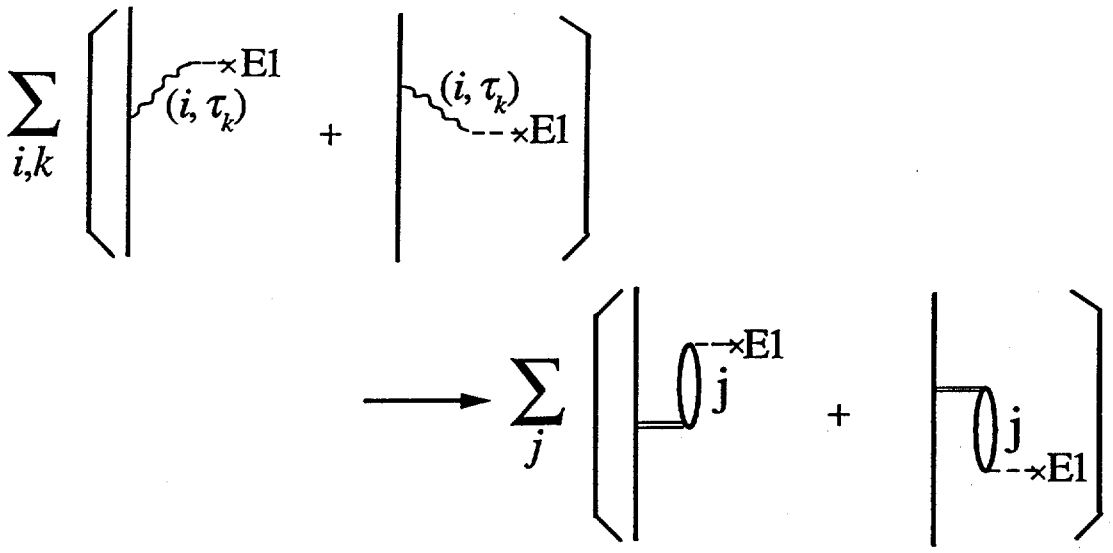

Fig. 4. Illustration of the renormalization of octupole-octupole interaction strength coming from the replacement of summation over octupole RPA modes in eq.(2) by summation over $\Delta N = 1$ 2qp excitations.

excitation energies will be presented in a forthcoming article[4]. In the r.h.s. part (i.e. for protons) of fig. 5 we show the contributions from a pair of blocked configurations, [411 1/2] and [541 1/2]. The blocking effect leads to the appreciable reduction of the final b_0 value in this case. In contrast, the blocking effect coming from the configurations, [514 9/2] and [404 7/2], turns out to be negligibly small.

Now, assuming that the difference in the b_ν values (δb_ν) calculated for two sets of observed E1 transitions in ^{169}Lu comes from the difference in blocking effects, we try to give the theoretical evaluation of δb_ν. In the calculations we use the model discussed in fig. 4, thus the bare strengths of the isoscalar (κ_0) and the isovector (κ_1) octupole-octupole interaction[1] should be renormalized due to $\Delta N = 3$ octupole excitations. Following the renormalization procedure given in ref.[1] we obtain: $\tilde{\kappa}_0 \approx 3 \times (-1.6 \times 10^{-5})$MeV fm^{-6} and $\tilde{\kappa}_1 \approx 0.2 \times (+7.9 \times 10^{-5})$MeV fm^{-6}, for the isoscalar and the isovector renormalized strengths for A=170, respectively. Using these values, we get:

$$\delta b_0^{theo} \approx -0.0013\text{fm}^{-2} \quad \text{and} \quad \delta b_1^{theo} \approx 0.0000\text{fm}^{-2} \tag{3}$$

for the theoretical estimates. These values should be compared with the δb_ν estimates obtained from the analysis of experimental data (see table 1):

$$\delta b_0^{exp} \approx -0.014\text{fm}^{-2} \quad \text{and} \quad \delta b_1^{exp} \approx 0.003\text{fm}^{-2} \tag{4}$$

From the comparison of the results given by eqs. (3) and (4) we see that the signs of δb_0^{theo} and δb_0^{exp} are the same as well as $|\delta b_0^{theo}| \gg |\delta b_1^{theo}|$ and $|\delta b_0^{exp}| \gg |\delta b_1^{exp}|$.

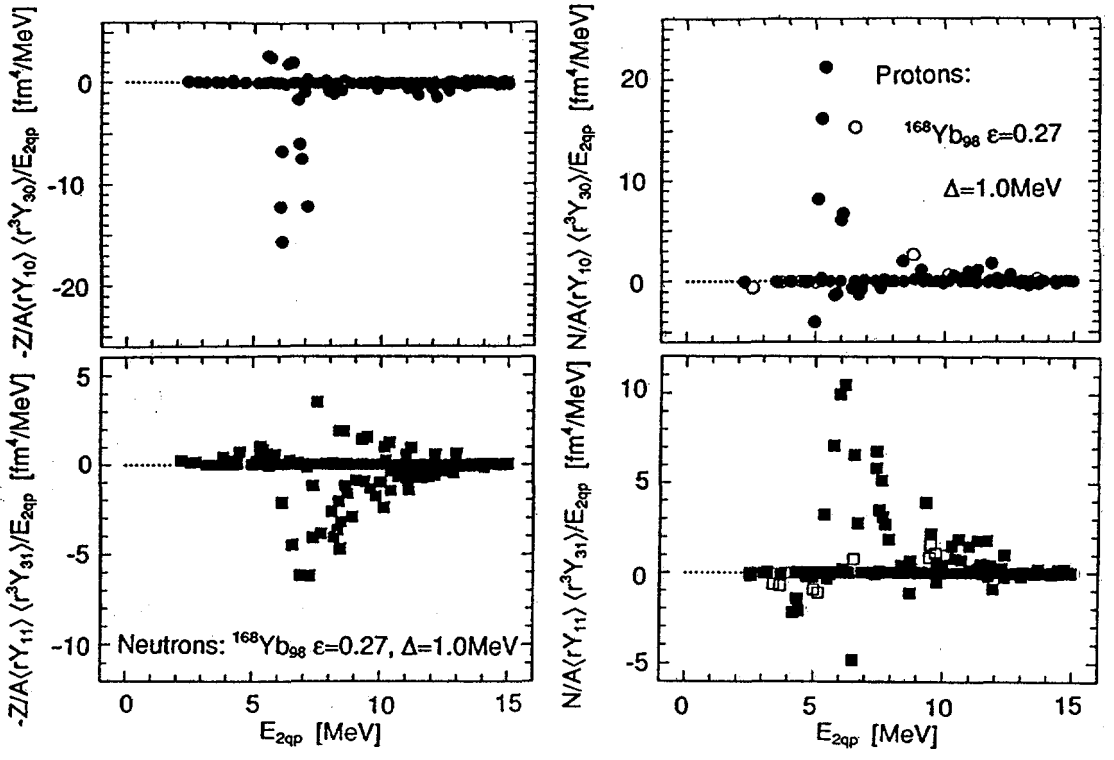

Fig. 5. Contributions to calculated b_ν values for ^{169}Lu (see eq. (2) and the discussion in the text concerning the method we use to estimate b_ν). Open symbols represent blocked orbitals for [411 1/2] and [541 1/2] configurations (see text for details).

However, the estimated magnitude of δb_0^{theo} is an order of magnitude smaller than δb_0^{exp}. Taking into account various ambiguities involved in the present theoretical analysis (such as ambiguities coming from our particle-rotor calculations as well as the assumed values of quadrupole moments to obtain B(E1) values from E2/E1 branching ratios, experimental uncertainties in measurements, and an approximations involved in the theoretical estimation procedure expressed in fig. 4), we might expect that the absolute magnitudes of δb_0^{theo} could have an ambiguity of a factor 2. However, the factor 10, which we have obtained in the comparison of δb_0^{theo} to δb_0^{exp}, seems to be a bit surprising and is presently difficult to understand.

References

[1] A.Bohr and B.R.Mottelson, Nuclear Structure, vol.2 (Benjamin, New York, 1975)

[2] S.Ogaza *et al.*, to be submitted to Nucl.Phys. A

[3] I. Hamamoto, J. Höller and X.Z. Zhang, Phys. Lett. **226B** (1989) 17

[4] G.B.Hagemann, I.Hamamoto and W.Satuła, to be published.

Intruder Bands in Odd-A $^{109-115}$Sb

V.P. Janzen,[a,b] H.R. Andrews,[a] T.E. Drake,[c] D.B. Fossan,[d] A. Galindo-Uribarri,[a] B. Haas,[a,e] A. Omar,[b] D.R. LaFosse,[d] J.R. Hughes,[d] S. Mullins,[b] E.S. Paul,[f] L. Persson,[b] S. Pilotte,[g] D. Prévost,[b] D.C. Radford,[a] J. Rodriguez,[b] M. Sawicki,[b] H. Schnare,[d] H. Timmers,[d] P. Unrau,[b] P. Vaska,[d] J.C. Waddington,[b] R. Wadsworth,[h] D. Ward,[a] J. Wilson,[f] R. Wyss[i] and G. Zwartz[c]

[a] *Chalk River Laboratories, AECL Research, Chalk River, ON K0J 1J0 Canada*
[b] *Department of Physics & Astronomy, McMaster University, Hamilton, ON L8S 4K1 Canada*
[c] *Department of Physics, University of Toronto, Toronto, ON M5S 1A7 Canada*
[d] *Department of Physics, State University of New York at Stony Brook, NY 11794 U.S.A.*
[e] *Permanent address: Centre de Recherches Nucléaires, F-67037 Strasbourg Cedex, France*
[f] *Oliver Lodge Laboratory, University of Liverpool, Liverpool L69 3BX U.K.*
[g] *Department of Physics, University of Ottawa, Ottawa, ON K1N 6N5 Canada*
[h] *Department of Physics, University of York, York Y01 5DD U.K.*
[i] *Joint Institute for Heavy Ion Research, Oak Ridge National Laboratory, Oak Ridge, TN 37831*

1. Introduction

The existence of rotational structures in nuclei bordering on the spherical $Z = 50$ closed shell has been known for some time (*eg.* [1]). Nevertheless, our understanding of collective effects in this region is remarkably incomplete; for example, before this work little high-spin data existed and there were no lifetime measurements to confirm the collectivity associated with the rotational bands observed in Sb ($Z = 51$) and Sn ($Z = 50$) nuclei. Furthermore, the role of the $h_{11/2}$ orbital was virtually unknown, although it has the highest angular momentum of the orbitals in this mass region and therefore is expected to have the most influence on the properties of high-spin states. In the $A \sim 130$ and $A \sim 180$ mass regions, where highly deformed intruder bands have been observed, it is the neutron $i_{13/2}$ and proton $i_{13/2}$ orbitals, respectively, which are preferentially lowered in energy by a combination of large deformation and fast rotation [2,3,4]. In lighter nuclei the $h_{11/2}$ orbital is expected to appear as an intruder configuration.

2. Experimental Results

We have populated high-spin states in odd-mass $^{109-115}$Sb nuclei using the reactions listed in Table I. Heavy-ion beams were provided by the Chalk River Tandem Accelerator Superconducting Cyclotron (TASCC) facility, and γ-γ coincidence data were acquired with the 8π spectrometer. Fig. 1 shows a γ-ray spectrum for the first excited $h_{11/2}$ intruder band found, in ^{113}Sb [5]. Analysis of the γ-ray centroid shifts from the backed-target data has yielded a quadrupole moment of $Q_0 \simeq 4.0$eb, which corresponds to an axial prolate deformation of $\beta_2 \simeq 0.3$. Subsequently similar bands were found in ^{109,111,115}Sb (present work) and ^{117,119}Sb (Stony Brook experiments [6]). For $Z = 51$ nuclei the rotational bands

Table 1: Reactions populating intruder bands in Sb (Z=51), Sn (Z=50) & In (Z=49) Isotopes.

Isotope	Reaction	E_{beam} (MeV)	Performed at	Type of Target
^{109}Sb	^{58}Ni(^{54}Fe,3p)	243	TASCC	Unbacked + Au-backed[1]
^{111}Sb	^{96}Ru(^{19}F,2p2n)	90	StonyBrook	Pb-backed[2]
	^{92}Mo(^{23}Na,2p2n)	120	TASCC	Unbacked
^{113}Sb	^{94}Mo(^{23}Na,2p2n)	117	TASCC	Unbacked + Au-backed[1]
^{114}Sb	^{96}Zr(^{23}Na,5n)	102	TASCC	Unbacked
^{115}Sb	^{96}Zr(^{23}Na,4n)	102	TASCC	Unbacked
	^{108}Pd(^{11}B,4n)	47	StonyBrook	Pb-backed[2]
^{106}Sn	^{58}Ni(^{54}Fe,α2p)	243	TASCC	Unbacked + Au-backed
^{108}Sn	^{58}Ni(^{54}Fe,4p)	243	TASCC	Unbacked + Au-backed[1]
^{111}In	^{96}Zr(^{19}F,4n)	85	TASCC	Unbacked

[1] Excited-state lifetimes measured using the Doppler Shift Attenuation Method.
[2] Provided high-resolution data on stopped transitions.

built upon the $h_{11/2}$ orbital appear to stabilize a well-deformed prolate shape up to high spin ($83/2\ \hbar$ in ^{111}Sb) and rotational frequency ($\hbar\omega \sim 1.4$ MeV in ^{109}Sb). This rotational frequency is the highest yet observed in heavy nuclei.

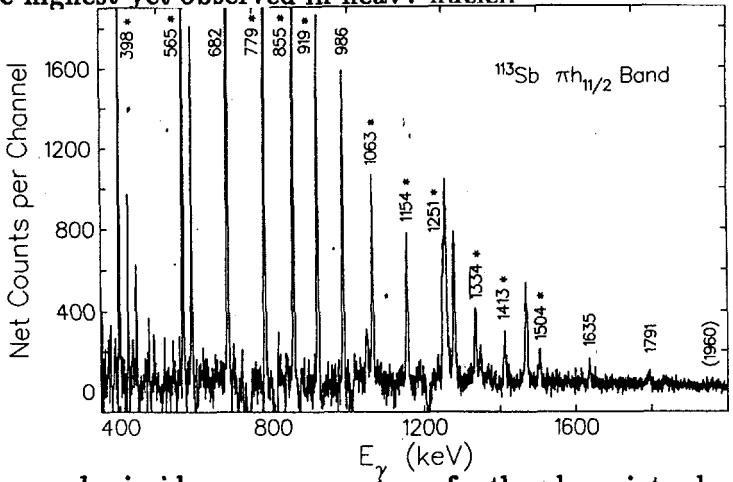

Fig. 1. Summed coincidence γ-ray spectrum for the $\pi h_{11/2}$ intruder band in ^{113}Sb.

Decoupled bands built on $K = 1/2$ positive-parity orbitals and on multi-quasiparticle states that involve the proton $h_{11/2}$ orbital have also been located in some of the odd-A Sb nuclei. Furthermore, decoupled bands have been populated in odd-odd ^{114}Sb and even-even ^{106,108}Sn (as byproducts), as well as ^{111}In. The In result is noteworthy since it represents the first observation of the $\pi h_{11/2}$ orbital in nuclei with $Z < 50$, *i.e.* below the $Z = 50$ "magic" shell gap.

As a result, we are presently able to identify 29 such intruder-type bands in the

$A \sim 110$ mass region. These are summarized in Fig. 2. The large number of observed bands is consistent with the view that the spherical-to-deformed transition is, for the most part, not caused by the occupation of one high-j orbital (*viz.* $\pi h_{11/2}$) but to the change in the Sn-like core from a spherical to a deformed 2-particle-2-hole (2p-2h) configuration.

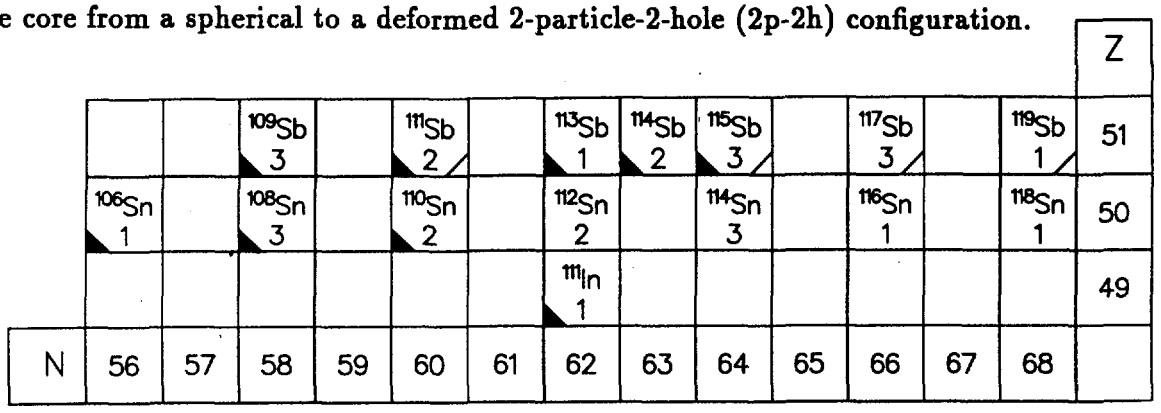

Fig. 2. Intruder-type rotational bands in the $A \sim 110$ mass region. Filled and open triangles denote experiments carried out at Chalk River and Stony Brook, respectively. The number of decoupled bands located in each nucleus is indicated.

3. Properties of the Sb $\pi h_{11/2}$ Intruder Bands

The $\pi h_{11/2}$ and $i_{13/2}$ intruder bands have certain experimental properties in common:

- The quadrupole deformations are much larger than those of low-spin states (*eg.* in the $A \sim 110$ region $\beta_2 \sim 0.3$ for the intruder-type states associated with the 2p-2h core, *vs.* $\beta_2 \leq 0.15$ for the normal states).
- They are excited configurations, brought down in energy at high spin by a combination of enhanced deformation and fast rotation.
- The observed frequencies and interaction strengths for band crossings associated with the rotational alignment of other high-j quasiparticles are much higher than expected (see below).

Some features observed in the $h_{11/2}$ intruder bands, however, are unique:

- The bandhead states lie relatively high in excitation energy ($E_x(11/2^-)$ = 2-to-4 MeV, as compared to $E_x(13/2^+) \sim 1$ MeV for the Re isotopes; the difference is related to the excitation energy of the deformed Sn 2p-2h core).
- Multiple rotational bands have been observed in the same nucleus (see Fig. 2).
- The γ-ray transitions between well-deformed and near-spherical states are observed, with the exception of ^{109}Sb.
- There is evidence for the influence of band-terminating states.
- Bands in the $N = 58$ isotones have constant relative alignment at high spin.
- At the highest spins one observes very low dynamical moments of inertia, corresponding to one-third to one-half the rigid-body values.

Here we briefly discuss two of these points: the anomalous characteristics of $\nu h_{11/2}$ band crossings in $\pi h_{11/2}$ intruder bands, and the alignment in ^{109}Sb bands relative to ^{108}Sn.

4. The Neutron $h_{11/2}$ Band Crossings

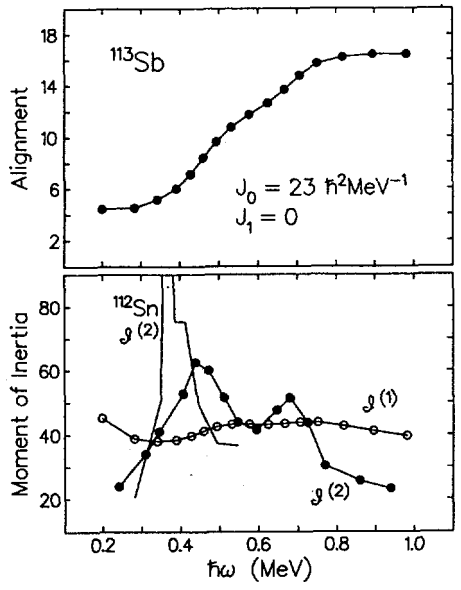

Fig. 3. (*a*) Quasiparticle aligned spin (i), and (*b*) kinematic ($\mathcal{J}^{(1)}$) and dynamic ($\mathcal{J}^{(2)}$) moments of inertia, for the $\pi h_{11/2}$ band in ^{113}Sb. Also shown is the $\mathcal{J}^{(2)}$ moment for the yrast rotational band in ^{112}Sn, which undergoes a sharp (*i.e.* weak-interaction) crossing at $\hbar\omega = 0.37$ MeV.

The characteristics of the $\nu h_{11/2}$ band crossings in the odd-A Sb nuclei are particularly intriguing. For example, the dynamic and kinematic moments of inertia for the $h_{11/2}$ band in ^{113}Sb are shown in Fig. 3. The two peaks in the $\mathcal{J}^{(2)}$ plot correspond to two distinct band crossings, at $\hbar\omega = 0.46$ and 0.69 MeV. Assuming a constant moment of inertia for the underlying core, and an interaction which is spin- and frequency-independent, we can obtain the interaction strength from the dynamic moment of inertia by

$$V_{int} = \frac{\Delta i^2/4}{\left(\mathcal{J}^{(2)}_{max} - \mathcal{J}^{(2)}_0\right)}, \qquad (1)$$

where $\mathcal{J}^{(2)}_0$ and $\mathcal{J}^{(2)}_{max}$ are the unperturbed and maximum value of the $\mathcal{J}^{(2)}$ moment of inertia, respectively, and Δi is the gain in alignment due to the crossing.[1]

Since the two band crossings in ^{113}Sb are observed in their entirety and since they lie far enough apart in frequency to be separated in the $\mathcal{J}^{(2)}$ plot it is reasonable to use Equation 1 to obtain a direct measure of the interaction strength, whereas this has not been possible in other nuclei. The resulting interaction strengths are 360 ± 60 keV and 210 ± 40 keV for the first and second crossing, respectively. There is reasonable agreement between cranked shell model predictions and experiment for the second crossing, which is associated with the rotational alignment of $\pi g_{7/2}$ quasiparticles. Regarding the first crossing, however, there is a very large discrepancy between the ^{113}Sb experimental result and the cranked shell model prediction of $|V_{int}| \simeq 80$ keV. In addition, the value extracted for the same crossing in the ^{112}Sn core nucleus is only $\simeq 20$ keV. The $\simeq 300$-keV interaction strength needed above and beyond the mean-field approach is similar to the values estimated for band crossings in $i_{13/2}$ intruder bands in heavier nuclei [11]. Further evidence of the influence of the $\pi h_{11/2}$

[1]Similar but incorrect expressions for V_{int} appear as Eq. 2 in Ref. [8] and Eq. 32 in Ref. [9]. We have used a derivation suggested by [10].

intruder orbital on the $\nu h_{11/2}$ crossing is revealed by the measured crossing frequency, which at $\hbar\omega = 0.46$ MeV is 0.09 MeV higher than in the even-even core nucleus ^{112}Sn (see Fig. 4). We propose that the band-crossing characteristics observed in ^{113}Sb are most likely related to a strong high-j neutron-proton interaction, since it is the presence of the *proton* $h_{11/2}$ intruder which affects the *neutron* $h_{11/2}$ crossing, and since the second crossing shows no such effect. The neutrons and protons occupy similar $h_{11/2}$ orbitals in the neutron-deficient Sb nuclei; $K = 3/2$-to-$5/2$ for the neutrons and $K = 1/2$ for the protons. In addition, both neutron and proton angular momenta are aligned along the axis of rotation at high spin. These conditions lead to a large overlap between neutron and proton wavefunctions, which leads in turn to a sizeable neutron-proton interaction. Measurements of the Sb band-crossing properties can thus probe those residual interactions which are neglected by standard mean-field theories.

A large interaction strength is also observed for the $\nu h_{11/2}$ crossing in ^{111}Sb. It is impossible, however, to measure interaction strengths for the remaining odd-A isotopes with the above method, since the $\nu h_{11/2}$ and $\pi g_{7/2}$ band crossings cannot be completely separated.

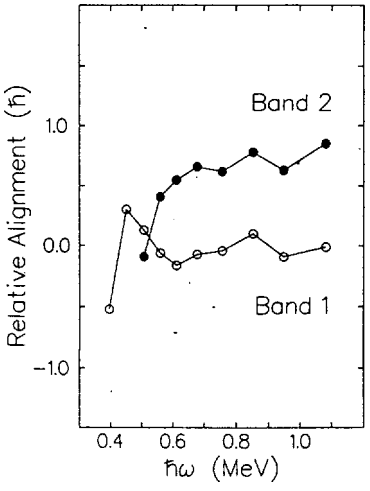

Fig. 4. Aligned spin for ^{109}Sb Bands 1 and 2 relative to Band 1 in the core nucleus, ^{108}Sn. The ^{109}Sb spins have been estimated; changing them by an integer amount will change the average aligned spin by the same amount, but will not alter the identical nature of the moments of inertia.

5. Relative Alignment for $N = 58$ Bands

As shown in Fig. 4, above a rotational frequency of $\hbar\omega \sim 0.5$ MeV ^{109}Sb Band 1 has a constant alignment of $i_{av} \sim 0$ relative to ^{108}Sn Band 1. Bands 1 in ^{109}Sb and ^{108}Sn are not "isospectral", that is they do not have identical γ-ray energies, but they do have identical moments of inertia. A similar analysis for ^{109}Sb Band 2 gives $i_{av} = 0.65\hbar$ over the same frequency range. These two cases are very good examples of non-superdeformed "identical" bands. It is interesting to note that they occur at high spin and very high rotational frequency, and are associated with the occupancy of low-K orbitals. These characteristics contrast with the majority of the "identical" bands found in the survey of Baktash *et al.* (contribution to these proceedings).

6. Summary

These experiments have revealed a large number of new intruder-type rotational bands, in a mass region which was largely unexplored at high spin before this work. The data analysis and interpretation are incomplete, but judging by these preliminary results, the spectroscopy of high-spin states in nuclei with $Z \simeq 50$ will prove extremely rewarding.

This work is supported by AECL Research, the Natural Sciences and Engineering Research Council of Canada, the U.K. Science and Engineering Research Council and NATO under grant # CRG.910192. The assistance of the staff of the TASCC facility is gratefully acknowledged.

References

[1] A.K. Gaigalas, R.E. Shroy, G. Schatz and D.B. Fossan, Phys. Rev. Lett. **35** 555 (1975); J. Bron, W.H.A. Hesselink, A. Van Poelgeest, J.J.A. Zalmstra, M.J. Uitzinger, H. Verheul, K. Heyde, M. Waroquier, H. Vincx and P. Van Isacker, Nucl. Phys. **A318**, 335 (1979).

[2] R. Wyss, J. Nyberg, A. Johnson, R. Bengtsson and W. Nazarewicz, Phys. Lett. **B215**, 211 (1988).

[3] E.S. Paul, R. Ma, C.W. Beausang, D.B. Fossan, W.F. Piel, Jr., S. Shi, N. Xu and J.-y. Zhang, Phys. Rev. Lett. **61**, 42 (1988).

[4] V.P. Janzen, *et al.*, Proc. of the Conf. on High-spin Nuclear Structure and Novel Shapes, Argonne National Laboratory, ANL-PHY-88-2, 216 (1988).

[5] V.P. Janzen, *et al.*, Contributions to the TASCC Workshop on Heavy-Ion Physics Research, Chalk River, 1990; V.P. Janzen, *et al.*, to be published.

[6] D. LaFosse, D.B. Fossan, J.R. Hughes, Y. Liang, P. Vaska, M.P. Waring and J.-y. Zhang, Vol. 1 of these proceedings, p. 8.

[7] R.E. Shroy, A.K. Gaigalas, G. Schatz and D.B. Fossan, Phys. Rev. **C19**, 1324 (1979).

[8] S. Åberg, Nucl. Phys. **A520**, 35c (1990).

[9] R. Bengtsson, S. Frauendorf and F.-R. May, Atomic Data and Nucl. Data Tables **35**, 15 (1986).

[10] W. Nazarewicz, private communication (1992).

[11] R.A. Wyss and A. Johnson, Proc. of the Int'l. Conf. on High Spin Physics and Gamma-Soft Nuclei, Pittsburgh/Carnegie-Mellon, ed. J.X. Saladin, R.A. Sorensen, C.M. Vincent, p. 123 (World Scientific, New Jersey, 1991).

TRACKING INTRUDER STATES

L.L. RIEDINGER, W.F. MUELLER, and C.-H. YU

Department of Physics, University of Tennessee, Knoxville, TN, 37996-1200, U.S.A.

Abstract

The deformation-driving effects of intruder states are studied by analysis of various types of data on rotational bands in rare-earth deformed nuclei. The sensitivity of four measurables (bandhead energy, $B(E2)$ value, neutron $i_{13/2}$ crossing frequency, and signature splitting) to increased deformation in an intruder band is shown. The analysis of signature splitting systematics is extended to known superdeformed bands.

1. Introduction

Single-particle states of large individual angular momenta, j, are surprisingly important in the properties of the nucleus as a whole. The promotion of single nucleons into such "intruder" states (the terminology that is appropriate when the high-j state lies significantly above the Fermi level) has a real effect on the nucleus in a number of observable ways. It is the purpose of this paper to summarize those examples of the influence of intruder states and to especially emphasize signature splitting, *i.e.* the energy shift between the two signatures of a high-j orbital. It is our thesis that this splitting or shift can be systematized and used as an indicator of the particular configuration in an odd-odd nucleus and furthermore as a measure of the shape influence of an intruder state present in the coupling. This analysis is done first for rotational bands of normal deformation and then applied to the more complex case of superdeformed bands. The natural paucity of specific information on observed superdeformed bands makes it very important to find ways to aid the classification of such structures.

In general there are four ways in which the shape-driving influence of a particular high-j intruder state can be observed when considering the "rare-earth" region of normal deformation: (1) lowered energy of bands built on intruder states due to the increased deformation, β_2; (2) increased $B(E2)$ values in such intruder bands; (3) shifts in the frequency of a "standard" band crossing (e.g. $i_{13/2}$ neutron alignment) due to the increased β_2 in the band; (4) changes in the $\nu i_{13/2}$ signature splitting in bands due to coupling with intruder proton orbitals. After demonstrating the signature-splitting systematics for this class of bands, we then use the observed shifts in the superdeformed $\pi i_{13/2}$ bands as a guide in understanding the physics of superdeformed bands in odd-odd Tl nuclei.

The discussion here is focused on the proton intruder states, $h_{9/2}$ and $i_{13/2}$, throughout the rare-earth region of normal deformation, and then on the $\pi i_{13/2}$ band as a "spectator" in superdeformed bands in Tl. The calculated single-proton level ordering is shown in Fig. 1. Note that the $K = 1/2$ $h_{9/2}$ level, 1/2[541], is clearly an intruder state (*i.e.* above the proton Fermi surface) for deformed (β_2 around 0.2) nuclei with $Z = 60$ (Nd) through 76 (Os), while the corresponding $i_{13/2}$ state retains its intruder status through Hg ($Z = 80$). However, at superdeformed shapes (β_2 around 0.5) there are four protons in the $i_{13/2}$ orbitals for Hg, which removes its status as an intruder orbital. For those cases, it is the $j_{15/2}$ neutron orbital that seems to have the largest shape-driving tendencies.

Some results discussed here are based on measurements led by our group: ^{179}Ir and ^{181}Ir [2,3], ^{175}Re

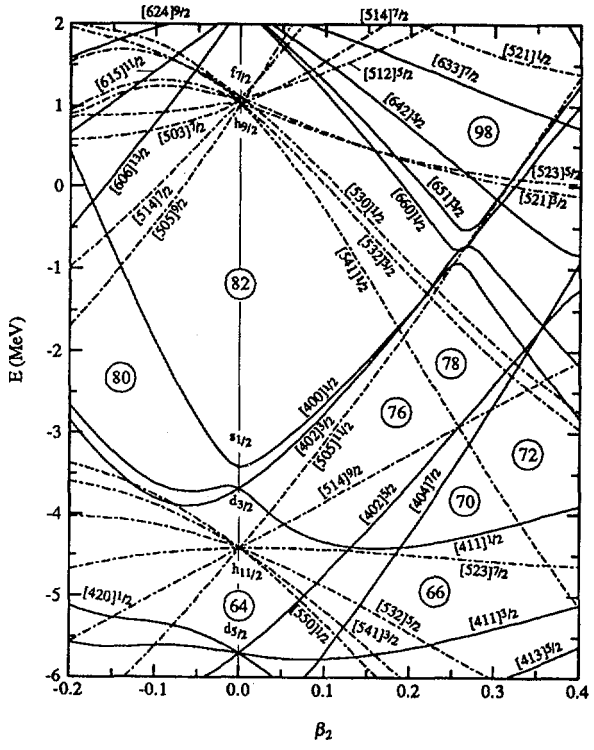

Fig. 1. Single-particle diagram for protons calculated by Wyss [1] using the Woods-Saxon potential. The calculation is done for β_4 and γ set equal to zero.

[4], ^{180}Ir [5], and ^{191}Tl [6].

2. Excitation Energies, Deformations, $B(E2)$ Values

The downsloping nature of the $\pi h_{9/2}$ and $\pi i_{13/2}$ orbitals in Fig. 1 should lead to a larger overall nuclear deformation if these are pure particle states (i.e. the Fermi surface is clearly below such orbitals). Indeed, Nazarewicz *et al.* [7] calculate that the deformation of the $\pi h_{9/2}$ bandhead in odd-A deformed nuclei throughout the rare-earth region is generally increased compared to the average of the ground-state values for the two adjacent even-even nuclei, e.g. a 20% increase for $^{165}_{71}Lu_{94}$. Such an increase in β_2 has the effect of lowering the expected energy of the single-particle excitation, to the point that it is easily observable in experiments on these nuclei, e.g. from around 1.2 MeV for the "normal" deformation in ^{165}Lu to half of that for the increased $\pi h_{9/2}$ deformation. The $\pi h_{9/2}$ band comes lower in energy as Z increases from 65 (Tb) to 73 (Ta), as the Fermi level of the nucleus increases closer to the $\pi h_{9/2}$ orbitals (see Fig. 1). An even more dramatic lowering in energy due to deformation occurs for the $\pi i_{13/2}$ excitation in this region, where the $\pi i_{13/2}$ band is observed regularly in isotopes of Re, Ir, and Au, even though it lies significantly above the $\pi h_{9/2}$ state in the single-particle scheme of Fig. 1.

While it is relatively easy to observe the bands built on proton intruder states throughout the rare-earth region, it is far more formidable to measure an increased deformation via a shorter state lifetime (increased $B(E2)$ value). Several measurements have been performed on $\pi h_{9/2}$ bands, e.g. that in ^{157}Ho by Gascon *et al.* [8]. Transition quadrupole moments, Q_t, were extracted in ^{157}Ho from lifetimes measured above $I = 37/2\ \hbar$ by the Doppler Shift Attenuation Method (DSAM) for states in both the $\pi h_{11/2}$ (7/2[523]) and $\pi h_{9/2}$ (1/2[541]) bands. Averaging over several states, Gascon *et al.* find that

Q_t is larger by $(28\ ^{+17}_{-15})\%$ in the latter compared to the former. This can translate to a similar β_2 difference, which compares favorably to the calculated ratio of 1.18 [7]. Thus, there is direct evidence for an increased deformation for the $\pi h_{9/2}$ intruder state. There is also evidence for an increased deformation for the $\pi i_{13/2}$ intruder state in Ir nuclei, e.g. in ^{179}Ir as measured by Jin *et al.* [2,3]. Lifetime results are compatible with the calculated deformations extracted from self-consistent Total Routhian Surface (TRS) calculations [1], $\beta_2 = 0.30$ for the $\pi i_{13/2}$ band compared to 0.24 for normal states in ^{179}Ir.

3. Delayed $\nu i_{13/2}$ Band Crossings

A band crossing due to the rotational alignment of a pair of quasiparticles can be described and systematized by three extracted quantities: the crossing frequency, $\hbar\omega_c$, the gain in quasiparticle alignment, i, in the crossing, and the interaction strength between the crossing bands. It is possible to use the $\nu i_{13/2}$ crossing frequency (the common first backbend throughout the rare-earth region) as a broad indicator of the deformation of the nucleus in a particular band. Compared to the smooth trend of measured $\nu i_{13/2}$ crossing frequencies in even-even nuclei (Dy through Pt), there is generally a delay in the $\nu i_{13/2}$ crossing frequency in $\pi h_{9/2}$ bands, e.g. in ^{157}Ho as discussed by Gascon *et al.* [8]. This delay is qualitatively correct, as the increased deformation measured in DSAM work (see the previous section) results in an increase in the crossing frequency according to Cranked Shell Model calculations. However, in ^{157}Ho the measured 28% or calculated 18% increase in β_2 is insufficient to raise the $\hbar\omega_c$ from the "normal" value of 0.30 MeV to the measured value of 0.35.

The delay in the $\nu i_{13/2}$ crossing frequency for $\pi h_{9/2}$ bands disappears in Ir nuclei [2,3,9]. This sudden change in behavior is clearly related to a Fermi level effect. As seen in Fig. 1, the valence proton for $Z = 77$ Ir occupies the 1/2[541] level, which therefore removes the intruder status of this $\pi h_{9/2}$ orbital. In such a situation this excitation is considered to be half particle and half hole, and the shape-driving tendency of the orbital is canceled. So, what was certainly a "good" intruder state in $Z = 65$ to 73 nuclei ceases to be such for Ir and above because of the increased Fermi level.

4. $\nu i_{13/2}$ Signature Splitting

Another measurable quantity related to the deformation of the nucleus is the signature splitting of the $\nu i_{13/2}$ band. The amount of signature splitting is deduced for such bands by plotting the energies in the rotating frame of the nucleus and extracting the difference in Routhian energies at a certain rotational frequency, $\hbar\omega = 0.2$ MeV. We have extracted these quantities, $\Delta e'$, from all known $\nu i_{13/2}$ bands in odd-A odd-N nuclei. The trend of signature splittings is quite smooth, being large low in the $\nu i_{13/2}$ shell ($N = 89$) and decreasing steadily as the neutron Fermi level increases through the $i_{13/2}$ shell. This trend is shown for the upper part of this region ($N = 99 - 107$) in Fig. 2.

Even for a given neutron number, there is a strong variation in the $\Delta e'$ value for different values of Z in Fig. 2. This results from the varying deformation, β_2, for these isotones. For example, TRS calculations [1] yield β_2 values of 0.282, 0.277, and 0.258 for the $Z = 70$, 72, and 74 $N = 99$ isotones, the larger deformation giving rise to the smaller splitting. This is an important point for addressing the deformation driving properties of intruder states. That is, the coupling of the $\pi h_{9/2}$ intruder orbital to the $\nu i_{13/2}$ structure forms a band (usually yrast) in odd-odd nuclei. If the intruder state changes the deformation of the nucleus, then the $\nu i_{13/2}$ signature splitting in the odd-odd nucleus should change compared to the adjacent odd-A nuclei, as is the case in Fig. 2. Note that the $\Delta e'$ value for the $\nu i_{13/2}\pi h_{9/2}$ band in ^{172}Ta is reduced from an expected value of 74 keV (that value on the $N = 99$ curve for $Z = 73$) to an actual value of 29 keV, which could suggest a 5% increase

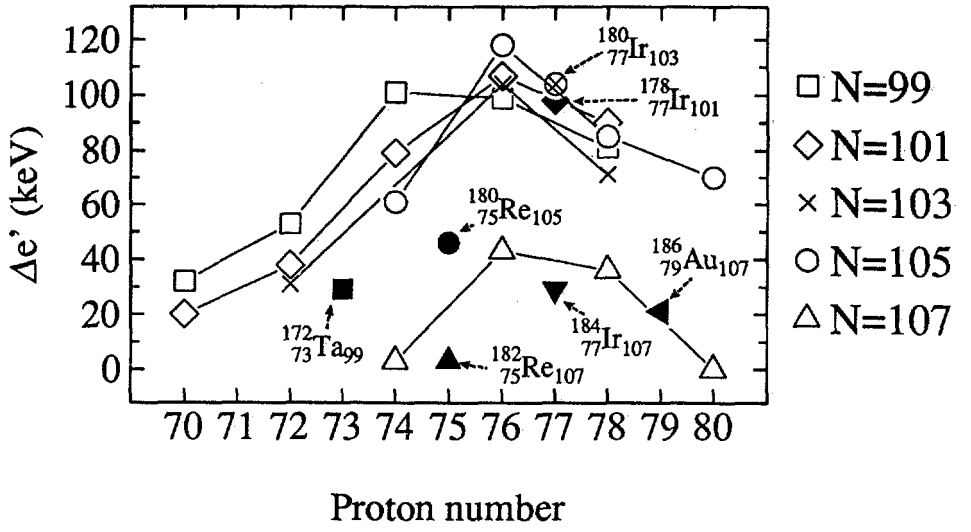

Fig. 2. Energy signature splittings, $\Delta e'$, for the $\nu i_{13/2}$ bands in odd-A odd-N nuclei and for the $\nu i_{13/2}\pi h_{9/2}$ bands in odd-odd nuclei. The values are extracted at $\hbar\omega = 0.20$ MeV from literature data on bands in these various odd-A nuclei, and from Kreiner *et al.* [10] for ^{172}Ta, Venkova *et al.* [11] for ^{180}Re, Slaughter *et al.* [12] for ^{182}Re, Yu *et al.* [5] for ^{178}Ir and ^{180}Ir, Kreiner *et al.* [13] for ^{182}Ir, and Kreiner *et al.* [14] for ^{184}Ir.

in β_2. Note also that the $\Delta e'$ decrease for odd-odd Re is still present (i.e. the $\pi h_{9/2}$ state is still a deformation-driving intruder orbital), but largely disappears for four known odd-odd Ir isotopes (two, ^{180}Ir and ^{178}Ir, from our measurements [5]). This correlates with the loss of intruder status by the $\pi h_{9/2}$ orbital, reflected also in the agreement in the $\nu i_{13/2}$ $\hbar\omega_c$ values in the $\pi h_{9/2}$ band of Ir nuclei, compared to the even-even cores. Thus, the measured $\Delta e'$ values in odd-odd nuclei do indeed reflect the change in shape induced by the coupling of the $\pi h_{9/2}$ intruder orbital to the $\nu i_{13/2}$ structure.

5. Energy Shifts in Superdeformed Bands

The superdeformed bands in the Hg region are generally thought to have a high-j composition of four protons in $i_{13/2}$ orbitals and two neutrons in $j_{15/2}$ levels (e.g. see [15]). It should be possible to do an analysis of signature splittings for the superdeformed bands now known in various isotopes of Hg and Tl in a manner similar to that described above. One difference is that the absolute energies of the levels are not known in the superdeformed cases. All one can measure at this time is the energies of the two sequences of $E2$ γ-ray energies, which are assumed to be related signatures of a strongly coupled superdeformed band. Until the next generation of 4π detectors is available, one can only make this association of γ-ray cascades into a strongly coupled band and hope that there are only a few confused cases. Since it is impossible to extract an actual signature splitting in these cases, we define instead an energy shift, ΔE, based on the average of two consecutive energies in one sequence to the comparable energy in the other signature:

$$\Delta E = E_\gamma(I \rightarrow I-2) - 1/2[E_\gamma(I+1 \rightarrow I-1) + E_\gamma(I-1 \rightarrow I-3)]$$

This quantity could be very different than the actual signature splitting, and thus one must be careful in the use of it. With this caution in mind, we attempt to systematize this quantity for the known superdeformed bands in Hg and Tl nuclei, as shown in Fig. 3.

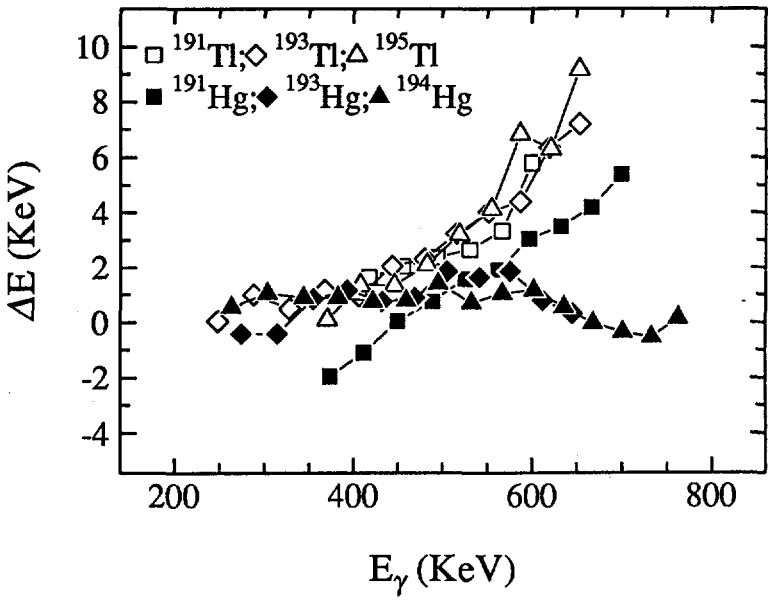

Fig. 3. Energy shifts, ΔE, for known superdeformed bands in Hg and Tl: ^{191}Tl [6], ^{193}Tl [16], ^{195}Tl [17], ^{191}Hg [18], ^{193}Hg [19], and ^{194}Hg [20].

Note first the essentially identical behavior for the superdeformed bands in the three odd-A Tl isotopes. In each case, these represent the two signatures of the $\pi i_{13/2}$ 5/2[642] band [6,16,17], and so the consistency is logical. For comparisons to the others, all three Tl isotopes show a ΔE of around 6 keV at a transition energy of 600 keV. By comparison, the three sets of bands in the Hg isotopes represent smaller energy shifts at 600 keV. The bands in ^{191}Hg are assigned [18] to the $\nu i_{11/2}$ 3/2[642] orbital, in ^{193}Hg to 9/2[642] $\nu i_{13/2}$ [19], and in ^{194}Hg likely to the coupling of this $\nu i_{13/2}$ orbital to neutron 5/2[512] ([20]). There is little signature splitting found in the calculations for any of these orbitals, and thus it is logical that the resulting ΔE values would be smaller than those in odd-A Tl.

The values of the energy shifts for ^{194}Tl are shown in Fig. 4, assuming the same association of energy cascades into bands as done by the original authors [21]. While none of the ΔE values is large, it is probably safe to conjecture that the pair with the largest values (called band 3 in Fig. 4) are associated with the odd-A structure with the largest shift, $\pi i_{13/2}$. The two signatures of this orbital are coupled to the only signature of the $\nu j_{15/2}$ orbital, 3/2[761], observed in ^{193}Hg [19]. The reduction of the ΔE for this ^{194}Tl band from 6 keV at 600 keV (the measured value for the $\pi i_{13/2}$ bands in odd-A Tl) to not more than half that could be due to a deformation increase caused by the intruder orbital, $\nu j_{15/2}$. As with the systematic shown for normal-deformed bands in Fig. 2, a deformation increase reduces the signature splitting of the "spectator" orbital. By comparison, the other two sets of bands in ^{194}Tl could be associated with one signature of $\pi i_{13/2}$ 5/2[642] coupled to the two signatures of the neutron 9/2[624] and 5/2[512] orbitals, since both of these have small ΔE in Hg nuclei (as discussed above).

This analysis of energy shifts between possible signature partners gives a suggestion of quasiparticle assignments that unfortunately cannot be checked currently by other means. The pattern of the moments of inertia is rather similar for the six observed cascades [21]. Eventually more measurements will give the details necessary to test the assignments suggested here.

The situation in ^{192}Tl is more complex. One association of the six newly observed bands produces three structures with energy shifts shown in Fig. 5. As discussed by Liang *et al.* [22], an analysis of

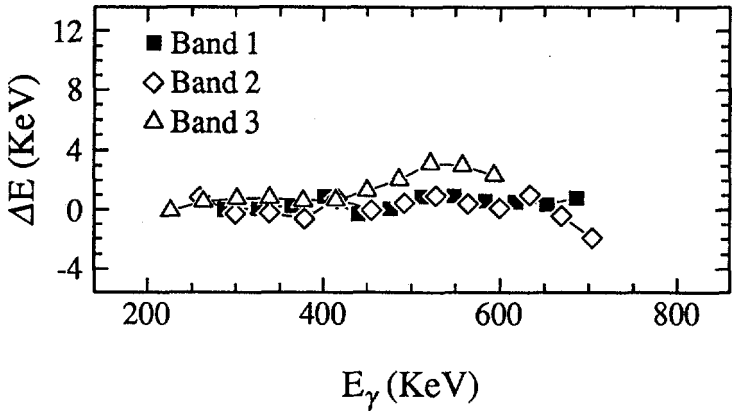

Fig. 4. Energy shifts, ΔE, for known superdeformed bands in ^{194}Tl [21].

the moments of inertia of the six cascades suggest the set labeled 2 in our Fig. 5 and called bands 3 and 4 there [22] should be assigned to $\nu j_{15/2}\pi i_{13/2}$ due to the unique flatness of the second moment as a function of frequency (double blocking of the expected crossing based on each of these orbitals). And this agrees with the trend discussed above, as the level of ΔE is reduced from the "expected" values for $\pi i_{13/2}$ (as in odd-A Tl) due to the deformation increase caused by the intruder orbital, $\nu j_{15/2}$.

The confusing aspects of ^{192}Tl correspond to the other structures labeled 1 and 3 in Fig. 5. Using 600 keV as the point of comparison, these two structures have ΔE values *larger* than any measured in adjacent odd-A nuclei. If one associates these two bands with the couplings of $\pi i_{13/2}$ 5/2[642] with $\nu i_{11/2}$ 3/2[642], then it is difficult to explain such significant changes from the smaller ΔE values observed for each in adjacent nuclei. This would suggest a *decrease* in the deformation of the nucleus to produce an *increase* in the energy shifts in odd-odd ^{192}Tl. That would be difficult to understand, but the association of the cascades into strongly coupled bands is probably too premature to allow one to make strong conclusions from this.

6. Conclusions

The role of intruder states in affecting the equilibrium deformation of nuclei is well known from a theoretical standpoint. The purpose of this work has been to demonstrate different ways in which the deformation changes might be observed, either by direct measurement (second effect discussed herein) or by deduction from measurements of three other quantities (bandhead energy, $\nu i_{13/2}$ crossing frequency, and $\nu i_{13/2}$ signature splitting). We have tried to show here that observing these effects and understanding their interpretation is important since these same fingerprints can be used to address the more complicated issues of superdeformed bands. Since it is even more difficult to measure the Q_t values for superdeformed bands than for bands of normal deformation, perhaps these indicators discussed here can be broadly used to give qualtitative measures of the configuration0dependent deformations, until more detailed spectroscopic information on families of superdeformed bands becomes available.

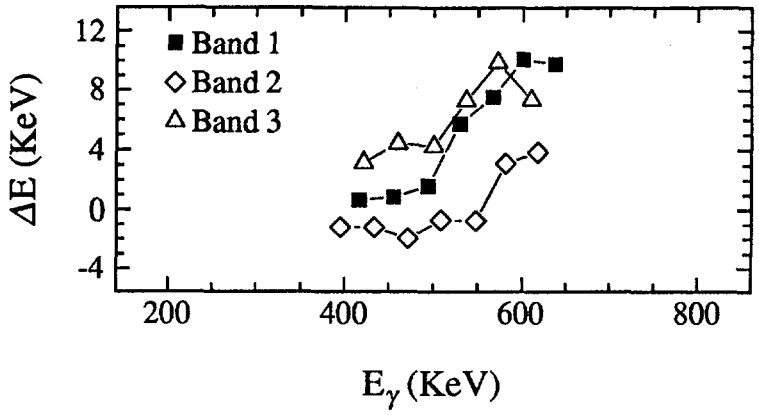

Fig. 5. Energy shifts, ΔE, for known superdeformed bands in ^{192}Tl [22].

Acknowledgements

The authors wish to thank Ramon Wyss for use of his TRS results, John Lewis for help in the preparation of this work, and Witek Nazarewicz and Jing-ye Zhang for their helpful discussions. This work has been supported by the U.S. Department of Energy under contract DE-FG05-87ER40361 with the University of Tennessee.

References

1. R. Wyss, private communication (1991).

2. H.Q. Jin, Ph.D. thesis, University of Tennessee (1991).

3. H.Q. Jin, L.L. Riedinger, C.-H. Yu, J.Y. Zhang, V.P. Janzen, C. Baktash, J.D. Garrett, N.R Johnson, I.Y. Lee and F.K. McGowan, to be published.

4. H.Q. Jin, L.L. Riedinger, C.-H. Yu, W. Nazarewicz, R. Wyss, J.Y. Zhang, C. Baktash, J.D. Garrett, N.R Johnson, I.Y. Lee and F.K. McGowan, Phys. Letters **B277**, 387 (1992).

5. C.H. Yu, H.Q. Jin, J.M. Lewis, L.L. Riedinger, L. Zhou, C. Baktash, J.D. Garrett, N.R. Johnson, I.Y. Lee, F.K. McGowan, J. McNeill, L. Chaturvedi, Y.R. Jiang, and H. Xie, to be published.

6. S. Pilotte, *et al.*, proceedings of this conference.

7. Nazarewicz, W., M.A. Riley, and J.D. Garrett, Nucl. Phys. **A512**, 61 (1990).

8. J. Gascon, C.-H. Yu, G.B. Hagemann, M.P. Carpenter, J.M. Espino, Y. Iwata, T. Komatsubara, J. Nyberg, S. Ogaza, G. Sletten, P.O. Tjøm, D.C. Radford, J. Simpson, A. Alderson, M.A. Bentley, P. Fallon, P.D. Forsyth, J.W. Roberts and J.F. Sharpey-Schafer, Nucl. Phys. **A513**, 344 (1990).

9. L.L. Riedinger, J. Avakian, H.Q. Jin, W.F. Mueller, and C.H. Yu, Proceedings of International School of Nuclear Physics, Erice, Italy, 1991.

10. A.J. Kreiner, D. Hojman, J. Davidson, M. Davidson, M. Debray, G. Falcone, C.W. Beausang, D.B. Fossan, R. Ma, E.S. Paul, S. Shi, and N. Xu, Phys. Letters **B215**, 629 (1988).

11. Ts. Venkova, R.M. Lieder, T. Morek, W. Gast, G. Hebbinghaus, A. Krämer-Flecken, J. Schäffler-Kräh, W. Urban, G. Sletten, H. Kluge, and K.H. Maier, Nucl. Phys. **A514**, 87 (1990).

12. M.F. Slaughter, R.A. Warner, T.L. Khoo, W.H. Kelly, and Wm. C. McHarris, Phys. Rev. **C29**, 114 (1984).

13. A.J. Kreiner, J. Davidson, M. Davidson, P. Thieberger, and E.K. Warburton, Phys. Rev. **C42**, 878 (1990).

14. A.J. Kreiner, J. Davidson, M. Davidson, P. Thieberger, E.K. Warburton, S. Andre, and J. Genevey, Nucl. Phys. **A489**, 525 (1988).

15. R.V.F. Janssens and T. L. Khoo, Ann. Rev. Nucl. Part. Sci. **41**, 321 (1991).

16. P.B. Fernandez, *et al.*, Z. Phys. **A517**, 386 (1990).

17. F. Azaiez, *et al.*, Phys. Rev. Lett. **66**, 1030 (1991).

18. E.F. Moore, *et al.*, Phys. Rev. Lett. **63**, 360 (1989).

19. D.M. Cullen, *et al.*, Phys. Rev. Lett. **65**, 1547 (1990).

20. M.A. Riley, *et al.*, Nucl. Phys. **A512**, 178 (1990); C.W. Beausang, *et al.*, Z. Phy. **A335**, 325 (1990).

21. F. Azaiez, *et al.*, Phys. Rev. Lett. **66**, 1030 (1991).

22. Y. Liang, *et al.*, proceedings of this conference.

WORKSHOP ON LARGE GAMMA-RAY DETECTOR ARRAYS

Chalk River

SESSION 1: STATES OF NEW INSTRUMENTS (I)

EUROGAM - A High Efficiency Escape Suppressed Spectrometer Array

P. J. NOLAN
Oliver Lodge Laboratory
University of Liverpool
Liverpool
L69 3BX

1. Introduction

EUROGAM is a UK-France collaboration to develop and build a high efficiency escape suppressed spectrometer array. The project has involved the development of both germanium (Ge) and bismuth germanate (BGO) detectors to produce crystals which are both bigger and have a more complex geometry. As a major investment for the future the collaboration has developed a new electronics and data acquisition system based on the VXI and VME standards. The array will start its experimental programme in mid 1992 at the Nuclear Structure Facility at Daresbury, U.K. At this stage it will have a total photopeak efficiency (for 1.33 MeV gamma-rays) of ~4.5%. This will give an improvement in sensitivity (relative to presently operating arrays) of a factor of about 10. When EUROGAM moves to France in mid 1993 its photopeak efficiency will have increased to about 8.5% which will result in an increase in sensitivity of a further factor of about 10. In this article I will concentrate on the array which will operate at Daresbury in 1992 and only briefly cover the developments which will take place for the full array before it is used in France in 1993.

2. Detector Developments

The detector module to be used in the first phase of EUROGAM is shown in Figure 1. It consists of a large n-type hyperpure Ge detector surrounded by a BGO escape suppression shield. The high resolution Ge detector is tapered over the front 30 mm of its length to allow for closer packing when in the array. The detectors to be used in EUROGAM typically have (for 1.33 MeV gamma-rays) a resolution of 2.1 keV and a relative efficiency of 75%. The BGO detectors are divided into 10 optically isolated elements, each with a photomultiplier readout. The complex shape of the detectors can be seen in the diagram shown in Figure 2. The individual BGO elements have resolutions (for 662 keV gamma-rays) of 18 - 22% when the source is placed in the germanium detector position. For its initial operation EUROGAM will consist of 45 of the detector modules shown in Figure 1.

A new four element detector is being developed for the second phase of EUROGAM. The detector shape is shown schematically in Figure 3. The improved granularity of this detector will help reduce Doppler broadening, especially when it is positioned at 90° to the beam direction. The properties and status of this detector are discussed in more detail in the contribution of Duchêne[1] (also in this proceedings).

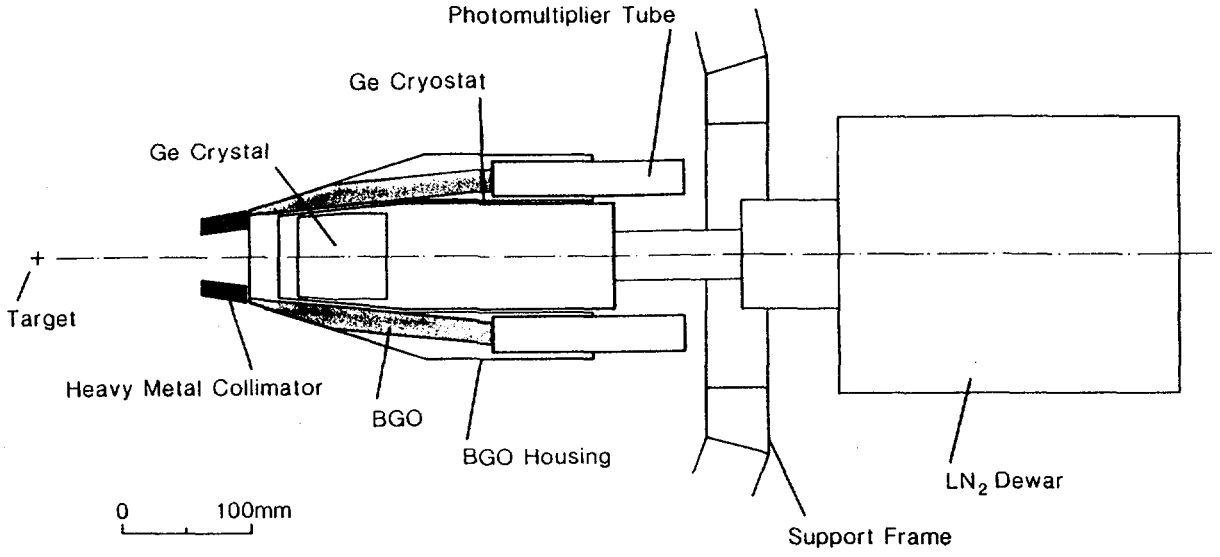

Figure 1 The escape suppressed spectrometer to be use in the first phase of EUROGAM.

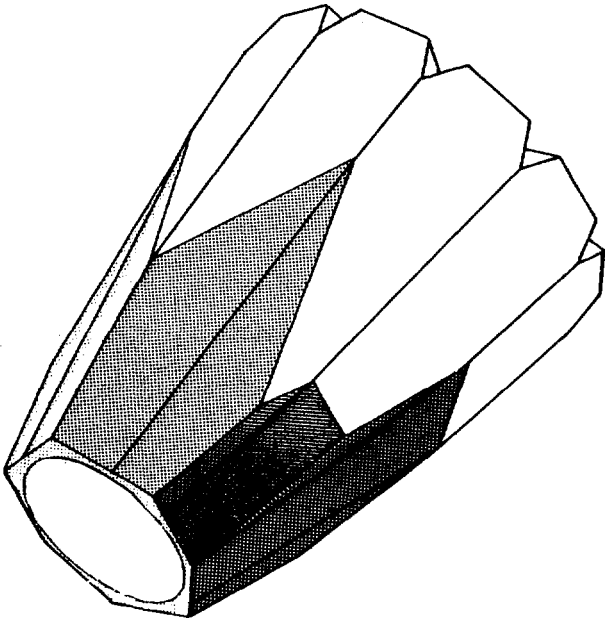

Figure 2 Schematic drawing of the BGO shield to be used in EUGOGAM. It consists of 10 optically isolated elements.

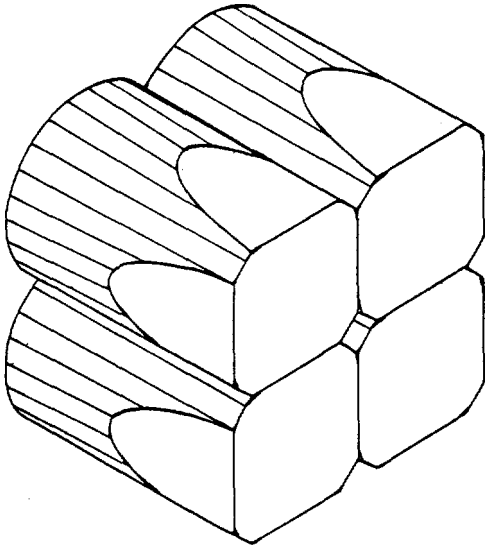

Figure 3 The four element clover detector being developed for EUROGAM phase 2.

3. Measurements on the Prototype Detectors

An extensive set of measurements has been carried out both with sources and in-beam for a 'mini' array of five escape suppressed spectrometers. These were all of the type shown in Figure 1. The results of these tests have been published[2] and will be discussed briefly here.

The design of an escape suppressed array has to incorporate many features. These include a high photo-peak detection efficiency, a good response function and a low cost. Achieving these aims means that many items need to be considered. It is the optimisation of all of these that leads to a successful design. In the test measurements a number of these items have been measured. These include the effects of isolated hit probability, reduced efficiency due to neutrons and random vetoes from the suppressors, peak to total and Doppler broadening. All except the latter will be discussed in the next paragraphs. The Doppler broadening measurements are discussed by Duchêne[1].

A schematic diagram showing the arrangement of the detectors for the tests is shown in Figure 4. The peak to total for ^{60}Co measured for shield A is 55 - 59% (depending on the Ge detector used) when only its surrounding shield is used as a suppressor (individual suppression). In shared suppression mode (using also the surrounding shields as indicated) this value increased to 63 - 65%. Two shared suppression modes were tried. In the first (mode 1) no account was taken of whether germanium detectors B - G also fired. In the second (mode 2) the event was not rejected if a second germanium fired. No major difference was found in the peak to total for the two modes. For ^{137}Cs typical peak to total values are 70% (individual suppression) and 73% (shared suppression).

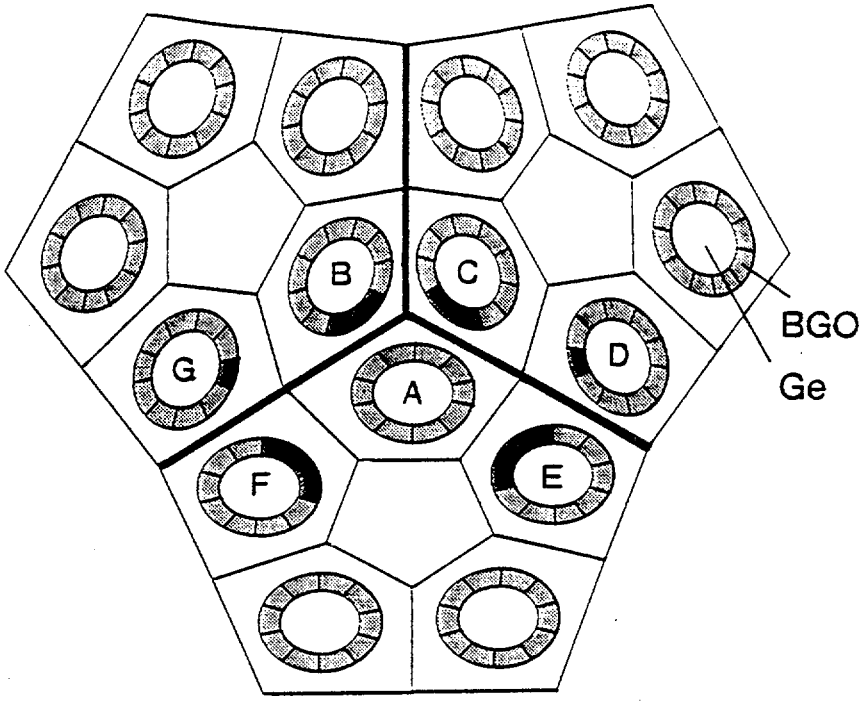

Figure 4 Schematic diagram of the detector arrangement for the test experiments

The amount of data lost was also measured. This is the intensity of a photopeak when a suppressed spectrum was compared to an unsuppressed spectrum. The data were taken following the $^{100}Mo + ^{32}S$ reaction at a beam energy of 132 MeV where the gamma-ray multiplicity is expected to be ~15. The data are shown in Figure 5. There are two causes of losses in this case. The first is due to bad vetoes from the suppressors due to scattered gamma-rays. This should depend on gamma-ray multiplicity. The second is bad vetoes due to neutrons hitting the suppressors. This will depend on the neutron multiplicity. The data confirm that at forward angles the loss rate is higher due to the forward peaking of neutrons in this reaction.

The effect of gamma-ray multiplicity can be measured with sources. Full details of the method are given by Beausang et al[2]. The results are shown in Figure 6. These data show that for multiplicity 30 (1.33 MeV gamma-rays) the loss rate is between 10% and 23% depending on the suppression mode used. The expected losses for multiplicity 15 are 5%, 8% and 12% for individual, shared suppression 2 and shared suppression 1 respectively. These are in good agreement with the measured in beam loss rates (at background angles) of 5%, 8% and 10% respectively for the three modes. The additional loss rates at forward angles are due to the effect of neutrons.

An additional loss of photopeak events arises from the isolated hit probability. That is the effects of more than one gamma-ray hitting a particular detector. This effect was again measured by sources [2], the results being shown in Figure 7. There is an additional 12% loss in the photopeak intensity for multiplicity 30.

The combination of peak to total and loss rates needs to be considered for individual experiments before deciding on the best mode of operation.

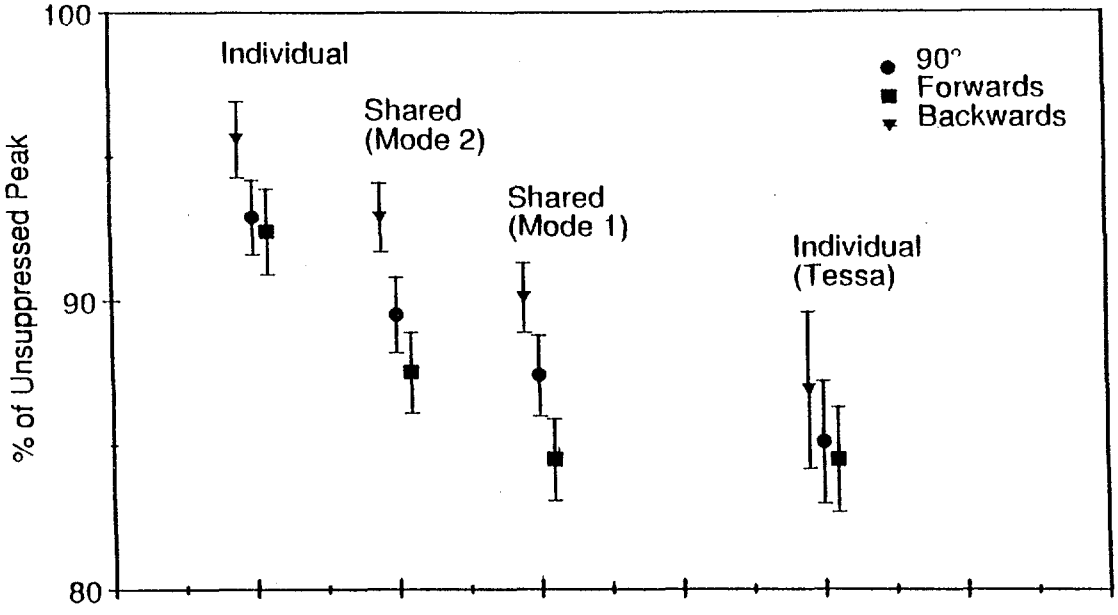

Figure 5 Comparison between suppressed and unsuppressed spectra to determine loss rates due to suppression. The terms are defined in the text. The forward angle used was 72°, the backward angle used was 158°.

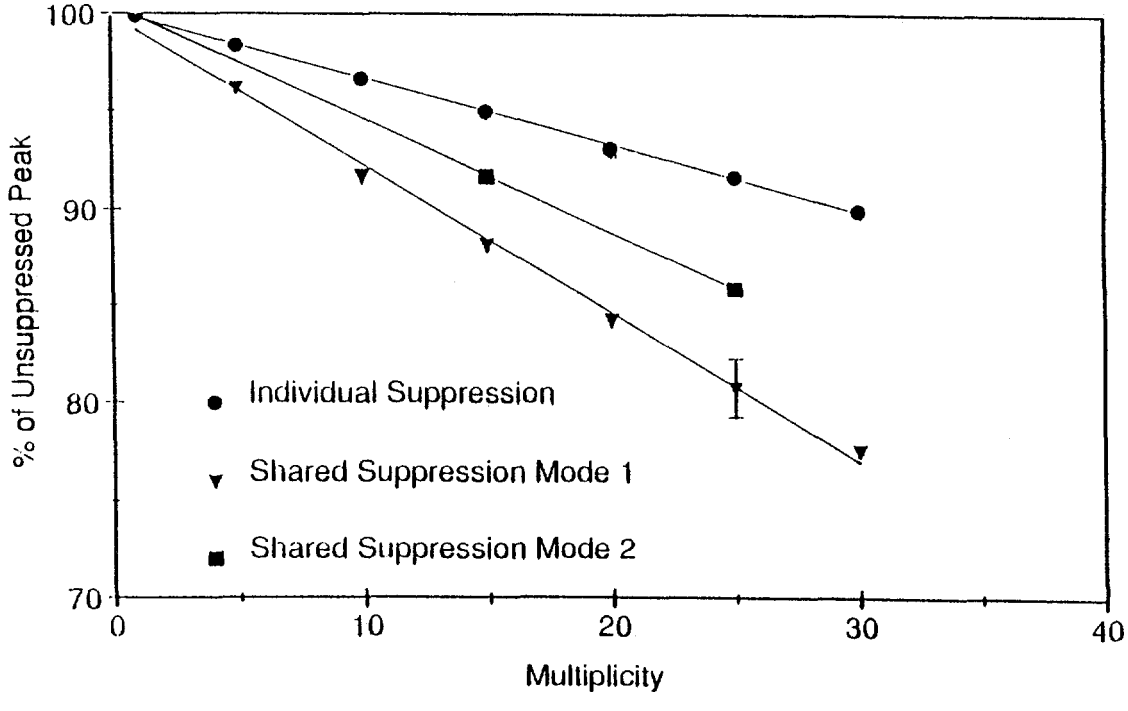

Figure 6 Percentage of unsuppressed peak area remaining in various suppressed spectra as a function of gamma ray multiplicity. A ^{60}Co source was used.

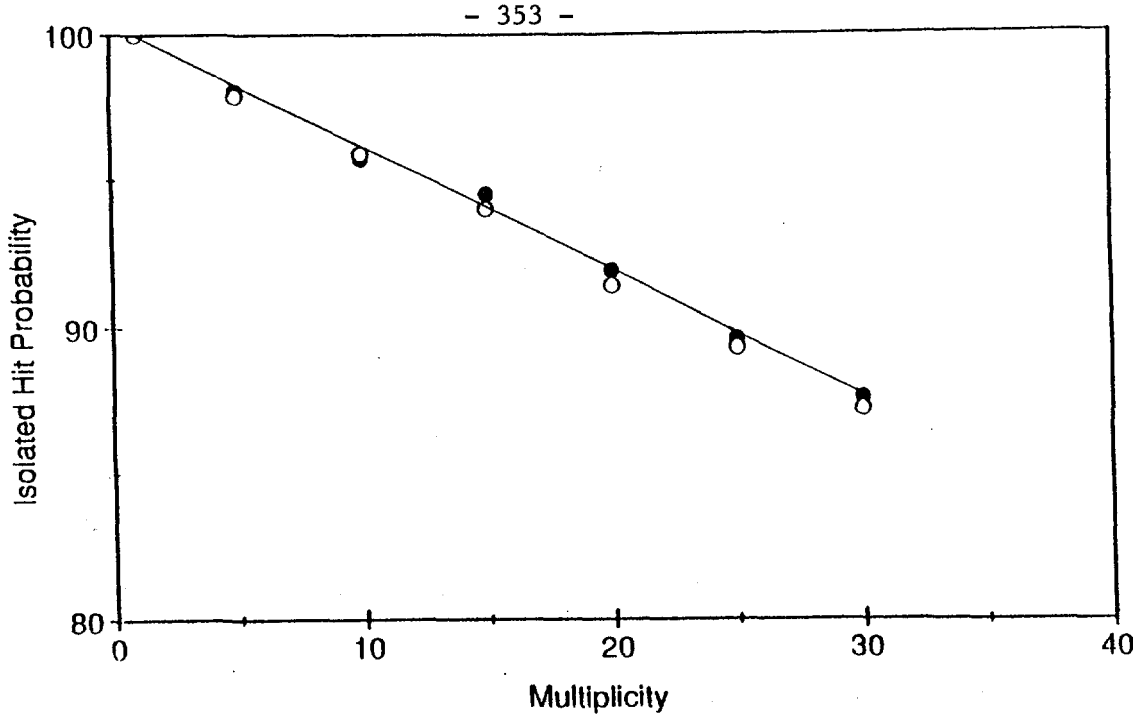

Figure 7 Isolated hit probability measured (see text) as a function of gamma ray multiplicity for ^{60}Co (1.33MeV) and ^{207}Bi (0.57MeV).

4. System Commissioning Tests

A series of in-beam commissioning tests were carried out using 25 - 30 escape suppressed detectors with conventional NIM electronics. One of these will be reported briefly here, others are discussed by Duchêne[1] and Hannachi [3].

The superdeformed band [4] in ^{132}Ce was populated using the ^{100}Mo (^{36}S,4n) ^{132}Ce reaction at a beam energy of 150 MeV. For this experiment 27 EUROGAM detectors were used at the following angles: 7 @ 134°, 12 @ 108°/72°, 8 @ 94°/86° (note the other angles available in EUROGAM are 158°/22° and 46°).

The measured experimental rates are given in Tables 1 and 2 for a target thickness of 0.5 mg cm^{-2} and a beam current of 2 pnA.

Table 1 **Measured Detector Rates**

Angle	Ge		BGO
(Deg)	Unsuppressed (kHz)	Suppressed (kHz)	(kHz)
134	2.7	1.4	0.28
108	2.8	1.5	0.34
94	2.7	1.3	0.33
86	2.5	1.2	0.39
72	2.5	1.2	0.44

Table 2 **Measured and Predicted Coincidence Rates**

Fold	Measured* (27 Ge) (kHz)	Predicted** (45 Ge) (kHz)
≥2	7.2	59
≥3	2.3	29
≥4	0.55	11
≥5	0.10	3
≥6		0.7

* beam 2pnA

** beam 8pnA giving a singles unsuppressed Ge rate of ~10 kHz

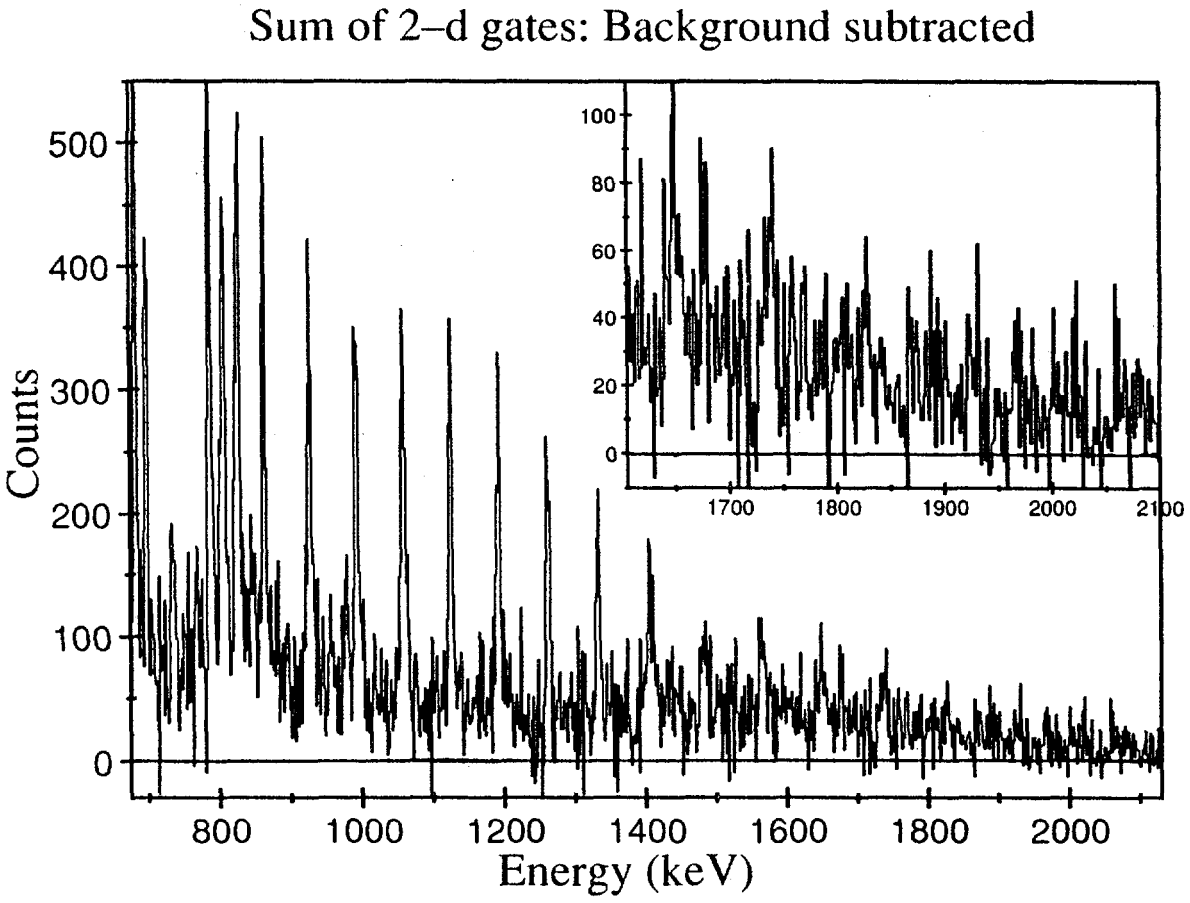

Figure 8 Spectrum (derived from triples data) of the superdeformed band in ^{132}Ce in coincidence with 13 pairs of gates on transitions in the superdeformed band.

The higher fold coincidence events can be unfolded to give many doubles, triples etc. The predicted figures given on Table 2 result in the following unfolded rates: triples 86 kHz, Quadruples 32 kHz, quintuples 9 kHz etc. In about 100 hours of beam time the data set available will be ~ 3 x 10^{10} triples and ~ 1.1 x 10^{10} quadruples.

The ^{132}Ce superdeformed band spectrum obtained in this experiment is shown in Figure 8. All the previously seen transitions are in the spectrum with approximately

the same peak to background. EUROGAM data was taken in about 4 hours of beam time (assuming 8 pnA) while the original TESSA3 data were collected in about 100 hours of beam time.

5. Electronics and Data Acquisition

The layout of the system is shown in the schematic diagram in Figure 9. The signals from the detectors are processed in VXI based electronics. The Germanium VXI based card takes signals from 6 detectors and outputs two energies (0 - 4 MeV and 0 - 20 MeV), a time based on a constant fraction discriminator and a time based on a cross over circuit. The latter is used for pile up rejection and pulse shape analysis. The BGO VXI card takes signals from 60 BGO crystals and is designed to correspond to the channels in an adjacent Ge card. The BGO card outputs energy, time and the pattern of BGO crystals in an event. Also in VXI electronics are the Master Trigger (which controls the logic for the event), the Readout Controller and a Resource Manager. Components of the system are described in more detail in references 5 - 11.

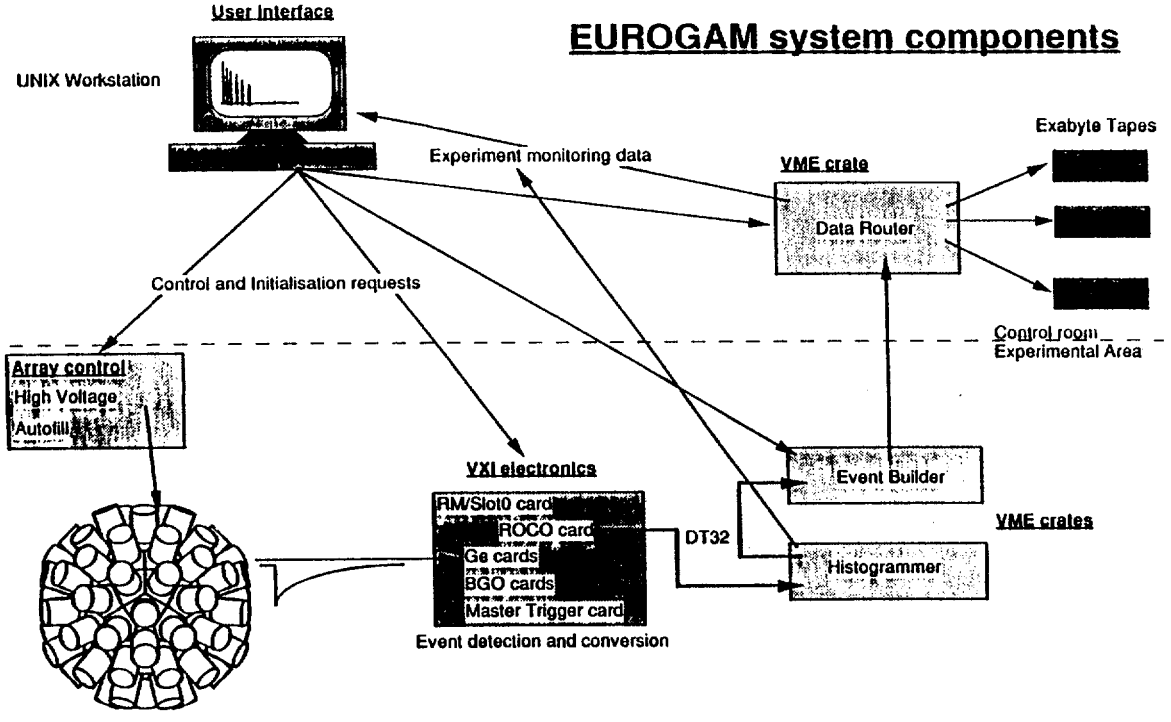

Figure 9 The EUROGAM electronics and data acquisition system

The data are read out from the VXI crate along a 32 bit bus into the data acquisition system which is VME based[12]. A histogrammer module can produce spectra for all parameters flowing along this bus. The data are built into events using commercially available VME modules and then passed to the data sorter and data router. The latter allows different sub sections of the data (e.g. triples, quadruples etc) to be directed to different storage devices. The system is designed to handle a rate of ~ 2 Mbytes/sec, but can be upgraded to 5 - 6 Mbytes/sec.

All the above components have been tested (including the software) and work to specification. Currently (May 1992) the final system tests are underway.

In addition to the above a VME based control and monitoring system has been developed for the liquid nitrogen autofill system, the detector HV modules and the environmental monitoring.

6. Auxiliary Detectors

The power of a device like EUROGAM is enhanced when it is operated in conjunction with additional detectors. During the EUROGAM commissioning tests a downstream isomer detector and the Daresbury recoil mass separator [13] have been used in coincidence with EUROGAM. In addition several other devices are being designed. These include gas detectors, an inner ball for some energy/multiplicity determination apparatus for recoil distance and g-factor measurements, neutron detectors etc.

As an illustration of the power of such devices some of the data taken using the recoil mass separator in coincidence with EUROGAM will be discussed. The $^{104}Ru + ^{34}S$ reaction was used at a beam energy of 160MeV. The data recorded were multifold suppressed γ-coincidences (fold $\geq$ 3) and recoil - γ (fold $\geq$ 2) coincidences.

Figure 10 shows spectra corresponding to the known highly deformed band in ^{133}Nd. The band can clearly be seen in both spectra, the mass gating reducing the contamination.

7. Current Status (May 1992)

The experimental programme on EUROGAM will start in summer 1992 using a system consisting of 45 detectors. This will have a photopeak efficiency (for 1.33 MeV gamma-rays) of ~ 4.5%. EUROGAM will move to France in summer 1993 and be upgraded to include some new 4 element clover detectors. The EUROGAM arrangement, shown in Figure 11, will then comprise 30 detectors from phase 1 (placed around 0° and 180°) and 24 clover detectors (place near 90°). This array should have a total photopeak efficiency of ~8.5%.

Acknowledgements

The EUROGAM collaboration is jointly funded in France by IN2P3 and in the UK by SERC. I would like to thank all those who have contributed to the EUROGAM project.

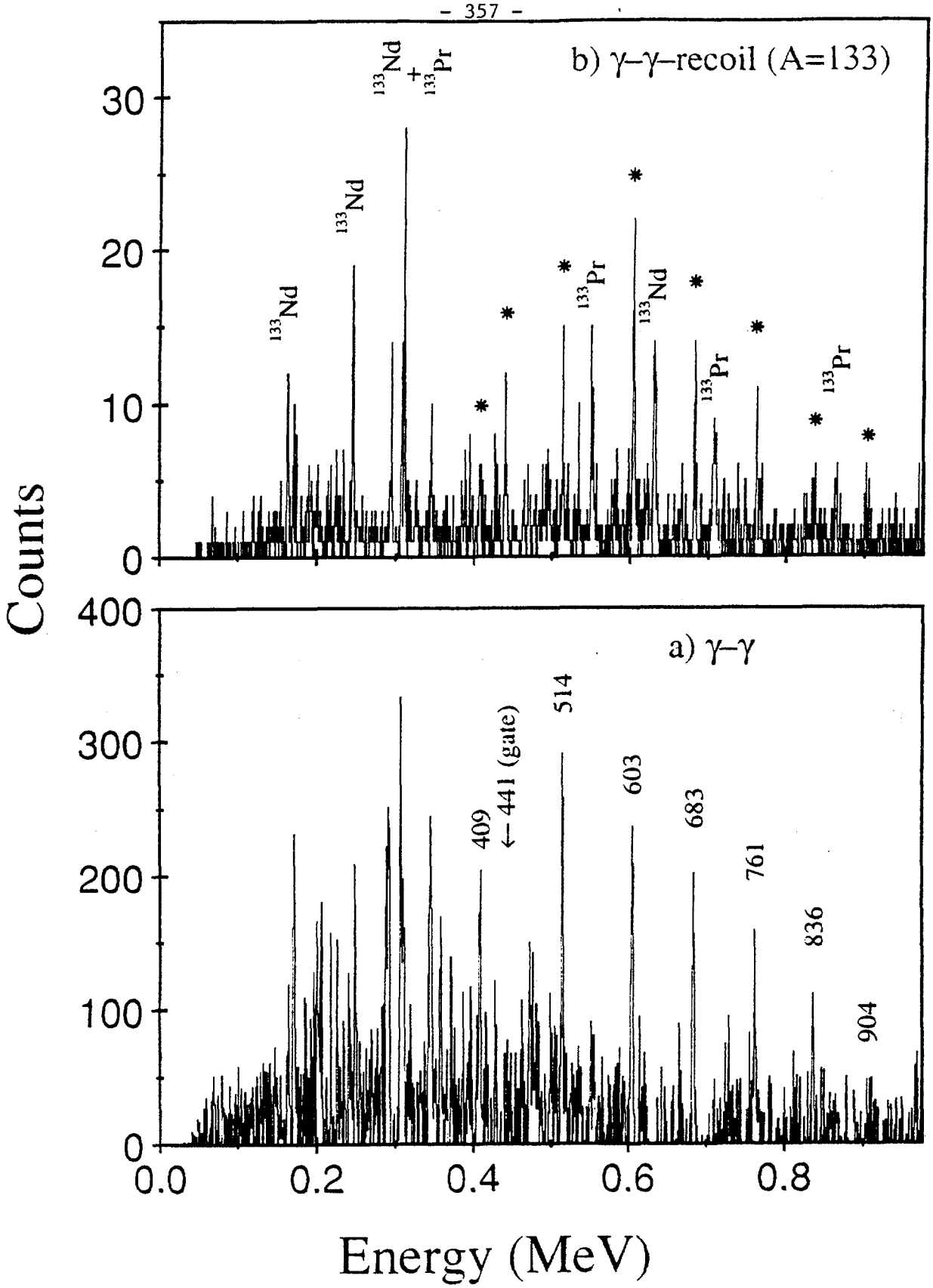

Figure 10 Spectra from γ-γ and mass (A=133) gated γ-γ data for the highly deformed band in ^{133}Nd. (a) a single gate on the 441 keV transition, (b) a sum of gates on 6 transitions in the band. Memebers of the band are marked *.

References

1) Duchêne G., Proceedings of the Workshop on Large Gamma-ray detector arrays, Canada May 1992 AECL 10613 (1992)

2) Beausang C. W. et al, Nucl. Instrum. Meth. A313 37 (1992)

3) Hannachi F., Proceedings of the Workshop on Large Gamma-ray detector arrays, Canada May 1992 AECL 10613 (1992)

4) Kirwan A. et al, Phys. Rev. Lett. 58 467 (1987)

5) Richard A. et al, IEEE Nuclear Science Symposium, New Mexico, USA, 1991

6) Bosson G. et al, IEEE Nuclear Science Symposium, New Mexico, USA, 1991

7) Pouxe J., IEEE Nuclear Science Symposium, New Mexico, USA, 1991

8) Berst J. et al, IEEE Nuclear Science Symposium, New Mexico, USA, 1991

9) Lazarus I. et al, IEEE Nuclear Science Symposium, New Mexico, USA, 1991

10) McPherson G. M. et al, IEEE Nuclear Science Symposium, New Mexico, USA, 1991

11) Alexander J. et al, IEEE Nuclear Science Symposium, New Mexico, USA, 1991

12) Pucknell V. and Aleonard M. M., Proceeding of the Real Time 91 Conference, Julich, Germany 1991

13) James A. N. et al, Nucl. Instrum. Meth. A267 144 (1988)

SIMULATION CALCULATIONS USING THE CODE GEANT III FOR THE EUROGAM DEVICE.

F.A.Beck, D.Curien, G.Duchêne, G.de France, L.Wei
Centre de Recherches Nucléaires, IN_2P_3/Université Louis Pasteur - BP 20, 67037 Strasbourg Cedex 2, France

Simulation calculations are good tools to determine, at a low cost, the characteristics of a detector. It enables to change the geometry of the counter in an iterative way to optimize its response leading to the best performances for the whole multi-detector device. This kind of calculations have been performed using the Geant III code for the EUROGAM device.

1. Tests of Geant III Code

Before performing simulation calculations on EUROGAM's Ge counters, we have tested the code on standard coaxial Ge detectors. Photopeak efficiencies $\epsilon_p\omega$ and peak to total ratios P/T (with a threshold set at 100 keV) have been measured for two coaxial Ge detectors, a large one and a small one, using a ^{60}Co source placed at 25 cm from the crystals. The experimental data have been compared to the calculated ones (see table I). Both set of photopeak efficiencies agree within the error bars whereas the calculated P/T overestimate the measured ones by about 10 %. These trends apply for the whole range of efficiencies and P/T (see fig. 3.5 and 3.6 of ref. [1]) showing a general agreement between calculations and experiments.

Detector Characteristics	Sm.Vol.	La.Vol.	EUROGAM Phase I
L(mm)	64.2	78	76.2
$\emptyset$(mm)	45.9	69	71.5
$(\varepsilon_p\omega)_R$ (%)	19.2 (0.6)	72.5(2.1)	74.0(2.1)
	19.3	*73.8*	*76.0*
$(P/T)_{100}$	0.189(0.013)	0.261(0.017)	0.283(0.019)
	0.21	*0.28*	*0.28*

Table I :*Detector characteristics, length L, diameter $\emptyset$, relative photopeak efficiency $(\varepsilon_p\omega)_R$ and peak to total ratio $(P/T)_{100}$ for three coaxial Ge counters : a small one, a large one and the EUROGAM Phase I detector. The calculated values are given in italic. The data have been obtained for a ^{60}Co source at 25 cm from the crystals.*

Sure of the reliability of the Geant III code we have performed simulation calculations to find the geometry of a single coaxial Ge crystal leading to the maximum $\varepsilon_p\omega$ value for a given solid angle ω. Figure I shows the geometry finally adopted for

EUROGAM Phase I and table I summarizes the performances of this counter. The crystal tapered along 3 cm, is only hold by the rear side and the distance to the can is only 3 mm. This shape of the detector enables a close packing of 70 counters around the target (target-crystal distance: 20.5cm). Note in this case that a better agreement is obtained between calculation and experiment for P/T, probably due to the reduction of the dead material around the crystal.

2. Doppler Broadening

The large crystal diameter compared to current devices (increase of the solid angle by about a factor of 2) introduces a larger Doppler broadening. Simulation calculations have been performed to estimate the degradation of the Ge energy resolution. They take into account the intrinsic energy resolution of the counter (1.2 keV at 122 keV and 2.3 keV at 1332 keV), the target thickness, the variation of the recoil velocities, the aperture of the recoil cone $\Delta\alpha$, the aperture $\Delta\theta$ and the angular position θ of the Ge detector.

We have calibrated the calculations on experimental data obtained at TESSA3 with the reaction ^{108}Pd(^{48}Ca,4n)^{152}Dy at a bombarding energy of 205 MeV. With stack of two targets (2 x 0.5 mg/cm^2) the recoil velocities β range from 2.8 to 3.0 % and the recoil cone is about 5°. In TESSA3 geometry ($\Delta\theta/2 = 6.2°$), at $\theta = 90°$ and for a gamma ray of 967 keV, the measured and calculated energy resolutions $E_{1/2}$ equal 4.8 keV and 4.7 keV respectively. Applying this calculations to EUROGAM ($\Delta\theta/2 = 8$ °), $E_{1/2}$ is found equal to 6.7 keV which is quite large.

A reduction of the Doppler broadening is obtained by use of a reduced collimation along the beam axis (fig.II). The calculations performed for the reaction ^{130}Te($^{27}A\ell$,6n)^{151}Tb at $E_{Lab} = 150MeV(\beta \simeq 1.8\ \%)$ are shown in table II for two collimations : the standard one ($\Delta\theta/2 = 8$ °) and a reduced one ($\Delta\theta/2 = 4°$).

EUROGAM angles	$\Delta\theta/2 = 8°$ (standard)		$\Delta\theta/2 = 4°$ Reduced	
94 °	5.6(0.3)	*5.9*	4.6 keV	*4.5*
108°	5.3	*5.5*		*4.3*
134°	4.6	*4.5*		*3.8*
158°	4.2	*3.4*		*3.3*

Table II : *Energy resolutions for a γ-ray energy of 1322 keV measured and calculated (italic) at the different EUROGAM angles with the standard and the reduced collimations. The reaction is given in the text.*

The Doppler broadening calculations have been compared to the data obtained during commissioning runs of EUROGAM using six different fusion-evaporation reactions. The recoil velocities β ranged from 1.7 to 6.8 % and an overall agreement between experiment and calculation is observed . The Ge energy resolution have also been measured with a reduced collimation ($\Delta\theta = 4°$) for ^{151}Tb residue and data are

reported in table II. The agreement between calculated and measured data is excellent except for the most backward (forward) angle where the target inhomogeneity could have some influence.

This new collimation leads to a loss in photopeak efficiency of about 20 % however fully compensated by the improved energy resolution (about + 20 %) and peak to background ratio (about + 15%).

3. Doppler broadening correction

How to reduce the Doppler broadening without loosing in photopeak efficiency? Electrically segmented detectors is in principle the best solution however this technology does not apply at present for N-type Ge crystals. The only solution is to mount in the same can several crystals in a close packed geometry.

About one year ago, we have imagined for the second phase of EUROGAM a new composite detector, the Clover detector, which consists of four coaxial N-type Ge crystals arranged like a four-leaf clover (fig.III). This counter is descripted in the contribution "The Clover detector". Two such prototypes have already been delivered by the company INTERTECHNIQUE with crystals of 50 mm diameter and 70 mm length.

Simulation calculations have shown that, in case of scattering events (when a gamma ray has scattered from one crystal to its neighbour), the first scattering interaction happen close to the common surface of the firing Ge crystals. The calculated distributions of scattering probability is shown in figure IV for three different γ-ray energies : 200, 1332 and 5000 keV. The half width half maximum of these distributions is smaller than 1.5cm and is almost independent of the γ-ray energy. Therefore a simple Doppler broadening correction method can be used. After proper orientation of the Clover counter relative to the beam axis, the composite detector can be divided in two halfs perpendicular to this axis. Each half has a reduced aperture ($\Delta\theta/2 = 5.1°$). The detection of one gamma ray in only the right (left) hand side half of the Clover detector leads to correct the Doppler shift using the angular position θ of this half. For scattering events where both halfs of the Clover detector fire, the energies collected are summed and the total energy is corrected for Doppler shift using the center of the whole Clover counter. As most of the scattering events (more than 75 %) happen in a range of $\pm$ 2 cm around the separation surface of the crystals firing, which is about the front size (4.1 cm) of the shaped crystals of the Clover detector, the FWHM for scattering events is about the same as the one obtained in each half (see table III). Only the few scattering events happening beyond $\pm$ 2 cm will slightly worsen the FWTM of the gamma line. Table III shows the calculated FWHM and FWTM obtained at 90° in the geometry of EUROGAM phase II with the reaction ^{108}Pd(^{48}Ca,4n)^{152}Dy at E_{Lab} = 205 MeV for a γ-ray energy of 967 keV.

The final corrected energy resolution of the whole Clover detector is highly improved (table III) as shown in figure V and is equivalent to the one obtained in the same conditions with the TESSA3 array (4.7 keV). The excellent energy resolution of the Clover detector without any loss in photopeak efficiency give raise to a very

good resolving power for EUROGAM phase II. This Doppler broadening correction method will be tested during the first experiments performed with EUROGAM I.

Peak Shape	Uncorrected Clover	Left Half	Right Half	Coinc. Events	Corrected Clover
FWHM(keV)	8.2	4.5	4.3	4.7	4.5
FWTM(keV)	11.7	7.6	7.5	9.3	7.9

Table III : *FWHM and FWTM in keV obtained at 90° in the geometry of EUROGAM phase II with a Clover detector. These values are calculated for a γ-ray energy of 967 keV for the reaction given in the text.*

Conclusion

Simulation calculations using the code Geant III have enabled us i) to improve the design of the coaxial Ge detectors of EUROGAM phase I, ii) to reduce the Doppler broadening by use of an optimized reduced collimation, iii) to imagine a new segmented detector, the Clover detector, devoted to phase II and to determine its main characteristics and iv) to invent a Doppler broadening correction method leading to excellent energy resolutions.

Reference [1] Eurogam, A french-U.K. Proposal, ed. CRN Strasbourg (1990).

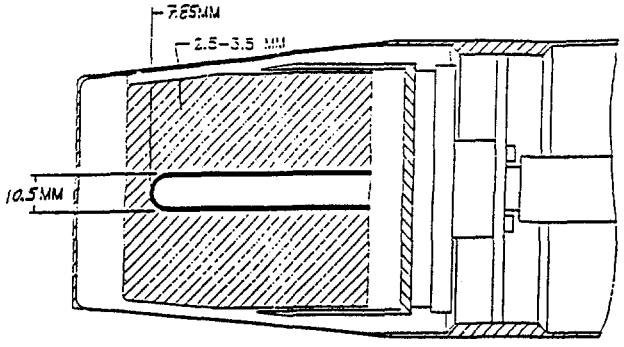

Figure I *(top) : Cross-section of the EUROGAM phase I Ge detector.*

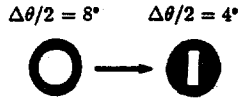

^{151}Tb

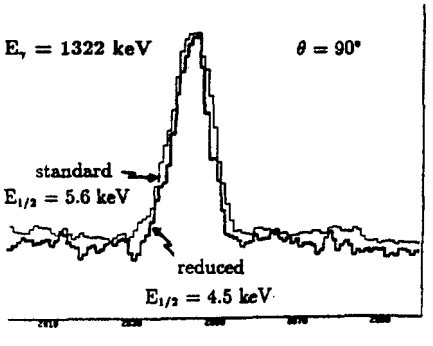

Figure II *(right) : The 1322 keV gamma line experimentally observed at 90° in the reaction $^{130}Te(^{27}Al,6n)^{151}Tb$ at E_{Lab} = 150 MeV. The energy resolutions $E_{1/2}$ obtained in the standard (thin line, $\Delta\theta/2 = 8°$) and the reduced (thick line, $\Delta\theta/2 = 4°$) collimations are given.*

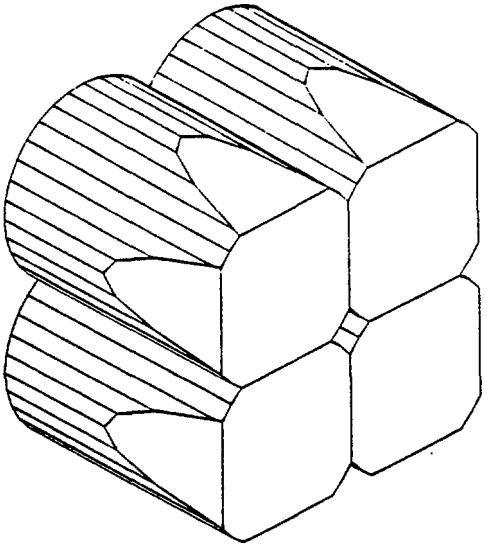

Figure III *(top left) : Schematic view of the Clover detector.*

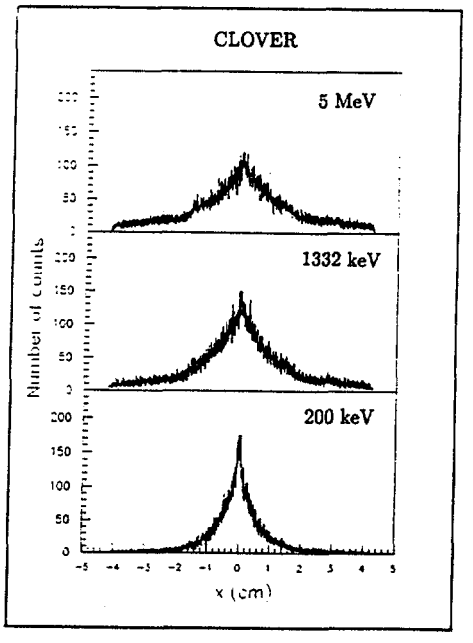

Figure IV *(top right) : Probability distributions of the gamma ray scattering from one crystal to its neighbour versus the distance x between the first interaction point and the separation surface of both crystals. The calculation apply for three γ-ray energies: 200, 1332 and 5000 keV.*

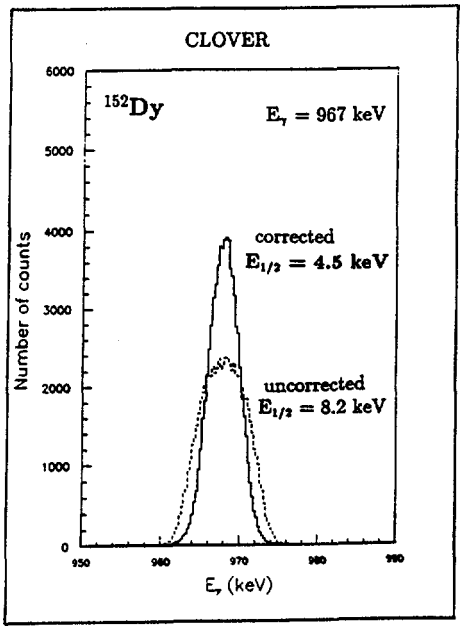

Figure V *(bottom right) : Doppler broadening correction. Uncorrected and corrected gamma lines calculated for the γ-ray energy 967 keV using the Clover detector placed at 90° relative to the beam axis at 23 cm from the target (phase II geometry). The reaction used leading to ^{152}Dy is given in the text.*

THE CLOVER DETECTOR

F.A.Beck, Th.Byrski, D.Curien, G.Duchêne, G.de France,B.Kharraja, L.Wei
Centre de Recherches Nucléaires, IN_2P_3/Université Louis Pasteur - BP 20, 67037 Strasbourg Cedex 2, France

P.Butler, G.Jones, P.Jones
Oliver Lodge Laboratory, University of Liverpool
Oxford Street, p.o. Box 147
LIVERPOOL L69 3BX, U.K.

F.Hannachi
SERC Daresbury Laboratory
Daresbury, Warrington WA4 4 AD, U.K.

The EUROGAM Phase I device is almost running for experiments and new technical developments are in progress for its second phase. For example, a composite Ge detector should enable i) a very large photopeak efficiency with good energy and timing resolutions and ii) the covering, with Ge, of a large portion of 4π-Str. The Clover detector, proposed by the CRN, Strasbourg, is one of this new generation of Ge detectors. It is currently developed in France by the EUROGAM collaboration. The design, the technical characteristics of the counter and the first results of the prototype tests are discussed in this contribution.

1. CLOVER GEOMETRY

The Clover detector consists of four coaxial N-type Ge-detectors, arranged like a four-leaf clover. Each crystal has a square front face with round edges obtained by tapering it on two adjacent faces with an angle of 7.1° starting at around the half of the length (see fig.I a)) and by cutting the two remaining faces parallel to the crystal axis and along its whole length. This enables a close packing of the crystals (Ge-Ge distance of about 0.2mm) and retains most (89 %) of the original crystal volume. For Ge crystals of 50 mm diameter and 70 mm length, the remaining active volume in the Clover detector is about 470 cm^3, 55 % more than the large monolithic coaxial crystals used in EUROGAM Phase I. The crystals are held only by the rear-side which reduces the amount of material around the detector and improves its P/T response. The four crystals are mounted in a common cryostat of tapered rectangular shape. To save space the gap between the tapered edges of the crystals and the inside of the cryostat is as small as 3.5 mm. To enable the close packing of the Ge crystals the outer surfaces of the crystals are at ground whereas the high voltage (common for the 4 crystals) is applied on the inner contacts. Energy and timing signals are obtained for each crystal through AC-coupling..

Beside the reduction of Doppler broadening, other advantages support the Clover detector :

1. its sensitivity to the linear polarisation of the gamma rays,
2. its reduced vulnerability to neutron damage,
3. the good timing particularily for low energy gamma rays.

2. CLOVER PROTOTYPES

Two prototypes built by the company Intertechnique, Strasbourg with Ge crystals of 50 mm diameter are currently being tested at the CRN, Strasbourg and another prototype with 55 mm diameter crystals has been ordered from EG&G Ortec, Oak Ridge. The response of the second Intertechnique prototype is summarized in table I.

The detection of the full energy of a gamma ray in a composite Ge detector made of N segments (crystals) proceeds in two ways :

i) the detection in one of the N segments (M = 1 in table I) called single event,

ii) the detection in several segments (M> 1 in table I) called multiple events.

In the latter case the full energy of the gamma ray is obtained by summing (add-back) the energies deposited in the M segments firing. The add-back factor $F_{a.b.}$ is thus defined as the ratio of the full efficiency in add-back mode over the efficiency in singles :

$$F_{a.b.} = \frac{(\varepsilon_p\omega)_{M=1} + (\varepsilon_p\omega)_{M\geq 1}}{(\varepsilon_p\omega)_{M=1}}$$

For the Clover detector (N = 4) the average photopeak efficiency $(\varepsilon_p\omega)_{ind}$ of the individual crystals at 1.33 MeV is 2.58 x 10^{-4} at 25 cm from the ^{60}Co source, whereas the total photopeak efficiency in add-back mode is 16.1 x 10^{-4} (table I). The latter value corresponds to a large add-back factor of 1.56 and to an increase in efficiency, compared to the detectors of EUROGAM I ($\varepsilon_p\omega \simeq 8.5$ x 10^{-4} at 25cm), of nearly 85%. The multiple events (M> 1) are mainly doubles at 1.33 MeV and the P/T response of the bare Clover detector is 0.30 (table I).

	$(\varepsilon_p\omega)_{ind.}$	$(\varepsilon_p\omega)_{\Sigma}$	M				$F_{a.b.}$	$(P/T)_{\Sigma}$
	x10^4	x10^4	1	2	3	4		
meas.	2.58	16.1	100	49.4	6.1	0.3	1.56	0.30
	(20.7 %)	(129 %)						
calc.	2.68	16.3	100	46.7	5.0	-	1.52	0.29
	(21.5 %)	(131 %)						

Table I :*Average individual* $(\varepsilon_p\omega)_{ind}$ *and total* $(\varepsilon_p\omega)_{\Sigma}$ *photopeak efficiencies are given as well as the corresponding relative efficiencies in percent. M is the number of segments in the Clover counter hitted by a 1332 keV gamma ray. The associated values give in % the proportion of doubles (M=2), triples (M=3) and quadruples (M=4) normalized to the singles (M=1).* $F_{a.b.}$ *is the add-back factor. P/T is the peak to total ratio obtained in add-back mode for a* ^{60}*Co source and with a threshold of 100 keV. Table I compares calculated to measured values.*

The energy resolutions of the four crystals shaped and placed in the definitive cryostat are about 2.0 keV at 1.33 MeV and 900 eV at 122 keV. The line shape is symmetric with FWTM/FWHM between 1.85 and 1.90. The energy resolution in add-back mode is excellent : 2.14 keV at 1.33 MeV and almost unaltered at low energy because $F_{a.b.}$ equal 1 up to 120 keV.

The timing response of the individual crystals mesured with a ^{60}Co source in coincidence with a small BaF_2 scintillator is good: the average FWHM is about 5.5 ns and FWTM/FWHM is smaller than 3.0 for a CFD threshold of about 50 keV.

3. SIMULATION CALCULATIONS USING THE CODE GEANT III.

The calculated performances of the Clover counter are compared to the experimental data in table I. The agreement is fairly good. Simulation calculations using the code Geant III have been performed to optimize the geometry of the composite detector and to determine the best procedure for the Doppler broadening correction. The calculations led to the geometry shown in fig.Ia). Concerning Doppler broadening, the energy resolution of the Clover detector after correction, despite the large opening angle of the counter, is predicted to be equivalent to the energy resolution obtained on TESSA3 array with 25 % efficiency Ge counters. More details are given in the contribution "Simulation calculations using the Code Geant III".

4. POLARISATION SENSITIVITY OF THE CLOVER COUNTER

The polarisation sensitivity Q of the Clover detector has been measured using four reactions (see table II) producing strongly polarised gamma-rays of E_2 multipolarity. The scattering asymmetry A of the Clover detector can be written as :

$$A = \frac{a(E_\gamma)N^c_\perp(90°) - N^c_\parallel(90°)}{a(E_\gamma)N^c_\perp(90°) + N^c_\parallel(90°)} \qquad where \qquad a(E_\gamma) = \frac{N^c_\parallel(0°)}{N^c_\perp(0°)}$$

$N^c_{\perp(\parallel)}$ represents the coincidence counting rate between two adjacent crystals located in a plan perpendicular (parallel) to the reaction plan (see fig.Ib). $a(E_\gamma)$ is the relative efficiency of the two adjacent crystals and is measured at 0°. It is a function of the γ-ray energy E_γ.

Target	Level J	E_γ(keV)	E_p(MeV)	Reaction
^{19}F	$5/2^+$	197	2.4	Coulomb Excitation
$^{107,109}Ag$	$5/2^-$	418/423	2.45	Coulomb Excitation
^{56}Fe	2^+	845	3.0	Resonance
^{24}Mg	2^+	1368	2.45	Resonance

Table II : *The reactions used for linear polarisation sensitivity calibration.*

The theoretical polarisation is calculated from the experimental angular distribu-

tion of the gamma-rays. For stretched E_2 it is defined by :

$$P_{th} = \frac{3a_2 + \frac{5}{4}a_4}{2 - a_2 + \frac{3}{4}a_4}$$

where a_2 and a_4 are the normalised angular distribution coefficients. The polarisation sensitivity Q is the ratio of the asymmetry over the theoretical polarisation ($Q = A/P_{th}$). The data obtained are compared in figure II to these published by J.Simpson et al. [1] for a segmented Ge(Li) detector of 17 % total photopeak efficiency at ^{60}Co and to a classical 3 Ge(Li) polarimeter. The Clover detector is about 20 % less sensitive to polarisation then the segmented Ge(Li) and by a factor of 2 compared to the 3 Ge(Li) polarimeter. This is due to the very compact geometry of the Clover (large scattering angle from the scatterer segments to the analyser crystals).

Let us define a figure of merit F as :

$$F = Q^2(\varepsilon_p\omega) \qquad where \qquad (\varepsilon_p\omega)_c = \frac{\mathcal{N}_{\parallel}^c + \mathcal{N}_{\perp}^c}{2} \cdot \frac{(\varepsilon_p\omega)_\Sigma}{N_{Tot}}$$

and N_{Tot} is the total number of counts in the Clover counter measured in add-back mode. For the 1368 keV transition, F (x 10^8) equals about 20 for the 3 Ge(Li) polarimeter, 43(4) for the segmented detector and 102(15) for the Clover detector which shows the importance of the large coincidence probability in this latter counter. As 24 such counters will be placed at 75° or 105° relative to the beam axis in EUROGAM phase II, the polarisation of very weak intensity gamma rays (as in superdeformed band) will be possible.

CONCLUSION

The Clover detector presents good energy and timing resolutions for a high photopeak efficiency. It enables a large correction of the Doppler broadening effect and may be used as a γ-ray polarimeter.

Reference [1] J.Simpson et al., *NIM* **204** (1983) 463

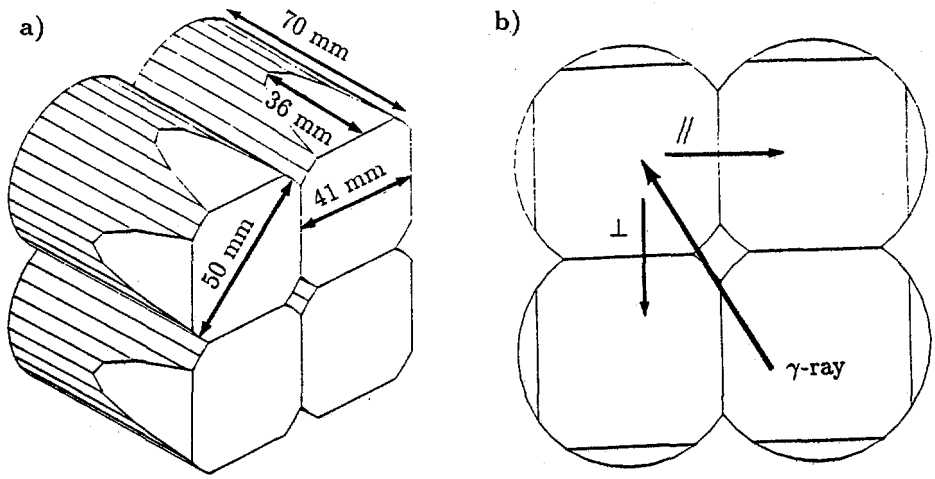

Figure I : *Schematic view of the Clover detector. Crystal sizes are given in a). In b) the upper left crystal is used as a scatterer segment. The vertical (⊥) and horizontal (//) coincidences with the adjacent segments are also shown.*

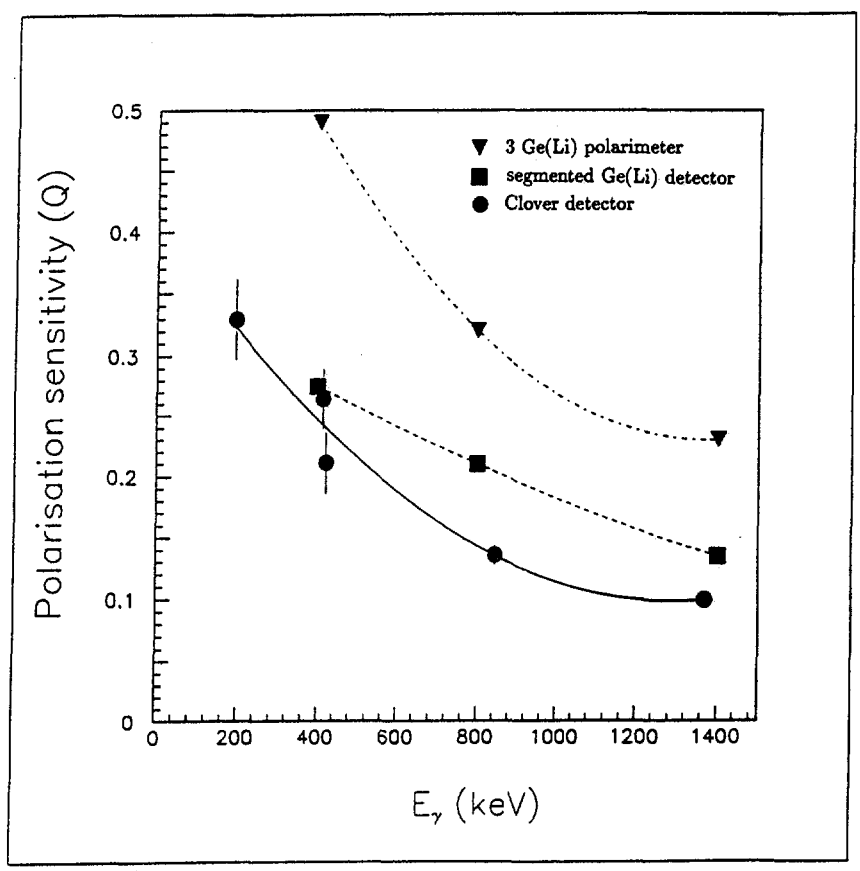

Figure II : *Polarisation sensivity versus γ-ray energy for the Clover counter (cercle), the segmented detector (square) and 3 Ge(Li) polarimeter (triangle).*

WORKSHOP ON LARGE GAMMA-RAY DETECTOR ARRAYS

Chalk River

SESSION 2: STATUS OF NEW INSTRUMENTS (II)

COMPTON SUPPRESSION TESTS ON Ge AND BGO PROTOTYPE DETECTORS FOR GAMMASPHERE

A. M. Baxter**, T. L. Khoo, M. E. Bleich*, M. P. Carpenter, I. Ahmad, R. V. F. Janssens, E. F. Moore†
Argonne National Laboratory, Argonne, IL 60439, USA

I. G. Bearden
Purdue University, West Lafayette, Indiana 47907, USA

J. R. Beene and I. Y. Lee
Oak Ridge National Laboratory, Oak Ridge, TN 37831, USA

During the last decade the application of arrays of 10–30 Compton Suppressed germanium (CSG) detectors in the field of γ-ray spectroscopy has led to a number of significant advances in studies of nuclear structure. Despite the success of these instruments, most of them are limited to detecting two-fold (and in a few cases three-fold) coincidences from high-multiplicity cascades. To increase the detection sensitivity for weak cascades, proposals have recently emerged for construction of much larger arrays. In the U.S.A., the proposed array, called GAMMASPHERE [1], is to have 110 large CSG detectors which will subtend a solid angle of almost 2π steradians, sufficient to permit routine acquisition of up to 5-fold coincidences from high-multiplicity cascades. This together with other improvements, will yield a resolving power [1] several orders of magnitude greater than currents arrays. In Europe, an array of similar size and power, called EUROGAM [2], is currently being constructed. In this paper, we report on measurements of the Compton suppression and overall P/T ratio of two Ge detectors in a BGO shield of the honeycomb pattern illustrated in fig. 1. These were the first prototype CSG detector assemblies for GAMMASPHERE. A more detailed description of these results can be found in ref. 3.

INDIVIDUAL BGO AND GE DETECTOR PERFORMANCE

The BGO shield was manufactured by Solon Technologies and represents the original honeycomb design. As can be inferred from fig. 1, this shield consists of six BGO elements which surround a Ge detector (in the honeycomb implementation, close-neighbor Ge detectors share a common BGO detector). There is also a backplug of BGO behind each Ge detector to suppress forward-scattered photons. This backplug is cylindrical except for a slot to accommodate an off-axis tube containing the cold finger and electrical cable connecting the Ge crystal to its remote liquid nitrogen dewar and preamplifier.

For efficient suppression of events in which a photon undergoes multiple scattering, it is desirable that the BGO discriminator threshold be set as low as possible. The low-energy response of the shield was measured using 59.5 keV γ rays from a ^{241}Am source. Peak/noise ratios of 20/1 – 36/1 were measured for the different BGO sectors, where lower energy γ rays and L-x rays from ^{237}Np were absorbed by a 0.25 mm copper disc and the aluminum cladding of the BGO. This excellent low energy response allowed us to easily place the discriminator

**On leave from the Australian National University, Canberra, Australia
*Present address: Summer student from Wesleyan Univ., Middletown, CT 06457
†Present address: GSI, Darmstadt, Germany

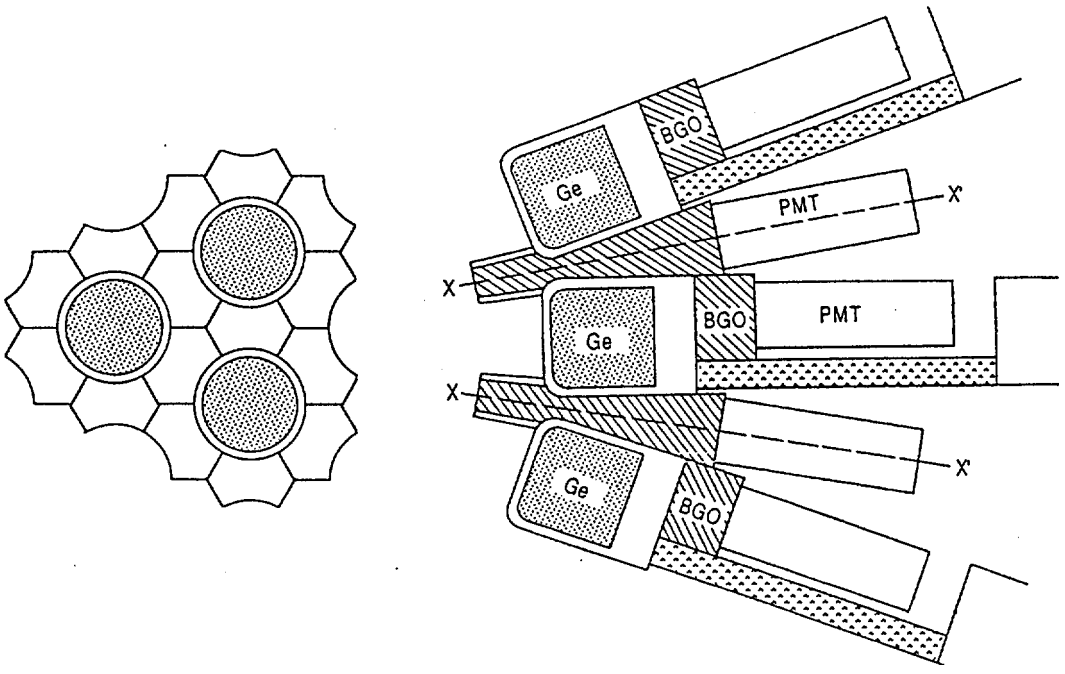

Figure 1: Schematic diagram of the GAMMASPHERE honeycomb arrangement of Ge detectors and their BGO Compton-suppression shields. One diagram shows a section through one Ge crystal, its neighbors on opposite sides and their shared BGO shields. The other shows a view, from the center of the array, of three neighboring Ge detectors and their shields.

thresholds at 10 keV for the suppression tests. The energy resolution of the individual BGO detectors at 662 keV (^{137}Cs) was typically 18%, while the time resolution (with a leading edge discriminator set near the single-electron noise) averaged 2.5 ns FWHM for full-energy ^{60}Co γ-ray interactions.

Suppression tests were carried with on two high-purity n-type Ge detectors which have very similar characteristics, e.g. they have full-energy peak efficiencies at 1.33 MeV of 75% and 76% for detector I and II, respectively. These detectors had time resolutions of $\sim$ 8.5 ns FWHM using a ^{60}Co source and an energy resolution of 2.23 and 2.25 keV at 1.33 keV using an amplifier shaping time of 6 μsec.

COMPTON-SUPPRESSION TESTS

The Compton-suppression measurements were performed by recording, for each event, the pulse height from the Ge detector and a logic bit which indicated whether or not there was a coincidence, within a time window of approximately 400 ns, between the Ge detector and the BGO shield. It was therefore possible to acquire suppressed and unsuppressed spectra simultaneously. The radioactive sources were suspended from a string well away ($\geq$ 1 m) from walls, the floor or other substantial matter in order to minimize the background caused by scattered photons from such material. The source was on the Ge detector axis at 25.9 cm (the original design distance for GAMMASPHERE) from the front face of the detector.

The effectiveness of the BGO Compton-suppression shield in suppressing the Compton background is demonstrated in fig. 2. In the bottom panel, the spectrum from a ^{60}Co source

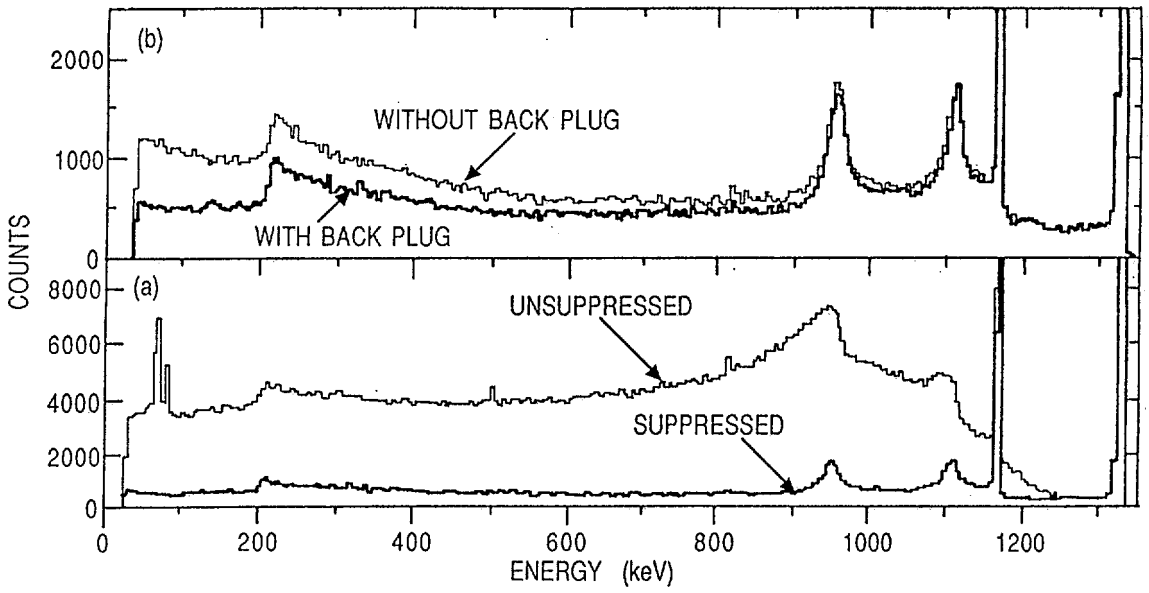

Figure 2: Plots showing the effect of Compton suppression on Ge detector spectra of a ^{60}Co source. (a) Suppressed and unsuppressed versions of the same spectrum are compared. (b) Properly normalized suppressed spectra are shown, with and without the backplug contributing to the suppression.

is shown with and without suppression. The performance of the shield is usually summarized in terms of a single parameter, the peak-to-total (P/T) ratio, which is defined here as the ratio of the area of the full-energy peaks to the total number of counts in the spectrum at energies greater than 100 keV. For the unsuppressed spectrum shown in fig. 2a, a P/T of 0.246 was measured while the suppressed spectrum (active backplug) gives P/T of 0.678.

Without the backplug, the P/T ratio is reduced to 0.622. The 10% difference that the backplug makes to the P/T is significant; it would improve the resolving power when detecting triple and quadrupole coincidences by about 30% and 40%, respectively. For comparison, fig. 2b shows two suppressed spectra of ^{60}Co, one with the backplug contributing and the other with the backplug in place but electronically disconnected. Clearly, the backplug contributes significantly to the suppression, not only in the low energy portion of the spectrum, as one would expect from a single scattering, but also up to the highest energies, indicating that multiple scattering in the Ge crystal is significant.

MONTE CARLO SIMULATIONS

Ge detector spectra, calculated using Monte Carlo simulations based on the GEANT library [4], were used to develop and optimize the GAMMASPHERE design. To simplify the calculations, the experimental geometry under which measurements were made was not reproduced in complete detail. The most important idealization used was to consider the radiation source to be a massless, monochromatic (or dichromatic for ^{60}Co) source which emitted γ rays only into the part of space occupied by the suppression shield and the Ge detector. Thus, the effect of γ rays scattered off materials other than the suppressor was not

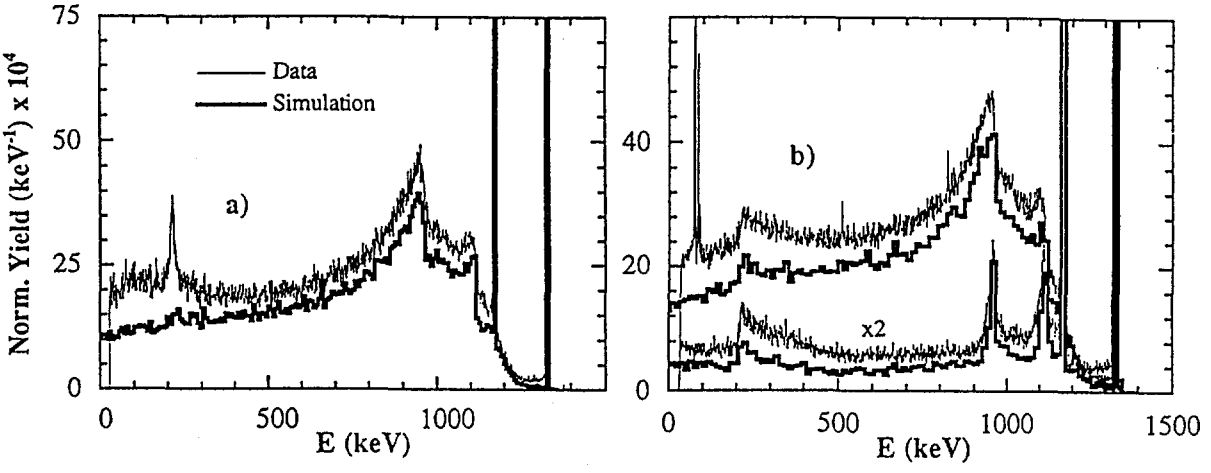

Figure 3: (a) Comparison of calculated and measured spectra of a bare Ge detector which is located away from scattering material to the maximum extent possible. (b) Comparison of calculated and measured unsuppressed and suppressed spectra. Suppressed spectra are multiplied by a factor of 2.

taken into account.

Simulated ^{60}Co spectra for the bare Ge detector and for the Ge detector in its shield are compared with experiment in fig. 3. Though qualitative similarities are obvious, there are large disagreements between the simulations and experiments. An immediate concern is whether the poorer results obtained experimentally reflect some problem with the implementation of the design or result primarily from idealizations in the simulations. To access these two possible explanations, it is instructive to compare the simulations to specific aspects of the data which should not be affected by a continuum arising from scattering. One such feature is the two peaks near the Compton edges for the ^{60}Co lines. The size, width and mean position of these peaks depends strongly on the design and performance of the "backscatter lip" region of the suppressor which extends out beyond the front face of the Ge detector. We find excellent absolute agreement between the simulated and experimental Compton-edge peaks. In fact, we can conclude that the experimental trigger efficiency in this lip region for $\sim$220 keV γ rays is 94$\pm$7% of that of the idealized simulations. This is important since there was concern about light collection from the lip region due to the complex light path. Other aspects which can be isolated for comparison are: (i) the performance of the backplug behind the Ge, and (ii) the percentage of γ rays which are transparent to the BGO shield. In both cases, excellent absolute agreement is obtained when the experimental data are compared to the simulations.

The quantitative agreement on these three aspects gives us confidence that there are no serious problems with the performance of the prototype suppressor resulting from the combination of the comparatively low light output of BGO and the complex geometry of the suppression shield. It also shows that simulations, based on widely used codes like the

GEANT package are sufficiently accurate to guide the design of Compton suppressor arrays.

It is also important to understand the origin of the discrepancies between the simulated and observed spectra. Since the calculations appear to simulate the performance of the suppressor, the differences between the simulated and measured spectra must result from an incorrect description of the spectrum of radiation incident on the detector system in the simulations. Further investigations of scattering makes it clear that the bulk of the scattering contribution to the continuum background would have to originate from material very near the source or the Ge detector. For example, the ^{60}Co source used in the measurements was encapsulated in a 24 mm × 10 mm × 2 mm plastic container. Simulations predict that scattering from this material produces a continuum amounting to 13% of the photopeak yield. This accounts for 40% (13 of 33%) of the scattered background, without a detailed treatment of the experimental environment.

We conclude that Monte Carlo simulations can accurately describe the performance of these prototype Compton-suppressed spectrometers. However, to obtain agreement with the measured spectra, it is necessary to include a background contribution from scattering materials near the source and detector. This emphasizes that the design of experimental apparatus (target chambers, ladders, frames etc.) requires great care to fully realize the high P/T values possible with Compton-suppressed arrays such as GAMMASPHERE.

CONCLUSIONS

Compton suppression tests have been carried out on two large n-type Ge detectors and a BGO shield which are prototypes for GAMMASPHERE. With a ^{60}Co radiation source, a peak-to-total ratio of 0.678 is obtained for a 75% Ge detector when operated with the shield. It is also found that a cylindrical BGO backplug behind the Ge crystal makes an important contribution to the effectiveness of the shield. The performance of the Ge detector and its shield can be well reproduced in Monte Carlo simulations if account is taken of γ rays which scatter from material near the source and Ge detector. The peak-to-total ratio, energy resolution and timing characteristics of these prototypes confirm that GAMMASPHERE will be capable of dramatic improvements in resolving power over that of the current generation arrays.

This work was supported by the U.S. Department of Energy, Nuclear Physics Division, under contract W-31-109-ENG-38, DE-FG02-87ER40346, and DE-AC05-84OR21400. The first prototype Ge detector and the BGO shield used in these tests were purchased with Argonne Exploratory Development Funds.

REFERENCES

1. GAMMASPHERE, A National γ-ray Facility, eds. M.A. Deleplanque and R.M. Diamond (Lawrence Berkeley Laboratory, Berkeley, PUB-5202, 1988).

2. EUROGAM, eds. M.M. Aleonard, F.A. Beck, J.C. Lisle, P.J. Nolan, E.G.C. Owern, C. Ring, H. Sergolle and P.J. Twin (Centre des Recherches Nucleaires, Strasbourg, 1990).

3. A.M. Baxter, T.L. Khoo, M.E. Bleich, M.P. Carpenter, I. Ahmad, R.V.F. Janssens, E.F. Moore, I.G. Bearden, J.R. Beene and I.Y.Lee, Nucl. Inst. Meth., in press.

4. R. Brun, F. Bruyant, M. Maire, A. C. McPherson, P. Zanarini, GEANT3 User's Guide, DD/EE/84-1, CERN 1987 (GEANT library ver. 3.14.07 was used in the simulations).

WORKSHOP ON LARGE GAMMA-RAY DETECTOR ARRAYS

Chalk River

SESSION 3: STATUS OF NEW INSTRUMENTS (III)

The gamma ray spectrometer GA.SP

D. Bazzacco for the GA.SP Collaboration

Istituto Nazionale di Fisica Nucleare, Sezione di Padova, Padova, Italy

GA.SP is a general purpose 4π detector array for advanced γ-spectroscopy and, in the same time, a suitable system for reaction mechanism studies. The detector is sited at the LNL Tandem+Linac accelerator and has been built as a joint project of INFN Padova, LNL, Milano and Firenze. The array consists of 40 Compton suppressed HPGe detectors and of a 4π calorimeter composed of 80 BGO crystals. The detector houses a reaction chamber of 34 cm diameter where a charged particles multiplicity filter composed of 40 Si detectors is going to be installed. Evaporation residues produced in the centre of GA.SP can be injected into the recoil mass spectrometer (RMS, named CAMEL) in use at LNL, without the need to remove any of the gamma detectors. The coupled operation of GA.SP, RMS and Si ball will give a unique instrument for identification and study of weak reaction channels.

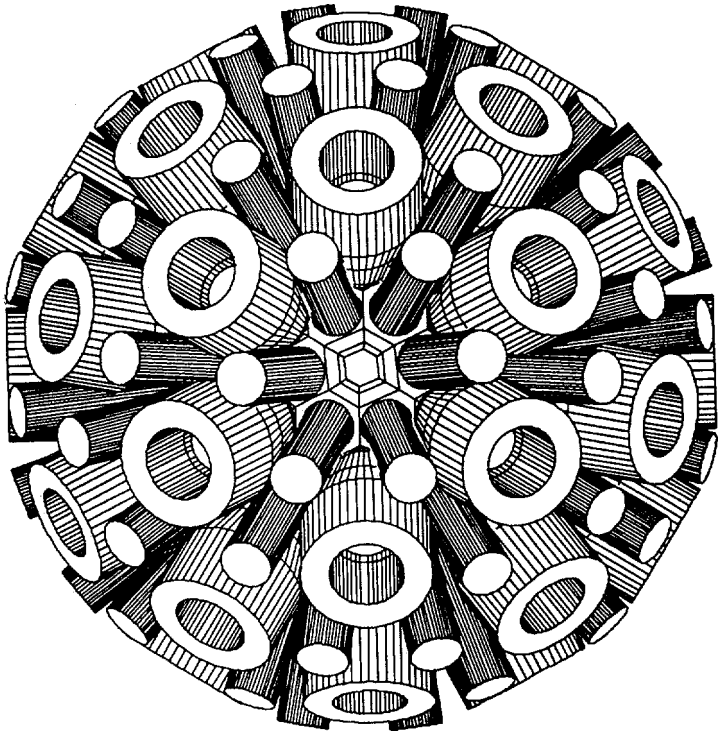

Figure 1: Downstream view of the array (and Logo of GA.SP).

The geometry of the detectors array is based on the polyhedron with 122 faces which can be built starting from the icosahedron or from its dual, the dodecahedron. The inner ball uses 80 of these faces while the remaining 42 faces are used for the beam ports and for the 40 Ge+Ac systems. Fig. 1 shows an artist's view of the

array. In order to simplify the drawing only the active parts of the detectors and the photomultiplier tubes of the inner ball are shown.

The 4π γ-detection systems proposed in recent years try to maximize the photopeak efficiency by means of non-standard germanium designs and of shared Compton suppressors. In this respect GA.SP is a detector system of the standard type as it uses individual Compton suppression shields. The increase of efficiency is obtained using the big volume germanium crystals which became available in recent years. Our HPGe detectors are built out of n-type cylindrical crystals of 72 mm diameter and about 82 mm length. The detectors have a taper of 10 degrees on the last 3 cm and are housed in an 87 mm diameter end cup. The mean relative photopeak efficiency of the detectors delivered until the time of this writing (36) is (see Fig. 2) about 83% at 1332 keV. The average energy resolution of these detectors is 2.2 keV.

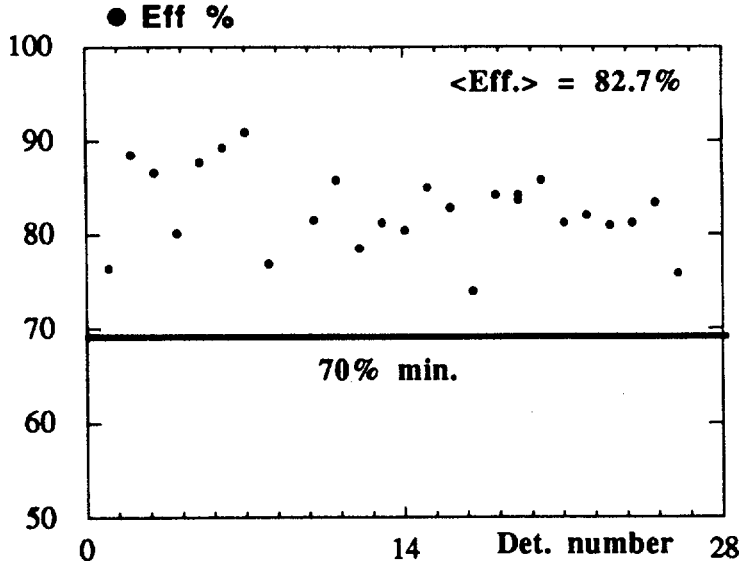

Figure 2: Relative photopeak efficiency at 1332 keV for the first 28 germanium detectors.

Compton suppression is performed by symmetric BGO shields composed of eight 19.5 cm long optically isolated crystals. Each of the 8 pieces has its own photomultiplier tube although the individual anode signals are summed together before being sent to the processing electronics. The dimensions and the cost of the BGO crystals have been optimized by means of extensive Montecarlo calculations exploiting the benefits of the higher intrinsic P/T of the big volume germanium crystals.

When using the inner BGO ball, the germanium detectors are positioned at 27 cm from the target; the detectors of the inner ball act as a partial collimator and the solid angle subtended by the germanium detector is 0.26%. In this situation the calculated absolute photopeak efficiency is 0.086% and the P/T is about 70% at 1 MeV. A measurement of the absolute photopeak efficiency at 1332 keV, performed using the sum energy of the two ^{60}Co lines, has given 0.074% which translates to about 3% for the complete system. Tests performed with the ^{60}Co source have given

Compton suppressed spectra with a P/T of 65%, as shown in Fig. 3. This results confirm that, as planned, GA.SP has the best response function among the arrays being built at present.

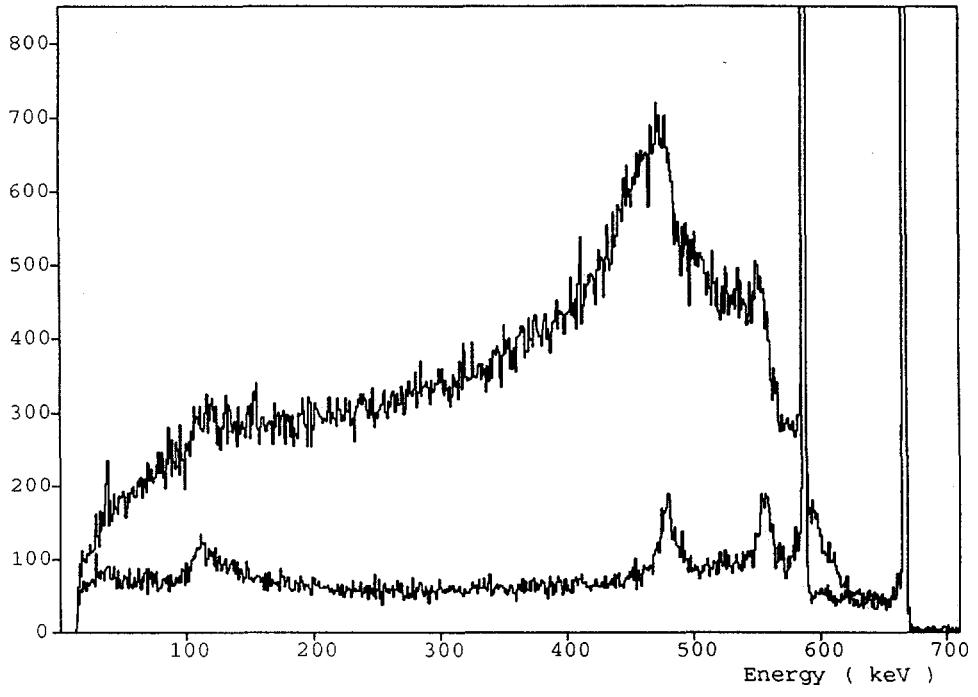

Figure 3: ^{60}Co spectra with (P/T = 65%) and without (P/T = 29%) Compton suppression.

The target-germanium distance can be reduced to 20 cm if the inner ball is removed and if the increased doppler broadening (which, for a recoil velocity of 4% changes, on the average, from 7 keV FWHM to 9 keV at 1332 keV) can be accepted. As in this way one could gain about a factor of two in detection efficiency the holding structure has been designed in order to allow for this option. However the detection efficiency is not the relevant feature and one should better compare the resolving power. This is defined normally as

$$R = \frac{SE_\gamma}{\Delta E_\gamma} \frac{P}{T} \qquad (1)$$

where SE_γ is the average separation of the gamma lines, ΔE_γ is the width of the peaks and P/T is full energy fraction of the response function. Under the usual assumptions of a gamma multiplicity of 30, a neutron multiplicity of 4, and a recoil velocity of 4% and a separation energy of 60 keV we have R=4.8 for the configuration with the inner ball and R=3.3 without it. In view of the different efficiency of the two configurations the average fold is 0.84 and 1.4 respectively. Finally if one takes as a figure of merit the expression $R^{<F>}$ and keeping in mind that the affect of the inner ball is estimated to give roughly a factor of two one ends up with about 8 and 5 for the two cases respectively.

For detection of high energy gamma rays the AC+Ge system can be operated in the add-back mode. At 20 MeV the calculated total efficiency is 0.36% ; the full energy peak has a FWHM of 1% and the P/T is about 20% .

The inner ball is built out of 80 hexagonally shaped 6 cm thick BGO crystals of two slightly different shapes but with almost exactly the same efficiency. The ball covers a solid angle of 80% and, according to Montecarlo simulations, it has an absolute efficiency of about 75% at 1 MeV and a resolution of 30% for a cascade of 30 transitions. Tests with radioactive sources are in progress in order to obtain the detailed response function of the BGO ball. In the first phase of operation of GA.SP only a reduced set of parameters will be taken from the inner ball and namely the fold k and the sum energy H. A planned improvement foresees the acquisition of both energy and time for every detector of the ball in order to obtain the details of the hit pattern and of the timing and total energy of the event.

One of the most interesting characteristics of this project is the coupled operation of GA.SP and RMS. As this is achieved without removing any gamma detector we get an increased resolving power without sacrificing detection efficiency.

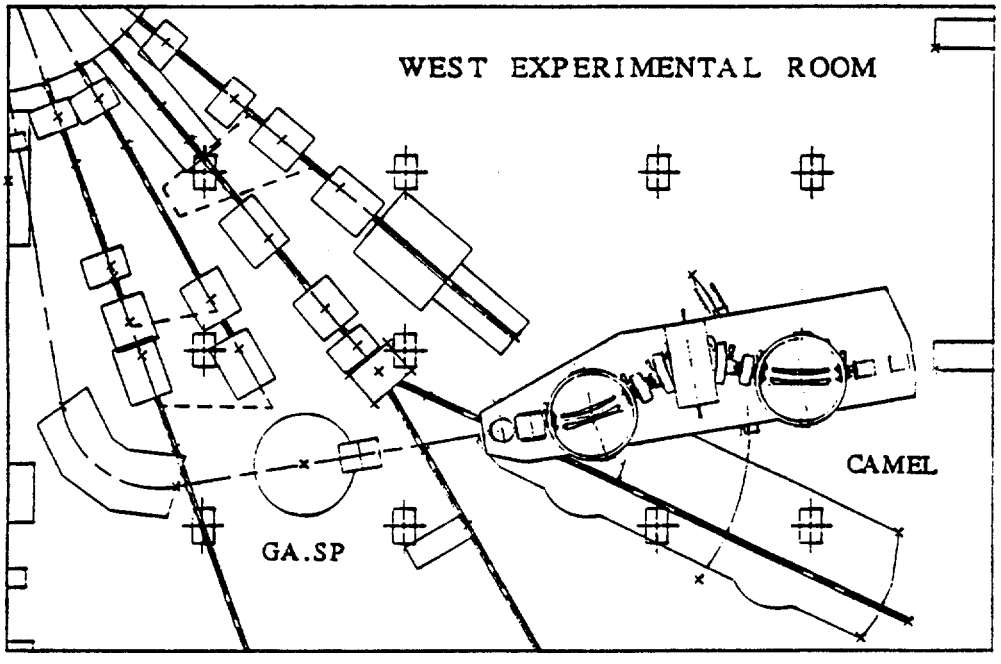

Figure 4: The experimental area with GA.SP and RMS.

The distance between the two spectrometers, as one can see in the layout of the experimental area shown in Fig. 4, is about 4 metres and the coupling of the two instruments is obtained by means of a magnetic quadrupole doublet, positioned at 70 cm from GA.SP, which focuses the recoils on the actual target position of RMS. Ray tracing calculations give an overall acceptance of the coupled system of about 5 msr (compared with 10 msr when the target in the RMS chamber) with $\Delta E/E$ of 10% and a mass resolution of 1/170 for a central mass A=100. This acceptance

is sufficient to collect almost 100% of the residues from HI induced reactions with evaporation of only neutrons and protons.

The signals from the 160 gamma detectors are worked out by dedicated electronics and acquisition system. Most of the electronics has been designed and home built with the goal of having a compact and reliable system with computer control of some of the most important features. Among the modules we will just mention the four channels Camac Constant Fraction Discriminator (which contains a Timing Filter Amplifier, the logics to perform the Compton suppression and a Gate and Delay Generator for the output signals) the Linear and Logic Multiplexers, used to inspect the relevant signals without disconnecting cables, and the Linear Gate and Stretcher module which acts as an interface to the ADC system. Considerable effort has been spent in order to obtain the best performances from the germanium detectors both in terms of energy resolution and of throughput. In order to increase the throughput and reduce the effects of pile-up, which are particularly severe for the high folds, it is foreseen that the main amplifier will be operated at a shaping time of $1\mu s$ and that the ballistic deficit will be recovered by an active filter integrator stage placed in the Linear Gate and Stretcher.

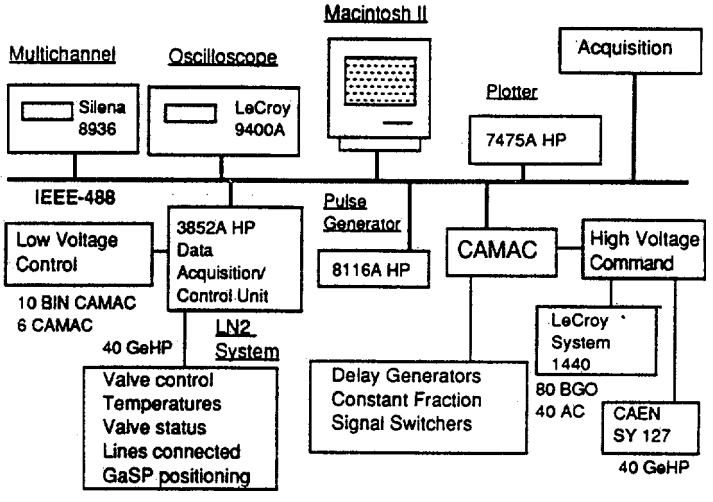

Figure 5: Layout of the control system for the LN2 and the electronics.

The detectors of GA.SP are controlled by a Macintosh based system which, is responsible for the liquid Nitrogen filling and for the HV settings. Beside these two tasks the Macintosh system (as shown in Fig. 5) is used to set up the CFD timings, to control the quality of the signals from the preamplifiers an PMTs and to maintain a data base of the relevant parameters and the history of the used detectors. It is planned that the user can, to a great extent, check and adjust the electronics set-up just by typing commands to the system through a very easy to use and intuitive graphical interface.

The rate of coincidences from the germanium detectors after Compton suppression can easily reach 20-30 kHz for doubles and this corresponds to a data flow in

excess of 1 Mbyte per second when considering only the gamma detection part of the system. The aim of the project is to have a reliable on-line analysis of the data, including automatic gain matching and ballistic deficit correction for the germanium detectors. This last will be achieved by taking the peaking time of the linear germanium signal, which is given by the LGS module, and using its empirical correlation to the amplitude loss as determined looking to $E_\gamma - T_{peak}$ matrices. The on-line system should furthermore be able to produce several gamma-gamma matrices in order, for example, to extract information from the two fold coincidences also when only higher folds are written on magnetic tape (usually EXABYTE).

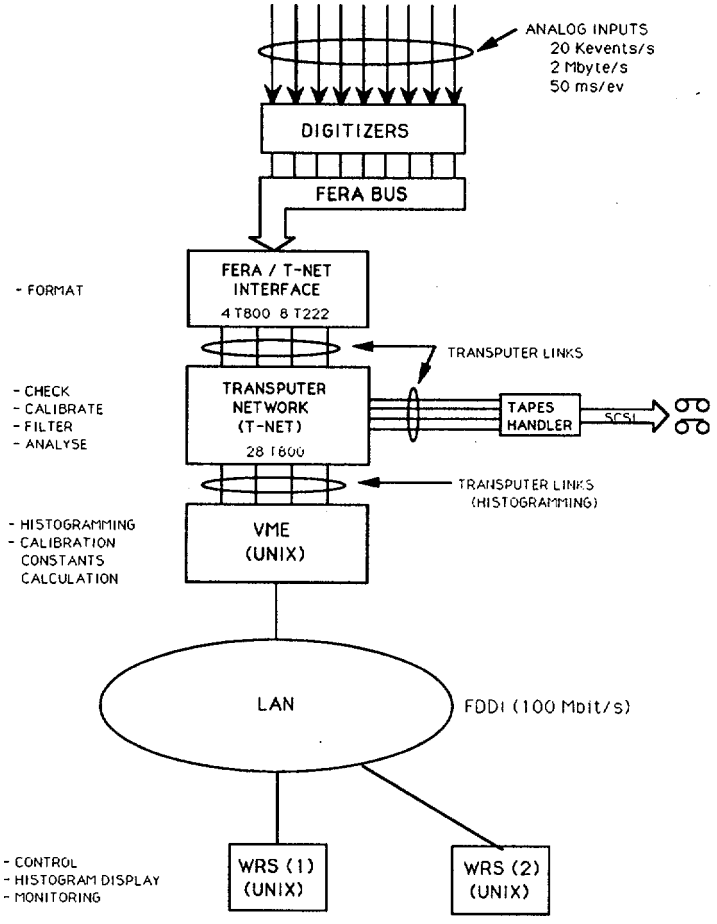

Figure 6: Layout of the Transputer based data acquisition system.

The computer power needed for all these tasks has been obtained with the development of a Transputer based distributed system. Its layout is shown in Fig. 6 : the several chains of transputer modules get the digitized data from the FERA read-out system, format the events in a user defined way, produce projections of the raw data, match the gains, perform the requested on line analysis and store the events on tape.

The user interacts with the system through applications running on a standard UNIX based computer. The building of events and their on-line analysis are performed in the Transputer system which is controlled by programs written in a high level language explicitly defined and implemented for this project. This language (called NEO for Nuclear Events Oriented language) contains primitives for the most common sorting operations and has the main function of hiding the parallel structure of the system to the user. In its present implementations the NEO compiler produces native Transputer code (OCCAM); a C code producing compiler is being presently written in order to use the same sorting language also in the off-line analysis running on standard serial computers.

Installation of GA.SP has begun in late fall 1991 and has been completed in March 1992. Commissioning of the system (using 28 Ge+Ac systems and the full BGO inner ball) has been performed in May 1992. A test of coupled operation of GASP and RMS has also been performed but the detailed study of the matching of the two systems has been moved to the second part of the year. Experimentation has been started shortly after the commissioning runs. Test experiments performed during commissioning(e.g. the $^{105}Pd+^{32}S$ reaction at 155 MeV with a beam current of about 10 pnA such to have 10 kHz of singles in the germaniums) have shown that the system can give about 5 kHz of triple coincidences. Several measurements are now scheduled and the main topics are the search for the linking transitions between superdeformed and normal states, search for hyperdeformation, study of the nuclei of the region around ^{100}Sn, search for octupole deformation and so fort. The detection system should be running in its full configuration for the beam times scheduled for the second part of the year.

WORKSHOP ON LARGE GAMMA-RAY DETECTOR ARRAYS

Chalk River

SESSION 4: NEW INSTRUMENTS: FREE DISCUSSION

Study of the superdeformed band in ^{194}Pb with EUROGAM

F Hannachi[1,2], M G Porquet[2], G Bastin[2], I Deloncle[2], B Gall [2], C Schuck[2], A G Smith[2], F Azaiez[3], C Bourgeois[3], J Duprat[3], A Korichi[3], N Perrin[3], N Poffé[3,4], H Sergolle[3], A Astier[5], Y Le Coz[5], M Meyer[5], N Redon[5] ,M Bentley[1,6], J Simpson[1], J F Sharpey-Schafer[7], M J Joyce[7], C W Beausang[7], P Fallon[7], E S Paul[7], P J Dagnall[7], S A Forbes[7], S Gale[7], P M Jones[7], R Wadsworth[8], R M Clark[8], M M Aléonard[9], D Curien[10]

1- SERC, Daresbury Laboratory, Warrington WA4 4AD, UK
2- C.S.N.S.M, IN2P3-CNRS, bat 104-108, F-91405 Orsay Campus
3- I.P.N, F-91406 Orsay Cedex
4- University of Oxford, Dept of Physics, Keble Road, Oxford
5- I.P.N, Université Lyon-1, F-69622 Villeurbanne Cedex
6- Staffordshire Polytechnic, Stoke-on-Trent, ST4 2DE, UK
7- Oliver Lodge Laboratory, University of Liverpool, P O Box 147 L69 3BX, UK
8- University of York, Dept of Physics, Helsington, York, YO1 5DD, UK
9- C.E.N.B.G, domaine du Haut Vigneau, F-33175 Gradignan Cedex
10- C.R.N, F-67037 Strasbourg Cedex

Abstract: *An experiment has been carried out using a subset of the Eurogam array to investigate the decay out of the superdeformed (SD) band in ^{194}Pb. Two new band members and a new decay pattern into the low lying states at normal deformation (ND) have been established for this band. New spectroscopic information about the level scheme at normal deformation has also been extracted.*

Over the last two years more than 20 SD bands have been found in the A=190 mass region. Almost all these bands have similar transition energies and dynamic moments of inertia and are observed down to spins I= 6-10 $\hbar$. However their excitation energies are unknown and their spins are subject to controversal discussions. This is because in all these cases the linking transitions between the SD and the ND states have not been established. For this purpose, we have investigated, during an Eurogam test experiment, the decay out of the SD band in ^{194}Pb where the lowest SD transition energy has been reported to date[1,2].

EXPERIMENTAL PROCEDURE

High spin states in ^{194}Pb were populated via the ^{36}S+^{162}Dy reaction at a beam energy of 162 MeV. The beam was provided by the Tandem accelerator of Daresbury Laboratory. A backed target of 1mg/cm^2 on 14mg/cm^2 Au has been used for two reasons. Firstly, from lifetime measurements[3] it is known that all the transitions below 420 keV in the SD band of ^{194}Pb do not exhibit any Doppler shift, hence all the "linking transitions" will be emitted by a stopped

nucleus and will appear as sharp peaks in the energy spectra. Secondly, ^{194}Pb exhibits several isomeric low-lying states with lifetimes ranging from a few to hundreds nanoseconds[4] and therefore it is crucial to stop the recoiling nuclei if the deexcitation of the SD band through an isomeric state is to be considered.
The experimental setup consisted of 30 Eurogam escape suppressed Ge detectors located at 158° (5 Ge), 134° (10), 108° (5), 86° (4) and 72° (6) with respect to the beam axis. The peak/total ratio measured with a ^{60}Co source was on average 55% (details of the Eurogam array can be found in the contribution of P Nolan).

Standard NIM electronics, the Daresbury Laboratory event manager and data acquisition system were used. During 40 hours of beam time, with the requirement that at least three Ge detectors fired, a total of 85 x 10^6 events were recorded on tape out of which 17 x 10^6 corresponded to a Ge fold $\geq$ 4. As a result of unfolding higher fold events, we obtained 136 x 10^6 events containing 3 Ge energies and 28 x 10^6 events containing 4 Ge energies. These were sorted in several 1D and 2D spectra corresponding to different gating conditions. Figure 1 shows typical spectra obtained using only quadruple and higher fold events. Spectrum (a) is a projection of all events. Spectrum (b) (resp.c,d) is constructed from all events containing at least 1 (resp.2,3) energy out of 7 selected ones (169, 213, 256, 298, 339, 457, 495 keV) in the SD band of ^{194}Pb. No background subtraction has been performed for any of these spectra. The peak/background ratio for the 379 keV SD band member increases from 0.15 in spectrum (a) to 20 in spectrum (d). This illustrates the improvement in the quality of the spectra which can be achieved with high fold Ge data by setting multigates on the energies . The most striking feature in Fig.1 is that very little background is present in spectrum (d) and therefore no background subtraction is needed for the analysis of such spectra.

RESULTS

a) The SD band in ^{194}Pb : Fig 2 displays a spectrum built with all triple and higher Ge fold events containing at least 2 energies out of six in the SD band (transitions indicated with dots on the spectrum). Besides the previously reported γ-ray transitions[1,2], two new band members at 672 keV and 705 keV have been observed. A weak transition is also visible at 739 keV and tentatively assigned to the SD band. The addition of these new data to the J^2 moment of inertia plot confirms the steady increase with rotational frequency already observed and discussed in ^{192}Hg[5].

b) The deexcitation of the SD band : From previous experiments[1,2], only the 965 keV ($2^+ \rightarrow 0^+$), 575 keV ($4^+ \rightarrow 2^+$) and 280 keV ($5^- \rightarrow 4^+$) yrast transitions were reported in coincidence with the SD band. In this work, we have identified 4 new transitions. These are the 1309 keV ($2^+_2 \rightarrow 0^+$)(see Fig.3), 595 keV ($6^+ \rightarrow 4^+$), 302 keV ($8^+ \rightarrow 6^+$) and 419 keV ($7^- \rightarrow 5^-$) low lying transitions in the level scheme[4,6] of ^{194}Pb. The intensities of these transitions (calculated for the decay of 100 SD nuclei) are given in table 1. The SD band feeds with similar probabilities all available states around spin I = 6-8 $\hbar$ while the decay of the high-lying ND states, as reported previously[4], proceeds mainly via the yrast line. In addition , we have identified several other transitions involved in the SD

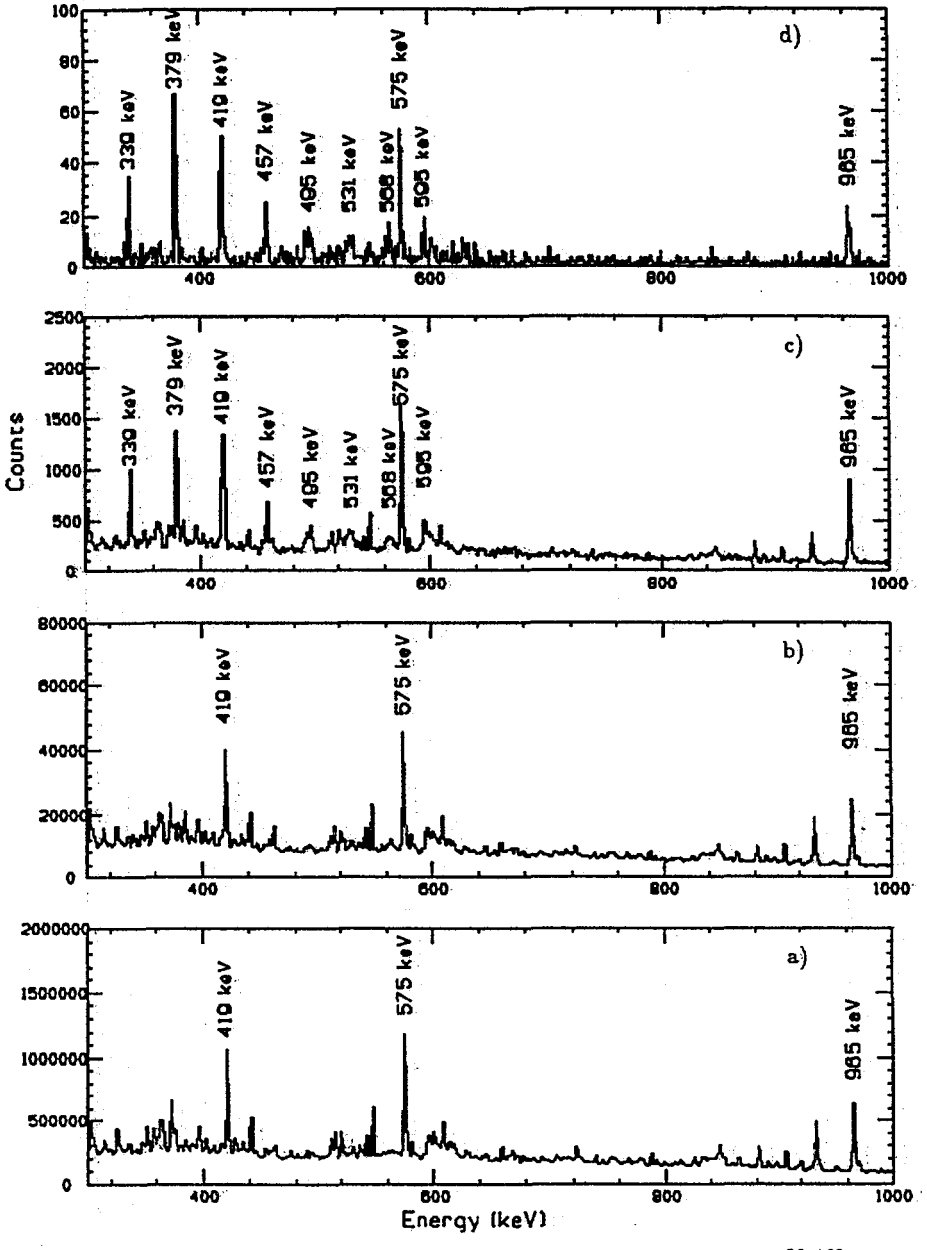

Fig.1 : Total projection (a) and 1,2,3 SD gated spectra (b,c,d) in the $S^{36}(^{162}Dy,4n)$ at E_b=162 MeV.

band decay however it has not yet been possible to place them in the level scheme.

Fig 2 :
The SD band in ^{194}Pb.

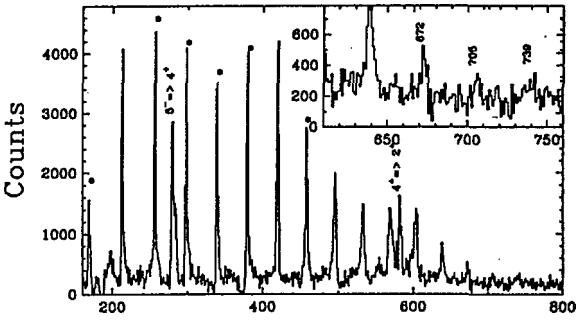

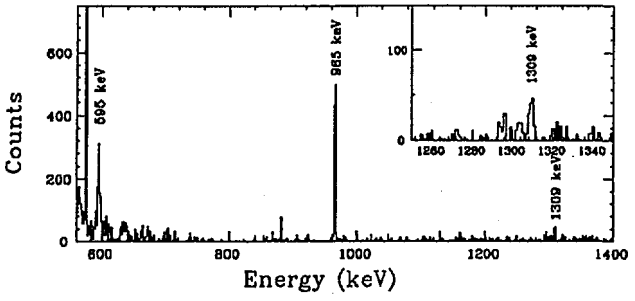

Fig 3 :
2 SD gated spectrum (background subtracted) showing the 1309 keV ($2_2^+ \rightarrow 0^+$) transition in coincidence with the SD band.

E_γ(keV)	$I_i \rightarrow I_f$	Intensity	E_γ(keV)	$I_i \rightarrow I_f$	Intensity
280	$5^- \rightarrow 4^+$	54±4	595	$6^+ \rightarrow 4^+$	32±5
302	$8^+ \rightarrow 6^+$	17±3	965	$2^+ \rightarrow 0^+$	82±4
421	$7^- \rightarrow 5^-$	18±5	1309	$2_2^+ \rightarrow 0^+$	16±3
575	$4^+ \rightarrow 2^+$	83±5			

Table 1: Intensities of low-lying transitions in ^{194}Pb in coincidence with the SD band.

c) The Δ I=1 structure : A Δ I=1 band of 14 transitions has been reported previously [4] in ^{194}Pb. However, the linking transitions between this structure and the low-lying ND states were not found. In our data, this band has a 5% intensity and we have established its missing deexcitation paths. Some of them are shown in Fig 4. The first state of this complex structure lies now at 4.3 MeV excitation energy and decays through several transitions (of about 1% intensity each) to the yrast states.

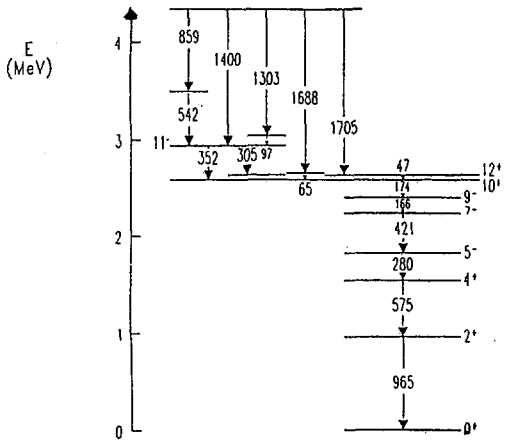

Fig 4 :
partial level scheme of ^{194}Pb.

d) Lifetime measurements in the SD band : The D.S.A.M. method has been used to determine transition quadrupole moments (Q_t) for six transitions in the SD band (420, 458, 496, 532, 569 and 602 keV) . The data were sorted into spectra representative of each of the five different angles of the Eurogam array with the condition that each event contained at least two members of a set of the six "stopped" SD transitions energies. A Monte Carlo type simulation of the recoil stopping process was performed [7]. The code Sisyphus [8] was used to fit the line shapes. Initial fitting assumed a constant Q_t as well as a constant side band quadrupole moment (Q_s) and resulted in $Q_t = 21\pm3$(eb) and $Q_s = 20\pm8$(eb) (χ^2=1.08 with 769 data points). Further fitting relaxed the constraint that all the SD states have the same Q_t and Q_s. We conclude that, within the experimental errors, Q_t is not changing with spin and has a value of about 21 eb. This is a similar conclusion to that drawn from the results of previous Q_t measurements[3,9] and is a further confirmation that the $\approx$40% rise in the dynamic moment of inertia may not be attributed to centrifugal stretching.

REFERENCES :

1- K Theine et al. Z. Phys. A336 (1990) 113 and H Hubel et al. Nucl. Phys. A520 (1990) 125
2- M J Brinkman et al. Z. Phys. A336 (1990) 115
3- P Willsau et al. Int. conf. on 4π high resolution γ-ray spectroscopy Erice 1991
4- B Fant et al. J. Phys. G. 17 (1991) 319-340
5- T. Lauritsen et al. Phys. Lett. B279 (1992) 239
6- P. Van Duppen et al. Phys. Rev. C35 (1987) 1861
7- J C Bacelar et al. Nucl. Phys. A442 (1985) 547
8- A G Smith, PhD thesis (1992), University of Manchester
9- E F Moore et al. Phys. Rev. Lett. 64 (1990) 3127

We are deeply indebted to all the physicists and engineers who are involved in the realisation of EUROGAM. We would also like to thank the Daresbury Tandem crew and B. Darlington for their assistance. F. H and N. R would like to express their gratitude to the Royal Society of London for financial support.

Digital Approach to High-Resolution Pulse Processing for Semiconductor Detectors

A. Georgiev[1] , W. Gast, A. Büchner[2] , J. Stein[3] , R.M. Lieder
Institut für Kernphysik, Forschungszentrum Jülich, D-5170 Jülich, FRG
1. Perm. address: Institute for Nuclear Research, BG-1184 Sofia, Bulgaria
2. Perm. address: Forschungszentrum Rossendorf, D-O-8101 Rossendorf, FRG
3. Target systemelectronic GmbH, D-5650 Solingen, FRG

A new design philosophy for processing signals produced by high resolution, large volume semiconductor detectors is described. These detectors, to be used in the next generation of spectrometer arrays for nuclear research (i.e. EUROBALL, etc.), present a set of problems like resolution degradation due to charge trapping and ballistic deficit effects,low resolution at a high count rate, poor long term stability, etc.. To solve these problems a new design approach has been developed. It includes three new advances:

(i) Reconstruction of the charge destribution produced by any radiation event. A new digital algoritm has been developed which incorporates as a main process a simple and fast deconvolution.

(ii) To obtain an optimal performance with respect to the energy resolution and the throughput a moving window processing has been implemented. That provides for the dead-time to peaking time ratio a value close to one, where one is the theoretical limit.

(iii) To transfer the problems from an analog to a digital world and to find for them an adequate digital solution, a totally digital signal processing system has been designed. The preamplifier signals are sampled at a very early stage, i.e. before any shaping which otherwise could introduce additional distortion of the charge distribution.

Reconstruction of the event charge

The basic elements of the semiconductor system are a detector followed by a charge sensitive preamplifier and a main (linear or shaping) amplifier. Any radiation event produces an amount of charge proportional to the absorbed energy. That charge results in a steplike waveform at the preamplifier output. In the system of our interest, i.e. a high resolution and high throughput system, preamplifiers with resistor discharge are mainly used, so the output step is followed by a decay with a very long time constant compared to the charge collection interval. The preamplifier output signal $U_p(t)$ is described by a convolution between the charge distribution function $g(t)$ and the preamplifier transfer function $f(t)$:

$$U_p(t) = \int_{-\infty}^{+\infty} g(\tau) f(t-\tau) d\tau \qquad (1)$$

If the charge collection time is instantaneous $g(t)$ becomes a delta function and the eq. (1) can be rewritten as:

$$U(t) = G f(t) \qquad (2)$$

where G is the total charge and is proportional to the absorbed energy.

The existing analog processing systems employ a differentiator, to extract G,

followed by a set of integrators. They differ mainly in respect to how the integrations are realized (i.e. active integrators, active integrator plus gated integrator, weighted sum of the integrators outputs [1], etc.). These processing sequence works correctly only when the charge function is a delta one, which has been the condition for the convolution integral (eq. 1) to become a product (eq. 2). Still it works well if the charge collection time is very short compared with any shaping time constant used in the processing channel. In the case of large coaxial Ge detectors the electron-holes drifting time cannot be neglected. The interplay between that time and the shaping constant(s) leads to a degradation of the resulution, known as ballistic deficit. The problem becomes even more severe for the detectors used for in-beam spectroscopy. The defects produced by the neutron irradiation are playing the role of trapping centers which introduce an additional delay in the charge collection time. Under such circumstances the substitution of the convolution integral (eq. 1) with eq. 2 is no more tolerable. It means that the processing sequence should be reconsidered. One natural solution is to employ a deconvolution as the first processing step. The effect of that approach is obvious - the original charge distribution of the detector signal is reconstructed from the preamplifier output signal hence a true ballistic measurement of the total charge can be performed. In this way an optimal suppression of ballistic deficit and charge trapping effects will be achieved.

To perform a deconvolution by analog means is practically impossible. Therefore, our approach involves as a first processing step the digitalization of the preamplifier signal. In the digital world the convolution integral becomes a sum:

$$U_P(it_S) = \sum_{j=0}^{\infty} g(jt_S) f(it_S - jt_S) \qquad (3)$$

Where t_S is the sampling interval, i.e. the interval of the repetetive digitizing of the preamplifier function $U_P(t)$. If the time scale is normalized to t_S , eq. 3 becomes:

$$U_P(i)\,|_{i=0}^{\infty} = \sum_{j=0}^{\infty} g(j)\ f(i-j) \qquad (4)$$

In fact, eq. 4 is a set of equations to be solved with respect to g(j). This task is difficult to be performed in real time even by a big computer, but some facts help to simplify the process. First, the deconvolution can be perform in a window with a limited size M, which reduces the number of equations in (4) to M. The assumption is correct if the time interval Mt_S is bigger than the maximum possible charge collection time. This requirement is easy to meet because under normal conditons the total distribution due to the electron-holes drifting and majority trapping delay does not exeed 1 μs even for very large Ge detectors. Second, for the energy analysis we are interested in the total charge in the window but not in its actual distribution. And third, the preamplifier transfer function f(i) is known or easy defineable in a real conditions. Even more, for the resistor-discharged preamplifiers it is exponential. Some deviation of the transfer function from the pure exponent could exist due to the nonresistivity behavior of the discharging resistor at high frequencies. But that will not influence the final result, i.e. the total amount of charge, as soon as the window size is bigger than the settling time of the preamplifier response.

These three assumptions permit to solve the equations (4) by applying a simple

recurrent procedure which employs only one multiplication-accumulation, one summation and one subtraction operation per sample. It means that only little hardware or relatively small computing power is required to run this process continuously in real time. We call the corresponding new processing unit Moving Window Deconvolver (MWD).

Noise shaping

Recently noise analyses for semiconductor detectors were carried out in the time domain [2,3]. The equivalent detector noise circuit includes two generators - for the serial and the parallel noise. The parallel noise is considered as a random sequence of delta charge pulses, and the serial - as a similar sequence followed by another one with reverse polarity. As the deconvolution in a window extracts all charges (signal and noise as well) belonging to that time interval the size of the window plays an important role. In analogy to the analog system it could be considered as the shaping constant of the digital system.

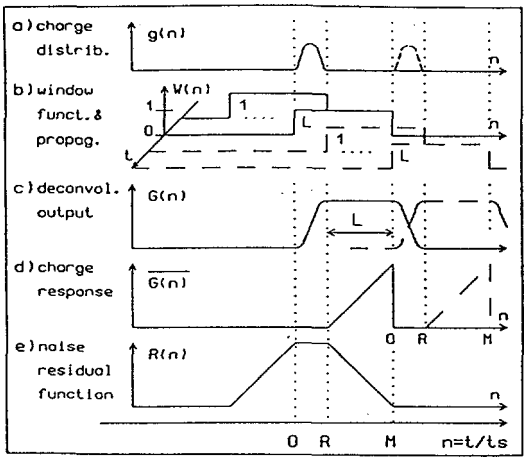

Fig. 1: Development of the charge response and the noise residual function.

If the window is by L sampling intervals bigger than the charge distribution produced by a single radiation event, then L consequent windows, shifted by one sampling interval, will cover that distribution. It means that L consequent results of the deconvolution will represents one and the same event. Taking the mean value of these L results the signal to noise ratio increases. To obtain an analytical expression for the noise contributions the time domain method has been used. On fig. 1d the step (charge) response of the system is shown produced by shifting the deconvolution window (fig. 1b) stepwise L=M-R times over the charge distribution (fig. 1a) and accumulating the results. The zero time reference corresponds to the beginning of the event and the zero to R time interval - to the maximum possible charge collection time. Shifting the delta noise charge, normalized to the event charge, from minus to plus infinity the noise residual function of the system is obtained (fig. 1e). As the residual function is a pure trapeziodal, the parallel and serial noise indexes are:

$$\overline{N_P^2} = \int [R(t)]^2 dt = \frac{2}{3} L t_s + R t_s \qquad (5a)$$

$$\overline{N_S^2} = \int [R'(t)]^2 dt = \frac{2}{L t_s} \qquad (5b)$$

Three remarks should be made in connection with eq. 5. First, due to the sampling process the residual function is not smooth but contains steps with a magnitude 1/L. It is obvious that the parallel noise index will not be affected but the serial

will increase. To eliminate that influence a low-pass filter has been placed in front of the sampling ADC with the time constant equal to one sampling interval. Second, the resolution of the sampling ADC should be higher than the signal to RMS noise ratio of the preamplifier output. If it is fulfilled the digitalization noise could be considered as a separate serial noise but the shape of the noise residual function will remain unchanged. The suppression of the digital noise will be discussed later. Third, the parallel noise has been considered as a sequence of charges with a constant rate. This assumption is not correct with respect to the low frequency interference, the detector "microphonic" effect and the temperature induced baseline fluctuations of the detector-preamplifier arrangement. To deal properly with these problems, a separate processing unit named Moving Average (MAU - see fig. 2) has been included in the system. The unit takes the results of the deconvolution in any S windows in which there are no radiation charges.

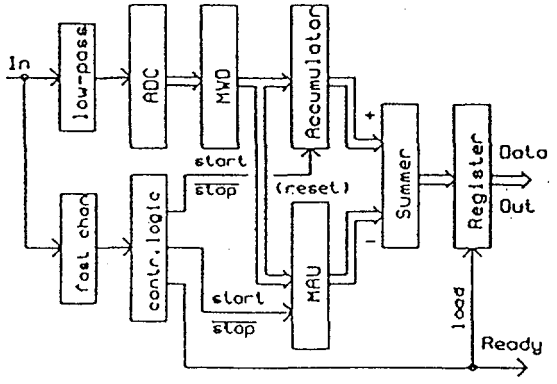

Fig. 2: Block diagram of the whole digital pulse processor.

Thus, the unit contains at any moment the mean value of the parallel noise. As this value is subtracted from the total event charge, two terms have to be added to the eqs. 5a and 5b, respectively:

$$\overline{N^2_{PP}} = \overline{N^2_P}\ \frac{L}{S}\ ; \qquad \overline{N^2_{SP}} = \overline{N^2_S}\ (\frac{L}{S})^3\ ; \qquad (5c)$$

If the number of windows S is at least 10 times bigger than the number of the charge windows L, than the impact of the MAU over the noise performance of the system is negligible, but still the unit suppresses perfectly the low frequency interferences.

The full pulse processing system is shown in a block form in fig. 2. It is best characterized by assuming 12-bit resolution, 25 MSPS sampling ADC (i.e. 40 ns sampling interval t_S), a MWD window size of 125 samples (i.e. 5 μs), 100 L-type windows (i.e. 4 μs effective shaping constant and 1 μs protection time for full charge collection) and 1000 S-type windows (i.e. 40 μs shaping constant for the low frequency interferences). The particular features of the design include:

(i) The charge collection time does not influence the resolution of the system. This comes as a result of the new design philosophy which uses a deconvolution as a first process in the signal processing channel. Fig. 3a shows the comparison of calculated peak deficits due to ballistic effects as function of the normalized charge collection time for two different analog shapers and for the new pulse processing system adjusted to equivalent effective shapings (PPADC-1). While for the Gauss shaper and the Gated Integrator no further improvement is possible because their peaking and shaping times are related, an additional free parameter of the pulse processing system, called Collection Time Protection (CTP) interval, can enhance its ballistic deficit performance even more without any degradation of

the delta-noise performance (PPADC-2). In fig. 3b the measured ballistic deficit performance of a Silena spectroscopy amplifier with 2 μs shaping is compared to our new system with the same effective shaping for various charge collection times, as simulated by pulser signals of equal amplitude but different risetimes of 20, 50, 100, 200, and 500 ns respectively.

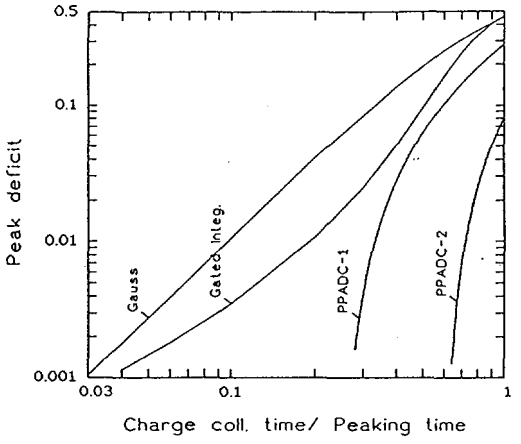

Fig. 3a: Calculated peak deficits due to ballistic effects as function of the normalized charge collection time for two analog shapers compared to the Pulse Processing ADC (see text).

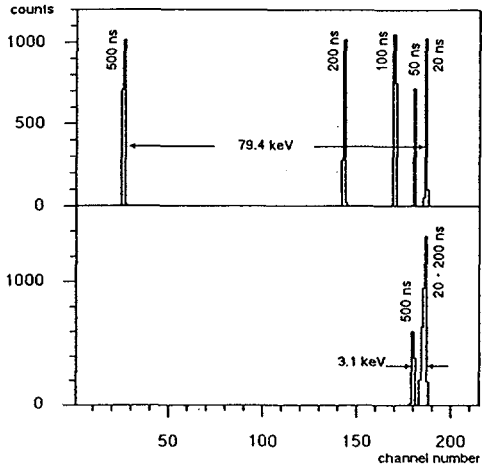

Fig. 3b: Measured ballistic deficit of the Silena 7611 L spectroscopy amplifier with 2 μs shaping for risetimes of the input signal of 20, 50, 100, 200, and 500 ns (upper spectrum) compared to that of the Pulse Processing ADC under the same conditions (lower spectrum).

(ii) The noise shaping function is a pure symmetrical triangular (in fact trapeziodal with a short flat top part). That shape is the best choise with respect to an optimal resolution - count rate performance [3,4]. As that shape cannot be realized by analog means in a pure form we consider it the second main achievement of the digital design. In the applications of our interest where the total processing time should be kept below 10 μs, i.e. where the serial noise is dominant, the slight increase of the parallel noise index, due to the flat top part of the shaper, does not contribute significantly to the overall noise performance of the system. Moreover, due to the moving window processing the dead-time is equal to the peaking time and both are defined by the size of the window. This feature combined with the pure symmetrical trapezoidal noise shaping function defines the highest possible noise-rate performance for the new system. The calculated noise-rate performance of the digital pulse processing system (PP) is compared to that of the 7^{th}-order Gauss shaper (GS) and the Gated Integrator (GI) in fig. 4a for identical effective shaping parameters. The improved countrate performance of the new system as represented by the low count losses as function of the input rate (solid lines) is not achieved at the expence of the noise performance as indicated by the comparable small increase of the Delta-Noise-Index (DNI) with increasing input rate (dashed lines). The experimentally measured resolutions of one and the same detector for the 1332 keV γ-line of ^{60}Co in fig. 4b show how in an high rate application with 10 μs total processing dead-time (TDT), i.e. 1μs shaping constant for the Gauss shaper, the conventional analog processing system employing an Silena 7611 L spectroscopy amplifier and a Silena 7423 UHS converter (2.9 keV FWHM, upper spectrum) is significantly overperformed by the new system (1.9 keV FWHM, lower spectrum). Even for shaping constants of 6 μs, optimized to

give the highest possible resolution for the given detector however leading to a huge total processing dead-time of approx. 60 μs, the analog system cannot compete (2.1 keV FWHM, middle spectrum).

(iii) The low frequency disturbances (microphonic effect, 50 Hz interference, etc.) are practically eliminated thanks to the parallel moving average channel. Due to its long shaping constant, compared with the constant of the main channel, it does not virtually change the noise performance of the system.

(iv) As the full processing is performed in a digital environment a number of advantages emerge: digital control of the processing parameters, reliability, on-line optimization and testing, etc. The final result, i.e. the radiation energy, is produced by the system directly in a digital form. As the system incorporates all necessary processing components we call it a Pulse Processing ADC (PPADC) to stress on its completeness. The utilization of the PPADC as a building unit of a new generation data acquisition system is discussed in ref. [5].

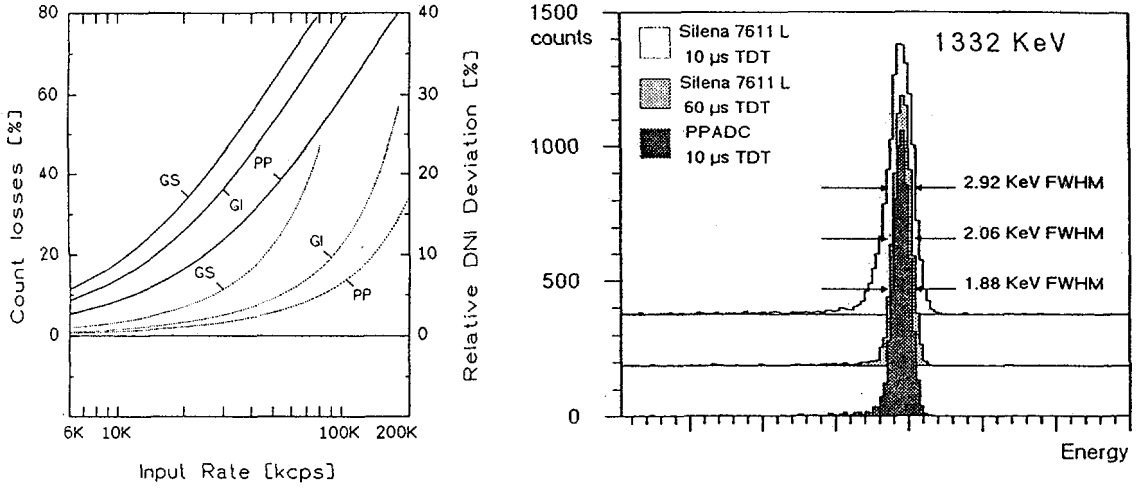

Fig. 4:

a) Comparison of the calculated noise-rate performance of the Gauss shaper (GS), the Gated Integrator (GI and the Pulse Processing system (PP)

b) Measured noise performance of the Silena 7611 L spectroscopy amplifier compared to that of the Pulse Processing ADC (PPADC) for a shaping parameter adjustment suitable for high rate applications with 10 μs total processing dead-time or 1 μs shaping constant of the Gauss shaper. As a reference the maximum achievable noise performance (resolution) of the analog Gauss shaper, obtained for 6 μs shaping is given, too. For a shaping parameter adjustment providing the same resolution the PPADC would yield an approx. 9 times higher peak-throughput.

Digital noise

The analog to digital conversion introduces two new sources of error namely quantization error and sampling clock uncertainty error (i.e. clock jitter error). These errors are very low compared with the detector parallel and serial noise, but to complete the picture of our digital processing system their contribution will be estimated. A natural way of their representation is to assume a sequence of delta noise charges with RMS amplitudes as follows:

$$(N_d)_{rms}=\frac{2^{-B}}{\sqrt{12}}\sqrt{t_s}\ ; \qquad (N_{jFS})_{rms}=\frac{1}{\sqrt{12}}\ \frac{t_s}{\tau}\ \sqrt{t_s}\ ; \qquad (6)$$

where B is the resolution of the sampling ADC in bits. The clock jitter error has a linear amplitude dependence, therefore it is estimated for the worst case, i.e. for the full scale (FS) of the system. As these errors are randomly positive or negative, they fit well to the serial noise model and their noise indexes can be determined solving the similar integral as in eq. 5b. The results are:

$$\overline{N_{dd}} = \frac{2^{-B}}{\sqrt{6L}}; \qquad \overline{(N_{dj})_{FS}} = \frac{t_s}{\tau_{pre}} \frac{1}{\sqrt{6L}}; \qquad (7)$$

The quantization noise contribution depends on the resolution of the ADC whereas the clock jitter noise depends on the sampling frequency. To estimate their contribution we will take the actual design parameters (see above) for B, L, t_s and assume a preamplifier with a 40 μs time constant. The calculated values are both below 40 ppm of the full processing scale. These results show that the digital noise has no practical influence on the performance of the system.

References:

1. F.S. Goulding et al, IEEE Trans. Nucl. Sci., NS-30, No. 1 (1983) 301.

2. M.O. Deighton, NIM 58 (1968) 201-212.

3. F.S. Goulding, D.A. Landis, IEEE Trans. Nucl. Sci., NS-29, No. 3 (1982) 1125.

4. E. Fairstein, IEEE Trans. Nucl. Sci., Vol. 37, No. 2 (1990) 382.

5. W. Gast et al., Annual report 1992, IKP-KFA Jülich.

WORKSHOP ON LARGE GAMMA-RAY DETECTOR ARRAYS

Chalk River

SESSION 5: DATA ANALYSIS

Multi-dimensional analysis of high resolution γ-ray data

S. Flibotte, U.J. Hüttmeier, P. Bednarczyk†, G. de France, B. Haas, P. Romain, Ch. Theisen, J.P. Vivien and J. Zen

Centre de Recherches Nucléaires,
IN2P3-CNRS/Université Louis Pasteur,
F-67037 Strasbourg Cedex, France

† Institute of Nuclear Physics Krakow (Poland).

High resolution γ-ray multidetectors capable of measuring high-fold coincidences with a large efficiency are presently under construction (EUROGAM, GASP, GAMMASPHERE). The future experimental progress in our understanding of nuclear structure at high spin critically depends on our ability to analyze the data in a multi-dimensional space and to resolve small photopeaks of interest from the generally large background. Development of programs to process such high-fold events is still in its infancy and only the 3-fold case has been treated so far. As a contribution to the software development associated with the EUROGAM spectrometer, we have written and tested the performances of computer codes designed to select multi-dimensional gates from 3-, 4- and 5-fold coincidence databases. The tests were performed on events generated with a Monte Carlo simulation and also on experimental data (triples) recorded with the 8π spectrometer [1] and with a preliminary version of the EUROGAM array [2].

Our principal goal was to develop appropriate software to analyze large sets of f-fold coincidence events by setting (f-1)-dimensional gates to obtain the resulting spectra as fast as possible. For technical and efficiency reasons, the classical method developed to analyze γ-γ coincidences — the slicing of a 2-dimensional 4096×4096 channel matrix — cannot be extended to higher-fold data. The memory requirement can be reduced by storing the data in the form of lists of events. In list mode, the memory needed to save the complete database is proportional to the total number of events and also to the number of bytes used to store each individual event.

The database structure and the algorithms of the programs are simplified when the analysis is restricted to one particular fold f at a time. In practice, a physical event which has triggered m Ge detectors ($m \geq f$) will be interpreted as $\binom{m}{f}$ f-fold coincidence events. The minimal number of bits required to store each event is reduced if the f-dimensional space

is divided and subdivided into smaller subspaces. All events located in a given subspace share a common f-dimensional energy offset associated with the position of the subspace and only the energy differences relative to this offset have to be stored. Furthermore, this data structure increases the speed of the slicing process since only a certain number of subspaces need to be treated for a particular gate. In order to decrease the total number of subspaces, the f energy parameters representing an event can then be stored in numerical order.

Fig. 1 shows a graphical representation of the database structure for the 2-fold case. In this example, the total dispersion on each axis is divided into four equal sections to obtain ten 2-dimensional subspaces. The term "file" will be used to denote these subspaces since they correspond to UNIX files in our implementation. Each file is further subdivided into subspaces called "lists" where the events are actually stored.

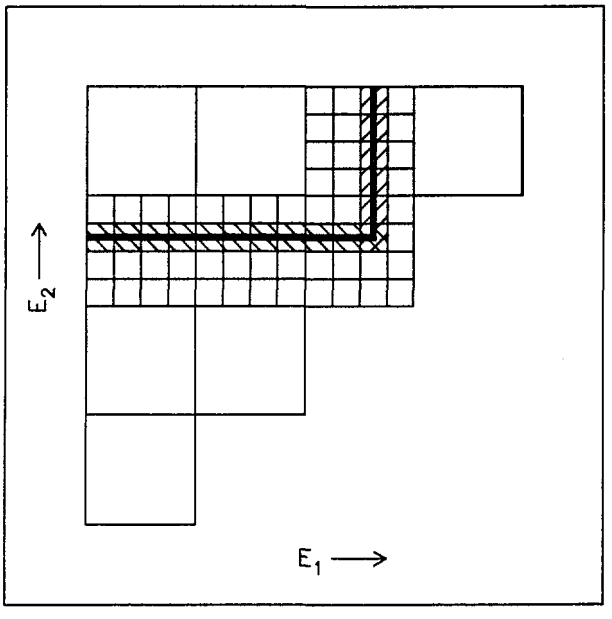

Fig. 1: Schematic representation of the database structure for a 2-fold coincidence analysis.

Besides reducing the memory requirement, the adopted database structure permits a fast slicing algorithm. An example of a slicing trajectory is indicated by the black area in Fig. 1, while the relevant lists from the relevant files are indicated by the hatched area. In this particular example, the window test is performed on the parameter E_2 for the horizontal portion of the slicing trajectory and on the parameter E_1 for the vertical one. For the list located on the diagonal, both parameters are tested. For a given event, if the tested parameter (corrected for the energy offsets)

falls inside the energy window of the gate, the channel associated with the other energy parameter is incremented in the projection histogram. With our database structure, the slicing technique can be easily generalized to perform (f-1)-dimensional gates on f-fold coincidences.

The problem of multi-dimensional gating can be artificially divided into three phases. In our implementation, an independent computer program corresponds to each different phase. The first phase program has the responsibility of reading the data recorded by the multidetector and extracting only the events corresponding to the requested fold, the events of higher-fold being "unfolded" to the studied fold. Other tests and processes such as a gain alignment can also be performed on the raw data in this initial step. The selected events are then stored on hard disk using the file structure described earlier. In the second phase, each individual file is processed to create the list structure. The third step corresponds to the slicing procedure. The program reads a gate file created by the user and extracts the resulting spectrum from the database. This third phase can be repeated as many times as desired with different gate files.

The total number of channels per axis and the width of each file and list are selected by the user. The optimal set of parameters depends on the total number of events to be processed and also on the available hardware configuration. The values chosen in the present work are presented in Table 1 for 3-, 4- and 5-fold data analysis. Real experimental events are usually recorded on magnetic tape using two bytes per energy parameter. A data compression factor of up to four is achieved with the adopted set of parameters given in Table 1.

Table 1. Total number of channels per axis (C_T) and width in channels of each file (C_F) and each list (C_L) used to analyze f-fold events.

f	C_T	C_F	C_L
3	4096	128	16
4	2048	128	16
5	2048	256	64

All the programs were written in C++ [3], an objet-oriented programming language. Programs were developed and tested on a single-processor Sun SPARC-2 with a performance of about 28 MIPS and 6.2 Mflops. The system was equipped with a 1.2 Gb Seagate hard disk with a mean access time of 15 ms and a SCSI-2 interface with a tested data transfer rate of about 4 Mb/s for reading and 500 kb/s for writing operations. In the computer codes, input/ouput operations are performed with functions

from the standard Sun C library [4]. The resulting spectra are stored in a format compatible with GPSI [5], the spectral analysis program used in Strasbourg. The software presently handles data written in 8π [6] and in Daresbury formats, and is easily modified for other formats.

Presently, there is no existing experimental data set large enough to provide high statistics test of our analysis programs for a fold larger than three. To get around this situation, f-fold events were generated using a Monte Carlo technique. The Monte Carlo simulation has the advantage of giving a better control over the data set characteristics, which facilitates programming error tracking and the comparison of the software performance between different folds. A superdeformed (SD) generator was selected for 5% of the events. The software performance was tested by gating on SD transitions to study our ability to isolate an SD spectrum from the large background simulated by a normal-deformed generator.

The CPU time required to execute the first two phases described earlier are presented in Table 2 for a data set comprising 1.5×10^8 events. The phase I CPU time is proportional to the number of generated events. In an analysis of real experimental data, this time is dominated by the data transfer rate of the Exabyte tape drive. The time required to execute the second phase increases less rapidly with the number of events. For example, the phase II CPU time for 4-fold data is roughly proportional to the cube root of the number of events processed, at least in the studied range (5 to 150 million events).

Table 2. CPU times required to generate and compress 1.5×10^8 events. The reported CPU times include both the user time and the system time used [4].

Fold	Phase I (min.)	Phase II (min.)	Total (min.)
3	369	44	413
4	481	40	521
5	602	164	766

Superdeformed band spectra were obtained by summing all combinations of multi-dimensional gates placed on 17 SD transitions. The average width of the selected energy windows was equal to 6 keV and the same set of energy windows was used for every studied fold. The slicing CPU time presented in Table 3 does not strongly depend on the fold and it stays within very acceptable values. This time depends on the specific gate file used and also on the number of events present in the database. For the same number of events in the database, the number of counts in a specific photopeak in the final SD spectrum decreases by a factor of $\sim$6 by going

from a given fold to the next higher one. It may be very important to know this factor since it could help to evaluate the beam time required to perform some specific high-spin experiments with the new generation of multidetectors.

Table 3. Slicing program statistics as a function of the fold when 17 superdeformed transitions are selected. The total number of gate combinations are presented together with the CPU time (user + system [4]) required for the slicing procedure. Databases containing 3×10^8 events were processed except for the 5-fold case where two data sets of 1.5×10^8 events each were used.

fold	number of gates	CPU time (sec) total	per gate
3	136	386	2.84
4	680	165	0.24
5	2380	2×456	2×0.19

In the present work, we have developed algorithms to analyze high-fold events in a multi-dimensional space. The algorithms were implemented for 3-, 4- and 5-fold coincidences. The performances of the programs were tested with large data sets generated with a Monte Carlo simulation. The slicing process requires typically less than one second of CPU time per gate on a Sun SPARC-2. The needed hard disk storage space was reduced to four bits per energy parameter for 3- and 4-fold events and down to 6 bits in the 5-fold case. More details can be found in ref. [7].

References

[1] B. Haas *et al.*, Phys. Rev. C **42** (1990) R1817.

[2] C.W. Beausang *et al.*, this conference.

[3] B. Stroustrup, The C++ Programming Language, Addison-Wesley, Reading, Massachusetts, (1986).

[4] SunOS Reference Manual, Sun Microsystems Inc., Mountain View, California, (1988).

[5] J. Zen and P. Wagner, unpublished.

[6] J.P. Martin *et al.*, Nucl. Instr. and Meth. **A257** (1987) 301.

[7] S. Flibotte *et al.*, Nucl. Instr. and Meth. A, in press; preprint CRN 92-22.

ESCL8R AND LEVIT8R - INTERACTIVE GRAPHICAL ANALYSIS OF γ-γ AND γ-γ-γ COINCIDENCE DATA FOR LEVEL SCHEMES

D.C. RADFORD
AECL Research, Chalk River Laboratories,
Chalk River, Ontario, Canada K0J 1J0

Abstract: The extraction of complete and consistent nuclear level schemes from high-fold coincidence data will require intelligent computer programs. These will need to present the relevant data in an easily assimilated manner, keep track of all γ-ray assignments and expected coincidence intensities, and quickly find significant discrepancies between a proposed level scheme and the data. Some steps in this direction have been made at Chalk River. The programs ESCL8R and LEVIT8R, for analysis of two-fold and three-fold data sets respectively, allow fast and easy inspection of the data, and compare the results to expectations calculated on the basis of a proposed level scheme. Least-squares fits directly to the 2D and/or 3D data, with the intensities and energies of the level scheme transitions as parameters, allow fast and easy extraction of the optimum physics results.

1. Introduction

The advent of large γ-ray detector arrays such as EUROGAM and GAMMASPHERE will soon provide us with high-fold Ge coincidence data in useful quantities. It may be anticipated that our lack of new techniques to analyse such data sets in general, powerful ways will form a major obstacle to extracting all of the interesting physics in an expeditious and reliable fashion. The analysis of specific experiments, such as the study of known superdeformed bands and damping widths, should present few technical problems; more general analysis, however, may require substantial enhancements to our present techniques.

General analysis of high-fold coincidence data to extract complete and consistent nuclear level schemes will require intelligent computer programs to extract the physically interesting numbers from the raw data and present them to the physicist in an easily assimilated manner, to keep track of all γ-ray assignments and expected coincidence intensities, and to quickly find and report major discrepancies between a proposed level scheme and the data so that they can be understood and corrected.

A few first steps in this direction have been made previously at Chalk River; for example, double- and triple-coincidence data sets can be fitted and all relevant coincidence intensities extracted, stored in data bases, inspected and compared to expected values with programs such as LF8R [1]). However, this program is non-graphical, i.e. it presents the data to the user numerically. This paper reports on the development of new *graphical* analysis programs which meet many of the above criteria.

2. Level Scheme Files

In order to achieve the goals of having a program keep track of γ-ray assignments and compare the observed results with those expected on the basis of a proposed level scheme, we have developed a format for files to describe level schemes, together with a set of routines to decode such files. These were then interfaced with a routine, adapted from a program

provided by the National Nuclear Data Center, to calculate internal conversion coefficients from the Hager-Seltzer tables [2]). Additional routines were written to modify and rewrite the files, to draw and edit level scheme figures, and to check intensity balances and energy sums.

By incorporating these level-scheme file routines, an analysis program can now calculate predicted gate spectra to be compared to the observed spectra. That is, the program can work backwards from the proposed level scheme, and attempt to reproduce the observed γ-γ matrix (or γ-γ-γ cube), on the basis of the proposed intensities, branching ratios and conversion coefficients. It can also modify the level scheme file, and fit the γ-ray energies and intensities directly to the 2D (or 3D) data, to improve the agreement with the observed results.

A level scheme file to be used with such a program should include data on all bands or levels observed with significant intensity in the matrix, whether or not they are assigned to the principal isotope being studied, so that the program can correctly reproduce contaminated coincidence gates.

3. Program ESCL8R

ESCL8R is a new graphical γ-γ data-analysis program for the extraction of level schemes. It allows fast and easy inspection and fitting of the γ-γ matrix, making use of parameterized values of the peak shape, peak width and detector efficiency and energy calibrations. It makes use of an algorithm for two-dimensional background subtraction similar to that of ref. 3, but with several significant improvements. It also reads and updates a level scheme information file as discussed above, specifying a proposed level scheme which is modified continually as the analysis of a data set proceeds. Least-squares fits to the matrix may be performed to extract the optimum energies and intensities of transitions in the level scheme, with fitting of up to 500 parameters simultaneously.

The data set used by ESCL8R is a 2k x 2k-channel raw (symmetrized) γ-γ matrix, with the two-dimensional background defined as the sum of one-dimensional spectrum cross-products [3]). The full background is subtracted from each gate as it is read from the matrix. This is done to allow the program to keep track of the uncertainties on the counts-per-channel in the gate spectrum.

The user is able to take and view a gate simply by typing the energy required. The program sets a gate centered at that energy, with a default width of one FWHM. Logical and arithmetic combinations of gates can also be taken just as easily. Lists of gates can be created, or read from a file, and the sum of such gate lists calculated with a single command. Alternatively, gates can be placed by using the graphics cursor to specify the limiting channels of the gate.

As each gate is taken, the program reports all level-scheme transitions included between the limiting energies. It displays the observed and calculated spectra, the difference between them, and the residual spectrum (i.e., the difference spectrum divided by the experimental uncertainty). In this way, it is now easy for the user to find places where the proposed level scheme fails to reproduce the observed results. An example of an ESCL8R graphics display, showing the sum of a set of gates placed on the ground band of ^{157}Ho [4]), is approximately reproduced in fig. 1.

Since the level scheme file is also interfaced with routines to draw and edit level scheme figures, these may also be generated quickly and easily. This has the added advantage of facilitating the use of such figures for documentation of an ongoing analysis.

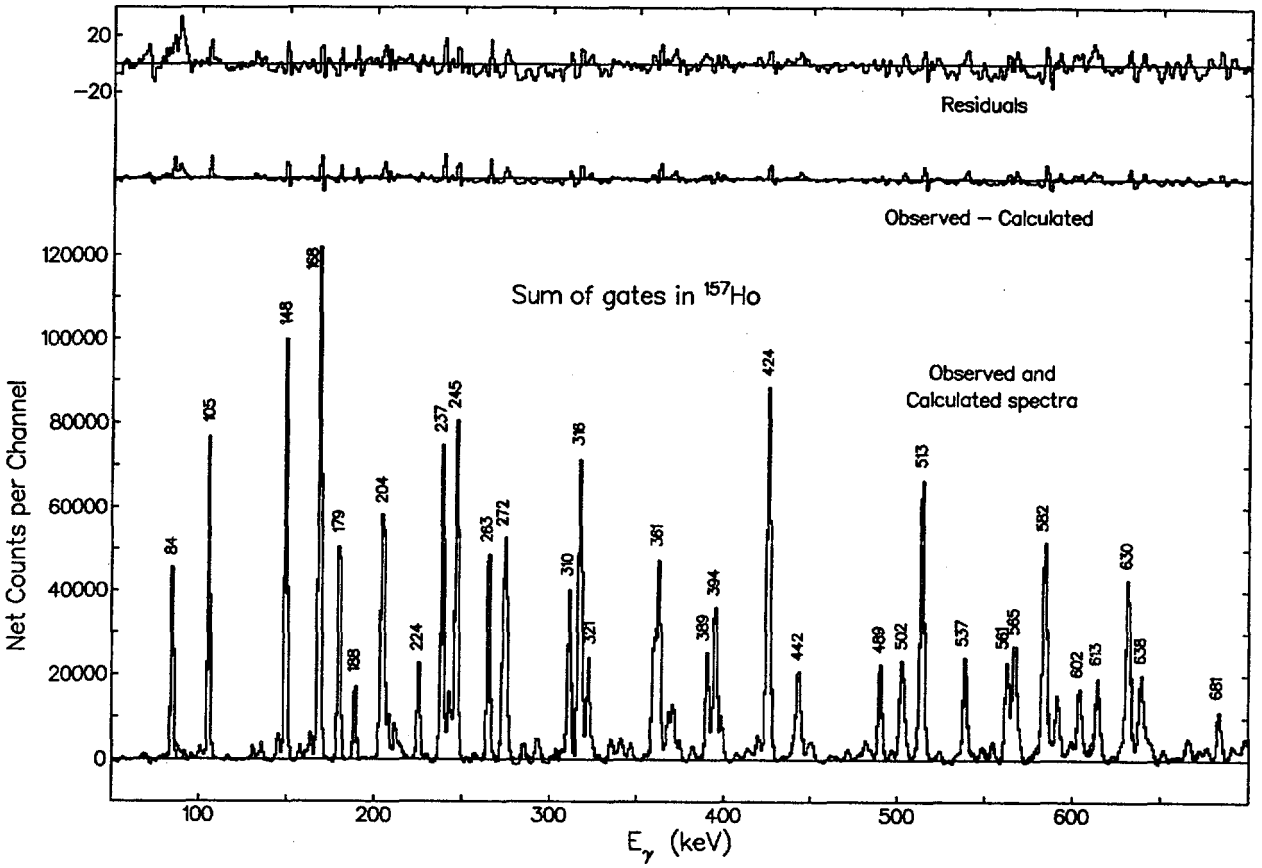

Figure 1. Partial spectrum from a sum of background-subtracted gates set on the ground band of ^{157}Ho. Both the observed and calculated spectra are shown in the lower portion; the upper portion shows the difference between these two spectra and the residuals (see text.)

4. Program LEVIT8R

LEVIT8R is a new program for graphical analysis of γ-γ-γ data; essentially, it is a three-dimensional version of ESCL8R. It uses the same type of parameterized peak shape, peak width, and detector efficiency and energy calibrations, and an algorithm for three-dimensional background subtraction. It also reads and updates the same type of level scheme file, and uses it to calculate expected gate spectra.

One major difference from ESCL8R is that LEVIT8R allows use of non-linear gain (i.e. an energy-dependent dispersion) for storage of the experimental data. This is usually set up to yield a constant FWHM (in channels) of the peaks, independent of energy. This approach produces a considerable saving in disk storage required for the data, especially for high-fold data, without sacrificing usable resolution at low energies. When such non-linear spectra are displayed, the counts-per-keV (rather than the more conventional counts-per-channel) are shown, as a function of energy (rather than channel number); that is, the spectra are displayed linearly with energy, so that the displayed bin width is energy-dependent.

The use of such an energy-dependent dispersion is illustrated in fig. 2, for a typical heavy-ion fusion-evaporation reaction with a detector array such as the 8π spectrometer. In this example, a constant FWHM of two channels is used, and the non-linear gain saves a factor of 2.2 in data storage space for each dimension, over the range 0 to 2000 keV. For the triples data, this amounts to a reduction in the required storage space by a factor of 11.

Again, the data set used by LEVIT8R is the raw γ-γ-γ cube. One-half of the full cube is stored; although only one sixth of the cube contains unique data, three times that space is used in order to speed up disk access. The three-dimensional background is subtracted from each gate as it is read from the cube, allowing the program to keep track of the uncertainties on the counts-per-channel in the gate spectrum.

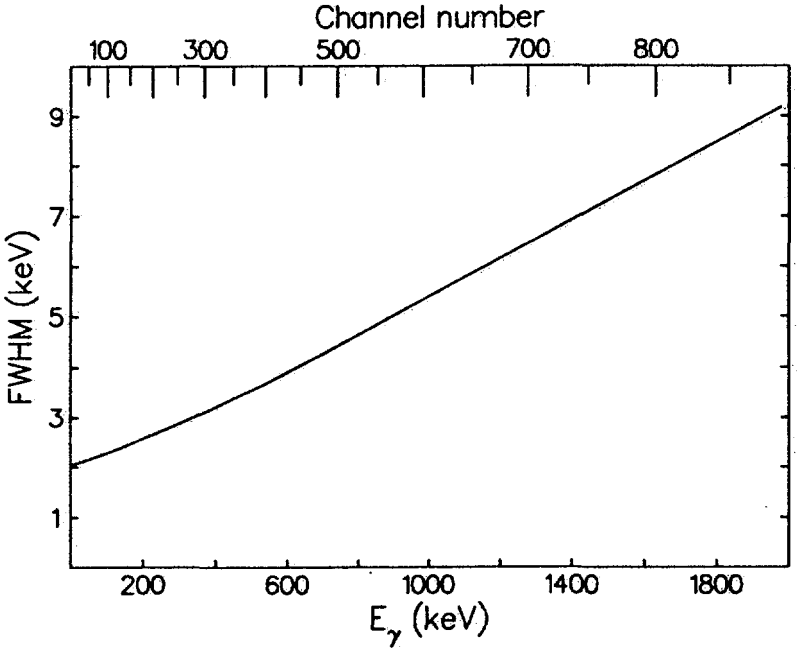

Figure 2. Example of the use of an energy-dependent dispersion. In this example, the energy dispersion is 1.0 keV/ch. at low energies and 4.5 keV/ch at 2 MeV, to give a constant FWHM of 2.0 channels.

By analogy to ESCL8R, the user is able to take and view a gate on the two-dimensional projection simply by typing the energy of the required gate. A double-gate on the triples set requires the typing of two energies; the program uses both gates to generate the one-dimensional spectrum. The default gate width is one FWHM; different widths are easily specified. Combinations of gates can also be taken just as easily; for example, the sum of all pairs of gates taken from two gate lists can be generated with a single command. As with ESCL8R, least-squares fits to the data set may be performed to extract the optimum energies and intensities of transitions in the level scheme. At present, the fitting may only be done to the two-dimensional projection; extensions to allow fitting of the full three-dimensional data set, or to selected two-dimensional subsets, are planned.

An example of a LEVIT8R display, showing the sum of double-gates placed on the yrast band of ^{154}Dy, is reproduced in fig. 3.

5. Conclusion

Programs ESCL8R and LEVIT8R, for interactive graphical analysis of two-fold and three-fold data respectively, allow fast and easy inspection of the data, and compare the results to expectations calculated on the basis of a proposed level scheme. In this way, it is now easy for the user to find places where the proposed level scheme fails to reproduce the observed results. In addition, the book-keeping of the analysis is simplified; it is no longer necessary to memorize the entire level scheme as is typically done when using more

conventional analysis techniques. Consistency checks on the level scheme (such as energy sums and intensity balances) can also be readily performed.

Least-squares fits directly to the 2D and/or 3D data, with the intensities and energies of the level scheme transitions as parameters, allow expeditious extraction of the optimum physics results from the data. Since the level scheme file is also interfaced with routines to draw and edit level scheme figures, these may be generated quickly and easily, as can tables of the level and transition data. This approach considerably enhances our capabilities for detailed and reliable data analysis, especially of higher-fold data sets.

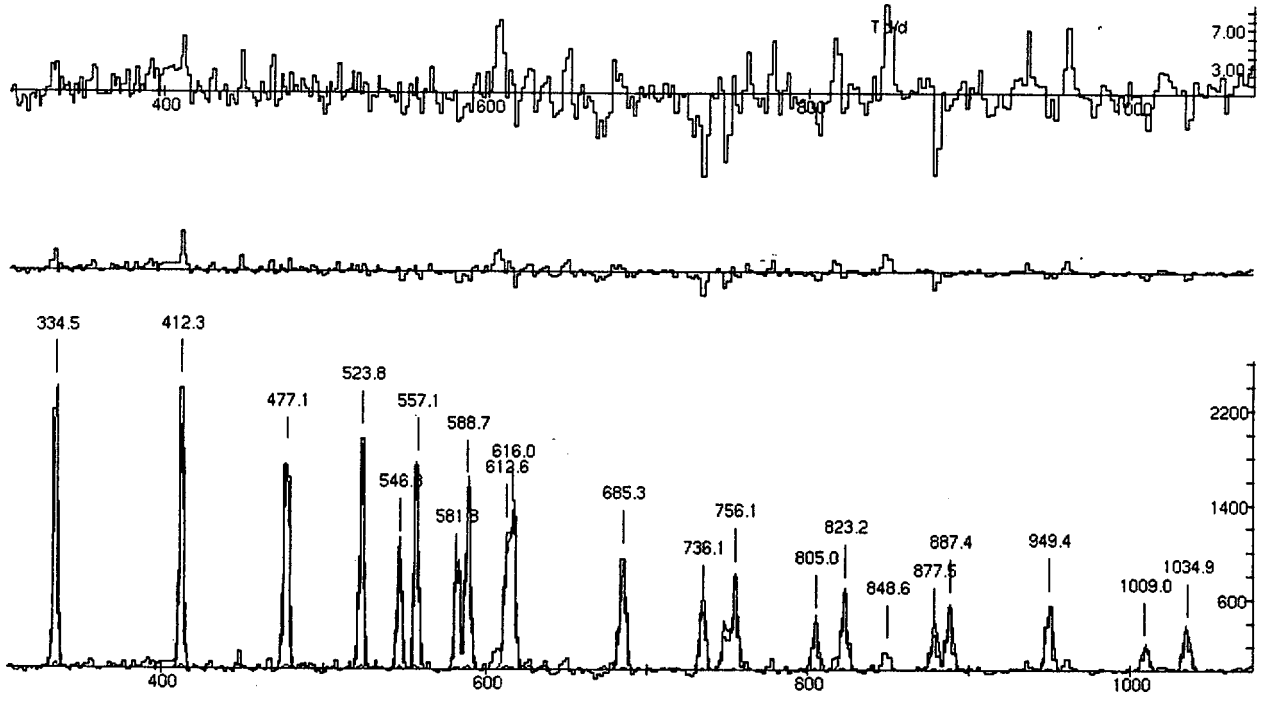

Figure 3. Example of a sum of two-dimensional gates on a triples data set, from the program LEVIT8R. Both the observed and calculated spectra are shown in the lower portion; the upper portion shows the difference between these two spectra and the residuals (see text.)

References

1) D.C. Radford, Proc. 1989 Int. Nucl. Phys. Conf., São Paulo, Brazil, August 1989
2) R.S. Hager and E.C. Seltzer, Nucl. Data Tables A4 (1968) 1
3) G. Palameta and J.C. Waddington, Nucl. Instr. and Meth. **A234** (1985) 476
4) D.C. Radford et al., Nucl. Phys. (in press)

A Lossless One–Pass Sorting Algorithm for Symmetric Three–Dimensional Gamma–Ray Data Sets

M. J. Brinkman, D. R. Manatt, J. A. Becker and E. A. Henry
Lawrence Livermore National Laboratory, Livermore, California 94550

Abstract: An algorithm for three–dimensional sorting and storing of the large data sets expected from the next generation of large gamma–ray detector arrays (i.e., EUROGAM, GAMMASPHERE) is presented. The algorithm allows the storage of realistic data sets on standard mass storage media. A discussion of an efficient implementation of the algorithm is provided with a proposed technique for exploiting its inherently parallel nature.

I. Introduction

The next generation of large Compton–suppressed germanium detector arrays for discrete gamma–ray spectroscopic studies (e.g., EUROGAM, GAMMASPHERE) are currently being constructed for precision energy determinations. These arrays will provide an unprecedented volume of high–multiplicity (i.e., three– and higher–fold) gamma–ray event data. Analysis of the higher–fold events in such data sets will take advantage of existing techniques, such as setting gates on known transitions in coincidence with the transitions of interest, and requires the development of new techniques designed to work in three– and higher–dimensionality event spaces. All of these techniques require the ability to sort and store the data in three– and higher–dimensional event spaces for efficient implementation. We will detail a new algorithm for sorting these data sets into three–dimensional event spaces, designed to run on computers available to nuclear structure experimentalists.

There are four goals of an ideal sorting algorithm: 1) The algorithm *must* be capable of handling realistic data sets. The next generation of large gamma–ray detector arrays will routinely provide multiples of 10^9 three– and higher–multiplicity events per experiment. 2) The sorted data *must* be small enough for practical storage. Ideally, the sorted data would fit within the 2 GB limit of available hard disks, and at maximum require no more than the 5 GB available on 8–mm tape cartridges. 3) The sort *must* be achievable within a reasonable amount of time—on the order of the time required to collect the data or less. 4) The sorting *should*, if possible, include all data over the entire useful dynamic range of the detectors, typically 4096 channels, without loss of information.

These goals, however, are difficult to achieve. In particular, the goal of a lossless sort must be reconciled with the practical storage constraint. A three–fold event can, in this case, take on any of 4096^3 possible combinations of three gamma–ray energies. If a byte of memory is required for hold the intensity for each of these combinations, one would require 64 GB of total storage. By symmetrizing the data (i.e., storing only the unique combinations of three gamma–ray energies) and requiring a single byte of storage per position, one can reduce the total storage required to ~11.5 GB, which far exceeds the practical limit of available storage (see figure 1). Thus, an ideal algorithm must be capable of reducing the required storage beyond what is can be achieved through the use of a simple symmetrized cube structure.

In the following sections we discuss sorting algorithms currently used for three–dimensional data sets. This is followed by a presentation of a new algorithm, the bitstream merge algorithm, for sorting data into symmetric three–dimensional event spaces. Results from our initial

implementation are discussed with regard to the four goals of an ideal sorting algorithm proposed above. We conclude with a brief look at extending this algorithm to parallel architectures.

II. Current Sorting Algorithms

Current sorting algorithms can be divided into three groups. The first of these is a list mode recording of the raw event data, in which one creates a list of the three gamma–ray energies which comprise the event. This list is then sorted and used in future data analysis [Ju90,Fl92]. The storage requirement for this sorting algorithm increases linearly with the number of events (see figure 1). This is an effective sorting strategy for data collected using the current generation of arrays, where data sets are on the order of 10^8 three– and higher–fold events in a typical experiment. It is not clear, however, that these methods can be readily extended to handle data sets containing multiples of 10^9 three–fold events that are expected from the next generation of large gamma–ray detector arrays.

A second set of sorting algorithms takes advantage of the fact that the energy resolution from large gamma–ray detector arrays is less than the energy resolution available from the ADC's. One can sum a number of adjacent channels commensurate with the energy resolution of the array and store the result [Ra92]. This method has a marked advantage when it comes to direct analysis in three–dimensional event space, since in addition to reducing the storage required, it also reduces the number of positions in the three–dimensional space that must be visited during analysis. This allows exponential improvement in the speed of the analysis programs. This process, however, sacrifices some of the hard won improvements in the energy resolution of the array and reduces the statistical quality of the data. Furthermore, traditional analysis techniques, such as gating on coincident transitions, depend on the ability to separate contributions from gamma–rays with nearly identical energies, which is sacrificed to a certain extent by the summing algorithms. Thus, while these sorting techniques provide a substantial advantage for direct analysis in three–dimensions, it is at a cost of reducing the information contained in data.

The final set of sorting methods discussed here involves the application of data compression techniques to the symmetrized cube to reduce the storage required. The symmetrized cubes are not amenable to standard data compression algorithms, however, due to the Poisson statistical nature of gamma–ray coincidence data. Mika and coworkers [Mi90] have presented a simple compression algorithm for nuclear spectrum files, which uses adaptive channel sizes in multiples of four–bit "nibbles" to store the intensity values. This method is readily extensible to symmetrized three–dimensional data sets. W. Urban has implemented such an algorithm for use with EUROGAM data sets [Be92]. This algorithm approximately halves the required storage (see figure 1).

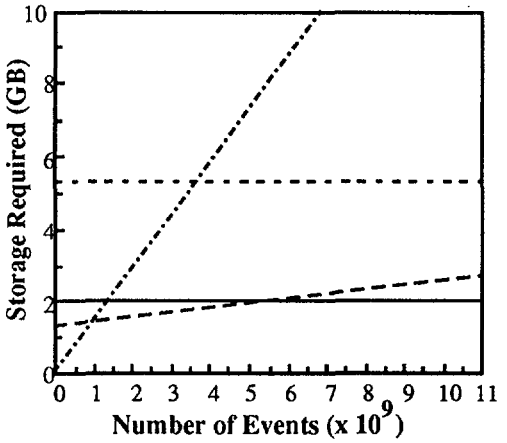

Figure 1. The storage required in GB's for (4096 channel)^3 cubes using list mode techniques assuming 4 bits per energy (dot-dashed line) [Fl92], the compressed cube assuming 4 bits per bin (dotted line) [Mi90], and the BSM algorithm (dashed line) as a function of the number of events. The solid line is the 2 GB limit of available hard disks.

III. The Bitstream Merge Algorithm

The Bitstream Merge Algorithm (BSM) sorts the three–fold event data into a consecutive string of bits (i.e., the bitstream). The 0–bits are used as bin separators, while the number of 1–bits preceding a given 0–bit denote the intensity at that position. Thus, the BSM reduces to a simple double counting algorithm.

The BSM has six steps: 1) Cube initialization, 2) Event decomposition, 3) Symmetrization of the event, 4) Indexing each event and appending to a list, 5) Sorting the index list, and 6) Merging the index list into the existing bitstream. The initialization of the cube starts by allocating one bit per bin, N_n, given by

$$N_n = \frac{n(n+1)(n+2)}{6} \qquad (1)$$

with n the length of a side of the cube in channels (typically 4096). The value of each bit is set equal to 0. This string serves as the initial bitstream, and the 0–bits are retained throughout the sorting procedure as bin separators.

Each event of the raw data stream is broken out into its component three–fold events. Each of these three–fold combinations is symmetrized such that $E_{\gamma 1} \leq E_{\gamma 2} \leq E_{\gamma 3}$, and an index value is assigned to each event using

$$I = \frac{E_{\gamma 3}(E_{\gamma 3}+1)(E_{\gamma 3}+2)}{6} + \frac{E_{\gamma 2}(E_{\gamma 2}+1)}{2} + E_{\gamma 1} \qquad (2),$$

which is the position in the symmetrized cube for the event. These index values are appended to an output buffer. Once the output buffer is filled the index values are sorted in ascending order, and the sorted list of index values, I_i, is passed to a program which merges it into the existing bitstream.

The BSM reads the existing data bitstream until the I_0^{th} 0–bit is found, when a single 1–bit is inserted in front of the I_0^{th} 0–bit, thereby increasing the length of the bitstream by one bit. The position in the index list is incremented, and the process continues until the index list is exhausted. An example for a four–fold event is provided in figure 2.

IV. Implementation of the Bitstream Merge Algorithm

The simple BSM presented above is extremely inefficient, with multiple instances of single bit insertions followed by the duplication of the remaining bitstream. Combining adjacent bits into bytes significantly improves the efficiency in two ways. 1) The output byte that resulting from a single bit insertion is uniquely defined by the input byte and the position of the inserted bit. Multiple repetitions of the bit manipulations can be eliminated by creating a lookup table containing the 256 distinct bit patterns in a byte created following in the 1–bit insertion process. 2) Each event adds a single bit to the length of the stream and moves all following bits one position to the right, "pushing" the rightmost bit off the input byte. Every eight bits pushed off the input stream forms a new byte, which can be treated as the next byte in the input stream, avoiding the costly duplication step.

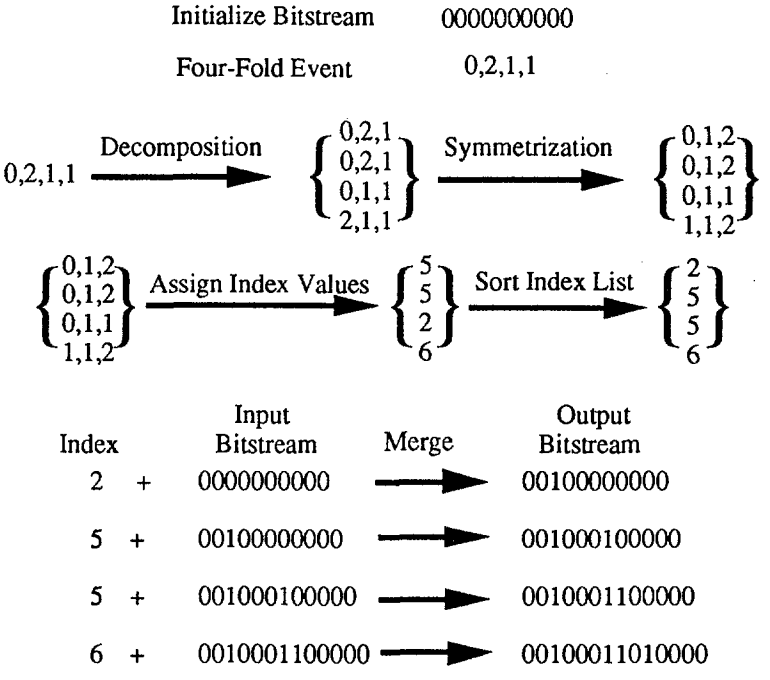

Figure 2: A sample bitstream merge for four–fold event with energies {0, 2, 1, 1} using a (3 channel)^3 symmetric cube. The bitstream is initialized with 10 zero valued bits (see Eq. 1). The four–fold event is decomposed to four three–fold events, and symmetrized. The symmetrized events are assigned an index value, and the index list is sorted. The sorted list is passed to a program which merges the index values into the bitstream.

The BSM, modified as above, is acceptably fast. In figure 3, the BSM sorting rate compared to the streaming speed of a 2 GB 8-mm tape, is presented for symmetric cubes of three different sizes. The BSM rate compares favorably with the streaming speed of the tape for symmetrized cubes as large as (1024 channels)^3.

The storage for the symmetric (4096 channel)^3 cube created with the BSM is given by

$$S = (N_{4096} + n_{events}) / 8 \qquad (3)$$

with S the memory required in bytes, N_{4096} defined in Eq. 1, and n_{events} the number of events in the data set. In figure 1, a comparison of the storage requirements for a symmetrized (4096 channel)^3 cube created using the BSM and other algorithms, as a function of the n_{events}, is given. For data sets with $1 \times 10^9 \leq n_{events} \leq 3\ N_{4096}$, the BSM is the most efficient algorithm in terms of storage required. List mode recording and the compressed cube are more efficient for smaller and larger data sets, respectively. Furthermore, for the $n_{events} \leq 5 \times 10^9$ expected from typical experiments at the next generation of large gamma–ray detector arrays, the BSM sorted symmetric (4096 channel)^3 cube meets the 2 GB storage goal for an ideal sort.

V. Future Extensions

Currently, sorting a symmetric (4096 channel)^3 cube is markedly slower than the streaming speed of the 2 GB 8–mm tape, as shown in figure 3. Furthermore, the total number of positions in a symmetric (4096 channel)^3 cube is greater than 2^{32}, which means integer arithmetic cannot

be used in the merging portion of the BSM. Both problems are alleviated by extending the algorithm to incorporate parallel processing techniques.

The original bitstream can be divided into smaller segments, each updated by a separate process which receives only the sorted index lists appropriate to that segment of the bitstream. This domain decomposition approach is a standard parallel processing technique. A relatively small number of independent processors are required, each with a relatively large amount of dedicated memory. Making the BSM algorithm amenable to a distributed workstation environment.

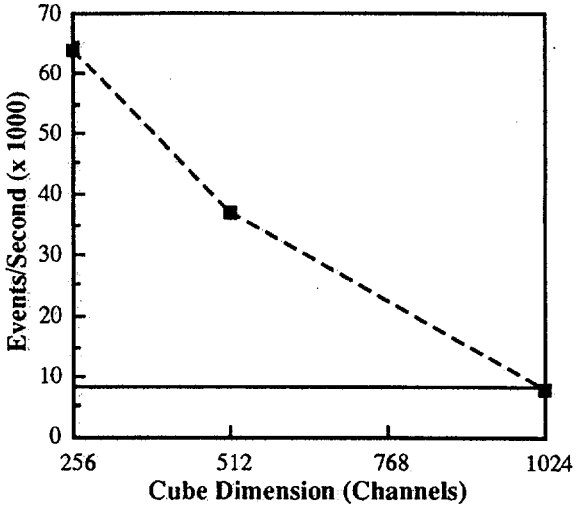

Figure 3: BSM sorting rate (dashed line) versus 2 GB 8–mm tape streaming speed. These results were achieved on a dual–processor Model 5 Solbourne computer with 256 MB of RAM.

We have successfully implemented a simple parallel version of the bitstream merge algorithm on a dual processor machine (see the caption of figure 3). A symmetrized (2048 channel)^3 cube was divided into 64 separate segments. Although this provided a proof in principle for the parallel processing extensions described above, we have yet to test the BSM in the distributed workstation environment required for marked increases in sorting speed.

*This work is supported by the U. S. Department of Energy under contract W-7405-ENG-48.

Be92 C. W. Beausang, private communication (this workshop).

Fl92 S. Flibotte, U. J. Hüttmeier, G. de France, B. Haas, P. Romain, Ch. Theisen, J. P. Vivien, and J. Zen, "Multi–dimensional Analysis of High Resolution γ–Ray Data", presented at the Workshop on Large Gamma–Ray Detector Arrays, Chalk River, Canada, May 22–23, 1992.

Ju90 J. Junikka and A. Lampinen, *Nucl. Inst. Meth.* **A292** (1990) 677.

Mi90 J. F. Mika, L. J. Martin, and P. N. Martin, *Nucl. Inst. Meth.* **A295** (1990) 276.

Ra92 D. C. Radford, "Interactive Graphical Analysis for Level Schemes", presented at the Workshop on Large Gamma–Ray Detector Arrays, Chalk River, Canada, May 22–23, 1992.

CUBEAID - AN INTERACTIVE METHOD OF QUICKLY ANALYZING 3-DIMENSIONAL GAMMA-RAY DATA SETS

J.A. Kuehner, J.C. Waddington and D. Prévost,
McMaster University

With the advent of very high efficiency gamma-ray detector arrays capable of producing significant 4- and 5-fold data a new challenge will be to develop appropriate data analysis techniques. One route may be to exploit the relatively fast analysis possible using 3D analysis of sorted higher-fold data as can be done using the CubeAid software running on a PC. This paper describes some of the capabilities of CubeAid.

The main idea is to construct and use a 3D array (a cube) of triples data of dimension suitable to the capabilities of a PC using VGA mode or higher. So far we have used a cube of edge size 640 and typically 2 or 3 keV per channel. In order both to make data extraction fast and to reduce disk space we have used a symmetrized 1/2 cube with the depth dimension having been compressed. In making this cube we first sort into a symmetrized 1/6 cube from tape to our VAX harddisk. Using 16-bit data this requires 1/6 x 640 x 640 x 640 x 2 = 87.4 Mbytes of storage. We then download to the PC where we convert the 1/6 cube to a compressed 1/2 cube. The size of the resulting compressed cube depends on the data density but can be as small as 10 Mbytes. The largest cube produced so far has 51 Mbytes for a cube containing 100 million events. Figure 1 shows data on the degree of compression obtained as a function of the data density and for two separate compression schemes. Method 1 simply records the position in the cube for any non-zero data and is useful only for very sparse data. Method 2 uses a variation of Huffmann compression where one uses short tokens to store the most

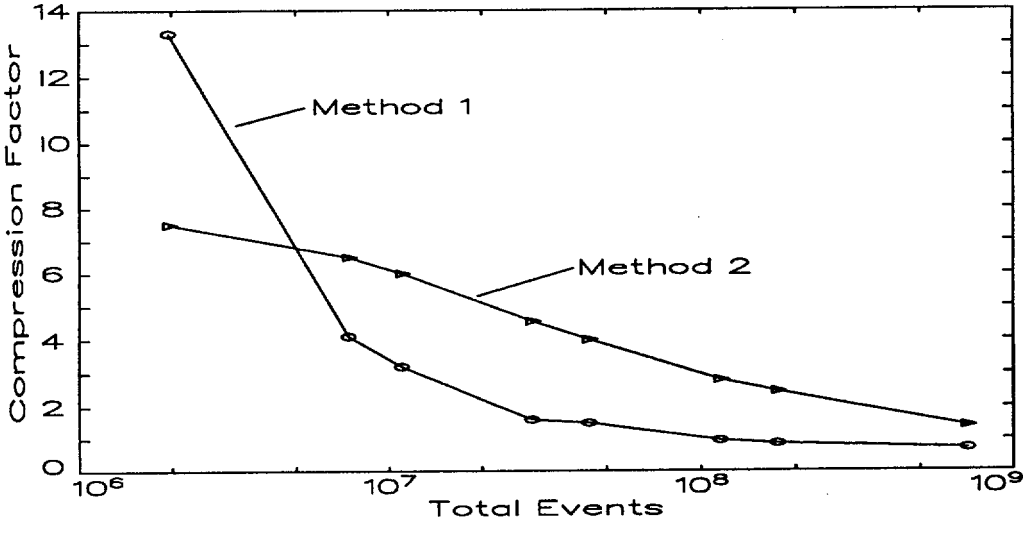

Figure 1

frequent values. It should be noted that there is no overhead penalty in using file compression but rather a gain since the limitation on speed is the harddisk access time.

The whole process of sorting the data and making the compressed cube takes about two days. Once the cube has been generated together with some subsidiary support files the process of looking at the data is very fast and interactive. The program allows one to define up to 15 energies (gates). Then, for example, one can generate and display a spectrum of all 15x14 double gate combinations in about 5 seconds. One can quickly and interactively move individual gates, turn them on and off, widen them etc. by using the keyboard. The same list of 15 energies can be used to project out the sum of 15 planes from the cube to make a 2D array (taking about 5 minutes). This 2D array can then be displayed and studied using functions contained in CubeAid. Some additional functions available include the ability to display the spectrum of the sum of two gamma-rays as a function of the third, the spectrum in coincidence with two separate lists of gamma-rays and the spectrum in coincidence with double gates corresponding to continuum features such as the "ridges". An additional feature allows one to search for regularly spaced features in the entire cube, which one would identify as a possible new superdeformed band.

The demonstration of CubeAid used 149Gd data obtained using the Chalk River 8pi detector. As an example of data analysis it was shown that two-dimensional data projected from the cube and associated with the superdeformed planes contains ridges indicating that the superdeformed continuum, partially at least, feeds into the discrete superdeformed band. A further description of this is contained in abstract C11 by Waddington et al. Figure 2 (top) shows this two-dimensional data while Figure 2 (bottom) shows two-dimensional data projected from the cube using planes displaced from the superdeformed band energies by 20 keV each. This latter data do not contain the ridge structures. The inset spectrum at the bottom right of each part of Figure 2 is the spectrum obtained by extracting the perpendicular cut across the ridge region using a width and location to fall between the data due to the discrete superdeformed band. These spectra clearly show the presence of the ridge structure in the data associated with the discrete supedeformed band.

In conclusion, CubeAid is allows quick, interactive analysis of 3-dimensional data. In the context of the new multi-dimensional data that we expect to have in the near future CubeAid should allow quick looks at many sorted 3D data sets extracted from the multidimensional data.

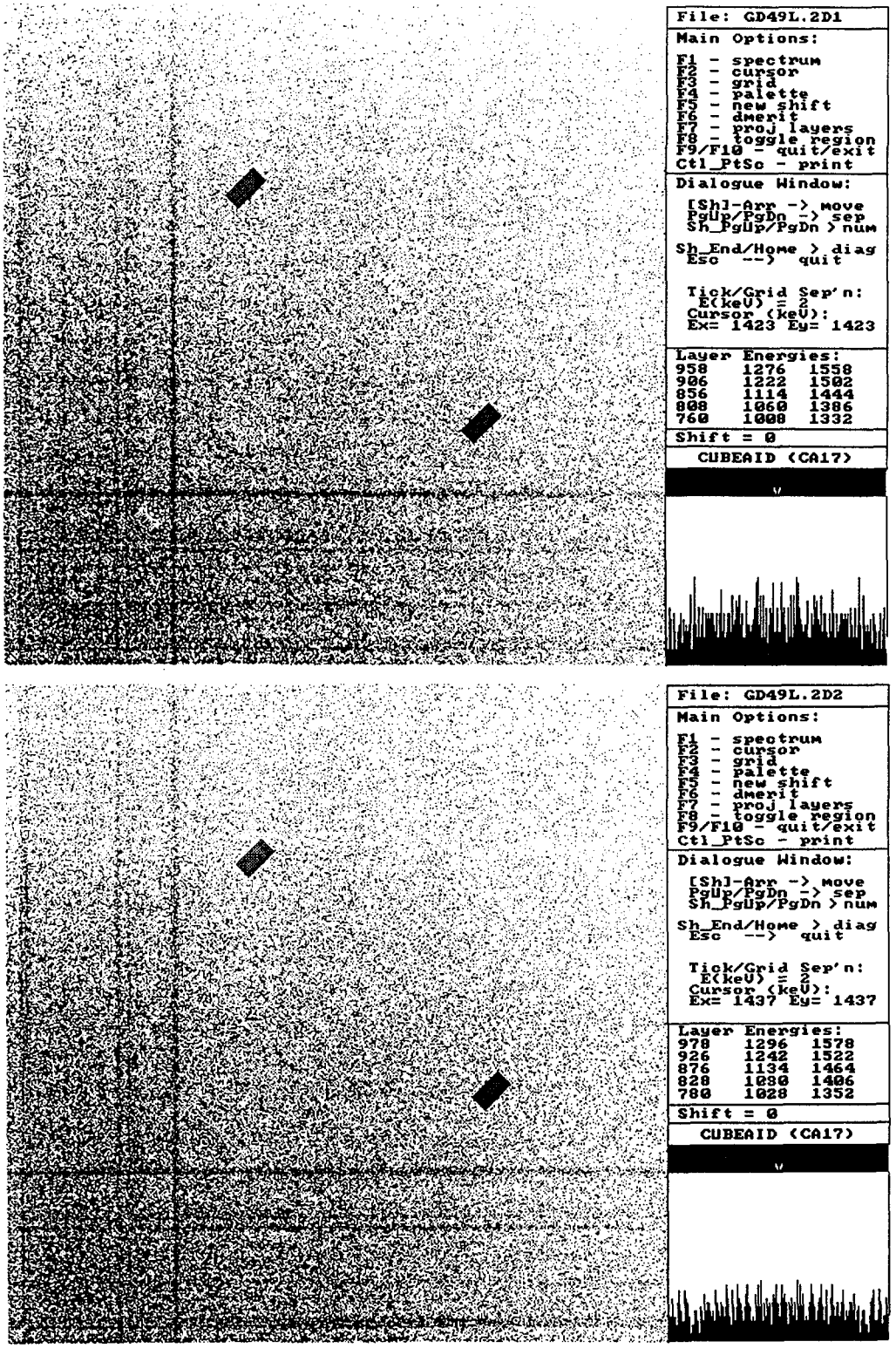
File: GD49L.2D1
Main Options:
F1 - spectrum
F2 - cursor
F3 - grid
F4 - palette
F5 - new shift
F6 - dmerit
F7 - proj layers
F8 - toggle region
F9/F10 - quit/exit
Ctl_PtSc - print
Dialogue Window:
[Shl-Arr -> move
PgUp/PgDn -> sep
Sh_PgUp/PgDn > num
Sh_End/Home > diag
Esc --> quit
Tick/Grid Sep'n:
E(keV) = 2
Cursor (keV):
Ex= 1423 Ey= 1423
Layer Energies:
958 1276 1558
906 1222 1502
856 1114 1444
808 1060 1386
760 1008 1332
Shift = 0
CUBEAID (CA17)
File: GD49L.2D2
Main Options:
F1 - spectrum
F2 - cursor
F3 - grid
F4 - palette
F5 - new shift
F6 - dmerit
F7 - proj layers
F8 - toggle region
F9/F10 - quit/exit
Ctl_PtSc - print
Dialogue Window:
[Shl-Arr -> move
PgUp/PgDn -> sep
Sh_PgUp/PgDn > num
Sh_End/Home > diag
Esc --> quit
Tick/Grid Sep'n:
E(keV) = 2
Cursor (keV):
Ex= 1437 Ey= 1437
Layer Energies:
978 1296 1578
926 1242 1522
876 1134 1464
828 1080 1406
780 1028 1352
Shift = 0
CUBEAID (CA17)

Figure 2

THE STARS IN A CUBE

SEARCH PROGRAMME FOR TRIPLE GAMMA SPECTROSCOPY

D.G. Popescu

Tandem Accelerator Laboratory, McMaster University,
Hamilton, L8S 4K1, Canada

Abstract:

We extend to three dimensions our algorithm developed for the case of two dimensional peak searches with the aim of finding an extremely fast procedure to detect the stars i.e. coincidences (centroids, widths, and intensities). For instance, the part of the local background studies was shortened for simplicity. When the variation from the local density is appreciable, we calculate with the mentioned algorithm, the stars' characteristics. We applied this procedure to a small cube (1/4*1/4*1/4 k**3 k=1024 channels) of simulated data, and we estimate that for a 1*1*1 k**3 symmetric cube that is less than half a day of CPU time will be enough to locate all the inner stars (more than 10^4).

WORKSHOP ON LARGE GAMMA-RAY DETECTOR ARRAYS

Chalk River

SESSION 6: PARTICLE DETECTION SCHEMES

The Argonne Silicon Strip-Detector Array

A. H. Wuosmaa, B. B. Back, I. G. Bearden*, R. R. Betts, M. Freer, J. Gehring, B. G. Glagola, Th. Happ, D. J. Henderson, P. Wilt
Argonne National Laboratory†, Argonne IL, 60439, USA

Many nuclear physics experiments require the ability to analyze events in which large numbers of charged particles are detected and identified simultaneously with good resolution and high efficiency, either alone, or in coincidence with γ rays. Such experiments cover a wide range of topics. These include breakup reactions, which have attracted some attention recently due to their potential astrophysical significance, inelastic scattering and transfer reactions leading to particle-unbound final states, and the detection of particle-unstable reaction products such as ^{8}Be nuclei. In the case of fusion-evaporation reactions where charged particles are emitted, it is useful to detect these charged particles in coincidence with photons, for instance, in conjunction with a large array of gamma-ray detectors. Such an arrangement could permit high-efficiency reaction-channel selection, measurement of the energy spectra of evaporated particles, the reconstruction of compound-nucleus excitation energies and, through the reconstruction of the velocity of the heavy reaction product, facilitate better Doppler-broadening corrections[1].

To study these processes, it is frequently necessary to detect the emitted particles with both good energy and spatial resolution. To perform these measurements, we encounter a number of technical requirements which apply to any kind of particle-detector array dedicated to study these types of reactions. The detector-device should be compact, especially if it is to operate in conjunction with a large gamma-ray detector array. It should be highly segmented, in order to be able to detect simultaneously several charged particles. The device should also provide good energy resolution. Finally, to provide high efficiency for the reconstruction of many-particle final states, the detector system should have a rather large solid angle.

Some solid-state detector devices which very nicely satisfy all of these criteria are double-sided silicon strip detectors (DSSDs)[2]. The detectors used in this work detectors are fabricated from 5 cm $\times$ 5 cm square silicon wafers, with the front and back diode junctions divided into two orthogonal sets of 16 strips, thus effectively segmenting the detector into 256 pixel regions within the 5 cm $\times$ 5 cm square. In addition to this high degree of segmentation, these devices provide excellent energy and time resolution, and their 2500 mm^2 area does indeed yield a large solid angle. The unique capability of these devices, which makes them particularly useful for the kinds of studies described above, is that when properly instrumented, they can provide $X-Y$ position sensitivity for events in which more than one particle strikes the detector at once.

In order to take advantage of this capability, each of the 32 separate segments of the DSSD must be read out independently. For an array consisting of several DSSDs,

many channels of electronics must be used. With conventional NIM electronics, this requirement leads to an leads to an bulky, complicated and expensive setup. We have developed a readout system for several DSSDs designed to be modular, compact, and relatively inexpensive. The heart of this readout system is a high-density, preamplifier module that contains 16 channels of FET charge preamplification and fast time pick-off circuitry within one single-width NIM module. The charge preamplification is performed using two hybrid integrated circuits manufactured by LeCroy, called the HQV810. These circuits each contain 8 channels of FET preamplifier and feedback circuitry within a single chip. The time pickoff circuits were designed at ANL. Using these modules, the entire energy and time preamplification requirements for one DSSD are contained within a very compact package of two NIM modules[3].

The remainder of the electronics relies upon commercially available high-density CAMAC units. The energy signals are sent directly into 16-channel charge-to-digital converters, and the time signals are fed to 16-channel constant-fraction or leading-edge discriminators which also reside in CAMAC. The outputs of these discriminators are used to trigger time-to-digital converters for time-of-flight information, as well as pattern registers which are used to control the event readout. The hit multiplicity information from these discriminators is also used to develop the logic required for event triggering.

To demonstrate the performance of the strip detectors and readout systems, we have performed tests with radioactive sources. These data were obtained using a detector with a thickness of 300 μm, and a leakage current of $\approx$15-20 nA/cm^2 at a bias voltage of 35 V, corresponding to 1.5 times the full depletion voltage[4]. Figure 1 shows an energy spectrum for alpha particles emitted by a ^{252}Cf source, with a strong peak at an energy of E_α=5.812 MeV, obtained from a single pixel region of the detector. The observed resolution is approximately 40 keV (FWHM), and is dominated by the leakage current, the detector dead layer and the electronic noise contribution of the preamplifier.

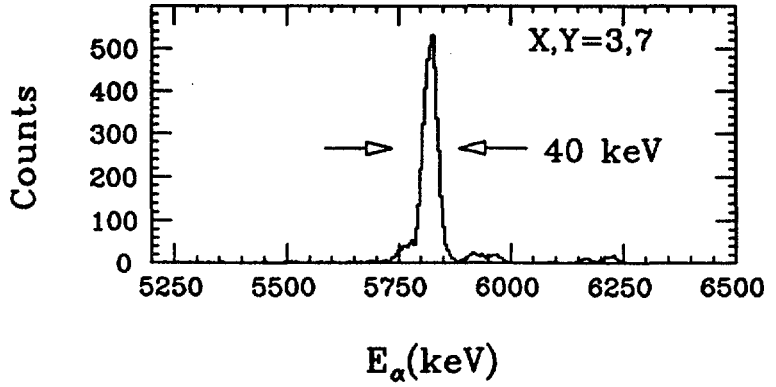

Figure 1. α-particle energy spectrum for one pixel region of the DSSD.

In order to take advantage of the multi-particle $X-Y$ position sensitivity of the DSSDs, certain ambiguities inherent to these devices must be resolved. Since the signals from the two sides of the DSSD are independent from each other, a multi-particle

event yields a set of X coordinates from one side of the detector, which must be correctly associated with a set of Y coordinates obtained from the other side of the device. To do this, we take advantage of the property of the DSSD that from the front and back of the device, we obtain two independent measurements of the energy of each particle striking the detector, and by correlating these energy signals we can readily assign the correct X and Y coordinates for each particle. The ability to perform this correlation depends upon the combined energy resolution of both sides of the detector. As a measure of this combined resolution, a spectrum of the measured difference between the alpha-particle energy signals obtained from the front and back of the DSSD for one pixel region appears in Fig. 2. The resolution of this difference spectrum is ≈55 keV (FWHM). Therefore, in a multi-particle event, if the particles have energies that differ by more than 60 to 100 keV, we can very efficiently assign them their correct X and Y coordinates.

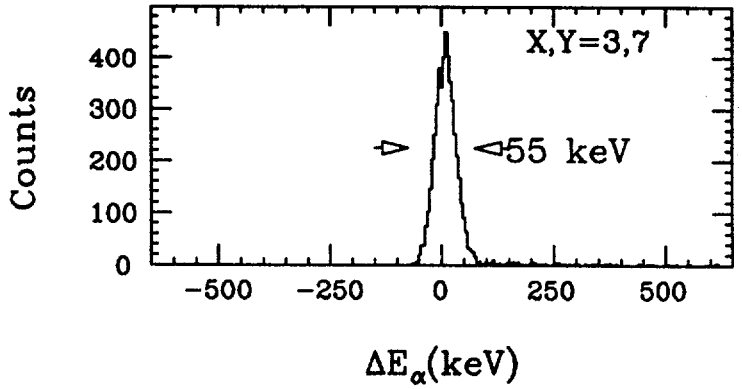

Figure 2. Spectrum of the front-back energy difference for 5.812 MeV alpha particles obtained for one pixel region of the DSSD.

To demonstrate the powerful capabilities of the DSSD for studying multi-particle final states, we present some data obtained from a measurement in which we studied $^{12}C+^{12}C$ inelastic scattering and transfer leading to several different particle-unbound final states[5]. The experimental setup for this measurement included two DSSDs positioned at 35° on either side of the beam, 15 cm from the target. Here, the vast majority of many-particle final states involve several alpha particles. For events in which two or more of these alpha particles strike one DSSD, assuming the alpha particles come from the decay of a composite object, the measured angles and energies of those alpha particles can be used to reconstruct a number of quantities which describe that composite object, including its kinetic energy, scattering angle, and excitation energy. For example, if N alpha particles hit the detector, the composite excitation energy is given by the simple expression $E_X = \sum_{i=1}^{N} E(\alpha)_i - E_K + E_{sep}$, where $E(\alpha)_i$ are the alpha particle kinetic energies, E_K the reconstructed kinetic energy, and E_{sep} a separation energy constant.

Figure 3a shows the resulting excitation-energy spectrum for events where two alpha-particles are detected in the DSSD. The ^{8}Be ground state is cleanly reconstructed with

a resolution better than 50 keV (FWHM). The corresponding spectrum for events in which three alpha particles are detected appears in Fig. 3b. Here, the first excited 0^+ state in ^{12}C is easily identified at $E_X(^{12}C)$=7.65 MeV, just 379 keV above the threshold for decay of ^{12}C into three alpha particles. This level is reconstructed with a resolution of ≈65 to 70 keV (FWHM). The 3^- level at 9.64 MeV is somewhat broader and weaker, due mainly to the effect of the much larger average opening angle for the three alpha particles on the excitation-energy resolution and detection efficiency, respectively .

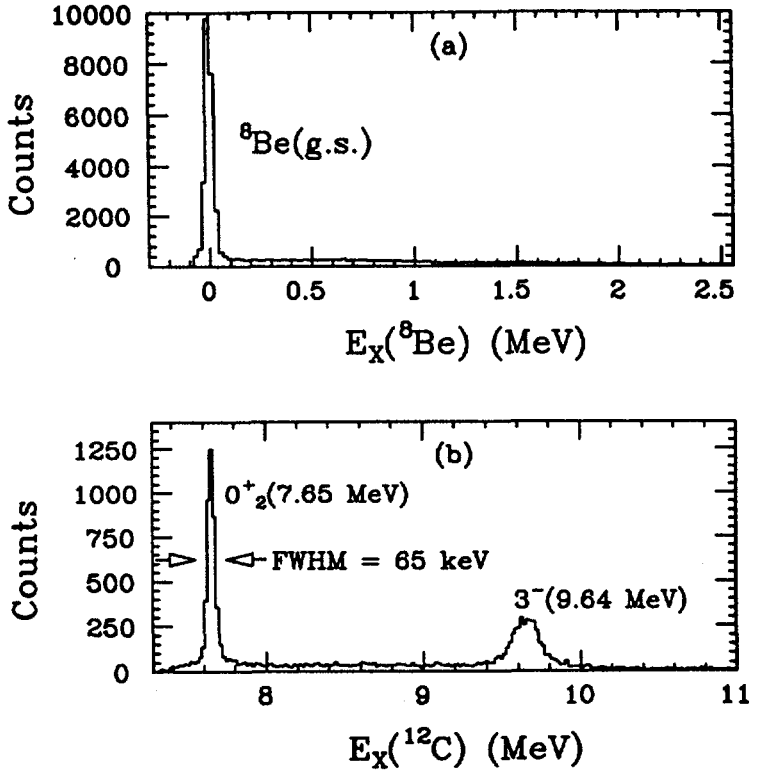

Figure 3. Reconstructed (a) ^{8}Be and (b) ^{12}C excitation energy for events with two and three alpha particles, respectively, detected in one DSSD.

Using this setup, we are also able to identify more complicated final states. For events in which both ^{12}C nuclei are dissociated into three alpha particles, we can, in some cases detect and identify all 6 alpha particles, three in each DSSD. In this case, the excitation-energy calculation shown in Fig. 3b can be performed for each set of alpha particles, and the sum of those two excitation energies yields the total excitation energy in the final state. Figure 4 shows the resulting total excitation-energy thus spectrum obtained at a beam energy of 64 MeV. The peak at a total excitation energy of 15.30 MeV corresponds to the final state where both ^{12}C nuclei are left in their excited 0^+ levels. Despite the fact these events represent 6 charged-particle final states, the rather powerful capabilities of the DSSD allow us to kinematically reconstruct and fully characterize this reaction process.

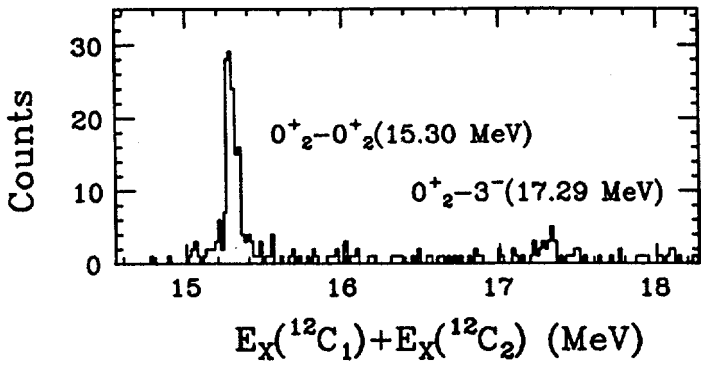

Figure 4. Total excitation-energy spectrum for 6 alpha-particle coincidence events in $^{12}C+^{12}C$ inelastic scattering.

We have begun implementation of a number of improvements and additions to our strip-detector array. One modification is to add a second large-area detector to each array element, thereby making each element a two-detector sandwich. The front element is a DSSD, and the second, backing, element a 5 cm× 5 cm wafer divided into 4 quadrants. Such an arrangement can serve two purposes. For instance, for events in which particles with high energy penetrate the front DSSD, if those events are uninteresting, the quadrant detector provides a very effective veto. Also, for events with moderate charged-particle multiplicity, a thin DSSD combined with a thick backing detector could be used as a highly segmented, large-area silicon $E - \Delta E$ counter. A box configuration with several of these units packed closely around the target could easily serve as a large solid angle, high segmentation detector for studies of charged-particle fusion-evaporation reactions.

In conclusion, the present results demonstrate that the highly segmented, high resolution double-sided silicon strip detectors are very powerful tools for studying nuclear reactions resulting in many-charged-particle final states. A readout system for these detectors has been constructed that is compact, modular, and inexpensive. The flexibility of these detectors, combined with the modularity of the readout system, suggest many further applications for arrays of these devices, both alone, or in conjunction with other detector systems.

*Department of Physics, Purdue University, West Lafayette, IN 47907, USA.

†Work supported by the U. S. Department of Energy, Nuclear Physics Division, under contract W-31-109-Eng-38.

[1]J. Nyberg, Talk presented at this workshop.

[2]T. Davinson, *et al.*, Nucl. Instrum. and Meth. Phys. Res. **A288** 254 (1990).

[3]A. H. Wuosmaa, *et al.* submitted to Nucl. Instrum. and Meth.

[4]Detectors manufactured by Micron Semiconductor, Lancing, UK.

[5]A. H. Wuosmaa, *et al.*, Phys. Rev. Lett. **68** 1295 (1992).

Correction of Doppler broadening of γ-ray lines induced by particle emission in heavy-ion induced fusion-evaporation reactions

J. Nyberg[a], D. Seweryniak[a], C. Fahlander[a], P. Insua-Cao[a], A. Johnson[b], E. Adamides[c], A. Ataç[d], B. Cederwall[b], E. Ideguchi[e], R. Julin[f], S. Juutinen[f], W. Karczmarczyk[g], J. Kownacki[g], S. Mitarai[e], L-O. Norlin[d], M. Piiparinen[c], R. Schubart[h], S. Törmänen[f], A Virtanen[f]

[a] The Svedberg Lab. and Dept. of Radiation Sciences, Uppsala Univ., Uppsala, Sweden
[b] Manne Siegbahn Inst. and The Royal Inst. of Technology, Stockholm, Sweden
[c] National Centre for Scientific Research, Ag. Paraskevi, Attiki, Greece
[d] The Niels Bohr Institute, University of Copenhagen, Copenhagen, Denmark
[e] Department of Physics, Faculty of Science, Kyushu University, Fukuoka, Japan
[f] Department of Physics, University of Jyväskylä, Jyväskylä, Finland
[g] Institute of Experimental Physics, University of Warsaw, Warsaw, Poland
[h] Hahn-Meitner Institute, Berlin, Germany

Abstract: The effect of particle emission on the peak shape of γ-ray lines have been investigated using the NORDBALL detector system. By detecting neutrons, protons and α particles emitted in the ^{32}S (95 MeV) + ^{27}Al reaction, the energy and direction of emission of the residual nuclei could be determined and subsequently used for an event-by-event Doppler correction of the detected γ rays. Extensive Monte Carlo simulations were performed to study how the different Doppler phenomena influence the peak shape and in particular which particle detector properties are important for the Doppler correction.

1. Introduction

The result of Doppler effects on γ-ray spectra recorded in-beam in connection with heavy-ion induced fusion-evaporation reactions is a well known phenomenon. These effects are in some techniques, like in DSAM and RDM, used intentionally in order to determine for example the life-time of a nuclear state. In most experiments, when Ge detectors and thin self-supporting targets are used, the Doppler effects are, however, unwanted and introduce a broadening of the peaks in the γ-ray spectra.

The total γ-ray peak width W_T (e.g. the FWHM) can be written as

$$W_T = [W_i^2 + W_{\Omega_\gamma}^2 + W_{\Delta\Theta_{Rt}}^2 + W_{\Delta v_{Rt}}^2 + W_{\Delta\Theta_{Rp}}^2 + W_{\Delta v_{Rp}}^2]^{1/2} \quad (1)$$

where the different terms are due to: Ge intrinsic resolution (W_i), Ge opening angle (W_{Ω_γ}), angular ($W_{\Delta\Theta_{Rt}}$) and velocity ($W_{\Delta v_{Rt}}$) spread of the γ-ray emitting evaporation residues (ER) due to target effects and angular ($W_{\Delta\Theta_{Rp}}$) and velocity ($W_{\Delta v_{Rp}}$) spread of the ER's due to particle emission.

The contribution of the different terms in eq. (1) depends on several experimental parameters, like e.g. the solid angle of the Ge detector and its angle relative to the direction of motion of the ER, the velocity of the ER, the target thickness, etc. In this work we are mainly interested in the last two terms of eq. (1), namely the Doppler effects caused by the energy and angular spread of the ER due to emission of particles.

Using the non-relativistic formula for conservation of momentum and ignoring target effects, one can write the velocity of the residual nucleus as

$$\vec{v}_R = \frac{m_{CN}}{m_R}\vec{v}_{CN} - \sum_{i=1}^{n}\frac{m_i}{m_R}\vec{v}_i \quad (2)$$

where, $\vec{v}_R$, $\vec{v}_{CN}$ and $\vec{v}_i$ are the velocities in the laboratory system of the residual nucleus, the Compound nucleus and the i:th particle, respectively, and m_R, m_{CN} and m_i are the corresponding masses. The well known non-relativistic Doppler formula is written as

$$E_\gamma = E_{\gamma 0}\,(1 + \frac{\vec{v}_R \cdot \vec{d}_\gamma}{c}) \tag{3}$$

where E_γ is the energy of the γ ray in the laboratory system, $E_{\gamma 0}$ it's energy in the rest system of the residual nucleus and $\vec{d}_\gamma$ is a unit vector defining the direction of emission of the γ ray in the LAB system. Combining eqs. (2) and (3) one can write

$$E_\gamma = E_{\gamma 0}\,(1 + \Delta E_0 - \sum_{i=1}^{n} \Delta E_i) \tag{4}$$

where

$$\Delta E_0 = \frac{m_{CN}}{m_R}\,\frac{\vec{v}_{CN} \cdot \vec{d}_\gamma}{c};\ \Delta E_i = \frac{m_i}{m_R}\,\frac{\vec{v}_i \cdot \vec{d}_\gamma}{c} \tag{5}$$

ΔE_0 leads to a Doppler shift of the γ-ray energy and to the usual Doppler broadening due to the finite opening angle of the Ge detector. ΔE_i also gives rise to a Doppler broadening of the γ-ray peaks and can in certain cases be very large and completely dominate the total peak widths. This is the situation e.g. when several 'heavy' particles of high energy like e.g. α particles are emitted in a reaction with a relatively light Compound nucleus. By measuring the mass (m_i), the velocity and direction of emission ($\vec{v}_i$) of all the particles emitted in the reaction one can determine ΔE_i for each event and thus correct for the Doppler broadening introduced by particle emission. The formulas given above will be partly modified if relativistic effects, effects of a finite target thickness and effects due to a non-ideal particle detector are taken into account.

2. Experiment

To test this Doppler correction scheme we have analysed the data from a recent NORDBALL experiment performed at the Tandem Accelerator Laboratory of the Niels Bohr Institute in Denmark. In this experiment the reaction ^{32}S (95 MeV) + ^{27}Al (stack of one 0.4 mg/cm^2 and one 0.7 mg/cm^2 thick target) was used with the aim of studying high spin states of the doubly magic nucleus $^{56}_{28}Ni_{28}$. The NORDBALL detector system (see fig. 1) was in this experiment equipped with a 4π charged particle detector (the Silicon Ball with 21 detectors) [1]. a 2π γ-ray calorimeter (the BaF_2 Ball with 30 detectors), a $\sim 1\pi$ neutron detector array (the Neutron Wall with 11 detectors) [2] and 15 Ge-BGO spectrometers. In table 1, some details of the geometry of the Silicon Ball are shown. A total of 160 million events, each consisting of information about the detected γ rays, neutrons, protons and α particles were collected.

In the off-line analysis, γ-ray spectra were sorted by gating on different neutron, proton and α particle multiplicities. The data have been sorted in two different ways. In the first sorting no Doppler corrections were applied to the Ge energies, which will be referred to as 'uncorrected' below. In the second 'corrected' sorting the Doppler correction scheme of eqs. (3), (4) and (5) was used. Due to the fact that no energy information was available for protons and α particles, constant values of $|\vec{v}_i|$ were used in eq. (5) for each reaction channel. These values were taken as the average particle energies obtained from a Monte Carlo version of the program CASCADE.

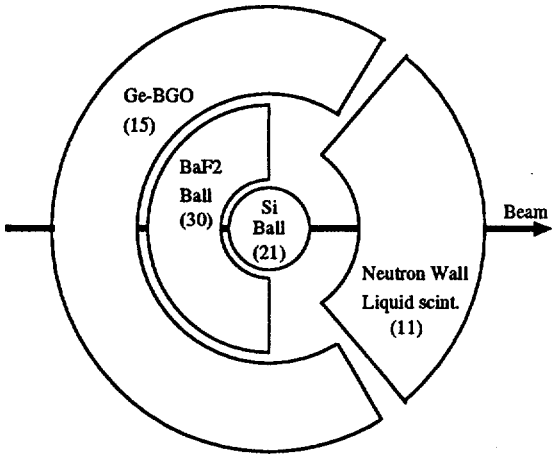

Fig. 1. Schematic figure of the NORDBALL detector system as used in the current experiment and equipped with the selective devices: the Silicon Ball, the BaF_2 Ball and the Neutron Wall.

Detector shapes	Nr. of detectors	<θ> (deg)	Ω/4π per det. (%)
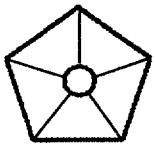	1x5	23°	1.3
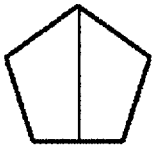	5x2	57° 78°	3.7
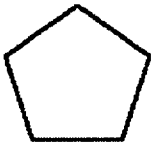	5x1	114°	7.4
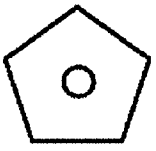	1x1	180°	6.6
	Σ=21		Σ= 87%

Table 1. Table showing some details of the geometry of the Silicon Ball.

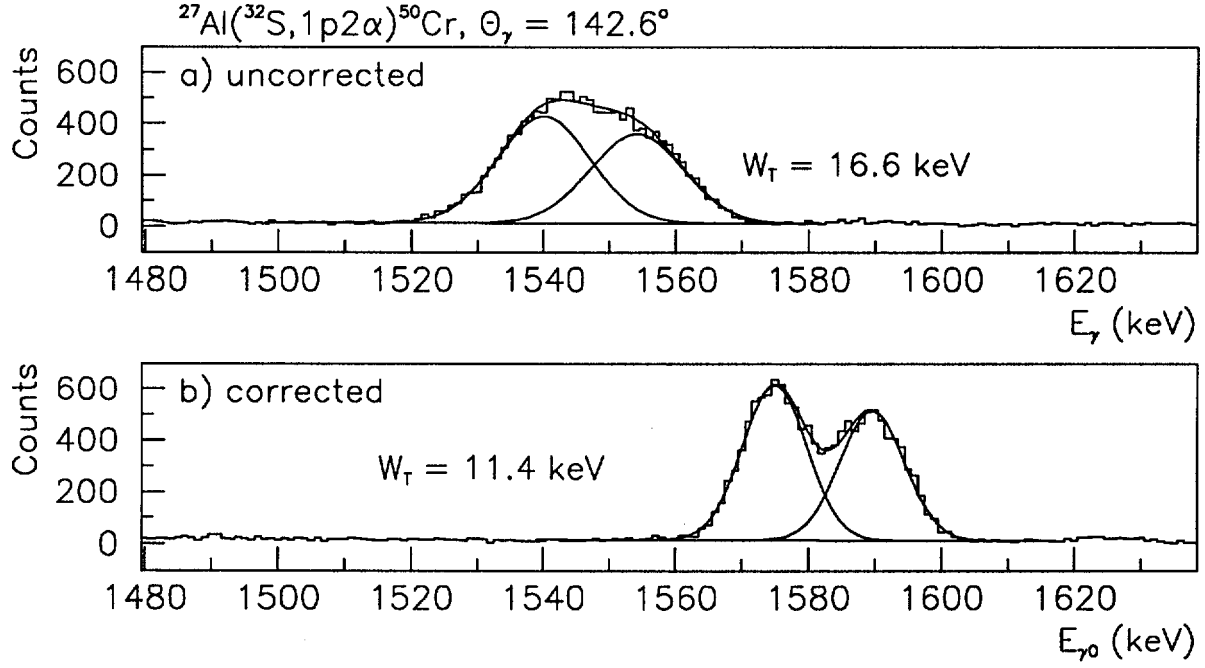

Fig. 2. a) Uncorrected and b) Doppler corrected γ-ray spectra. The histograms show the experimental data while the smooth curves correspond to a fit of two Gaussian peaks to the data.

An example of a) an uncorrected and b) a corrected γ-ray spectrum is shown in fig. 2. The spectra

were produced by gating on $1p2\alpha$ and summing events from the Ge detectors at $\theta_\gamma = 143°$. The peaks shown in fig. 2 form a doublet and correspond to the $8^+ \rightarrow 6^+$ and $10^+ \rightarrow 8^+$ transitions of ^{50}Cr at $E_{\gamma_0} = 1582$ and 1596 keV, respectively. The average particle energies used for the Doppler correction in fig. 2b) were $\langle E_p^{CM} \rangle = 5.5$ MeV and $\langle E_\alpha^{CM} \rangle = 12.0$ MeV. As can be seen in the figure there is a considerable reduction of the total peak width W_T (=FWHM), from 16.6 to 11.6 keV, when applying the Doppler correction.

In fig. 3 the total uncorrected and corrected experimental peak widths are shown as a function of γ-ray energy for peaks in the $1p2\alpha$ gated spectrum and for Ge detectors placed at $\theta_\gamma = 143°$.

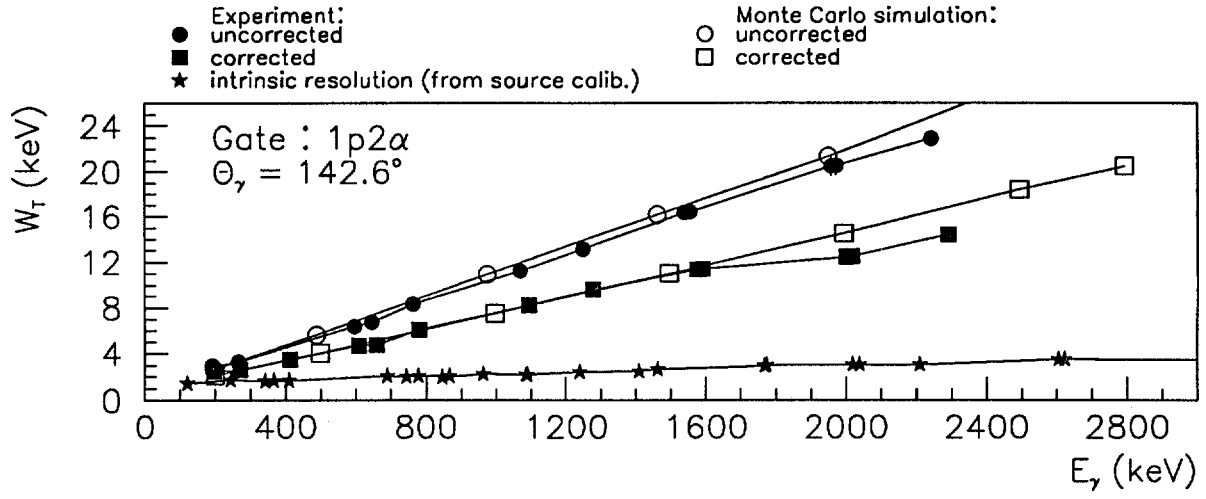

Fig. 3. Total uncorrected (circles) and corrected (squares) peak widths (=FWHM) as a function of γ-ray energy, extracted from the $1p2\alpha$ gated spectrum. Experimental results (filled symbols) are shown together with results from a Monte Carlo simulation (open symbols). The intrinsic Ge energy resolution ($\star$) is also shown in the figure.

All the peaks analysed in fig. 3 correspond to transitions in ^{50}Cr. The average recoil velocity was $\langle v_R/c \rangle = 3.3\%$ for this reaction channel. Similar results have also been obtained for the other reaction channels.

3. Monte Carlo simulations

Extensive Monte Carlo simulations of the γ-ray peak shapes were also performed. A computer program was written in which 'all' possible effects contributing to the peak shape were taken into account, e.g. Ge solid angle, target effects, imperfect particle detection, etc. Results from one of the simulations are shown in fig. 3. As seen, the calculated total peak widths agree very well with the experimental ones.

From the Monte Carlo simulation we can extract the separate contributions to the peak width. For the case shown in fig. 3 we get for $E_\gamma = 1$ MeV (see eq. (1)): $W_i = 2.3$ keV, $W_{\Omega_\gamma} = 3.3$ keV, $[W^2_{\Delta\theta_{Rt}} + W^2_{\Delta v_{Rt}}]^{1/2} = 3.1$ keV, $[W^2_{\Delta\theta_{Rp}} + W^2_{\Delta v_{Rp}}]^{1/2} = 9.9$ keV (uncorrected) and $= 5.5$ keV (corrected). From the last two values we conclude that we are able to correct for $\sim 45\%$ of the Doppler broadening due to particle emission. This is reasonable considering the relatively poor angular resolution of the Silicon Ball and the absence of any energy information for this detector.

The different properties of the particle detector important for the Doppler correction are illustrated in fig. 4, where the corrected peak width is shown as a function of a) efficiency, b) angular and c)

energy resolution of the particle detector for the $^{27}Al(^{32}S,2\alpha)^{51}Mn$ reaction at E(^{32}S)= 100 MeV and for $E_\gamma = 1$ MeV and $\theta_\gamma = 45°$.

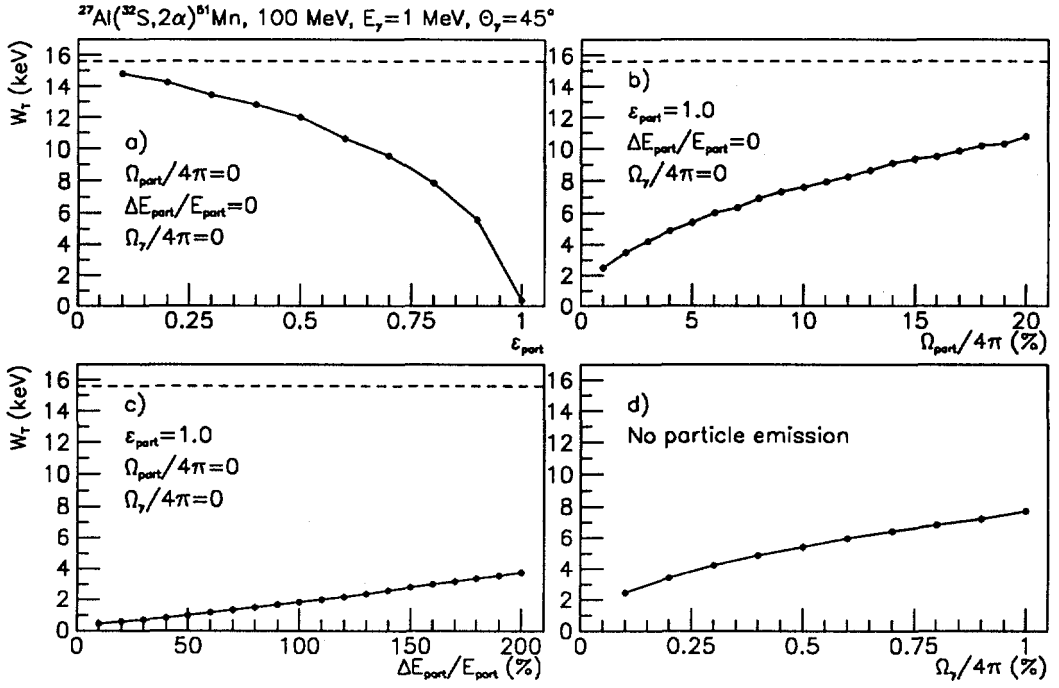

Fig. 4. Monte Carlo simulation of the influence of different particle detector properties on the corrected peak width. The dashed line corresponds to the uncorrected total peak width. No target effects were included in this calculation.

In fig. 4a-c) two of the particle detector parameters were kept fixed with 'ideal' values while changing the third parameter and the Ge solid angle was set = 0. For reference the total peak width is shown in fig 4d) as a function of Ge solid angle in the case of no particle emission. I can be conclude that the corrected peak width is strongly dependent on the efficiency of the particle detector, moderately dependent on the angular resolution and rather independent of the energy resolution. It is thus essential to have a particle detection efficiency as close to 100% as possible.

4. Conclusion

In this work it is demonstrated that already with a relatively modest particle detector, like the Silicon Ball, one can partly correct for the Doppler effects induced by particle emission in heavy-ion induced fusion-evaporation reactions. Monte Carlo simulations were performed to study the different contributions to the peak shape and in particular how the particle detector properties influence the Doppler corrections. The results of the simulations are used in a preliminary study of a future 4π charged particle detector ball for EUROBALL.

Acknowledgements

This work was partially supported by the Swedish National Science Research Council.

References

[1] T. Kuroyanagi et al., Nucl. Instr. Meth. in print.
[2] S.E. Arnell et al., Nucl. Instr. Meth. A300(1991)303.

The 8π MINIBALL CHARGED-PARTICLE DETECTOR ARRAY

G.C. Ball[1], A. Galindo-Uribarri[1], H.R. Andrews[1], N.C. Bray[1], T.E. Drake[2], J.D. Lori[1], D.C. Radford[1], L.V. Smith[1], G.A. Tapp[1], J.C. Waddington[3] and D. Ward[1]

1 *AECL Research, Chalk River Laboratories, Ontario Canada, K0J 1J0*
2 *Department of Physics, University of Toronto, Toronto, Ontario, Canada M5S 1A7*
3 *Department of Physics, McMaster University, Hamilton Ontario, Canada, L8S 4K1*

A modular miniature array of 24 CsI(Tl) crystals (0.5 cm thick) coupled to large-area photodiodes has been constructed to operate inside the 8π spectrometer. The array was designed to have good resolution, high efficiency and adequate granularity for detecting light charged particles emitted in coincidence with the γ-rays from the decay of high-spin states populated in heavy-ion fusion-evaporation reactions. The 24 detector elements are arranged in a closely-packed geometry in the shape of a rhombicuboctahedron. This figure of 26 faces consists of 18 squares and 8 equilateral triangles. Two opposing squares are used for beam entrance and exit. Commercially available 4 cm^2 square photodiodes and specially made triangular ones were used. In this configuration there were three rings of eight detectors centered at 45°, 90° and 135°. The geometrical solid angle of the miniball is 91% of 4π. However, at the present time the target frame and the detector absorber mounts reduce the coverage to ≈75% of 4π.

In general, the requirements for a charged-particle detector array used with large γ-ray detector arrays are: large solid angle, good particle identification and energy resolution, low threshold, linearity and gain stability, high count-rate capability, resistance to radiation and a small influence on the γ-ray array. Table 1 summarizes the "4π sr" charged-particle detector arrays that are or have been used for γ-ray spectroscopy[1-6]. A comparison of the advantages and disadvantages of these devices as well as a detailed description of the 8π miniball have been given elsewhere[5]; some of the unique features of the 8π miniball are discussed below.

Particle identification for the miniball is determined by pulse-shape discrimination, with a common start signal obtained from the BGO ball and individual stop signals derived for each CsI(Tl) element from the zero crossover of a bipolar pulse from a spectroscopy amplifier operating with a 3 μs shaping-time constant. Excellent p-α discrimination is achieved down to a low energy threshold of ~ 3 MeV protons. Absorber foils are placed in front of the detectors at forward angles to stop scattered beam particles. Thin Au/Al absorbers are used at other angles to reduce the flux of low-energy x-rays. The pre and post pile-up rejection circuitry available for the 8π spectrometer allow us to operate the individual

CsI(Tl) particle detectors of the miniball at counting rates up to ~10 KHz.

Of particular concern was the effect of the miniball on the performance of the 8π spectrometer. Every effort was made to minimize the attenuation of γ-rays. The support structure and the vacuum chamber were made of "Delrin" plastic, and the preamplifiers for the thin (300 μm) photodiodes were located outside the BGO ball. The thickness of the CsI(Tl) crystals (0.5 cm) was chosen to stop ~35 MeV protons. The resulting transmission coefficient for γ-rays is $\geq$0.75 for E_γ > 0.5 MeV. However, the γ-γ coincidence efficiency for low energy ($\leq$ 200 keV) transitions is significantly reduced. The effect of the miniball on the peak-to-total ratio for the Compton-suppressed HPGe γ-spectra was also determined. For a ^{137}Cs source the P/T ratio was found to decrease by only ~5% (see Figure 1).

For each event we record the Compton-suppressed HPGe energies and times, the total energy (H), multiplicity (K) and hit pattern for the BGO ball and the particle-detector energies, times and hit pattern. This information allows us to select a specific reaction channel and/or study charged-particle yields, spectrum shapes, angular distributions and particle-gamma correlations for residual nuclei or specific bands within a given nucleus selected by γ-rays observed in the HPGe array.

The first experimental results, a study of charged-particle spectra associated with superdeformed bands in ^{133}Nd were reported previously[7]. Since that time the device has been used in ten different experiments for: i) studying discrete spectroscopy, ii) searching for new SD bands, iii) searching for nuclear-structure effects in particle-evaporation spectra and iv) looking for evidence of hyperdeformation. These are summarized in Table 2 and include five contributions to the 1992 Inter. Conf. on Nuclear Structure at High Angular Momentum[7-15].

Channel selection is the most important criterion for nuclear-spectroscopy studies. This requires good particle identification as well as high efficiency when more than one charged particle is emitted from the compound nucleus. Figure 2 shows γ-ray spectra obtained from the reaction ^{58}Ni + ^{58}Ni at 250 MeV with gates set on two or more protons (bottom panel) and an alpha particle plus two or more protons (top panel). From the difference spectrum in the middle panel we can distinguish between γ-rays associated with "yp" exit channels (downward peaks) and "α yp" channels (upward peaks). For this symmetric reaction where kinematics results in the emission of a large number of particles at forward angles θ_L<23° not covered by our array, the efficiency for detecting a single proton was found to be ~55%. Significantly higher values have been obtained for asymmetric reactions.

For the study of charged-particle evaporation spectra associated with the decay of nuclei formed in heavy-ion fusion reactions, both channel selection and good energy resolution are required. The 8π miniball is ideally suited to these experiments. Figure 3 shows the overlaid proton

energy spectra from the reaction $^{32}S + ^{105}Pd$ for the four square detectors positioned at θ_L=45°. No measurable differences were observed over five orders of magnitude in intensity.

Recently, Sarantites et al.[16] reported large shifts and changes in the shape of the proton spectra associated with different rotational bands populated in the $^{52}Cr(^{34}S, 2p2n)^{82}Sr$ reaction. However, in the miniball experiments carried out so far to study these phenomena (see Table 2) no evidence has been found for similar structural effects.

To extend the present experimental program with the 8π miniball to near-symmetric or inverse reactions, we are upgrading the array to increase the granularity at forward angles by segmenting each of the four front square photodiodes into four 1 cm^2 detectors mounted on a single ceramic substrate. In addition, a miniature forward wall will be added consisting of nine 1 cm^2 detectors on a 3x3 matrix. The zero degree detector will be removable. These modifications will provide higher efficiency for more exclusive measurements and complete kinematical reconstruction where charged-particle evaporation dominates. Corrections for Doppler broadening[17] will also be implemented as required. The upgraded array should be operational within six months.

REFERENCES

1. D.G. Sarantites et al., Nucl. Instr. and Meth. A264 (1987) 319 and Nucl. Instr. and Meth. A294 (1990 485.

2. T. Chapuran et al., Nucl. Instr. and Meth. A272 (1988) 767.

3. F. Azaiez et al., Nucl. Instr. and Meth. A281 (1989) 133.

4. F. Liden, Nucl. Instr. and Meth. A288 (1990) 455.

5. A. Galindo-Uribarri, Prog. Part. Nucl. Phys. 28 (1992) 463.

6. Kuroyanagi et al., Nucl. Instr. and Meth., to be published.

7. A. Galindo-Uribarri et al., Inst. Phys. Conf. Ser. No. 109 Chapter 6 (1990) 179 and to be published.

8. V.P. Janzen et al., Vol 1. AECL-10613 (1992) F6.

9. S.M. Mullins et al., Vol. 1 AECL-10613 (1992) A5 and to be published.

10. Pilotte et al., private communication.

11. D.J. Blumenthal., et. al. Phys. Rev. Lett. 66 (1991) 3121.

12. G. Zwartz et al., Vol. 1 AECL-10613 (1992) C25.

13. M. Cromaz et al., Vol. 1 AECL-10613 (1992) B4.

14. A. Galindo-Uribarri, Vol. 1 AECL-10613 (1992) A16.

15. J. Cameron et al., private communication.

16. D.G. Sarantites et al., Phys. Rev. Lett. 64 (1990) 2129.

17. J. Nyberg, Vol. 1 AECL-10613 (1992) G8.

TABLE 1

4π CHARGED PARTICLE DETECTOR ARRAYS FOR γ-RAY SPECTROSCOPY

Array	Number of Detectors	Type	Application	Reference
Dwarf Ball	72	Fast/Slow Plastic Fast Plastic/CsI	ORNL Spin spectrometer	Sarantites et al.[1]
Pennsylvania Array	24	Fast Plastic/CaF_2	(+2 Ge)	Chapuran et al.[2]
Plastic Cube	17	Fast plastic	Chateau de Cristal	Azaiez et al.[3]
Hystrix	12	Fast/slow plastic	POLYTESSA NORDBALL	Liden[4]
Miniball	24	CsI/photodiode	8π spectrometer	Galindo-Uribarri et al.[5]
Silicon Ball	21	Thin Si	NORDBALL	Kuroyanagi et al.[6]

TABLE 2

SUMMARY OF EXPERIMENTS WITH 8π MINIBALL

1. Nuclear Spectroscopy

Nucleus	Channel	Reference
^{109}Sb	3p, 3pα	Janzen et al.[8]
^{141}Gd	2pn	Mullins et al.[9]
^{138}Sm	αp2n	" "
^{141}Eu	2p2n	" "
^{169}Re	p2n	Pilotte et al.[10]

2. Nuclear Structure Effects in Particle Evaporation Spectra

^{133}Nd	2p2n	Galindo-Uribarri et al.[7]
^{152}Dy	p4n	Galindo-Uribarri et al.[7,8]
^{84}Zr	2pn	Blumenthal et al.[11]
^{81}Sr	2pα	" "

3. Search for New Superdeformed Bands

^{197,198}Pb	xn	Zwartz et al.[12]
^{195,196}Hg	αxn	
^{195}Tl	pxn	

4. Search for Evidence of Hyperdeformation

^{167}Hf	α5n	Cromaz et al.[13]
^{152}Dy	p4n	Galindo-Uribarri et al.[14]
^{48}Cr	α	Cameron et al.[15]

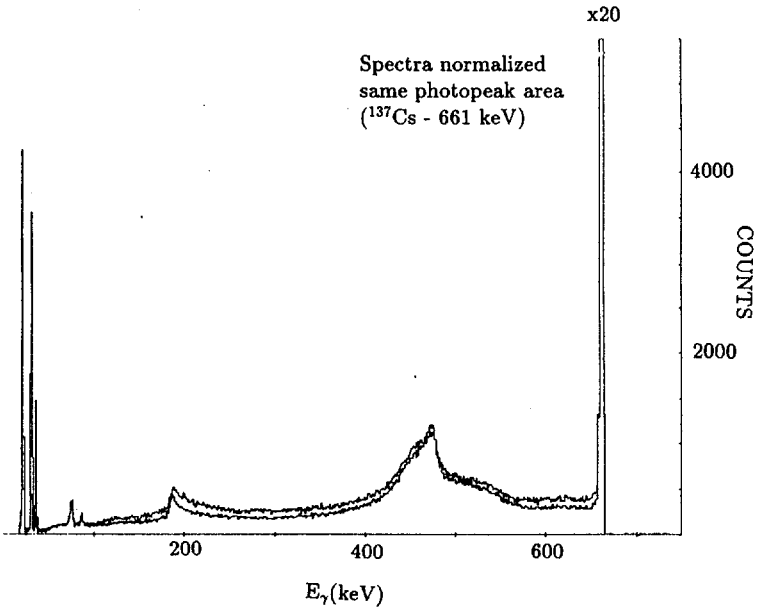

Figure 1 Compton suppressed HPGe γ-spectra measured with and without the miniball.

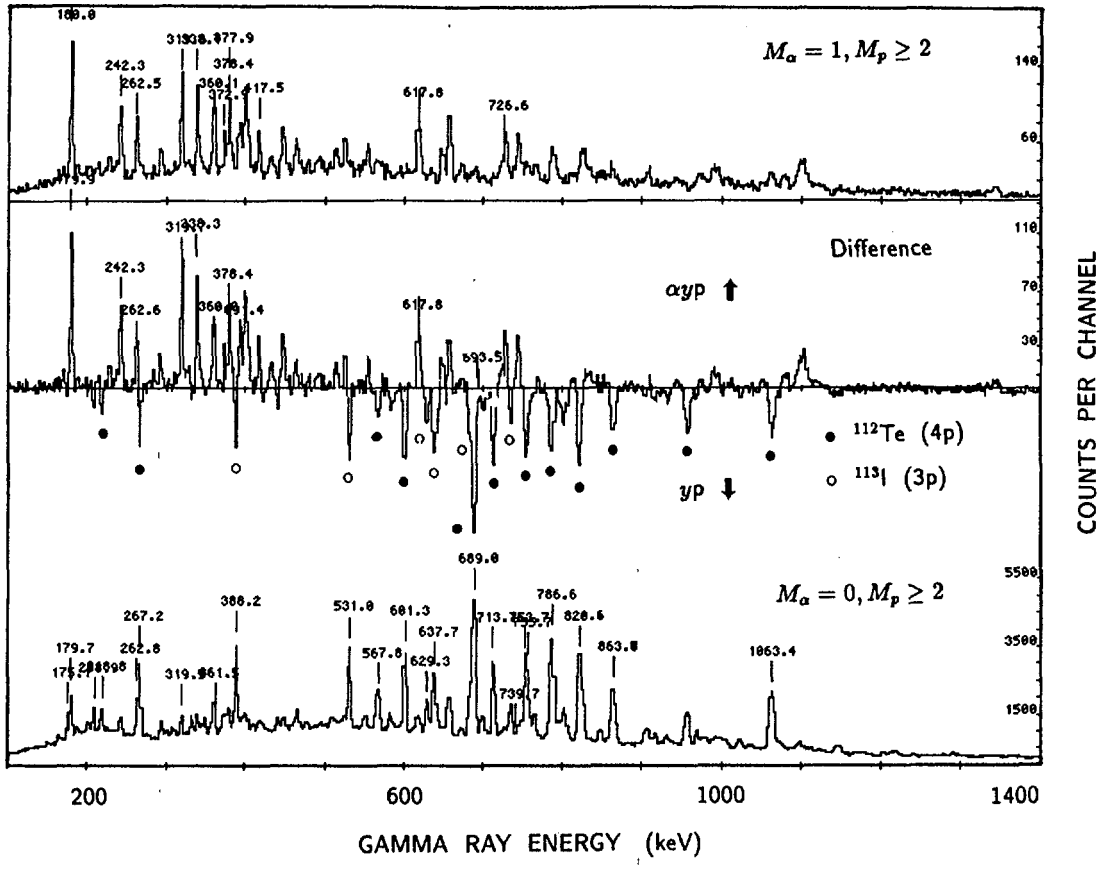

Figure 2 *Gamma ray spectra from the reaction ^{58}Ni + ^{58}Ni at 250 MeV gated by proton and/or alpha particles detected in the 8π miniball (see text).*

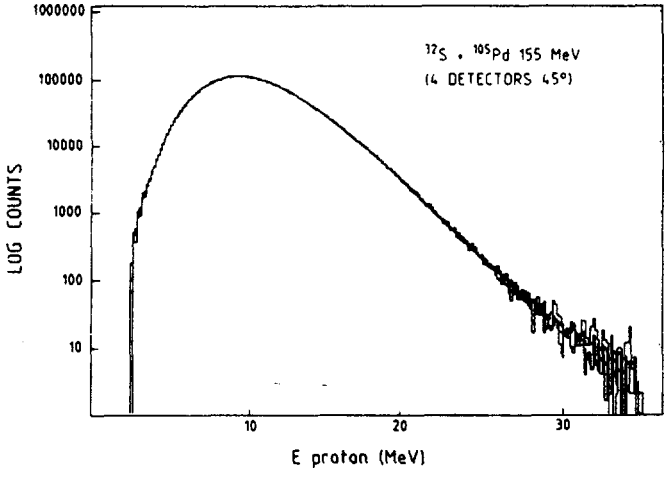

Figure 3 *Overlaid proton energy spectra from 4 detectors at $\theta_L = 45$.*

Octupole Deformation in ^{148}Nd

R. Ibbotson[a], C.A. White[b], T. Czosnyka[c], B. Kotlinski[a], P.A. Butler[b], N. Clarkson[b], R.A. Cunningham[d], D. Cline[a], M. Devlin[a], K.G. Helmer[a], T.H. Hoare[b], J.R. Hughes[e], A.E. Kavka[a], G.D. Jones[b], R.J. Poynter[e], P. Regan[e], E.G. Vogt[a], R. Wadsworth[e], D.L. Watson[e], C.Y. Wu[a]

a) Univ. of Rochester
b) Univ. of Liverpool
c) Univ. of Warsaw
d) SERC, Daresbury
e) Univ. of York

Abstract

E1, E2 and E3 matrix elements have been determined for transitions between states up to spin 13 in ^{148}Nd. These values were obtained from Coulomb excitation data using ^{58}Ni and ^{92}Mo ions, projectile excitation using a ^{208}Pb target, and from recoil distance lifetime measurements. The results are consistent with a description of ^{148}Nd having fairly constant intrinsic-frame moments of Q_{20} =+400 efm^2 ($\beta_2^{rms} \approx$+0.22), $Q_{30}^{sum} \approx$1600 efm^3 ($\beta_3^{rms} \approx$0.16) for the positive parity states and Q_{20} =+330 efm^2 ($\beta_2^{rms} \approx$+0.18), $Q_{30}^{sum} \approx$2000 efm^3 ($\beta_3^{rms} \approx$0.21) for the negative parity states.

The experimental study of nuclei with Z=54-60 and N≈88 populated by α induced reactions, e.g. [1] and fission, e.g. [2], has revealed the presence of low-lying negative parity states which are coupled to the positive parity members of the g.s. band by strong E1 transitions. These have been interpreted using geometric models within the mean field approach as arising from the presence of a octupole deformation, i.e. $\beta_3 \neq 0$ [3, 4]. The experimental evidence for this interpretation is sparse for these nuclei as compared with the light actinides: the interleaving of the positive and negative parity states is well established for nuclei with N=88. In ^{148}Nd many transitions have already been identified, e.g. the octupole band observed by Urban et al. [1], recently extended to high spin by Durell et al. [7] and the many low lying states populated by β decay [8]. The partial level scheme is shown in fig. 1. Measurement of the E1 transition strength is known not to be a reliable indicator of octupole correlations because it is strongly affected by fluctuating single particle contributions [5, 6]. The best measurement of collective octupole strength is the E3 transition strength, which can be related directly to this particular degree of freedom. While observation of real photon E3 emission is not yet technically possible in these transitional nuclei, the determination of E3 matrix elements from Coulomb excitation (C.E.) measurements is feasible. It is necessary to perform many independent measurements of observables which are sensitive to the electric matrix elements connecting the states in ^{148}Nd in order to determine these matrix elements. Presented here are the results of such measurements for E1, E2 and E3 matrix elements in ^{148}Nd following excitation with ^{58}Ni ions, ^{92}Mo ions, and a ^{208}Pb target in which both C.E. yields and lifetimes were determined.

i) Gamma ray intensities were measured in coincidence with the detection of ^{58}Ni ions, using 5 Compton suppressed Ge spectrometers (CSS) positioned 15 cm from the

target. The beam of 200 MeV ^{58}Ni was provided by the Rochester tandem Van de Graaff. The Nd and Ni ions were detected using position sensitive avalanche detectors (PSAD) covering the angular ranges $14° \leq \theta \leq 76°$ and $110° \leq \theta \leq 150°$. This detector system is described elsewhere [10, 11]. Measurements of the coincidence γ-ray yields were made for 4 ranges of scattering angle, so that the dependence of the Coulomb excitation on impact parameter could be exploited.

ii) Particle-γ and particle-γ-γ coincidences were measured following bombardment with 330 MeV ^{92}Mo ions, provided by the Nuclear Structure Facility, Daresbury. The γ-rays were detected in POLYTESSA [9] consisting of 20 CSS's and the scattered ions were detected in PSADs subtending an angular range of 104° - 154 ° [6]. In this experiment transitions from both the positive and negative parity states in the octupole band were observed up to spins 10^+ and 9^- respectively (see fig. 1). Gamma-ray intensities were determined, in coincidence with all backscattered Mo ions, at four selected Ge detector angles. A self supporting foil of 1mg/cm^2 Nd, enriched to 93% in ^{148}Nd, was used in the measurements of yields using both Ni and Mo beams. In these two measurements, the 9^- state was the highest observed, since the 615 keV γ-ray ($10^+ \rightarrow 8^+$) is a doublet with the $0_2^+ \rightarrow 2_1^+$ transition and the 338 keV transition ($10^+ \rightarrow 9^-$) is contaminated by the $6^+ \rightarrow 4^+$ transition in ^{150}Nd. The $3^- \rightarrow 2^+$ transition also was obscured by the lowest ($2^+ \rightarrow 0^+$) transition in ^{144}Nd for these measurements. E2 transitions within the negative parity band were not observed, but transitions de-exciting the quasi-β and γ-vibrational band [8] were observed.

iii) An isotopically pure beam of ^{148}Nd, provided by HHIRF, at the Oak Ridge National Laboratory, was excited by a 0.2 mg/cm^2 ^{208}Pb target. Both Nd and Pb ions were detected using a PSAD covering $14° \leq \theta \leq 76°$ [10], and the γ-rays were detected

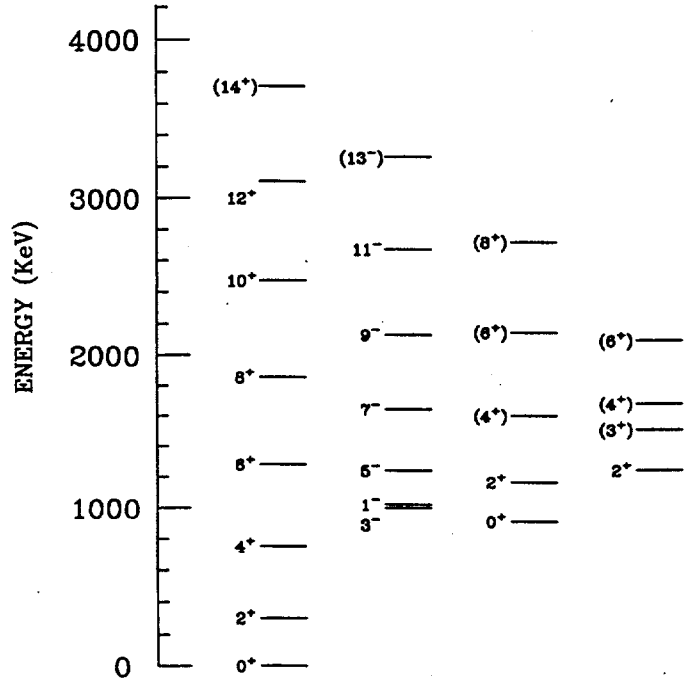

Figure 1: level scheme for ^{148}Nd

in 16 CSS's in the Spin-Spectrometer, which served as a multiplicity filter. Particle-γ-γ events were used in conjunction with the γ-ray multiplicity to make assignments of unknown γ-transitions. Level assignments made on the basis of the Mo and Pb data are shown in parenthesis in fig. 1.

iv) Lifetimes of 9 excited states in ^{148}Nd were measured using the recoil distance method, following inelastic scattering of ^{58}Ni ions at a bombarding energy of 210 MeV. In this experiment, also performed at the University of Rochester, the backscattered ions were detected in a PSAD subtending 140°-170° [12], and γ-rays were detected in a CSS placed at 0°. The target used was 0.2mg/cm^2 ^{148}Nd evaporated onto a stretched 0.5mg/cm^2 Ni foil. Lifetimes were determined by measuring the γ-ray yield emitted before and after the Nd recoil passed through a slowing down foil, made of 2.8 mg/cm^2 Ni. The distance between the target and the slowing down foil was varied between 10 and 2000 μm. This experiment has been described in more detail elsewhere [13].

A total of $\approx$2100 independent data points (C.E. yields, lifetimes, and a previous measurement of $\Gamma_{1^- \to 0^+}$ [14]) were used with the semiclassical Coulomb-excitation least-squares search code, GOSIA [15], to extract the E1, E2 and E3 matrix elements for ^{148}Nd. In order to take into account virtual excitation effects, the rigid rotor model was used to constrain the possible values of matrix elements with λ=1,2,3 for unobserved transitions involving states with I> 13. In these calculations the E4 matrix elements were constrained to lie within a range of values determined by a previous measurement of $< 0^+||E4||4^+ >$ [16] and the predictions of the rigid rotor model. The extracted values are given in fig. 2 for the E1 and off-diagonal E2 matrix elements and fig. 3 for the E3 matrix elements. The errors shown take into account cross-correlation effects. Matrix elements connecting states in the quasi-β and -γ bands were also included in the fit, the fitted values will be presented elsewhere [17]. The overall value of the χ^2, normalized to

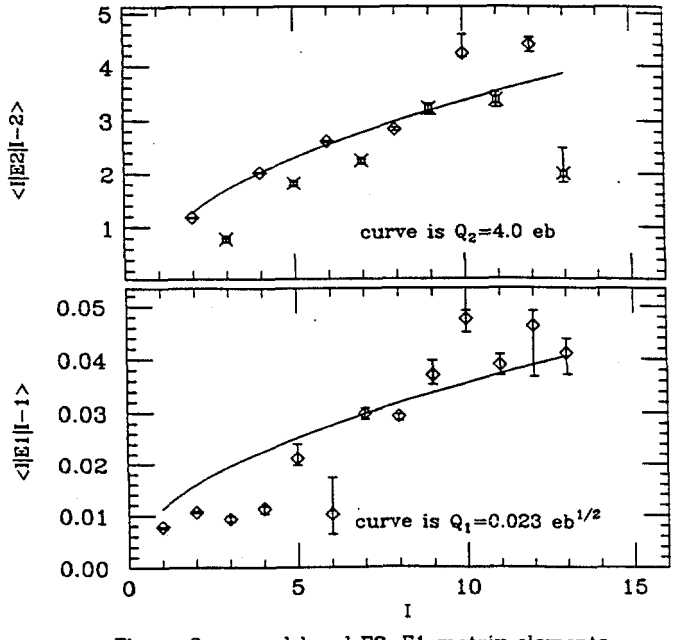

Figure 2: ground band E2, E1 matrix elements

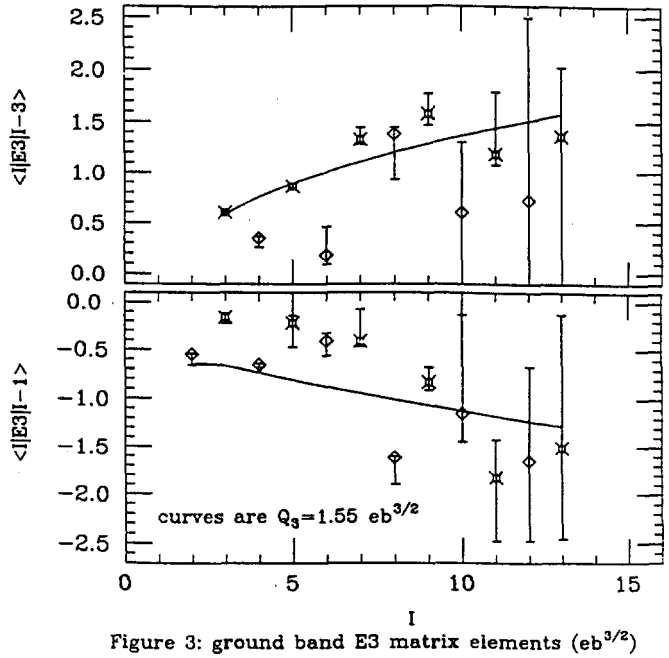

Figure 3: ground band E3 matrix elements (eb$^{3/2}$)

the number of data points in the fit, was 1.24. The relative phases of the wavefunctions were chosen by fixing the sign of one in-band E2 transition matrix element connecting each state, and one E3 between the positive and negative parity bands. The other signs are observables.

The positive parity band closely follows the predictions of the rotational model, with a value of Q_{20}=+400 efm^2 (β_2^{rms} =+0.22) ($Q_{\lambda 0}$ is the intrinsic Eλ moment). The negative parity band shows a systematically smaller value of Q_{20} =330 efm^2 (β_2^{rms} =+0.18) for states above the 3^-. The measured static E2 moments are consistent with the assumption of a prolate shape for this nucleus except that the static E2 moment for the 1^- state is considerably smaller than the rotor prediction.

The E3 matrix elements exhibit a considerable staggering, (shown with different symbols in fig. 3), which could be indicative of mixing with higher K$\neq$0 states. One group of the E3 matrix elements follows approximately the rotational model predictions with a value of Q_{30} =1550 efm^3 (β_3^{rms} $\approx$0.16). The E3 matrix elements connecting the negative parity states to the beta band are unexpectedly large, accounting for $\approx$30% of the B(E3) strength observed in these experiments, while the E3 matrix elements to the gamma band account for <10%. This shows a considerable fractionation of the E3 strength among the K=0 bands. The actual matrix elements will be presented in [17]. The summed B(E3) strengths are fairly constant with a Q_{30}^{sum} $\approx$2000 efm^3 (β_3^{rms} $\approx$0.21) for the negative parity states and a Q_{30}^{sum} $\approx$1600 efm^3 (β_3^{rms} $\approx$0.16) for the positive parity states.

The E1 matrix elements exhibit an increase in their value with spin through the band(fig. 2). At high spins the values of $< I||\mathrm{E1}||I-1 >$ stabilize and are consistent with the value of Q_{10}=0.23 efm given by recent experiments [1, 21], and are comparable to calculations [1, 22]. The relative signs of the E1 and the E3 matrix elements have been fixed in the above analysis so that Q_{10} and Q_{30} have the same sign. This relative phase is taken from ref [20] and is the same as that expected for a deformed liquid drop [23] alone with Strutinski's method for the dipole moment. This phase could not be determined uniquely, since comparable fits were obtained with either choice of this phase.

Mean field calculations which allow octupole deformation have been made for ^{148}Nd [1]. These give an octupole deformed configuration at spin 7-8 with mean values of the deformation parameters of $\overline{\beta}_2$=0.20, $\overline{\beta}_3$=0.075 lying close in energy to the reflection symmetric minimum with $\overline{\beta}_2$=+0.22 and $\overline{\beta}_3$=0. The value of β_3^{rms} is extracted from the Q_{30}, which depends on the magnitude of the octupole moment at the minimum, and the softness of the nucleus to octupole deformation [18]. Calculations including this effect, performed by Nazarewicz and Tabor [22], predict a rather constant Q_{30} for this octupole-soft nucleus.

In summary, a comprehensive set of E1, E2 and E3 matrix elements are presented for ^{148}Nd. The electric quadrupole and octupole matrix elements are consistent with predictions of a model which assumes a rotating shape having prolate quadrupole and octupole deformation in the mass co-ordinates, with fairly constant Q_{20} =400 efm^2 ($\beta_2^{\rm rms}$ $\approx$+0.22), $Q_{30}^{\rm sum}$ $\approx$1600 efm^3 ($\beta_3^{\rm rms}$ $\approx$0.16) for the positive parity states, and Q_{20} =330 efm^2 ($\beta_2^{\rm rms}$ $\approx$+0.18), $Q_{30}^{\rm sum}$ $\approx$2000 efm^3 ($\beta_3^{\rm rms}$ $\approx$0.21) for the negative parity states.

We are very grateful to W. Nazarewicz for stimulating discussions. This work was supported by the U.K. Science and Engineering Research Council, and by the U.S. National Science Foundation. C.A.W., N.C., T.H.H., J.R.H. and P.R. acknowledge S.E.R.C. studentships. R.J.P. acknowledges an S.E.R.C. fellowship. T.C. and J.S. acknowledge grants from the British Council and the University of Liverpool respectively, and grants from the Polish Ministry of Science.

References

[1] W. Urban et al; Phys. Lett. 200B (1988) 424.
[2] W.R. Phillips et al.; Phys. Rev. Lett. 57 (1986) 3257.
[3] G.A. Leander et al.; Phys. Lett. 152B (1985) 284.
[4] S. Cwiok and W. Nazarewicz; Nucl. Phys. A469 (1989) 367.
[5] G.A. Leander et al.; Nucl. Phys. A453 (1986) 58.
[6] R.J. Poynter et al.; Phys Lett. 232B (1989) 447.
[7] J.L. Durell et al.; Daresbury Annual Report (1987/88) p. 28.
[8] T. Karlewski et al.; Z. Phys. A-Atom. Nucl. A330 (1988) 55.
[9] P.J. Nolan et al.; Daresbury Annual Report (1984-85) p. 104,106
[10] D. Cline et al.; NSRL Annual Report (1987) p. 149.
[11] F.C. Kowalik et al.; NSRL Annual Report (1988) p. 183.
[12] A. Renalds et al.; NSRL Annual Report (1988) p. 185.
[13] R. Ibbotson et al.; Nucl. Phys. A530 (1991) 199.
[14] H.H. Pitz et al.; Nucl. Phys. A509 (1990) 587.
[15] T. Czosnyka et al.; Bull. Am. Phys. Soc. 28(1983) 745.
[16] A. Ahmad et al.; Phys. Rev. C37 (1988) 1836.
[17] R. Ibbotson et al.; to be submitted to Nucl. Phys.
[18] W. Nazarewicz and P. Olanders; Nucl. Phys. A441 (1985) 420.
[19] O. Scholten et al.; Ann. Phys. 115 (1978) 325.
[20] P.A. Butler and W. Nazarewicz; Nucl. Phys. A533 (1991) 249.
[21] A.S. Mowbray et al.; Daresbury Annual Report (1988-89) p. 22.
[22] W. Nazarewicz and S.L. Tabor; Phys. Rev. C45 (1992)2226.
[23] A. Bohr and B. Mottelson; vol. 2, (W.A. Benjamin, Inc., 1975)

A new Recoil Filter for γ-Detector Arrays

J. Heese, W. Lahmer, K.H. Maier
Hahn-Meitner-Institut GmbH, Berlin, Germany

M. Janicki, W. Meczynski, J. Styczen
Henryk Niewodniczanski Institute of Nuclear Physics, Cracow, Poland

The operation of large arrays of Compton suppressed HP Germanium detectors in coincidence with electromagnetic recoil mass separators (RMS) has allowed the investigation of many nuclei near the proton dripline and therefore yielded information about the shell structure which stabilises nuclei [1-3]. The observation of nuclei populated in heavy-ion induced fusion-evaporation reactions with only 10^{-3} of the total cross section was possible because the γ ray spectra were filtered with the Z and A information of the evaporation residue. However, the price for this unique exit channel selection is the low efficiency of the existing recoil mass separators. In addition, RMS are less effective in the spectroscopy of heavy nuclei when A and Z cannot be resolved. However, a considerable improvement of γ spectra can still be achieved when γ rays are detected in coincidence with evaporation residues without Z and A information. This coincidence suppresses γ rays from competing fission or transfer processes, Coulomb excitation and reactions with target contaminations and therefore cleans γ spectra and improves the peak/background ratio. In addition, the determination of the recoil velocity vector allows Doppler corrections and therefore a gain in energy resolution. With this in mind, a sturdy time-of-flight filter for evaporation residues has been designed as an additional detector for the OSIRIS spectrometer consisting of 12 Compton suppressed Ge detectors and a 48 element BGO multiplicity filter [4]. The schematic setup is shown in figure 1. Since the recoil filter detector (RFD) requires only a narrow forward cone (200 mrad), it can be used with all 48 elements of the BGO ball, only the most forward Ge detector had to be removed for mechanical reasons.

The RFD consists of two rings of 6 and 12 individual detector elements mounted 73 cm from the target under forward angles between 2.7° and 12.1° to the beam axis. In each RFD element, nuclei hitting a thin aluminised Mylar foil produce secondary electrons which are electrostatically accelerated up to 20 keV and focussed onto a thin plastic scintillator as shown in figure 2. Electron yields of n$\approx$200/ion are expected from slow and heavy evaporation residues [5]. Since the heavy ion-induced secondary electron yields are proportional to the electronic energy loss of the projectile [5,6], recoiling evaporation residues can be discriminated from scattered beam not only via time of flight but also by the pulse height of the scintillator signal. This signal is fast enough (20 ns double pulse resolution) to allow the detection of evaporation residues even if scattered beam hits the detector before. During experiment, 1-2% of the initial beam is scattered into the inner RFD ring causing high countrates. Therefore, signals from scattered beam are suppressed by selecting only RFD signals in an appropriate time window for evaporation residues relative to the pulsed beam. In a second stage a γ-γ-RFD coincidence is required. Parameters measured are the time-of-flight with respect to the RF of the VICKSI cyclotrone and the fired RFD element that determines the angle of the evaporation residue.

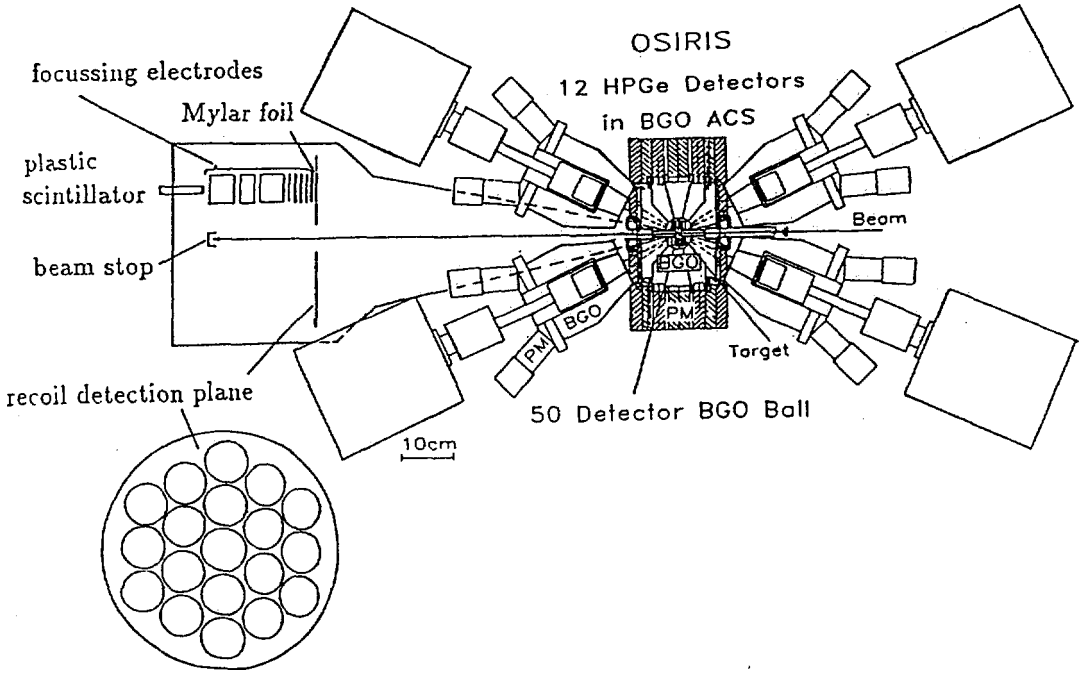

Figure 1: Schematic setup of OSIRIS plus RFD. The 18 detection elements are arranged in the detection plane on concentric rings as shown, the central hole holds the beam stop. For reasons of clearness only one detector element is shown which is magnified in figure 2.

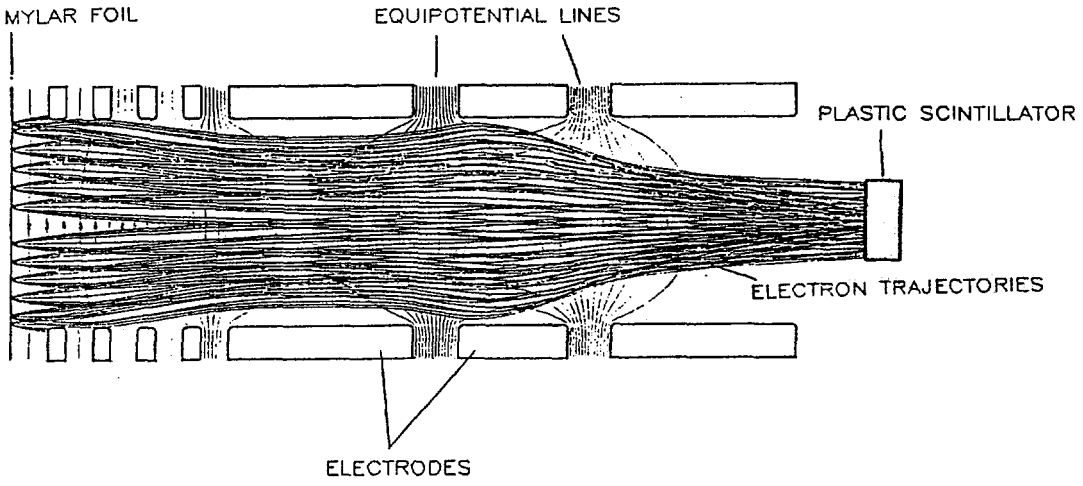

Figure 2: A single RFD element consisting of a thin foil, an electrostatic electron lense and an electron detector. Secondary electrons induced by ions hitting the thin Mylar foil are accelerated and focussed onto a thin plastic scintillator.

The detection efficiency of the RFD depends on the geometrical efficiency and on the fraction of recoils scattered into the sensitive angular range of the device and therefore depends on the reaction and target thickness. The amount of beam and evaporation residues scattering into the active RFD area can be calculated using Monte-Carlo-simulations of ion-beam interaction with solids, e.g. the program TRIM [7]. Efficiencies between 20 % and 50 % can be expected e.g. in the reaction ^{124}Sn(^{40}Ar,5n)^{159}Er at 185 MeV for target thicknesses between 0.5 and 1.4 mg/cm^2.

First in-beam test experiments with only four Compton suppressed Ge detectors and RFD were performed with the reactions ^{40}Ar + ^{124}Sn and ^{40}Ar + ^{152}Sm at 185 MeV. In these runs, γ singles and recoil gated γ spectra were recorded. The recoil detection efficiency determined from (recoil-γ)/γ intensity ratios was 31% in the first run (using a 1.4 mg/cm^2 target) and 18% in the second run (with a 0.7 mg/cm^2 target) which is only about half of the theoretical efficiency. The peak/background ratio in the recoil gated spectra compared to γ singles was improved by a factor of 1.5 and 3, respectively.

First experiments using the full OSIRIS array plus RFD aimed at the spectroscopic investigation of the very neutron deficient Pb isotopes ^{186,188}Pb. The reactions ^{154,156}Gd(^{36}Ar,4n)^{186,188}Pb at 175 MeV and with 1.2 mg/cm^2 targets were used. Figure 3 shows a $\gamma\gamma$ projection from the ^{188}Pb run compared to the corresponding recoil-$\gamma\gamma$ projection. The $\gamma\gamma$ data were gated with a total γ multiplicity m $\geq$ 5 and corrected for Doppler broadening using the average recoil velocity and Ge detector angles measured with respect to the beam axis. The recoil-$\gamma\gamma$ data were Doppler-corrected event-by-event using the measured recoil velocity and angles between Ge detector and RFD element. It can be seen from figure 3 that the background in the recoil-$\gamma\gamma$ spectra is reduced by a factor of 85 compared to $\gamma\gamma$ data. The effect of Doppler corrections is most pronounced for α evaporation channels. The measured recoil detection efficiency in this run was 12 %.

γ transitions in the previously unknown isotopes ^{188}Pb and ^{186}Pb were identified from γ-X-ray coincidences. Figure 4 shows a sum of coincidence spectra for observed ^{188}Pb lines, the inset shows the level scheme established from this work. The 2^+ assignment of the 724 keV state is suggested for two reasons: (i) the line at 724 keV is the most intense one and (ii) a 2^+ energy of about 730 keV in ^{188}Pb is expected from systematics. All other lines were placed in the level scheme according to their intensities. DCO ratios measured in coincidence with the 724 keV line indicate a stretched E2 nature of the 341, 370, 434 and 499 keV transitions. The transitions 370, 434, 499, 558, 606 and 634 keV thus seem to form a rotational band starting with fairly constant energy spacings of ΔE_γ=60-65 keV. A similar sequence of γ rays was observed in ^{186}Pb. While the occurence of collective structures in the neutron deficient Pb isotopes is known [8,9], the excitation energy of the first rotational levels is surprisingly low. Calculations using the Strutinsky shell correction method with a Woods-Saxon potential and a monopole pairing interaction have predicted well-developed prolate minima of the potential energy surface in all Pb isotopes with N$\leq$108 [10]. The so far known deformed structures are ascribed to proton excitations and oblate shape. The lowest predicted excitation energy of the prolate second minimum is 1.5 MeV in

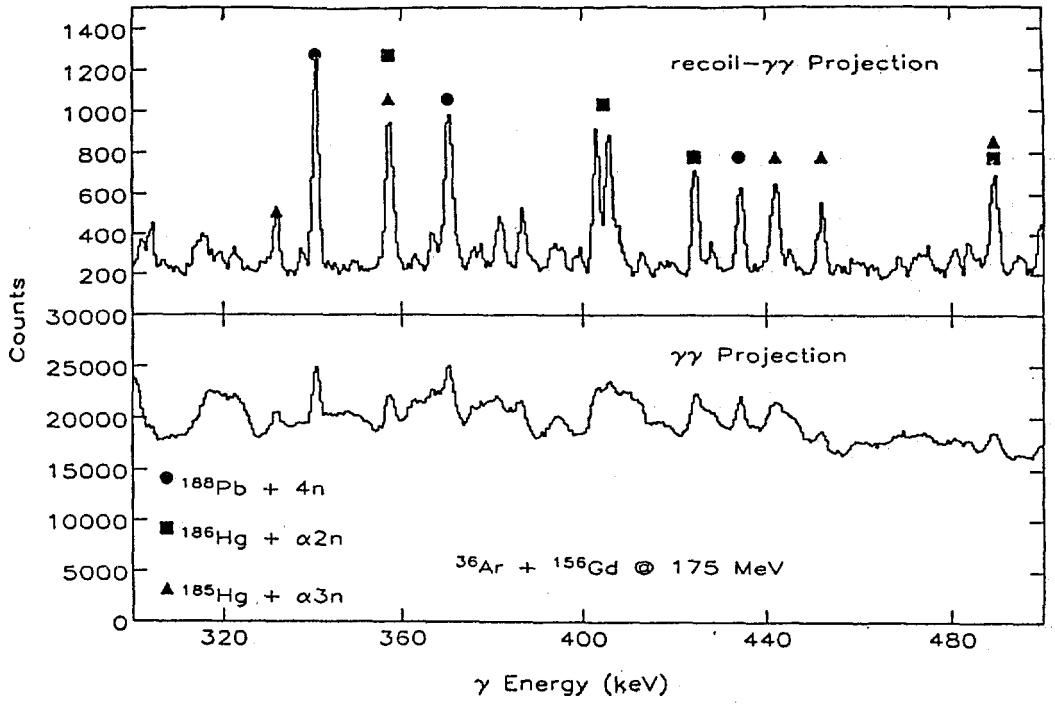

Figure 3: Comparison of a $\gamma\gamma$ projection with a recoil gated $\gamma\gamma$ projection. For details see text.

^{186}Pb with a calculated deformation parameter $\beta_2 = 0.26$. Experimentally, the lowest rotational levels in ^{186,188}Pb are found around 1 MeV.

In summary, we have shown that a RFD is a helpful additional detector for Germanium detector arrays with respect to background suppression and exit channel selection. This is particularly true for the spectroscopy of heavier nuclei where fission dominates. Although the measured efficiencies are still somewhat low compared to expected values, first experimental results obtained with the RFD look very promising. We have identified the previously unknown isotopes ^{186,188}Pb. In both nuclei low-lying rotational bands have been observed for the first time.

The authors would like to acknowledge the help of H. Kluge, H. Grawe, R. Schubart, M. Schramm and K. Spohr during the experiments. We would also like to thank J. Grebosz for writing the data sorting software. This work was supported by the Polish-German co-operation treaty.

References

[1] C.J. Lister et al., Phys. Rev. C 42, R1191 (1990)
[2] C.J. Gross et al., Phys. Rev. C 44, R2253 (1991)
[3] P.J. Ennis et al., Nucl. Phys. A 535, 392 (1991)
[4] R.M. Lieder et al., Nucl. Instr. Meth. A 220, 363 (1984)
[5] H.G. Clerc et al., Nucl. Instr. Meth. 113, 325 (1973)
[6] H. Rothard et al., in 'Particle Indudced Electron Emission II', Springer Tracts

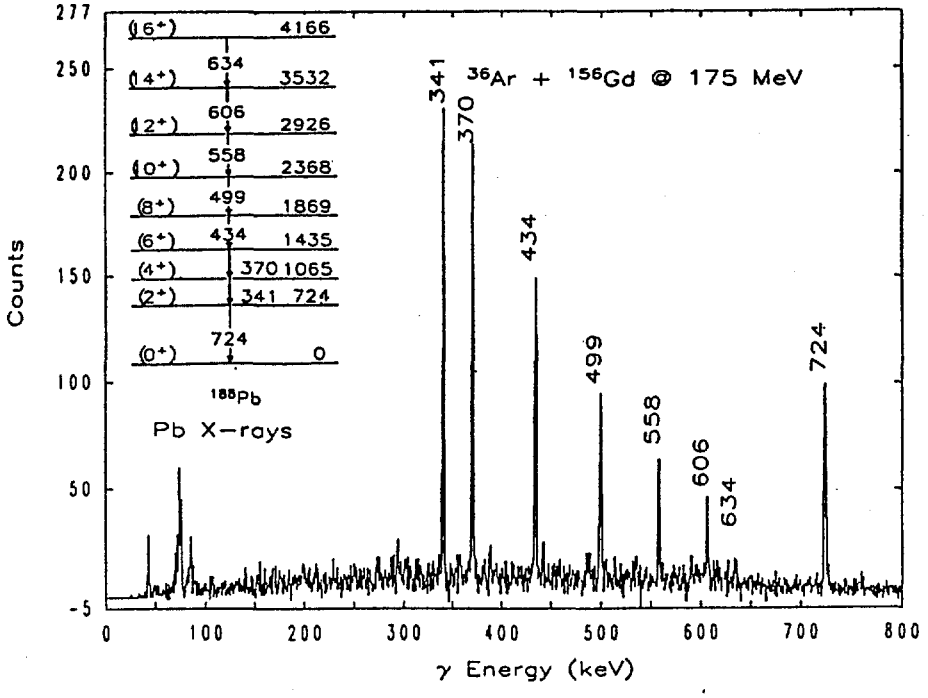

Figure 4: Summed coincidence spectra of the labeled transitions in ^{188}Pb from recoil-$\gamma\gamma$ data. The inset shows the deduced level scheme.

in Modern Physics, Vol. 123, Springer 1991
[7] J.P. Biersack, L.G. Haggmark, Nucl. Instr. Meth. 174, 257 (1980)
[8] P. van Duppen et al., Phys. Rev. Lett. 52, 1974 (1984); Phys. Lett. B 154, 354 (1985)
[9] G. Baldsiefen et al., Phys. Lett. B 275, 252 (1992)
[10] R. Bengtsson and W. Nazarewicz, Z. Phys. A 334, 269 (1989)

High Spin Study and Lifetime Measurements of Neutron Rich Co Isotopes.

P.H.Regan, J.W.Arrison, U.J.Hüttmeier and D.P.Balamuth

Dept. of Physics, University of Pennsylvania, 209 South 33rd St,
Philadelphia, Pa 19104, USA

Abstract

The neutron rich nuclei ^{61,63}Co have been studied using the reactions ^{16}O(^{48}Ca,p2n)^{61}Co at 110 MeV and ^{18}O(^{48}Ca,p2n)^{63}Co at 110 MeV respectively. Discrete lines from the channels of interest were investigated using pre-scaled γ singles, charged-particle-γ, neutron-charged-particle-γ and charged particle$-\gamma-\gamma$ data. Decay schemes, with level spins deduced from angular distribution data are presented togther with preliminary information on the lifetimes of some higher excitation states. These data represent the first study on the medium to high spin states in these nuclei.

Introduction

The advent of large Van de Graaff heavy ion accelerators has allowed nuclear structure scientists to gain a vast array of spectroscopic information on proton-rich nuclei via heavy ion fusion-evaporation reactions. While the data gained in such pursuits has provided a rich testing ground for present day nuclear models, the neutron-rich side of the nuclear mass table remains largely unexplored by these methods. In the main, such nuclei are inaccessible via such reactions due to the limited choice of stable nuclei for target and beam materials. It is however possible to reach some neutron rich systems by choosing high T_z beam/target combinations and studying the relatively low cross-section charged particle evaporation channels. Here we report results from a program of work using ^{48}Ca beams on a variety of light targets. Specifically we have investigated ^{61,63}Co via the $p2n$ evaporation channel on ^{16,18}O targets. These nuclei have been studied previously via β decay [1, 2] and light ion pickup and stripping experiments. [3, 4]. However, none of these experiments identified the medium to high spin yrast states that are preferentially populated by heavy ion fusion reactions. The extension of the yrast parts of these decay schemes allows further comparison with model predictions at higher spins which is important for a full understanding of such nuclei.

Experimental Procedure and Data Analysis.

In order to identify γ ray transitions in ^{61,63}Co, separate experiments were performed at the University of Pennsylvania tandem accelerator using gold-backed $W^{16}O_3$ and $W^{18}O_3$ targets of thickness 400 μg/cm^2 and 1 mg/cm^2 respectively. The targets were bombarded by 110 MeV ^{48}Ca beams to populate states in the cobalt nuclei of interest via the $p2n$ evaporation channel. In-beam γ-rays were identified using an array of six germanium detectors (three Compton suppressed) with the Penn 4π segmented charged particle array [5]. Three of the Ge detectors were placed at 90° to the beam direction, with two at 135° and one at 140°. The charged particle array utilised phoswhich detector telescopes to distinguish between protons and α particles, thereby giving excellent element identification spectra. A large tank of liquid scintillator was placed at 0° downstream to measure coincident neutrons. Data was written to optical disc on γ singles, charged particle-γ, neutron-charged-particle-γ and charged particle-$\gamma-\gamma$ events for off-line analysis.

Figure 1 shows typical proton gated identification spectra for the two reactions. Note the apparent increase in yield for the higher neutron multiplicity $px n$ channels in the neutron gated spectra. The circled peaks in the ^{18}O data are due to contaminantion of the target with ^{16}O.

States in ^{61}Co were identified using the following three criteria: (a) their presence in the ^{16}O+^{48}Ca proton-γ spectrum (b) their absence in the $\alpha-\gamma$ spectrum and (c) their relative neutron efficiency compared to known states in ^{60,62}Co [7, 8]. States populated via $p2n$ evaporation were expected to have about two thirds the single neutron detection efficiency of the $p3n$ channel since the only two-thirds as many neutrons are produced per event. States in ^{63}Co were identified in essentially the same manner as those in ^{61}Co, but using the ^{18}O reaction.

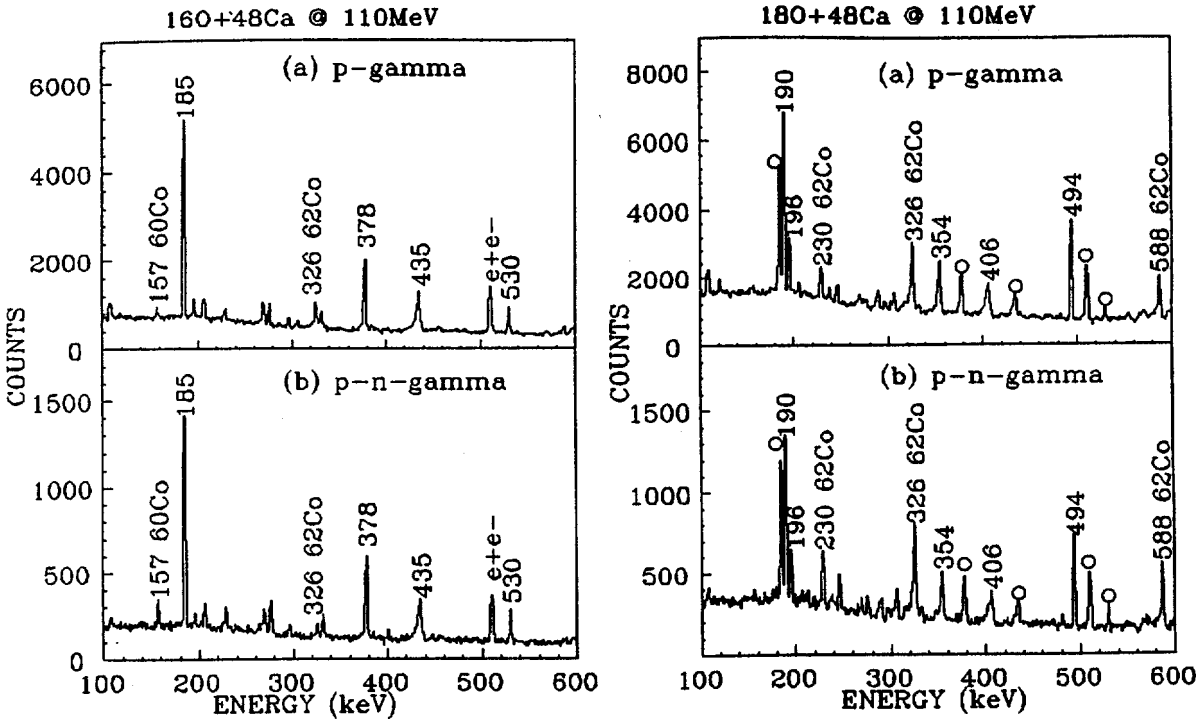

Figure 1: Typical spectra used in the identification of ^{61,63}Co.

The total evaporation cross-section was divided up into a number of different residual channels with the strongest channels being $3n$ and $4n$. The xn evaporation cross-section is enhanced for a more neutron rich compound system and this effect was evident in the ^{18}O+^{48}Ca reaction where xn evaporation accounted for approximately 70% of the total fusion cross section. The data highlights the effectiveness of 4π array for studying such systems, by selecting the pxn and αxn decay channels and separating them from the xn residues.

The decay schemes of ^{61,63}Co were constructed by investigating the coincidence relationships between transitions identified in these nuclei by the the $p-\gamma$ and $p-n-\gamma$ data. A $\gamma-\gamma$ matrix gated on the condition that a coincident proton was also observed in the 4π array was used to set coincidence gates on the identified transitions. Typical examples of the spectra used to build up the decay schemes are shown in figure 2. The ordering of transitions was deduced using intensity measurements, corrected for dectector efficiency and any angular anisotropy using the $p-\gamma$ data. Some information on the γ-ray multipolarities was obtained from a two point angular distribution analysis assuming the A_4 coefficients were negligibly small.

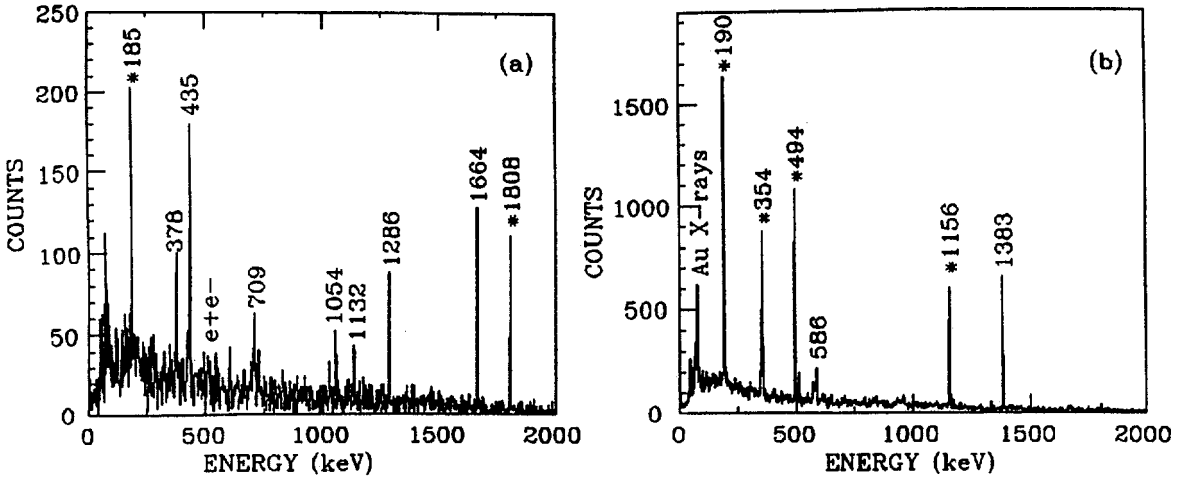

Figure 2: Sums of individual $p-\gamma-\gamma$ gates (*) for (a) ^{61}Co and (b) ^{63}Co.

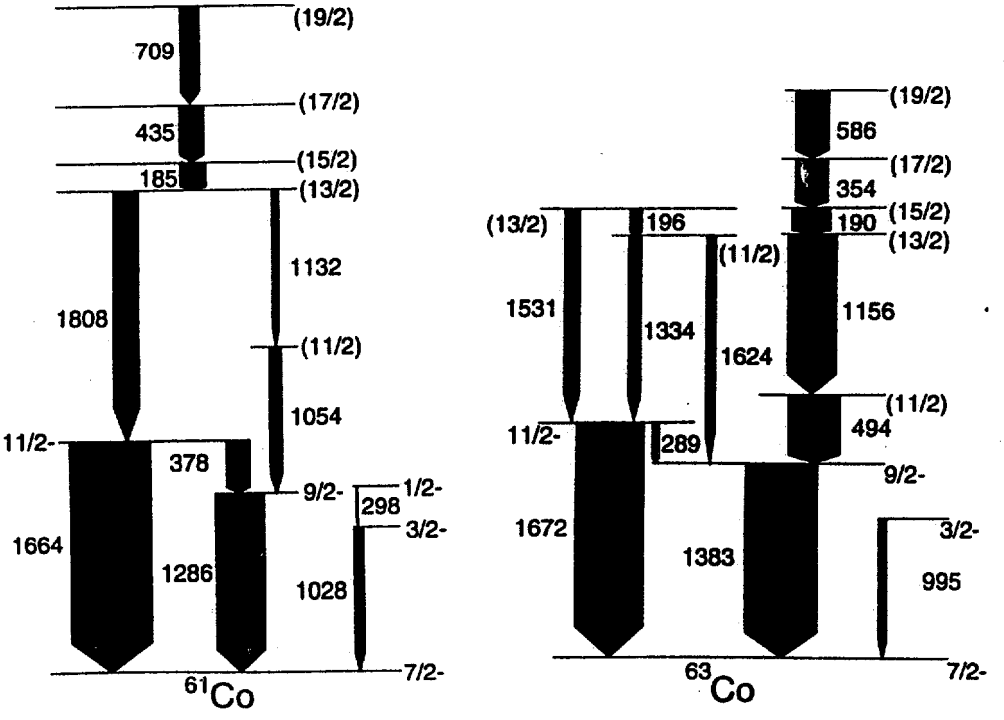

Figure 3: Partial decay schemes of ^{61,63}Co observed in the present work.

A ground state spin of $\frac{7}{2}^-$ was deduced for ^{61}Co following the β decay of ^{61}Fe [1]. The low-lying $\frac{9}{2}^-$ and $\frac{11}{2}^-$ states at 1286 keV and 1664 keV have been identified previously by Mateja *et al* [3] using the ^{64}Ni(p,α)^{61}Co reaction. These assignments are consistent with the present work which suggests ΔJ=1 for the 378 keV transition and ΔJ=2 for the 1664 keV crossover. The angular distribution for the 1286 keV transition could not be measured accurately due to uncertainties associated with the Doppler shifted lineshape at 135°. The high spin yrast levels in the present work have not been previously observed which is consistent with the usual expectation that heavy ion fusion-evaporation reactions preferentially populate yrast and near yrast states.

The $\frac{7}{2}^-$ ground state of ^{63}Co was deduced from β decay studies of ^{63}Fe [2]. As in the ^{61}Co decay scheme, the low lying 1383 and 1672 keV states had also been previously observed [4] using a light-ion reaction. However, the spin assignment in the previous work for the 1383 keV state differs from the present assigment. The light ion data assigned an ambiguous $(\frac{5}{2}, \frac{7}{2})$ spin for the 1383 keV state. However, the γ-ray angular distribution for this transition was consistent with a dipole, suggesting a spin of $\frac{9}{2}$ assuming the preferential population of yrast states. In addition, the observation of a dipole decay from the spin $\frac{11}{2}^-$ 1672 keV level appears to confirm the 1383 keV level spin of $\frac{9}{2}^-$. As figure 3 shows, the yrast decay scheme for ^{63}Co consists, in part, of a simple cascade of six dipole γ-rays from the $\frac{19}{2}$ state to the $\frac{7}{2}^-$ ground state.

Whilst the parity of most of the high spin states could not be deduced from the simple two point angular distributions, it is likely that the levels have negative parity due to the occupation of the negative parity f and p states. The yrast states in ^{57}Co, for example, are all negative parity upto spin $\frac{19}{2}$ [6]. However, the possibility of postive parity states resulting from the population of the $g\frac{9}{2}$ orbital can not be ruled out. Indeed such positive parity states have been observed in neighbouring Fe and Ni nuclei with N=33 and 35 at excitation energies of about 1-2 MeV [8, 7].

A number of other γ-rays were identifed in these nuclei which could not be placed with certainty into the decay schemes. The strongest of these were 530 keV, 710 keV and 752 keV in ^{61}Co and 405 keV, 555 keV and 1248 keV in ^{63}Co.

Lifetime Measurements.

The particle-γ spectra obtained with the Penn 4π array were also used to obtain information regarding the lifetimes of some of the higher spin states. The three 90° germanium detectors were used to get accurate values for the unshifted energies, whilst the average shifted energies were obtained by measuring the centroids of the backward shifted peaks in the two 135° detectors. Figure 4 shows the 90° and 135° spectra for shifted states in ^{61,63}Co. The experimental fractional Doppler shifts were converted to apparent lifetimes assuming simple LSS stopping theory [9]. Table 1 gives a summary of the DSAM results for shifted transitions observed in the present work.

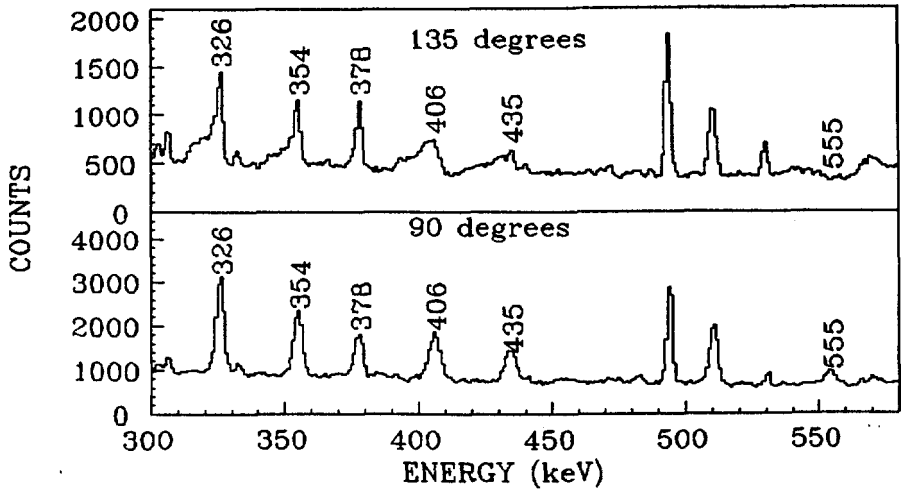

Figure 4: Proton-γ coicidence data for detectors at (a) 90° and (b) 135° for the ^{16,18}O+^{48}Ca reactions.

Since the nature of feeding into the shifted transitions is not well known only the apparent lifetimes of resolved transitions are quoted here. The experimental B(M1)s were calculated with the apparent lifetimes of the states and therefore should only be regarded as lower limits to the true intrinsic values.

Nucleus	E_o (keV)	$F(\tau)$	τ_{app} (ps)	B(M1)
^{61}Co	434.8(5)	0.26(3)	1.2(4)	0.58(23)
^{63}Co	353.6(5)	0.06(1)	6(3)	0.21(9)
^{63}Co	405.4(5)	0.16(2)	2.2(7)	0.34(12)
^{63}Co	554.7(1.0)	0.38(10)	0.8(3)	0.21(8)
^{63}Co	585.6(1.0)	0.36(12)	0.8(3)	0.17(7)

Table 1: Measured fractional Doppler shifts for shifted states in ^{61,63}Co. The B(M1) are given in units of $\frac{e\hbar}{2Mc}$. The B(M1) values include corrections of the experimentally observed branching ratios as measured from the $p-\gamma$ intensity data.

For some of the higher lying (and therefore more shifted) transitions where the angular distribution measurements can have larger errors, the lifetime measurements can be used as a way of deducing the multipolarity of the decay. All of the transitions listed in table 1 for example, have lifetimes consistent with dipoles but not with electric quadrupoles.

Summary and Conclusions.

The decay schemes of the neutron rich isotopes, ^{61,63}Co have been investigated using heavy ion fusion reactions and the medium spin yrast states studied for the first time. Two point angular distributions have been used to gain information on the multipolarities of these transitions. Clear evidence of Doppler shifts in some higher lying transitions have been measured allowing lifetimes and lower limits for reduced transition probabilties to be deduced.

Two of the germanium detectors and one Compton suppression shield used in this work were kindly loaned to us by the group at Rutgers University. This work is supported by the N.S.F.

References

[1] J.Bron *et al. Phys. Rev.* **C11** (1975) p996

[2] E.Runte *et al. Nucl. Phys.* **A441** (1985) p237

[3] J.F.Mateja *et al. Phys. Rev.* **C13** (1976) p2269

[4] M.Seeger *et al. Nucl. Phys* **A533** (1991) p1

[5] T.Chapuran *et al. Nucl. Inst. Meth.* A272 (1988) p767

[6] N.Bendjaballah *et al. Nucl. Phys.* **A280** (1977) p228

[7] E.K.Warburton *et al. Phys. Rev.* **C16** (1977) p1027

[8] E.K.Warburton *et al. Phys. Rev.* **C18** (1978) p1637

[9] T.Alexander and J.S.Forster, *Advances in Nuclear Physics,* Baranger-Vogt **10** (1978) p258

Gamma-ray Spectroscopy of Nuclei Near ^{100}Sn

D. Seweryniak[a], B. Cederwall[b], J. Nyberg[a], C. Fahlander[a], E. Adamides[c], A. Ataç[d], G. de Angelis[e], H. Grawe[f], E. Ideguchi[g], A. Johnson[b], R. Julin[h], S. Juutinen[h], W. Karczmarczyk[i], A. Kerek[b], J. Kownacki[i], S. Mitarai[g], L-O .Norlin[b], M. Piiparinen[d], R. Schubart[f], G. Sletten[d], S. Törmänen[h], A Virtanen[h]

[a] The Svedberg Laboratory and Department of Radiation Sciences, Uppsala University, Uppsala, Sweden
[b] Manne Siegbahn Institute of Physics and Department of Physics, The Royal Institute of Technology, Stockholm, Sweden
[c] National Centre for Scientific Research, Ag. Paraskevi, Attiki, Greece
[d] The Niels Bohr Institute, University of Copenhagen, Copenhagen, Denmark
[e] Laboratori Nazionali di Legnaro, Legnaro, Italy
[f] Hahn-Meitner Institute, Berlin, Germany
[g] Department of Physics, Faculty of Science, Kyushu University, Fukuoka, Japan
[h] Department of Physics, University of Jyväskylä, Jyväskylä, Finland
[i] Institute of Experimental Physics, University of Warsaw, Warsaw, Poland

Abstract: Proton rich nuclei close to ^{100}Sn have been investigated in an in-beam γ-ray spectroscopic study using the NORDBALL detector array, including arrays of charged particle and neutron detectors. Excited states were identified for the first time in ^{102}In, ^{106,107,108}Sb and tentatively in ^{108,109}Te. The nucleus ^{110}Te was also populated and studied for the first time in an in-beam experiment.

The study of exotic proton rich nuclei close to ^{100}Sn is of great interest for investigating the validity of the nuclear shell model in general and single-particle energies and the residual proton-neutron interaction in particular. For ^{100}Sn the effective proton-neutron interactions might even be strong enough to cause deformation of the ground state of the nucleus. The nucleus ^{100}Sn in itself is a very interesting and challenging study object because it is the heaviest self-conjugate (N=Z) doubly magic nucleus which can be assumed to be stable against particle decay in its ground state. The possibility to investigate the entire range of tin isotopes between the doubly magic nuclei ^{100}Sn and ^{132}Sn is also of great significance since it will provide a deeper insight into the role of the residual interactions as one sequences through a series of valence orbitals. To produce and study the structure of ^{100}Sn it will probably be necessary to use radioactive nuclear beams and/or targets together with very efficient detector systems. Until such facilities are available one is left with the challenge to study nuclei as close as possible to ^{100}Sn using more conventional techniques. We have, therefore, recently performed heavy-ion in-beam γ-ray spectroscopy in this mass region.

The experiment was performed at the Tandem Accelerator Laboratory of the Niels Bohr Institute in Denmark using the reaction $^{58}_{28}Ni_{30}$ (270 MeV) + $^{54}_{26}Fe_{28}$ ($10mg/cm^2$, 99.8%) leading to the compound nucleus $^{112}_{54}Xe_{58}$. The emitted γ rays, charged particles and neutrons were detected in the NORDBALL detector system, equipped with 15 Ge-BGO spectrometers, one of which was a LEP detector, a 4π charged particle detector consisting of 21 ΔE-type Si detectors, a 2π γ-ray calorimeter consisting of 30 BaF_2 crystals in the upstream hemisphere and a $\sim 1\pi$ neutron detector array comprising 11 liquid scintillator detectors in the downstream hemisphere. The detector system is shown schematically in fig. 1.

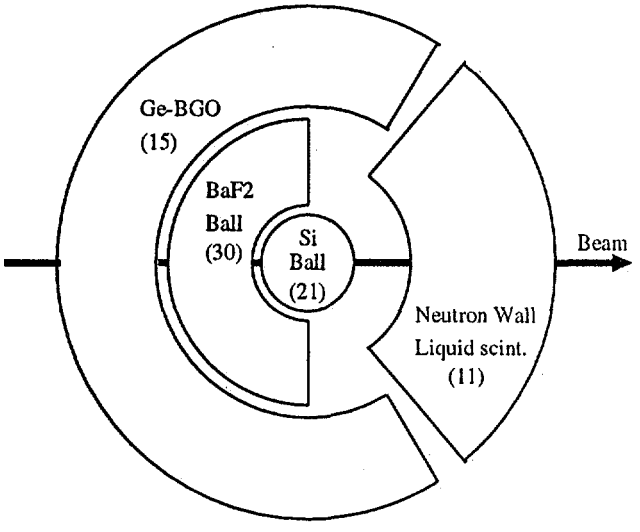

Fig. 1. Schematic figure of the NORDBALL detector system as used in the present experiment and equipped with 15 Ge-BGO spectrometers and the selective devices Silicon Ball (21 detectors), Neutron Wall (11 detectors) and the BaF_2 Ball (30 detectors).

The compound nucleus ^{112}Xe is very neutron deficient which means that reactions leading to evaporation of neutrons are rare. Since such reactions are of the greatest interest, producing the most exotic nuclei, a major emphasis was put on the performance of the neutron detector system. By using both neutron time-of-flight and pulse shape discrimination techniques it was possible to improve the neutron-γ separation by an order of magnitude compared to earlier results, where only pulse shape discrimination was used. A total of about 420 million γ-γ-coincidence events containing information about the detected γ rays, neutrons, protons and α particles were collected.

In the data analysis, γ-γ-coincidence matrices gated by different combinations of charged particles, neutrons, γ-ray fold and sum-energy have been produced. These matrices are not clean since reaction channels with higher particle multiplicities may leak into channels with lower multiplicities, but by using a special subtraction technique, 'clean' matrices have been extracted, each containing events from one specific reaction channel. From these final matrices γ-ray spectra were projected.

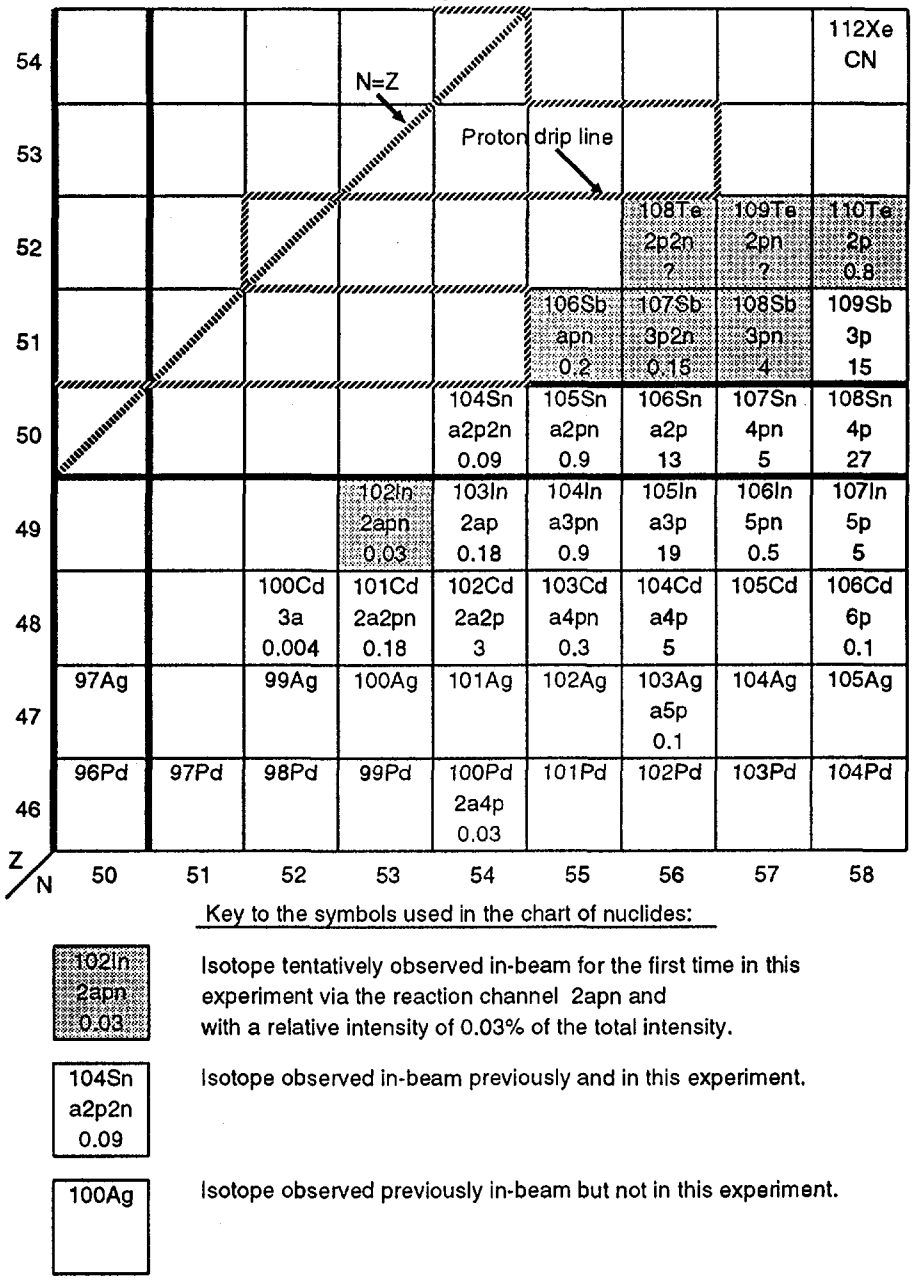

Fig. 2. An overview of the residual nuclei observed in the present experiment.

In a preliminary analysis we have so far been able to identify in-beam γ rays tentatively from 26 nuclei. They are shown in fig. 2 with their relative intensities. No excited states were previously known in six of these nuclei, namely ^{102}In, ^{106,107,108}Sb and ^{108,109}Te. High-spin states of ^{110}Te were populated for the first time in an in-beam experiment. Only the 2^+ state was previously known for this nucleus from decay work. An example of a γ-γ-coincidence spectrum for ^{102}In is shown in fig. 3.

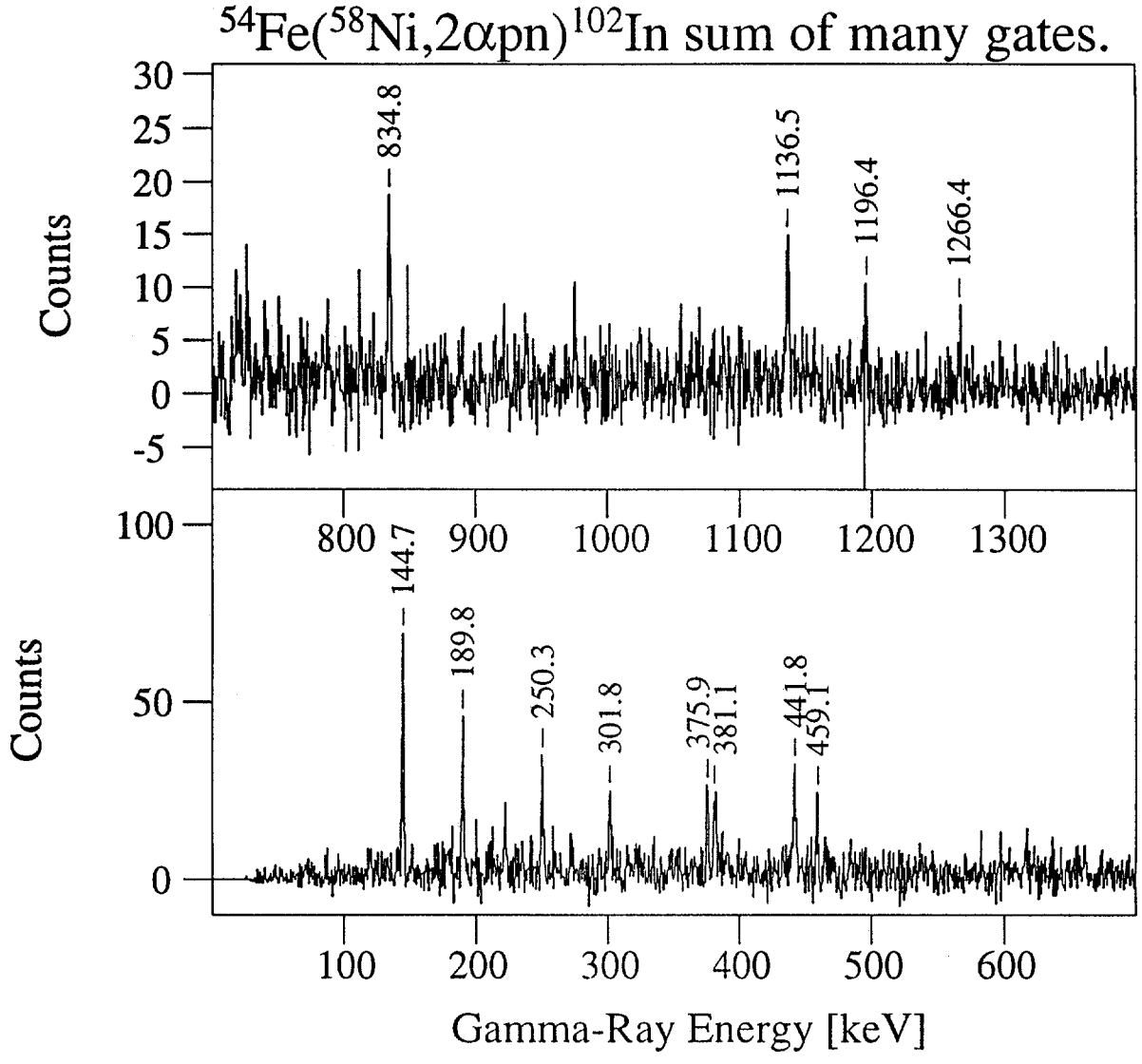

Fig. 3. A summed γ-γ-coincidence spectrum gated by $2\alpha pn$. All strong lines seen in this spectrum are in coincidence with each other and are believed to belong to ^{102}In.

The experimental evidence for our assignments are summarized in fig. 4, where the observed intensity ratios of characteristic γ-ray transitions in spectra gated by different conditions are shown. The intensity ratios depend on the particle multiplicities and on the detection efficiencies. Since the detection efficiency for a specific type of evaporated particle is almost independent of the reaction channel, combinations of such ratios and comparisons with γ rays from previously known nuclei that were populated in the experiment suggest the assignments of the final nuclei. All the ratios shown in fig. 4 agree nicely with the suggested assignments, except maybe for the $2p$ channels, where the experimental ratios seem to lie in between proton multiplicity 2 and 3. The reason for this is not completely understood at the moment. However, it is necessary to be cautious with the assignments since γ rays from fission or from reactions with light target contaminations may be present. These effects are presently being studied.

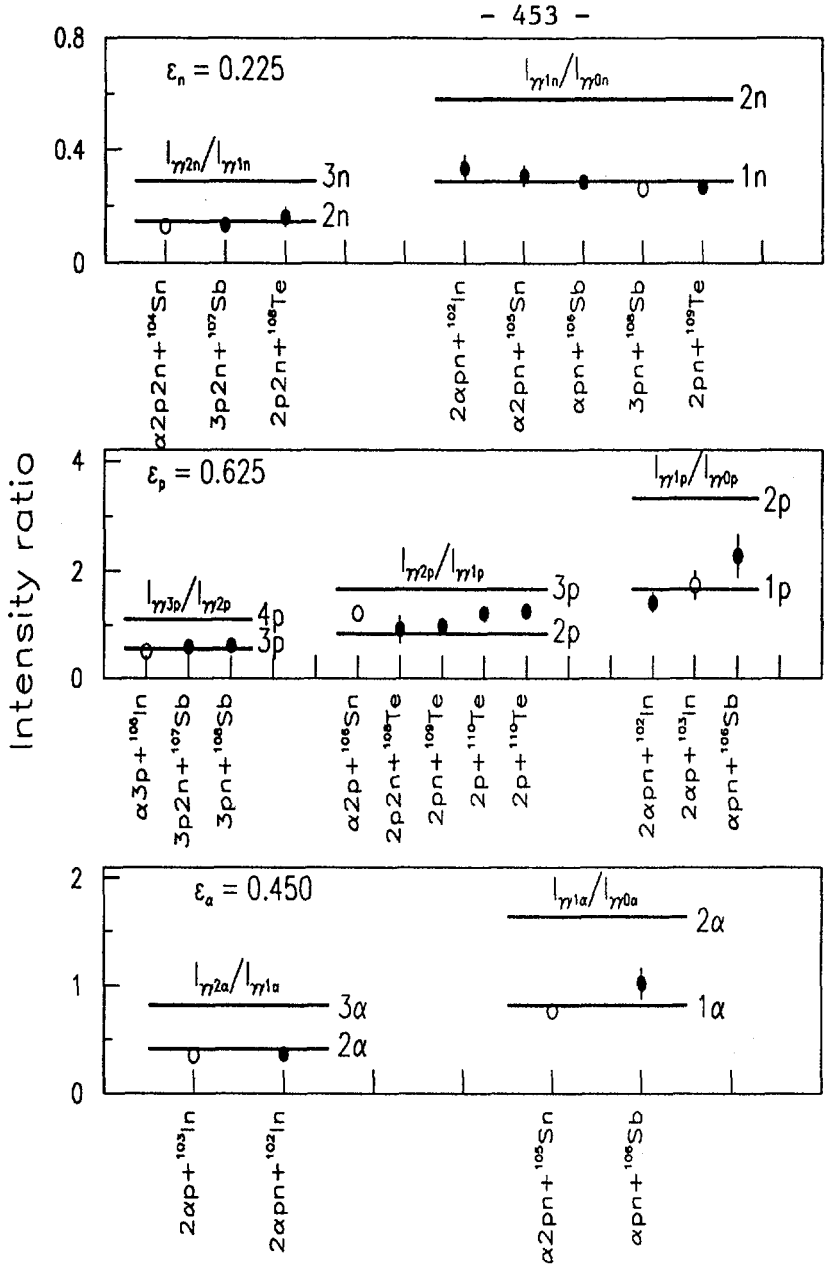

Fig. 4. Experimental intensity ratios for characteristic γ rays in the spectra gated by different numbers of neutrons, protons and α particles. The solid lines are values calculated for different particle multiplicities using the average total particle efficiencies given in the figure.

In addition to the identification of previously unobserved nuclei, the present experiment will yield new information on the high-spin structures of the nuclei $^{103-107}$In, $^{104-108}$Sn and ^{109}Sb.

Acknowledgements:
This work was partially supported by the Swedish Natural Science Research Council.

WORKSHOP ON LARGE GAMMA-RAY DETECTOR ARRAYS

Chalk River

SESSION 7: FAR VISIONS (I)

High Spin Studies with Radioactive Ion Beams

J. D. Garrett
Physics Division, Oak Ridge National Laboratory
Oak Ridge, Tennessee 37831-6371, USA

ABSTRACT

The variety of new research possibilities afforded by the culmination of the two frontier areas of nuclear structure: high spin and studies far from nuclear stability (utilizing intense radioactive ion beams) are discussed. Topics presented include: new regions of exotic nuclear shape (e.g. superdeformation, hyperdeformation, and reflection-asymmetric shapes); the population of and consequences of populating exotic nuclear configurations; and complete spectroscopy (i.e. the overlap of state of the art low- and high-spin studies in the same nucleus).

I. INTRODUCTION

Probably today's two most exciting frontiers of nuclear structure are rapidly-rotating nuclei and nuclei far from stability. The current renaissance in both frontier areas is based on recent technical innovations: *to wit,* the advent of large Compton-suppressed germanium detector arrays (e.g. EUROGAM and GAMMASPHERE) based on the ability to grow large crystals of high-purity germanium,[1] and new breakthroughs in producing and accelerating high-intensity beams of radioactive ions. Therefore, it is imperative to consider the culmination of these two initiatives, high-spin research possibilities afforded by intense beams of radioactive ions.

The large angular momentum imparted to the residues of heavy-ion induced fusion-evaporation reactions produces two major nuclear structure effects: (i) a stabilization of highly-deformed nuclear shapes; and (ii) a major rearrangement of the nuclear single-particle states generated by the Coriolis and centrifugal forces acting on the nucleons due to the rotation of the nucleus. The increased stability of superdeformed nuclei is well known to this audience. The modification of the single-particle spectrum of states by rotation is illustrated in Fig. 1. The Coriolis plus centrifugal term in the single-nucleon hamiltonian[5] ($= -\omega j_1$, where ω is the angular frequency of rotation, and j_1 is the component of the intrinsic nucleonic angular momentum along the rotational axis) can produce perturbations as large as those resulting from nuclear deformation. Such rotationally-induced single-particle effects are the bases of a variety of high-spin phenomena as diverse as "backbending" (band crossings),[6,7] loss of pair correlations,[8,9] the nuclear shrinking paradox,[4] and an enhancement of residual interactions[10] based on an increased overlap of nucleonic states.[4,11]

Radioactive ion beams will provide experimental access to a variety of even more exotic shapes and combinations of single-particle orbitals in nuclei far from stability. Some examples are described in Sections 2 and 3, respectively. Likewise, the possibility and consequences of comprehensive high spin studies of nuclei, whose low angular momentum

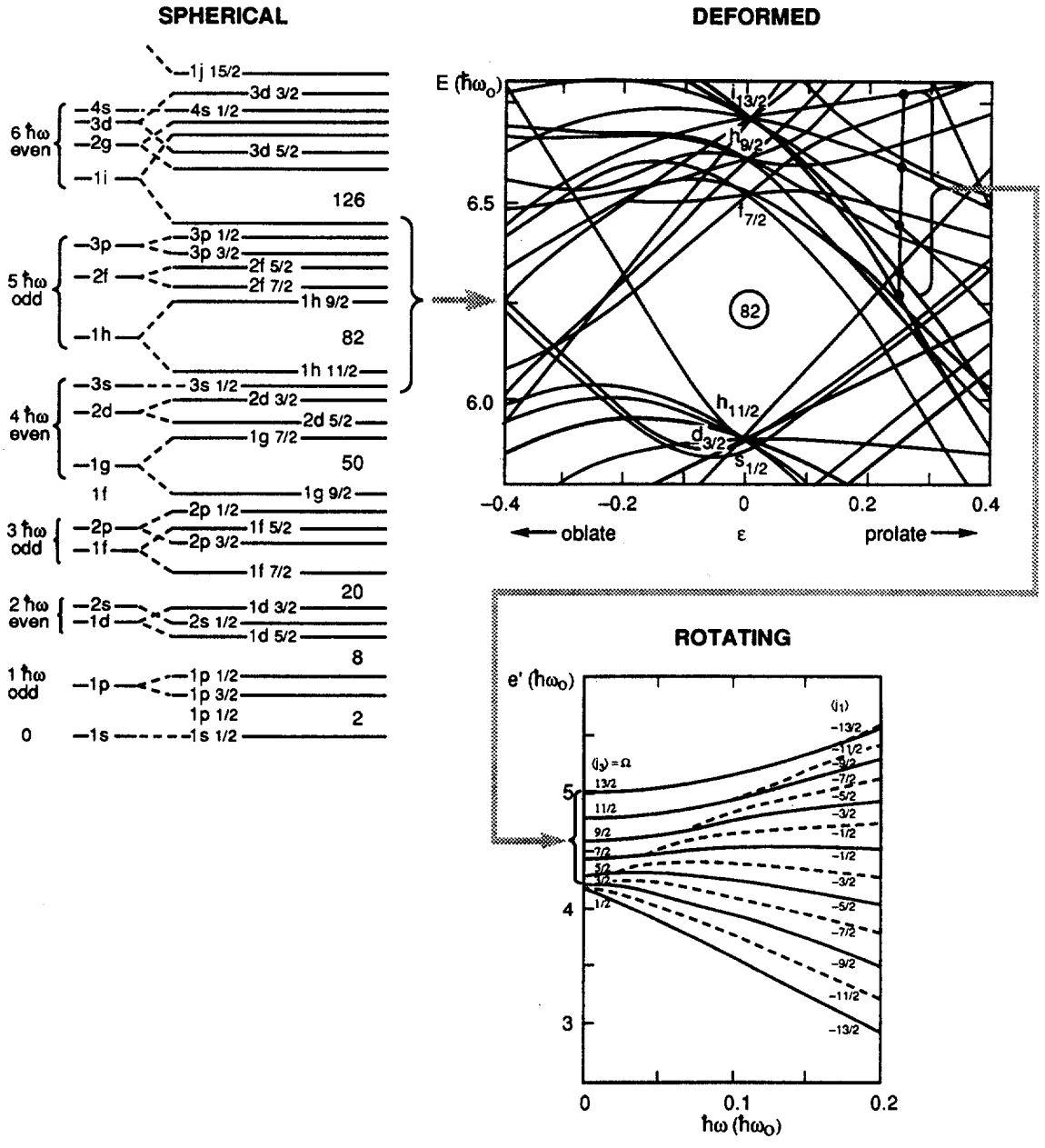

Fig. 1. Comparison of the spectra of single-particle states from spherical, deformed, and rotating deformed nuclear potentials taken from refs. 2-4, respectively (see also Figs. 4 and 6). Because of the greater complexity of the single-particle states with increasingly-complex approximations to the nuclear potentials, only the subset of states indicated in the figure is shown for the deformed and rotational cases.

properties also are well known, are discussed in Section 4. Whereas the neutron-rich portion of this research will require large ISOL facilities, for example, the proposed IsoSpin Laboratory,[12] nearly all of the proton-rich studies also can be made using "first generation" facilities, such as the Oak Ridge RIB Facility.[13] For a more comprehensive discussion of the structure of rapidly-rotating nuclei with radioactive beams the reader is referred to ref. 14.

II. EXOTIC NUCLEAR SHAPES ACCESSIBLE WITH RADIOACTIVE ION BEAMS

The observations of high-spin superdeformed states (2:1 ratio of the major to minor axes) in A ≈ 150 and 190 nuclei (refs. 15,16 and 17,18, respectively) and deformations intermediate between normal and superdeformed in A ≈ 130 and 186 (refs. 16, 19 and 20, respectively) have focused an intense interest on highly-deformed nuclear shapes. Such states correspond to secondary minima in the nuclear potential energy at large deformations resulting from major gaps in the single-particle levels.[21-23] This striking illustration of the interplay of single-particle and collective degrees of freedom was developed[21] to describe isomeric fission of actinide nuclei.[24,25] Already in 1968 it was realized that such secondary minima should also exist in lighter nuclei; indeed the proton and neutron numbers of the occurrence of such shell corrections were predicted.[26] However, it wasn't until 1986 that the technique of populating superdeformed minima at high spin and observing the gamma-ray cascade based on the rotating superdeformed intrinsic state succeeded[15] in establishing additional superdeformed states at high spin.

The high-spin superdeformed states near A = 150 and 190 and the actinide fission isomers all occur at or near predicted minima in both the proton and neutron shell energy, see Fig. 2. Other regions of the table of isotopes where the proton and neutron shell energies are predicted to act coherently to produce additional minima in the potential energy at superdeformed deformations, also are indicated in this figure, as are the projected "new" nuclei that can be studied[14] using the radioactive ion beams planned for the IsoSpin Laboratory.[12] Though a large number of "new" neutron-rich nuclides become accessible to study with radioactive beams, these cannot be populated by heavy-ion fusion-evaporation reactions, the traditional technique for studying high-spin superdeformed states.[16,18] Therefore, new techniques are necessary to populate high-spin superdeformed states to the right of the valley of beta stable nuclei. For example, Coulomb excitation of neutron-rich radioactive beams can provide some high spin information, but this process has a vanishingly-small probability of populating superdeformed states. On the other hand, Coulomb excitation plus few-particle transfer may offer some chance of studying superdeformation in these neutron-rich nuclei; however, the associated cross sections also are small at very high spin. So far, the probability of populating superdeformed states has not been demonstrated by these mechanisms.

Indeed, the known A ≈ 150 and 190 high-spin superdeformed nuclei[16,18] are on the proton-rich side of stable nuclei, see Fig. 2. Although some of the best candidates[28,29] of the light superdeformed nuclei, Z = 33-35 and 38-42 and N = 29-47 are accessible with stable beams and targets and have been investigated, no discrete transitions attributed to superdeformed states have been observed.[30] This lack of success may be the result of the

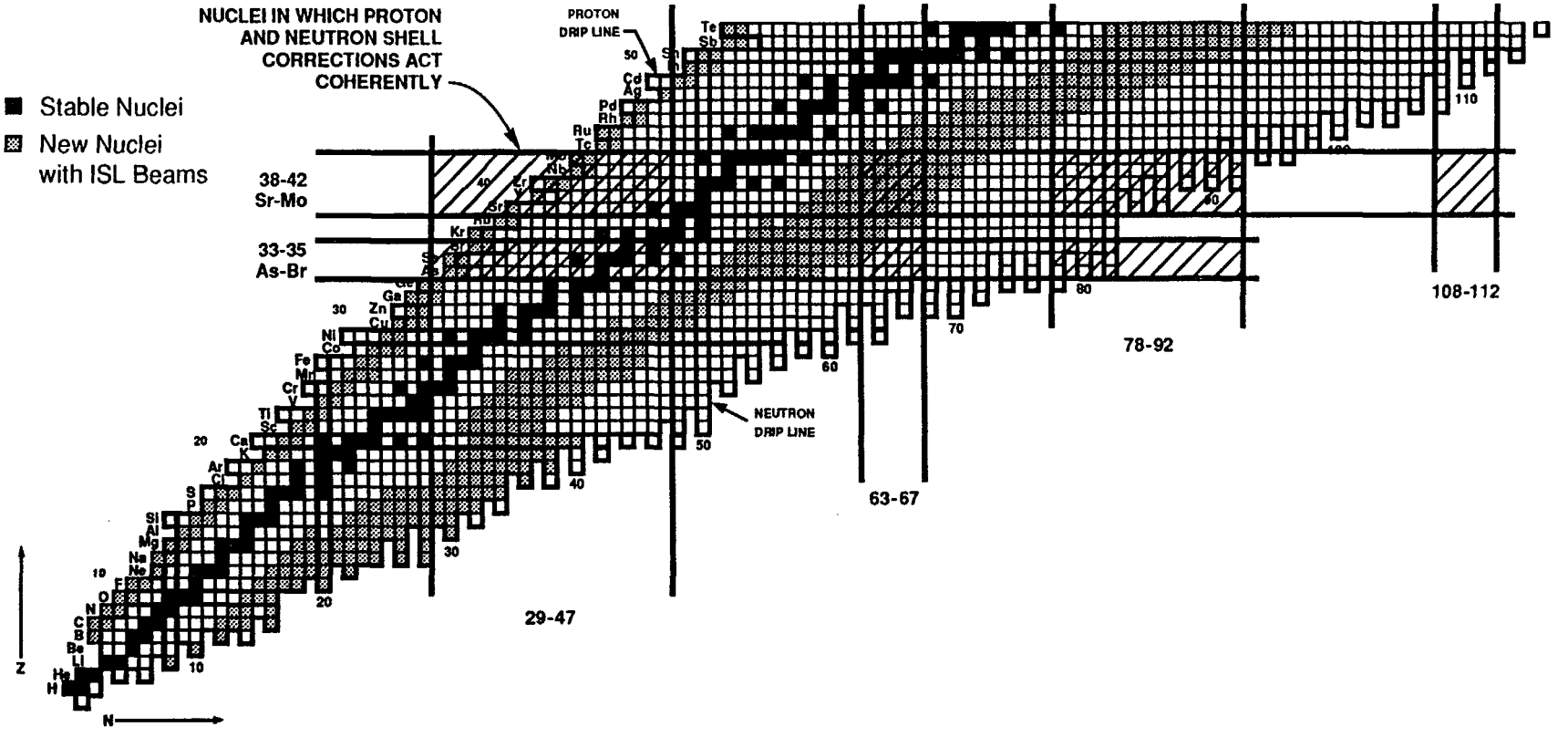

Fig. 2. Comparison of regions of nuclei in which the proton and neutron shell energy corrections act coherently at high spins producing stable prolate superdeformed shapes and the "new" nuclei which can be produced with high intensity radioactive ion beams. The proton and neutron numbers of the minimum shell energy corrections are taken from refs. 45 and 46, and the regions of overlapping proton and neutron shell energy minima are indicated by diagonal shading. The lower Z boundary of the heaviest regions has been decreased to include Hg, Tl, and Pb, since superdeformed states have been identified for isotopes of these elements.[18] The predicted "new" nuclei that can be studied with radioactive ion beams, but which cannot be studied with stable beams and stable targets are estimated[14] using the projected beams of the IsoSpin Laboratory.[12] Smaller "first generation" facilities, such as the Oak Ridge RIB Facility[13] could produce most of the proton-rich nuclei indicated with $Z \leq 82$, see ref. 14. See next page for heavier nuclei.

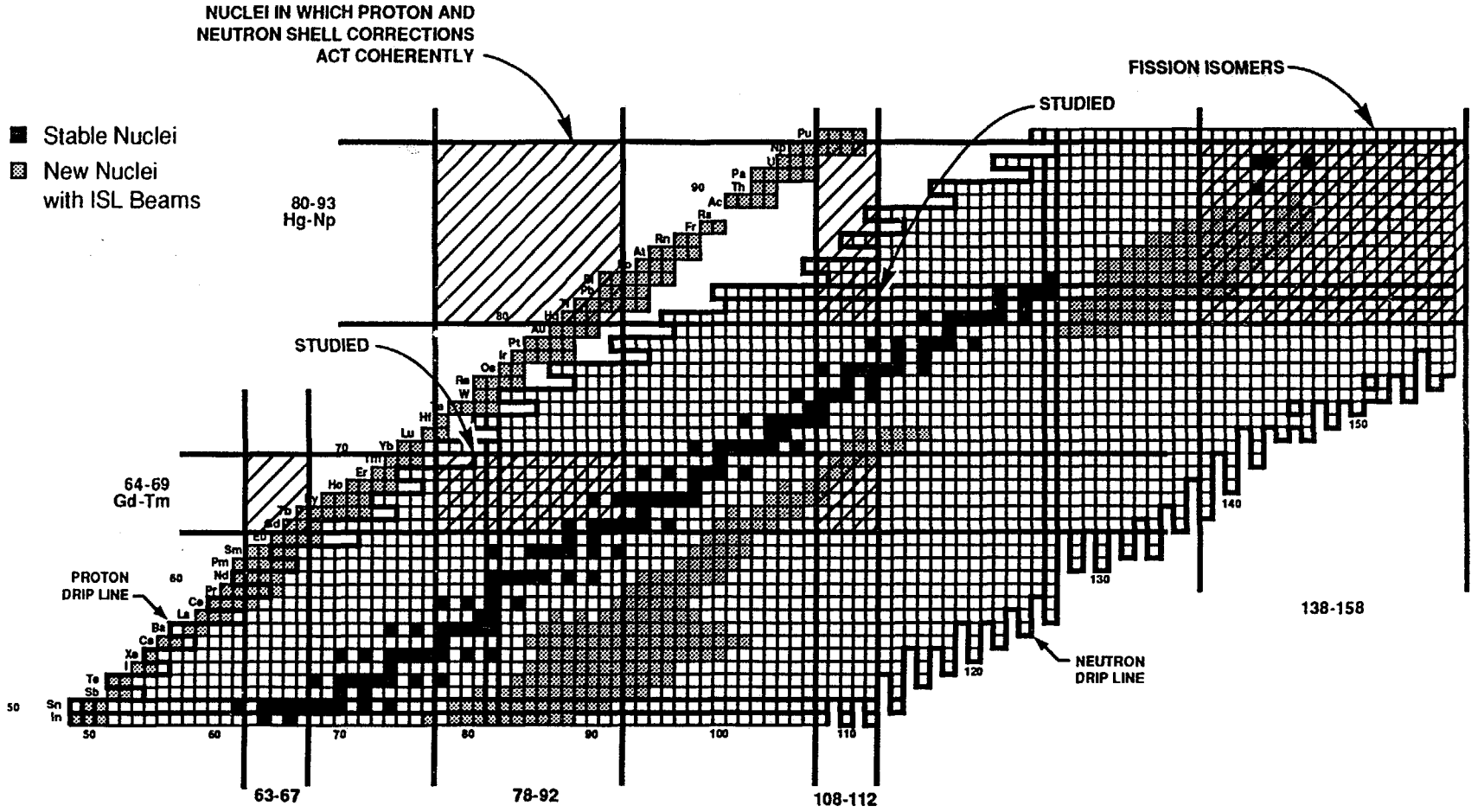
NUCLEI IN WHICH PROTON AND NEUTRON SHELL CORRECTIONS ACT COHERENTLY
FISSION ISOMERS
STUDIED
STUDIED
Stable Nuclei
New Nuclei with ISL Beams
80-93 Hg-Np
64-69 Gd-Tm
PROTON DRIP LINE
NEUTRON DRIP LINE
63-67
78-92
108-112
138-158

large Doppler shift and low photopeak efficiency associated with the high-energy gamma-ray transitions between superdeformed states of light nuclei (due to the smaller moment of inertia). It also may be that the nuclei with the most stable superdeformed minimum at the lowest excitation energy (i.e. the best candidates for superdeformation) in this mass region are too proton-rich to be populated with stable beams and targets.[31]

Two unstudied proton-rich regions of superdeformation that should become accessible to experiments with radioactive ion beams are indicated by Fig. 2. These are the light (N = 63-67) isotopes of Gd - Tm nuclei (Z = 64-69) and the light (N = 70-92) isotopes of Hg - Np (Z = 80-93). Indeed, the proton and neutron numbers for the very proton-rich mercury - lead nuclei suggested to be superdeformed are the combination of the proton number of the known superdeformed mercury - lead nuclei and the neutron number of the known superdeformed europium - dysprosium nuclei. However, the larger ratio of protons to neutrons will lead to increased fission especially at high angular momentum for these very proton-rich heavy nuclei. Thus, the lighter region of very proton-rich Gd - Tm (Z = 64-69) isotopes perhaps is the favored new region for superdeformation studies with proton-rich radioactive ion beams.

The preceding discussion of possible new regions of superdeformation accessible to radioactive ion beams is primitive; such a discussion could have been given nearly a quarter century ago.[26] The complete potential energy surface, minimized with respect to a variety of deformations, must be calculated systematically for the new nuclei that can be populated at high spin using radioactive ion beams. The first results of a systematic program of such state-of-the-art calculations for the mercury isotopes[32] are shown in Fig 3. Indeed, these calculations correctly predict the minima associated with the known low-lying normally-deformed prolate states ($\beta_2 \approx 0.25$) in $^{180\text{-}190}$Hg (ref. 33) and the known superdeformed states[18] in $^{189\text{-}194}$Hg ($\beta_2 \approx 0.47$) that coexist with the oblate ground-state configuration. These superdeformed states, predicted to occur at an excitation energy of between 3 and 4 MeV for ^{188,190}Hg in the absence of rotation ($\omega = 0$), should become yrast at I ≈ 30-40. An unobserved high-lying hyperdeformed (3:1 ratio of the major to minor axis) configuration ($\beta_2 \approx 0.8$, $\beta_3 \approx 0$) also is predicted for ^{188,190}Hg. Another superdeformed configuration ($\beta_2 \approx 0.56$, $\beta_3 \approx 0$, but "soft" with respect to the reflection-assymetric, β_3, degree of freedom is predicted to occur quite low in excitation energy for some of the light mercury isotopes that are on the verge of experimental study at high spin with stable beams and targets and which should be easily accessible with radioactive beams. This superdeformed configuration can be associated with the shell corrections shown in Fig. 2, and described in the preceding paragraphs of this section. Likewise, a hyperdeformed ($\beta_2 \approx 0.8, \beta_3 \approx 0.15$) configuration is predicted at an ever lower excitation energy for $^{178\text{-}184}$Hg than for the heavier mercury isotopes.

Both the superdeformed and hyperdeformed minima predicted for the lightest mercury isotopes, see the calculations for ^{170}Hg and ^{180}Hg shown in Fig. 3, are "soft" with respect to the octupole degree of freedom. This "softness" can probably be attributed to the occurrence of both proton and neutron $1i_{13/2}$ -- $2f_{7/2}$ $\Delta\ell = 3$ pairs near the Fermi level for these lightest mercury isotopes at large deformation, see Fig. 4. The lowest fission barrier of these nuclei is associated with a large octupole deformation. Indeed, the predicted decrease in the fission barrier associated with the octupole degree of freedom could lead to isomeric fission for the light mercury isotopes!

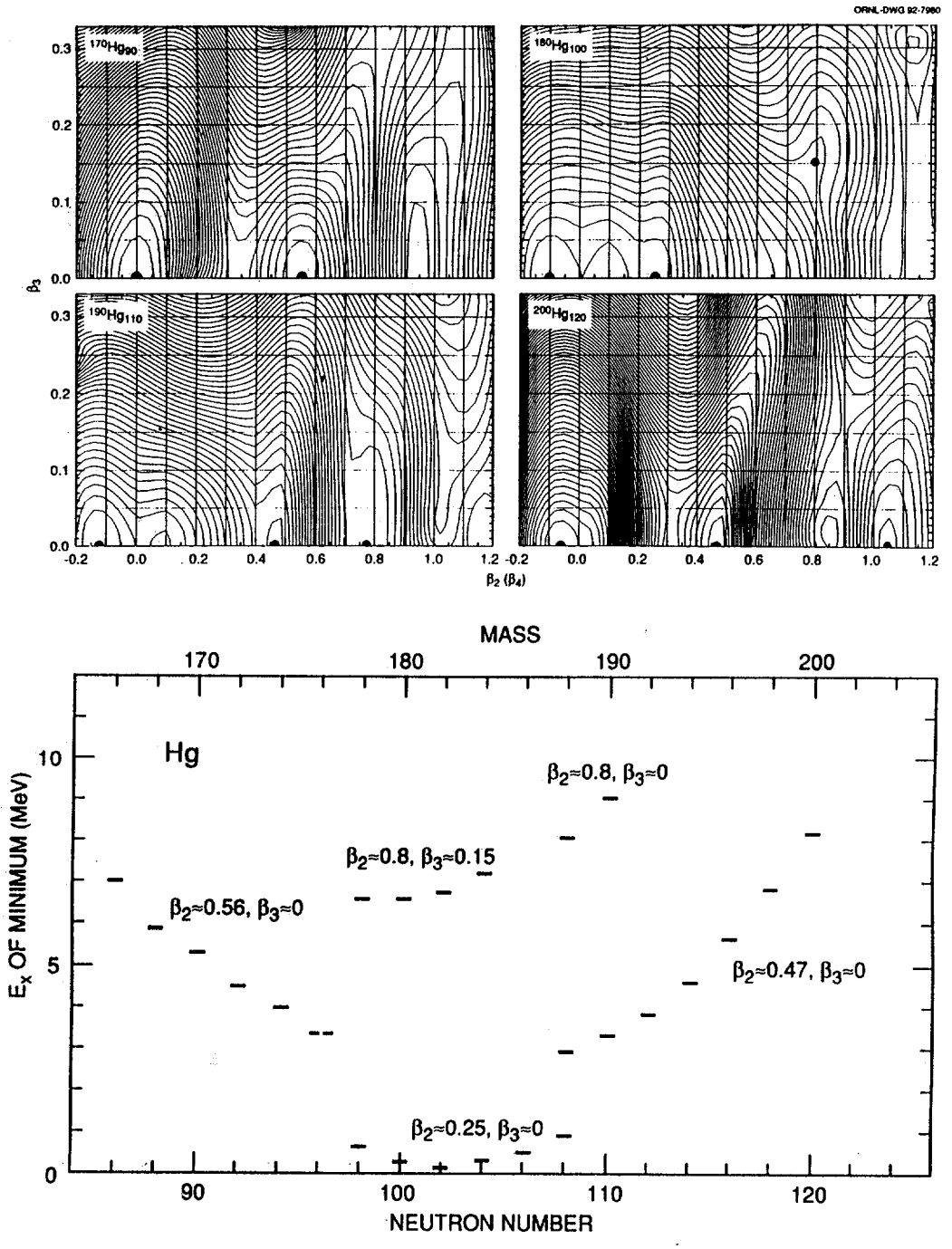

Fig. 3. (Top) Calculated zero rotational frequency potential energy surfaces[32] for $^{170}Hg_{90}$, $^{180}Hg_{100}$, $^{190}Hg_{110}$, and $^{200}Hg_{120}$ as a function of the quadrupole deformation, β_2, and the octupole deformation, β_3. These calculations also have been minimized with respect to β_4-β_8 deformations. The loci of the various minima are indicated by solid points. (Bottom) Calculated excitation energies of selected secondary minima in the potential energy surface for mercury isotopes. The approximate β_2 and β_3 values are given for each set of minima, and the complete potential energy surfaces for $^{170,180,190,200}Hg$ are shown in above.

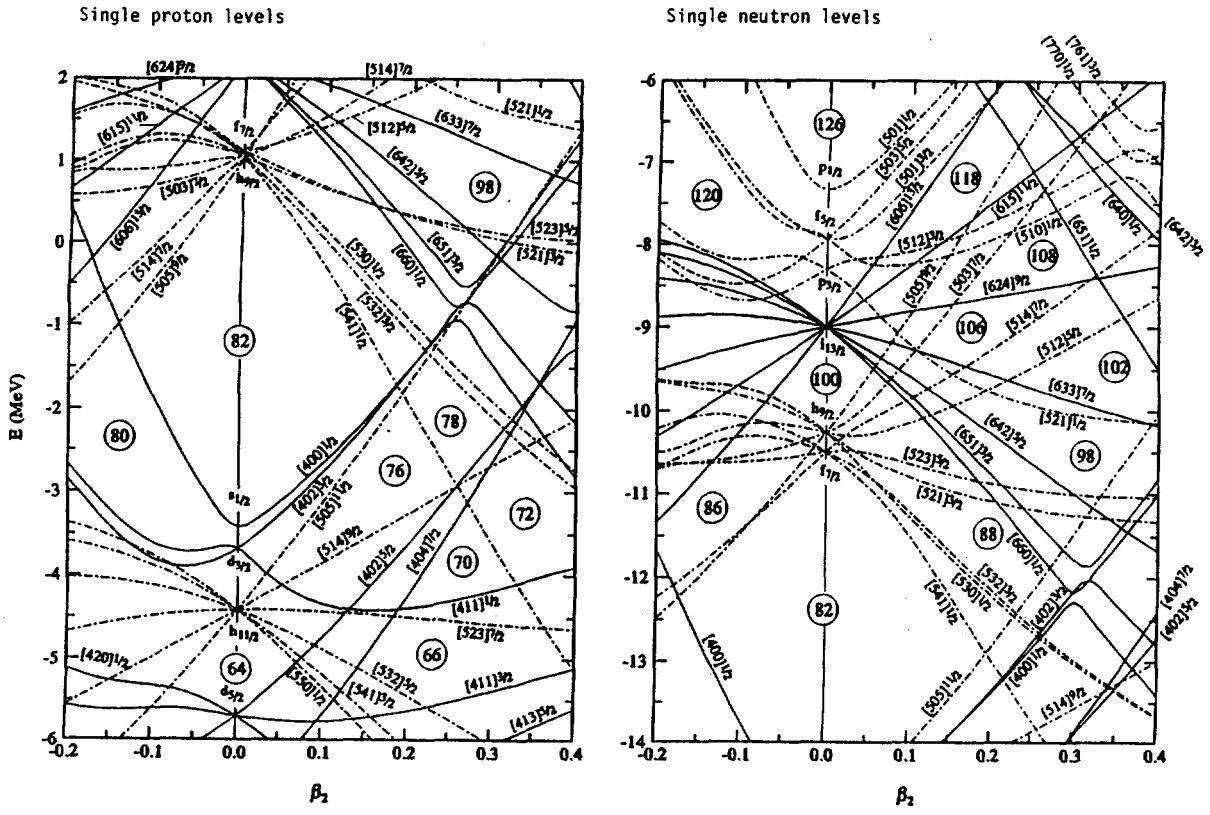

Fig. 4. Plot of predicted single-proton (left) and single-neutron (right) energies for Nilsson configurations as a function of the quadrupole deformation (β_2). These single-particle levels, calculated using Woods-Saxon potential[34] and assuming $\beta_4 = \gamma = 0$, are taken from ref. 35.

III. EXOTIC NUCLEAR CONFIGURATIONS ACCESSIBLE WITH RADIOACTIVE BEAMS

The major rearrangement of the spectrum of single-particle states associated both with a prolate quadrupole deformation of the mean nuclear field (most deformed nuclei are prolate) and with nuclear rotation (see Fig. 1) have a common feature. Both favor (i.e. decrease the energy of) the high-j, low-Ω configurations. (Ω, the projection of j on the nuclear symmetry axis, = 1/2, 3/2, ..., j.) These are the states whose wave functions are most highly localized. The spacial localization of the high-j Nilsson states is a result of the quantization of axially-deformed nuclei (nonrotating) with respect to Ω. Plots of the probability distribution of wave functions as a function of the intrinsic angular momentum and the angles of the orbital median plane, shown in Fig. 5, help to demonstrate the concept of quantal localization. The localization is enhanced for large j, since a large number of states (reflecting the large number of Ω values) must be accommodated in the same phase space, i.e. angular range. Likewise, for a specific j the localization is further enhanced for small values of Ω, see refs. (4,12).

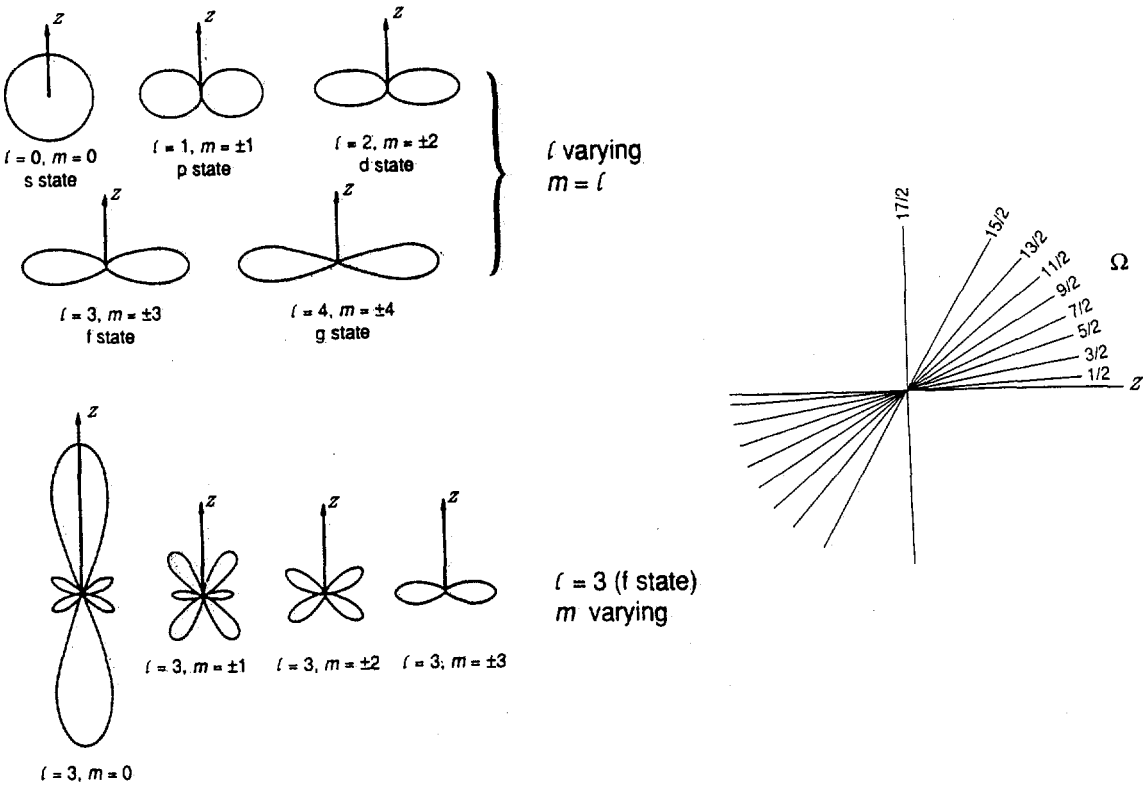

Fig. 5. Pedagodical depiction of the concept of quantal localization. (Left) Probability distributions relative to the polar axis for the m = ℓ component as a function of the orbital angular momentum (ℓ) and for the ℓ = 3 (f state) as a function of the magnetic quanutm number (m). Adapted from ref. 36; see also refs. 4 and 12. (Right) Semiclassical depiction of the median angles of the orbital planes for different Ω states of a $1k_{17/2}$ orbit in a deformed nucleus. Note the extreme localization for the lowest Ω, equatorial orbits. Adapted from ref. 12.

In a rotating system the Coriolis interaction destroys[8] the nuclear pair correlations by decreasing the energy of the state corresponding to the highly-localized, low-Ω components of the wave function that orbit the nucleus in the direction of the nuclear rotation and increasing the energy of those orbiting in the opposite direction, see Fig. 6. Indeed, this interaction not only enhances the spacial localization, but in the limiting case it also restricts the valence nucleons (i.e., those of non-filled shells) to equatorial orbitals in the direction of nuclear rotation, see Fig. 7. The large overlap of such orbits is a necessary, though not sufficient, condition for new types of rotationally-induced correlations.[4]

Such quantal localization effects (which will produce, e.g. coexisting nuclear shapes, large residual interactions,[4,10,11] and perhaps even new types of nuclear correlations[4]) become increasingly important for heavy nuclei, where many of the intrinsic (i.e. shell-model) configurations occupied have large angular momentum, j, see e.g. Figs. 1 and 4. Even larger enhancements are expected in regions where the low-Ω states of the nuclear wave functions and/or the same neutron and proton configurations are selectively

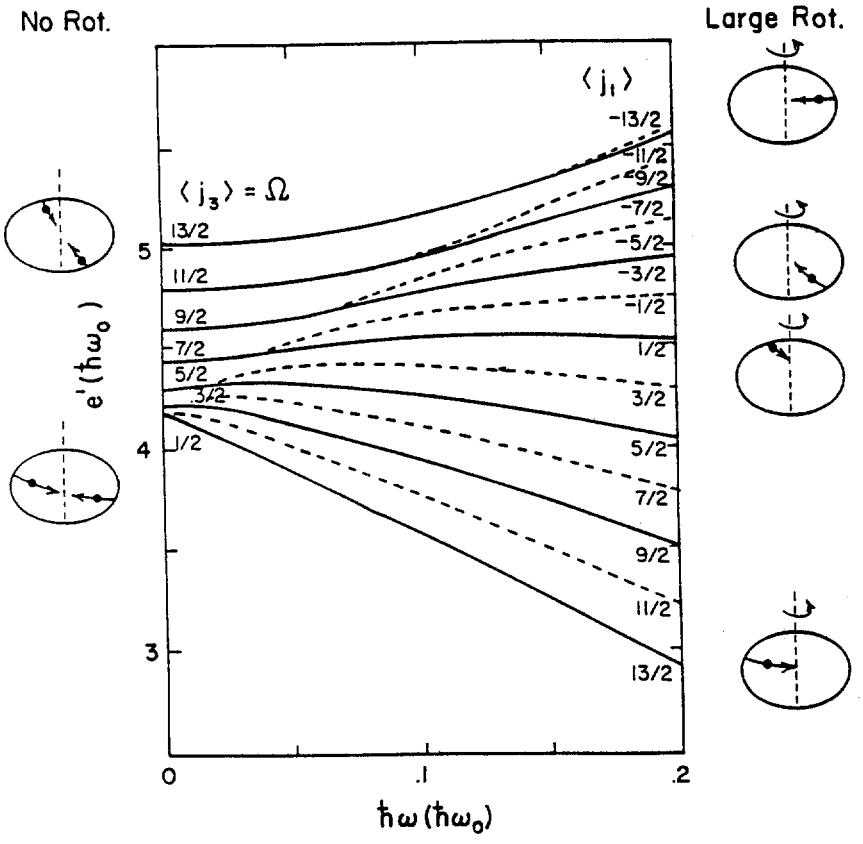

Fig. 6. Calculated spectrum of single-particle states for a single-j shell in a rotating axially-deformed nucleus ($\varepsilon_2 = 0.25$) in the absence of pair correlations. Solid and dashed curves correspond to states of signature (α) 1/2 and -1/2, respectively. Though the details of the calculation correspond to $i_{13/2}$ neutrons, this spectrum of states is typical of any high-j shell. Values of $\langle j_3 \rangle = \Omega$ and $\langle j_1 \rangle$ are given in the limiting case of no rotation and infinite rotation, where they are conserved quantities. Schematic diagrams depicting selected nucleonic orbital with respect to the nuclear-symmety and rotational axes also are shown in the right- and left-hand portions of the figure. Adapted from ref. 4.

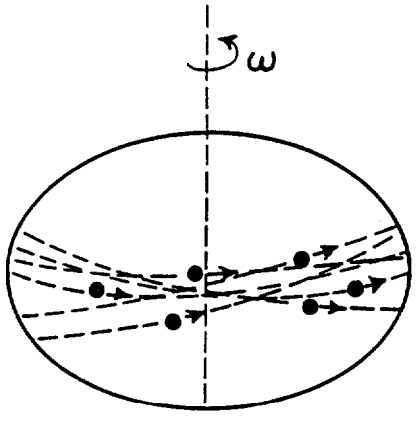

Fig. 7. Idealized figure depicting the valence nucleonic motion in a very rapidly-rotating deformed nucleus.

occupied. Indeed, all these conditions are met for the "new" proton-rich isotopes of xenon - neodymium ($Z \approx N = 54 - 60$) which can be studied with proton-rich radioactive beams, see Fig. 2 and ref. 14. Even more dramatic examples of quantal localization perhaps can be studied in the "new" very proton-rich isotopes of platinum to lead[35] ($Z = 78 - 82$). For the prolate deformations, associated with the occupation of down-sloping orbitals on the Nilsson diagram, the low-Ω components of the intruding $i_{13/2}$, $h_{9/2}$, and $f_{7/2}$ proton orbitals have nearly maximal overlap with each other and even more importantly with the same neutron orbitals which are occupied just above the $N = 82$ neutron shell, see Fig. 4.

IV. COMPLETE SPECTROSCOPY -- OVERLAPPING HIGH- AND LOW-SPIN DATA IN THE SAME NUCLEUS

A dream of nuclear structure physicists (see e.g. refs. 5 and 47) since the advent of heavy-ion beams -- obtaining state of the art low- and high-spin data in the same nucleus -- can be realized for the first time utilizing beams of heavy neutron-rich radioactive nuclei. The combination of the increased neutron excess in heavy stable nuclei (to counteract the repulsive Coulomb interaction), the emission of neutrons from highly-excited nearly-stable and neutron-rich compound nuclei, and the necessity of heavy ions for imparting angular momentum to the system (in heavy-ion induced fusion evaporation reactions), has confined previous high spin studies to proton-rich nuclei. For example, nuclei such as $^{168}Er_{100}$, which are studied[37,38] in great detail at low spin in (n,γ) studies and transfer reactions, cannot be populated at high spin using heavy-ion induced fusion, evaporation reactions with stable beams and targets.

Figure 8 illustrates the population of erbium isotopes by a variety of reactions utilzing both stable and radioactive ions. All of the stable erbium isotopes can be studied at high, as well as at low, spin using the neutron-rich radioactive beams planned for the IsoSpin Laboratory[12] (and other similar second-generation ISOL facilities). Likewise, the predicted[39] best cases for hyperdeformation, $^{166\text{-}168}Er$, also can be populated at high spin with these radioactive beams. Indeed, for complete spectroscopic studies a variety of light-, intermediate-, and heavy-ion induced fusion-evaporation reactions are needed to populate the nucleus with the complete range of angular momenta. Of course, this nucleus also must be studied at low spin with (n,γ), (e,e'), and transfer reactions and Coulomb excited.

Besides the obvious use of "complete spectroscopic studies" for more stringent tests of nuclear models, several other interesting nuclear structure questions can be addressed by "complete" data. For example, statistical analyses of level spacing distributions, often associated with the order or chaos of the nuclear system,[40,41] can be studied as a function of angular momentum.[42] Likewise, detailed studies of strongly-correlated nuclear states, such as the γ-, β-, and octupole-vibrations, at larger angular momentum, will be greatly facilitated by the use of radioactive ion beams to overlap low- and high-spin studies in the same nucleus. Such data can provide information on the spin dependence of the microscopic basis of such correlations, see e.g. refs. 43 and 47.

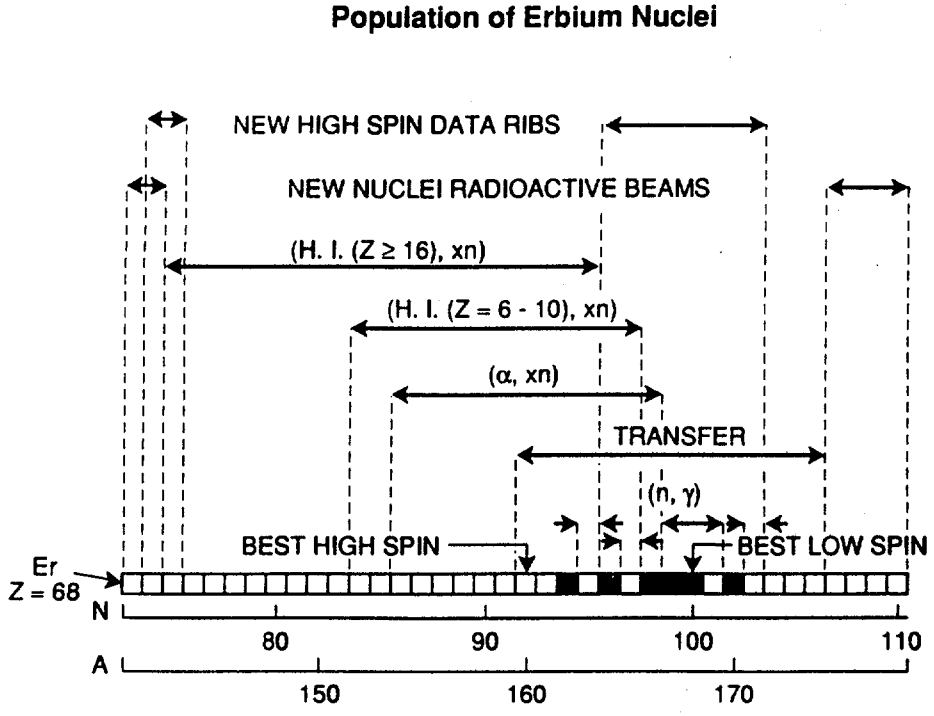

Fig. 8. Comparison of the population of erbium isotopes by a variety of nuclear reactions using both stable and radioactive ion beams (RIBS). The stable erbium isotopes are shown by filled squares, and the best studied cases at both low and high spin are indicated.

VI. CONCLUSION

The purpose of this report is to present a flavor of the rich and exciting nuclear structure studies of rapidly-rotating exotic nuclei afforded by radioactive ion beams. It is not intended to be a comprehensive review of this frontier field. Indeed, the possibilities for studies on the limits of both angular momentum and isospin are just starting to be seriously considered. Additional information is contained in refs. 12-14, 35, and 44.

ACKNOWLEDGMENTS

Discussions with C. Baktash, R. Casten, I.Y. Lee, W. Nazarewicz, D. Winchell, R. Wyss, and C.H. Yu are acknowledged. The author also would like to thank W. Nazarewicz for permission to use Fig. 3 prior to publication. Oak Ridge National Laboratory is managed by Martin Marietta Energy Systems, Inc. for the Department of Energy under contract No. DE-AC05-84OR21400.

REFERENCES

1. GAMMASPHERE Proposal, ed. by M.A. Deleplanque and R.M. Diamond, 1988.
2. M.G. Mayer and J.H.D. Jensen, Elementary Theory of Nuclear Shell Structure (Wiley, 1955, New York) pg. 58.
3. M.A. Riley, J.D. Garrett, J.F. Sharpey-Schafer, and J. Simpson, Phys. Lett. **B177** (1986) 15.
4. J.D. Garrett, J. Nyberg, C.H. Yu, J.M. Espino, and M.J. Godfrey, in Contemporary Topics in Nuclear Structure Physics, ed. by R.F. Casten, et al. (World Scientific, 1988, Singapore), pg. 699.
5. See e.g., R. Bengtsson and J.D. Garrett, in International Review of Nuclear Physics, Vol. 2 (World Scientific, 1984, Singapore) pg. 194.
6. A. Johnson, H. Ryde, and I. Sztarkier, Phys. Lett. **34B** (1971) 605.
7. F.S. Stephens and R.S. Simon, Nucl. Phys. **A183** (1972) 257.
8. B.R. Mottelson and J.G. Valatin, Phys. Rev. Lett. **5** (1960) 511.
9. J.C. Bacelar, M. Diebel, C. Ellegaard, J.D. Garrett, G.B. Hagemann, B. Herskind, A. Holm, C.-X. Yang, J.-Y. Zhang, P.O. Tjøm, and J.C. Lisle, Nucl. Phys. **A442** (1985) 509.
10. S. Frauendorf, L.L. Riedinger, J.D. Garrett, J.J. Gaardhøje, G.B. Hagemann, and B. Herskind, Nucl. Phys. **A431** (1984) 511.
11. J.Y. Zhang, J.D. Garrett, R.F. Casten, D.S. Brenner, C. Wesselborg, C.-H. Yu, and M. Carpenter, Nucl. Phys. **A520** (1990) 251c.
12. R.F. Casten, J.M. D'Auria, C.N. Davids, J.D. Garrett, J.M. Nitschke, B.M. Sherrill, D.J. Vieira, M. Wiescher, and E.F. Zganjar, The Isospin Laboratory, Research Opportunities with Radioactive Nuclear Beams, LALP 91-51 (Los Alamos National Laboratory, 1991, Los Alamos).
13. A Proposal for Physics with Exotic Beams at the Holifield Heavy Ion Research Facility, ed. J.D. Garrett and D.K. Olsen, Physics Division, ORNL, February 1991.
14. J. D. Garrett, in Proc. of the Workshop on the Techniques of Secondary Nuclear Beams, Dourdan, France, March 1992 (Editions Frontieres, 1992, Paris), in press.
15. P.J. Twin, B.M. Nyakó, A.H. Nelson, J. Simpson, M.A. Bentley, H.W. Cranmer-Gordon, P.D. Forsyth, D. Howe, A.R. Mokhtar, J.D. Morrison, J.F. Sharpey-Schafer, and G. Sletten, Phys. Rev. Lett. **57** (1986) 811.
16. P.J. Nolan and P.J. Twin, Ann. Rev. Nucl. Part. Sci. **38** (1988) 533.
17. E.F. Moore, R.V.F. Janssens, R.R. Chasman, I. Ahmad, T.L. Khoo, F.L.H. Wolfs, D. Ye, K.B. Beard, U. Garg, M.W. Drigert, Ph. Benet, Z.W. Grabowski, and J.A. Cizewski, Phys. Rev. Lett. **63** (1989) 360.
18. R.V.F. Janssens and T.L. Khoo, Ann. Rev. Nucl. Part. Sci. **41** (1991) 321.
19. A.J. Kirwan, G.C. Ball, P.J. Bishop, M.J. Godfrey, P.J. Nolan, D.J. Thornley, D.J.G. Love, and A.H. Nelson, Phys. Rev. Lett. **58** (1987) 467.
20. W.C. Ma, J.H. Hamilton, A.V. Ramayya, L. Chaturvedti, J.K. Deng, W.B. Gao, Y.R. Jiang, J. Kormicki. X.W. Zhao, N.R. Johnson, I.Y. Lee, F.K. McGowan, C. Baktash, J.D. Garrett, W. Nazarewicz, and R. Wyss, Vanderbilt, ORNL, JIHIR Preprint, 1992.
21. V.M. Strutinsky, Nucl. Phys. **A95** (1967) 420.
22. Aa. Bohr and B.R. Mottelson, Nuclear Structure (Benjamin, 1975, Reading), Vol. II, pgs. 591-607.
23. J. Dudek, W. Nazarewicz, Z. Szymanski, and G.A. Leander, Phys. Rev. Lett. **59** (1987) 1405.

24. S.M. Polikanov, V.A. Druin, V.A. Karnauchov, V.L. Mikheev, A.A. Pleve, N.K. Skobelev, V.G. Subotin, G.M. Ter-Akapoian, and V. A. Fomichev, Zh. Eksp. Teor. Fiz. **42** (1962) 1016.
25. S. Bjørnholm and J.E. Lynn, Rev. Mod. Phys. **52** (1980) 725.
26. V.M. Strutinsky, Nucl. Phys. **A122** (1968) 1.
27. C.Y. Wu, W. von Oertzen, D. Cline, and M.W. Guidry, Ann. Rev. Nucl. Part. Sci. **40** (1990) 285; and refs. therein.
28. W. Nazarewicz, J. Dudek, R. Bengtsson, T. Bengtsson, and I. Ragnarsson, Nucl. Phys. **A435** (1985) 397.
29. J. Dudek, W. Nazarewicz, and N. Rowley, Phys. Rev. **C4** (1987) 1489.
30. See e.g., C. Baktash, G. Garcia-Bermudez, D.G. Sarantites, W. Nazarewicz, V. Abenante, J.R. Beene, H.C. Griffin, M.L. Halbert, D.C. Hensley, N.R. Johnson, I.Y. Lee, F.K. McGowan, M.A. Riley, D.W. Stracener, T.M. Semkow, and A. Virtanen, Phys. Lett. **B225** (1991) 174.
31. I. Ragnarsson, in Proceedings of the Workshop on the Science of Intense Radioactive Ion Beams, ed. J.B. McClelland and D.J. Vieira Los Alamos National Laboratory Report LA-11964, 1990, pg. 199.
32. W. Nazarewicz, private communication and to be published in these proceedings.
33. J.L. Wood, K. Heyde, W. Nazarewicz, M. Huyse, and P. Van Duppen, Phys. Rep. (1992), in press; and refs. therein.
34. W. Nazarewicz, J. Dudek, R. Bengtsson, T. Bengtsson, and I. Ragnarsson, Nucl. Phys. **A435** (1985) 397.
35. J.D. Garrett, in Reflections and Directions in Low Energy Heavy-Ion Physics, ed. J.H. Hamilton, et al. (World Scientific, 1992, Singapore), in press.
36. L. Pauling and E.B. Wilson, Introduction to Quantum Mechanics (McGraw-Hill, New York, 1935).
37. W.F. Davidson, D.D. Warner, R.F. Casten, K. Schreckenbach, H.G. Börner, J. Simic, M. Stojanovic, M. Bogdanovic, S. Koicki, W. Gelletly, G.B. Orr, and M.L. Stelts, J. Phys. **G7** (1981) 455 and 843.
38. D.D.Warner, R.F. Casten and W.F. Davidson, Phys. Rev. **C24** (1981) 1713.
39. J. Dudek, T. Werner, and L.L. Riedinger, Phys. Lett. **B211** (1988) 252.
40. R.U. Haq, A. Pandey and O. Bohigas, Phys. Rev. Lett. **48** (1982) 1086.
41. O. Bohigas and H.A. Weidenmüller, Ann. Rev. Nucl. Part. Sci. 38 (1988) 421.
42. J. Garrett, in Future Directions in Nuclear Physics with 4p, Gamma Detection Systems of the New Generation, ed. J. Dudek, et al. (American Institute of Physics, 1991, New York), in press.
43. S. Jönsson, N. Roy, H. Ryde, W. Walus, J. Kownacki, J.D. Garrett, G.B. Hagemann, B. Herskind, R. Bengtsson, and S. Åberg, Nucl. Phys. **A449** (1986) 537.
44. R. Casten and J.D. Garrett, in Proceeding of the Workshop on the Science of Intense Radioactive Ion Beams, ed. J. B. McClelland and D. J. Vieira, Los Alamos National Laboratory Report LA-11963-C, 1990, pg. 18.
45. T. Bengtsson, M.E. Faber, G. Leander, P. Møller, M. Ploszajczak, I. Ragnarsson, and S. Åberg, Phys. Scrip. **24** (1981) 200.
46. S. Åberg in Proc. XXV International Winter Meeting on Nuclear Physics, Bormio, Italy, ed. E. Iori (Ricerca Scientifica ed Educazione Permanente, Milano, 1987), p. 661.
47. J.D. Garrett, Nucl. Phys. **A421** (1984) 313c.

Spectrum Fluctuations from Regular- and Damped Rotational Structures in ^{168}Yb and ^{163}Tm Nuclei.

B. Herskind[a], T. Døssing[a], S. Leoni[b], M. Matsuo[c], N. Ninel[a], E. Vigezzi[b], A. Ataç[a], P. Bosetti[b], M. Bergström[d], A. Bracco[b], A. Brockstedt[d], R. A. Broglia, [b], H. Carlsson[d], P. Ekström[d], H. J. Jensen[a], J. Jongman[e], G. B. Hagemann[a], F. Ingebretsen[f], R. M. Lieder[a], T. Lönnroth[g], A. Maj[a], B. Million[b], A. Nordlund[d], J. Nyberg[a], M. Piiparinen[a], H. Ryde[d], M. Sugawara[a], P. O. Tjøm[f], A. Virtanen[a]

[a] *The Niels Bohr Institute, University of Copenhagen, Denmark.*
[b] *Dipartmento di Fisica, University of Milano, Italy.*
[c] *Yukawa Institute, Kyoto, Japan.*
[d] *Department of Physics, University of Lund*
[e] *Kernfysisch Versneller Institut, Groningen, The Nederlands*
[f] *Department of Physics, University of Oslo, Norway*
[g] *Department of Physics, Åbo Akademi, Finland*

A new method has been developed for analyzing fluctuations of counts in 2-D γ-ray coincidence spectra. The collective E2 γ-decay from high spin states formed in Compound reactions mainly flow through regions of high level density. The method [ref. 1,2] is based on a statistical analysis, only making assumptions about the average properties of the excited states. Two regions with different decay characteristics are considered, i): a low energy region below $U_0 \approx 800$ keV, with many regular rotational bands as is well known from level schemes of deformed nuclei, and ii): the region above U_0, where the decay is dominated by damped rotational motion, caused by mixing of the rotational states connected by E2 matrix elements. Transition energies along discrete rotational bands may be viewed as randomly selected from a continuous distribution of rotational frequencies and moments of inertia. For the damped region a random matrix model is assumed, with transition strength distributions of the Porter-Thomas type, leading to smooth energy spectra, but with strong fluctuations in the transition strength distributions.

The fluctuations of counts is analyzed in spectrum intervals, corresponding to one consecutive transition-path per cascade in average, which can give information about how many different two-step decay paths the nucleus effectively uses at different rotational frequencies. The experimentally determined effective number of decay paths $N^{(2)}_{path}$ is compared with the number calculated from models assuming either regular or damped rotational motion.

The fluctuations in a given 2-D spectrum (fig. 1a) are analyzed by making a fitted average spectrum (fig. 1b) and calculating the normalized standard deviation μ_2/μ_1 from this average, as illustrated in (fig 2a) for ^{168}Yb. Diagonal cuts at 840 $\pm$ 30 keV on the 2-D spectra are shown to the left of the 2-D spectra. All known transitions from level schemes has been removed from the right part of the spectra corresponding to $E_{\gamma 1} > E_{\gamma 2}$. The data on ^{167,168}Yb were made in Daresbury with the European Suppression Spectrometer Array ESSA-30, and the fluctuation analysis is discussed in more detail in [ref. 1, 2].

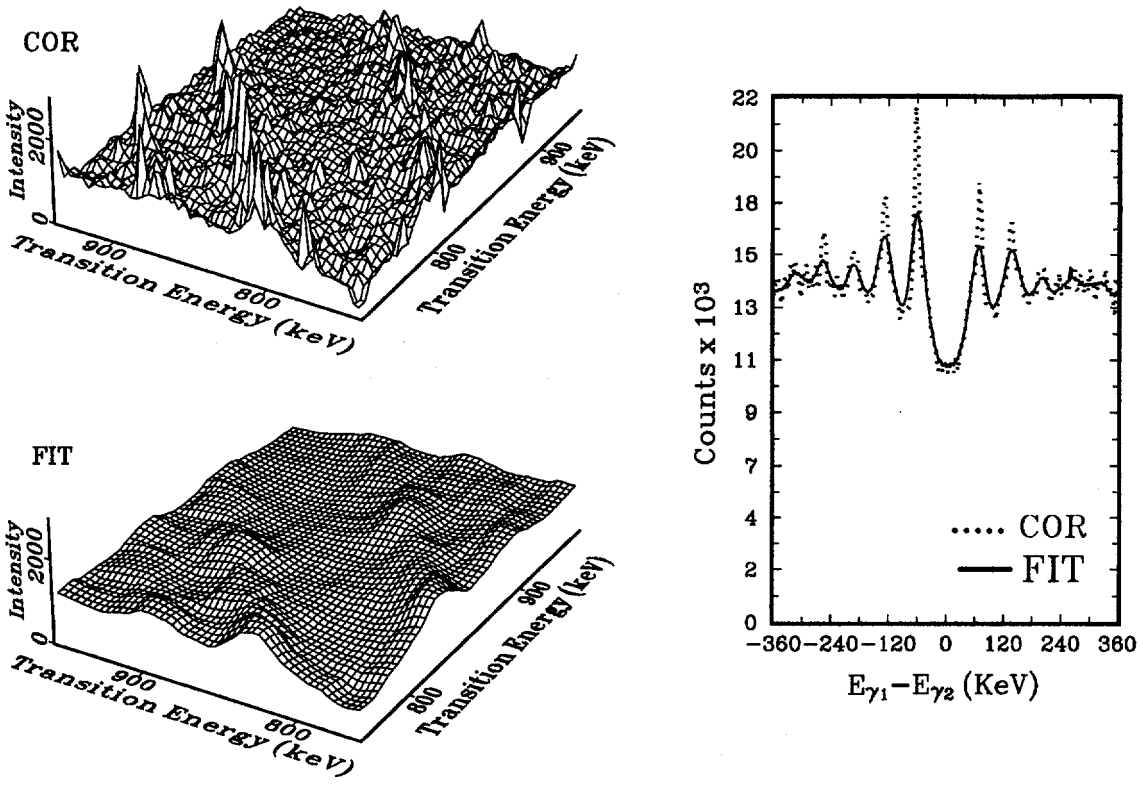

Fig. 1 *A selected range of a background subtracted COR-spectrum for* $^{167,168}Yb$ *are shown and marked a), together with a spectrum b) which shows a so-called fitted average of the COR-spectrum [ref. 2] for the same range. The spectra in c) show perpendicular cuts at 840 ± 30 keV on the spectra shown in a) and b).*

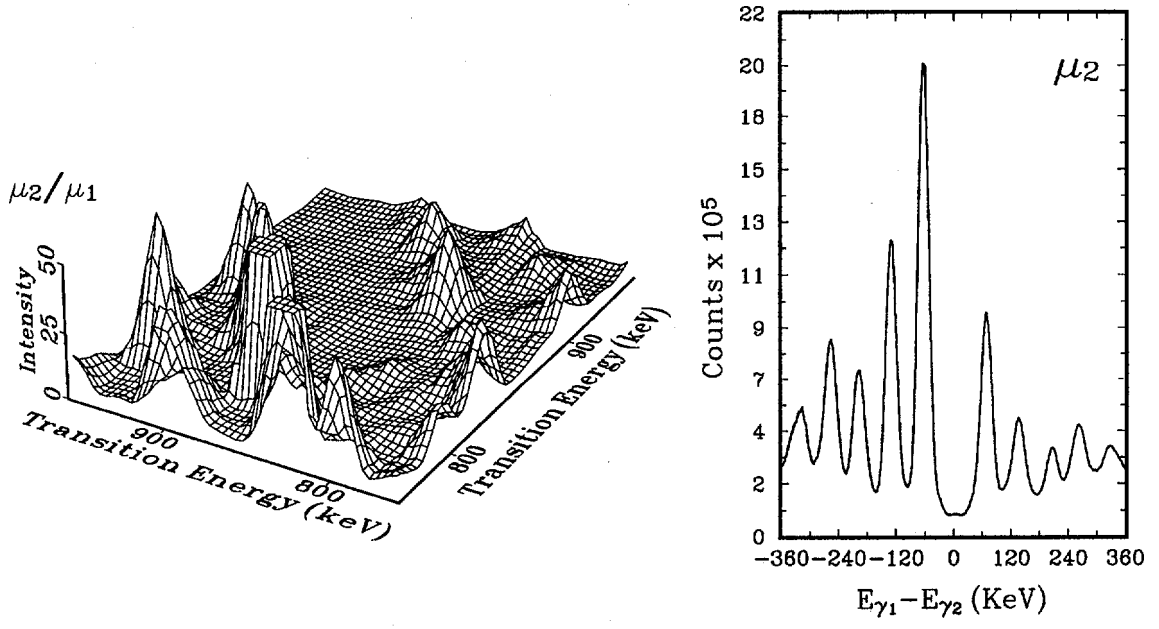

Fig. 2 *The normalized fluctuation spectrum* μ_2/μ_1 *deduced from the spectra shown in fig. 1a and 1b is displayed in part a). The spectrum in part b) at the left show a perpendicular cut across a* μ_2 *spectrum at 840 ± 30 keV (not normalized to* μ_1*).*

It is also shown in [ref. 1,2] that the number of effective path can be calculated from the following expression:

$$N_{path}^{(2)} = \frac{N_{event}}{\mu_2/\mu_1 - 1} \cdot P_2/P_0 \cdot f^2$$

with P_2/P_0 and f^2 expressing correction factors for resolution and Compton scattering in 2-D spectra respectively.

The fluctuation spectrum in fig. 2a displays large fluctuations along the so-called ridges, where transitions in regular rotational bands are found. Since large fluctuations imply a small number of paths, according to equation (1), this shows that the number of paths, and thereby the number of regular rotational bands, is rather low. In contrast, small fluctuations, close to the statistical limit $\mu_2/\mu_1 \approx 1$, are found along the central valley where $E_{\gamma_1} = E_{\gamma_2}$ and no regular rotational structures in principle occur, indicating thousands of paths at higher excitation energies.

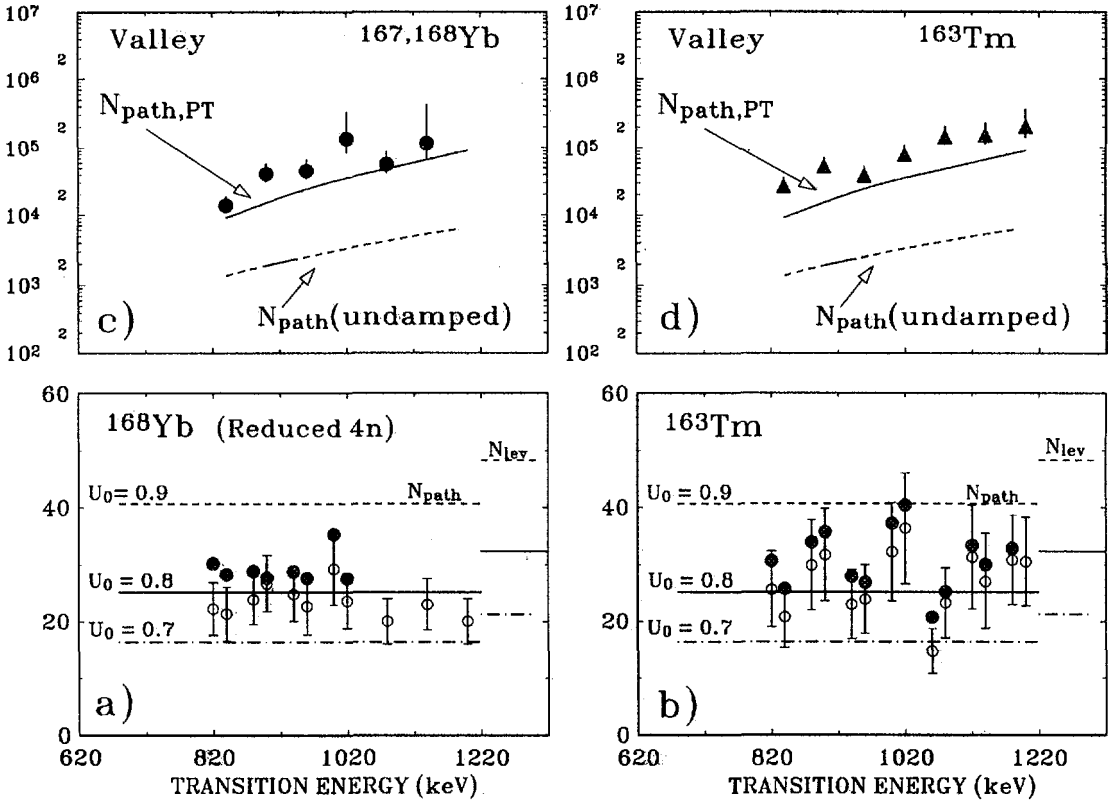

Fig. 3 *The effective number of decay paths $N_{path}^{(2)}$ extracted from fluctuations along the 1. ridges in ^{168}Yb and ^{163}Tm spectra are shown in panels a) and b) respectively. Also shown are model calculations of the effective $N_{path}^{(2)}$ and the actual N_{lev} number of discrete bands up to the energy U_o. A procedure for subtracting known low-lying bands was applied with the results shown as open circles. The known bands are added to $N_{path}^{(2)}$ with the totals shown as closed circles. The effective number of decay paths $N_{path}^{(2)}$ extracted from fluctuations along the diagonal valleys in ^{168}Yb and ^{163}Tm spectra are shown in panels c) and d) respectively. Also shown are model calculations of the effective $N_{path}^{(2)}$ with no damping assumed (dashed lines), and with damping included (full drawn lines.)*

A new data set for ^{162,163}Tm with a high intensity of 2.5 $\cdot 10^9$ 2-fold event has recently been made with the NORDBALL array equipped with a 39 elements BaF_2 calorimeter for γ-multiplicity and sum-energy selection, using a 160 MeV ^{37}Cl beam on 2-3 500μg/cm^2 targets of ^{130}Te evaporated on very thin gold backings. The experimental details together with a discrete lines analysis of this data set is discussed in [ref. 3].

Figure 3 displays the experimental number of paths extracted from a multiplicity and sum-energy selected spectrum of ^{163}Tm, compared to similar results from the Yb experiments. Fig. 3a and 3b show the number of paths $N^{(2)}_{path}$ extracted from the 1. ridges whereas figs. 3c. and 3d show $N^{(2)}_{path}$ extracted from the diagonal valley for the two nuclei. The values are reduced taking into account the simultaneous population of the neighboring nuclei ^{167}Yb and ^{162}Tm as function of transition energy. A rather small number of paths $N^{(2)}_{path} \approx 30$ is found along the first ridges for both nuclei. This is in accordance with the hypothesis that the discrete rotational bands extend from the yrast line and up in excitation energy to about $U_o \approx 800$ keV, both in the odd ^{163}Tm and in the even ^{168}Yb nuclei.

Above U_o, rotational damping may be expected to dominate with branching of the transition strength at each decay-step out to many final states. The diagonal valley around $E_{\gamma_1} \approx E_{\gamma_2}$ in the coincidence spectrum is the place to look for decay along the mixed bands. The large number of paths, $N^{(2)}_{path} \sim 10^5$ extracted for the valley region, for both ^{168}Yb and ^{163}Tm shown in figure 3c and 3d respectively, ***displays evidence for a strong branching in the decay.*** As shown on the figure, a model without branching predicts 10 times too few decay paths. In contrast, a model including damping assuming Porter-Thomas strength distributions, full branching within a damping width of Γ_{rot}=100 keV, yields consistent results as shown with full drawn lines in fig 3c and 3d. The rather small and constant damping width found from the analysis by the ***Rotational Plane Mapping Method*** on the same data sets of Yb and Tm is also consistent with this result. All together we may conclude that there are evidence for rotational damping in the two rotational nuclei discussed.

We can also try to address the question: Does the intensive data on Tm show a motional narrowing effect? By use of the NORDBALL calorimeter it is possible by a low and a high sum-energy gate to select two different entry distributions for the same spin range defined by a common γ- multiplicity gate. This is illustrated in fig. 4, where the number of paths N_{path} are found to be significant larger for the high gates than for the low gates close to the entry points in the region of highest transition energies both for the 4n and 5n channels separately (fig. 4a and 4b respectively), and for the totals of the 4n and 5n channels (fig. 4c). At lower transition energies the results from the gates merge and the gating show no effect. These results were expected and in good agreement with the simulation calculations shown in figure 4d. Accordingly, *it is only possible to trace different temperature regions close to the entry spin.*

The same gates which show a different selection of states by different $N^{(2)}_{path}$ were also used for the evaluation of the damping width as function of transition energy discussed in the contribution of Leoni et. al. and shown in the upper part of fig. 3 in [ref. 4]. Unfortunately it was only possible on basis of the present experiment to extract the Γ_{rot} values for the low energy region where the sensitivity to different

temperature region is minimal, and only a small trace of the effect may be seen.

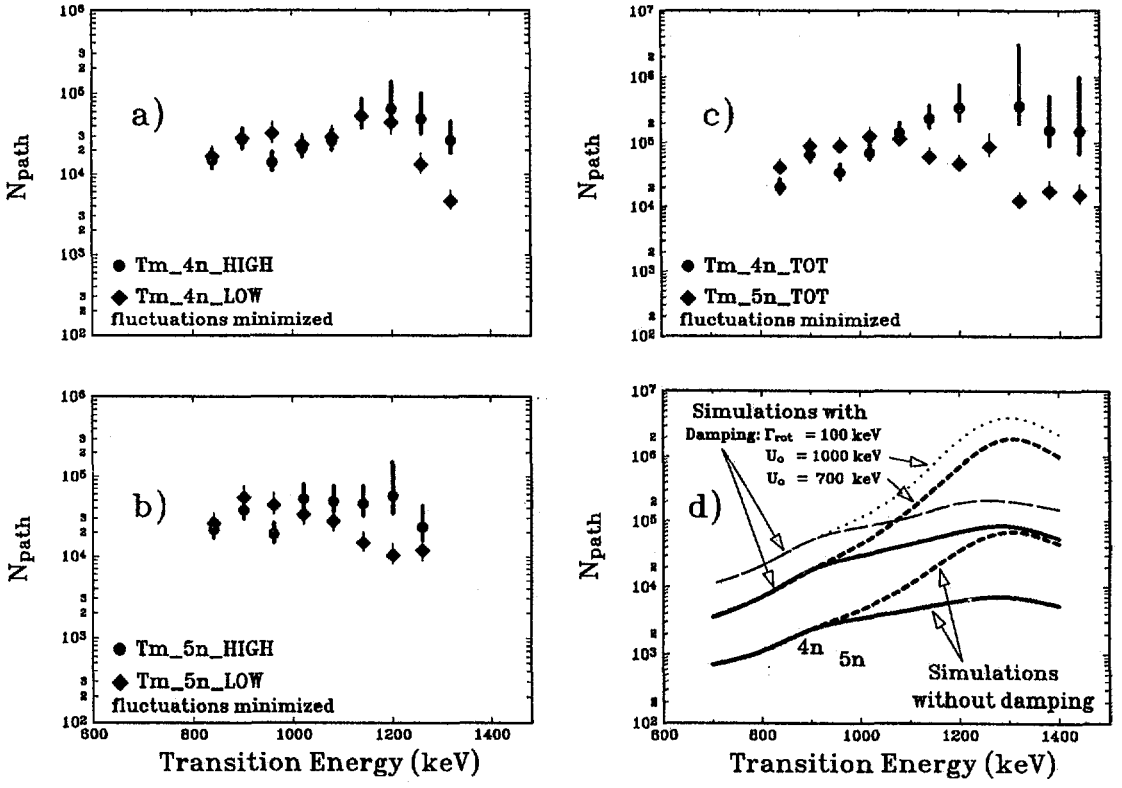

Fig. 4 *The effective number of decay paths N_{path} extracted from fluctuations along the diagonal valleys in ^{163}Tm spectra gated by high and low sum-energy for the same γ-multiplicity selected xn channels by the calorimeter of NORDBALL are shown in a), b), and c) as indicated in the legends. Also shown in d) are model calculations of the effective N_{path} corresponding to low and high gates, with no damping assumed, and with a damping width Γ_{rot} = 100 keV, and two different lower integration limit of U_o, the borderline where the damping sets in.*

References:

1 B. Herskind, A. Bracco, R. A. Broglia, T. Døssing, A. Ikeda, S. Leoni, J. Lisle, M. Matsuo and E. Vigezzi,
Phys. Rev. Lett., **68**, (1992).

2 B. Herskind, T. Døssing, S. Leoni, M. Matsuo and E. Vigezzi.
Int. Conf. on Progress in Particle and Nuclear Physics, Vol, 28, ERICE Volume, Pergamon Press, UK, ed. by A. Faessler, (1992).

3 H.J. Jensen, G. B. Hagemann, P. O. Tjøm, S. Frauendorf, et al.
Z. Phys. A - Hadrons and Nuclei **340**, 351-362 (1991).

4 S. Leoni, B. Herskind, T. Døssing, P. Rasmussen et al.
ibid.

WORKSHOP ON LARGE GAMMA-RAY DETECTOR ARRAYS

Chalk River

SESSION 8: FAR VISIONS (II)

WHERE TO LOOK FOR HYPERDEFORMED STATES ?

T. R. Werner[a,b] and J. Dudek[b]

a) Institute of Theoretical Physics, Hoża 69, 00-681 Warsaw, Poland

b) Centre de Recherches Nucléaires, 22, rue du Loess, 67-200 Strasbourg, France

Supported in part by the Polish State Committee for Scientific Research, Contract # 204509101

1. INTRODUCTION

The discovery of superdeformed rotational bands has been one of the most spectacular achievements in nuclear structure physics during the last decade. Such bands have been identified in nuclei around ^{152}Dy and, later, also in the region around ^{194}Hg. The phenomenon was predicted by theoretical calculations based on the so called total routhian surfaces (TRS) at high spin. The existence of superdeformed states in these regions seems to be intimately connected with the structure of single particle spectrum at high deformation. It turns out that at certain deformations (corresponding to 2:1 or 3:2 axis ratio), new shells (and gaps) are formed which stabilise high spin states of superdeformed nuclei in some particular regions of the periodic table. The same mechanism may be also expected to hold for hyperdeformation[1], *ie* for 3:1 axis ratio (in oscillator model; using realistic potentials, we get this ratio slightly differrent.) Both super- and hyperdeformed states provide – due to weak pairing correlations – a test ground for analysing the single particle nuclear spectrum, the role of the so called intruder states, the role of pseudo–SU_3 or pseudo–spin symmetry *etc.* Although superdeformed states has been known experimentally since pioneering work of Daresbury group[2], the hyperdeformed nuclear states seemed to be far beyond the reach of the experimentalists. However, construction of very large gamma–ray detector arrays gives a hope that such extreme states will soon become accessible (or, possibly, has already been observed[3].)

In this contribution, we present our results concerning theoretical predictions of existence of hyperdeformed high spin states for nuclei with $58 \leq Z \leq 92$ and for more than 10 isotopes for each element (only even–even nuclei.) The calculations were based on cranking method and Strutinsky's shell corrections. As the two most important criteria for the possibility of existence of hyperdeformed states we took: *a)* energy of hyperdeformed state with respect to the yrast line, and *b)* minimum height of the barrier separating the hyperdeformed minimum from normal states and from fission.

2. METHODS OF CALCULATIONS

In the calculations the shape of a nucleus is parametrised in terms of the spherical harmonics of the second and fourth order. The equation specifying the surface of a nucleus is

$$\Sigma: \quad \mathcal{R}(\vartheta,\varphi) = c(\alpha) r_0 A^{1/3} \left(1 + \sum_{\lambda=2,4} \sum_{\mu=-\lambda}^{\lambda} \alpha_{\lambda\mu} Y^*_{\lambda\mu}(\vartheta,\varphi) \right)$$

where r_0 is a parameter, and $c(\alpha)$ ensures that the volume enclosed by Σ does not depend on deformation. In the frame of coordinates connected with the principal axes of the tensor of inertia, the shape can be described[4] by two real parameters β_2 and γ:

$$\alpha_{20} = \beta_2 \cos\gamma \quad \alpha_{22} = \alpha_{2-2} = \frac{1}{\sqrt{2}} \beta_2 \sin\gamma \quad \alpha_{21} = \alpha_{2-1} = 0$$

where three other degrees of freedom correspond to the orientation of the nucleus as a whole in space and are described by Euler's angles. The hexadecapole part of the deformation is introduced in such a way that neither the rotational invariance of the deformation tensor, nor the $\mathcal{D}_2$ symmetry of the quadrupole part is violated[5]. Only one parameter (β_4) describing hexadecapole deformation was used. In terms of β_4 the coefficients $\alpha_{4\mu}$ can be expressed as follows:

$$\alpha_{40} = \beta_4(5\cos^2\gamma + 1)/6 \quad \alpha_{42} = \alpha_{4\text{-}2} = \beta_4\sqrt{\frac{15}{72}}\sin(2\gamma) \quad \alpha_{44} = \alpha_{4\text{-}4} = \beta_4\sqrt{\frac{35}{72}}\sin^2\gamma$$

the other coefficients $\alpha_{4\mu}$ being zero. The nuclear shape is therefore parametrised by three parameters: β_2, γ, and β_4.

Single particle spectra are generated by the hamiltonian:

$$\hat{\mathcal{H}} = \frac{\hbar^2}{2m}\nabla^2 + V_{WS} + V_{SO} + \frac{1}{2}(1+\tau_3)V_{Coul}$$

where $V_{WS}(\vec{r},\alpha)$ and $V_{SO}(\vec{r},\alpha)$ are standard Woods–Saxon central and spin–orbit potentials[6, 7]. The Coulomb potential for protons is calculated as the electrostatic potential of uniformly charged deformed drop. The form of the potential and its parameters are those used in the previous calculations of this type[8].

In order to investigate the structure of high spin nuclear states, we use the cranking model[9, 10]. In this approach one solves the Schrödinger equation in a rotating, body fixed coordinate frame; the hamiltonian is then:

$$\hat{H}^\omega = \hat{H}_{WS} - \omega\hat{J}_x = \sum_\nu h^\omega(\nu) = \sum_\nu (h(\nu) - \omega j_x(\nu))$$

where $\hat{H}_{WS}$ is the intrinsic hamiltonian (which, in our case, corresponds to Woods–Saxon potential, as described above), multiplier ω has the interpretation of angular velocity (times Planck's constant $\hbar$), and $\hat{J}_x$ is the operator of x–projection of angular momentum. One thus diagonalises the problem

$$h^\omega|\chi_\nu^\omega\rangle = e_\nu^\omega|\chi_\nu^\omega\rangle$$

to obtain single particle energies in the rotating frame e_ν^ω (routhians) — the true energies e_ν are then defined as the expectation values of the hamiltonian $h(\nu)$ with the eigenfunctions $|\chi_\nu^\omega\rangle$:

$$e_\nu = e_\nu(\omega) = \langle\chi_\nu^\omega|h|\chi_\nu^\omega\rangle = e_\nu^\omega + \omega\langle\chi_\nu^\omega|j_x|\chi_\nu^\omega\rangle.$$

The total energy and spin are then expressed as the sums over occupied states:

$$\mathcal{E}(\omega) = \sum_\nu e_\nu^\omega + \omega\sum_\nu\langle\chi_\nu^\omega|j_x|\chi_\nu^\omega\rangle \quad I(\omega) \approx I_x(\omega) = \sum_\nu\langle\chi_\nu^\omega|j_x|\chi_\nu^\omega\rangle.$$

Having calculated the total energy and spin of a nucleus as functions of ω, we can eventually obtain (by interpolation) the dependence of energy on spin.

In order to take the shell effects into account, the Strutinsky method[11, 12] has then been used. The smooth (macroscopic) part of the energy was replaced by 'folded-Yukawa' liquid drop energy[13, 14].

For every deformation point, the value of $\beta_4^{\text{l.d.}}(\beta_2,\gamma)$ was first selected as that minimising liquid drop energy. Then the calculations were repeated for a few values of β_4 above and below $\beta_4^{\text{l.d.}}$. The final value of β_4 was found by minimising the energy for each deformation (β_2,γ), single particle configuration, and value of spin separately.

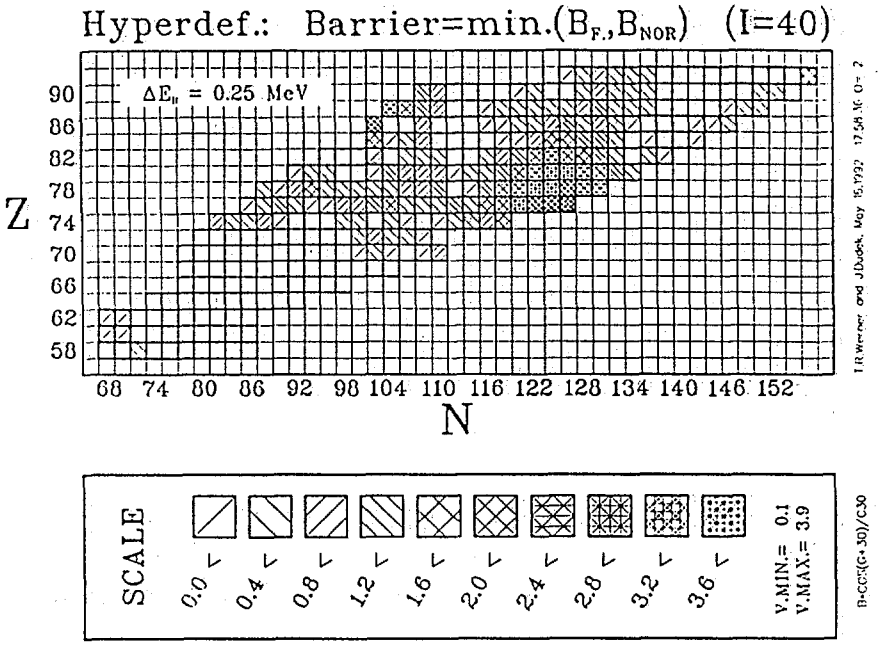

Fig. 1. Barriers separating hyperdeformed minima from other states – see text.

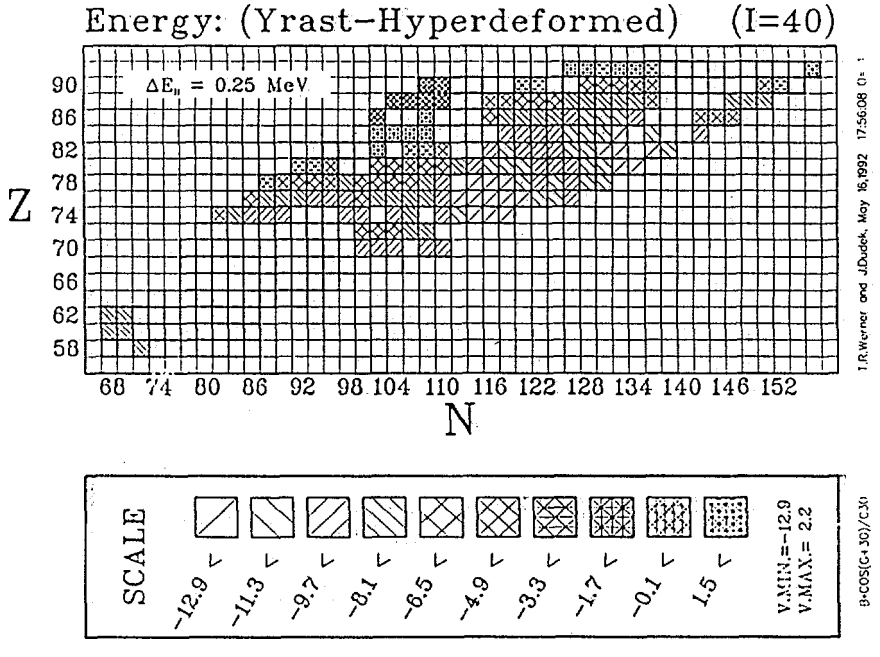

Fig. 2. The difference between the energy of the lowest non-hyperdeformed state and that of the hyperdeformed state – see text.

3. RESULTS

The calculations have been performed for nuclei in both Rare Earth and Actinide regions:

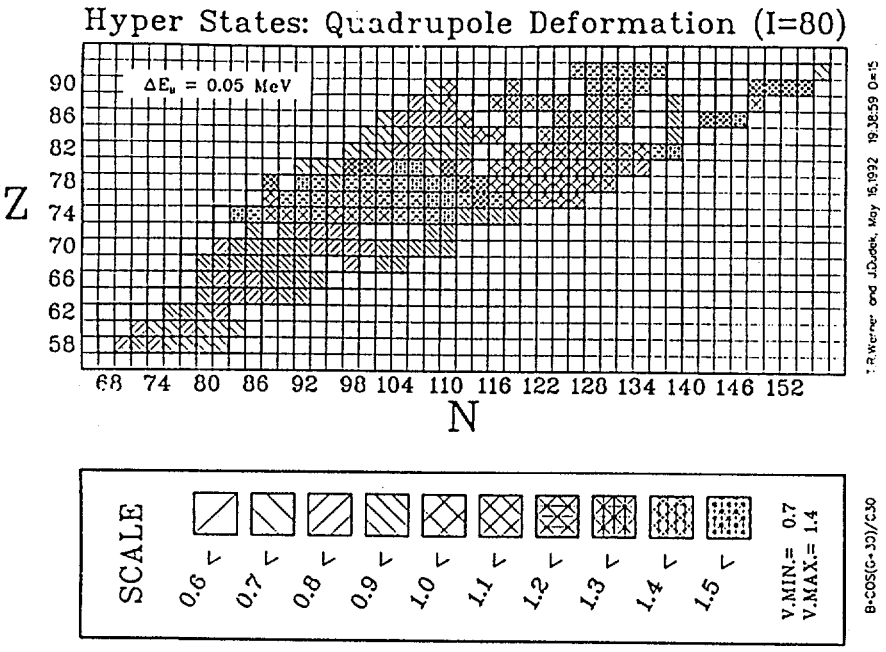

Fig. 3. Quadrupole deformation (β_2) of hyperdeformed states.

$58 \leq Z \leq 92$ with more than 10 isotopes for each element (only even–even nuclei.) Some of the isotopes cannot be studied at present (in particular their high spin states); however, in view of big experimental projects in the U.S. and Europe, one can hope that many of them will soon become reachable.

The results are presented in the Figs. 1 and 2. The former shows the barrier separating hyperdeformed minimum from non–hyperdeformed ones (normal or superdeformed), or from fission, whichever is smaller. Nuclei for which this value is less than $\Delta E_B = 0.25$ MeV, or for which no hyperdeformed minimum exists, have been rejected — they correspond to blank 'tiles' in the figure. Calculations were performed for the value of spin $I = 40\hbar$. The best cases can be found for nuclei with $Z \approx 76$ and for a quite wide range of neutron numbers. Another region, more exotic, corresponds to $Z \approx 86$ and $N \approx 102$ — here, however, the deformation is much smaller ($\beta_2 \approx 0.74$) than in the former region, where $\beta_2 \geq 1.1$ (see Fig. 3.) The existence of even large barrier is not sufficient for the hyperdeformed state to be observed. As the level density blows up exponentially with excitation energy, one has to impose the additional condition: the energy of the hyperdeformed state should not be too high above the yrast line. This condition can easily be met for very large values of spin — however, for such states, the barrier towards fission rapidly decreases. Fig. 2 shows the difference between the energy of the lowest non–hyperdeformed minimum and that of the hyperdeformed one (consequently, positive values indicate that the hyperdeformed minimum *is* yrast.) The figure corresponds to the value of spin $I = 40\hbar$. The hyperdeformed states of neutron–rich nuclei with $Z \approx 76$ are rather high in energy (more than 8 MeV above the yrast line), while for proton–rich isotopes of the same elements this value can be as low as 3 MeV. This energy difference decreases with spin — this can be seen in Fig. 4, where energy cuts along the steepest descent path are shown for several values of spin.

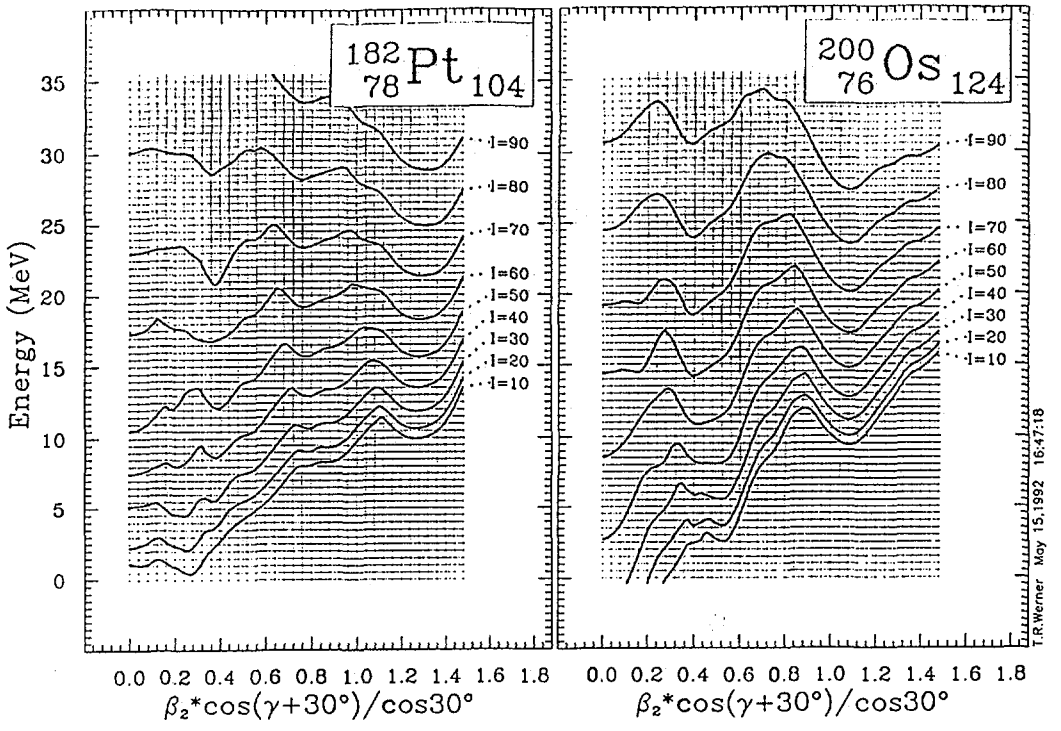

Fig. 4. Energy cuts along the steepest descent path as a function of spin.

Analysing Figs. 1 and 2, one can see that nuclei from the Rare Earth region are not the best candidates to look for hyperdeformed states. Similar figures for higher spins[15] (not shown here) indicate that in this region hyperdeformed states can be only expected for spins around $70\hbar$ and larger; the depth of the hyperdeformed minimum is then still quite substantial (about 1 MeV), while its energy is already close to the yrast.

References:

1. J. Dudek, T.R. Werner and L.L. Riedinger, *Phys. Lett.* **B211** (1988) 252
2. P.J. Twin *et al* , *Phys. Rev. Lett.* **59** (1986) 811
3. A. Galindo-Uribarri *et al* , these proceedings
4. D.L. Hill and J.A. Wheeler, *Phys. Rev.* **89** (1953) 1102
5. W. Nazarewicz and P. Rozmej, *Nucl. Phys.* **A369** (1981) 396
6. J. Dudek, Z. Szymański and T.R. Werner, *Phys. Rev.* **C23** (1981) 920
7. S. Ćwiok, J. Dudek, W. Nazarewicz, J. Skalski and T.R. Werner, *Comput. Phys. Commun.* **46** (1987) 379
8. T.R. Werner and J. Dudek, *Atomic Data and Nucl. Data Tables* **50** (1992) 179
9. D.R. Inglis, *Phys. Rev.* **96** (1954) 1059, *Phys. Rev.* **97** (1955) 701
10. Z. Szymański *Fast Nuclear Rotation*, 1983, Oxford University Press, Oxford
11. V.M. Strutinsky *Nucl. Phys.* **A95** (1967) 420, *Nucl. Phys.* **A122** (1968) 1
12. Brack *et al* , *Rev. Mod. Phys.* 44 (1972) 320
13. H.J. Krappe, J.R. Nix and A.J. Sierk, *Phys. Rev.* **C20** (1979) 992
14. P. Møller and J.R. Nix, *Nucl. Phys.* **A361** (1981) 117
15. T.R. Werner and J. Dudek, to be published

INTERNATIONAL CONFERENCE ON NUCLEAR STRUCTURE AT HIGH ANGULAR MOMENTUM

Radisson Hotel - Ottawa

TUESDAY, MAY 19

Session 1		**SUPERDEFORMATION IN NUCLEI (I)** **Chairperson: R.M. Diamond** **Welcome Speech: J.C. Waddington**
Pilotte	(Ottawa)	Superdeformed Bands in ^{191}Tl
Janssens	(ANL)	Higher Superdeformed Band Members in ^{190}Hg
Henry	(LLNL)	Superdeformation in the A~190 Lead Nuclei
Lee	(ORNL)	Lifetimes of the Superdeformed Band in ^{192}Hg
Session 2		**SUPERDEFORMATION IN NUCLEI (II)** **Chairperson: R.M. Diamond**
Nazarewicz	(Warsaw/ORNL)	New Vistas in Superdeformation
Atac	(NBI)	Decay out of a Superdeformed Band in ^{143}Eu
Galindo	(CRL)	New Features in the Spectrum of ^{152} Dy at Very High Spin
Session 3		**FUSION AND HIGH ANGULAR MOMENTUM RESIDUES** **Chairperson: B. Herskind**
Leigh	(ANU)	Fusion and Fission
Beausang	(Liverpool)	Entrance Channel Effects in ^{152}Dy
Lauritzen	(ANL)	Entrance Channel Effects in ^{191}Hg
Session 4		**NUCLEI AT HIGH TEMPERATURE** **Chairperson: C.J. Lister**
Leoni	(NBI)	Spin Dependence of Rotational Damping
Farris	(Rutgers)	Statistical Gamma Transitions in ^{174}Hf
Bracco	(Milano)	The Giant Dipole Resonance and the Shape of Hot Nuclei
Goodman	(Tulane)	Statistical Orientation Fluctuation

WEDNESDAY, MAY 20

Session 5 — **NUCLEAR SPECTROSCOPY (I)**
Chairperson: R. Wadsworth

Hagemann	(GSI)	Delayed Band Crossing in ^{163}Tm
Dracoulis	(ANU)	Spectroscopy of Very Light Hf and W Nuclei
Hubel	(Bonn)	Collective Oblate Bands in Pb Nuclei
Johnson	(ORNL)	Transition Probabilities up to I=36^{+} in Light Yb Nuclei

Session 6 — **PHYSICS OF HIGH SPIN NUCLEAR STATES**
Chairperson: R. Janssens

Wyss	(Stockholm/ ORNL)	Physics of High Spin Nuclear States
Walker	(Surrey)	High K Structures in ^{180}W
Baktash	(ORNL)	Low-Spin Identical Bands

Session 7 — **NUCLEAR THEORY (I)**
Chairperson: P. Semmes

Matsuyanagi	(Kyoto)	Octupole Correlations in Superdeformed States
Frauendorf	(ISP)	Tilted Cranking Classification of Multi-band Spectra

Session 8 — **SUPERDEFORMATION IN NUCLEI (III)**
Chairperson: J. Sharpey-Schafer

Strahle	(Julich)	Search for Superdeformation in ^{144,145}Gd
Lucas	(Sarclay)	Search for Low Spin Superdeformed States
Mullins	(McMaster)	Superdeformation in ^{142}Sm
Liang	(ANL)	Identical Superdeformed Bands in ^{192}Tl

THURSDAY, MAY 21

Session 9		**NUCLEAR SPECTROSCOPY (II)** **Chairperson: J. Cizewski**
Paul	(Liverpool)	Non-collective Oblate States in Odd-A Iodine Isotopes
Piiparinen	(Jyvaskyla)	Two to One-phonon E3 Transitions in ^{148}Gd
Oliveira	(LBL)	High Spin Spectroscopy of ^{168}Yb
Garg	(Notre Dame)	Electromagnetic Properties of ^{181}Ir
Session 10		**NUCLEAR THEORY (II)** **Chairperson: I. Hamamoto**
Skalski	(Warsaw)	Exotic Nuclear Shapes in Atomic Nuclei
Khanna	(Alberta)	Symmetry Breaking in Nuclei
Shimizu	(Kyushu)	Nuclear Wobbing Motion
Session 11		**EXOTIC SHAPES, CLUSTERS ETC.** **Chairperson: C. Broude**
Haxton	(Washington)	Large Basis Shell Model Calculations
Betts	(ANL)	Clusters and Superdeformation
Session 12		**SYSTEMATION OF NUCLEAR STATES** **Chairperson: D. Fossan**
Tabor	(Florida)	Triaxiality and Alternating M1 Strength
Hamamoto	(Lund)	Low-energy E1 Transitions and Octupole Softness
Janzen	(CRL/ McMaster)	Intruder Bands in $^{109-115}$Sb
Riedinger	(Tennessee)	Tracking Intruder States

WORKSHOP ON LARGE GAMMA-RAY DETECTOR ARRAYS

Chalk River Laboratories

FRIDAY, MAY 22

Session 1		**STATUS OF NEW INSTRUMENTS (I)** **Chairperson: D. Cline**
Nolan	(Liverpool)	Status of EUROGAM
Duchene	(Strasbourg)	Simulation Calculations and Tests of Eurogam Detectors
Session 2		**STATUS OF NEW INSTRUMENTS (II)** **Chairperson: R. Lieder**
Stephens	(LBL)	Status of GAMMASPHERE
Carpenter	(ANL)	Development of GAMMASPHERE Prototypes
Session 4		**STATUS OF NEW INSTRUMENTS (III)** **Chairperson: M.A. Deleplanque-Stephens**
Schwalm	(Heidelberg)	Status of Euroball
Bazzacco	(Padova)	The GA.SP Spectrometer
Session 4		**NEW INSTRUMENTS: FREE DISCUSSION** **Chairperson: J. Simpson**
Contributions to be called		
Hannachi	(Strasbourg)	Study of Superdeformed Band in ^{194}Pb with Eurogam
Martini	(ORNL)	Present and Future Ge Detectors

SATURDAY, MAY 23

Session 5 — **DATA ANALYSIS**
Chairperson: I. Yang Lee

Flibotte	(Strasbourg)	Multi-dimensional Analysis of High Resolution γ-ray Data
Radford	(CRL)	Interactive Graphical Analysis for Level Schemes
Brinkman	(LLNL)	Lossless One-Pass Sorting Algorithm and Feature Evaluation
Kuehner	(McMaster)	Three-Dimensional γ-ray Data Set Analysis

Session 6 — **PARTICLE DETECTION SCHEMES**
Chairperson: D. Balamuth

Wuosmaa	(ANL)	The Argonne Si-strip Detector Array
Nyberg	(Uppsala)	Correction for Doppler Broadening
Ball	(CRL)	The 8π Miniball
Ibbotson	(Rochester)	Octupole Deformation in ^{148}Nd

Session 7 — **FAR VISIONS (I)**
Chairperson: T.L. Khoo

Garrett	(ORNL)	High Spin Physics with Radioactive Beams
Herskind	(NBI)	High Fold Studies in the Continuum

Session 8 — **FAR VISIONS (II)**
Chairperson: G. Dracoulis

Selected and Invited Short Comments

Dudek	(Strasbourg)	Future Development of Nuclear Structure Physics

TOUR OF TASCC

Registered Participants

Y.A. Akovali
Bldg. 6000 Mail Stop 6371
Oak Ridge National Laboratory
P.O. Box 2008
Oak Ridge TN
U.S.A. 37831-6371

H.R. Andrews
Chalk River Laboratories
Chalk River Ontario
Canada K0J 1J0

A. Atac
Tandem Accelerator Lab
Niels Bohr Institute
Riso, DK-4000 Roskilde
Denmark

F. Azaiez
Institute de Physique
Nucléaire - ORSAY
B.P. No. 1
91406 ORSAY
France

C. Baktash
Oak Ridge National Laboratory
P.O. Box 2008
Bldg. 6000, MS-6-371
Oak Ridge Tennessee
U.S.A. 37831-6371

D.P. Balamuth
Physics Dept.
University of Pennsysvania
Philadelphia PA
U.S.A. 19104-6396

G.C. Ball
Chalk River Laboratories
Chalk River Ontario
Canada K0J 1J0

D. Bazzacco
I.N.F.N.
Sez. Padova
Via Marzolo 8
I-35131 Padova
Italy

I. Bearden
Purdue University
Argonne National Laboratory
Argonne IL
U.S.A. 60439

C. Beausang
Dept. of Physics
Oliver Lodge Laboratory
University of Liverpool
U.K. L69 3BX

J.A. Becker
Lawrence Livermore National Laboratory
L-280
Livermore CA
U.S.A. 94501

L. Bernstein
Dept. of Physics
Rutgers University
Piscataway N.J.
U.S.A.

R.R. Betts
Physics Division
Argonne National Laboratory
9700 South Cass Avenue
Argonne IL
U.S.A. 60439

M.P. Carpenter
Physics Division
Argonne National Laboratory
9700 South Cass Avenue
Argonne IL
U.S.A. 60439-4843

A. Bracco
University of Milano
Institute of Physics
Via Celoria 16
I-20133 Milano
Italy

P. Chowdhury
Yale University
Wright Nuclear Structure Lab
P.O. Box 6666, 272 Whitney Avenue
New Haven CT
U.S.A. 06511

M.J. Brinkman
Lawrence Livermore National Laboratory
P.O. Box 808
L-280
Livermore CA
U.S.A. 94550

J.A. Cizewski
Dept. of Physics
Rutgers University
P.O. Box 849
Piscataway NJ
U.S.A. 08855-0849

C.M. Broude
Physics Department
Weizmann Institute of Science
Rehovot
Israel 76100

R. Clark
Physics Department
York University
Heslington
York
U.K. Y01 5DD

J. Burde
Lawrence Berkeley Laboratory
70A-3307 Nuclear Science Division
University of California
1 Cyclotron Road
Berkeley California
U.S.A. 94720

D. Cline
Nuclear Structure
Research Laboratory
University of Rochester
Rochester New York
U.S.A. 14627

J.A. Cameron
Tandem Accelerator Laboratory
McMaster University
GS 105
HAMILTON Ontario
Canada L8S 4K1

M. Cromaz
Physics Department
University of Toronto
60 George Street
Toronto Ontario
Canada M5S 1A7

D.M. Cullen
Oak Ridge National Laboratory
P.O. Box 2008
Oak Ridge Tennessee
U.S.A. 37831-6371

G.D. Dracoulis
Department of Nuclear Physics
Australian National University
GPO Box 4
Canberra ACT 2601
Australia

J. De Graaf
Physics Department
University of Toronto
60 St. George Street
Toronto Ontario
Canada M5S 1A7

T.E. Drake
Physics Department
University of Toronto
60 St. George Street
TORONTO Ontario
Canada M5S 1A7

J.P. Delaroche
Service PTN
C.E. Bruyerès-le-Châtel BP12
91680 Bruyères-le-Châtel
France

M. Drigert
Idaho National Eng Lab
EG&G Idaho, Inc
P.O. Box 1625
Idaho Falls, ID
U.S.A. 83415-2211

M.A. Deleplanque
NSD 70A-3307
Lawrence Berkeley Laboratory
1 Cyclotron Road
Berkeley California
U.S.A. 94720

G. Duchêne
Group R.S.N.
Centre de Recherches Nucléaire
67037 STRASBOURG Cedex
France

R.M. Diamond
Nuclear Science Division
Lawrence Berkeley Laboratory
Berkeley CA
U.S.A. 94720

J. Dudek
Physique Theorique
Centre de Recherches Nucléaires
B.P. 20
67037 STRASBOURG Cedex
France

J. Doering
Dept. of Physics
Florida State University
Tallahassee Florida
U.S.A. 32306

P. Fallon
Oliver Lodge Laboratory
University of Liverpool
Liverpool L69 3BX
U.K.

S. Flibotte
Centre de Recherches Nucléaires
23, rue du Loess
67037 STRASBOURG Cedex
France

D.B. Fossan
Physics Dept.
SUNY-Stony Brook
Stony-Brook NY
U.S.A. 11794

S.G. Frauendorf
Zentralinstitut für
Kernforschung
FZ Rossendorf
0-8054 Dresden
Germany

A. Galindo-Uribarri
Chalk River Laboratories
Chalk River Ontario
Canada K0J 1J0

U. Garg
Physics Dept.
University of Notre Dame
Notre Dame IN
U.S.A. 46556

J. Garrett
Physics Division
M.S. 6371
Oak Ridge National Laboratory
Oak Ridge, TN
U.S.A. 37831

J.S. Geiger
Chalk River Laboratories
Chalk River Ontario
Canada K0J 1J0

J. Gerl
G.S.I.
Postfach 110552
Planckstr. 1
D-6100 Darmstadt 11
Germany

A.L. Goodman
Physics Dept.
Tulane University
New Orleans LA
U.S.A. 70118

G.S. Hackman
McMaster University
1280 Main St. W.
Hamilton Ontario
Canada L8S 4M1

G.B. Hagemann
Tandem Accelerator Laboratory
Niels Bohr Institute
4000 Roskilde
Denmark

I. Hamamoto-Kuroda
Dept. of Mathematical Physics
Lund Institute of Technology
P.O. Box 118
Lund S-221 00
Sweden

F. Hannachi
Centre de Spectrometrie Nucléaire
Batiment 108-104
91405
ORSAY
France

J.C. Hardy
TASCC Division
Physical Sciences
Chalk River Laboratories
Chalk River Ontario
Canada K0J 1J0

R.W. Hoff
Lawrence Livermore National Laboratory
P.O. Box 808
Mail Stop L-234
Livermore CA
U.S.A. 94550

W. Haxton
Department of Physics
FM15
University of Washington
Seattle Washington
U.S.A. 98195

H.C. Hubel
Universitat Bonn
Institut Fur Strahlen-und Kernphysik
Nussallee 14-16
D-5300 Bonn 1
Germany

A. Hayes
Chalk River Laboratories
Chalk River Ontario
Canada K0J 1J0

R. Ibbotson
Nuclear Structure
Research Laboratory
University of Rochester
Rochester New York
U.S.A. 14627

J. Heese
Hahn-Meitner-Institut
Berlin GmbH
Glienicker Str. 100
W-1000 Berlin 39
Germany

R. Janssens
Physics Division
Argonne National Laboratory
9706 South Cass Avenue
Argonne Illinois
U.S.A. 60439

E. Henry
L-234
Lawrence Livermore National Laboratory
P.O. Box 808
Livermore, CA
U.S.A. 94550

V. Janzen
Chalk River Laboratories
Chalk River Ontario
Canada K0J 1J0

B. Herskind
Tandem Accelerator Laboratory
Niels Bohr Institute
4000 Roskilde
Denmark

H. Jin
Dept. of Physics
University of Tennessee
Knoxville TN
U.S.A. 37996-1200

J. Johansson
G.S.B. 105
McMaster University
Hamilton Ontario
Canada L8S 4K1

N. Johnson
Physics Division
Oak Ridge National Laboratory
P.O. Box 2008
Bldg. 6000 MS 6-371
Oak Ridge Tennessee
U.S.A. 37831

F. Khanna
University of Alberta
Edmonton AB
Canada

T.L. Khoo
Physics Division
Argonne National Laboratory
9700 South Cass Avenue
Argonne IL
U.S.A. 60439

H. Kluge
Hahn Meitner Institute
Gleinicker Str 100
W-1000 Berlin 39
Germany

A. Korichi
Institut de Physique
Nucléaire - ORSAY
B.P. No. 1
91406 ORSAY
France

W. Korten
Tandem Accelerator Laboratory
Niels Bohr Institute
Riso
DK4000
Roskilde
Denmark

J.A. Kuehner
Department of Physics
McMaster University
GSB 105
Main Street West
Hamilton Ontario
Canada L8S 4K1

A.C. Kuhnert
Lawrence Livermore National Laboratory
P.O. Box 808
L-280
Livermore CA
U.S.A. 94550

D. LaFosse
Physics Dept.
SUNY
Stony Brook
N.Y.
U.S.A. 11794

T. Lauritsen
Physics Division
Argonne National Laboratory
Building 203
Argonne IL
U.S.A. 60439-4843

M. Lederer
Lawrence Berkeley Laboratory
Berkeley CA
U.S.A.

I.Y. Lee
Oak Ridge National Laboratory
P.O. Box 2008
Bldg. 6000 MS 6-371
Oak Ridge TN
U.S.A. 37831-6371

J.R. Leigh
Department of Nuclear Physics
Research School of Physical Sciences
Australian National University
GPO Box 4
Canberra ACT 2601
Australia

S. Leoni
Universite di Milano
Fisica del Nuclear
Via Celoria 16
Milano
Italy

Y. Liang
Physics Division
Argonne National Laboratory
9700 South Cass Ave.
Argonne IL
U.S.A. 60439

R.M. Lieder
Institut für Kernphysik
Kernforschungsanlage
D-5170 Julich
Germany

C.J. Lister
Yale University
272 Whitney Avenue
New Haven CT
U.S.A. 06511

G. LoBianco
Dipartimento di Fisica
Universita di Milano
Milano 20133
Italy

R. Lucas
DAPNIA SPHN
CE Saclay
91191 Gif sur Yvette
France

W. Ma
Department of Physics & Astronomy
Vanderbilt University
P.O. Box 1807
Station B
Nashville TN
U.S.A. 37235

R. MacLeod
Chalk River Laboratories
Chalk River Ontario
Canada K0J 1J0

M. Maier
Lawrence Berkeley Laboratory
B29
1 Cyclotron Road
Berkeley California
U.S.A. 94720

D.R. Manatt
Nuclear Chemistry Division
L-231
Lawrence Livermore National Laboratory
7000 East Avenue
P.O. Box 808
Livermore California
U.S.A. 94550

E.R. Marshalek
Dept. of Physics
University of Notre Dame
Notre Dame Indiana
U.S.A. 46556

M. Martini
EG&G ORTEC
100 Midland Road
Oak Ridge TN
U.S.A. 37830

K. Matsuyanagi
Dept. of Physics
Kyoto University
Kitashirakawa
Kyoto 606
Japan

W.C. McHarris
Dept. of Chemistry
Michigan State University
East Lansing MI
U.S.A. 48824

V. Meot
DAPNIA SPHN
CE Saclay
91191 Gif sur Yvette
France

B. Million
Sezione di Milano
Instituto Nazionale
di Fisica Nucleare
Via Celoria 16
Milano 20133
Italy

B. Moftah
TINA BOX
TRIUMF
4004 Wesbrook Mall
Vancouver B.C.
Canada V6T 2A3

S. Mullins
Tandem Accelerator Lab
GSB-105
McMaster University
Main Street West
Hamilton Ontario
Canada L8S 4M1

W. Nazarewicz
Joint Institute for Heavy Ion Research
ORNL, P.O. Box 2008
Bldg. 6008, MS 6374
Oak Ridge TN
U.S.A. 37831

P.J. Nolan
Oliver Lodge Laboratory
University of Liverpool
Oxford Street
Liverpool L69 3BX
U.K.

A. Nordlund
Department of Physics
University of Lund
Solvegatan 14
S-223 62 LUND
Sweden

J. Nyberg
The Svedberg Laboratory
Box 533
S-75121 Uppsala
Sweden

J.R. Oliveira
Nuclear Science Division
Lawrence Berkeley Laboratory
70A-3307
1 Cyclotron Road
Berkeley CA
U.S.A. 94720

A. Omar
Physics Department
McMaster University
Hamilton Ontario
Canada L8S 4M1

E.S. Paul
Oliver Lodge Lab
University of Liverpool
Oxford St.
P.O. Box 147
Liverpool
U.K. L69 3BX

L. Persson
Physics and Astronomy Dept
McMaster University
1280 Main Street West
Hamilton Ontario
Canada L8S 4M1

M. Piiparinen
Tandem Accelerator Lab
Niels Bohr Institute
DK-4000 Roskilde
Denmark

S. Pilotte
Physics Department
University of Ottawa
150 Louis Pasteur
Ottawa Ontario
Canada K1N 6N5

K.R. Pohl
University of Pennsylvania
209 S. 33rd Street
Philadelphia PA
U.S.A. 19104

D. Popescu
I.P.N. Orsay
Campus Orsay Bat. 104
91406 Orsay Cedex
France

M.G. Porquet
Centre de Spect. Nucl.
et de Spect. de Masse
Batiment 104
B.P. 1
F-91405 ORSAY
France

D. Prevost
McMaster University
ABB 241
Main Street West
Hamilton Ontario
Canada L8S 4M1

D. Radford
Chalk River Laboratories
Chalk River Ontario
Canada K0J 1J0

P. Regan
University of Pennsylvania
Physics Department
209 S. 33 SE
Philadelphia PA
U.S.A. 19106

W. Reviol
Physics Department
University of Notre Dame
Notre Dame Indiana
U.S.A. 46556

H. Schnare
Physics Department
SUNY
Stonybrook NY
U.S.A.

L. Riedinger
Physics Department
University of Tennessee
Knoxville Tennessee
U.S.A. 37996-1200

D. Schwalm
Physikalisches Institut
der Universität Heidelberg
D-6900 Heidelberg 1
Philosophenweg 12
Heidelberg
Germany

J.L. Rodriguez
c/o Jim Waddington
G.S.B. 105
McMaster University
Hamilton Ontario
Canada L8S 4K1

P.B. Semmes
Dept. of Physics
Tennessee Technological University
Box 5051
Cookeville TN
U.S.A. 38505

D.J. Rowe
Department of Physics
University of Toronto
60 St. George Street
Toronto Ontario
Canada M5S 1A7

J.F. Sharpey-Schafer
The Oliver Lodge Laboratory
University of Liverpool
Liverpool
U.K. L69 3BX

J.X. Saladin
Department of Physics
University of Pittsburg
Pittsburg PA
U.S.A. 15260

Y.R. Shimizu
Dept. of Physics
Kyushu University
Fukuoka 812
Japan

D. Santos
ISN
53, Av. Des Martyrs
38026 Grenoble Cedex
France

J.J. Simpson
SERC
Daresbury Laboratory
Daresbury Warrington
U.K. WA44AD

N.C. Schmeing
Chalk River Laboratories
Chalk River Ontario
Canada K0J 1P0

B. Singh
Tandem Accelerator Lab
GSB-105
McMaster University
Main Street West
Hamilton Ontario
L8S 4K1

J. Skalski
Physique Nucleaire
Universite Libre de Bruxelles
CP 229
Boulevard du Triomphe
B1050 Bruxelles
Belgium

G. Sletten
Niels Bohr Institute
Tandem Accelerator Laboratory
4000 Roskilde
Denmark

F.S. Stephens
Lawrence Berkeley Laboratory
Nuclear Science Division
Berkeley CA
U.S.A. 94720

M.A. Stoyer
Lawrence Livermore National Laboratory
Livermore CA
U.S.A. 94550

A. Stuchbery
Dept. of Nuclear Physics
Australian National University
GPO Box 4
Canberra ACT 2601
Australia

K. Sugawara-Tanabe
Department of Physics
School of Social Information Studies
Otsuma Women's University
Tama-shi
Tokyo 206
Japan

S.L. Tabor
Physics Dept.
Florida State University
Tallahassee Florida
U.S.A. 32306

K. Tanabe
Dept. of Physics
Saitama University
Urawa 338
Japan

H. Timmers
Physics Dept.
SUNY
Stony Brook New York
U.S.A. 11794-3800

E. Vigezzi
INFN Milano
via Celoria 16
Italy

J.C. Waddington
Dept. of Physics
McMaster University
GSB 105 Main Street West
HAMILTON Ontario
Canada L8S 4K1

R. Wadsworth
Department of Physics
University of York
York Y01 5DD
U.K.

P.M. Walker
Department of Physics
University of Surrey
Guildford GU2 5XH Surrey
U.K.

D. Ward
Chalk River Laboratories
Chalk River Ontario
Canada K0J 1J0

M. Waring
Physics Department
SUNY-SB
Stony Brook New York
U.S.A. 11794

T.R. Werner
Department of Physics
Institute of Theoretical Physics
Warsaw University
00-681 Warsaw
ul. Hoza 69
Poland

D. Winchell
Physics Division
Oak Ridge National Laboratory
P.O. Box 2008
Bldg. 6000
Oak Ridge Tennessee
U.S.A. 37831-637

H.-J. Wollersheim
Gesellschaft für
Schwerionenforschung mbH
Planckstraase 1
Postfach 110 552
D-6100 Darmstadt 11
Germany

C.Y. Wu
Nuclear Structure
Research Laboratory
The University of Rochester
Rochester N.Y.
U.S.A. 14627

A.H. Wuosmaa
Physics Division
Argonne National Laboratory
9700 S. Cass Avenue
Argonne IL
U.S.A. 60439

R. Wyss
Joint Institute for Heavy Ion Research
Oak Ridge National Laboratory
P.O. Box 2008
Bldg. 6008 MS 6374
Oak Ridge Tennessee
U.S.A. 37831

W. Younes
Dept. of Physics
Rutgers University
Piscataway N.J.
U.S.A. 08855-0849

C.-H. Yu
Dept. of Physics
University of Tennessee
Knoxville TN
U.S.A. 37996-1200

G. Zwartz
Physics Department
University of Toronto
60 St. George Street
Toronto Ontario
Canada M5S 1A7